MOLECULAR DYNAMICS SIMULATIONS OF MACHINING, MATERIALS TESTING, AND TRIBOLOGY AT THE ATOMIC SCALE

By

NAGASUBRAMANIYAN CHANDRASEKARAN

Bachelor of Science
University of Madras
Madras, India
1995

Master of Science
Oklahoma State University
Stillwater, Oklahoma
1997

Submitted to the faculty of the
Graduate College of the
Oklahoma State University
in partial fulfillment of
the requirements for
the degree of
DOCTOR OF PHILOSOPHY
May, 2001

MOLECULAR DYNAMICS SIMULATIONS

OF MACHINING, MATERIALS TESTING,

AND TRIBOLOGY AT THE

ATOMIC SCALE

Thesis Approved:

Thesis Adviser

Dean of the Graduate College

ACKNOWLEDGEMENTS

"Annaiyum Thanthaiyum Munneri Theivam"

This verse in Tamil language emphasizes that 'mother' and 'father' are the first and foremost God for any individual. There are not enough words to express my sincere gratitude to my parent's for their love, support, understanding, and encouragement at times of difficulty. Special thanks are due to my sister (Dr. Padmapriya Darsini) for her inspiration, motivation, love, and guidance.

"Guru Brahma Guru Vishnu Guru Devo Maheshwaraha

Guru Saakshat Para Brahma Tasmai Sree Gurave Namaha"

This Sanskrit sloka says that 'Guru' is the representative of Brahma (creator), Vishnu (protector), and Shiva (destructor). He creates, sustains knowledge, and destroys the weeds of ignorance. I salute such a Guru, my advisor, Prof. Komanduri. I thank him for his constant support, motivation, guidance, and above all, his friendship.

I would like to extend my appreciation to Prof. Raff for introducing me to the concept of Molecular Dynamics simulation technique. During the course of the project, he has spent numerous hours in listening to our problems and providing the solutions. This thesis would have been impossible without his constant guidance. I would also like to thank Prof. Price for guiding me with some problems related to the orientation studies and his constructive criticisms regarding the thesis manuscript. My sincere appreciation

extends to Dr. Lu for his invaluable guidance and motivation. The discussions with Dr. Lu in his class on 'Continuum Mechanics' provided valuable insight in designing and solving some of the nano-scale problems discussed in this thesis.

I wish to express my gratitude to Dr. Ali Noori Khajavi for his assistance and encouragement during the early stages of the project. Thanks are also due to Prof. Hou, David Stokes, Robert Stewart, Sony Verghese, P. R. Mukund and other research members of our group at AMPMRL for assistance with the simulation, support, motivation, and helpful conversations. I also wish to thank my friends and family members for their support.

This project was supported by grants from the Manufacturing Processes and Machines Program (DMI-9523551) of the Division of Design, Manufacture, and Industrial Innovation (DMII) and the Tribology and Surface Engineering Program (CMS-9414610) of the Division of Civil and Mechanical Structures of the National Science Foundation. Thanks are due to Drs. P. Rajurkar, Delcie Durham, B. M. Kramer, L. Martin-Vega of DMII and J. Larsen Basse of the Tribology and Surface Engineering Program for their interest in and support of this investigation.

Finally, I would like to thank the Department of Mechanical and Aerospace Engineering for providing the opportunity to pursue my Ph.D. at Oklahoma State University.

TABLE OF CONTENTS

Chapter **Page**

LIST OF TABLES

LIST OF FIGURES

CHAPTER 1

INTRODUCTION

1.1. INTRODUCTION TO ULTRAPRECISION MACHIING (UPM)

Today, a wide range of materials, including, metals (e.g., copper, aluminum), semiconductors (e.g., silicon, germanium), ceramics (e.g., silicon nitride, alumina), and glasses (e.g., fused silica, soda-lime) of different compositions and metallurgical structures are being used in a variety of precision mechanical, electronic, magnetic, and optical applications. Precision aluminum discs are used extensively for disc drives in the computer industry and precision aluminum mirrors for numerous optical applications, including lasers. Silicon is widely used in the semiconductor electronic industries and for optical components and high resolution thermal imaging systems. Silicon as well as germanium continue to be the most widely used materials operating in the middle infra-red wavelength regions because of their unique properties (Zhong and Venkatesh, 1994). Ceramics find a wide range of applications, including, mechanical, electromagnetic, optical, thermal, biochemical, and energy oriented fields (Komanduri et al., 1997). Glasses are widely used as optical components in infra-red systems, beam deflectors in

synchrotron radiation equipment, lenses, mirrors, and recently even as hard disc substrates.

Precision engineering applications (as listed above) require the components to be finished to a high degree of surface finish (in the order of a few nanometers) and form accuracy with minimum surface and subsurface damage or good surface integrity. The damage includes micro cracks, structural changes, extensive plastic deformation, and residual stresses (Komanduri, 1996). This is enabled by material removal at very small depths of cut (a few μm to nm) associated with significantly low loads (a few μN to nN) on a highly rigid, precise, and environmentally controlled ultraprecision machine tool. Material removal at such small depths of cut is enabled by such precision processes as ultraprecision machining (UPM), ultraprecision grinding (UPG), and polishing. Since, the material removal in UPM is only on the order of a few nanometers it is also termed as nanometric cutting. This technology was pioneered by Bryan (1979) of the Lawerence Livermore National Laboratory (LLNL) and subsequently for UPG by McKeown (1987) of the Cranfield Unit of Precision Engineering (CUPE).

Taniguchi (1983) defines UPM as those processes or machines by which the highest possible dimensional accuracy can be achieved at a given point in time. Figure 1.1 referred to as the "Taniguchi Curve" shows the progress of machining accuracy with time. Taniguchi's predictions in 1983 are in line with today's achievable machining accuracy (1 nm). As the technology advances, the geometric accuracy and finish requirement of parts increases. From Figure 1.1, it can be seen that what was considered

to be the highest achievable accuracy 10 years ago is considered as normal machining today. Taniguchi (1983) predicted that in the early years of the 21st century the attainable processing accuracy will reach the sub-nanometer level and it appears that today's UPM will be tomorrow's conventional machining. Such improvements in machining accuracy is made possible by constant improvements in the machine tool technology and a better understanding of the associated material removal mechanisms.

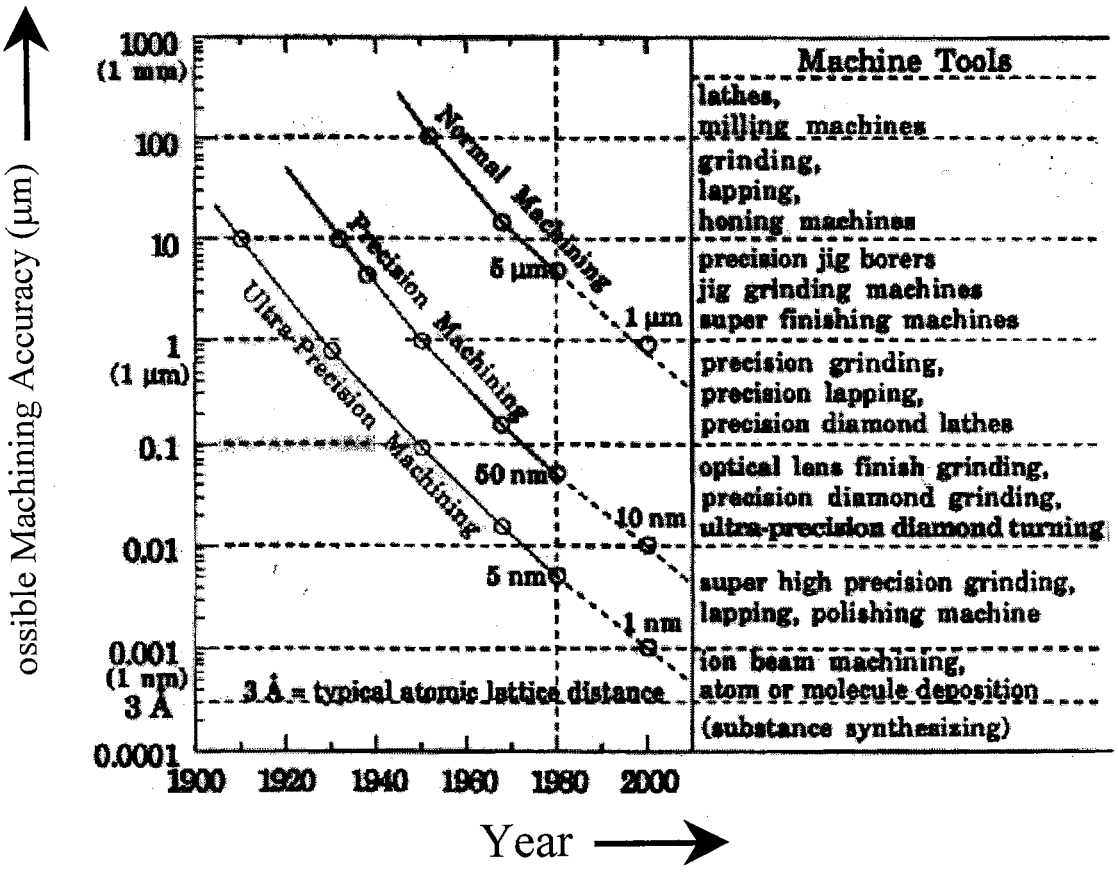

Figure 1.1. Progress of machining accuracy achieved with respect to time during the 20th century (after Taniguchi, 1983)

1.2. INTRODUCTION TO MICRO SYSTEM TECHNOLOGY (MST)

Micro system technology (MST) involves fabrication of micro- and nano-components used in micro-electro-mechanical systems (MEMS) and micro-opto-electro-mechanical systems (MOEMS) (Bhushan, 1995). This requires material processing at the nano and the atomic regime. Figure 1.2 shows a micromotor manufactured by thin film processing technology. The motor has a height of 100 μm and the clearance between the axle and the rotor is only 500 nm.

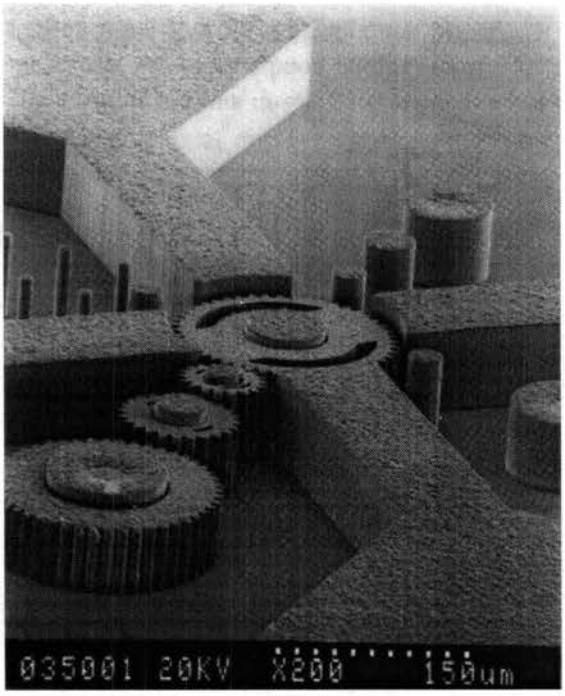

Figure 1.2. Magnetic micromotor with gear transmission manufactured By thin film processing techniques (after Fatikow and Rembold, 1997)

The micro- and the nano-structural elements are produced by such special processes that they are almost devoid of defects. These ideal materials (with no or very few defects and strength close to their theoretical values) are going to be the norm rather than

exception for nanocomponents in MEMS and MOEMS. Hence, an investigation of the strength and deformation behavior of defect-free materials at the nanometer level greatly facilitates the analysis of nano-components. For example, the performance of a (nano) transistor might be compromised by a shift of voltage if the residual stress in the deposited film is high. This may even cause cracking or warping of the thin film itself.

With the development of the micro system technology emerged another important field known today as nanotribology or tribology at the atomic scale. Tribology aims at reducing friction and wear between the contacting surfaces. Nanotribology aims to achieve a similar goal under low loads and small mass conditions. In conventional tribology, sliding surfaces sustain the applied load due to the pressure exerted by moving parts and the loads are usually large enough to cause plastic deformation of the surface. However, in micromechanical systems due to low mass and load conditions, the surface deformation is mostly restricted to elastic deformation.

In nanotribology, the physical and chemical properties of the contacting surface are a primary factor. For example, the use of Atomic Force Microscope (AFM) to characterize various surfaces and also to manufacture nanocomponents can result in significant friction, wear, and adhesion between the contacting bodies. The surface interactions between the tip and the nanocoatings can cause damage to the coatings during characterization, which can impair the performance characteristics of the coatings. Figure 1.3 shows the adhesive forces in ambient between various kinds of tips and

surfaces collected by several researchers over a period of time (Kohono and Hyodo, 1974; Miyamoto et al., 1990; Hamada and Kaneko, 1990).

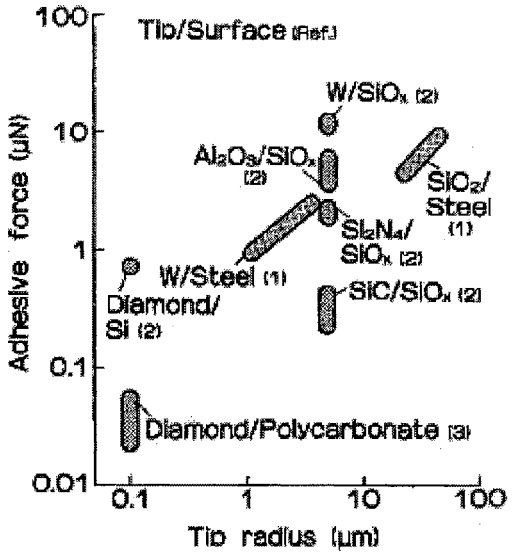

Figure 1.3. Adhesive forces between tips and surfaces (after Kaneko, 1991)

It can be seen from Figure 1.3 that depending on the contacting surfaces the adhesive forces can be significant (10 nN to 1 μN) even with an extremely sharp tip (0.1 μm). In ambient air the surface of a solid is usually covered with a thin oxide/liquid layer. Under such conditions, it is possible to have weak Van der Waals forces between the contacting surfaces or have solid-solid adsorption and liquid surface tension type adhesion forces as shown in Figure 1.4 (Kaneko, 1991). Kaneko points out that the mass of a micromotor rotor with 100 μm diameter and 10 μm thickness (10 nN) is less than the adhesive forces of only one contact point with a 0.1 μm tip. The bearing of the micromotor in such cases cannot support the load and will fail in use. Consequently, nanotribology (friction, wear, and adhesion in the nano-regime) and its effects on MOEMS need to be understood in detail.

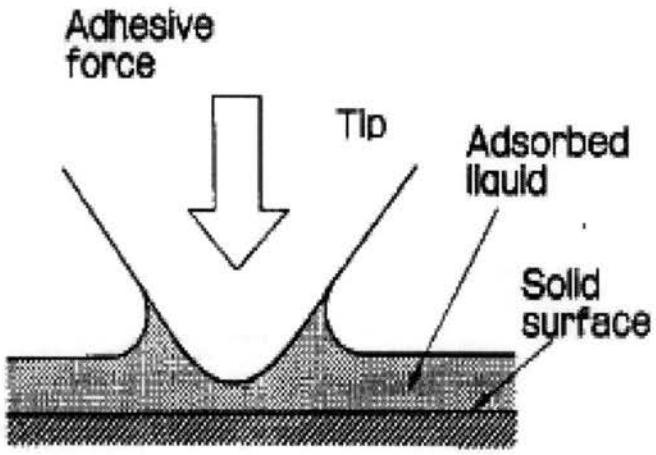

Figure 1.4. Adhesive force with liquid surface tension (Kaneko, 1991)

1.3. THEORETICAL ANALYSIS OF MATERIALS PROCESSING

While significant advances have been made in the field of UPM since their first use in manufacturing precision components, further advances in this field is somewhat limited by the technological difficulties and lack of a better understanding of the material removal mechanisms at the nanometer regime. Machine tool builders are constantly improving the process accuracy by building more accurate machines (see Komanduri et al., 1997 for details on UPM machine tools). However, other factors affecting the quality of the finished surface in nanometric cutting are yet to be investigated in detail.

To formulate the mechanism of chip formation and the mode of material removal in UPM based on experimental work, the chips generated and the machined surface, need to be correlated with the machining process. When the depth of the material removed is of the order of a few atomic layers, it becomes somewhat difficult and time consuming to

study the mechanism of material removal and the associated surface and subsurface damage. In order to study the effect of cutting conditions and tool geometry, expensive single crystal diamond tools have to be used. Consequently, the cost of experimentation can be significant and such experiments can only be conducted in those laboratories, which are equipped with expensive environmentally controlled ultraprecision machine tools.

A similar situation exists in the MST field. With increasing miniaturization and precision requirements, accurate determination of properties and performance characteristics of various materials and nanocomponents becomes extremely important, time consuming, expensive, and increasingly difficult. Consequently, it is necessary to investigate alternate methods, such as analytical and computational models, to improve our understanding of the mechanical and chemical behavior of materials under various loading conditions. Of course, for the validation of the theoretical results and models, need exists for experimental verification and this can be done either with the results reported in the literature or by selective experimentation.

The mechanics of chip formation has been investigated extensively by many researchers since the mid nineteenth century (Komanduri, 1993). Merchant (1944) studied the mechanics of continuous chip formation (or Type II chip) process for both orthogonal (2-D) and oblique (3-D) cutting. Merchant, in this classical work, pointed out that the chip should be considered as an independent body held in static equilibrium by two equal, opposite, and collinear forces, one acting at the shear plane and the other at the tool face. Merchant's model laid the foundation for much of the research that followed.

For example, Lee and Shaffer (1951) and Hill (1954) used the plasticity approach to metal cutting, and Oxley and his associates (1989) applied the slip-line field solutions to the metal cutting problem. Shaw (1950) and later von Turkovich (1963, 1967, and 1970) brought the dislocation approach to metal cutting. These analytical models have contributed significantly towards a better understanding of the metal cutting process.

Since the 1970's, continuum mechanics [Finite Difference Method (FDM) and Finite Element Method (FEM)] approaches have been applied to metal cutting problems (Tay et al., 1974; Usui and Shirakashi, 1982; Iwata et al., 1984; Strenkowski and Carroll, 1985; Benton and Kramer, 1988; Young and Chou, 1994; Li et al., 1995, to name a few), mostly to microcutting. Here, the material is considered as a continuum neglecting the microconstituents (chemistry, crystal structure, lattice spacing, grain size, and second phase particles, to name a few) of the workmaterial or the tool, except through some physical properties. In this approach, the workmaterial under study is divided into elements with the corner of the elements referred to as nodes. However, the number of nodes and the distance between the nodes were selected arbitrarily, a coarser mesh for processing speed and a finer mesh for details. This analysis, along with other methods, has contributed towards a better understanding of the mechanics of the cutting process from one vintage point, namely, computational.

1.4. INTRODUCTION TO MOLECULAR DYNAMICS (MD) SIMULATION

While the continuum mechanics approach provides a better understanding of the process mechanics at the micro-regime, it cannot be implemented to simulate the process

at the nano and the atomic regime (as it assumes the material to be a continuum). An alternative is to use the Molecular Dynamics (MD) simulation technique. MD simulation techniques give higher temporal and spatial resolution of the cutting process than is possible by continuum mechanics approach. MD also provides a clear picture at the atomistic level that gives a microscopic view, which is a compromise between analytical models and results from experiments. Unlike in FEM, nodes and the distance between nodes are selected in MD simulation not on an arbitrary basis but on more fundamental units of the material, namely, centers of the atoms as the nodes and interatomic distances as distance between nodes. Thus, the process can be reduced to its fundamental units for analysis. However, since a large number of atoms constitute any common material, one needs to consider the interactions of several thousands of atoms in MD simulation of machining. Since, such a simulation requires large mainframe computers with significant memory and fast processing times, this research was mostly confined to the U.S. national laboratories (chiefly LLNL) until recently. Today, the availability of fast workstations with significant memory has enabled MD simulation research to be conducted in this area at academic institutions.

MD simulations were initiated in the late 1950's at the Lawerence Radiation Laboratory (LRL) by Alder and Wainwright (1959, 1960) in the field of equilibrium and non-equilibrium statistical mechanics. The application of MD simulation to nanometric cutting and nanoindentation process was first introduced at LLNL in the late 1980's and early 1990's (Hoover, 1986; Hoover et al., 1989 and 1990; Belak et al., 1990, 1991, 1993, and 1994). Pioneering work in the field of MD simulation of indentation was conducted

by Landman et al. (1989-1992, 1996) at Georgia Institute of Technology followed by Belak and his colleagues at the LLNL. Since then, MD simulation has been applied to a wide range of fields including crystal growth, low-pressure diamond synthesis, laser interactions, nanometric cutting (Ikawa et al., 1991; Shimada et al., 1992-1995; Inamura et al., 1991-1994; Maekawa and Itoh, 1995; Chandrasekaran et al., 1998), indentation (Harrison et al., 1991; Tomagnini et al., 1993; Rentsch and Inasaki, 1994; Brenner et al., 1996; Yan and Komvopoulos, 1998), tribology (Hirano and Shinjo, 1990; Harrison et al., 1992; Kim and Suh, 1994; Buldum and Ciraci, 1998), materials testing (Selinger et al., 1991, 1993; Lynden-Bell, 1994-1995; Doyama, 1995; Kitamura et al., 1997; Heino et al., 1998a, 1998b), to name a few. The literature pertaining to MD simulations of nanometric cutting, indentation, materials testing, and tribology are of interest here and will be covered in the appropriate sections. While a sound foundation has been laid for MD simulation of materials processing at the nano and the atomic regime, many of the challenging problems are yet to be investigated in detail. An attempt is made to address some of these problems in this investigation.

1.5.THESIS OUTLINE

In Chapter 1, a general introduction to UPM discussing its unique features, advantages, and limitations has been provided. The progression of machining accuracy with time has been discussed, suggesting the possibility of the depths of cut approaching atomic dimensions in the near future, as predicted by Taniguchi (1983). This emphasized the importance of understanding the material removal mechanisms in the nano-regime and the atomic-regime. The field MST also requires a better understanding of the material

behavior under various processing conditions in the atomic regime. The alternatives to experimental techniques are presented and it is suggested that MD simulation is a powerful tool to investigate the process mechanics at the nano and the atomic regime.

In Chapter 2, the theory of MD simulation is presented in detail, including, the methodology of MD simulation, simulation models used in this study, potential energy equations, and computation of atomic trajectories. The advantages and limitations of MD simulation technique are also outlined. The scope of the current investigation and the approach are briefly outlined in Chapter 3.

Uniaxial tension simulations and nanoindentation simulations were conducted to measure the mechanical properties and understand the deformation behavior of different materials (both, ductile and brittle) under load. Chapter 4 discusses in detail the results of the uniaxial tension and nanoindentation MD simulations. Chapters 5 through 8 present the results of MD simulations of nanometric cutting addressing various issues, including tool geometry (Chapter 5), effect of crystal orientation and cutting direction (Chapter 6), exit failure in nanometric cutting (Chapter 7), and nanometric cutting of silicon (Chapter 8), respectively. In Chapter 9, the results of the MD simulations conducted to understand the nature of atomic scale friction and the frictional anisotropy are presented in detail. Chapter 10 lists the conclusions based on the current study and some suggestions for future research.

CHAPTER 2

PRINCIPLES OF MOLECULAR DYNAMICS (MD) SIMULATION

2.1. INTRODUCTION

There are two approaches to describe the atomic motion. In the first approach, known as MD simulation, the subject of this investigation, the position of each atom is obtained by solving the Newtonian equations of motion with a high time resolution (on the order of 10^{-15} sec or 1 fs), which is smaller than the period of vibratory motion of atoms. While the atoms vibrate around their minimum energy positions, the minimum energy positions themselves move as cutting progresses. This method, however, is computationally intense. For example, a physical phenomenon lasting 1 sec has to be simulated in 10^{-15} sec time steps. In the other approach, called Molecular Statics (MS) analysis, only the positions at which the resultant force on each atom is zero are followed. Of course, the atoms in this case follow the positions of minimum potential energy. It is thus a quasi static method. Only a few hundred atoms have to be considered in this simulation and, hence, should result in significantly shorter computational times. However, the interpretation and analysis of data by this simulation are rather complex.

MD simulations can be likened to the dynamic response of numerous nonlinear spring (potential or force) - mass (atoms or positive ions) systems under an applied load, velocity, or displacement conditions. From this point of view, MD simulation is similar to other analyses that mechanical engineers routinely conduct, such as the investigation of vibrations of a mechanical system, wherein a series of springless masses and massless springs are connected and the response of the system is investigated under a given external load (Komanduri and Raff, 1999).

The problem of simulating any molecular process, be it a chemical reaction, or, a physical process, such as machining, involves four essential parts, namely, (1) the formulation and integration of classical equations of motion for the atoms comprising the system of interest, (2) the choice of the molecular model, (3) the development of a sufficiently accurate potential energy function for the system, and (4) the simulation of the experimental conditions. If the results of the simulations are to be useful in the interpretation and prediction of experimental data, appropriate care must be exercised in each of these steps. In the following, each of these aspects are briefly considered.

2.2. METHODOLOGY OF MD SIMULATION

2.2.1. MD Simulation Model

Figure 2.1 is a general schematic of the model used in the MD simulation of nanometric cutting. The workmaterial is divided into three different zones, names the moving zone (P-zone), the peripheral zone (Q-zone), and the boundary zone (B-zone) (Riley et al., 1988). A layer of boundary and peripheral atoms are placed on all sides of the crystal except on the surface of the workmaterial where the chip is being formed. The motion of the atoms in the moving zone is determined solely by the forces produced by

the interaction potential and the direct solution of classical Hamiltonian equations of motion. These atoms are also termed as the Newtonian atoms. The motions of the peripheral atoms are also calculated from the solution of Hamiltonian equations, but modified by the presence of velocity reset functions associated with each atom in the peripheral zone. The boundary atoms are fixed in position and serve to reduce the edge effects and maintain proper symmetry of the lattice. It should be noted that the model shown in Figure 2.1 is a general schematic, and different models are used in this study based on the problem under investigation and will be presented in the respective sections. In the following, a detailed discussion on the function of the three zones are explained in detail for a better appreciation of the model.

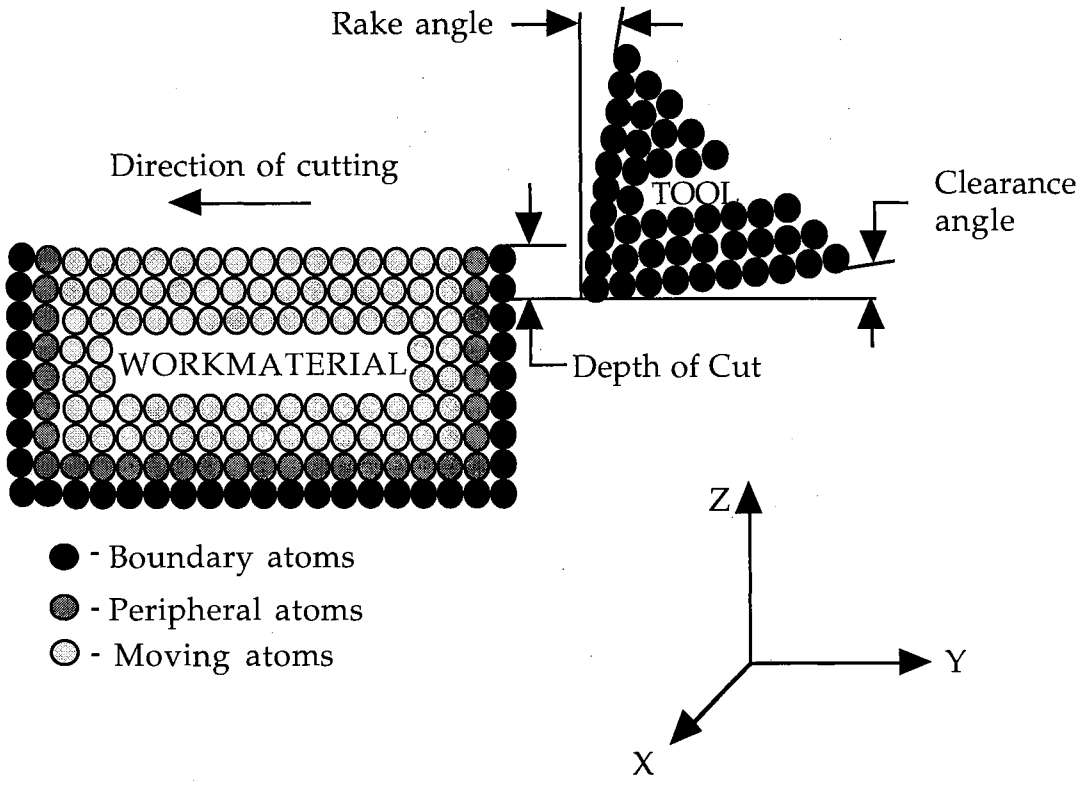

Figure 2.1. Schematic of the MD simulation model

2.2.1.1. Newtonian Atoms

In MD simulations, numerical integration of the classical Newtonian equations of motion is carried out for an ensemble of atoms (Newtonian atoms) (Goldstein, 1965). Thus,

$$m\frac{d^2\vec{r}_i}{dt^2} = \frac{d(m\vec{v}_i)}{dt} = \frac{d\vec{p}_i}{dt} = \vec{F}_i \tag{2.1}$$

where m is the mass of the atom and $\vec{r}_i$, $\vec{v}_i$, $\vec{p}_i$, and $\vec{F}_i$ are the position, velocity, momentum, and force exerted on atom i, respectively. The output of the simulation are trajectories of atoms as well as their velocities. The force, $\vec{F}_i$, on atom i, is the gradient of the potential energy function with respect to the position of atom i, i.e.

$$\vec{F}_i = -\nabla_i V\left(\vec{r}_1, \vec{r}_2, \ldots, \vec{r}_{N_a}\right) \tag{2.2}$$

where V is the potential energy function, N_a is the number of atoms, $\vec{r}_i = x_i\hat{i} + y_i\hat{j} + z_i\hat{k}$ is the position vector of atom i, x_i, y_i, and z_i are the coordinates of atom i, and

$$\nabla_i = \frac{\partial}{\partial x_i}\hat{i} + \frac{\partial}{\partial y_i}\hat{j} + \frac{\partial}{\partial z_i}\hat{k} \tag{2.3}$$

For an appreciation of the time involved in MD simulations, it may be noted that the number of differential equations to be solved is 6N, where N is the total number of atoms considered in the workpiece, which can vary from a few hundred to several thousand atoms. The larger the number the larger the processing time. Generally, 2 to 10 thousand atoms are considered in a simulation. Thus, a 2000 atom model requires integration of 12,000 coupled, first-order differential equations of motion. Considering that the potential energy function is a simple pairwise potential form, the total number of terms in such a potential is given by N(N-1)/2. Thus, for N=2000, some 2 million pairwise terms need to

be calculated each time a derivative is evaluated. Since, four such evaluations must be done for every integration step, some $8x10^6$ evaluations would be required for every trajectory calculation. Consequently, the computation time increases rapidly as the number of atoms considered increases.

2.2.1.2. Peripheral Atoms and Velocity Reset Functions

The plastic energy in the primary shear zone and the frictional energy at the tool-chip interface are converted into heat, which has to be dissipated continuously. In actual machining, much of this heat is carried away by the chip and the lubricant. It is essential that the effects upon the energy transfer within the solid that would be present for an extended lattice model be included in the calculations. This could, of course, be accomplished by using lattice models containing large number of atoms, say, 10^6 atoms or more. Such a procedure, however, is not computationally efficient. The most efficient method for simulating the removal of the heat generated in machining is the use of velocity reset functions. Velocity reset methods have been suggested by Agrawal et al. (1988) and by Riley et al. (1988). The latter of these is the more general in that the procedure permits statistical fluctuations about the equilibrium temperature. Under certain conditions, the method can also be shown to be equivalent to a Langevin procedure.

In the method proposed by Riley et al. (1988), the N lattice atoms are partitioned into three zones as mentioned earlier, namely, the moving zone, the peripheral zone, and the boundary zone (Figure 2.1). The motions of the atoms in the peripheral zone are modified by the presence of velocity reset or thermalization functions associated with each atom in the zone. The cartesian velocity components of each peripheral lattice atoms is reset at periodic time intervals, Δt, using the following algorithm:

$$v_{\alpha i}^{new} = (1-W)^{1/2} v_{\alpha i}^{old} + w^{1/2} V(T,\xi) \qquad (2.4)$$

where $v_{\alpha i}^{old}$ is the α-component (α = x, y, or z) of velocity of lattice atom i resulting from the solution of the Hamiltonian equations of motion and $v_{\alpha i}^{new}$ is the reset α velocity component. w is a parameter that controls the strength of the reset with w=0 corresponding to no reset and w=1 being a complete reset. $V(T,\xi)$ is a randomly chosen velocity from a Maxwell-Boltzmann distribution at temperature T. ξ is a random number whose distribution is uniform on the interval [0,1] that controls the random selection. To obtain Δt, Riley et al. (1988) recommend that Δt be approximately 1/5 of the Debye period of the lattice adapted. This procedure simulates the thermostatic effect of the bulk and guarantees that the equilibrium temperature will approach the desired value, which is 293 K in these calculations. The initial velocity for each of the atoms in the moving and the peripheral zone is chosen as to follow the Maxwell-Boltzmann distribution specific to the initial bulk temperature (293 K).

2.2.1.3. Boundary Atoms

The boundary atoms of the tool and the workpiece are assumed to be unaffected by the cutting process. Consequently, the positions of the boundary atoms with respect to one another will not change during the cutting process. In Figure 2.1, the tool is composed of only boundary atoms which simulates an infinitely hard (non-deformable) tool. This is generally the case where a soft workpiece such as copper or aluminum is machined by a hard tool such as diamond.

Alternately, the tool can be considered deformable by placing Newtonian atoms in the tool that can contact the workmaterial as shown in Figure 2.2. In this case the tool can deform similar to the workmaterial. This will be the case when machining copper workpiece with an iron tool or machining an iron workpiece with a diamond tool. Plastic deformation of the tool, tool wear, chemical interactions between the tool and the workpiece can be studied using this approach. It should be noted that the boundary atoms

do not participate in trajectory calculations. Also, a boundary atom can exert force on a moving atom but not on another boundary atom.

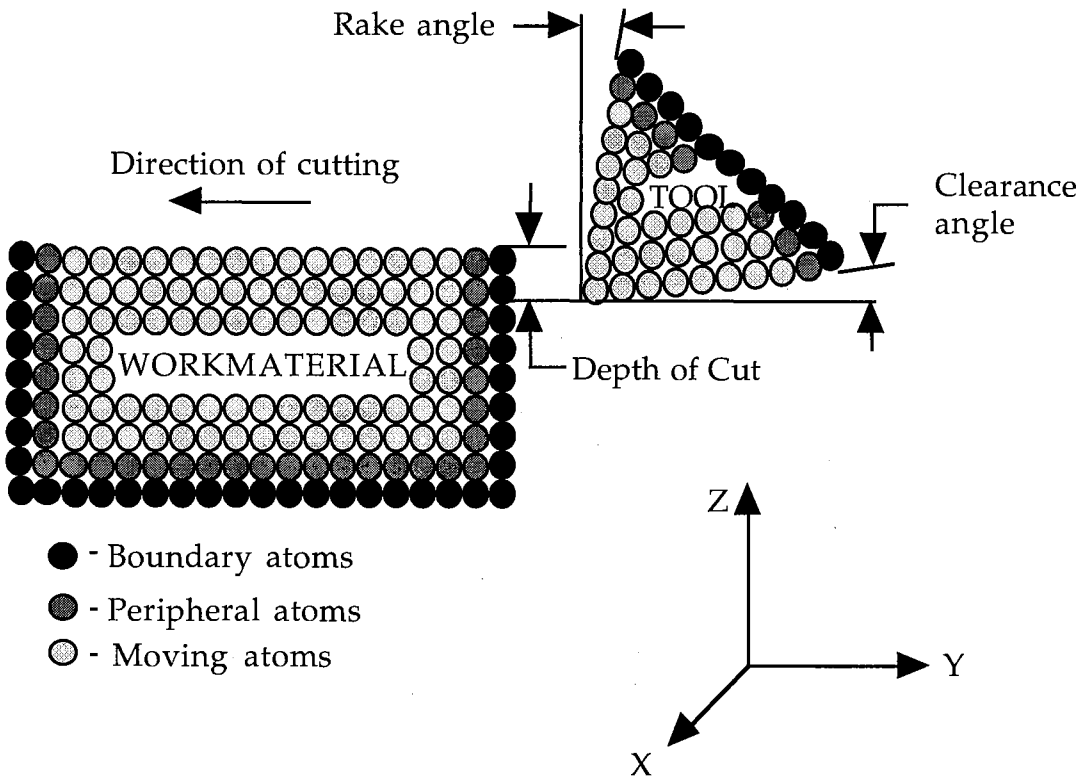

Figure 2.2 Schematic of MD simulation model showing a deformable tool

2.2.2. Computation of the Trajectories Using Numerical Integration

The computation of a trajectory requires numerical integration of the differential equations of motion from the initial state, which for machining would be the state in which the cutting tool is approaching the workpiece but has not touched yet, to some final state, which might be after a layer of material has been removed from the workmaterial. There are a variety of methods available for performing this numerical integration step of which the fourth-order Runge-Kutta procedure is the most frequently

used method because of several advantages (Conte, de Boor, 1972; Ralston, 1962). First, it is self starting in that it is not necessary to know the values of the elements of Y which is a column vector whose elements are the coordinates and their conjugate momenta at times prior to to. Second, the local error in a given integration step is of the order of h^5, where h is the integration time step. The method, therefore, provides good accuracy. Finally, the method is stable and easy to program. Two disadvantages associated with the procedure are: (1) it provides no estimate of the accuracy being achieved during the integration and (2) 24N derivatives must be evaluated in each integration step. In this investigation, this method is used to perform the numerical integration to compute the atomic trajectories.

The first disadvantage is not serious since an estimate of accuracy can be obtained bu monitoring the energy and other constants of the motion during the integration. Experience shows that if these quantities remain constant to four or five significant digits, the accuracy is usually sufficient in most applications. In addition, a step size reduction procedure can be used. In this method, the sensitivity of the final results to h is obtained by repeated integrations with smaller values of h. By empirical determination of the largest value of h for which the final results are essentially independent of h, an appropriate step size can be obtained. Finally, the accuracy of integration can be checked by back integration of a trajectory. In this procedure, after n integration steps, all P_k are replaced with $-P_k$ in Y, where P_k is the momentum conjugate to the coordinate Q_k, which is one of the 3N generalized coordinates needed to define a system of N atoms. The trajectory is then "back-integrated" n steps. The extent of agreement of the final values with the elements of Y in their initial state provides an excellent measure of the integration accuracy.

2.3. POTENTIAL ENERGY (PE) AND INTERATOMIC FORCES

It may be pointed out at the outset that the accuracy of the trajectories of atoms obtained from the MD simulation [based on Eqs. (2.1) and (2.2)] are highly affected by the choice of the appropriate potential energy (PE) function. Hence, selection of an appropriate PE function is a prerequisite. The total energy of the system is the sum of the kinetic energy (KE) and the potential energy (PE). The KE is simple to compute but the PE computation is rather complex as it depends on the position of all interacting atoms. The force acting on each atom is proportional to the first derivative of the potential energy function and the total energy must be carefully monitored during the MD simulation.

2.3.1. Classification of Potential Energy Functions

There are two approaches for the determination of interatomic potentials. The first approach is an *ab initio* method and the second approach uses essentially empirical potentials. In the *ab initio* method, the parameters of the PE function can, in theory, be determined by solving the Schrodinger's wave equation. However, in practice, it is difficult to solve except for very simple systems. For larger systems, empirical PE functions are used that take into account factors, such as covalent bond stretching, bond angle change due to bending, torsions, and non-bonded (Van der Waals and coulomb) interactions (Morse, 1929; Garifalco and Weizer, 1959; Torrens, 1972; Stillinger and Weber, 1985; Biswas and Hamann, 1985; Brenner and Garrison, 1986; Tersoff, 1988; Brenner, 1990; Bolding and Andersen, 1990; Voter, 1996). This is the second and the most commonly used method in which the parameters are determined on the basis of physical properties of the material under consideration. The parameters can be obtained either from experimental studies or using quantum mechanical calculations. The

interatomic potential energy is assumed to be the sum of empirical potentials which depend only on the distance between the atoms.

The empirical potentials are further classified into two-body, three-body, and multibody potentials depending on the unit of atoms on which the potential terms depend. Most of the empirical potential forms comprise an attractive and a repulsive term (discussed in detail below). The attractive force binds the atoms together while the repulsive force prevents them from coalescing.

The term "empirical" in empirical potential may be somewhat misleading as it may not be strictly empirical as the term suggests (Komanduri and Raff, 1999). In fact, these potentials often present a more realistic view of the atomic interactions than the potentials derived exclusively at great efforts from purely theoretical considerations which are themselves often approximate in nature (Torrens, 1972). The empirical potentials are based on simple mathematical expressions for pairwise interaction between two atoms or ions, which may or may not be justified from theory, and which will contain one or more parameters adjusted to the experimental data. The validity of the function as well as the stability of the crystal for a given material are checked for various properties including cohesive energy, Debye temperature, lattice constant, compressibility, and the elastic constants as well as the equation of state. Consequently, these potentials can be considered reasonably valid for simple cubic metals.

2.3.2. Attractive and Repulsive Forces

Figures 2.3 (a) and (b) show the dependence of the attractive, repulsive, and net forces and potential energies, respectively as a function of interatomic distance (r) for two

isolated atoms. By convention, repulsive forces are considered positive while attractive forces are negative.

The magnitude of both, attractive and repulsive forces, increases as the distance between them decreases. The repulsive force increases more rapidly than the attractive force. The curvature of the PE function is mainly determined by the repulsive force, which therefore dictates the elastic behavior of the solid. The length of the bond (r_o) is the center-to-center distance of the bonding atoms. Strong bonds pull the atoms closer and so have smaller bond lengths compared to weak bonds. At r_o, the attractive and repulsive forces exactly balance and the net force is zero. This corresponds to stable equilibrium with a minimum potential energy, the magnitude of which is the bond energy. The cohesive properties of the solid, its melting and vaporization behavior are determined by the magnitude of the maximum binding energy, which is governed by the attractive component of the interatomic force. In the case of metals, higher the bonding energy, the higher the melting temperature and the Young's modulus and lower is the coefficient of thermal expansion. The slope of the force curve at r_o gives the elastic modulus. In general, deep potential wells are more symmetrical about the equilibrium position r_o than shallow wells.

2.3.3. Cut-Off Distance

The potential energy functions generally extend over a modest range of pair separations though at vanishingly small energy levels. By neglecting the interatomic interactions beyond a cut-off point, a significant reduction in the computational time with minor loss in accuracy can be achieved. Truncation of the potential to a cut-off point also results in a small truncation of the force curve.

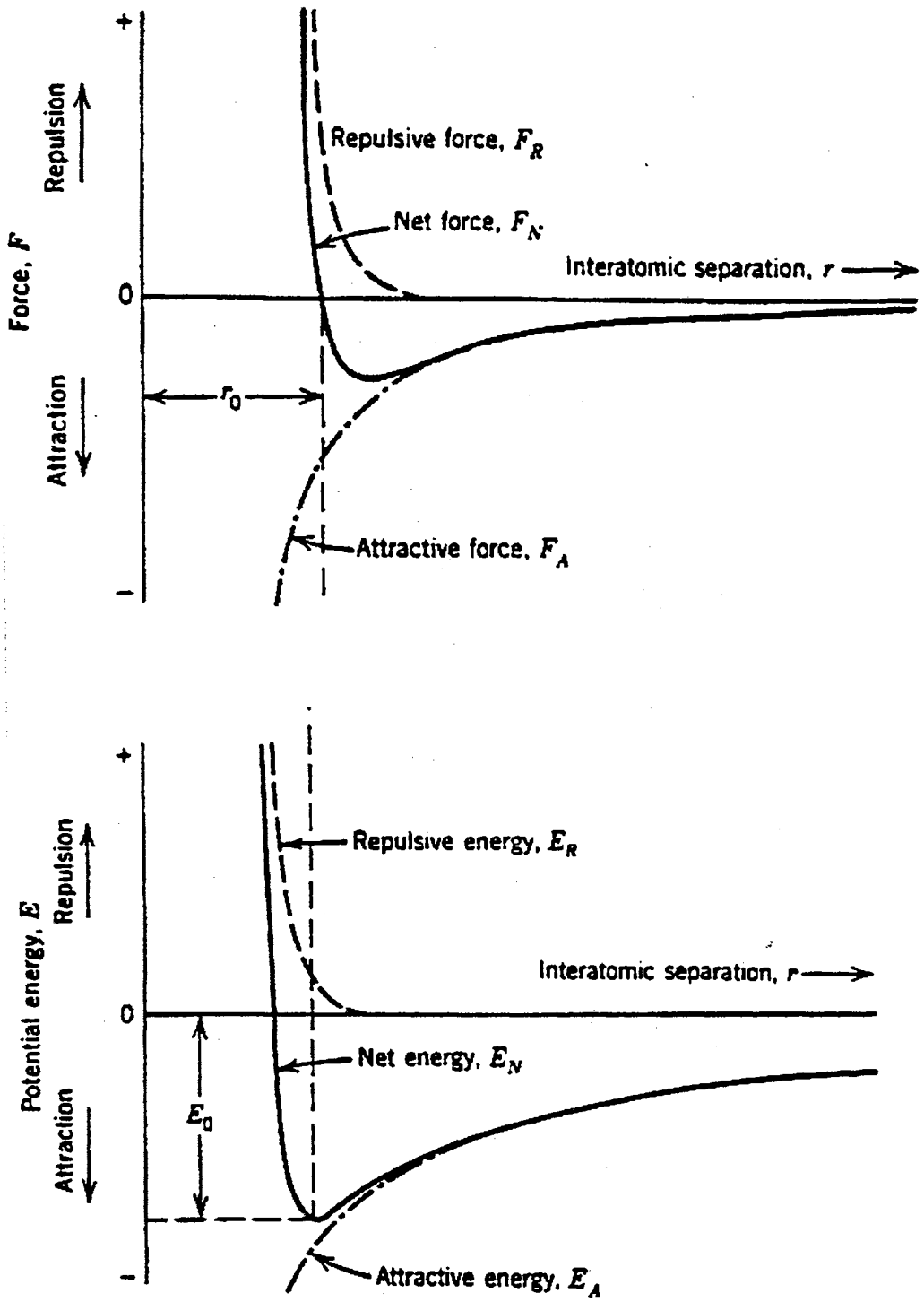

Figure 2.3 (a) and (b) Variation of the attractive, repulsive, and net forces as well as attractive, repulsive, and net potential energies as a function of interatomic separation, r between two isolated atoms

The cut-off distance can be of any value of choice but is generally taken as the distance where the value of the potential energy is ~3-5% of the equilibrium potential energy. In this investigation, this value is taken as 4%. Consequently, instead of strictly constant energy, one may find small fluctuations in energy, however, they exert little effect on the values computed for equilibrium properties.

2.3.4. Potential Energy Functions

Several empirical potential energy functions are in use today including the pair potentials, such as Morse potential (Morse, 1929), Lennard-Jones potential (Lennard-Jones, 1925), and Born-Meyer potential (Born and Meyer, 1933) and potentials for complex systems, such as, Embedded atom potential (Daw and Baskes, 1984), Bolding-Andersen potential (Bolding and Andersen, 1990), Brenner Potential (Brenner, 1990), Stillinger-Weber potential (Stillinger and Weber, 1985), and Tersoff potential (Tersoff, 1989). In this study two potentials are used to model metals and covalent systems. Morse potential is used to model metals and interaction forces between the tool and the workmaterial, while the Tersoff potential is used to model silicon, germanium, and diamond. In the following discussion, the Morse potential and the Tersoff potential are presented in detail.

2.3.4.1. Pair Potentials

Pairwise interactions are applicable for many atomistic studies and are used in most of the MD simulations. Pair potentials (Vitek, 1996) can be classified into two basic categories based on their contribution to the total energy. In the first type, the potential determines the total energy of the system under consideration, whereas, the second type determines change in energy when the atomic configuration of the system varies under

constant density conditions. In both cases, the total energy of the system composed of N particles is given by,

$$E_{total} = \frac{1}{2} \sum_{i\pi k=1}^{N} F_{ik}(r_{ik}) + U(\Omega) \tag{2.5}$$

where, F_{ik} is the pair potential, r_{ik} is the separation between atoms i and k, U=0 for first type potentials, and Ω is the average density of the material.

The simplest and the most commonly used form of pair potential is the Morse potential. In the case of metals, such as aluminum and copper, the potential used in the simulations is a pairwise sum of Morse potentials between the lattice atoms of the workmaterial plus a second summation of pairwise Morse potentials between the atoms of the tool and those in the workmaterial i.e.,

$$V_{total} = V_T = \sum_{i=1}^{N_W} \sum_{j>i}^{N_W} V_M^L(r_{ij}) + \sum_{i=1}^{N_W} \sum_{j=1}^{N_T} V_M^{TL}(r_{ij}) \tag{2.6}$$

where r_{ij} is the i-j interparticle distance and

$$V_M^L(r_{ij}) = D_L\left[\exp\{-2\alpha_L(r_{ij}-r_{eL})\} - 2\exp\{-\alpha_L(r_{ij}-r_{eL})\}\right] \quad \text{for } r_{ij} \le r_c, \tag{2.7}$$

$$V_M^L(r_{ij}) = 0 \quad \text{for } r_{ij} > r_c, \tag{2.8}$$

$$V_M^{TL}(r_{ij}) = D_T\left[\exp\{-2\alpha_T(r_{ij}-r_{eT})\} - 2\exp\{-\alpha_T(r_{ij}-r_{eT})\}\right] \quad \text{for } r_{ij} \le r_c, \tag{2.9}$$

$$V_M^{TL}(r_{ij}) = 0 \quad \text{for } r_{ij} > r_c. \tag{2.10}$$

N_W and N_T are the number of lattice atoms in the workmaterial and tool, respectively. The potential parameters for the workmaterial, D_L, α_L, and r_{eL} are adjusted to the measured sublimation enthalpy, Debye temperature, and nearest-neighbor spacings for aluminum. The three parameters for the tool-workmaterial potential, D_T, α_T, and r_{eT} are obtained by standard combining rules with the parameters for the pure materials. The cutoff radius (r_c) is chosen such that the ratio of the potential at the cutoff point to that at equilibrium is less than 4%. It should be noted that there are no potential terms connecting the atoms of the tool with the workmaterial atoms in the boundary zone (Figure 2.1). Consequently, the tool can, in effect, move through the B-zone atoms as if they are not present.

Garifalco and Weizer (1959) calculated Morse parameters using the experimental values for the energy of vaporization, lattice constants, and the compressibility. They computed the equation of state, the elastic constants, and stability conditions using the Morse parameters for both, FCC and BCC cubic metals and found the results to agree well with the experimental results. Table 2.1 gives the Morse potential parameters for the pairwise atomic interactions for some of the cubic metals of interest in this investigation.

2.3.4.2. Effect of Morse Potential Parameters

Figures 2.4 (a) and (b) show the variation of force with interatomic distance for various values of D_L (with α_L and r_{eL} fixed) and α_L-parameters (with D_L and r_{eL} fixed), respectively, used in the Morse potential. As two atoms are pulled apart, the forces between them transform from a short range repulsive to medium range attractive, subsequently, reaching an equilibrium position. Further separation (long range) leads to zero force.

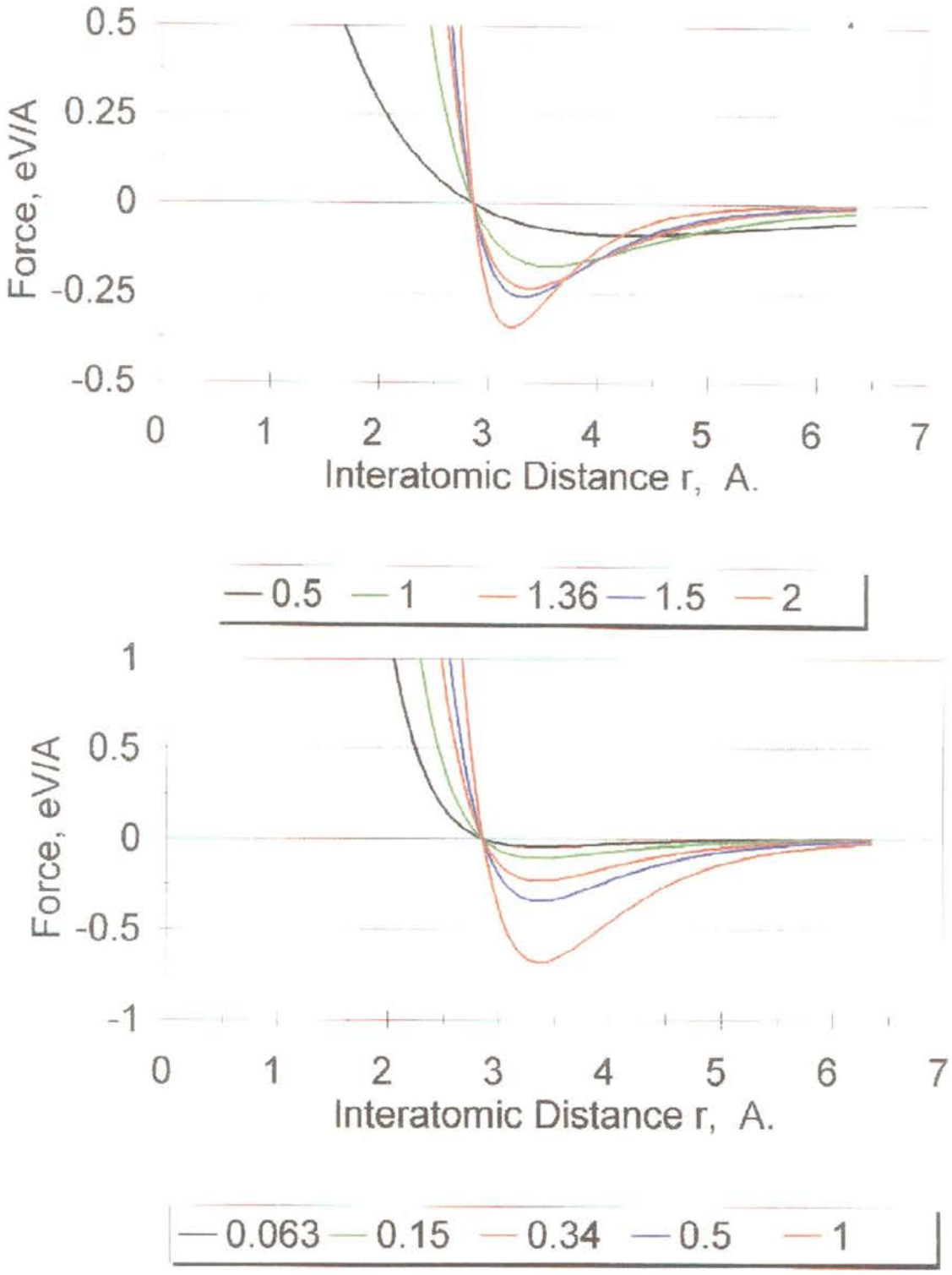

Figures 2.4 (a) and (b) Variation of force with interatomic distance for various values of D (with α and r_o fixed) and α-parameters (with D and r_o fixed), respectively, used in the Morse potential

As the D parameter of the Morse potential increases, the magnitude of the forces required to separate the atoms increases. As the α-parameter of the Morse potential increases, the long range forces tend to approach zero at shorter interatomic distance [Figure 2.4 (b)]. Consequently, the D-parameter and the α-parameter of the Morse potential can be used as an indication of the material property, such as, strength and ductility. Lower the value of the D-parameter and the α-parameter, the more ductile the material is with lower strength and vice-versa.

2.3.4.2. Bond Order Potentials

For the case of covalently bonded materials, such as silicon, germanium, and diamond pairwise Morse potentials are not applicable. In this study Si, Ge, and C are modelled using Tersoff potential (1988). Table 2.2 lists the parameters for Si, Ge, and C used in the Tersoff potential (Tersoff, 1988). As shown in Figure 2.5, assume that j and k are the neighboring atoms of atom i. Let the atomic bond lengths between atoms i and j and atoms i and k be r_{ij} and r_{ik}, respectively. Let the angle between the bonds ij and ik be h_{ijk}.

Table 2.1. Morse potential parameter for various metals (Garifalco and Weizer, 1959)

Metal	αa_o	β	$LX10^{-22}$ (eV)	α (A^{-1})	r_o (A)	D (eV)
Pb	2.921	83.02	7.073	1.1836	3.733	0.2348
Ag	2.788	71.17	10.012	1.369	3.115	0.3323
Ni	2.500	51.78	12.667	1.4199	2.780	0.4205
Cu	2.450	49.11	10.330	1.3588	2.866	0.3429
Al	2.347	44.17	8.144	1.1646	3.253	0.2703
Mo	2.368	88.91	24.197	1.5079	2.976	0.8032
Cr	2.260	75.92	13.297	1.5721	2.754	0.4414
W	2.225	72.19	29.843	1.4116	3.032	0.9906
Fe	1.988	51.97	12.573	1.3885	2.845	0.4174

Table 2.2. Parameters for Si, Ge, and C used in the Tersoff potential (Tersoff, 1989)

Parameter	C	Si	Ge
A (eV)	1.3936×10^3	1.8308×10^3	1.769×10^3
B (eV)	3.467×10^2	4.7118×10^2	4.1923×10^2
λ (A^{-1})	3.4879	2.4799	2.4451
μ (A^{-1})	2.2119	1.7322	1.7047
β	1.5724×10^{-7}	1.1×10^{-6}	9.0166×10^{-7}
n	0.72751	0.78734	0.75627
c	3.8049×10^4	1.0039×10^5	1.0643×10^5
d	4.384	16.217	15.652
h	-0.57058	-0.59825	-0.43884
R (A)	1.8	2.7	2.8
S (A)	2.1	3.0	3.1
	$\chi_{C\text{-}Si} = 0.9976$	$\chi_{Si\text{-}Ge} = 1.00061$	

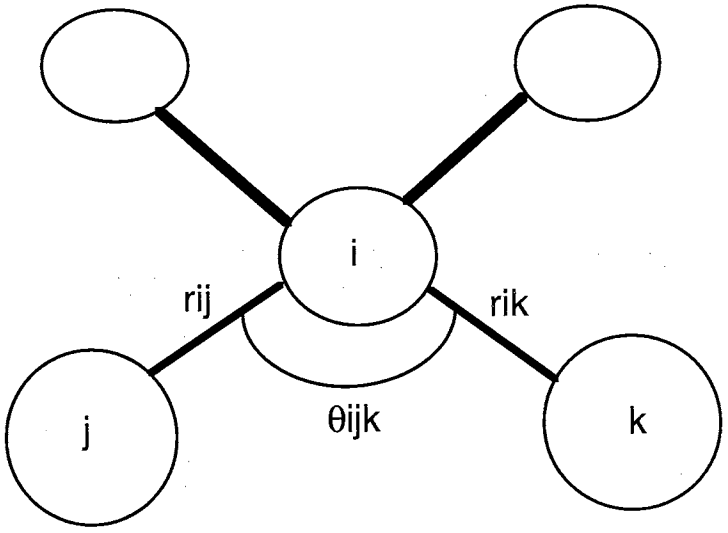

Figure 2.5. Atomic coordination of silicon

Then the total Tersoff energy is expressed as,

$$E = \frac{1}{2} \sum_{i \neq j} W_{ij} \tag{2.11}$$

where, W_{ij} is the bond energy so that summation in the equation is about all the atomic bonds in the control volume. W_{ij} is a function of repulsive pair potential f_R and attractive pair potential f_A. It is represented as,

$$W_{ij} = f_c(r_{ij})\left[f_R(r_{ij}) + b_{ij}\, f_A(r_{ij})\right] \tag{2.12}$$

where, $f_c(r_{ij})$ acts as a cut-off function which determines the number of atoms bonded to an atom i. The terms in the equation for W_{ij} are calculated as below (Tersoff, 1989).

$$f_R(r_{ij}) = A_{ij} \exp(-\lambda_{ij} r_{ij}) \tag{2.13}$$

$$f_A(r_{ij}) = -B_{ij} \exp(-\mu_{ij} r_{ij}) \tag{2.14}$$

$$f_c(r_{ij}) = \begin{cases} 1 & r_{ij} \leq R_{ij} \\ \frac{1}{2} + \frac{1}{2}\cos\left(\frac{r_{ij} - R_{ij}}{S_{ij} - R_{ij}}\pi\right) & R_{ij} \leq r_{ij} \leq S_{ij} \\ 0 & r_{ij} \geq S_{ij} \end{cases} \tag{2.15}$$

$$b_{ij} = \chi_{ij}\left(1 + \beta_i^{n_i}\, \zeta_{ij}^{n_i}\right)^{-\frac{1}{2n_i}} \tag{2.16}$$

$$\zeta_{ij} = \sum_{k \neq i,j} f_c(r_{ik})\, g(\theta_{ijk}) \tag{2.17}$$

$$g(\theta_{ijk}) = 1 + \frac{c_i^2}{d_i^2} - \frac{c_i^2}{d_i^2 + (h_i - \cos\theta_{ijk})^2} \tag{2.18}$$

$$\begin{aligned} \lambda_{ij} &= \frac{1}{2}(\lambda_i + \lambda_j) & \mu_{ij} &= \frac{1}{2}(\mu_i + \mu_j) \\ A_{ij} &= \sqrt{A_i A_j} & B_{ij} &= \sqrt{B_i B_j} \\ R_{ij} &= \sqrt{R_i R_j} & S_{ij} &= \sqrt{S_i S_j} \end{aligned} \tag{2.19}$$

2.4. SOME ASPECTS OF MD SIMULATION OF ATOMIC SCALE PROCESSES

Machining simulations using MD are usually performed at high speeds (100-500 m/s) to simulate the process in reasonable computational time frame. However, nanomachining experiments are performed at much slower cutting rates (10^{-6} to 10^{-9} m/sec), but if conducted at these rates, MD simulations would take extremely long processing times even with the fastest microprocessors. Currently, this is one of the drawbacks of MD simulations. It is possible that the large tool speeds may produce spurious effects. It is also possible that the properties that we are investigating are insensitive to tool speed so that no aphysical effects are produced. Since we cannot execute the MD simulations at experimental speeds of 10^{-6} to 10^{-9} m/sec, these theoretical methods cannot be used to investigate this point. However, it is possible to study nanocutting at tool speeds in the experimental range using Monte Carlo simulation techniques. A comparison of Monte Carlo results with MD simulations will provide a clear picture of the artifacts, if any, that are generated by employing high tool speeds.

The use of pairwise potential in the simulations also merits some comment. Numerous trajectory investigations of complex chemical reactions in the gas phase (Raff and Thompson, 1985) and in the solid state under matrix isolation conditions (Raff, 1998)

have shown that pairwise potentials yield accurate results so long as the process under investigation does not involve the scission and formation of covalent chemical bonds. This has been our experience as well, on a range of nanometric cutting and tribological applications (Komanduri et al., 1998-2001) [see Appendix I]. If the machining process involves covalently bonded materials such as silicon or diamond, more complex potential forms must be employed, such as the Tersoff potential (Tersoff, 1989). Other potential forms can, of course, be used for any system. The modified embedded atom potential (Baskes, 1992) has been shown to simulate a wide range of materials from metals to covalently bonded materials such as silicon and diamond.

It is interesting to point out that some theorists consider MD simulation as not an experimental technique as no measurements are done on real systems, i.e., MD simulations are the outcome of pure calculations. The experimentalists argue that simulations are used, like experiments, to test theories and are prone to problems of reproducibility and statistical errors (Haile, 1992). In the absence of accurate theory of nanometric cutting, in the present investigation, experimental results are looked upon as a guide to arrive at rational conclusions of the MD simulation of machining.

2.5. ADVANTAGES AND CURRENT LIMITATIONS OF MD SIMULATION

2.5.1. Advantages

1. Unlike in FEM, nodes and the distance between nodes in MD simulations are not selected arbitrarily but are chosen on the basis of more fundamental units of the material, namely, centers of the atoms as the nodes and interatomic distances as the distance between nodes.

2. MD techniques offer high temporal and spatial resolution of the atomic scale processes than is possible by any other technique, including the continuum mechanics approach. Hence, any physical phenomenon not accounted for in continuum analysis due to size limitations can be effectively investigated by MD simulation.

3. MD technique can be used effectively to simulate the mechanics of machining, materials testing, and tribology at the atomic scale.

4. MD techniques do not require the use of expensive equipment, such as ultraprecision diamond turning machine, diamond tools, and considerable experimentation to obtain data.

5. In MD simulation, since the process can be reduced to its fundamental units for analysis, MD data should provide the theoretical limits of the machining process.

6. Effects of such variables as edge radius, rake angle, depth of cut, etc. can be easily and effectively varied in MD simulation. The experimental work requires expensive single crystal diamond tools, careful characterization of the tool, and considerable testing on an ultraprecision machine tool which is both time consuming and costly. In MD simulations, one can define these variables and conduct simulations accordingly.

7. It is easy to vary the properties of the workmaterials and the cutting tools in MD simulations.

8. Contrary to general perception that MD simulations can only be done on perfect materials and cannot address real materials, it can be shown that defect structures,

such as grain boundaries, voids, second phase particles, dislocations etc. can be accurately modeled though on a limited scale (Komanduri and Raff, 1999).

9. Tool-work interactions that cannot be studied by FEM techniques, can be addressed in MD simulation. Thus, tool wear, plastic deformation of the tool, and subsurface deformation in the workmaterial can all be studied for some simple systems.

10. Effect of crystal orientation of the workmaterial and cutting direction on the mechanics of chip formation in machining can be investigated systematically. Similar experimental work would be expensive due to very high cost of single crystal materials and specimen preparation and orientation time.

2.5.2. Limitations (and Potential Solutions)

1. Number of atoms considered in the workmaterial is rather small (few hundred to a few thousand atoms) to reduce the computational time. Even then, it is rather time consuming to perform simulations at cutting speeds close to conventional (~ 2 m/s). However, it may be possible to simulate larger number by combining MD simulation with statistical mechanical approaches, such as Monte Carlo simulation.

2. Applied mainly to nano-scale materials processing problems and not to the general area of machining. This, however, is not a limitation especially when investigating the mechanics of nanometric cutting. Experimental results and their trends in conventional machining can be compared to the results in nanometric cutting. An alternative is to combine the MD and the FEM simulation techniques to increase the processing scale to micrometer range.

3. Cutting speeds used in MD simulations are extremely high (100-500 m/s) and somewhat unrealistic to overcome long processing times. This is a natural criticism of MD simulation of machining studies. But with the introduction of dedicated and faster workstations and with the use of parallel processing this speed can perhaps brought down significantly to almost close to the conventional machining speeds.

4. Currently, MD simulations are applied to only simple systems, such as single crystal elements. This will be the case until potential energy surfaces are developed for other material systems of interest. There are, however, a considerable number of applications of nanometric cutting of non-ferrous materials, such as Cu, Al, and semiconductor materials, such as Si and Ge with single crystal diamond tool. Also, one can conduct MD simulations of workmaterials which are alloys whose components are mutually soluble in both liquid and solid states, such as nickel-copper alloys. The distribution of the atoms in the workmaterial will be proportional to the atomic weight percent of the respective elements.

5. MD simulation is applied thus far for mostly pure materials with no defects such as voids, grain boundaries, second phase particles etc. Various aspects of these are addressed recently and it is possible to simulate the presence of grain boundaries, voids etc. Thus defect structure in the workmaterial can be taken into account in MD simulation (Komanduri and Raff, 1999).

6. Simulation time is long (can be from a few days to several weeks). Fortunately, with the availability of reasonably low priced workstations with high computational speeds and considerable memory, simulations can be done in reasonable time scale. Another approach to reducing computational time is developing new MD simulation techniques that can reduce the processing time and memory requirements, such as the

book-keeping technique, linked-list method (Rentsch and Inasaki, 1994), Area Restricted Molecular Dynamics [ARMD] (Maekawa and Itoh, 1995), Length Restricted Molecular Dynamics [LRMD] (Chandrasekaran et al., 1997) etc.

7. MD simulation is applied thus far mostly to quasi 2-D (mostly planar) cutting. This is not a real limitation but a practice by some researchers to reduce the computational time. A quasi 3-D cutting (plane strain) should be conducted even if that involves more processing time as it is more representative of the real process.

8. In most of the studies reported thus far, the tool is generally considered infinitely hard and hence, the tool-work interactions, tool wear, and tool deformation are generally neglected. However, this limitation can be relaxed. One has to develop interface parameters for the potential function to consider tool-work interactions.

CHAPTER 3

PROBLEM STATEMENT

In this investigation, MD simulation technique is used to obtain a better understanding of the material behavior (both, ductile and brittle) under various loading conditions. Machining, materials testing, and tribological problems at the atomic scale are investigated in detail. The objectives of the proposed investigation are briefly outlined below*.

1. Tension and indentation techniques are used extensively to measure the properties and behavior of various materials. In this investigation, MD simulations of uniaxial tension and nanoindentation are conducted on various materials (metals and semiconductors) to understand their deformation behavior under load and to measure their properties. The effect of material property, loading rate, indenter geometry, and indentation depth are investigated in detail.

---

* - The results reported in this report have been published in various technical journals. A list of publications resulting from the current investigation is given in Appendix I.

2. Conduct nanometric cutting experiments on ductile (aluminum and copper) and brittle materials (silicon and germanium) under various cutting conditions. The following problems related to nanometric cutting are investigated in detail.
    - Effect of cutting conditions, such as depth of cut, width of cut, tool geometry (both, rake angle and tool edge radius), crystal orientation and cutting direction, and workmaterial properties (ductile versus brittle) on the mode of material removal.
    - Effect of process variables (listed above) on the variation of cutting forces, force ratio, specific energy, and subsurface deformation.
    - Compare the mechanism of material removal in nanometric cutting and the variation of forces and specific energy with the experimental and simulation results reported in the literature.

3. Significant discrepancy exists between the results reported in the literature on the magnitude of friction coefficient at nano/atomic regime and on the frictional anisotropy. Friction coefficients varying from very low (~0.01) to extremely high (~20) have been reported in the literature. An attempt is made to understand the nature of atomic scale friction and the frictional anisotropy at atomic scale. The magnitude of friction coefficient at the atomic regime is also investigated in detail.

CHAPTER 4

MD SIMULATIONS OF NANO MATERIALS TESTING [a, b, c]

4.1. INTRODUCTION

Investigation of the strength and the deformation behavior of defect-free materials at the nanometer level are essential for the analysis of nano-components used in micro-electro-mechanical systems (MEMS) and micro-opto-electro-mechanical systems (MOEMS). Generally, the material properties of nano-components are determined using nanoindentation tests at extremely light loads in the range of nanonewtons (Pethica et al., 1983). While tensile tests are most common in determining the mechanical properties at macrolevel, such tests at the nanoscale are extremely difficult, if not impossible, to conduct. The two main issues concerning the measurement of mechanical properties of MEMS and MOEMS components are: (1) manufacturing microscale test specimens and (2) performing direct measurements on the microcomponents in a way representing the actual stress situation under which they operate.

---

a - R. Komanduri, N. Chandrasekaran, L. M. Raff, "MD Simulations of Uniaxial Tension," accepted for publication in J. Mat. Sci., 2001

b - R. Komanduri, N. Chandrasekaran, L. M. Raff, "Nano-Tensile Testing of Semiconducting Materials for MEMS Applications," submitted for publication

c - R. Komanduri, N. Chandrasekaran, L. M. Raff, "MD Simulation of Nanoindentation of Silicon," submitted for publication

Most of the problems of testing microsamples for MEMS could be avoided if the entire system including the load actuator is made on a chip. However, such integration is not simple due to the force-output requirement on the actuator. Many of the microactuators require fabrication processes that are complex and expensive. It is also difficult to calibrate the microactuator, as the force it delivers to the specimen should be known accurately. Thus, the MEMS testing techniques, while providing many important basic data, are not adequate for the accurate measurement of the desired information. Even though, the fracture stress of real crystals is based on their defect density, the ultimate strength of the material depends on the way defect-free crystals would deform and fail (Lynden-Bell, 1992). Consequently, it is necessary to determine the strengths of defect free crystals, which is made possible by MD simulation studies. In this investigation, the MD simulation process is employed to study the behavior of various single crystal materials [both, metals (Al, Cu, Ni, Cr, Fe, and W) and semiconductors (Si and Ge)] under different loading conditions (tension and nanoindentation).

4.2. UNIAXIAL TENSILE TESTING

4.2.1. Literature Review

MacMillan and Kelly (1972) conducted MD simulations of uniaxial tension on NaCl crystals using a simple, two-body, central force Born-Meyer potential. Marked anisotropy in the ideal tensile strength, with a pronounced minimum for the <100> plane was found. This is consistent with the observed cleavage on this plane. Also, the maximum strain the crystal can withstand before failure depended on the direction of the applied strain and whether the unit cell dimensions perpendicular to the stress direction are allowed to relax or not. Parinello and Rahman (1981) introduced a new Lagrangian formulation to perform MD simulations on systems under external stress. Using this

method, they applied uniaxial stress to a FCC cubic lattice (nickel) with periodic boundary conditions at 350 K. Under uniaxial compression, they suggest a transformation in the crystal structure from FCC to HCP. The maximum tensile strength under uniaxial tension was reported to be $11x10^{10}$ dyne/cm^2 is reported.

Selinger et al. (1991) investigated the statistical thermodynamics of stretched 2-D Lennard-Jones type perfect crystals. They report an increase in stress to a critical value after which the crystal became unstable and failed. The failure was attributed to the growth of defects caused by thermal fluctuations. It was suggested that a change to the stable state due to the thermal fluctuations is possible only when the applied stress is very close to the critical stress value. Selinger et al. (1993) investigated failure of a 3-D FCC metal (Pt) using a hybrid MD/ Monte Carlo computation technique that allowed changes in both the shape and volume of the periodic boundary condition. Under low temperature and slow loading conditions, a crystal-crystal phase transition is reported to precede the crystal failure. As the stretching force was increased, they observed the extension to increase steadily followed by a sudden jump to a longer extension. The crystal was then reported to stretch continuously in a steady manner until it broke. The authors attribute the sudden jump to a phase change undergone by the crystal as a result of the imposed stress. The phase change was reported to take place in order to enable the crystal to relieve the imposed stress. At higher temperatures, direct failure of the system due to stress-induced melting was reported.

Lynden-Bell (1994, 1995) conducted MD/Monte Carlo simulations of uniaxial tension at various temperatures ($0.04T_m$ - $0.7T_m$, where T_m is the bulk melting temperature of the material) on platinum, gold, rhodium, and silver. Failure of the crystals was reported to be due to void formation and their growth to nanocracks. At low temperatures, the stress was reported to increase to a maximum after which a series of

structural rearrangements of the crystal accompanied by a decrease in the stress magnitude was reported. Highly ductile metals, such as platinum/gold, were reported to develop local regions of disorder first, in comparison to slip between planes of atoms relative to each other observed with not highly ductile metals, such as rhodium/silver. At temperatures above half the melting point, all the metals were reported to be disordered before failure by void formation. A liquid like, highly disordered region was said to exist in the fracture region. This occurs when the free energies of the ordered and disordered states are equal. It appears that an investigation of the tensile behavior at various temperatures would require consideration of both short range as well as long range order in the material. Thus, the potential function used should incorporate many-body terms to represent the behavior of the metal in bulk.

Rentsch and Inasaki (1995) conducted MD simulations of uniaxial tension of silicon to verify the material representation of silicon in fracture. They reported a linear increase in the stress-strain relation followed by a sudden break down to zero. They also reported anisotropic deformation of silicon. The Young's modulus and the specific surface energy of silicon were found to be 171 GPa and 0.393 J/m^2, respectively.

Doyama (1995) conducted MD simulations of tension on iron and copper single crystals with free boundaries. The iron and copper specimens were prepared with a notch and pulled in the [111] and [001] directions, respectively. They suggest that the notch is normally a source of dislocations due to stress concentration. They observed no perfect dislocations in their simulations. With decreasing notch thickness, the effect of the crack was reported to decrease although interaction still exists across the notch. The initial stage of deformation was found to be due to dislocations followed by crossage between dislocations on different slip planes in the middle stage resulting in work hardening, with the final stage consisting of many dislocations and inhomogeneous deformation. Studies

of crack propagation, dynamic instability, and subsequent failure by MD simulations of tension have been reported by other researchers (Sieradzki et al., 1988; Abraham et al., 1994; Zhou et al., 1997).

Kitamura et al. (1997) conducted atomic simulations of tension on a nanoscopic wire, film, and a bulk nickel lattice without defects. To investigate the effect of constraint of transverse deformation on the fracture process, simulations for the bulk were conducted under two conditions: (1) free transverse stress condition and (2) full constraint condition. During the fracture process, the wire and the film were reported to exhibit multiple slip with the neck formation after a strain of 1.0. Concentrated shear deformation with the localization of slip in the necking region was reported to result in ductile fracture. However, with the bulk specimen, they reported absence of necking by the slip even at a strain of 1.0. The transformation was reported to be induced by the tensile strain. In the case of tension experiments with free transverse stress conditions, i.e. without the constraint of transverse deformation, yielding was reported to be brought about by the crystallographic slip on the (111) planes at about a strain of 0.1. The yield stress in tension was found to be ~ 15-20 GPa and very little difference in strength was reported between the wire, the film, and the bulk. Multiple slip, even after yielding of the crystal and significant plastic deformation, was reported to cause ductile shear fracture. In the simulations with constraint of transverse deformation, the yield stress was reported to reach 40 GPa. No plastic strain was generated. This is attributed to the restriction of dislocation glide. Cleavage cracks were observed and found to bring about brittle fracture and hence a change in the fracture mode.

Heino et al. (1998a) conducted MD simulations of tension and shear on copper for [100][010], [01-1][011], and [-1-12][111] orientations. The differences between the calculated and experimental tensile and shear moduli were reported to be in the range of

2-6% and 3-15% respectively. This difference was attributed to the effect of boundary conditions. With a free boundary condition, plastic deformation by slip on the {111} planes was reported. An increase in the strength with decreasing system size and a decrease with increasing disorder was also found. The computed failure strain was 8.5%. In the study of crack propagation, generation of microvoids and crack propagation as a result of coalescing of microvoids was observed.

Heino et al. (1998b) conducted MD simulations of tensile loading (periodic as well as free boundaries) on copper with various types of defects, namely, point defects, grain boundaries, and an initial void serving as a crack seed. With periodic grain boundaries, the tensile modulus of copper in the elastic region was reported to be 210 GPa. They concluded that the simulation results are in quantitative agreement with the experiments. They obtained the tensile modulus of the grain boundary to be ~40% less than the whole system. They also stated that the modulus of the grain boundary depend crucially on its microstructure. Cracking was reported to have initiated at a location where the strain concentration due to differences in the modulus of the grain boundary and the ordered bulk was largest. After initiation, the crack was reported to propagate along the grain boundaries. The strength of the system with periodic boundaries was reported to be ~10.3 GPa. In the tensile loading of a system with grain boundaries but with free boundaries, they reported absence of crack propagation with failure occurring due to grain boundary sliding. In this case, the system was reported to fail at low strain and stress values.

4.2.2. Methodology of MD Simulation

Figure 4.1 (a) is a schematic of a conventional tensile specimen and Figure 4.1 (b) is a schematic of the gage section used in the MD simulations of uniaxial tension of various workmaterials showing various regions of interest. The workmaterials studied in the

present investigation include FCC (aluminum, copper, nickel) and BCC (iron, chromium, tungsten) metals and covalently bonded semiconductors (silicon and germanium). A digital alpha-workstation (Model 500) with a clock speed of 500 MHz was used for the simulations. Simulations were conducted at loading rates of 500 to 10 m/s for Si and Ge to study the effect of rate of loading. The free surfaces (i.e., front and back surfaces as well as the sides of the specimen) are free from any external loads, as in conventional tensile testing. The top and bottom sides are fixed by boundary atoms. The regions above the top and below the bottom boundary atoms represent the material above and below the gage section [Figure 4.1 (a)], respectively similar to a conventional tensile specimen. The crystal was set up with the cube orientation and the uniaxial tensile force was applied along the [001] direction. Table 4.1 gives the dimensions of the workmaterial, potential used, rate of loading, loading condition, and the bulk temperature.

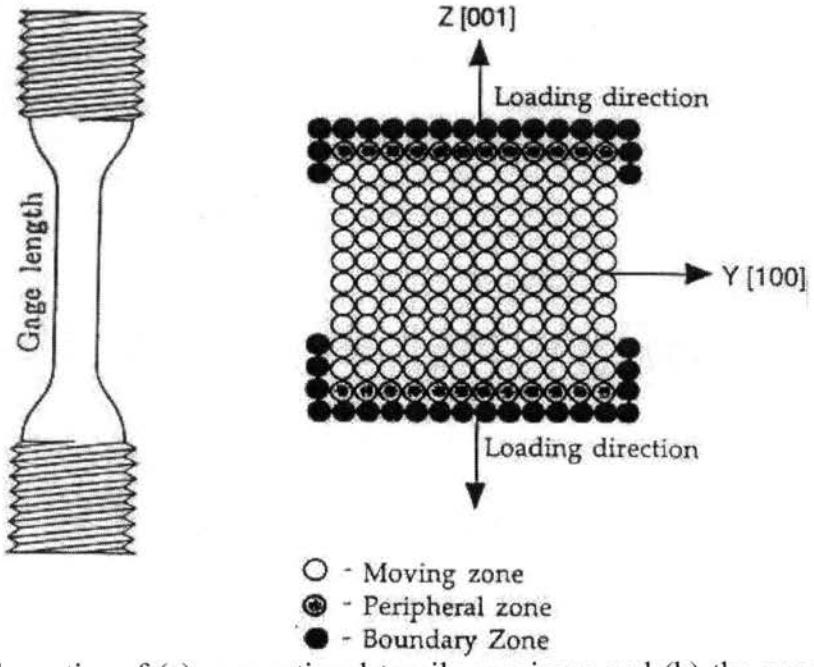

Figures 4.1 (a) - (b) Schematics of (a) conventional tensile specimen and (b) the gage section used in the MD simulations of different workmaterials showing various regions of interest

Table 4.1: Computational parameters used in the MD simulation of uniaxial tensile loading

Configuration	3-D
Potential used	Morse potential for metals and Tersoff potential for Si and Ge
Workmaterial dimensions	5a x 15a x 15a for metals and 5a x 5a x 5a for Si and Ge a - lattice constant
Tensile loading condition	Uniaxial
Speed of simulation	500 m/sec
Bulk temperature	293 K

4.2.3. On the Nature of Fracture and Deformation Under Tensile Loading

MD simulation plots of gage sections of the tensile specimens at various stages of uniaxial loading are shown in Figures 4.2 - 4.9. Figures 4.2 to 4.4 are for the FCC materials, Al, Cu, and Ni, respectively and Figures 4.5 to 4.7 are for the BCC materials, Fe, Cr, and W, respectively. Figures 4.8 and 4.9 are the MD simulation snapshots corresponding to Si and Ge, respectively. It may be noted that the discussion of the results presented here is based not only on the MD simulation plots of the various stages presented here but also on the detailed study of the animation process which was accomplished using a special program developed at OSU (Stewart, 1998).

For the FCC materials, the specimens after relaxation were found to be slightly under compression due to internal forces. Figure 4.2 (a) shows a slight compressive bulge of the specimen after relaxation for the case of Al. Similar situation is found for the case of the other two FCC metals investigated, namely, Cu [Figure 4.3 (a)] and Ni [Figure 4.4 (a)]. This, however, was not the case with the BCC materials [Compare Figures 4.5 (a), 4.6 (a) and 4.7 (a) with Figures 4.2 (a), 4.3 (a), and 4.4. (a)]. Considerable disorder in the

gage section of the crystal was observed during the early stages of loading for all FCC metals [see (b) and (c) of Figures 4.2-4.4]. As the workmaterial was pulled apart, bridging of the top and bottom portions of the crystal by a disordered neck of constantly decreasing diameter can be seen [(c) - (e) of Figures 4.2-4.4]. Al exhibited high ductility, with the atoms holding together for a larger strain, before the voids formed during the early stages of deformation coalesce and form a ductile fracture. Towards the later stages, the neck is elongated almost linearly to a very large strain [Figure 4.2 (f)]. On subsequent pulling, the necked region [Figure 4.2 (f)] separates culminating in the failure. The radius of the neck was found to increase with increase in the deformation of the specimen and decrease with decrease in the ductility of the material. The radius was observed to decrease monotonically as we go from Al to Cu to Ni. The region of disordered material as well as the extent of void formation was also found to decrease with decrease in the ductility of the material. Initially, dislocations at ~45° were observed in the animation for the case of Cu and Ni but due to the high disorder, further dislocation propagation was difficult to observe.

In the case of BCC materials, different behavior was observed during the early stages. As can be seen from Figures 4.5 (a), 4.6 (a), and 4.7 (a), the workmaterials seem to be in an excited state during its initial stage (i.e., after one time step). This localized disorder develops a weak region in the specimens, which results in subsequent necking. In the case of Fe, the layers above and below the necked region are arranged perpendicular to the loading direction with significant void volume fraction in the necked region [Figures 4.5 (c) & (d)]. The observed crystal order [Figure 4.5 (c)] is different than the initial crystal set-up [Figure 4.5 (a)]. On subsequent loading, the crystal order above and below the necked region disappears and the localized disorder spreads through the entire length of the workmaterial [Figures 4.5 (d) & (e)].

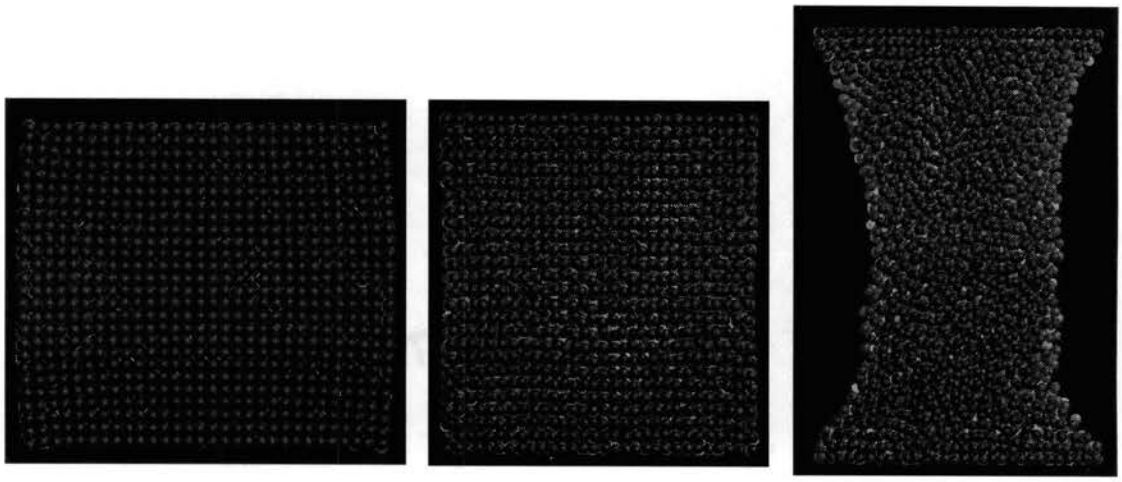

(a) Stage 1 (b) Stage 2 (c) Stage 3

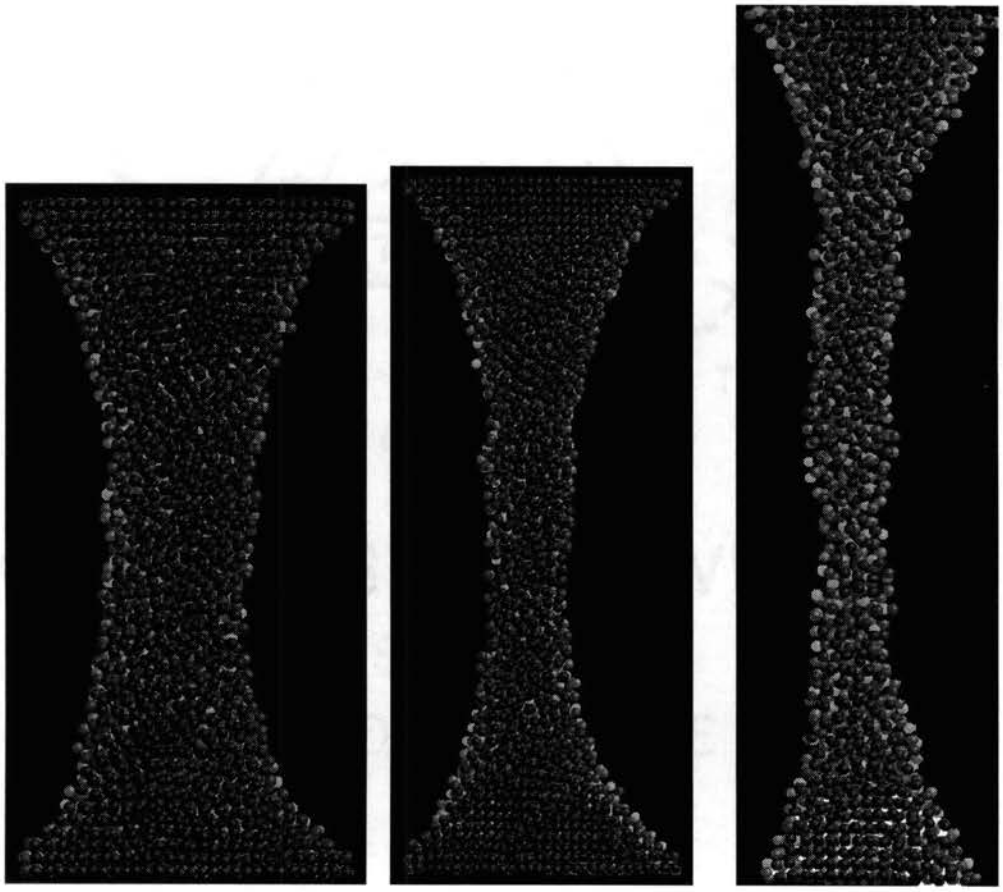

(d) Stage 4 (e) Stage 5 (f) Stage 6

Figures 4.2 (a) - (f) MD Simulation of Uniaxial Tension of Aluminum

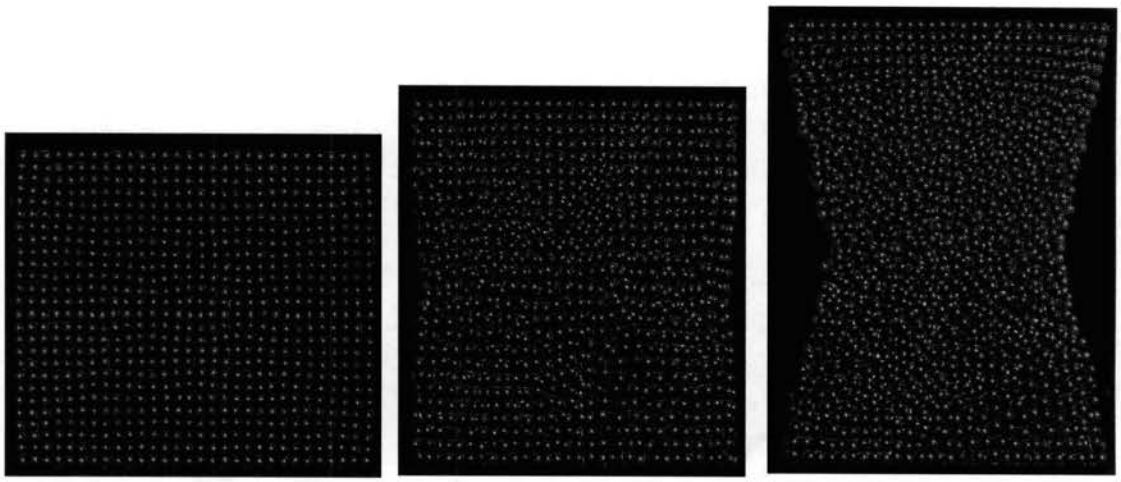

(a) Stage 1 (b) Stage 2 (c) Stage 3

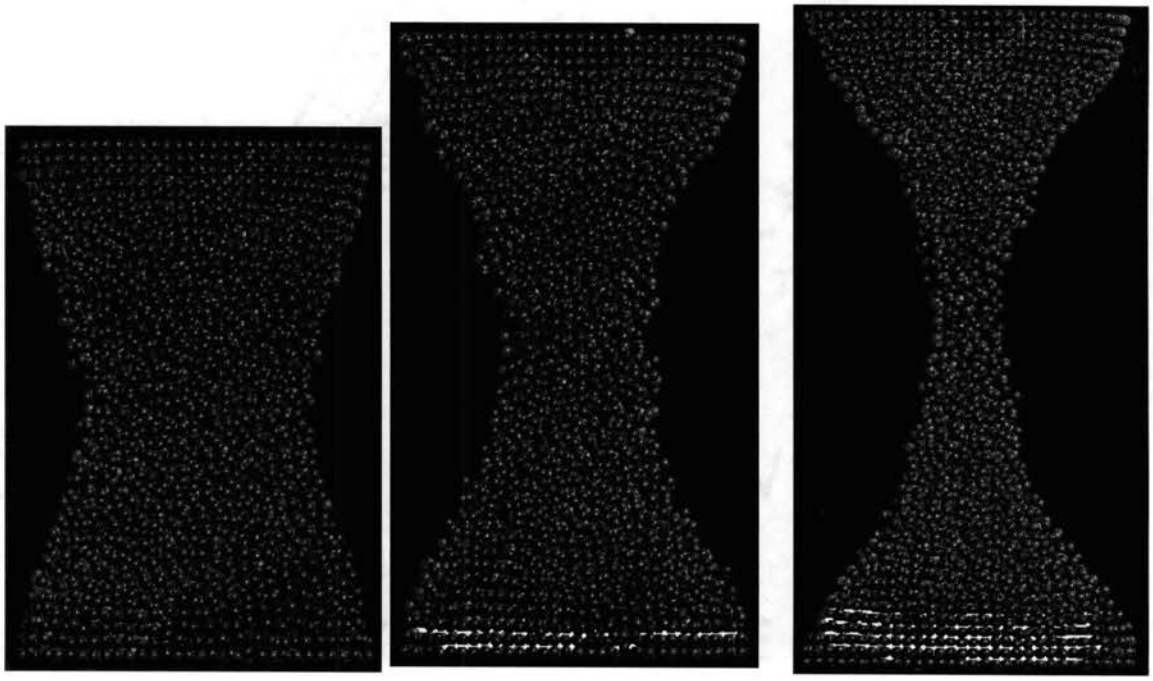

(d) Stage 4 (e) Stage 5 (f) Stage 6

Figures 4.3 (a) - (f) MD Simulation Plots of Uniaxial Tension of Copper

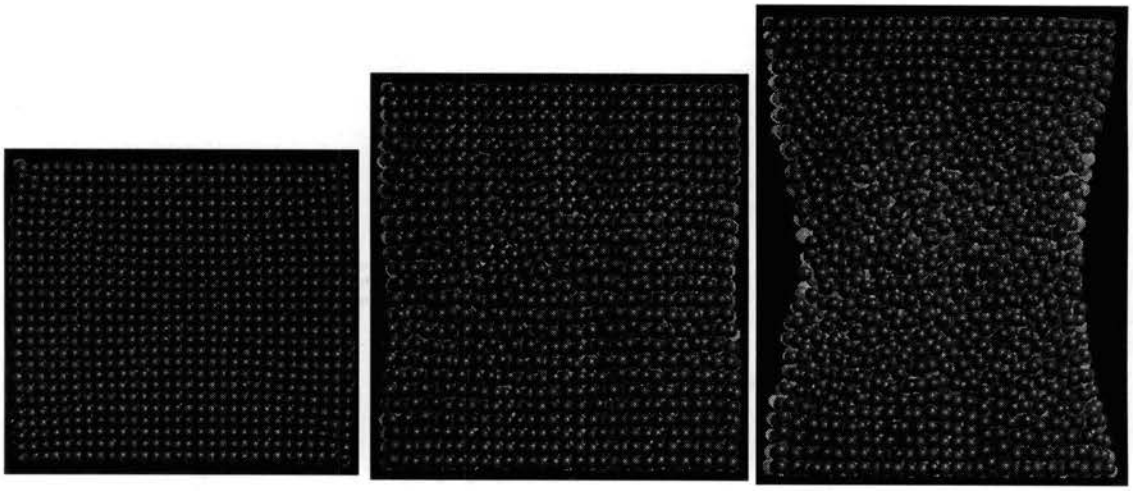

(a) Stage 1 (b) Stage 2 (c) Stage 3

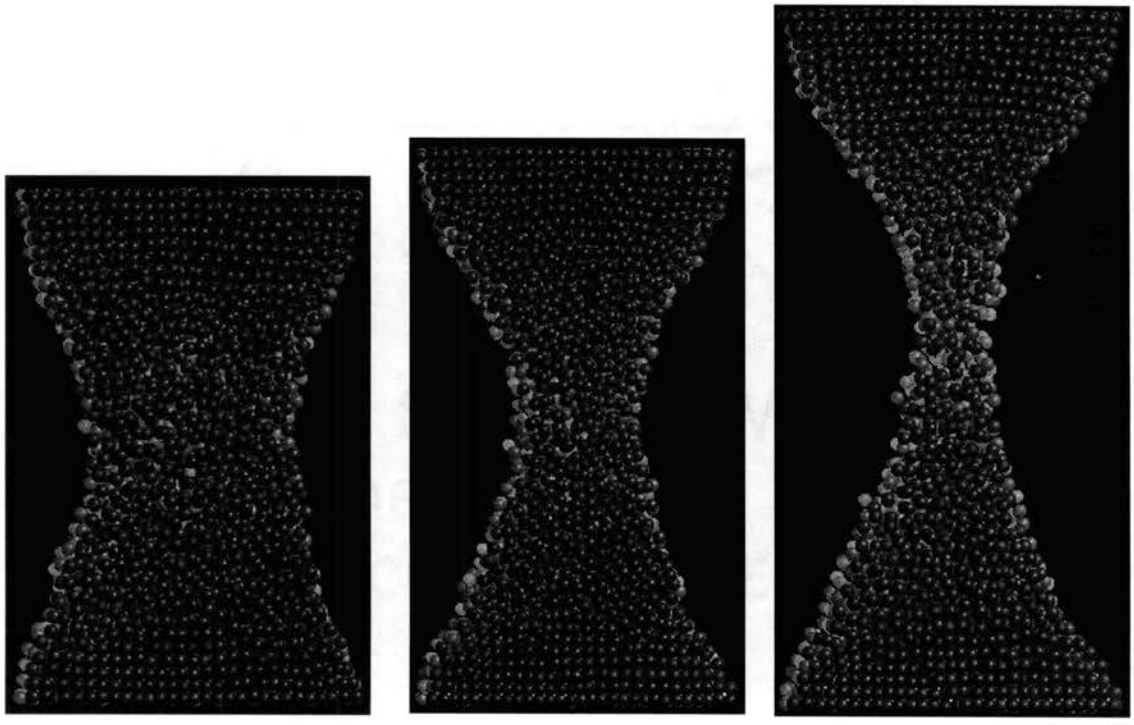

(d) Stage 4 (e) Stage 5 (f) Stage 6

Figures 4.4 (a) - (f) MD Simulations of Uniaxial Tension of Nickel

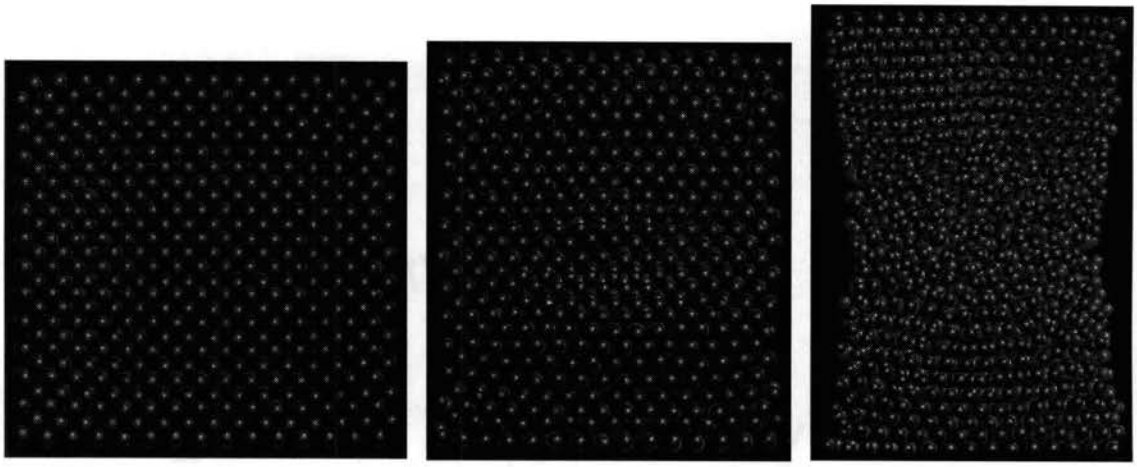

(a) Stage 1 (b) Stage 2 (c) Stage 3

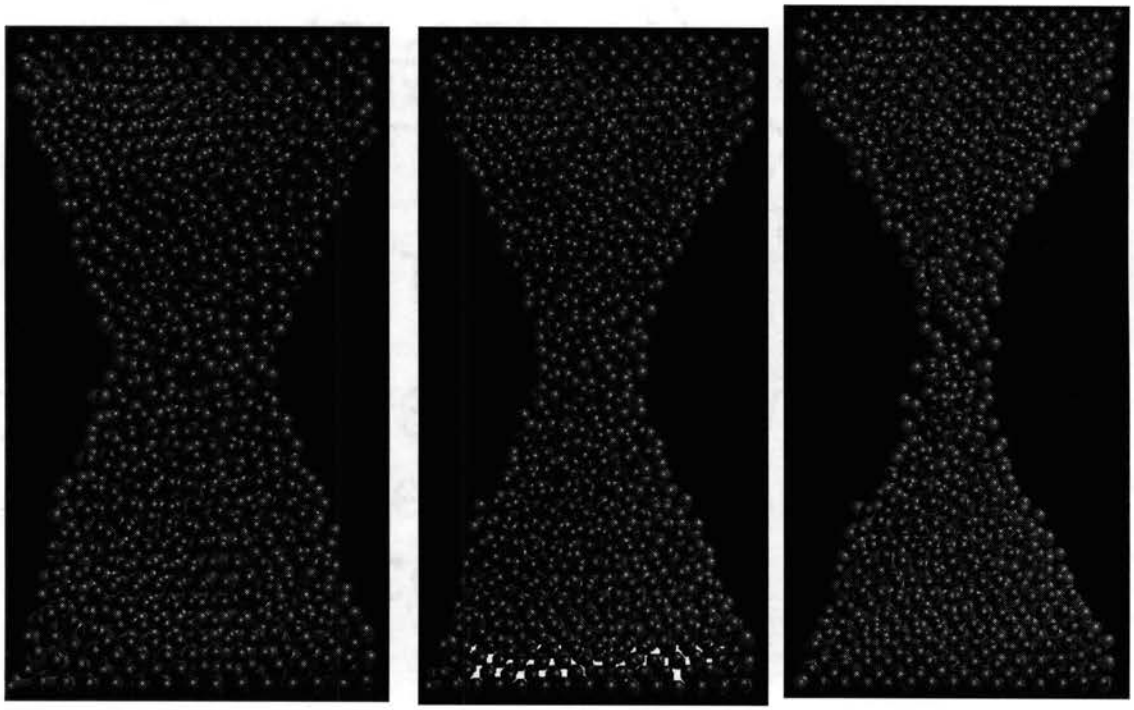

(d) Stage 4 (e) Stage 5 (f) Stage 6

Figures 4.5 (a) - (f) MD Simulations of Uniaxial Tension of Iron

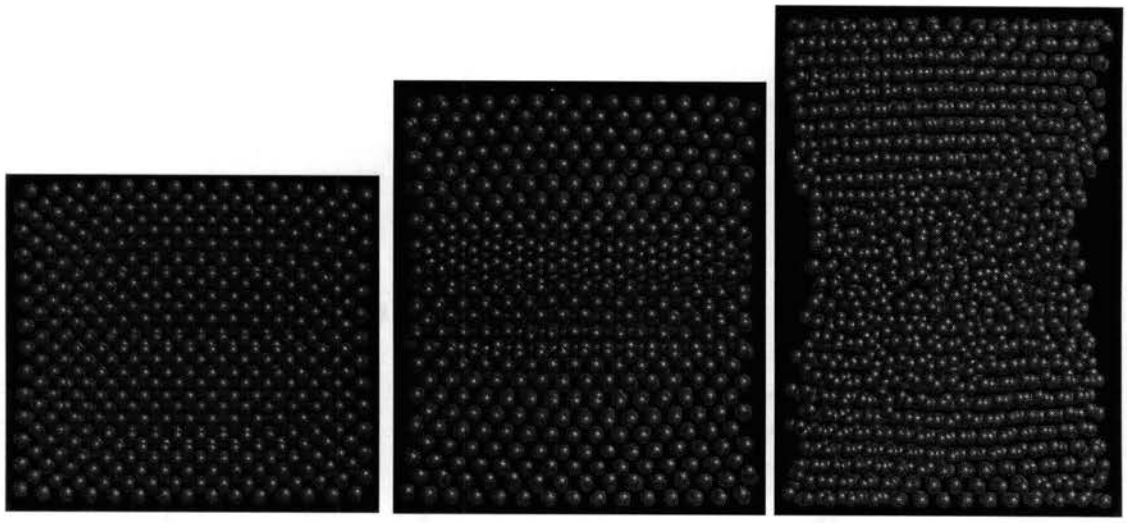

(a) Stage 1 (b) Stage 2 (c) Stage 3

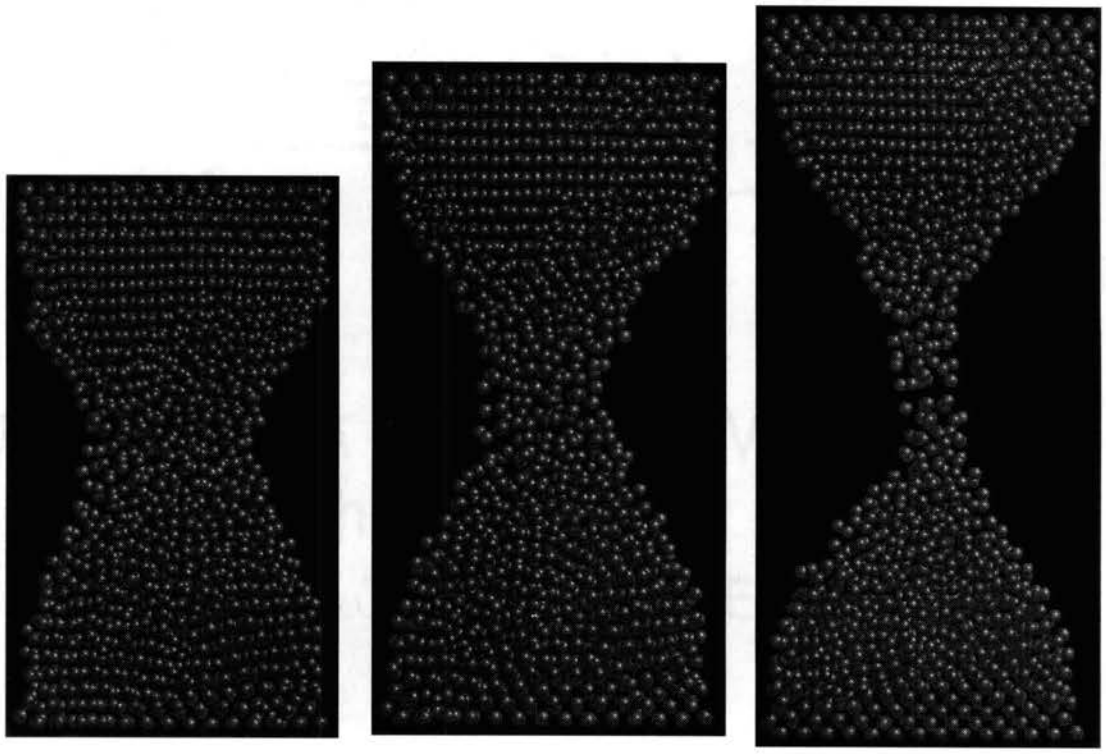

(d) Stage 4 (e) Stage 5 (f) Stage 6

Figures 4.6 (a) - (f) MD Simulation Plots of Uniaxial Tension of Chromium

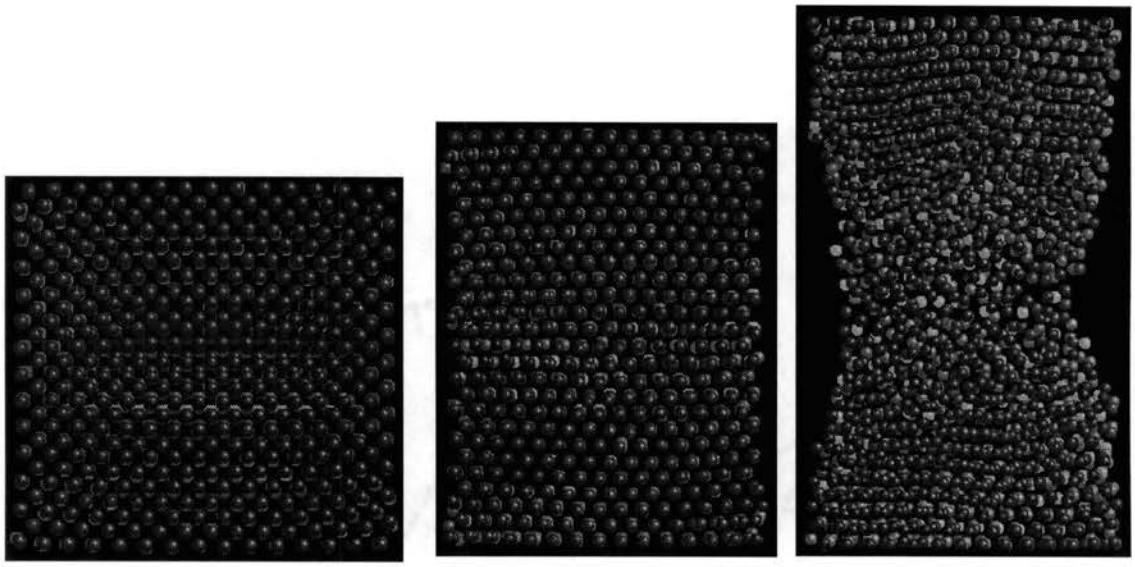

(a) Stage 1 (b) Stage 2 (c) Stage 3

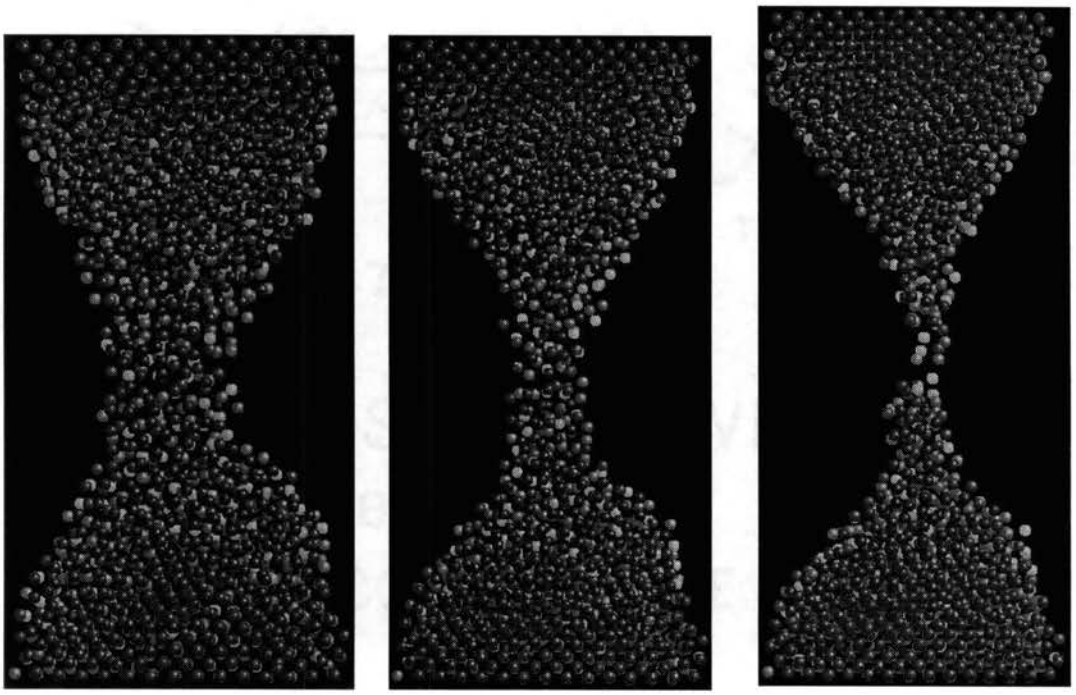

(d) Stage 4 (e) Stage 5 (f) Stage 6

Figures 4.7 (a) - (f) MD Simulation Plots of Uniaxial Tension of Tungsten

In the case of Cr, the disorder observed in the workmaterial during the initial step [Figure 4.6 (a)] disappears on further loading [Figure 4.6 (b)]. However, a localized disorder develops in the center of the workmaterial [Figure 4.6 (b)] as observed with Fe [Figure 4.5 (b)]. Similar to Fe, the regions above and below the weak region (mid-plane) are arranged perpendicular to the loading direction. The new crystal arrangement causes generation of voids in the weak region [Figure 4.6 (c) & (d)]. Subsequent elongation of the Cr crystal results in fracture [Figure 4.6 (f)].

In the case of W, as loading progresses, the disorder [Figures 4.7 (a) and (b)] disappears and the crystal assumes a new orientation [Figure 4.7 (c)]. Even though, the disorder still exists around the mid-plane of the crystal it is minimal in comparison to Fe and Cr. Due to the complete reorientation of the crystal and a definite order in the atomic positions, the disorder on subsequent elongation seems to concentrate around the mid-plane of the crystal [Figure 4.7 (d)]. A significant void fraction can be observed in the necked region. Once again, the layers above and below the necked region are arranged perpendicular to the loading direction [Figures 4.7 (d) & (e)]. Since the defects are highly concentrated in the necked region, subsequent loading results in early failure of tungsten [Figure 4.7 (f)].

Based on the animations as well as the plots at various stages of the deformation [Figure 4.2-4.7], the strain to fracture was observed to be lower with BCC materials compared to the FCC materials. This can be observed by comparing Figures 4.2 (f) - 4.7 (f), which shows a pictorial view of the variations in the strain to fracture of various crystals. Al behaves like an ideal ductile material extending significantly [Figures 4.2 (e) and (f)]. The amount of extension decreases as one moves from Al to Cu [Figure 4.3 (f)], to Ni [Figure 4.4 (f)], to Fe [Figure 4.5 (f)], and Cr [Figure 4.6 (f)] with W exhibiting minimum strain before fracture [Figure 4.7 (f)]. Also, the radius and length of the neck

was observed to be different for different materials [Figures 4.2 (e) - 4.7 (e)]. In the case of FCC materials, the workmaterial was disordered from the early stages of necking till the end. Consequently, it was not possible to observe any structural changes in the crystal. The disorder was observed to spread through the entire length of the workmaterial. The void volume fraction was distributed throughout the specimen with FCC materials while in the case of BCC materials they were concentrated around the necked region. Consequently, FCC materials were able to withstand higher strains before failure. In the case of BCC materials, the atoms tend to rearrange with their neighbors to form a different or modified crystal structure. The workmaterial above and below the necked region was observed to arrange itself perpendicular to the loading direction. The crystal symmetry in these regions resulted in a weak mid-plane with higher void volume fraction. Consequently, the crystal failed around this region at a lower strain in comparison to the FCC materials. This constant rearrangement of the atoms with the BCC materials will be shown to result in significant force variations. It will be shown, based on the force trends that structural transformations also occur with FCC materials, albeit to a lesser extent in comparison to BCC materials.

Figures 4.8 (a) - (f) and 4.9 (a) - (f) are snapshots of the MD simulation process of tensile loading performed on silicon and germanium, respectively. In contrast to the relatively ductile metals presented above [Figures 4.2 to 4.7], both silicon and germanium exhibit a tendency to fail by sudden fracture (as was also observed from the animations). Upon tensile loading, both silicon and germanium exhibit a distinct elastic behavior. Figures 4.8 (b) and 4.9 (b) show the state of the silicon and germanium workmaterials prior to failure. Absence of crystal disorder in the form of dislocations or voids can be observed. In contrast, the metals presented above showed the generation of dislocations and void formation much earlier during the loading process. Figure 4.8 (c) shows the initiation of crystal disorder along the mid-plane from ends of the silicon workmaterial.

At this point, the crystal fails by sudden fracture by propagation of the lattice disorder perpendicular to the loading direction along the mid-plane. Consequently, the crystal separates into top and bottom halves [Figure 4.8 (d)]. After this stage, further loading causes the crystal to break into two separate pieces [Figures 4.8 (d) - (f)]. Similar behavior can also be observed in the case of germanium [Figure 4.9 (c) - (f)]. This catastrophic failure of silicon and germanium was observed to result in a sudden drop in the stress-strain curve (as will be shown later). Both, silicon and germanium exhibit absence of an extended neck as was observed with aluminum [Figures 4.2 (a) - (f)], copper [Figures 4.3 (a) - (f)], and nickel [Figures 4.5 (a) - (f)]. The absence of neck formation is more pronounced with germanium where one can see the failure initiation in the middle of the workpiece [Figure 4.9 (c)] resulting in immediate breaking of the crystal into two separate pieces [Figures 4.9 (d) - (f)].

This difference in the deformation behavior between silicon and germanium can be due to silicon readily forming various types of clusters, crystals, and surfaces, in comparison to germanium. Raghavachari and Logovinsky (1985) have shown by *ab initio* molecular orbital calculations that numerous coordination, n (n up to 30) of silicon are possible under different conditions leading to the formation of various types of clusters, crystals, and surfaces of silicon

4.2.4. On the Nature of Force Variation Under Tensile Loading

Figures 4.10 (a) - (h) show the engineering stress-strain diagrams obtained by MD simulation of the tensile specimens of Al, Cu, Ni (FCC) [Figures 4.10 (a) - (c)], Fe, Cr, and W (BCC) [Figures 4.10 (d) - (f)] and Si and Ge (semiconductors) [Figures 4.10 (g) and (h)], respectively.

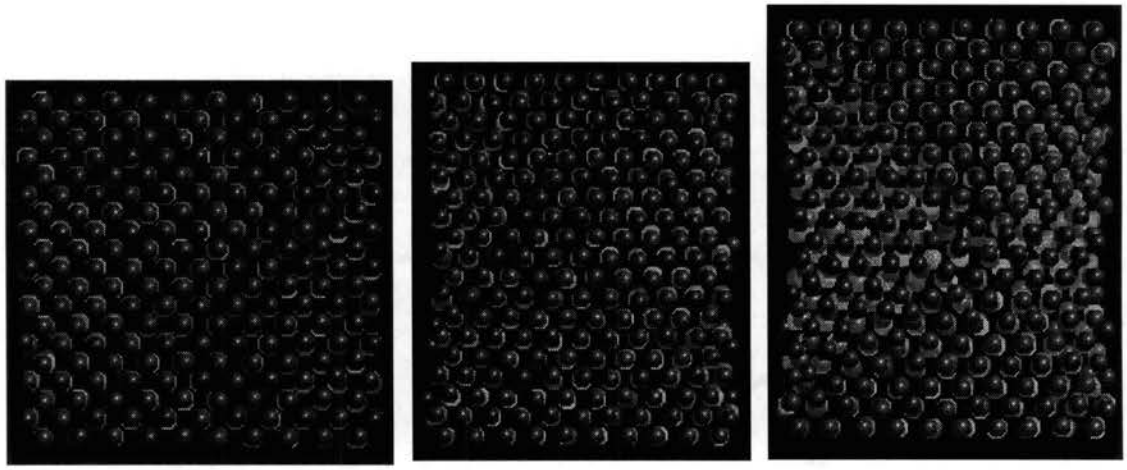

(a) Stage 1 (b) Stage 2 (c) Stage 3

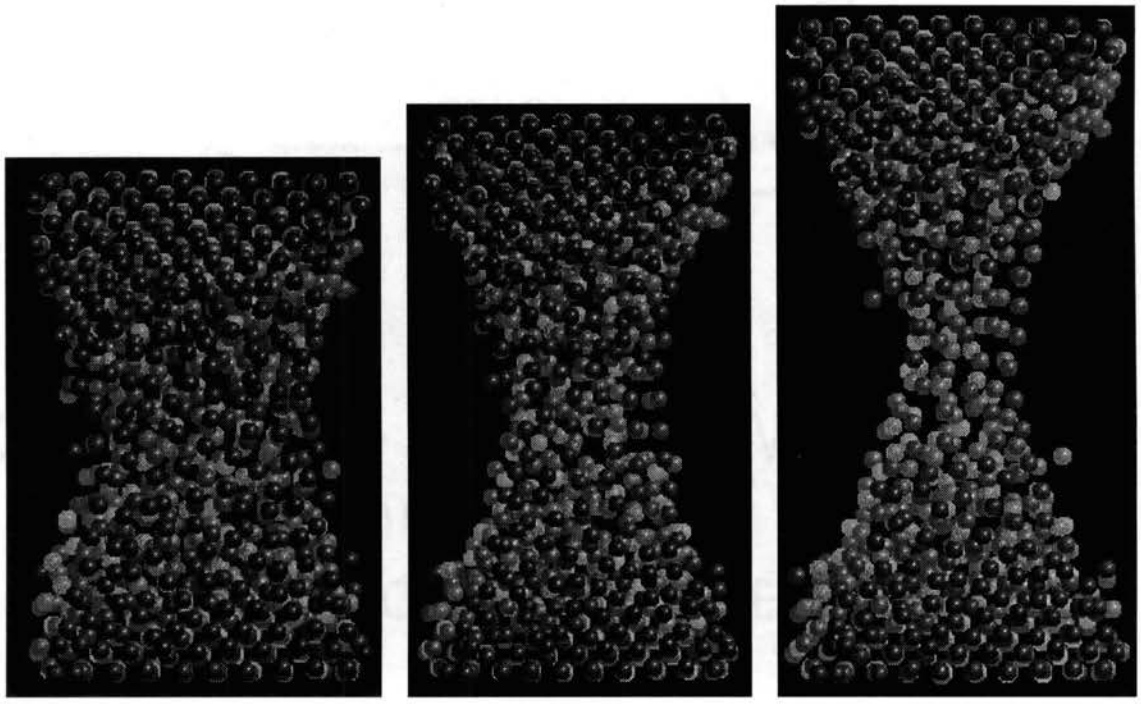

(d) Stage 4 (e) Stage 5 (f) Stage 6

Figures 4.8 (a) - (f) MD Simulation Plots of Uniaxial Tension of Silicon

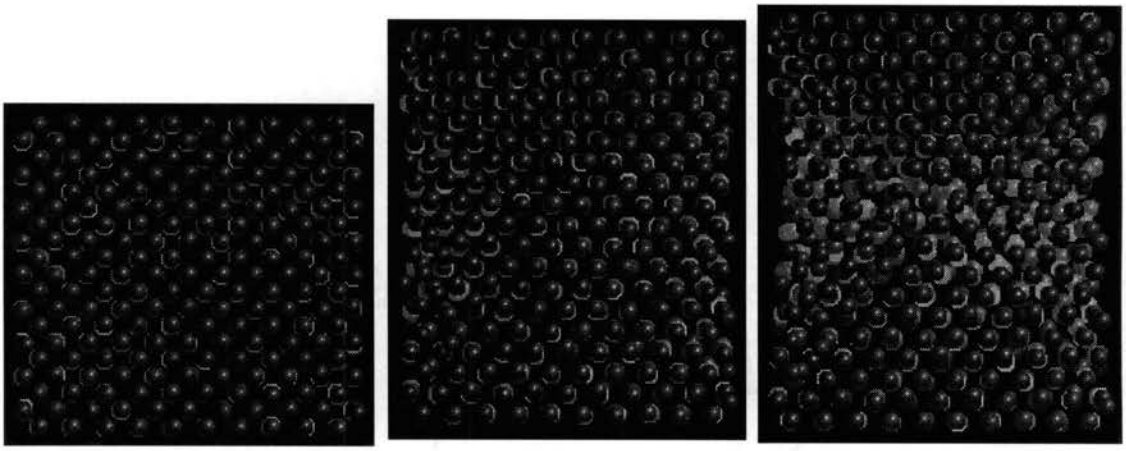

(a) Stage 1 (b) Stage 2 (c) Stage 3

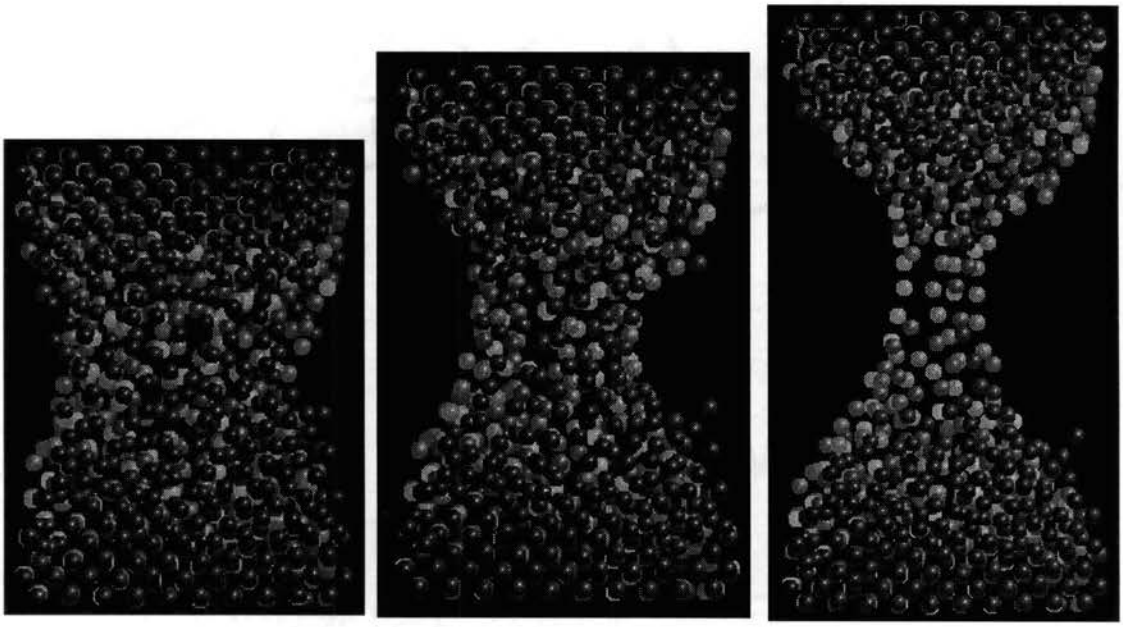

(d) Stage 4 (e) Stage 5 (f) Stage 6

Figures 4.9 (a) - (f) MD Simulation Plots of Uniaxial Tension of Germanium

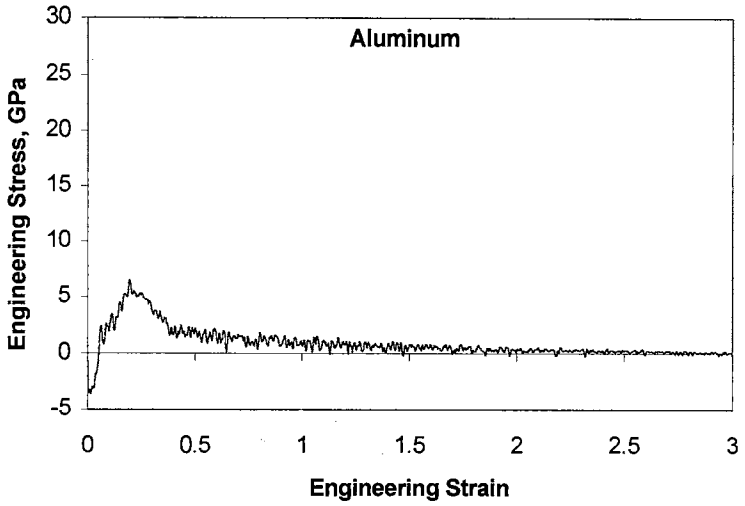
Aluminum
Engineering Stress, GPa
30
25
20
15
10
5
0
-5
0
0.5
1
1.5
2
2.5
3
Engineering Strain

(a)

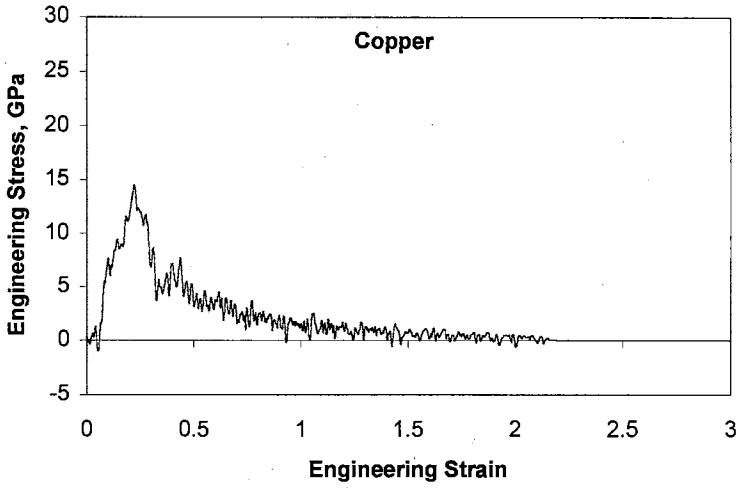
Copper
Engineering Stress, GPa
30
25
20
15
10
5
0
-5
0
0.5
1
1.5
2
2.5
3
Engineering Strain

(b)

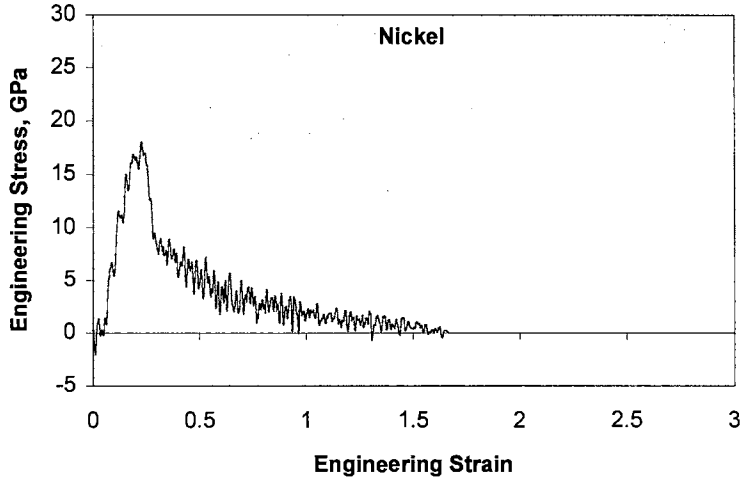
Nickel
Engineering Stress, GPa
30
25
20
15
10
5
0
-5
0
0.5
1
1.5
2
2.5
3
Engineering Strain

(c)

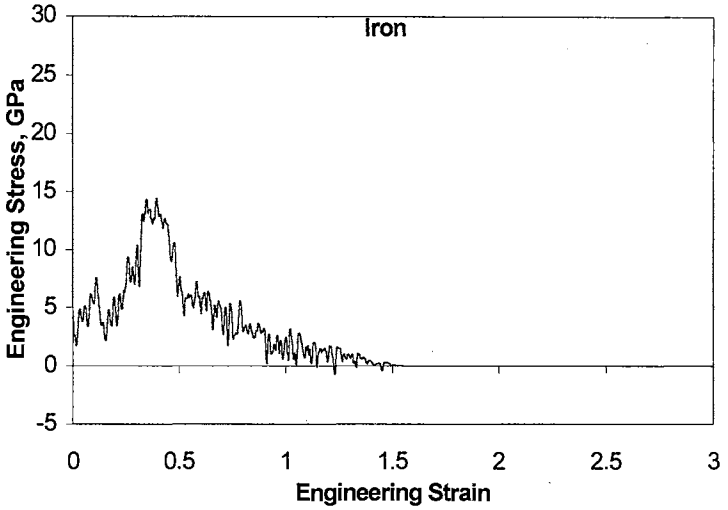
Iron
Engineering Stress, GPa
30
25
20
15
10
5
0
-5
0
0.5
1
1.5
2
2.5
3
Engineering Strain

(d)

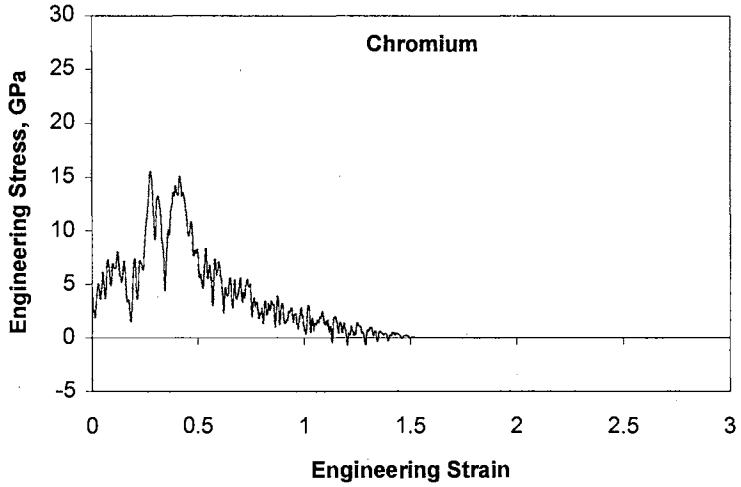
Chromium
Engineering Stress, GPa
30
25
20
15
10
5
0
-5
0
0.5
1
1.5
2
2.5
3
Engineering Strain

(e)

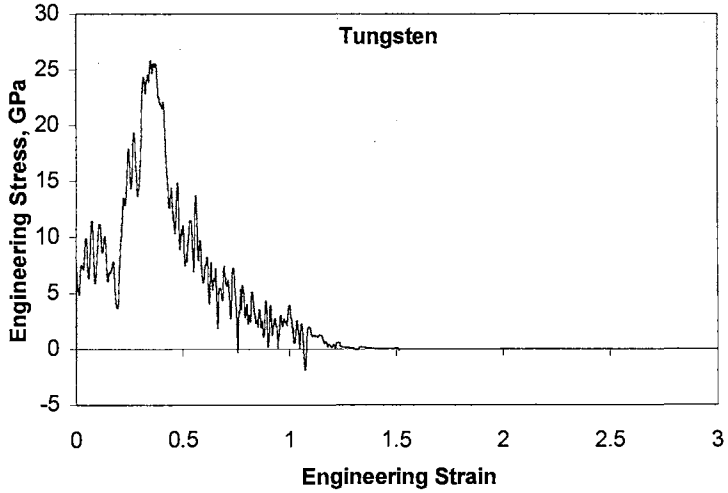
Tungsten
Engineering Stress, GPa
30
25
20
15
10
5
0
-5
0
0.5
1
1.5
2
2.5
3
Engineering Strain

(f)

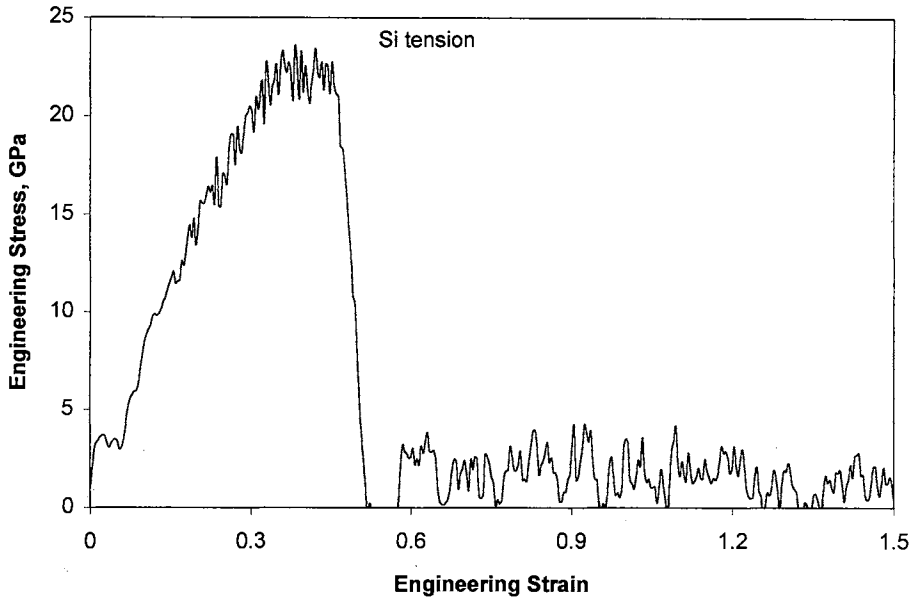

(g)

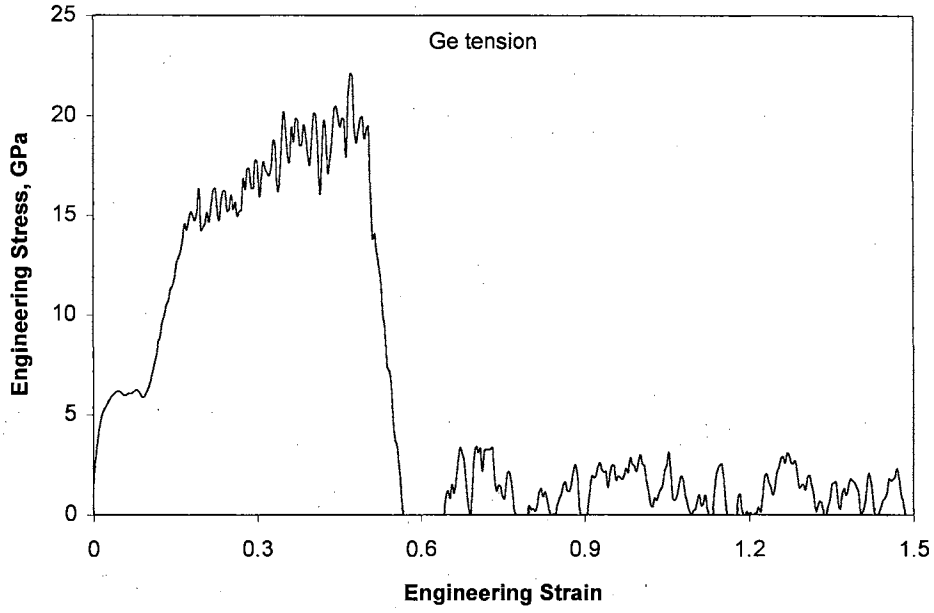

(h)

Figures 4.10 (a) - (f) Engineering stress-strain diagrams obtained by MD simulation of the tension specimens of various materials, namely, Al, Cu, Ni (FCC) [(a) - (c)]; Fe, Cr, and W (BCC) [(d) - (f)]; and Si and Ge (Covalently bonded) [(g) and (h)], respectively

In the case of FCC materials, especially Al and Ni [Figures 4.10 (a) and (c)], the forces start below the zero point prior to the application of tensile loading. It was pointed out earlier that after the relaxation procedure, the FCC specimens were under slight compression [Figures 4.2 (a) - 4.4 (a)] due to internal stresses. This compression causes the initial forces to be negative. The slope of the linearly increasing curve is more apparent in the case of FCC workmaterials with Ni exhibiting the maximum slope [Figure 4.10 (c)] followed by Cu [Figure 4.10 (b)] and Al [Figure 4.10 (a)]. Unlike in conventional tensile testing, where the stress-strain diagram is essentially smooth with a linear slope in the elastic region, in nano tensile testing, a series of steps of rise and fall in the stress values with engineering strain is observed. This behavior can be attributed to strain hardening and subsequent softening of the material associated with constant reorganization of the atoms in the workmaterial. Also, no clear demarcation of linear elastic range nor the yield point is visible. It is, therefore, difficult to calculate exact values of elastic moduli or the elastic constants with any degree of certainty. The general practice is to obtain the modulus for small values of strain from a second degree polynomial that was fitted to the stress-strain diagram (Heino et al., 1998a). This approach was used in this study, as well.

In the case of BCC materials, no distinct linear trend in the engineering stress-strain characteristics is observed [Figures 4.10 (d) - (f)]. The diagrams show a number of sudden jumps of rise and fall in the stress values. Cr shows a significant drop and rise after reaching the maximum tensile strength point followed by an increase to the global maximum tensile strength point before dropping down to zero [Figure 4.10 (e)]. Such high force drops can also be observed with Fe [Figure 4.10 (d)] and W [Figure 4.10 (f)]. In the case of Fe, Cr, and W [Figures 4.10 (d) - (f)], the fluctuations in the force curves during the early stages can be compared with the structural changes seen in the MD simulations, as have been discussed earlier. If the drop in the force curves can be

attributed to the rearrangement of atoms to a new crystal structure, it appears that BCC materials undergo significant changes in their structure and subsequent realignment in comparison to FCC materials.

Several differences can be observed by comparing the force curves of Si [Figure 4.10 (g)] and Ge [Figures 4.10 (h)] with that for the metals presented above [Figures 4.10 (a) - (f)]. The slope of the force curve for Si and Ge exhibit minimal fluctuations. This can be attributed to the absence of structural changes observed with Si and Ge. In contrast, metals (both, FCC and BCC) exhibit significant structural changes resulting in force variations even during the initial stages of the tensile loading process. The engineering stress-strain curves for both, Si and Ge, exhibit a catastrophic failure after reaching the maximum, as was also observed from the simulation plots [Figures 4.8 (a) - (f) and 4.9 (a) - (f)], in contrast to the gradual decay in forces to zero observed with metals [Figures 4.10 (a) - (f)]. This indicates the differences in the ductilities of the materials considered with metals indicating a ductile fracture mode while Si and Ge exhibiting brittle fracture.

Lynden-Bell (1995) suggested that the position of the maximum stress is the point of failure of the material and marks the change from reversible to irreversible behavior. Actually, reversible behavior stops after the elastic limit and once the yield point is reached. This is far below the position of maximum stress in the case of metals. In the MD simulations conducted here, we observed that in the case of FCC and BCC materials, even before the maximum stress point is reached the crystal has undergone significant amount of irreversible deformation, as would be expected. The fluctuations in the force curves observed for both the FCC and BCC workmaterials [Figs. 4.10 (a) - (f)] suggest the irreversibility of the process even before the maximum stress point is reached. If one considers the structural transformations and the subsequent drop in the force to be due to

plastic deformation in the crystal, then it no longer is a reversible process. However, in the case of Si and Ge no irreversible deformation was observed till the maximum stress point is reached.

Table 4.2 gives the measured (from MD simulation) tensile strength, elastic modulus, and strain at fracture of the various materials used in this study (for [001] direction). W exhibits the highest strength among metals (ultimate strength of ~26 GPa) while Al exhibits the lowest strength (ultimate strength of ~7 GPa). The strength of Ni was estimated to be ~18 GPa which is very close to the value (15-20 GPa) reported by Kitamura et al. (1997). The strength of Cu was estimated to be ~14 GPa. Heino et al. (1998b) reported a strength of 10.3 GPa for polycrystalline Cu. Since our simulations were performed on defect free single crystals the estimated strength of Cu should be higher than that reported by Heino et al. (1998b). The strength can be expected to decrease with increasing disorder in the workmaterial as reported by Heino et al. (1998a). The strain at fracture can also be observed to be different for the various materials used in this investigation. W showed an earlier fracture (~1.4) while in the case of Al the maximum strain before fracture is ~3.2. The BCC workmaterials studied in this investigation exhibit higher stress accommodation in comparison to the FCC workmaterials (Table 4.2). This can be attributed to the higher degree of structural transformations observed with BCC materials in comparison to the FCC materials.

Si and Ge exhibit an ultimate tensile strength of ~25 GPa and ~20 GPa, respectively. The UTS of Si (~24 GPa) is in agreement with the value (~23 GPa) reported by Rentsch et al. (1995) based on MD simulation study. The strain at fracture for silicon (~0.5) and germanium (~0.55) are much lower compared to the metals studied in this investigation [Table 4.2]. The estimated elastic modulus of silicon in the [001] direction (~130 GPa) is in agreement with the values reported in the literature based on macro- (Brantley, 1973

[130 GPa]) and micro-scale (Sato et al., 1996 [125 GPa] and Wilson and Beck, 1996 [130 GPa]) experimental work. The [001] elastic modulus of germanium (~103 Gpa) is also in agreement with the values reported in the literature*.

Table 4.2: Results of MD simulations of uniaxial tensile loading in [001] direction for various materials (Loading rate: 500 m/s)

Material	Ultimate strength, GPa	Evaluated elastic modulus, GPa	Strain at maximum stress	Strain at failure
Aluminum	6.51	69	0.20	3.19
Copper	14.32	124	0.22	2.17
Nickel	18.02	214	0.23	1.67
Iron	14.43	196	0.40	1.52
Chromium	15.55	289	0.28	1.52
Tungsten	25.57	406	0.34	1.40
Silicon	23.53	130	0.38	0.52
Germanium	22.1	103	0.47	0.55

4.2.5. On the Effect of Morse Potential Parameters On Fracture of Metals

It was shown earlier [Figures 2.4 (a) and (b), Chapter 2, section 2.3.4] that the long-range forces between atoms approach zero at higher interatomic distance with decreasing α-parameter and the forces required to break an atomic bond increases with increasing D parameter. Consequently, the D-parameter and the α-parameter of the Morse potential can be used as an indication of the material strength and ductility. Lower the value of the D-parameter and the α-parameter, the more ductile the material is with lower strength and vice-versa.

* - from various website refs., for example, 1. http://www.argusinternational.com/ge.html 2. http://www.ioffe.rssi.ru/SVA/NSM/Semicond/Ge/mechanic.html

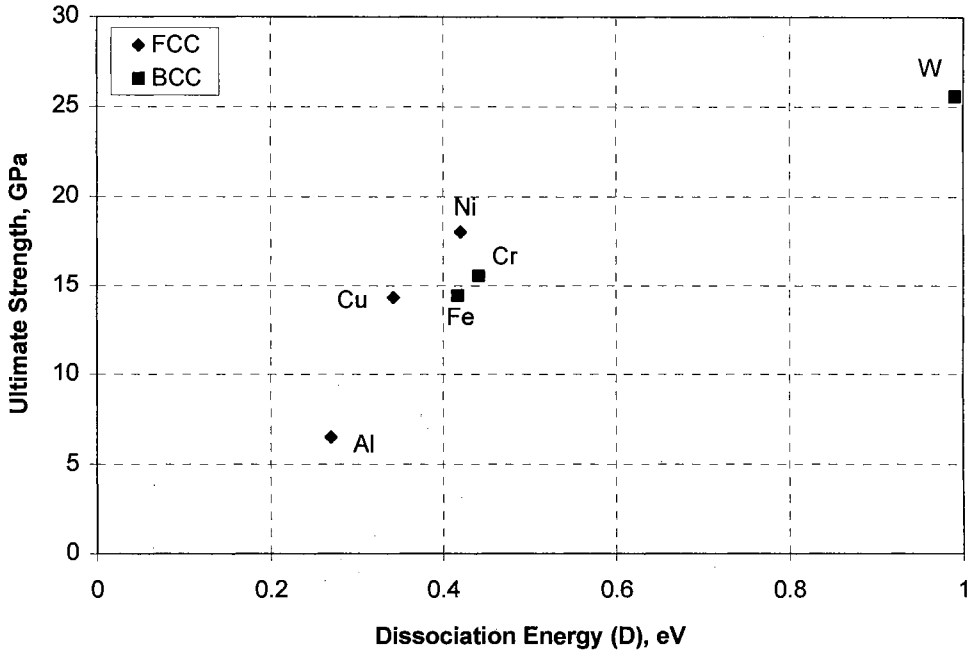

(a)

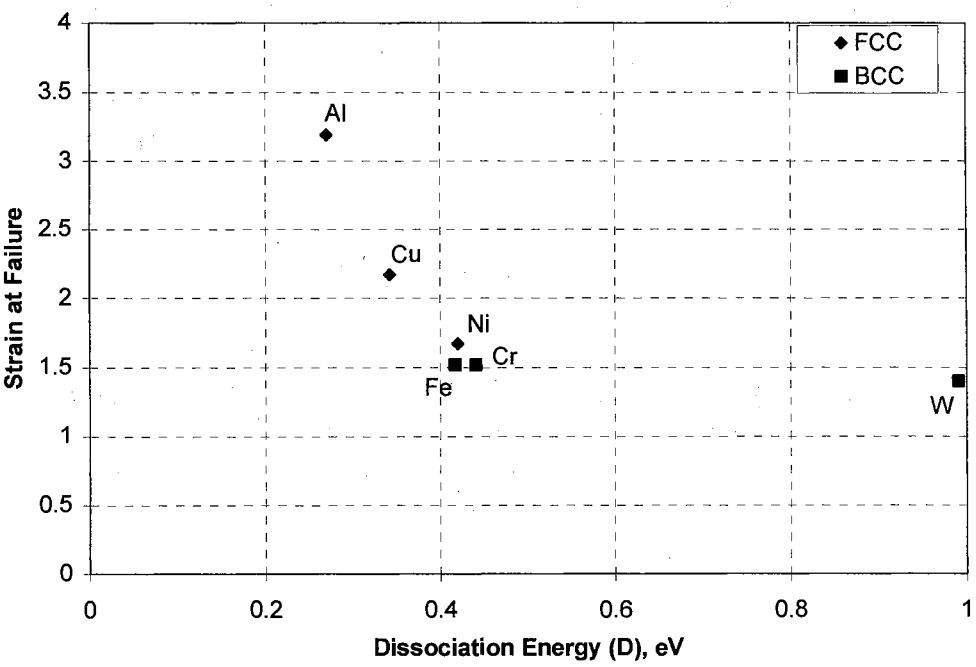

(b)

Figures 4.11 (a) - (b) Variation of (a) ultimate strength and (b) strain at failure with Dissociation energy (D parameter) of Morse potential

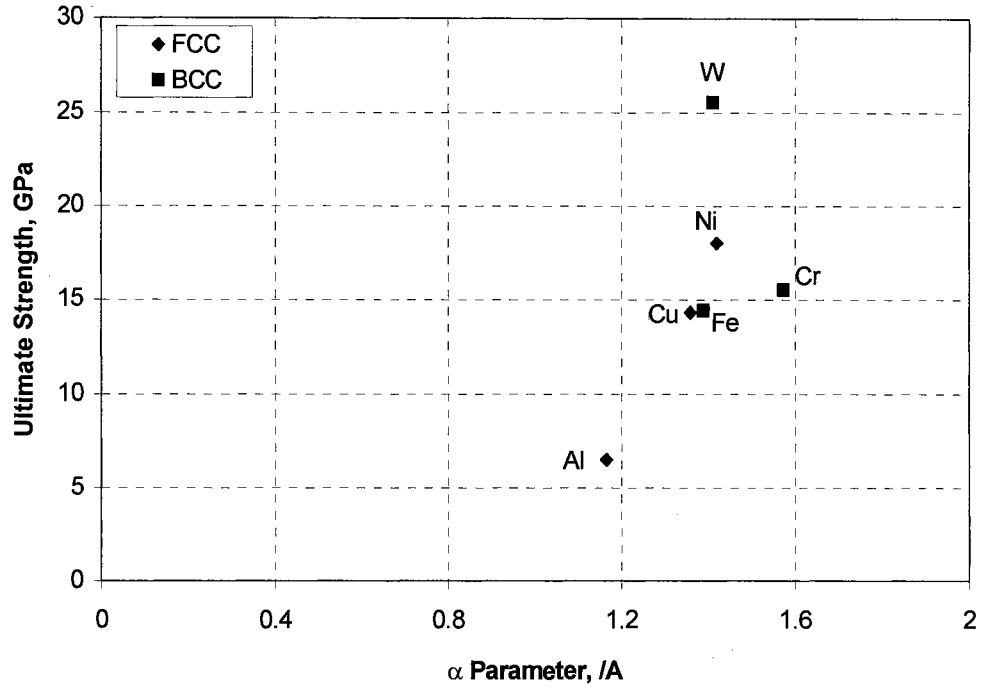

(a)

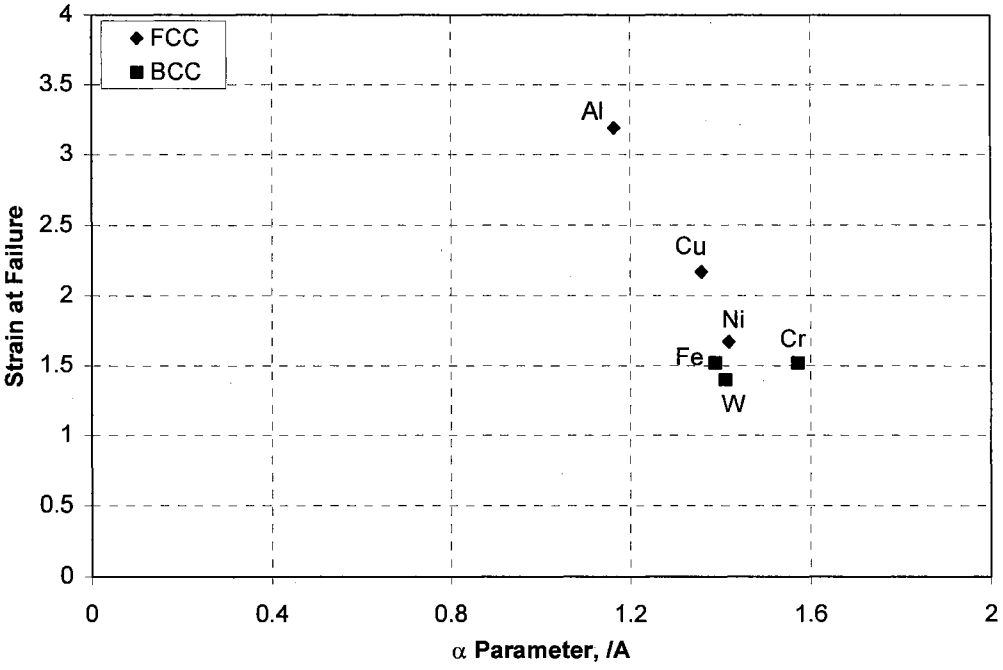

(b)

Figures 4.12 (a) - (b) Variation of (a) ultimate strength and (b) strain at failure α parameter of Morse potential

Figures 4.11 (a) and (b) and Figures 4.12 (a) and (b) show the variation of ultimate strength and the strain at failure for the various metals studied here with the D- and the α-parameters of the Morse potential [Refer to Table 2.1 for the D- and α-parameters of various metals]. It can be seen that, the ultimate strength increases almost linearly for the FCC materials, namely, Al, followed by Cu, and Ni [Figures 4.11 (a) and 4.12 (a)] with increase in the D-parameter and the α-parameter, respectively. In contrast, for the BCC metals, while there is an increase in the ultimate strength with increase in the D parameter [Figure 4.11 (a)], this is not so with increase in the α-parameter [Figure 4.12 (a)].

Similarly, the strain at fracture decreases almost linearly with increase in the D-parameter [Figure 4.11 (b)] and α-parameter [Figure 4.12 (b)], respectively, for the FCC materials, namely, Al, followed by Cu, and Ni. However, for the BCC metals the strain at fracture seems to be independent of both the D-parameter and the α-parameter [Figures 4.11 (b) and 4.12 (b)]. For example, even though, the dissociation energy (D parameter) of the BCC workmaterials used in this investigation is varied from ~0.4 to 1, the strain at fracture remains nearly constant [Figure 4.11 (b)]. It can be seen from this that it is rather difficult to interpret the variation of D- and α-parameters on the strength and strain behavior of BCC metals. Such behavior suggests that a Morse potential may not represent the deformation behavior of the BCC metals as well as the FCC metals.

4.2.6. Effect of Strain Rate or Rate of Loading On the Tensile Response

MD simulations of uniaxial tension was conducted at various strain rates (500 m/s to 10 m/s) for Si and Ge to study the effect of strain rate on the deformation behavior and the measured properties. Figures 4.13 (a) - (f) are the MD simulation plots of silicon at a given strain (~0.4) for various strain rates, namely, 500 m/s, 400 m/s, 300 m/s, 200 m/s 100 m/s, and 10 m/s, respectively.

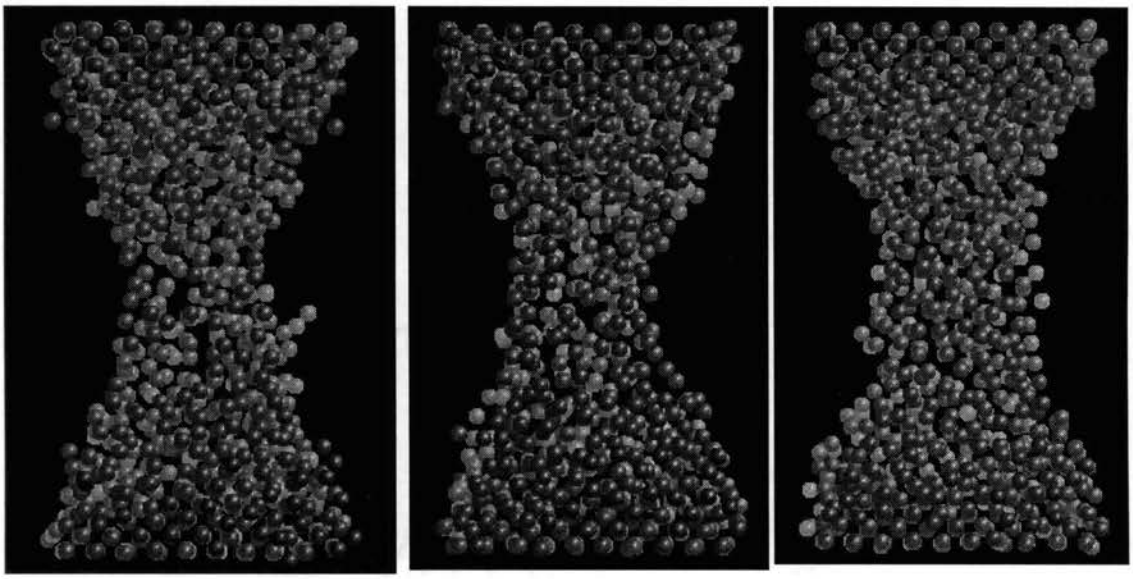

(a) Strain rate: 500 m/s (b) Strain rate: 400 m/s (c) Strain rate: 300 m/s

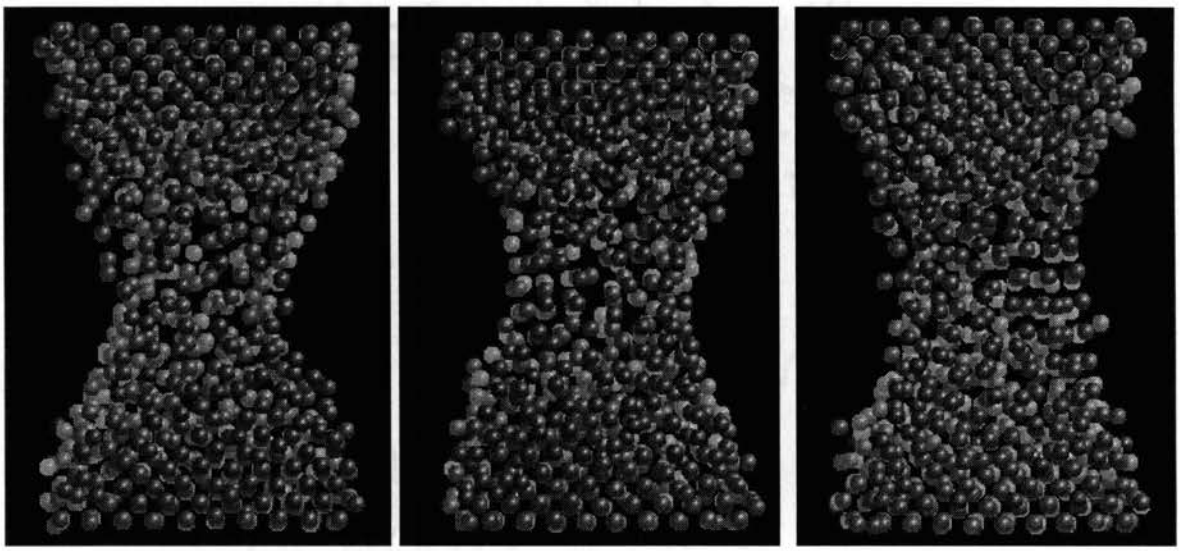

(d) Strain rate: 200 m/s (e) Strain rate: 100 m/s (f) Strain rate: 10 m/s

Figures 4.13 (a) - (f) MD Simulation Plots of Silicon at a Strain of ~0.4 Under Various Loading Rates

It can be seen that [by comparing Figures 4.13 (a) - (f)] while there are differences in the atomic positions to some extent, no noticeable differences in the deformation behavior is seen. At all strain rates, the deformation is due to generation of voids in the necked region and propagation of these voids along the mid-plane of the workmaterial. Figures 4.14 (a) and (b) are the engineering stress-strain curves for Si and Ge, respectively, at various strain rates of 500 m/s, 400 m/s, 300 m/s, 200 m/s, 100 m/s, 50 m/s, and 10 m/s, respectively. In both cases (Si and Ge), the ultimate strength and the strain at failure decrease with decreasing strain rate. The linear portion of the curves during the initial loading stages nearly overlap irrespective of the strain rate.

In the case of Si [Figure 4.14 (a)], as the strain rate decreases from 500 m/s to 100 m/s, the engineering stress-strain curves increase to a maximum and then exhibit a sudden drop to zero. Further loading causes the forces to oscillate around the zero line. At a strain rate of 50 m/s, the engineering stress-strain curve for Si drops to zero however, further loading results in an increase in the stress-strain curve. This secondary rise in the stress-strain curve reaches a maximum and then slowly decays to zero upon further loading. At 10 m/s loading rate, the engineering stress-strain curve for Si drops after reaching a maximum but does not reach the zero line. After the initial drop, the forces increase slightly and then decay to zero upon further loading. A similar situation can also be observed with germanium at a strain rate of 10 m/s [Figure 4.14 (b)]. As mentioned earlier, both Si and Ge (Si to a greater extent) have a tendency to form various clusters and structures. It is possible that at lower strain rates, after failure both Si and Ge form secondary clusters across the mid-plane (plane of fracture). As the specimen is loaded further these clusters result in the secondary peak observed with Si and Ge at lower strain rates. This phenomenon was not observed at higher strain rates and it is possible that at high loading rates there is not sufficient time for the material to form clusters.

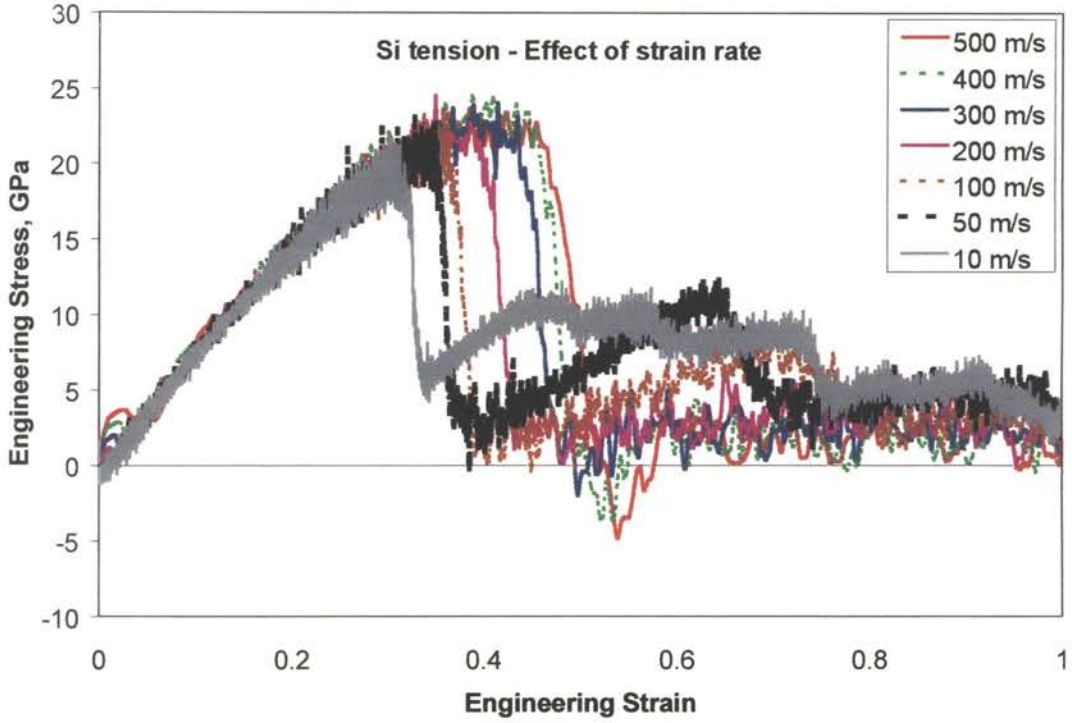

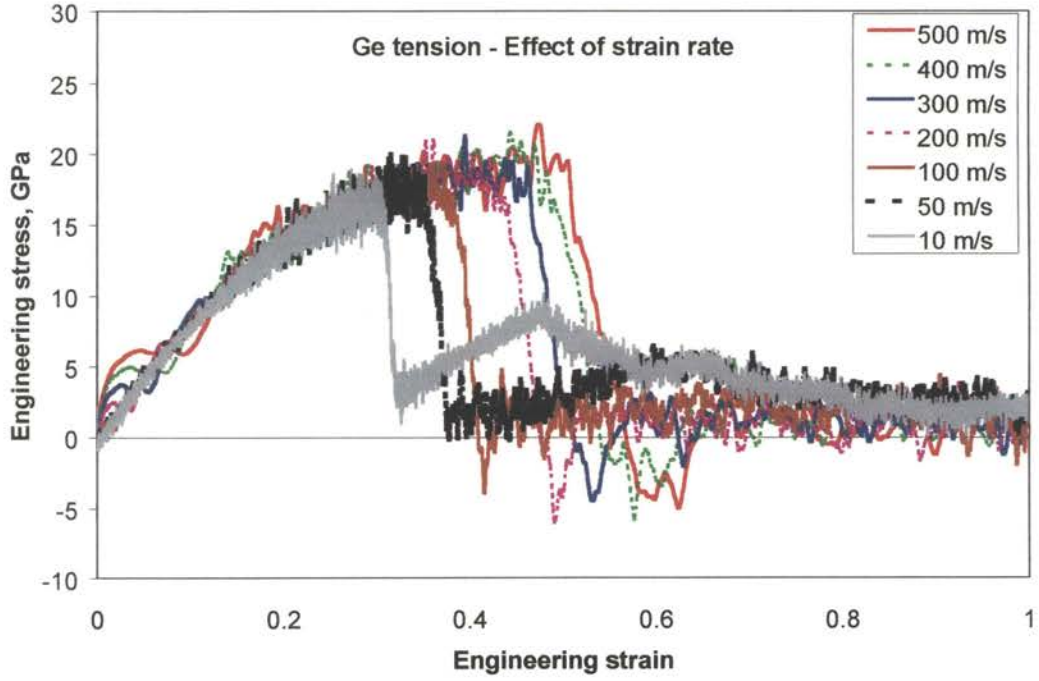

Figures 4.14 Engineering stress-strain curves for (a) Si and (b) Ge, respectively, at various strain rates

Figure 4.15 (a) shows the effect of strain rate on the measured ultimate tensile strength and elastic modulus for Si and Ge. The ultimate strength shows a decreasing trend with decreasing strain rate as was also observed from Figures 4.14 (a) and (b). The measured UTS decreases from ~24 GPa to ~21 GPa for Si and from ~22 GPa to ~19 GPa for Ge as the strain rate is decreased from 500 m/s to 10 m/s. The elastic modulus for both materials does not show a trend with strain rate but fluctuates between an upper and lower limit. It is possible that the elastic modulus is not affected by strain rate, which was also observed from the engineering stress-strain curves [Figures 4.14 (a) and (b)], where the initial linear part of the curves overlapped irrespective of the strain rate. The average elastic modulus (averaged over the measured elastic modulus at various strain rates) of Si and Ge in the [001] direction are estimated to be ~118 GPa and ~104 GPa which are in close agreement with those reported in the literature. Figure 4.15 (b) shows the effect of loading rate on the strain at ultimate strength point and the strain at fracture for Si and Ge. Both, the strain at UTS and the fracture strain decrease with decreasing strain rate.

Based on the data for fracture strain between 500 m/s and 10 m/s measured from the MD data, the fracture strain for Si and Ge was extrapolated to lower strain rate values. Figure 4.16 plots the effect of strain rate and strain at fracture for Si and Ge at strain rates down to 0.0001 m/s. The equations used for the extrapolation were evaluated from the best fit curves through the measured data from MD simulation [equations shown in Figure 4.16]. It can be seen that the strain at fracture decreases with decreasing strain rate. Consequently, the high fracture strain obtained from the MD simulations may relate to the high strain rates. It is possible that at high strain rates the temperature in the workmaterial increases significantly (without sufficient time for energy dissipation) resulting in the material behavior changing from brittle to ductile.

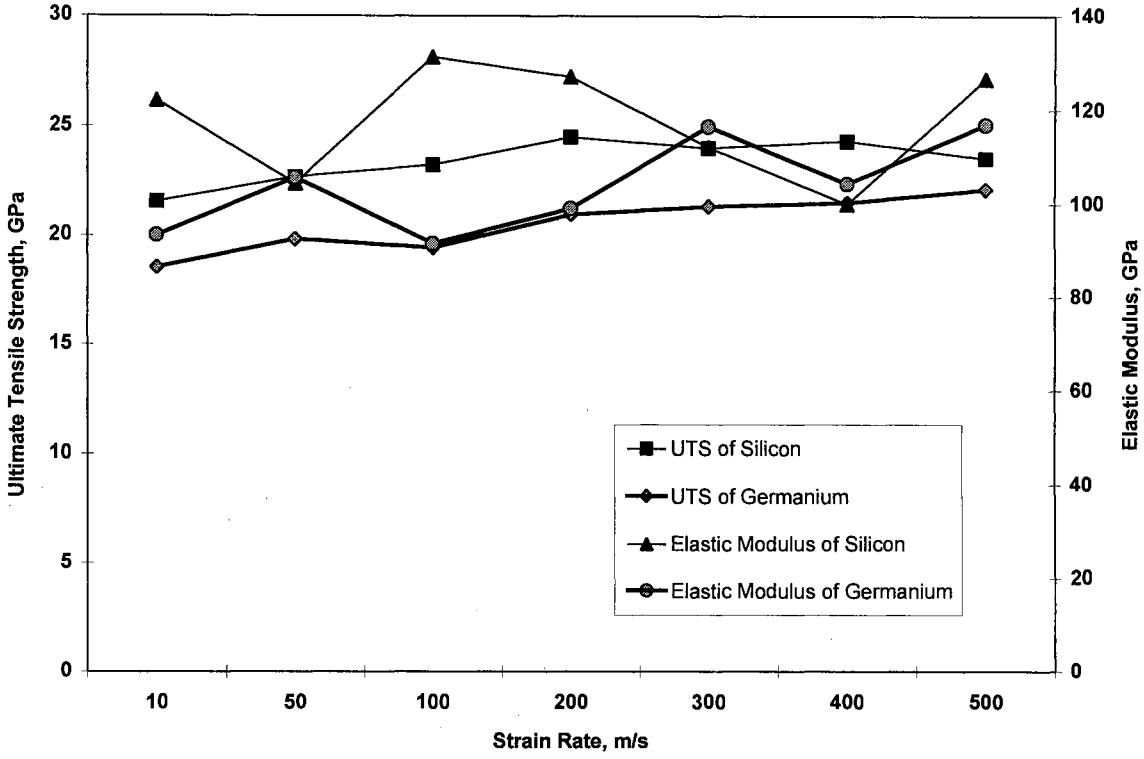

Figure 4.15 (a) Effect of Strain Rate on UTS and Elastic Modulus of Si and Ge

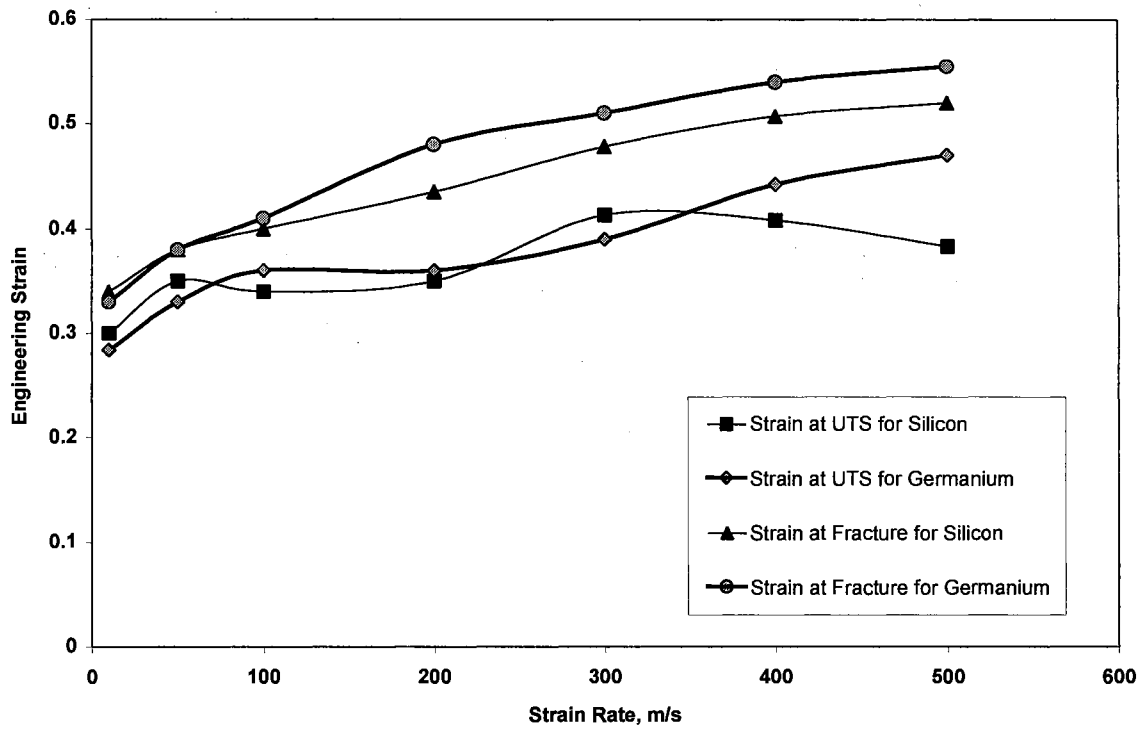

Figure 4.15 (b) Effect of Strain Rate on Strain at UTS and Fracture Strain

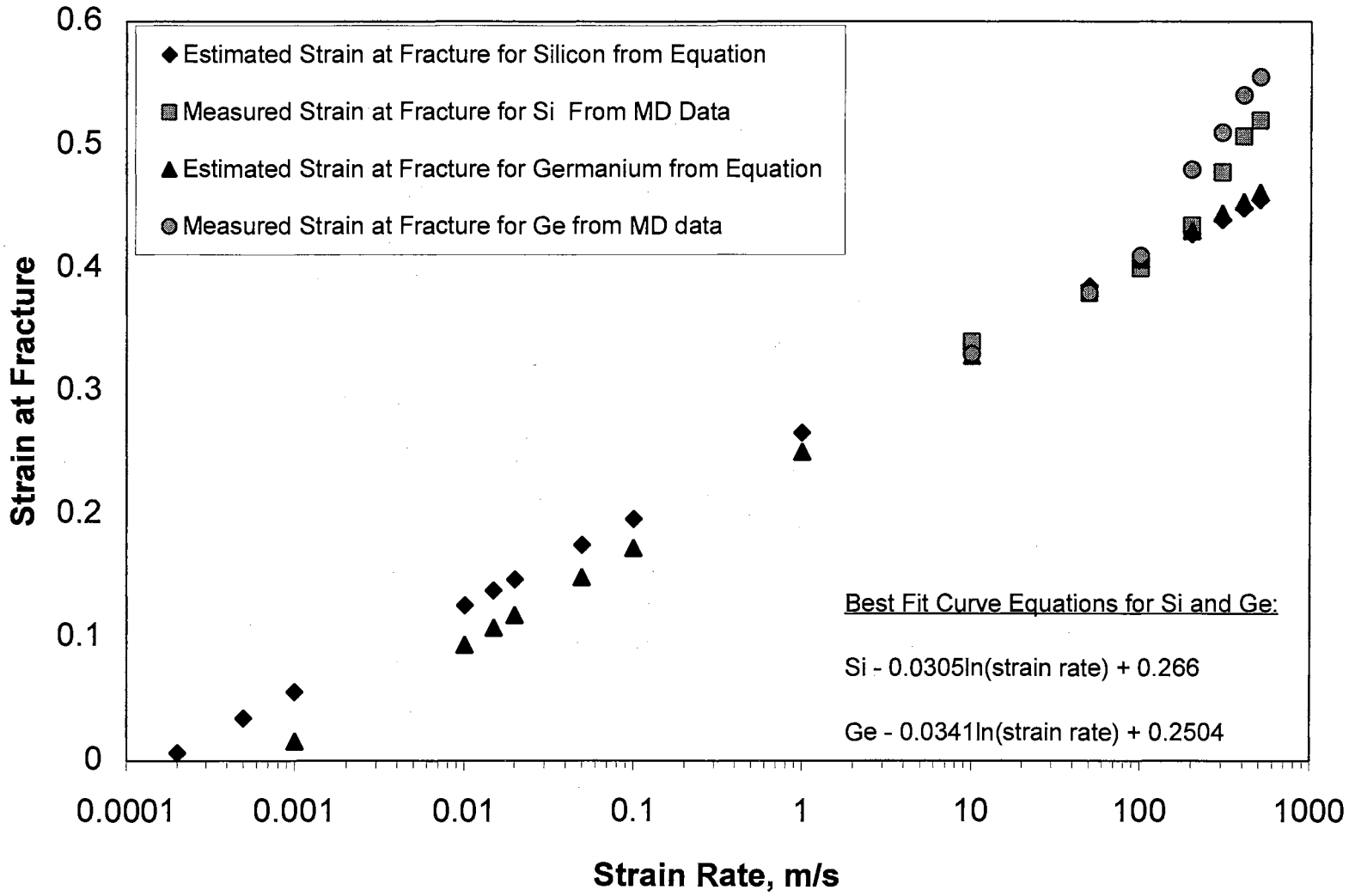

Figure 4.16 Effect of strain rate on fracture strain (extrapolated fracture strain values to lower strain rates)

MD simulations of uniaxial tension of an FCC (Ni) and BCC (Cr) material were conducted at three loading rates of 500 m/s, 250 m/s, and 100 m/s. This study was carried out specifically to investigate if the high stress-strain fluctuations observed with the BCC materials can be attributed to significant structural changes or due to an artifact at high loading rates (500 m/s) employed in the simulation. Figures 4.17 (a) and (b) show the variation of engineering stress-strain distribution at different loading rates for Cr and Ni, respectively. Both, Cr [Figure 4.17 (a)] and Ni [Figure 4.17 (b)], show an initial decreasing slope with increasing strain. They also show a decrease in the ultimate stress with decreasing loading rate as supported by both theory and experimentation (Hertzberg, 1996). The stress-strain distribution during the initial and final stages of tension overlap, irrespective of the strain rate.

Figure 4.17 (a) shows that the high fluctuations in the stress-strain curve for Cr at 500 m/s repeat themselves even at lower strain rates. For example, at a strain rate of 250 m/s for Cr, the stress fluctuates from point 'a' through 'd' finally reaching the maximum stress at 'e' before the stress decreases to zero [Figure 4.17 (a)]. Similar fluctuations can also be observed with other strain rates, namely 100 m/s and 500 m/s. However, the strain at which these fluctuations are observed seem to vary with strain rate. Based on this result, it appears that the high fluctuations in the stress-strain curve for BCC materials are not due to the high strain rates but due to the significant structural transformations observed with BCC materials in comparison to FCC materials as explained earlier.

In the case of Ni, a gradual and systematic drop in the ultimate tensile strength with decreasing strain rate is observed [Figure 4.17 (b)]. The ultimate tensile strength of Ni decreases by a factor of ~3 while the ultimate strength of Cr decreases by a factor <2 as the strain rate is reduced by 5 times. However, according to theory (Hertzberg, 1996), one would expect BCC metals to exhibit higher strain rate sensitivity than FCC metals. The

strain at which the ultimate strength is measured seems to remain constant for both BCC and FCC metals. These contradictions, observed with BCC materials, reascertain the possibility of lack of proper modeling of BCC metals using Morse type potential.

4.2.7. Conclusions

Molecular Dynamics (MD) simulations of uniaxial tension have been carried out at a constant rate of loading (500 m/s) on various single crystal materials, including FCC [Al, Cu, and Ni], BCC [Fe, Cr, and W], and covalently bonded [Si and Ge] materials to investigate the nature of deformation and fracture in these materials at the atomic scale. The following are some of the specific conclusions from the study.

1. Failure of the ductile materials was observed to be due to void formation, their coalescence into nanocracks, and subsequent fracture or separation. These observations are similar to their behavior at macroscale.

2. For FCC materials, considerable disorder in the gage section of the crystal is observed during the early stages of loading. Further loading resulted in the disorder spreading through the entire length of the workmaterial. In the case of BCC materials, the disorder is observed to be highly localized around the midplane of the workmaterial. The layers above and below the neck region are arranged perpendicular to the loading direction. The new crystal arrangement generates voids in the weak region.

3. No disorder was observed with Si and Ge until the maximum stress point was reached. Both, Si and Ge exhibited their brittle nature by displaying an extended elastic region and sudden failure by crack propagation after the maximum stress point was reached.

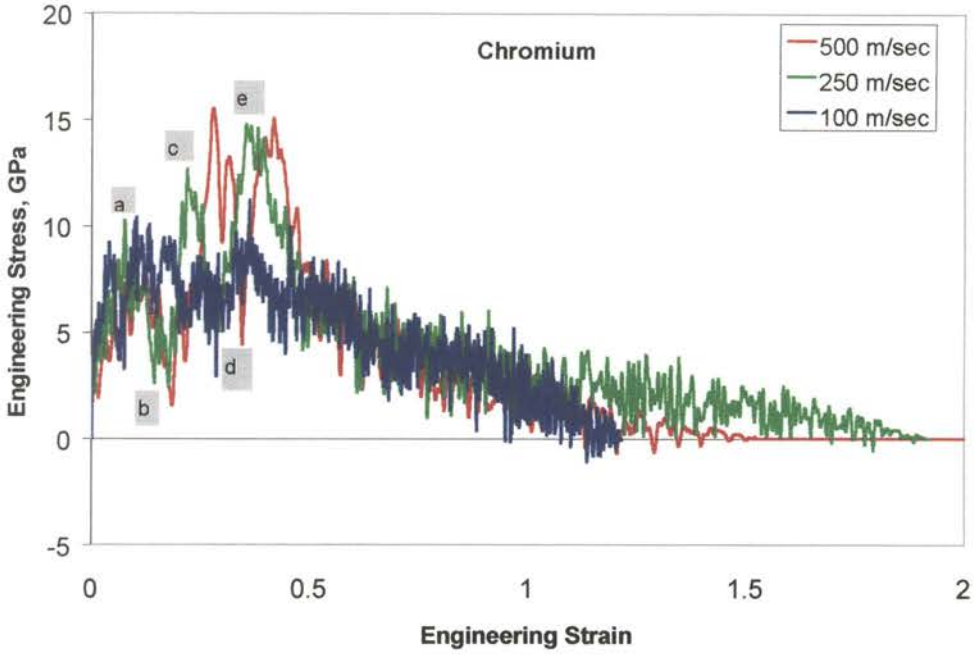

(a)

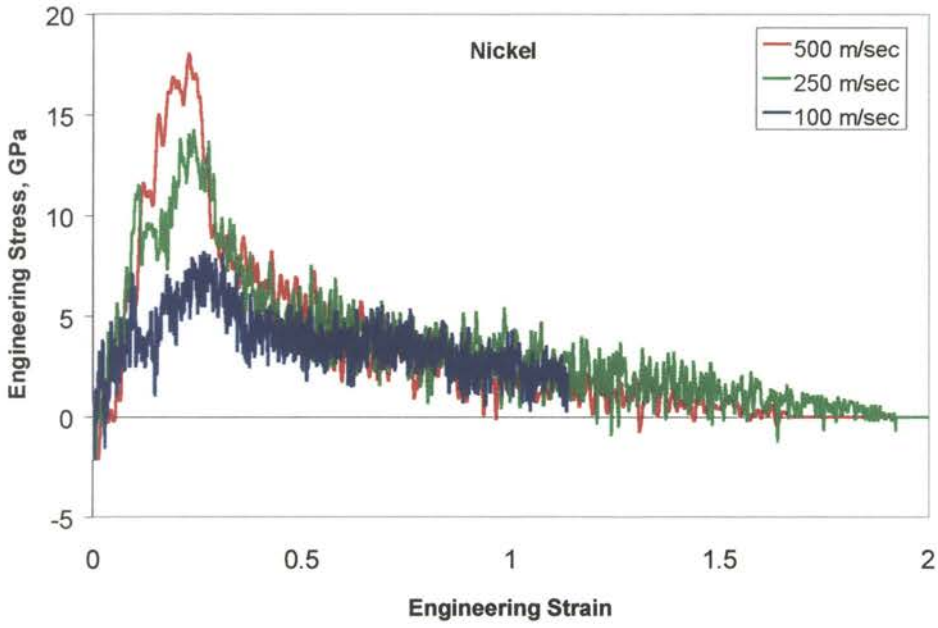

(b)

Figure 4.17 Variation of the engineering stress with strain at different loading rates (500 ms^{-1}, 250 ms^{-1} and 100 ms^{-1}) for (a) a BCC (Cr) and (b) an FCC (Ni) materials, respectively

4. The measured mechanical properties, including, elastic modulus and ultimate tensile strength of FCC materials and Si and Ge were observed to be in reasonable agreement with the values reported in the literature. However, the measured properties of BCC materials did not agree with the earlier reported results.

5. The effect of strain rate on the deformation behavior and measured properties was investigated by conducting MD simulations at lower strain rates (10 m/s). The deformation behavior of the gage section was observed to be similar irrespective of the strain rates. The ultimate tensile strength and the fracture strain exhibited a decreasing trend with decreasing strain rate. The elastic modulus was observed to be relatively constant irrespective of the strain rate. The high fracture strains at higher loading rates are attributed to the significant temperature rise of the specimen at higher loading rates.

6. While, good correlation was found between the D- and α-parameters of the Morse potential with the ultimate strength and the strain at failure for the FCC metals, no such correlation was found for the BCC metals. From this it appears that Morse potential may not represent the deformation behavior of the BCC metals as accurately as the FCC metals and an alternate potential may need to be considered.

4.3. MD SIMULATION OF NANOINDENTATION

4.3.1. Literature Review

Belak *et al.* (1993) reported MD simulation of nanoindentation of copper and silver (111) surfaces with a blunt indenter. The velocities used in the simulations were 1, 10,

and 100 m s^{-1}. An initial van der Waal's attraction followed by a linear increase in the load due to elastic response of the substrate was observed. The magnitude of the load was reported to be comparable to the experimental results in the literature using AFM's (Burnham et al., 1991; Salmeron et al., 1992). They reported the occurrence of a critical yielding phenomenon and a significant drop in the load after the tip had penetrated ~1.5 layers into the substrate. Pile up of atoms around the tool tip was observed as the tool was indented further into the substrate (~7 layers). The substrate was reported to show elastic-plastic deformation. The cross sectional plots through the tool tip showed the plastic deformation to be limited to a few lattice spacing surrounding the tip.

Landman and Luedtke (1991, 1996) conducted MD simulations of indentation on a gold substrate using a nickel tool. A gradual increase in the force between the tip and the substrate was observed followed by a region of instability. This increase was interpreted as an increase in the attractive force between the tip and the substrate. They noted that the gold atoms under the tip were displaced by ~0.2 nm towards the tool tip. Jump-to-contact (JC) was reported at a tip to substrate separation distance of 0.42 nm and this was accompanied by an increase in the attractive force.

Yan and Komvopoulos (1998) conducted MD simulations to analyze the deformation occurring during indentation of a dynamic substrate by a single atom or hard tip. They also studied the effects of substrate temperature and indentation speed on the force, deformation behavior, and energy dissipation. In their study of the single atom indentation process, they used both argon and copper as the substrates when a hard tip was used. They reported a hysterisis in the normal force versus separation distance curve for both cases (atom or rigid tip as indenter) studied. The direction of irreversible deformation coincided with the macroscopic plastic flow. They observed the material differences to exhibit a strong influence on the force-distance curve.

Buldum and Ciraci (1998) conducted MD simulation of nanoindentation and sliding of a nickel tip on a copper substrate. Specifically, they conducted tests with a sharp nickel (111) tool on copper (110) surface and a blunt nickel (001) tip on copper (001) surface. An Embedded atom potential was used to simulate the metallic bonds of nickel and copper. In the case of a sharp tool, movement of atoms from the tool tip towards voids in the substrate at a separation distance of 0.43 nm was reported. The forces were reported to be almost negligible at large separation distances and increased with decreasing separation distance between the tool tip and the workmaterial. They also reported the phenomenon of JC to take place as the tip was lowered into the substrate. When the tool was pulled away from the substrate, stretching of the junction formed by the indenter and consequent neck formation were reported. Contrary to the sharp tool, the JC was reported to initiate from the softer material (substrate) when a blunt tip was used in the simulations. Multiple JC's were observed when a sharp tip was used, in contrast to the single JC using a blunt tip. A quasi periodic variation in the force was reported during sliding of the sharp nickel tip on the copper substrate. This was attributed to the stick-slip process involving phase transitions.

Kallman et al. (1993) conducted MD simulations of silicon indentation and report results for both amorphous and single crystal silicon. The Stillinger-Weber potential was used to model the many-body silicon potentials. They observed the absence of crystallization for the amorphous solids while the crystalline phase exhibited near melting and a tendency to transform to the amorphous phase close to the indenter surface. The nanoyield strength of silicon is reported to be between 25 and 250 kbars depending on the structure, rate of deformation, and sample temperature. Brenner et al. (1996) conducted MD simulations of silicon (111) surface using an atomically sharp diamond tip to study

the tool wear in silicon nanoindentation. The tip is reported to maintain its integrity through out the simulation.

Rentsch et al. (1995) conducted MD simulations of silicon indentation using the Tersoff potential to study the influence of machining on the surface integrity of brittle materials. Indentations were performed with various indenter radius (r) and depth (d) combinations. They report a dependency of crack initiation with indenter tip radius, with no crack generation for indenters with a radius less than 2 nm and crack initiation for tips with a radius equal to or greater than 2 nm. The material in the direct vicinity of the tip is reported to deform plastically with elastic deformation taking place deeper into the workmaterial. They report the presence of an unstructured amorphous material in the vicinity of the 1 nm radius indent. On the other hand, the presence of a more crystalline looking phase beneath the tip is reported with the 2 nm and 5 nm radius indents.

Zhang and Tanaka (1999) and Cheong and Zhang (2000) have conducted MD simulation of nanoindentation of silicon single crystals. Their results show that elastic deformation occurs only in an extremely narrow regime, with no indication of dislocation generation. Densification beneath the indenter was found to involve a phase transition from α to β-silicon induced by the large pressures present in the simulation. The authors reach this conclusion by monitoring the positions of the atoms within the model crystal and noting that the distributions of Si-Si bond lengths and the number of nearest neighbors changes from those characteristics of α-silicon to a broader distribution that can be viewed as consisting of components of both α and β forms. They report that the effect of indenter edge radius and the indentation speed are negligible when the maximum indentation strain is less than unity.

4.3.2. Methodology of MD Simulation

Figure 4.18 is a schematic of the workmaterial and the indenter used in the MD simulations of nanoindentation of different workmaterials showing various regions of interest. The workmaterials studied in this investigation include FCC metals (aluminum, copper, silver, and nickel) and semiconductors (silicon and germanium). The FCC metals were modeled using a pairwise sum of Morse potentials while Si and Ge were modeled using the many-body type Tersoff potential. A digital alpha-workstation (Model 500) with a clock speed of 600 MHz was used for the simulations. The effect of workmaterial type, indentation depth, and indenter geometry were studied. The crystal was set up with the cube orientation and indentation force was applied along the [001] direction. Table 4.3 gives the dimensions of the indenter and the workmaterial, indenter geometry, indentation depth, rate of loading, bulk temperature etc.

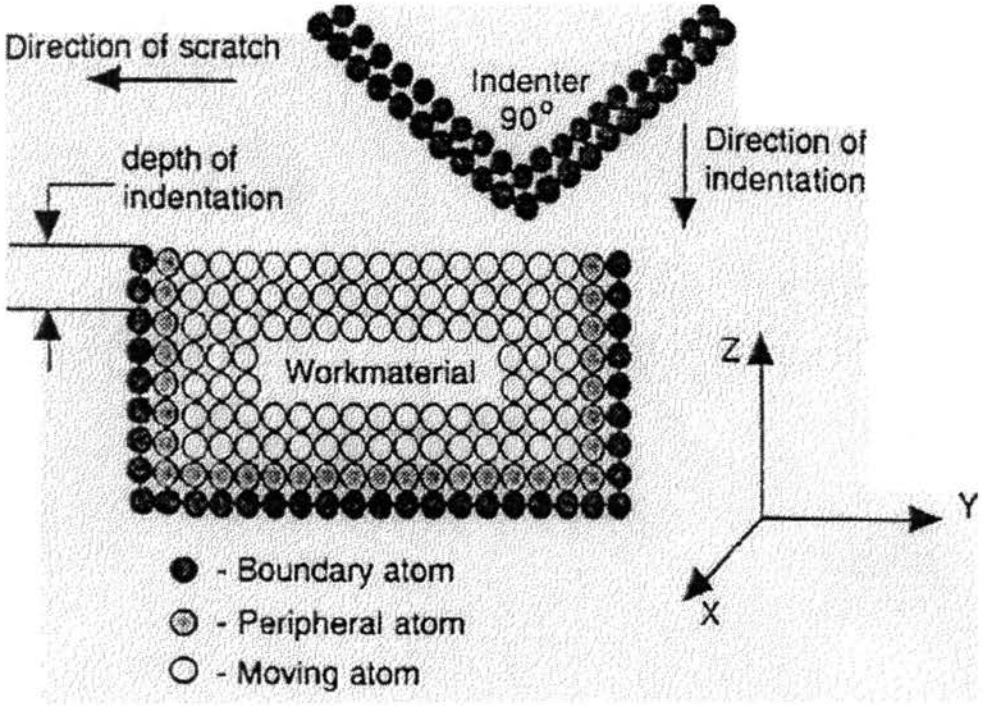

Figure 4.18. Schematic of the nanoindentation model

Table 4.3: Computational parameters used in the MD simulation of nanoindentation

Configuration	3-D indentation
Potential used	Morse and Tersoff potentials
Workmaterial dimensions	3a x 15a x 10a for Si and Ge 4a x 25a x 25a for Al, Cu, Ag, and Ni a - lattice constant
Indenter included angle	90° - 150°
Indentation Depth	0.543-2.172 nm
Indentation Speed	500 m/sec
Bulk temperature	293 K

4.3.3. Effect of Workmaterial Type

4.3.3.1. On the nature of deformation

Figures 4.19 (a) - (d) and 4.20 (a) - (d) are MD simulation plots of nanoindentation of aluminum and silicon, respectively, showing various stages of the nanoindentation process. Figures 4.19 (a) and 4.20 (a) show the initial set-up of the workmaterial before commencing the indentation process. Figures 4.19 (b) and 4.20 (b) show an intermediate stage during the indentation process while Figures 4.19 (c) and 4.20 (c) show the indenter at maximum indentation depth. Figures 4.19 (d) and 4.20 (d) show the workmaterial structure after the indenter was retracted from the workmaterial.

Comparison of Figures 4.19 and 4.20 shows significant differences in the nature of deformation in these two materials owing to the differences in their ductilities. In the case of aluminum, significant dislocation generation can be seen at ~ 45° to the indentation direction even during the early stages of the indentation process [Figure 4.19 (b)]. As indentation progresses further dislocations are generated and they propagate on either sides of the indent deep into the workmaterial at ~ 45° [Figure 4.19 (c)]. Figure 4.19 (c)

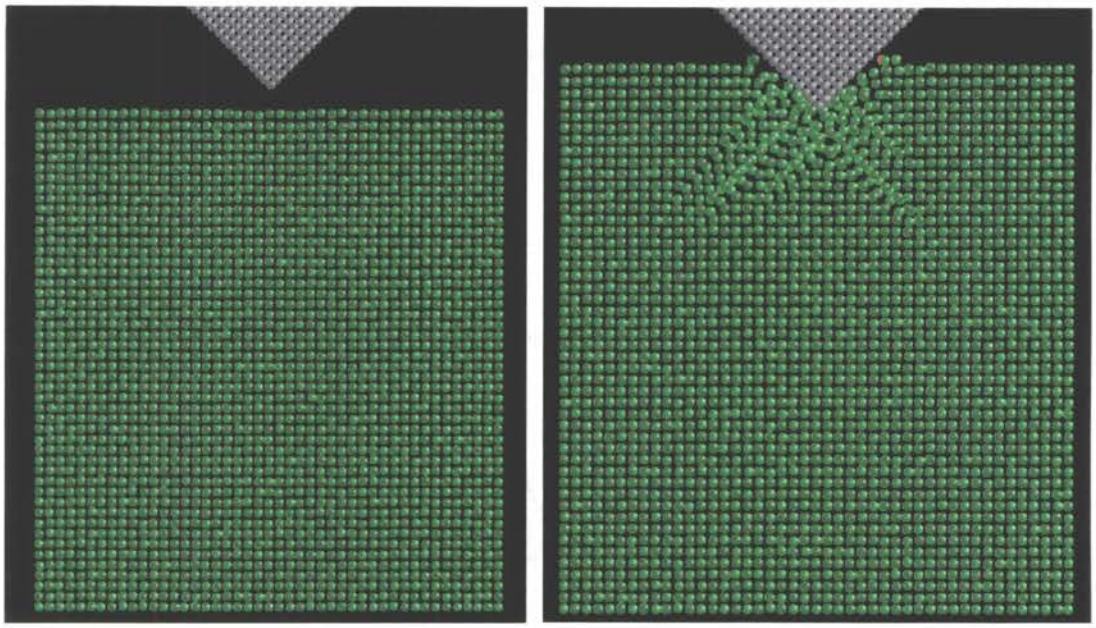

(a) Before Indentation (b) Indentation depth: 0.8 nm

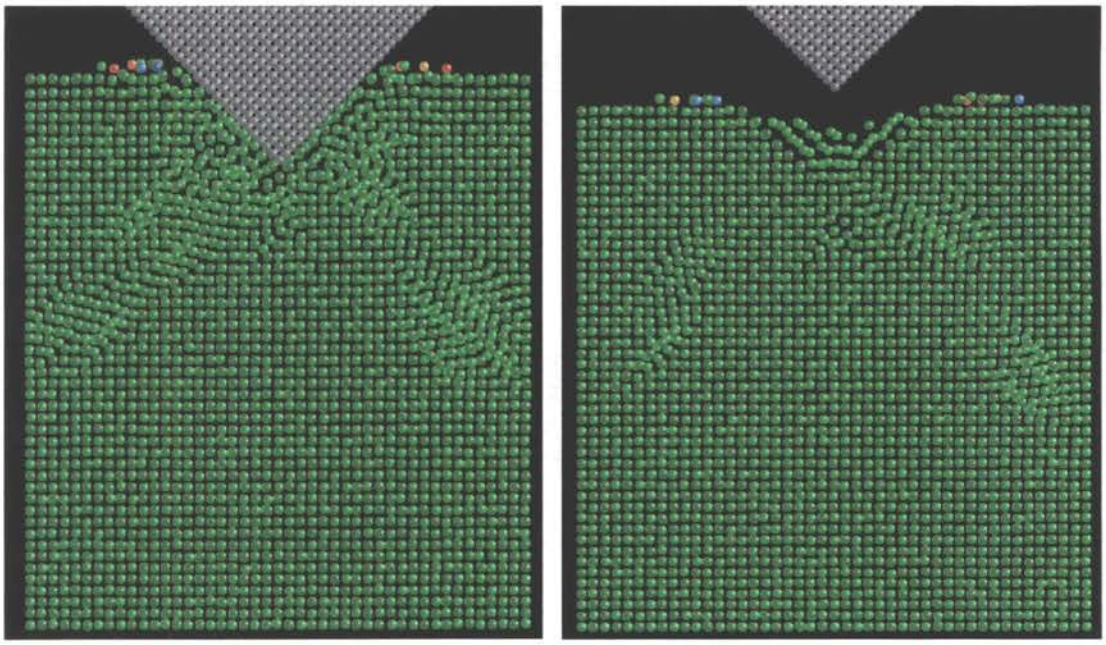

(c) Maximum Indentation Depth (1.62 nm) (d) After Retraction

Figure 4.19 (a) - (d) MD Simulation Plots of Nanoindentation of Aluminum

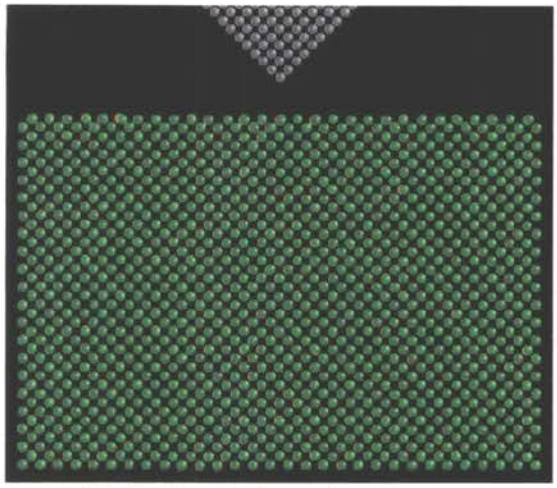

(a) Before Indentation

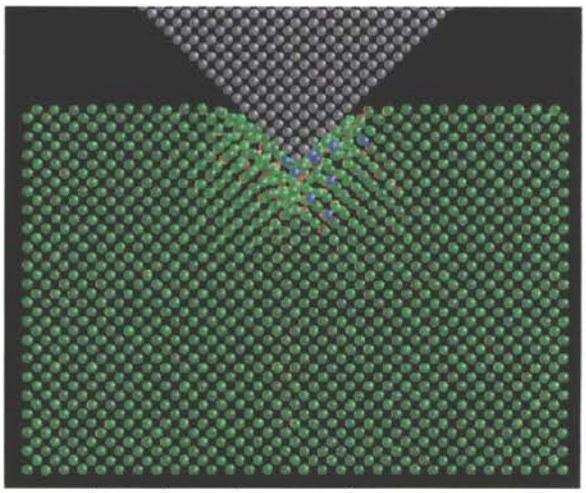

(b) Indentation Depth: 0.5 nm

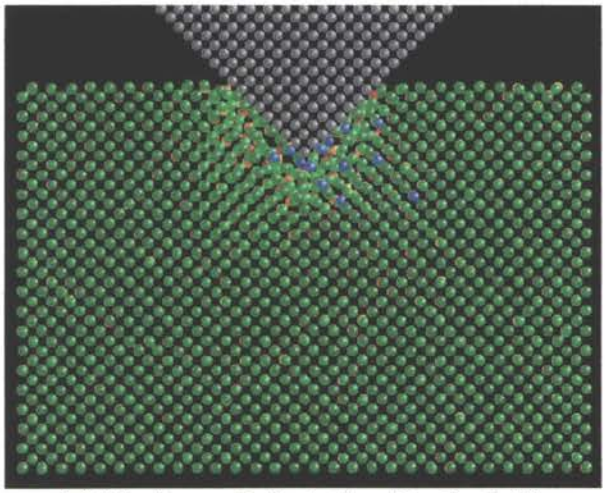

(c) Maximum Indentation Depth: 1.09 nm

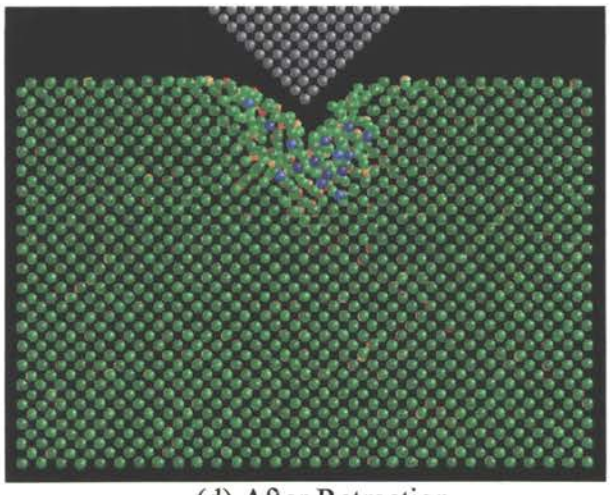

(d) After Retraction

Figures 4.20 (a) - (d) MD Simulation Plots of Nanoindentation of Silicon

shows the indenter at its maximum indentation depth. Plastic deformation around the indent can be seen, in addition to the generation and propagation of dislocations ahead of the tool and into the workmaterial. As the indenter was retracted from the workmaterial, significant elastic recovery of the indent area was observed [Figure 4.19 (d)]. The dislocations in the workmaterial observed at maximum indentation depth [Figure 4.19 (c)] recover elastically and terminate at the free surface of the workmaterial or the indent zone. Also, the plastic deformation observed around the indenter, at maximum indentation depth [Figure 4.19 (c)] is no longer present after retraction [Figure 4.19 (d)]. Instead, the area around the indent has regained its original crystal structure due to elastic recovery. A significant reduction in the indent area can also be observed by comparing Figures 4.19 (c) and (d). Nanoindentation of the other FCC metals, namely, copper, silver, and nickel exhibited similar deformation characteristics and the corresponding MD simulation plots of nanoindentation of these metals are given in Appendix II.

In contrast, no dislocation generation was observed with silicon even at maximum indentation depth [Figures 4.20 (b) and (c)]. The workmaterial region immediately around the indenter has undergone significant plastic deformation and subsurface deformation. However, the rest of the workmaterial maintains its crystal structure. For the case of aluminum, the dislocations generated at ~45° to the indentation direction were observed to penetrate deep into the workmaterial requiring the size of the workpiece to be increased considerably to avoid boundary effects. This was not found to be the case with silicon due to its limited ductility. Figure 4.20 (d) shows the silicon workmaterial after the indenter was retracted from maximum indentation depth. In contrast to aluminum, silicon exhibits limited elastic recovery. It will be shown based on the force curves that silicon also exhibits a tendency to recover elastically but to a limited extent compared to aluminum and other metals studied in this investigation. The plastically deformed zone around the indent has been referred to as amorphous silicon or crystalline β-silicon by

several researchers based on experimentation and simulation results. The highly compressed region underneath the indent is attributed here to the pressure-induced phase transformation of silicon under high hydrostatic pressure present under the tool during nanoindentation. The deformation mechanism of germanium upon nanoindentation was observed to be similar to that of silicon. A significantly plastically deformed layer around the indent was observed at maximum indentation depth and did not recover completely upon retraction of the indenter from the workmaterial. The MD simulation plots corresponding to nanoindentation of germanium are given in Appendix II.

4.3.3.2. On the pressure induced phase transformation in silicon

The damaged layer underneath the indenter in silicon nanoindentation has been attributed to the pressure induced phase transformation (from α to β-silicon) and/or an amorphous structure in various investigations on indentation (Zhang and Tanaka, 1999; Cheong and Zhang, 2000) and nanometric cutting (Tanaka et al., 1999; Belak et al., 1993). Figures 4.21 (a) and (b) are schematics of the α- and β-silicon structures. At atmospheric pressure, β-silicon has a lattice constant of 5.43 A, a bond distance of 2.352 A, and an atomic volume of 18.38 A^3. The high-pressure β-silicon phase has a body-centered tetragonal structure (β-tin structure) with the following lattice constants a = 4.686 A, c = 2.585 A, and c/a = 0.5516. In this structure, each silicon atom has four nearest neighbors at 2.43 A and the two next neighbors are at a distance of 2.585 A. The atomic volume is 14.19 A^3. The α to β transformation, therefore, results in a significant reduction in the atomic volume from 18.38 A^3 to 14.19 A^3 per atom or a densification reduction of ~22.8% (Donohue, 1974). Although, the Tersoff potential used in the present study does not include the long-range forces required to properly simulate sharp phase transitions, it should be possible to observe some of these features in the MD simulation of nanometric cutting of silicon, at least qualitatively.

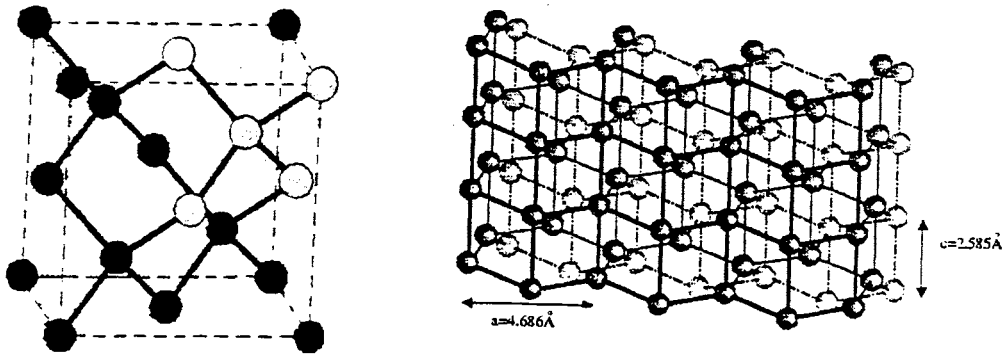

(a) (b)

Figures 4.21 Schematic of (a) crystal structure of α - silicon phase (diamond cubic structure) and (b) crystal structure of β silicon phase (after Cheong and Zhang, 2000)

Donohue (1974) and Recently Cheong and Zhang (2000) showed that the phase transformation from α- to β-silicon is accompanied by a change in the interatomic distance from 0.235 nm (diamond cubic structure) to 0.243 nm for 4 bonds and 0.258 nm for the remaining 2 bonds (β-silicon), resulting in a change in the coordination number between silicon atoms from 4 to 6. In this investigation, based on Cheong and Zhang's work (2000), the distribution of atoms in three dimensions at various interatomic distances and coordination were determined from the MD simulation data before and after nanoindentation in the region surrounding the indent.

Figures 4.22 (a) and (b) are plots of the distribution of atoms at various interatomic distances and the coordination structure for silicon at three stages during the indentation process (before, at maximum indentation depth, and after retraction) in the subsurface

deformed zone underneath the indenter. The number of atoms at various interatomic distances and the coordination number are normalized with respect to the corresponding values measured before indentation. Figure 4.22 (a) shows that before indentation, all the atoms are positioned at an equilibrium distance of 0.235 nm corresponding to α-silicon (diamond structure). At maximum indentation depth [Figure 4.22 (a)], a significant decrease in the number of bonds at 0.235 nm and a corresponding increase in the number of bonds at 0.243 nm and 0.258 nm interatomic distances can be noted. After retraction of the indenter from the workmaterial, the β-silicon remains stable and a small increase in the number of atoms at 0.243 nm interatomic distance can be seen [Figure 4.22 (a)]. Figure 4.22 (b) shows a high peak at 4 and a smaller peak at 2 coordination before nanoindentation. The peak at 4 for silicon is indicative of a covalently bonded system with a diamond cubic structure. The peak at 2 is indicative of the termination of bonds (dangling bonds) on the surface and sides of the workmaterial. At maximum indentation depth, the number of atoms with 4 coordination was found to decrease with a corresponding increase in the number of atoms of 5 and 6 coordination. A relatively small increase in the 7 and 8 coordination was also observed. The 5 and 6 coordination structure remain stable even after retraction [Figure 4.22 (b)].

Raghavachari and Logovinsky (1985) have shown by *ab initio* molecular orbital calculations that numerous other coordination, n (n up to 30) of silicon (such as 5 in this case) are possible under different conditions leading to the formation of various types of clusters, crystals, and surfaces of silicon. It may be noted that although silicon and diamond are both covalent, this is where their similarity ends. For example, within the diamond structure no other transformations are possible, whereas the Si (111) surfaces are known to undergo reconstruction into a 7x7 symmetric configuration (Lifshits and Saranin, 1994).

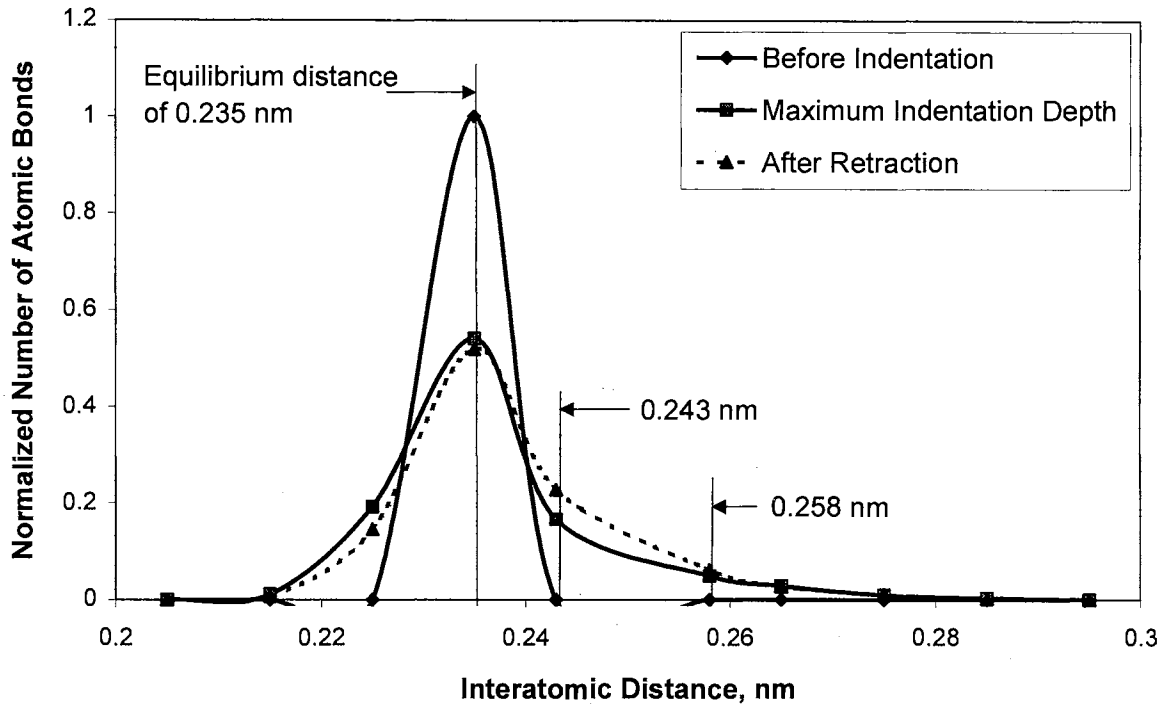

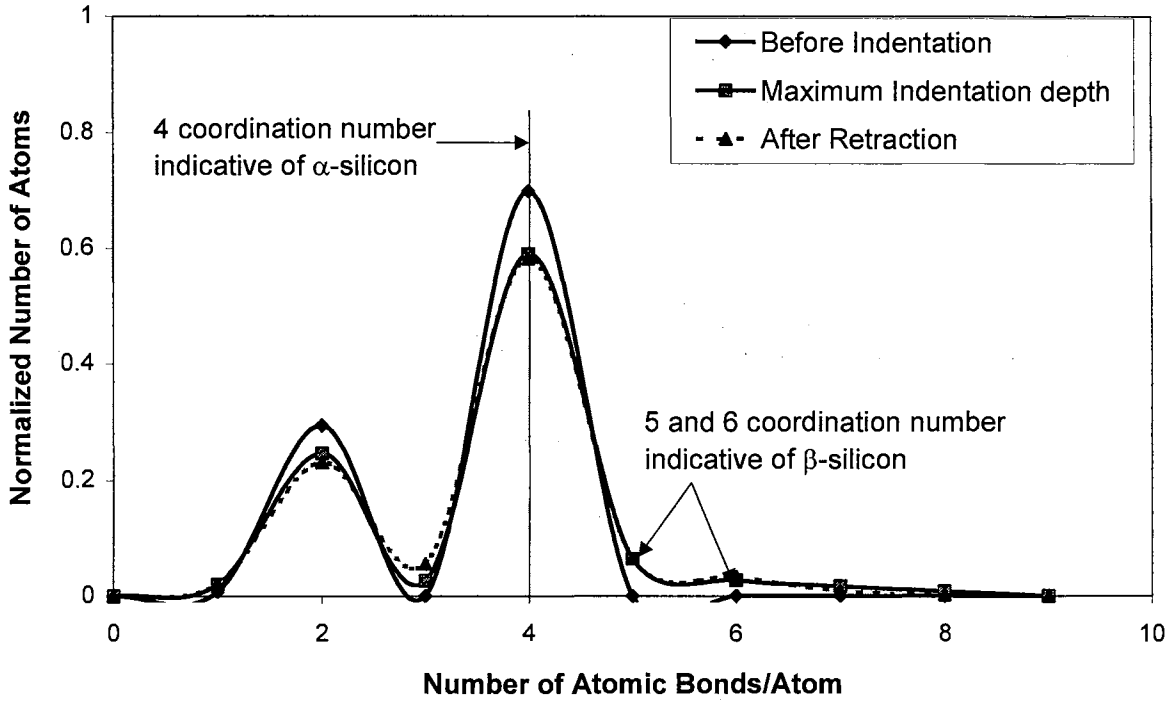

Figures 4.22 (a) and (b) Distribution of (a) atoms at various interatomic distances and the and coordination structure for silicon during the indentation process in the subsurface deformed zone underneath the indenter

The results presented here [Figures 4.22 (a) and (b)] indicate the possibility that the material around and underneath the indenter in the case of silicon can undergo a structural transformation (from α to β-silicon) and a significant densification as a consequence of nanoindentation. Without the presence of long-range forces in the Tersoff potential, a sharp, unequivocal phase transition may not be observable in the MD simulations. The existence of such a phase change can only be inferred by the broadened distributions seen in Figures 4.22 (a) and (b) and by the lack of elastic response of the lattice upon indentation and machining. Similar conclusions have previously been drawn by Zhang and Tanaka (1999) and Cheong and Zhang (2000).

This highly densified and not so well ordered structure underneath the indenter is also referred to as an amorphous structure by some researchers. Whether or not this material is body centered tetragonal or amorphous structure is an important side issue, as evidence was presented for the existence of both these forms using TEM (Pharr et al., 1991; Puttick et al., 1994; Shibata et al., 1994; Kunz et al., 1996). However, based on the distribution of atoms in three dimensions at various interatomic distances and the coordination numbers, it appears that the highly densified material underneath the indenter appears to be the phase transformed body centered tetragonal structure. This does not mean that there is no formation of amorphous structure in nanoindentation of silicon but merely states that at this time no means is available, to the knowledge of the author, for evaluating this aspect using the MD simulation results.

4.3.3.3. On the nature of forces

Figures 4.23 (a) to (c) are the force-displacement curves obtained in MD simulation of indentation for different materials, namely, aluminum, copper, silver, nickel, silicon, and germanium, respectively. They provide the raw data for further analysis.

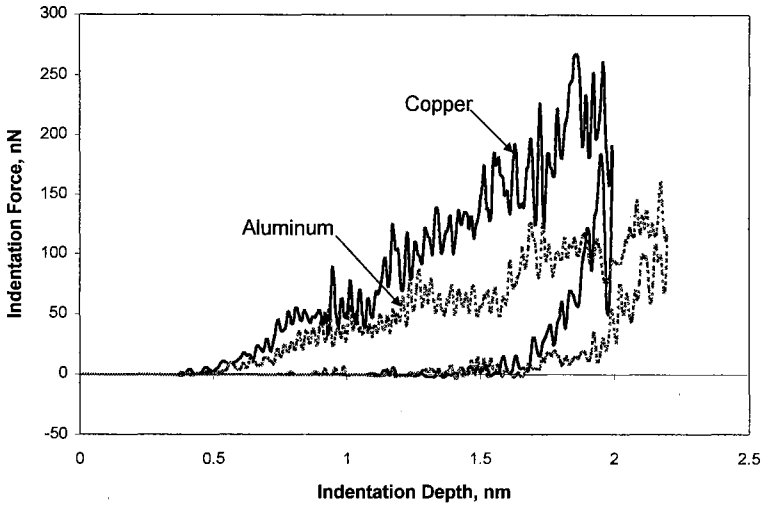

4.23 (a) Indentation Force Curves for Aluminum and Copper

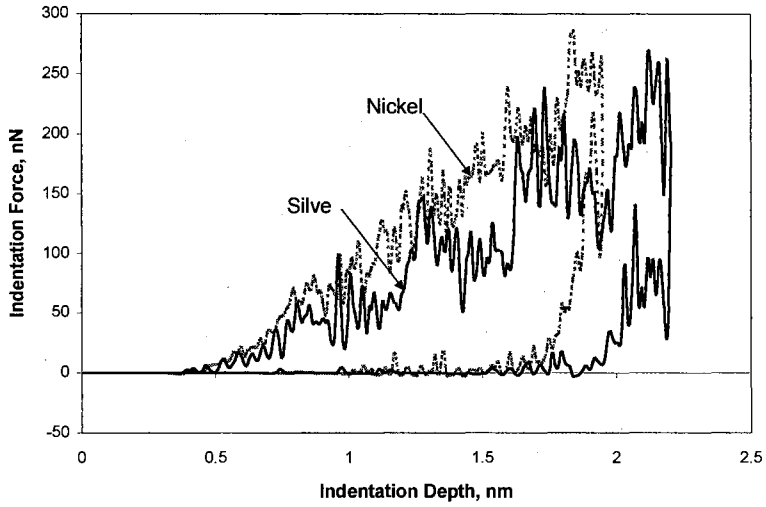

4.23 (b) Indentation Force Curves for Silver and Nickel

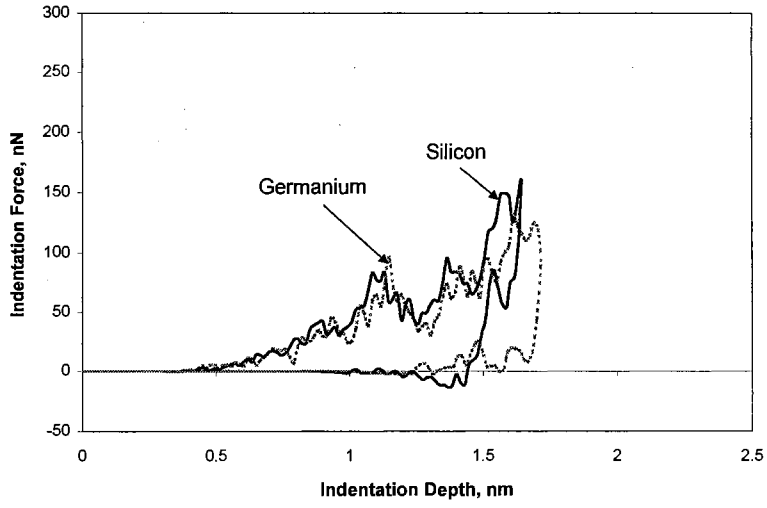

4.23 (c) Indentation Force Curves for Silicon and Germanium

During indentation, the indentation force increases rapidly to a maximum and then drops back to zero as the indenter is retracted from the workmaterial. The increase in the indentation force is essentially uniform exhibiting minor fluctuations. The force fluctuations during the indentation process are significant in the case of metals [Figures 4.23 (a) and (b)] compared to silicon and germanium [Figure 4.23 (c)]. This can be attributed to the extensive dislocation generation observed with the metals compared to the semiconducting materials. Once the indenter has moved through the specified indentation distance, it was retracted from the workmaterial. The force corresponding to this segment of the simulation drops to zero as the indenter-work separation increases. Hysterisis in the indentation-retraction curve can also be seen.

In general, indentation tests are conducted at constant load. However, in the present investigation, a constant velocity condition is used instead for convenience. Consequently, the indentation force is taken as the average of the forces during the entire indentation process. The hardness of the workmaterial is evaluated as the average force over the contact area of the indenter with the workmaterial. Table 4.4 summarizes the results of the MD simulation studies of nanoindentation conducted on different workmaterials. It shows the magnitude of the indentation hardness based on penetration depth (H_{PD}), indentation hardness based on corrected depth (H_{CD}), and elastic recovery for various materials. Indentation hardness based on the corrected depth corresponds to the ratio of the average force over the contact area where the contact area is evaluated based on the corrected depth. The corrected depth corresponds to the indent depth at zero load just prior to separation during retraction as suggested by Pethica et al. (1983). The hardness values of metals are close to their theoretical hardness values. Belak et al. (1993) reported a hardness of 5.4 GPa in the MD simulation of indentation of silver substrate, close to the value reported in this study (Table 4.4). Pethica et al. (1983) reported the hardness of silicon to be 19 GPa, which is in agreement with the value

reported here. The hardness value of silicon is also comparable to the hardness values reported by Bhattacharya and Nix (1988) [~11 GPa] and Doerner and Nix (1986) [~14 GPa]. The elastic recovery is considered to be the depth at which the force curve corresponding to the retraction part reaches zero (i.e., indent depth - corrected depth). Comparison of Figures 4.23 (a) - (c) suggests significant differences in the elastic recovery of the various materials with the maximum and the minimum elastic recovery observed with aluminum and germanium (also from Table 4.4).

Table 4.4. MD simulation results of nanoindentation

Material	H_{PD}	H_{CD}	% Elastic Recovery
Al	4.11	7.08	32.7
Ag	6.66	9.48	22.6
Cu	8.52	13.1	26.9
Ni	10.6	15.1	21.3
Si	19.1	24.8	18.42
Ge	13.52	16.0	12.4

4.3.4. Effect of Depth of Indentation

MD simulations of nanoindentation of silicon were conducted for various indentation depths, namely, 0.543 nm, 1.086 nm, 1.629 nm, and 2.172 nm, respectively to study the effect of depth of indentation on the mode of deformation, phase change, indentation hardness, and elastic recovery. Figures 4.24 (a) - (d) show the indenter at various indentation depths during nanoindentation of silicon. The degree of plastic

deformation underneath the indenter can be observed to increase with increasing indentation depth. Figure 4.25 shows the indentation-retraction force curves for the four indentation depth simulations. The initial part of the indentation force curve overlap each other indicating minimum statistical error in the force data collected based on different simulations. The maximum indentation force increases with increasing indentation depth while the elastic recovery or the retracted depth decreases with increasing indentation depth. Figure 4.26 shows the variation of the indentation hardness evaluated based on indentation depth and corrected depth and the % elastic recovery with depth of indentation. All three quantities decrease as the indentation depth increases. The hardness shows a constant decrease with increasing indentation depth indicating a size effect. However, the elastic recovery shows a significant decrease initially as the depth is increased from 0.543 nm to 1.086 nm. Further increase in the indentation depth results in a relatively smaller decrease in the elastic recovery. This suggests that at low indentation depths the deformation of silicon is highly elastic and as the indentation depth increases the plastic component of deformation increases significantly relative to the elastic component. Figures 4.27 (a) and (b) are plots of the distribution of atoms at various interatomic distances and the coordination structure for silicon at maximum indentation depth in the subsurface deformed zone underneath the indenter for various indentation depths. The degree of phase transformation from α- to β-silicon can be observed to increase with increasing indentation depth. This can be attributed to the constant increase in the magnitude and radius of the hydrostatic pressure zone with increasing indentation depth. Consequently, the degree of phase transformation from α- to β-silicon increases with increasing indentation depth. It should also be noted that the phase transformed layer remained stable even after retraction under all depths studied.

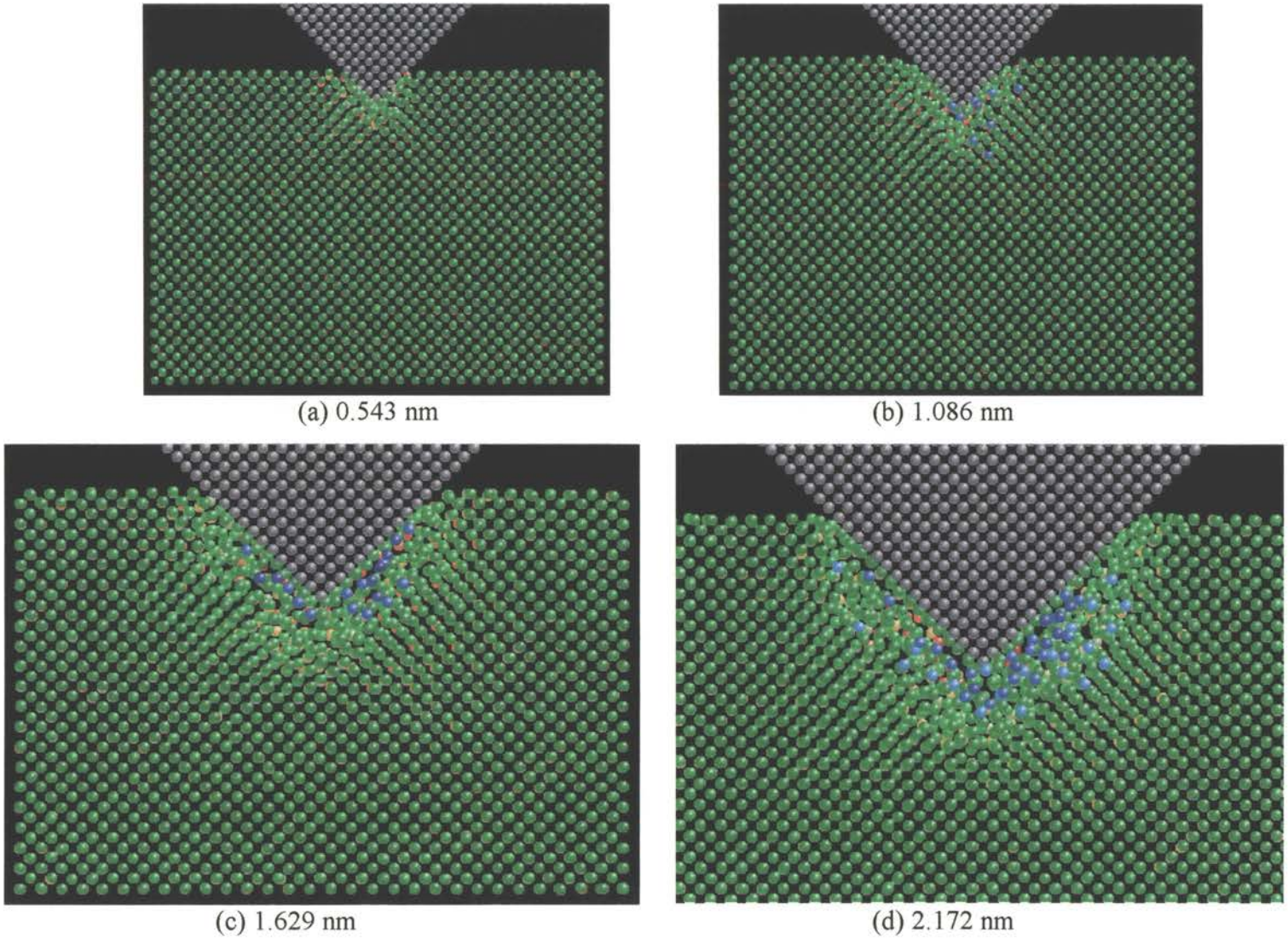

(a) 0.543 nm

(b) 1.086 nm

(c) 1.629 nm

(d) 2.172 nm

Figure 4.24 (a) - (d) Effect of Indentation Depth in Nanoindentation of Silicon

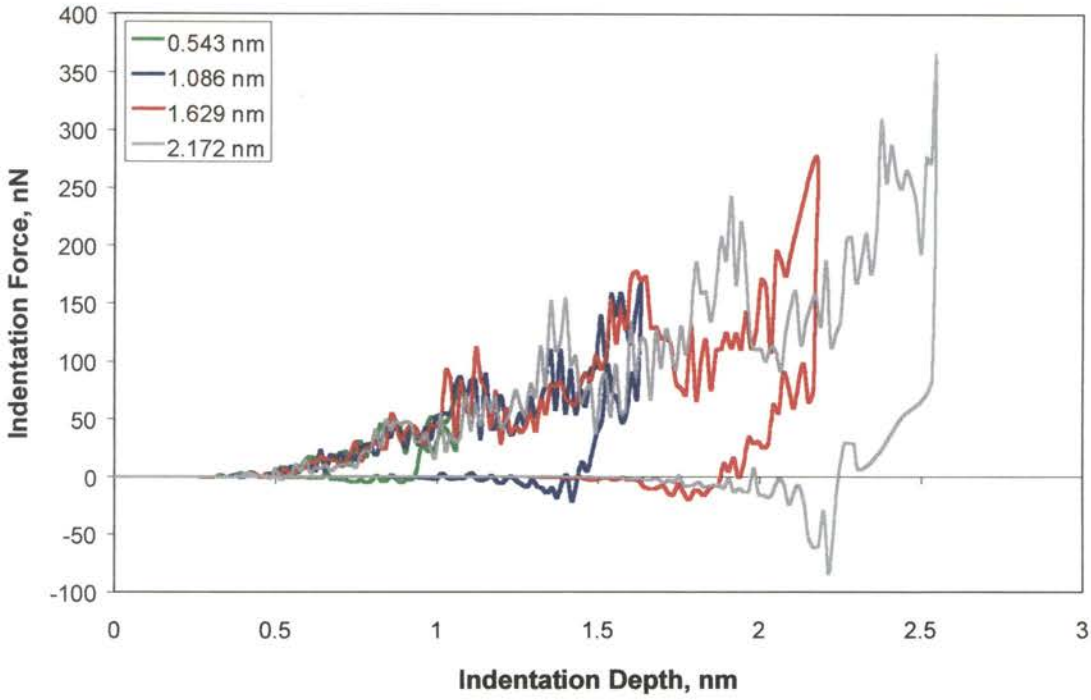

Figure 4.25 Effect of Depth of Indentation On Indentation - Retraction Force Curves

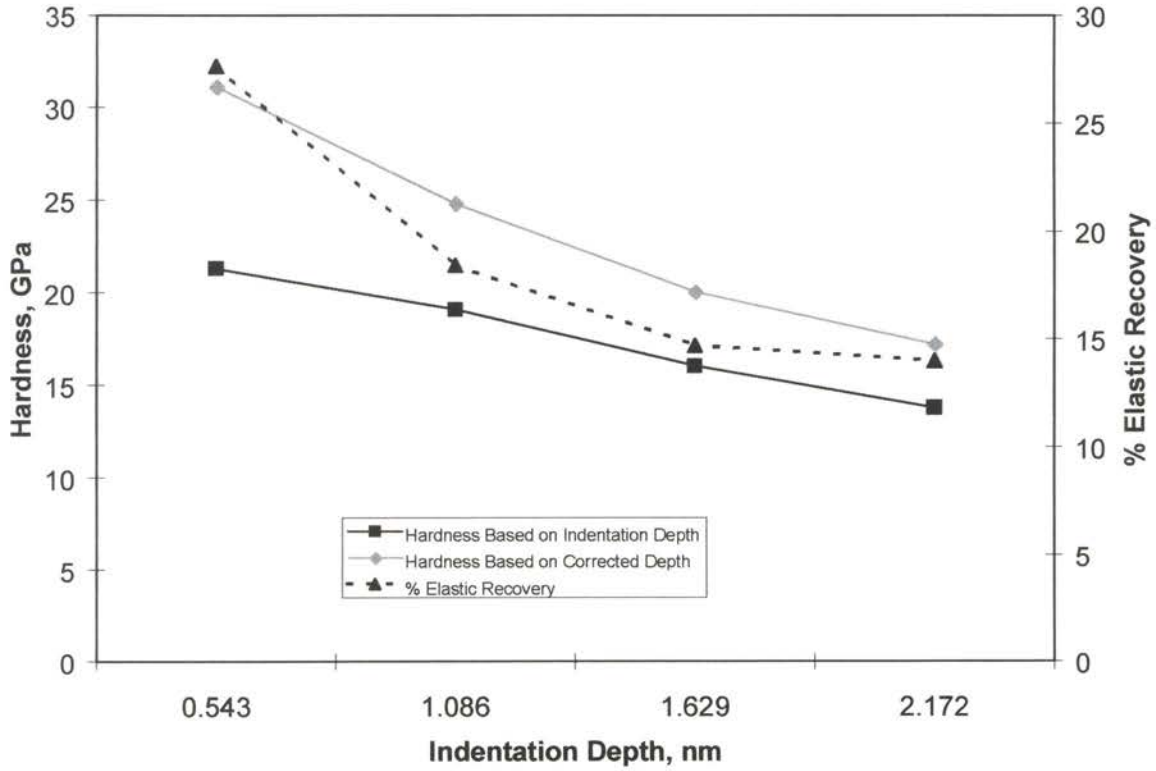

Figure 4.26 Effect of Indentation Depth On Hardness and Elastic Recovery

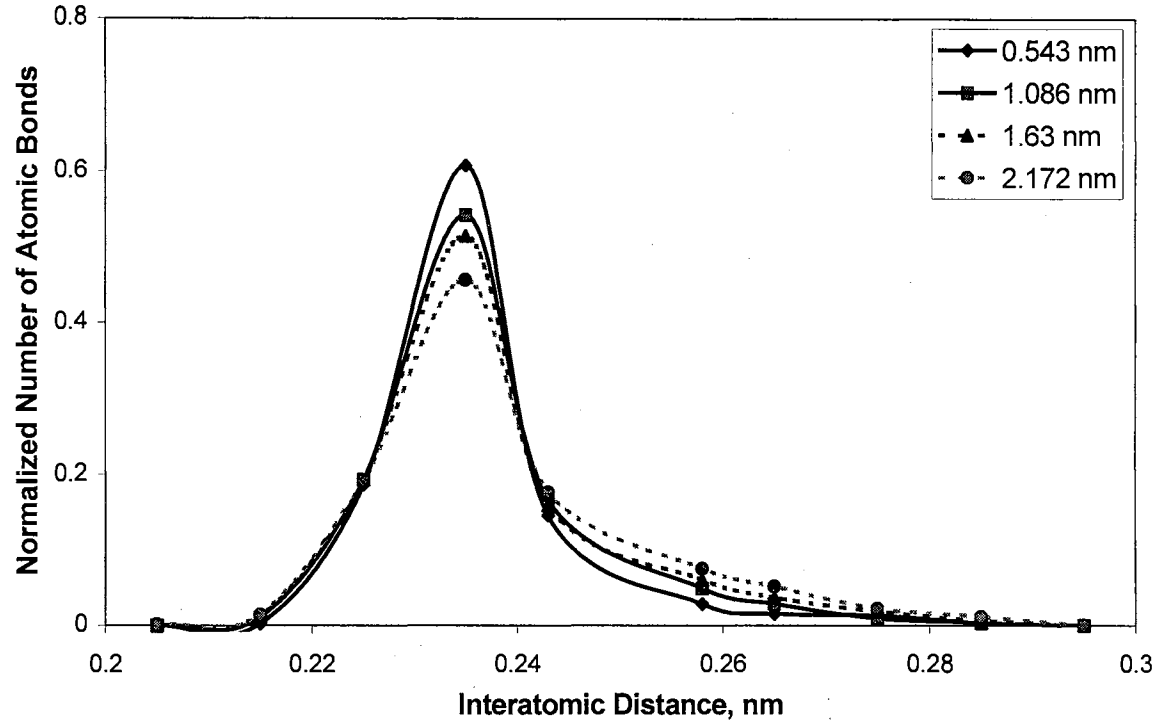

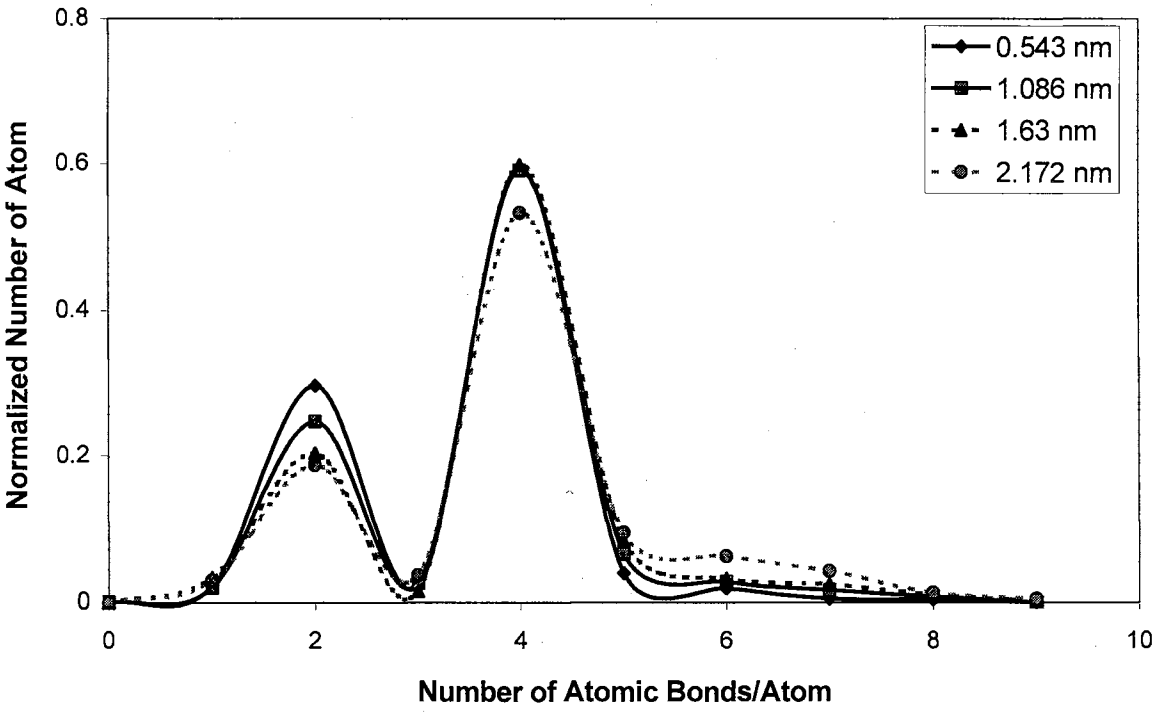

Figures 4.27 (a) and (b) Distribution of (a) atoms at various interatomic distances and (b) the coordination structure for silicon at maximum indentation depth in the subsurface deformed zone underneath the indenter for various indentation depths

4.3.5. Effect of Indenter Included Angle

MD simulations of nanoindentation of silicon were performed with different indenter included angles, namely, 90°, 120°, 136°, and 150°, respectively, to study the effect of indenter geometry on the measured hardness and phase transformation in silicon indentation. Figures 4.28 (a) - (d) are the MD simulation plots showing nanoindentation of silicon with various included angle indenters at maximum indentation depth. An increase in the amount of plastic deformation around the indenter can be seen. Both, the radius of the plastic deformation zone as well as the degree of compaction of atoms underneath the indenter increase with increasing indenter included angle. It was also observed that the degree of elastic recovery decreased with increasing indenter included angle. Figures 4.29 (a) and (b) are plots of the distribution of atoms at various interatomic distances and the coordination structure for silicon at maximum indentation depth in the subsurface deformed zone underneath the indenter for various indenter included angles. Figure 4.29 (a) shows an increase in the number of atomic bonds at 0.243 nm and 0.258 nm interatomic distance and a corresponding decrease at 0.235 nm interatomic distance with increasing indenter included angle. Figure 4.29 (b) shows a corresponding increase in the 6 coordination structure and an associated decrease in the 4 coordinated silicon structure with increasing indenter included angle. Both, Figures 4.29 (a) and (b), suggest an increase in the degree of phase transformation of silicon from α- to β-phase with increasing indenter included angle. Komanduri et al. (1997) suggested that in nanometric cutting, the hydrostatic pressure underneath the tool increases with increasing tool edge radius and/or tool negative rake angle. A similar situation might exist in nanoindentation of silicon with increasing indenter included angles, which can account for the increasing degree of phase transformation of silicon observed with increasing indenter included angle. The measured indentation hardness (H_{PD}) was observed to increase from 19.1 GPa to 26.2 GPa as the indenter included angle was increased from 90° to 150°.

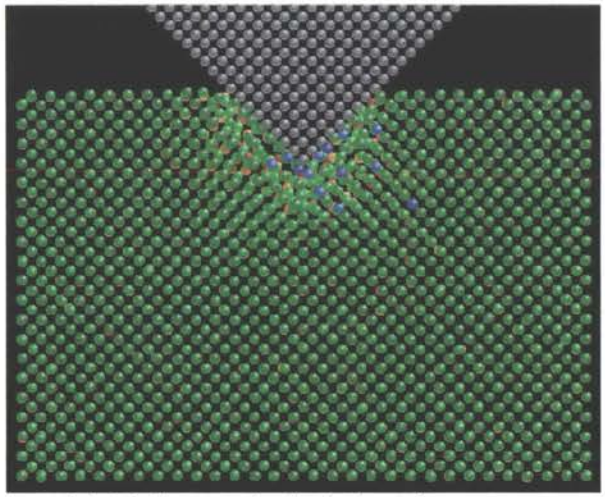

(a) 90 degrees included angle

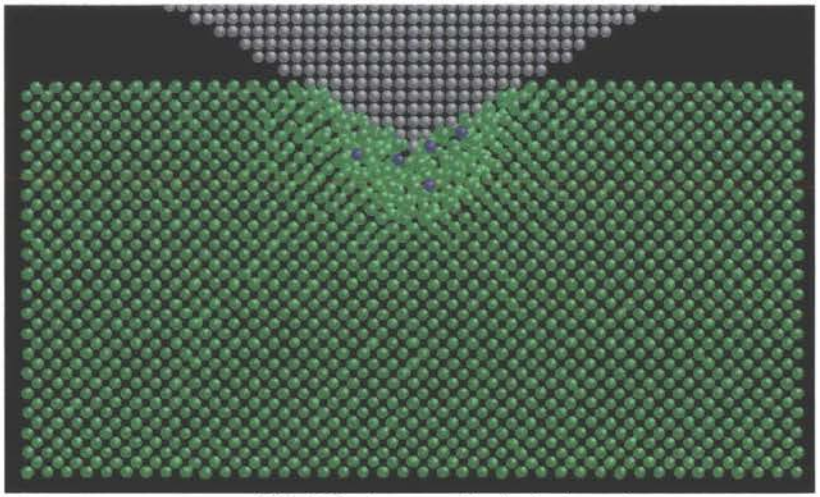

(b) 120 degrees included angle

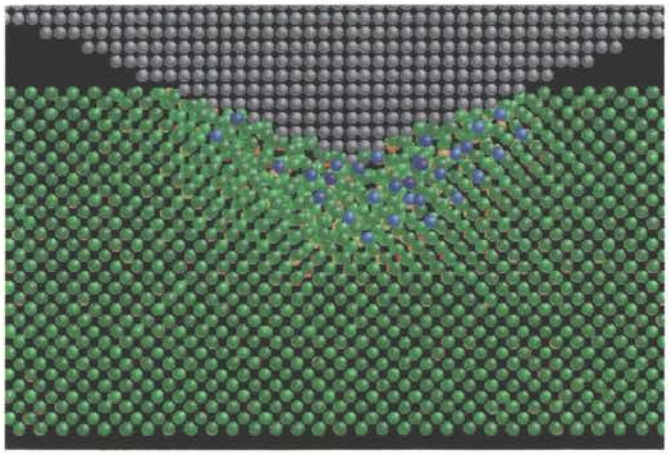

(c) 136 degrees included angle

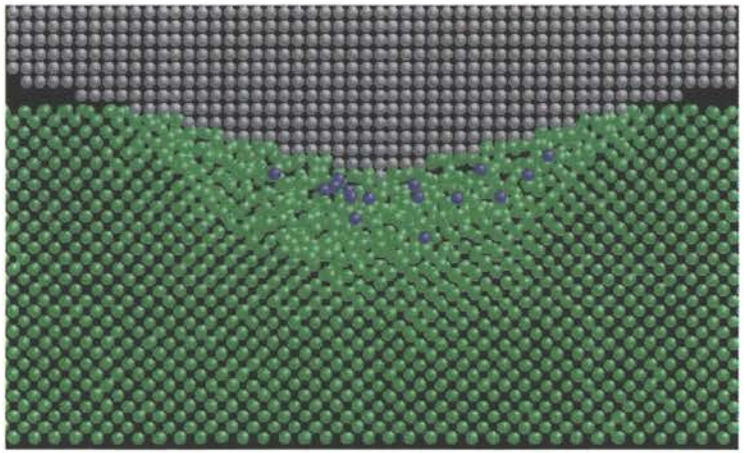

(d) 150 degrees included angle

Figures 4.28 (a) - (d) Effect of Indenter Included Angle in Nanoindentation of Silicon

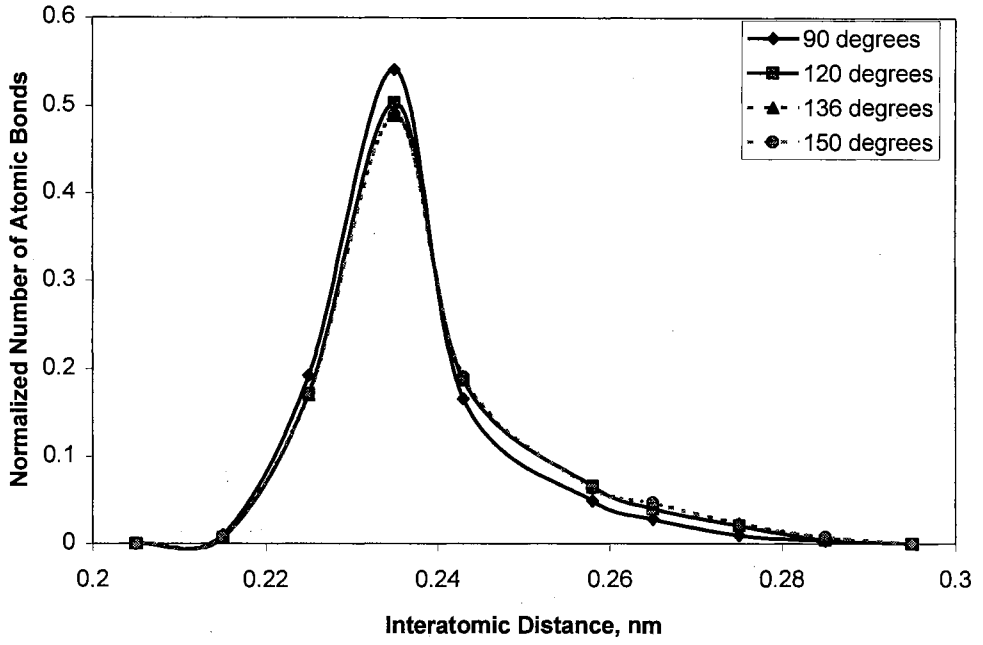

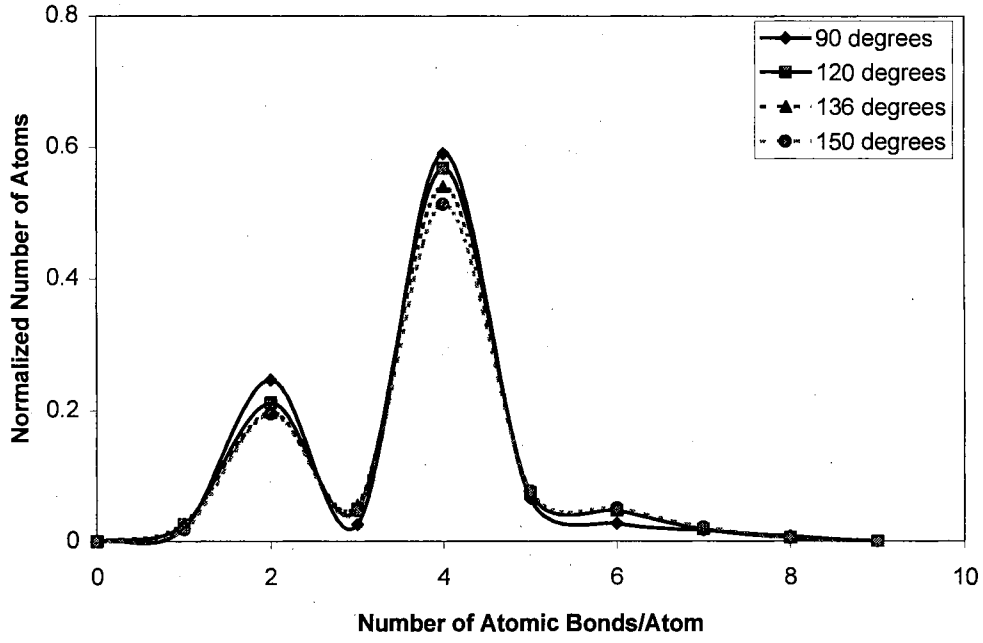

Figures 4.29 (a) and (b) Distribution of (a) atoms at various interatomic distances and (b) the coordination structure for silicon at maximum indentation depth in the subsurface deformed zone underneath the indenter for various indenter included angles

4.3.6. Conclusions

Molecular Dynamics (MD) simulations of nanoindentation have been carried out at a constant rate of loading (500 m/s) on various single crystal materials, Al, Cu, Ag, Ni, Si, and Ge to investigate the nature of deformation in these materials at the atomic scale. The following are some of the specific conclusions from the study.

1. The deformation of metals under indentation loading conditions was associated with the generation and propagation of dislocations at ~45° to the indentation direction. No dislocations were observed with Si and Ge.

2. The simulation results indicate the possibility that the material around and underneath the indenter in the case of silicon can undergo a structural transformation (from α to β-silicon) and a significant densification as a consequence of nanoindentation.

3. The elastic recovery was observed to decrease with decreasing ductility of the material. Al exhibited the maximum elastic recovery while Ge showed minimum elastic recovery after retraction.

4. The indentation hardness was measured from the MD simulations and found to be in reasonable agreement with the results reported in the literature. The indentation hardness was observed to decrease with increasing indentation depth and decreasing indenter included angle.

5. The degree of phase transformation in silicon nanoindentation was observed to increase with increasing indentation depth and indenter included angle.

CHAPTER 5

EFFECT OF TOOL GEOMETRY IN NANOMETRIC CUTTING [a, b]

5.1. INTRODUCTION

In UPM, be it single point diamond turning or grinding or polishing it is necessary to identify the conditions that involve the full development of plasticity underneath the tool or abrasive grain (indenter) prior to the ensuing fracture by median cracks. It has been postulated that the tendency of a brittle material to exhibit plastic deformation instead of brittle fracture decreases below a critical depth or load. This is termed as brittle-to-ductile transition (BDT). Interestingly, in all the works reported in the literature on precision machining of brittle materials, a tool with a high negative rake angle (-25° to -45°) or with a high tool edge radius relative to the depth of cut ($d/r \ll 1$) has been used.

---

a - R. Komanduri, N. Chandrasekaran, L. M. Raff, "Some aspects of machining with negative rake tools simulating grinding: a molecular dynamics simulation approach," Phil. Mag. B, 1999, 79/7, pp. 955-968

b - R. Komanduri, N. Chandrasekaran, L. M. Raff, "Efect of tool geometry in nanometric cutting: a molecular dynamics simulation approach," Wear, 1998, 219, 84-97

This is because at low depths of cut, the stresses generated by the high negative-rake-angle tools may not reach the values required to generate median vents in brittle materials. It has also been suggested that at shallow depths of cut, the energy required to propagate cracks may be larger than the energy required for plastic yielding resulting in material removal by plastic deformation (Blake and Scattergood, 1990).

Alternately, it is possible that such large negative rake angle tools and/or large tool edge radius relative to depth of cut used in practice for finishing of advanced materials, such as silicon, can induce significant hydrostatic pressure to plastically deform the material around the tool (Komanduri et al., 1997). It is well known that the hydrostatic pressure can increase the strain at fracture even in a nominally brittle material, such as chalk, marble, cast iron etc. (Bridgman, 1947; Crossland and Dearden, 1958; Handin et al., 1967). Yoshino et al. reported the possibility of defect-free machining of silicon under the application of external hydrostatic pressure (EHP) by both experimental (2001a) and simulation techniques (2001b). Chandrasekaran et al. also showed the possibility of an increase in the BDT depth and generation of defect-free surfaces in machining of silicon (2000) and glass (2001) under EHP.

Although, the critical load and depth play a significant role in determining the BDT depth, it is the state of stress, which determines whether fracture will occur or not. A reduction in the depth will result in a change in stress magnitude alone and not in the stress state, which is brought about by a change in the tool geometry. As the depth of cut (d) is reduced for a given tool edge radius (r), the d/r ratio decreases which results in a

subsequent increase in the effective negative rake angle presented by the tool. Consequently, the stress state underneath the tool changes from tensile to compressive enabling defect-free machining of brittle materials. The geometry of the tool or abrasive grain, coupled with the depth of cut and the workmaterial properties determine the resulting force system which acts at the surface and which determines whether fracture occurs in the case of a nominally brittle material. Consequently, the effect of tool geometry in UPM and UPG is of significant importance, which is the subject of this investigation.

5.2. MACHINING WITH NEGATIVE RAKE TOOLS SIMULATING GRINDING

5.2.1. Introduction

Grinding is technologically an important manufacturing operation for finishing. Recently, ultraprecision grinding (UPG) was developed specifically to meet the challenging needs of producing components of high form accuracy, complex geometry, and high surface finish for optical, electronic, magnetic, and other applications. The diamond or the cubic BN (c-BN) abrasive used in the grinding wheel removes extremely fine chips on the order of a few nanometers thickness. Hence, the term nanometric cutting is extended to UPG.

Unlike in cutting with a single, or, multiple point tool, the geometry of the abrasives in grinding is not well defined and changes continuously as the process proceeds due to wear and self sharpening action (friability) of the abrasive. Even though the shape and geometry of the abrasive grits are random, they can be modeled as a sphere as a sphere or a polyhedron as a first-order approximation [Figure 5.1] (Shaw, 1996). However, it may be noted that it is the geometry at the tip of the abrasive that is of concern (and not the geometry of the abrasive grit) as far as the material removal mechanism is concerned. The fine depths of cut, the continuously changing tool geometry and the high grinding speeds makes the analysis of the grinding process somewhat difficult.

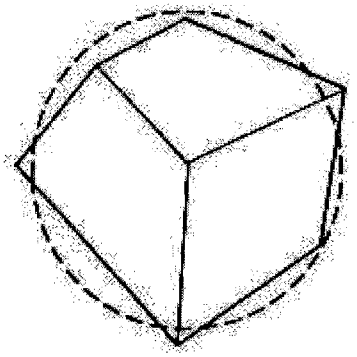

Figure 5.1. Schematic diagram of an abrasive grit modeled as a sphere or as a polyhedron (Shaw, 1996)

The rake angle in machining is measured between the tool rake face and the normal to the cutting velocity vector [Figure 5.2]. It is considered positive when this angle is measured in the clockwise direction from this normal to the tool face and negative when measured in the counterclockwise direction. When the rake face coincides with the normal to the velocity vector, the tool is designated as a zero-rake tool.

Generally, in conventional cutting using cemented-carbide inserted tools, a rake angle of -5^{o} and a clearance angle of $+5^{o}$ are used to enable the use of all eight corners of the insert as the tool holder is pre-set to provide these angles with a square insert.

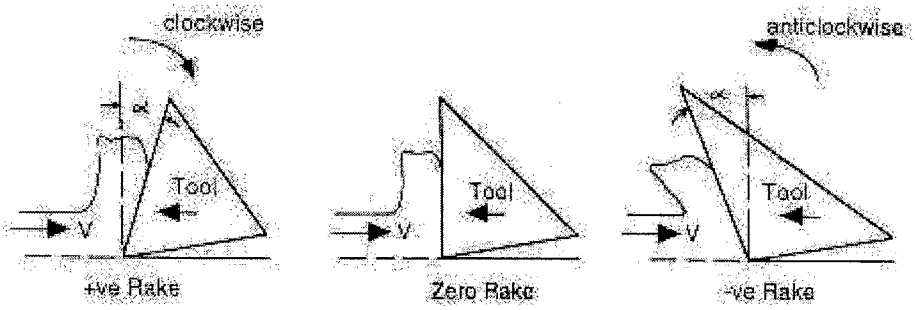

Figure 5.2. Nomenclature of a Cutting Tool in Machining Showing Positive, Zero, and Negative Rake Angles

It is generally recognized that abrasive grits in grinding present a large negative rake angle. This is based on a comparison of the ratio of cutting force to thrust force, partition of energy expended in grinding between the chip, the workmaterial, and the abrasive, the nature of residual stresses, and the subsurface deformation in grinding compared to machining. Consequently, the grinding process may be simulated by cutting with large negative rake angle tools. This way many features of the grinding process can be understood by comparing it with machining with large negative rake tools. As previously pointed out, alternatively, the abrasive grain can be modeled as a sphere with the edge radius as the tip radius of the abrasive.

5.2.2. Literature Review

In order to formulate the material removal mechanisms in grinding, it becomes necessary to conduct experiments with large negative rake tools. However, it is not clear whether with such high negative rake tools, especially at the higher end of the range, the material removal is by chip formation or by ploughing of the tool into the workmaterial. Rubenstein et al. (1967) concluded that no chips would be formed when cutting with tool rake angles more negative than -55°. This was based on the extrapolation of the results published by Crawford and Merchant (1953) for a tool with a zero rake angle to 55° rake angle. It may be noted that from a theoretical point of view there should not be such a limit almost up to or close to -90°, for at -90° there would be no space left between the tool face and the work surface for chip flow.

Hahn (1956) introduced the rubbing grain hypothesis to grinding according to which some abrasive grits may merely rub the work surface giving rise to high frictional forces on the clearance face but no cutting force on the tool rake face while other abrasive grits would participate in the chip formation process. According to Hahn, since the grinding process is similar to the milling process except on a microscale, there should be no reason for the forces in grinding to be different from those in cutting. However, in metal cutting with positive rake tools, the thrust force is generally about half the cutting force while in grinding the thrust force is twice the cutting force.

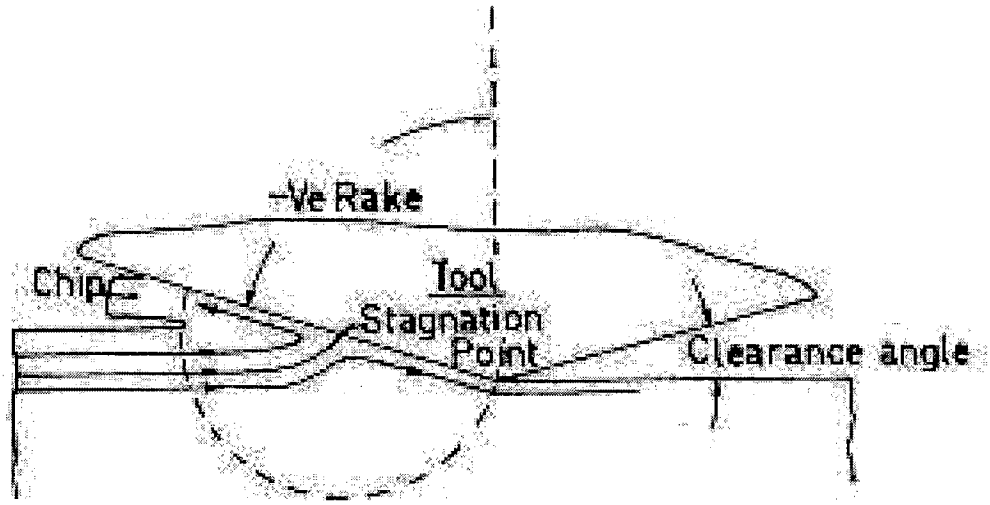

Figure 5.3. Schematic diagram of the chip formation process with a large-negative-rake tool (after Komanduri, 1971)

Figure 5.3 is a schematic of the chip formation process with a large negative rake tool (Komanduri, 1971). It can be seen that, if the stiffness of the tool support system is not sufficient to support the large thrust (or normal) forces without any deflection, then the tool will be forced to move upwards and away from the work material, thereby limiting the depth of cut and in the limit causing zero depth of cut or no cutting. Alternately, instead of forming a chip, material from the work can plough sideways without causing chip formation (Komanduri, 1971). This is because the chip is generally thicker than the uncut material and the space between the tool face and the work surface is somewhat limited in the case of large negative rake tools. The chip formation therefore

takes place along the path of least resistance. Thus, a rigid tool support system is a prerequisite for machining with large negative rake angle tools.

To simulate conventional grinding, Komanduri (1971) conducted single point turning tests with a wide range of negative rake tools (up to -85°) with a rigid tool support system. He found that the ability to form chips not only depends on the rake angle but also on the width of the workmaterial being machined for a given depth of cut. A reduction in the width of the workmaterial for the same cut depth minimizes the possibility of plane-strain conditions or promotes plane-stress conditions. This results in poor friction conditions on the rake face as well. In this case, material removal takes place predominantly by ploughing and side flow of the workmaterial. He also observed chip formation to take place with a negative rake angle as high as -76° yielding a long continuous chip and only with a -85° rake tool did he observe absence of chip formation (and not -55° rake as postulated by Rubenstein et al., 1967). The tool merely rubbed the work surface resulting in plastic deformation and side flow. This lack of chip formation at -85° is due to the limited space available between the tool face and the work surface for the cut depth used. As the rake angle was decreased to more negative values, the thrust force was found to increase initially slowly, up to about -50° followed by a sharp rise to about -85°. The ratio of thrust force to cutting force also increased from about 0.9 to close to 5 as the rake angle is changed from +10° to -85°.

In Komanduri's studies, however, the minimum cut depth used was ~10 μm as tests were conducted on a conventional lathe and not on an ultraprecision lathe which is

capable of nanometric cutting. Since the cut depths in nanometric cutting are several orders of magnitude smaller than in conventional machining, it is not clear if the results obtained in the latter can be extended to nanometric cutting. The purpose of this study is to investigate this and compare the results with the earlier results published in the literature.

5.2.3. Methodology of MD Simulations

Figure 5.4 is a schematic diagram of the model used for the MD simulation of nanometric cutting with a negative-rake tool simulating grinding showing various regions of interest. MD simulations were conducted on a Digital α-workstation (model 250) with a clock speed of 333 MHz. Table 5.1 gives the conditions used in the MD simulations with extremely sharp tools (i.e., no radius on the tool) of different rake angles giving the dimensions of the work material and the tool, the depth of cut, the length of cut, and the tool geometry. Copper workmaterial and an infinitely hard tool were used in the simulations. Cutting forces, specific energy, subsurface deformation, and size effect are studied by comparing with the experimental results of Komanduri (1971), Crawford and Merchant (1953), and Kita and Ido (1982). Some of these simulations were conducted using a new method termed as Length Restricted Molecular Dynamics (LRMD) to reduce the computational time and memory requirements. Details on the LRMD are explained elsewhere (Chandrasekaran, 1997).

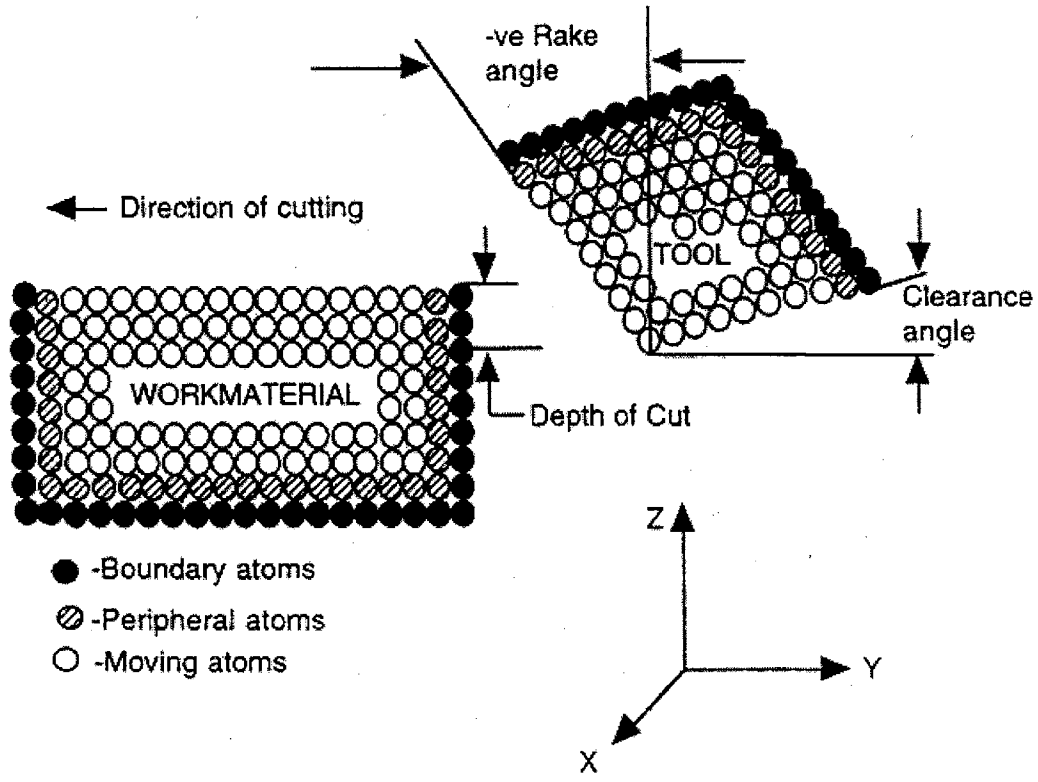

Figure 5.4. Schematic diagram of the model used for the MD simulation of nanometric cutting with a negative rake tool

5.2.4. Results and Discussion

5.2.4.1. MD Simulation Results

Figures 5.5 (a) - (f) are photographs of the MD simulation of nanometric cutting process conducted with an extremely sharp tool of different rake angles. Plastic deformation ahead of the tool tip and into the machined surface can be clearly seen. It can also be seen that the chip lengths decrease (or the chip thickness increase) with increasing negative rake angles. The photographs of the simulation process also suggest increased plowing of the tool into the workmaterial with increased negative rake.

Table 5.1. Computation Parameters Used in the MD Simulation of Nanometric Cutting

Configuration	3-D Cutting
Workmaterial	Copper
Potential Used	Morse Potential
Workmaterial Dimensions	4x21x20 and 4x16x20[a]
Tool Material	Infinitely Hard
Tool Dimensions	4x10x14
Rake Angle	-75^{o} to $+45^{o}$
Clearance Angle	5^{o}
Width of Cut	1.448 nm
Depth of Cut	0.724 nm
Length of Cut	7.5 nm
Cutting Speed	500 m/s
Bulk Temperature	293 K

a - Workmaterial dimension in LRMD simulation

A comparison of the photographs and the computer animated movies also showed an increase in the degree of subsurface deformation with increasing negative rake angle. Generation and movement of dislocations into the workmaterial can also be seen. Once the tool has passed the machined zone in the work material, the elastic recovery of the machined surface takes place as can be seen from the figure. From the animated movies of the simulations with various rake tools as well as from the plots of the MD simulation of nanometric cutting, it was observed that as the rake changes to more negative values the shear zone rotates towards the workmaterial due to decrease in the shear angle as well as the rotation of the resultant force vector.

Atomically sharp tools are possible in MD simulation of nanometric cutting while the experimental work is limited by the minimum edge radius that can be formed physically on a given cutting tool. Consequently, it is possible only to vary the rake angle without affecting the edge radius or wear of the tool. It may be noted that with the best technology available, the edge radius of the tool (i.e. between the rake face and the clearance face) would be of the order of several nanometers (20-50 nm) for the case of a single crystal diamond tool. Also, tool wear with such large negative rake angles can be significantly high especially in machining steels. This can change the geometry of the tool. Hence, data have to be taken in the very early stages of cutting before a wear land develops on the cutting tool.

Significant deformation underneath the tool due to indentation effect can also be observed in the case of high negative rake tool [Figure 5.5 (a)]. While MD simulation with negative rake tools reported above facilitates simulation of the grinding process, this study was extended to involve tools with extremely large positive rake angles (up to 45^{o}) as well to investigate the extent of decrease in forces and consequent energy savings at such large positive rake angles compared with a conventional -5^{o} rake tool. Figures 5.6 (a) - (d) are photographs of the MD simulation of the nanometric cutting process conducted with tools of various positive rake angles. An increase in the shear angle, a decrease in the tool-chip contact length (reduced friction), reduced subsurface deformation, and chip curl with increase in tool positive rake angle can be seen.

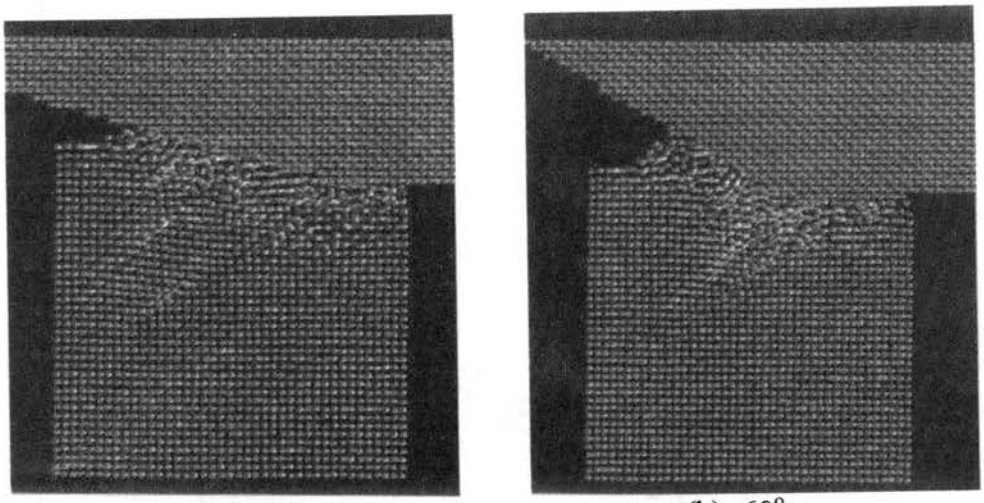

(a) -75°

(b) -60°

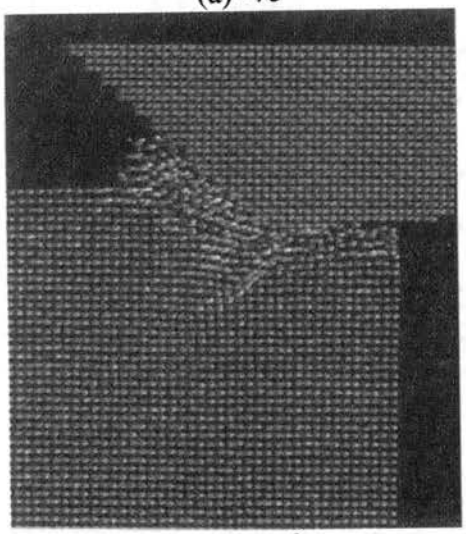

(c) -45°

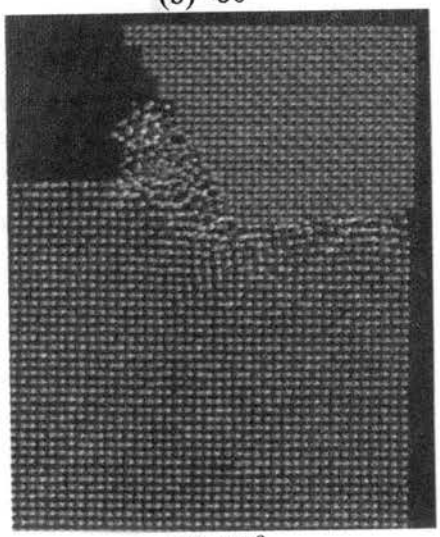

(d) -30°

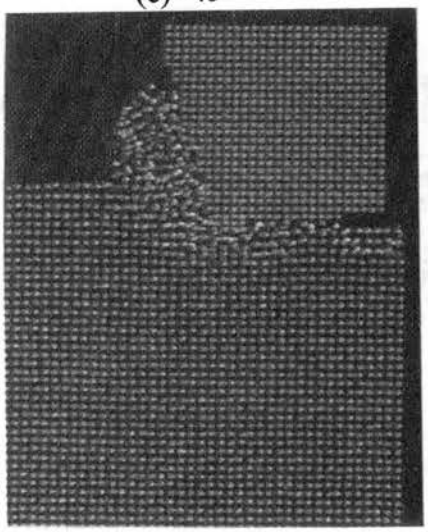

(e) -15°

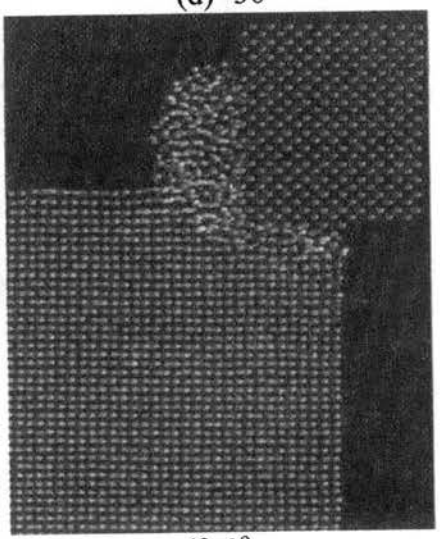

(f) 0°

Figures 5.5 (a) - (f) MD simulation plots of nanometric cutting process with various tool rake angles

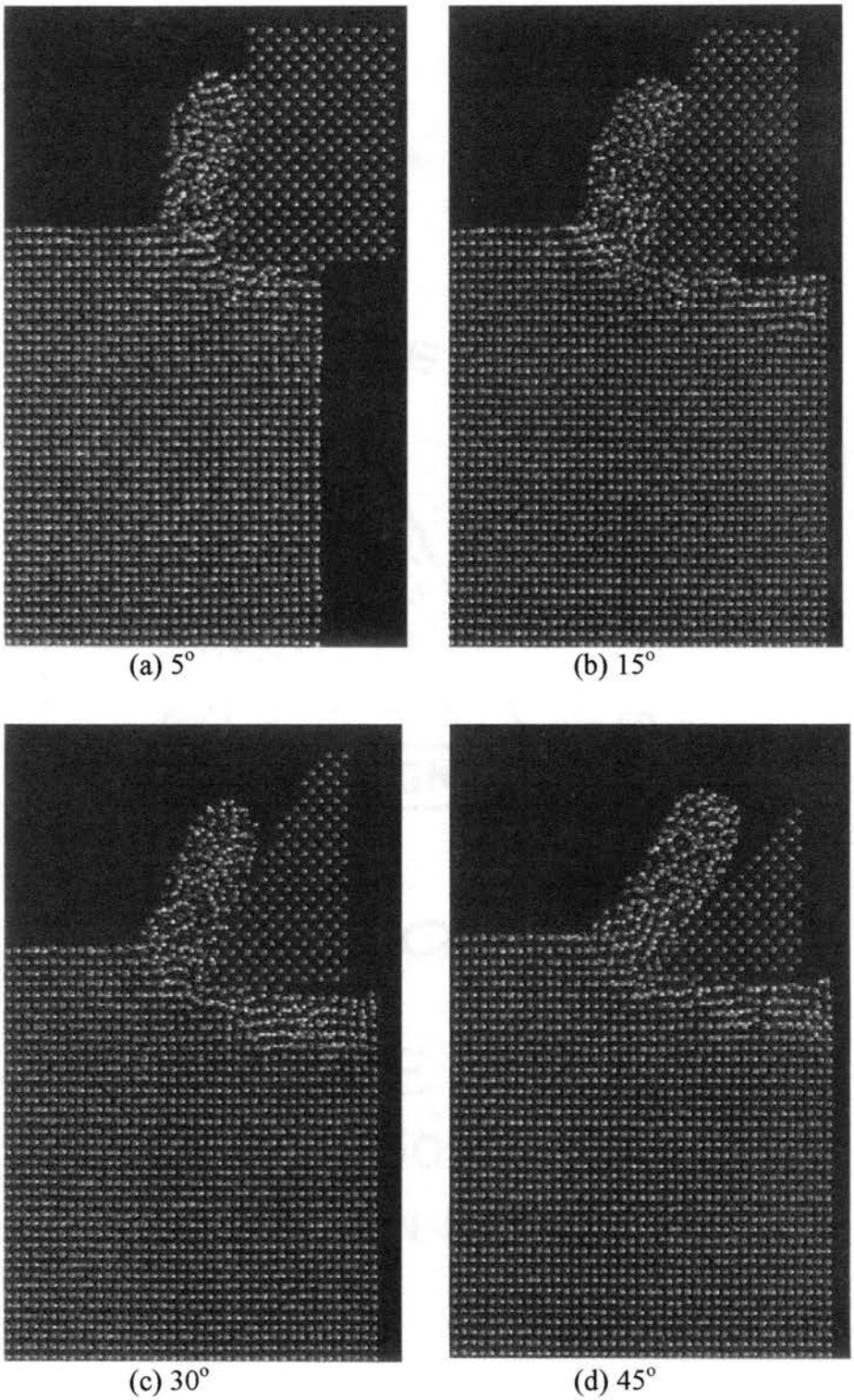

(a) 5°

(b) 15°

(c) 30°

(d) 45°

Figures 5.6 (a) - (d) Photographs of MD simulation of nanometric cutting with positive rake tools

5.2.4.2. Analysis of Forces

Table 5.2 gives the mean cutting and thrust forces per unit width of cut, the ratio of the thrust force to the cutting force, and the specific energy for the MD simulation of nanometric cutting with tools of different rake angles. Figures 5.7 (a) & (b) show the variation of the cutting and the thrust forces per unit width, as well as the ratio of the thrust force to the cutting force with rake angle in nanometric cutting. It can be seen from Figure 5.7 (a) that as the rake angle is changed from $+10^{o}$ towards negative rake, the thrust force increases rapidly up to -75^{o}. The cutting force also shows an increasing trend but at a slower rate. The force ratio also increases as the rake angle changes to more negative [Figure 5.7 (b)]. At 10^{o} rake, the thrust force is 0.6 times the cutting force. This ratio increases as the rake changes to more negative, for example at -75^{o} rake it is 2.4. It can be seen from Table 5.2 that the ratio of the thrust force to the cutting force at -60^{o} is 1.9 (about twice) as expected. These trends are similar to the results reported by Komanduri (1971) although exact values are somewhat different.

Figure 5.8 shows the variation of the force ratio with rake angle in MD simulation of nanometric cutting, and the results of conventional cutting by Crawford and Merchant (1953); Kita and Ido (1982); and Komanduri (1971). Except at very high tool negative-rake-angles where the MD simulation results are lower than the conventional tests, it appears that the agreement of the results is reasonable. Even this discrepancy can be attributed to the wear of the tools in conventional machining with large negative rake angles while no wear is involved in the MD simulation. Marshall and Shaw (1952) found the mean grinding coefficient, which is the ratio of cutting force to thrust force for

grinding to be 0.47 for silicon carbide wheel. Based on a comparison of all these values, it appears that there is a similarity between the UPG and the nanometric cutting with high negative rake tools, with the mean rake angle in grinding in the vicinity of -60°.

Table 5.2. Results of MD simulation of nanometric cutting with various rake angles

No	Rake Angle, degrees	Cutting Force/Unit Width (F_c), N/mm X 10^2	Thrust Force/Unit Width (F_t), N/mm X 10^2	F_t / F_c	Specific Energy, N/mm^2 X 10^{-5}
1	-75	7.321	17.286	2.361	1.011
2	-60	6.485	12.336	1.902	0.896
3	-45	6.132	10.6	1.729	0.847
4	-30	4.938	6.92	1.401	0.682
5	-15	4.506	4.887	1.085	0.622
6	-5	3.813	3.687	0.967	0.527
7	0	3.631	3.116	0.858	0.502
8	5	3.33	2.472	0.742	0.46
9	10	2.921	1.939	0.664	0.403
10	15	2.661	1.582	0.595	0.368
11	30	2.238	1.276	0.57	0.309
12	45	2.124	1.054	0.496	0.293

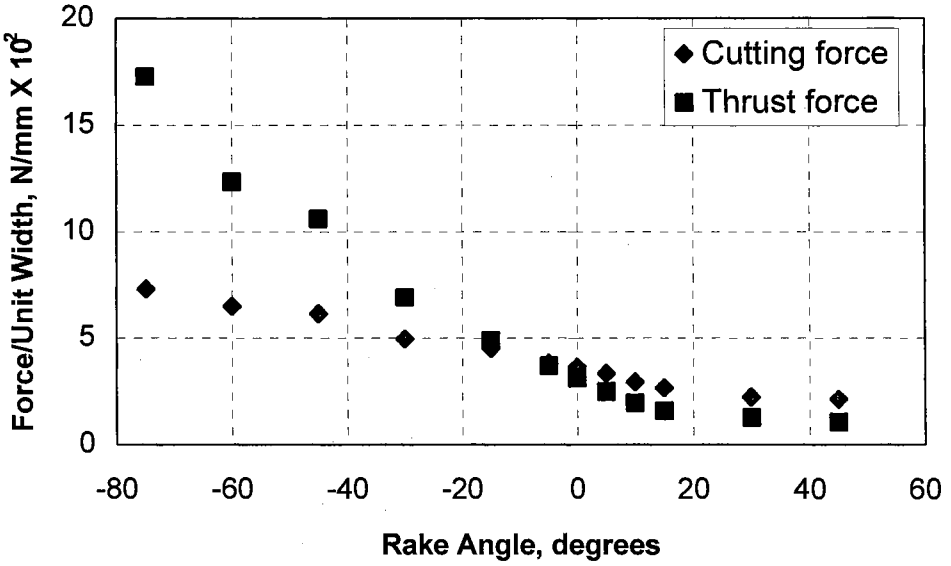

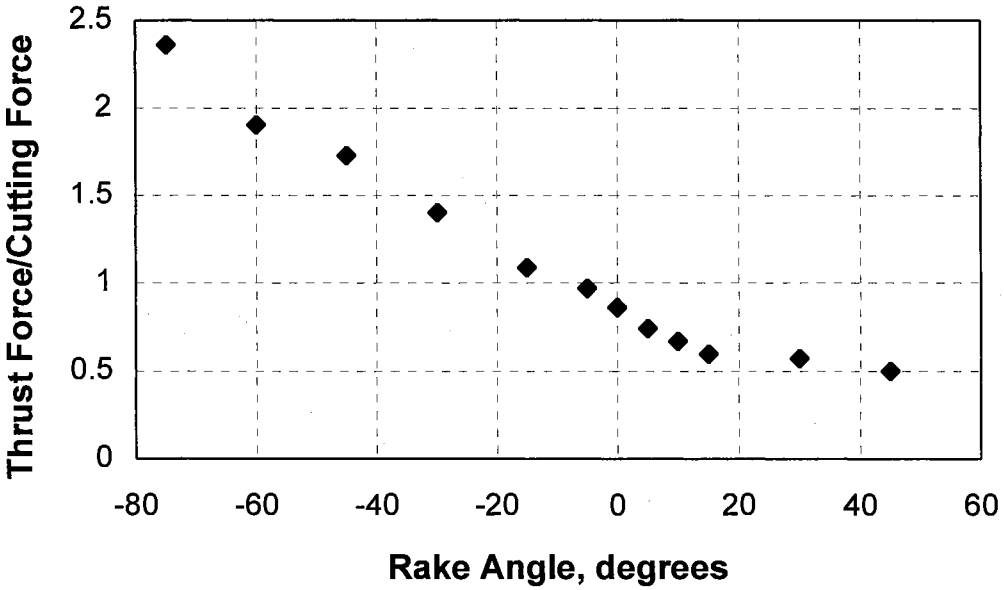

Figures 5.7 (a) and (b) Variation of (a) the cutting and the thrust forces per unit width and (b) the ratio of the thrust force to the cutting force with rake angle

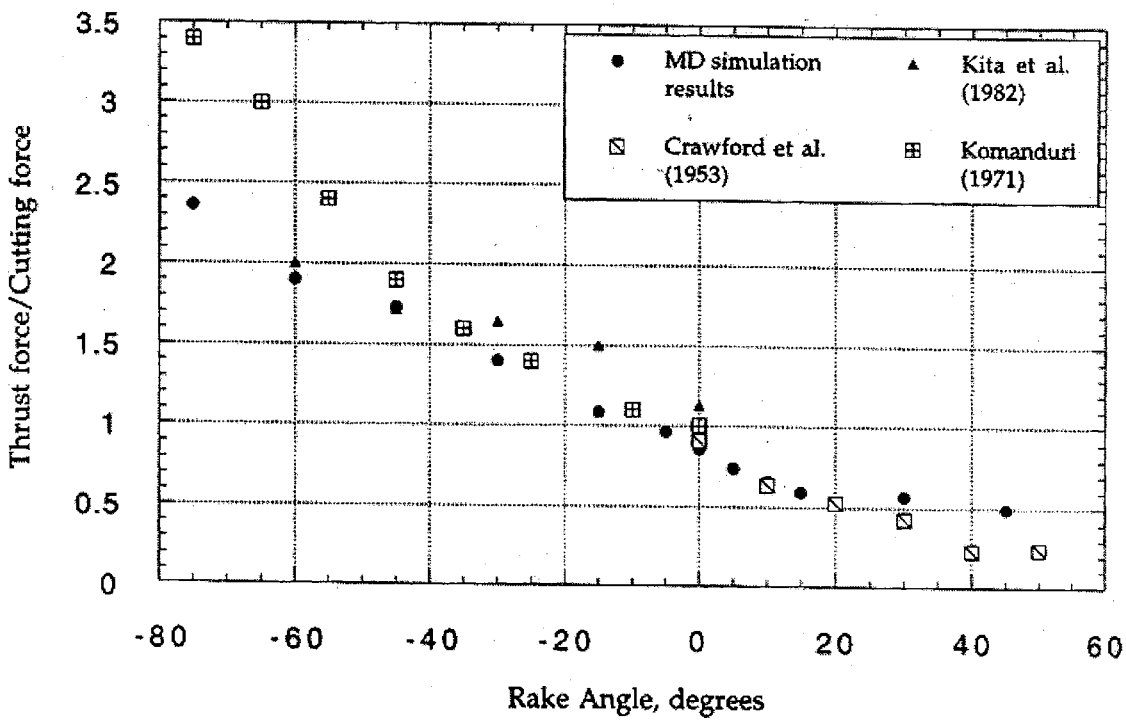

Figure 5.8. Variation of the force ratio with rake angle in MD simulation of nanometric cutting, and the results of conventional cutting by Crawford and Merchant (1953); Kita and Ido (1982); and Komanduri (1971)

Figure 5.9 shows the variation of specific energy (i.e. the energy required for removal of unit volume of the work material) versus rake angle from the results of MD simulation for a depth of cut of 0.724 nm. Also shown in the figure are the experimental data by Komanduri (1971) for a depth of cut of 10 μm and that of Crawford and Merchant (1953) for a depth of cut of 250 μm. An increase in specific energy with decreasing rake angle can be observed. However, the specific energy in nanometric cutting is found to an order of magnitude larger than conventional cutting. This increase in specific energy can be attributed to the size effect similar to that reported by many

other researchers (Backer et al., 1952; Nakayama and Tamura, 1958; Komanduri, 1971; Furukawa and Morunuki, 1988; Moriwaki and Okuda, 1989; Lucca et al., 1991). It should be noted that the workmaterial in nanometric cutting is initially free of any defects, such as point, line, or area defects and the size of the work material under consideration is only a few nanometers on each side of a parallel piped.

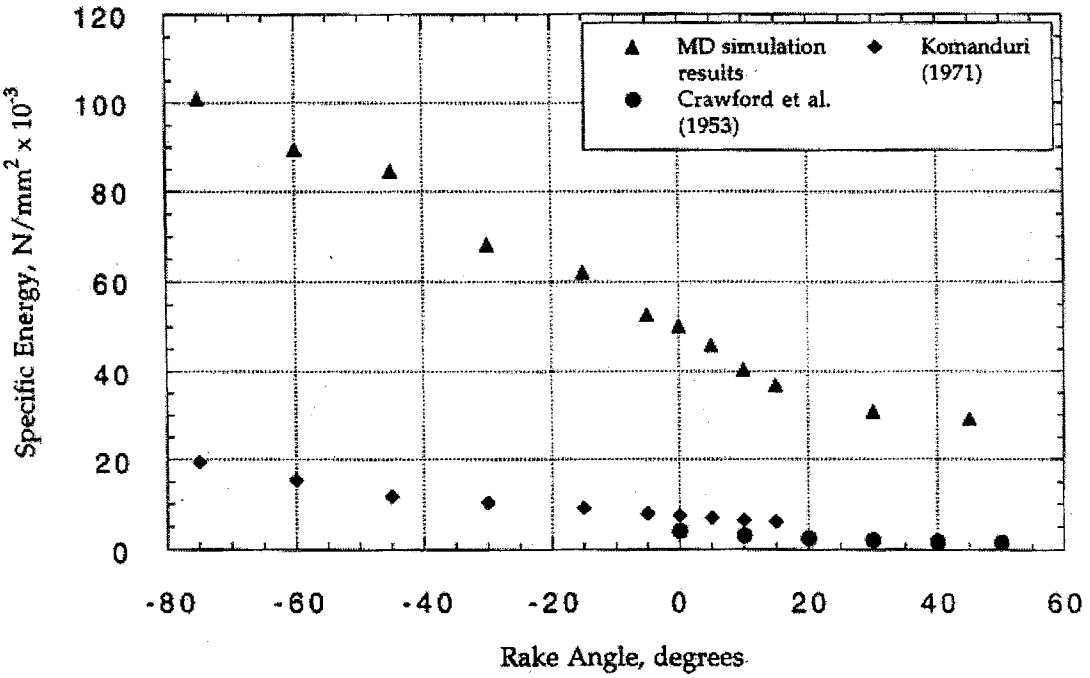

Figure 5.9. Variation of Specific Energy With Rake Angle in MD Simulation of Nanometric Cutting and the Results of Conventional Machining by Komanduri (1971) and Crawford and Merchant (1953)

If one were to use positive rake tools or very sharp tools, i.e., an edge radius small compared to the depth of cut, one may not induce adequate hydrostatic pressure to cause any plastic deformation and elastic deformation followed by the formation of median cracks which can result in brittle microfracture. However, with increasing emphasis on

the so-called dry machining, a significant decrease in energy will directly translate into a substantial decrease in tool temperature and consequent increase in tool life. While more refractory tools, such as multiple-layer nanocoatings, or advanced ceramics may enable machining without using a cutting fluid, large positive rake tool geometry will further extend the tool life or improved productivity by removing material at higher speeds. It can be seen from Figure 5.7 (a) that nearly a 50% reduction in cutting force and consequent cutting energy can be achieved by using high positive rake tools. The availability of new high-strength, submicrometer grain-tool materials enables the use of such large rake angles without compromising the life, especially for machining softer non-ferrous materials such as aluminum and copper. Hence, it would be possible to machine some of these materials without the use of a cutting fluid, at the same time, accomplishing a nearly equivalent tool life and/or higher productivity.

5.2.5. Conclusions

MD simulations of nanometric cutting were carried out with a range of negative rake tools to simulate the UPG process. A comparison of results with the experimental results published in the literature showed reasonably good agreement. The following are the specific conclusions that may be drawn from this study.

1. Chip formation was observed with negative rake angles as high as -75° similar to that reported by Komanduri (1971).

2. The ratio of the thrust force to the cutting force was found to be less than unity (about one half) for positive-rake tools while with high negative rakes this ratio was significantly higher (about 2 for -60° rake tool). The fact that, in grinding this ratio is about two suggests a close similarity of grinding and machining with large negative rake tools.

3. Both, the cutting and the thrust forces, the ratio of the thrust force to the cutting force, the specific energy, and the subsurface deformation increase with increase in the negative rake angle.

4. The specific energy in nanometric cutting is an order of magnitude higher than in conventional machining and this is interpreted as possibly due to a size effect.

5.3. EFFECT OF TOOL EDGE RADIUS AND DEPTH OF CUT

5.3.1. Introduction

Unlike in conventional cutting where the depth of cut (d) is significant compared to the edge radius (r) (i.e., the edge radius is negligible), in nanometric cutting this is generally not the case due to small depths of cut and minimum possible edge radius that can be produced on a single crystal diamond tool by the best manufacturing practice (20-70 nm) [Figures 5.10 (a) and (b)]. Consequently, factors usually neglected in conventional machining, such as flank wear and flank face friction become more

important in ultraprecision machining. Also, the tool edge radius relative to the depth of cut becomes an important factor as the change in one parameter results a change in the effective negative rake angle presented by the tool.

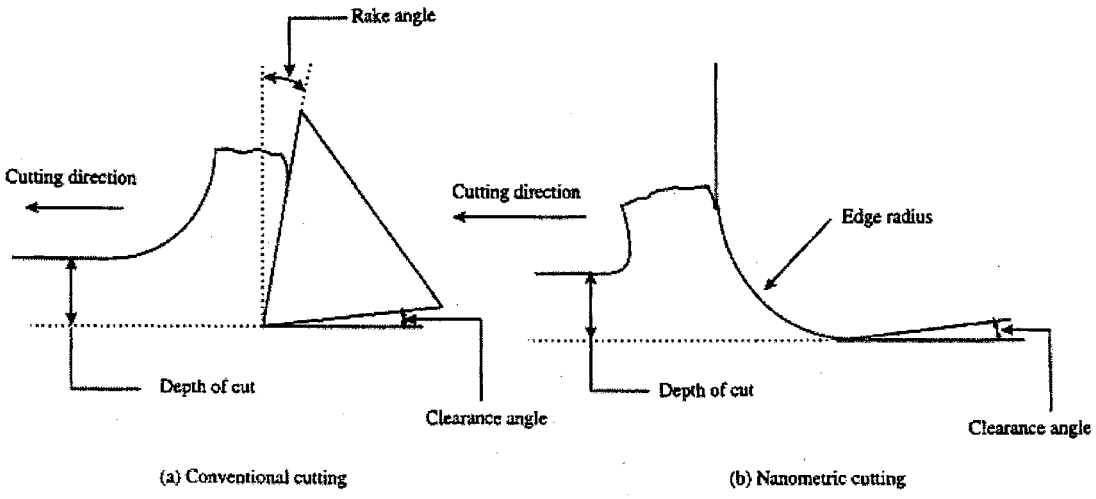

Figure 5.10. Schematics showing (a) conventional cutting and (b) nanometric cutting

It may be noted that in the indentation hardness field, pyramidal indenters, such as Vicker's, Knoop, and various conical indenters are classified as sharp indenters while spherical indenters are classified as blunt indenters. If we consider indentation-sliding to simulate ultraprecision machining, grinding, or abrasion then all these indenters do in fact fall into the category of blunt indenters [Figure 5.11]. For example, a Vicker's indenter with a 136° included angle would be equivalent to a high negative rake angle of -68°. A conical indenter with an included angle of 120° would represent a negative rake angle of -60°. A Knoop indenter with an included angle of 130° would represent a negative rake of -65° in one direction and with an included angle of 172.5° would present a negative rake angle of -86.25° in the other direction. The spherical indenter would be equivalent to a

varying high negative rake angle from close to -90° at the tool-workmaterial interface to whatever angle subtended by the tool at the depth of cut line. Thus, both the radius and the depth of cut of the spherical indenter come into picture in this case.

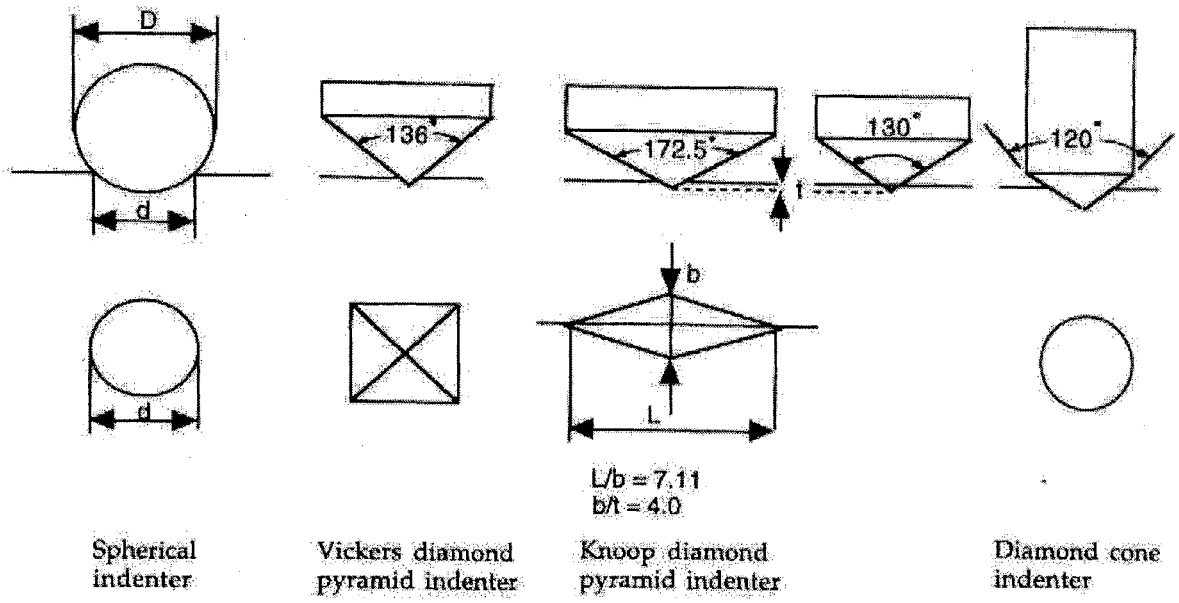

Figure 5.11. Geometry of Spherical, Vicker's, Knoop, and Diamond Indenters

Shaw (1972, 1996) proposed a mechanism of material removal involving extrusion of heavily deformed material ahead of a large edge radius tool in grinding of ductile metals [Figure 5.12] and Komanduri (1971) proposed a mechanism likening the grinding process to machining with high negative rake tools [Figure 5.3]. Puttick et al. (1989) used similar models to include the case of nanometric cutting of nominally brittle materials, such as silicon.

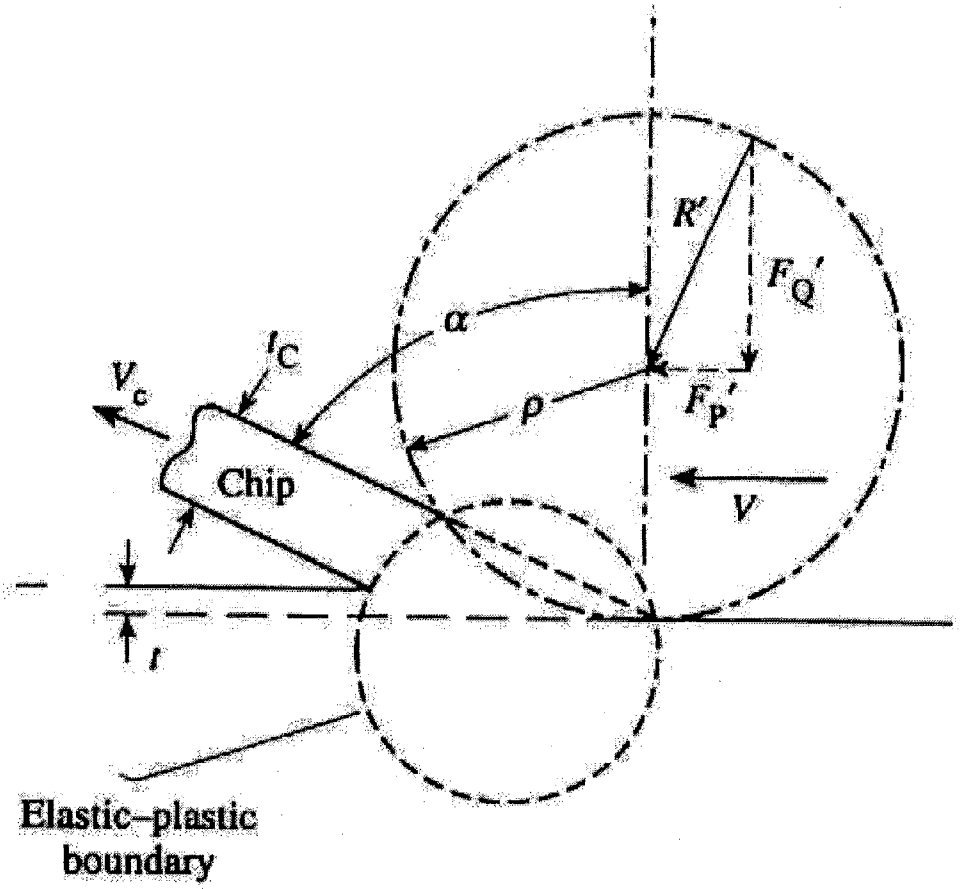

Figure 5.12. Mechanism of material removal involving extrusion of heavily deformed material ahead of a large radius tool in grinding of ductile Metals (Shaw, 1972, 1996)

As mentioned earlier, it is the state of stress, which determines whether fracture will occur or not. In UPM, the geometry of the tool coupled with the depth of cut and work material properties determine the resulting force system which acts at the surface, and which determines whether fracture occurs in the case of nominally brittle materials. The

edge radius and the depth of cut as well as their ratio play an important role in nanometric cutting, which is the objective of this investigation.

5.3.2. Methodology of MD Simulation

Figure 5.13 is a schematic of the model used in the simulations with a tool having large edge radius compared to the depth of cut showing various regions of interest. Copper workmaterial and an infinitely hard tool were used in these simulations. The potential used was a pairwise sum of Morse potentials. MD simulations were conducted on a Digital α-workstation with a clock speed of 333 MHz. The tool edge radius (r: 1.207 to 21.72 nm) and the depth of cut (d: 0.362 to 2.172 nm) were varied in specific combinations with the d/r ratio varying between 0.1 to 0.3.

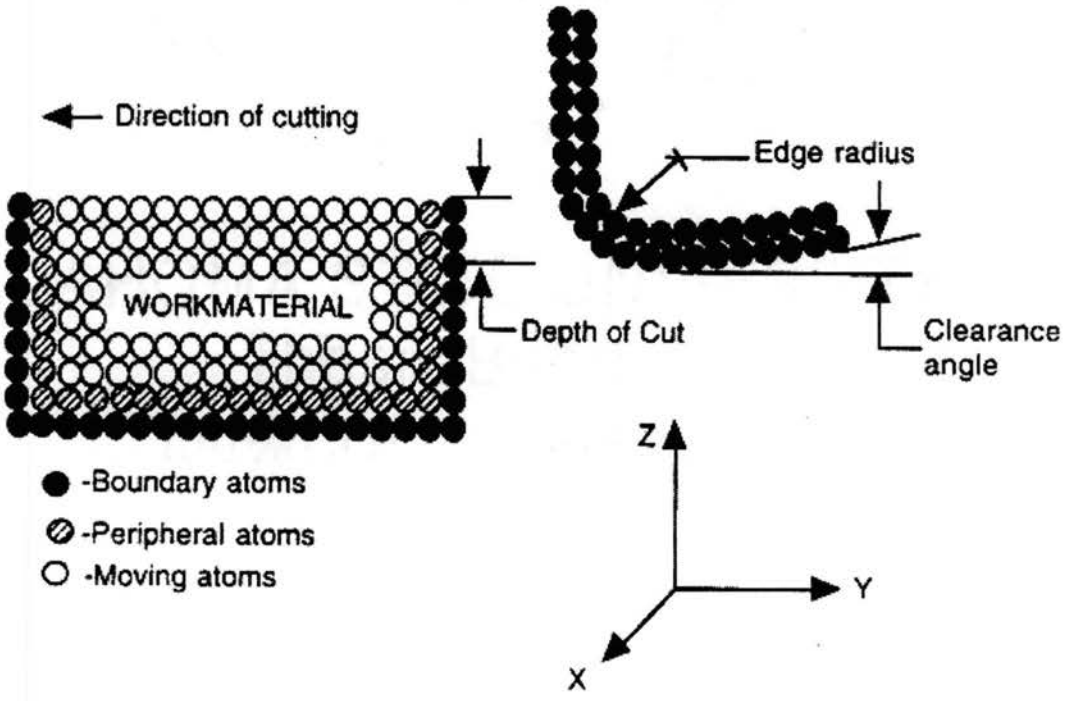

Figure 5.13. Schematic of the MD Simulation Model

5.3.3. Results and Discussion

5.3.3.1. Effect of Tool Edge Radius and Depth of Cut On the Mode of Deformation

Figures 5.14 (a) - (d) to 5.16 (a) - (d) are photographs of the MD simulation of nanometric cutting process conducted for various d/r ratios (0.1, 0.2, and 0.3, respectively) and for different depths of cut (0.362 nm - 2.172 nm). They show an increase in the extent of plastic deformation ahead of the tool as well as extensive subsurface deformation with increase in depth of cut for a given d/r ratio. The generation of dislocations can also be seen especially at higher depths of cut and with higher tool edge radii. The dislocation density for a given cutting condition increases, as the cutting process progresses because of the generation of additional dislocations along different directions due to barriers to the dislocation motion. Due to the absence of any inherent defects in the workmaterial, such as voids, inclusions, grain boundaries in the MD simulation model used, the only barrier to the dislocation motion are the dislocation interactions leading to additional dislocations. It is also found that the dislocation density increases with increasing depths of cut for a given d/r ratio due to increase in the force that can generate dislocations.

The extent of subsurface deformation appears to increase with decrease in the d/r ratio while the extent of the chip generated appears to increase with increase in the d/r ratio. This indicates increase in the cutting action and decrease in the ploughing or rubbing action between the cutting tool and the workmaterial as the d/r ratio increases.

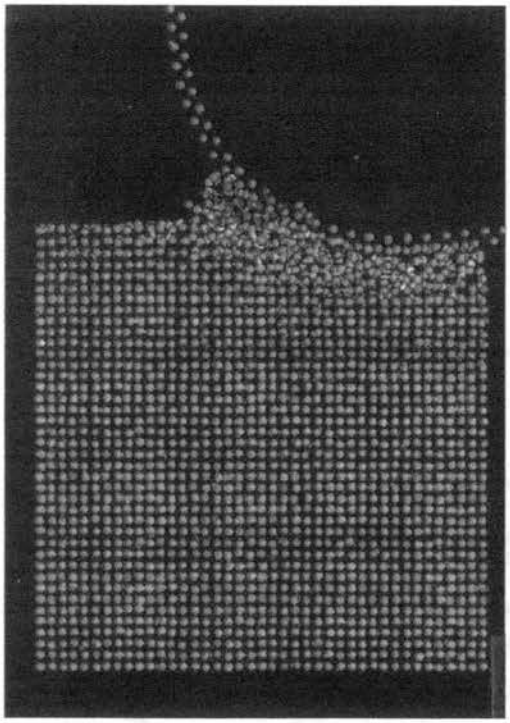

Cut depth: 0.362 nm, radius: 3.62 nm

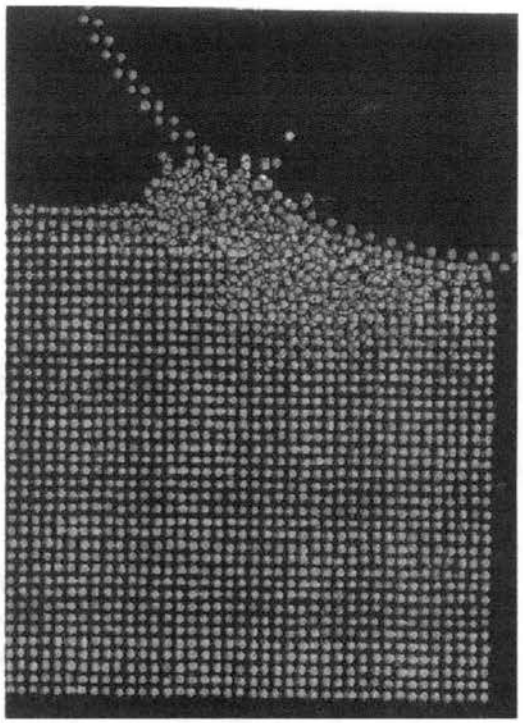

Cut depth: 0.724 nm, radius: 7.24 nm

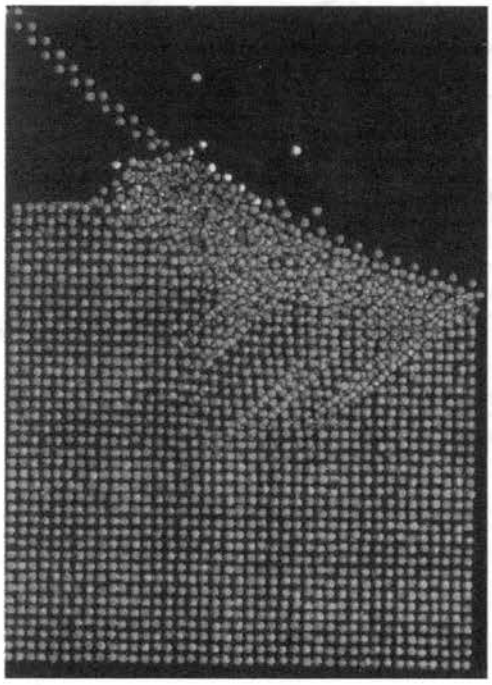

Cut depth: 1.448 nm, radius: 14.48 nm

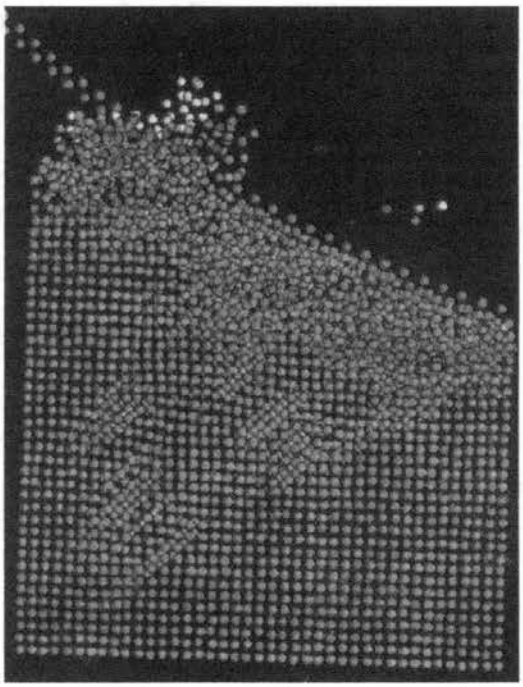

Cut depth: 2.172 nm, radius: 21.72 nm

Figure 5.14. Photographs of the MD simulation of nanometric cutting for a d/r ratio of 0.1

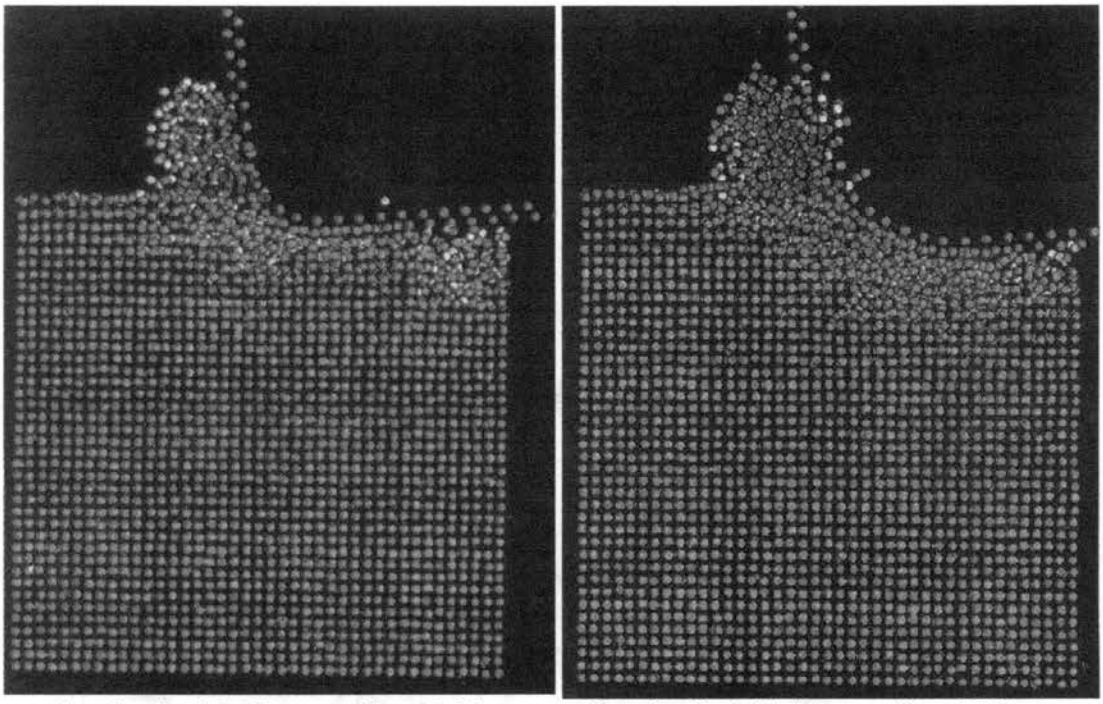

Cut depth: 0.362 nm, radius: 1.81 nm Cut depth: 0.724 nm, radius: 3.62 nm

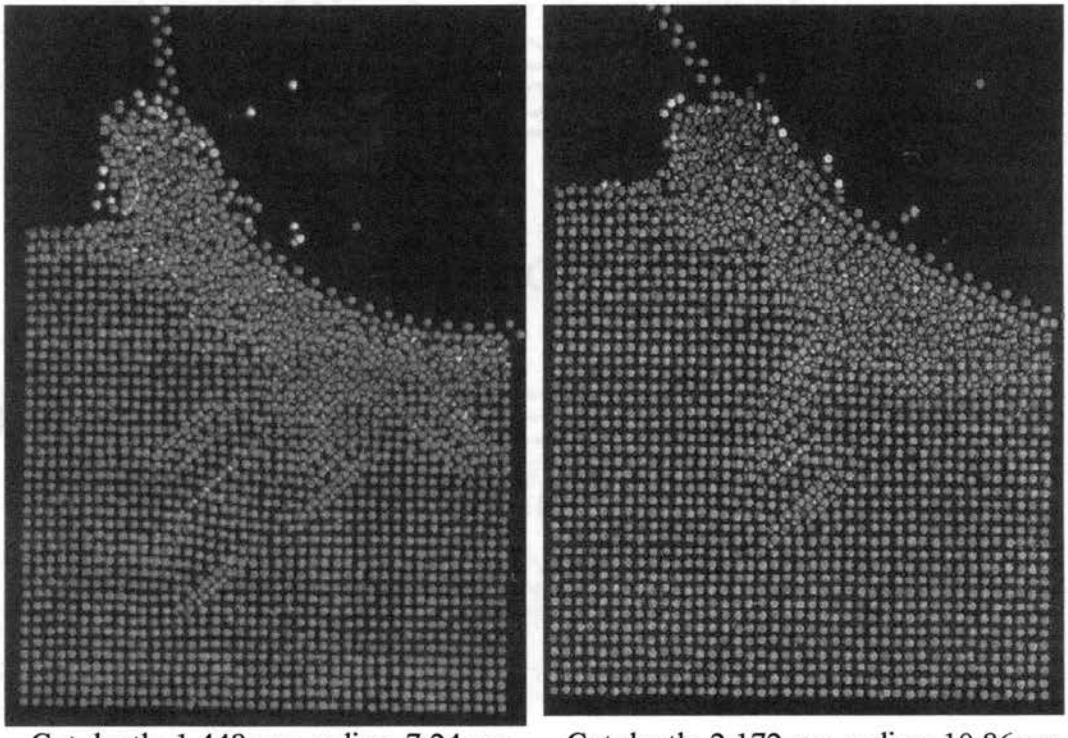

Cut depth: 1.448 nm, radius: 7.24 nm Cut depth: 2.172 nm, radius: 10.86 nm

Figure 5.15. Photographs of the MD simulation of nanometric cutting for a d/r ratio of 0.2

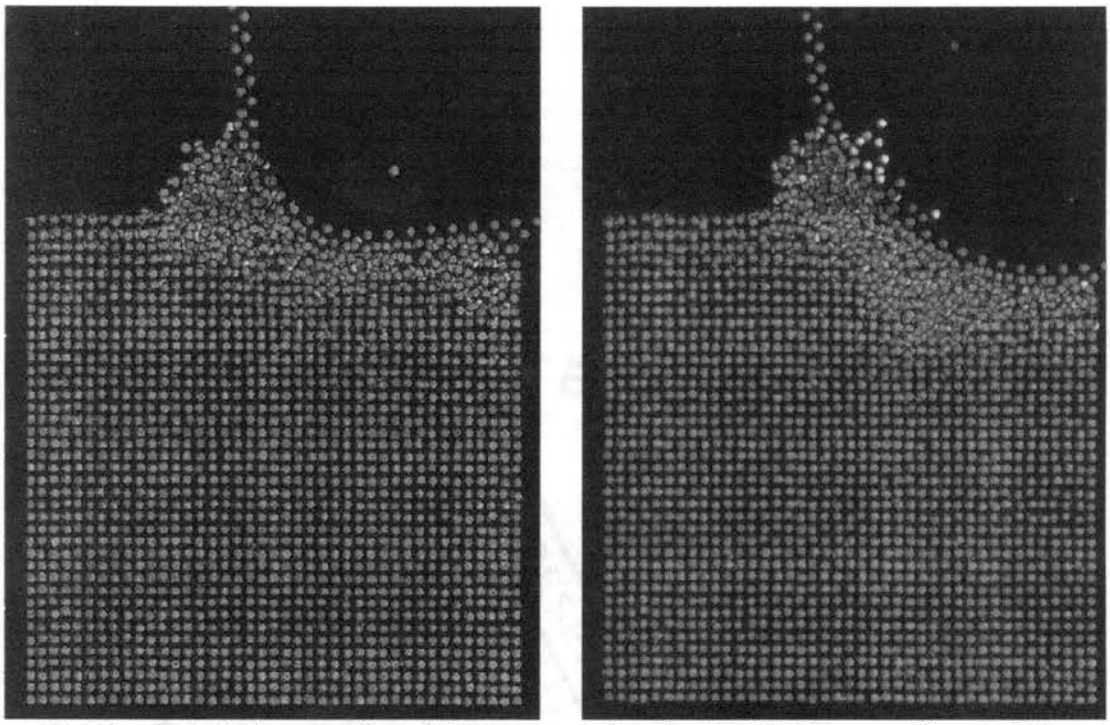

Cut depth: 0.362 nm, radius: 1.207 nm Cut depth: 0.724 nm, radius: 2.413 nm

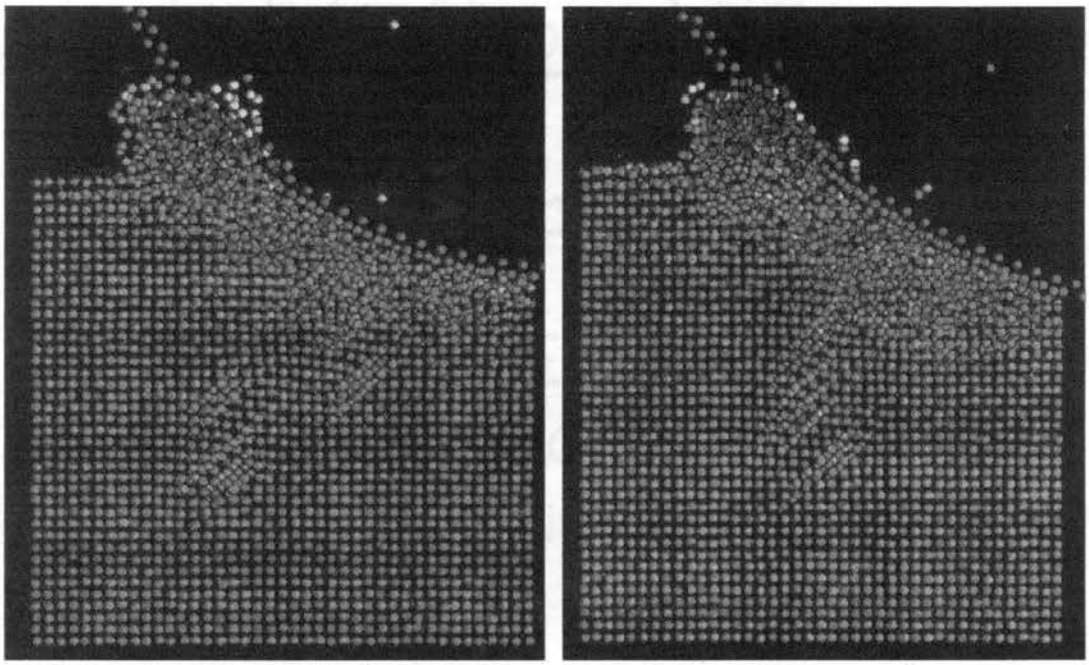

Cut depth: 1.448 nm, radius: 4.827 nm Cut depth: 2.172 nm, radius: 7.24 nm

Figure 5.16. Photographs of the MD simulation of nanometric cutting for a d/r ratio of 0.3

Also, for a given depth of cut, an increase in the tool edge radius (i.e., lower d/r ratios) seems to decrease the extent of chip formation. This is because at higher values of edge radius, the effective tool rake angle will be more negative, and hence less conducive to chip formation process. Further, for a given ratio of d/r, the increase in edge radius increases the negative rake angle and consequently, the shear region is rotated towards the workmaterial.

Table 5.3. Results of MD simulation study for a range of d/r ratios (0.1 to 0.3)

No	Depth of Cut (d), nm	Tool Edge Radius (r), nm	d/r	Cutting Force/Unit Width (F_c), N/mm X 10^2	Thrust Force/Unit Width (F_t), N/mm X 10^2	F_t/F_c	Specific Energy, N/mm^2 X 10^{-5}
1	0.362	3.62	0.1	2.86	6.056	2.117	0.79
2	0.724	7.24	0.1	3.763	7.977	2.12	0.52
3	1.448	14.48	0.1	5.564	9.254	1.663	0.384
4	2.172	21.72	0.1	6.98	9.747	1.396	0.321
5	0.362	1.81	0.2	2.773	4.67	1.684	0.766
6	0.724	3.62	0.2	3.774	7.576	2.007	0.521
7	1.448	7.24	0.2	5.509	9.079	1.621	0.38
8	2.172	10.86	0.2	6.946	9.5	1.37	0.32
9	0.362	1.207	0.3	2.654	4.155	1.566	0.733
10	0.724	2.413	0.3	3.653	6.739	1.845	0.505
11	1.448	4.827	0.3	5.407	8.839	1.635	0.373
12	2.172	7.24	0.3	6.783	8.941	1.32	0.312

5.3.3.2. On the variation of forces

Table 5.3 summarizes the results of MD simulation study for various depths of cut and tool edge radii for a range of d/r ratios. In the following, the effect of tool edge radius, the depth of cut, and the ratio of d/r in nanometric cutting will be analyzed.

5.3.3.2.1. Effect of tool edge radius

Figures 5.17 (a) - (c) show the variation of the cutting and the thrust force with tool edge radius for different depths of cut, respectively. It can be seen that while the forces increase with tool edge radius, especially at the smaller edge radius (this is more pronounced in the case of thrust force than the cutting force), they more or less become independent of the edge radius at higher values of tool edge radius. It can also be observed that this near constant forces with high tool edge radius is associated with high depths of cut. This is because at higher values of the tool edge radius (and high depths of cut), the equivalent negative rake angle varies in a narrow range while at the lower values of tool edge radius (and low depths of cut), it varies significantly. Also, at the higher edge radius, the ratio of the thrust to the cutting force remains more or less constant while at the lower edge radius, they increase with increase in the edge radius [Figure 5.17 (c)]. Also, this ratio decreases with increase in the depth of cut, indicating more cutting and less subsurface plastic deformation of the workmaterial. Figure 5.18 shows the variation of the specific energy with tool edge radius for different depths of cut. While the specific energy seems to increase with tool edge radius for small values of tool edge radius (and small values of depth of cut), it appears to be a constant and independent for higher values of tool edge radius (and higher depths of cut).

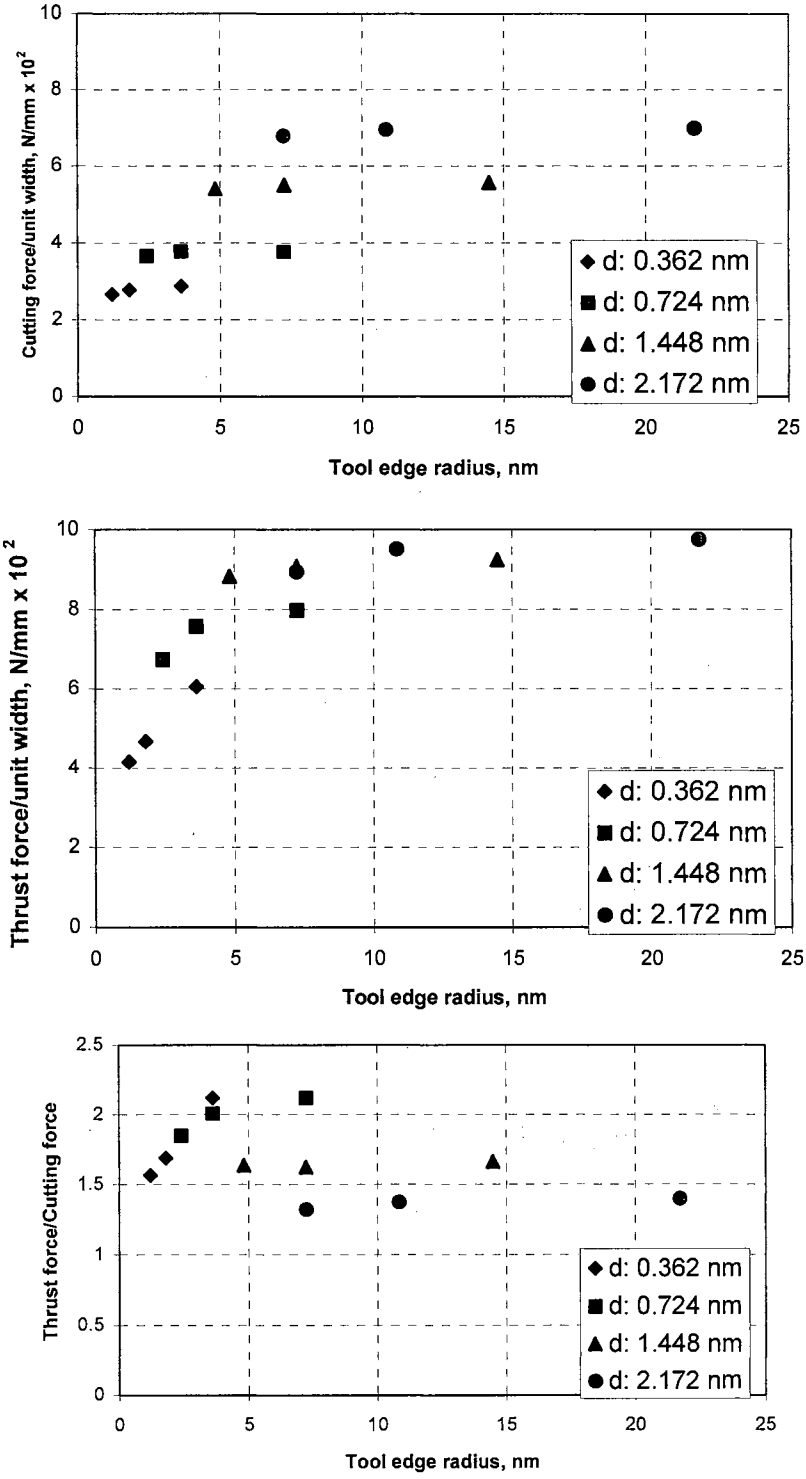

Figures 5.17 (a) - (c) Variation of the cutting and the thrust force and the force ratio with tool edge radius for different depths of cut, respectively

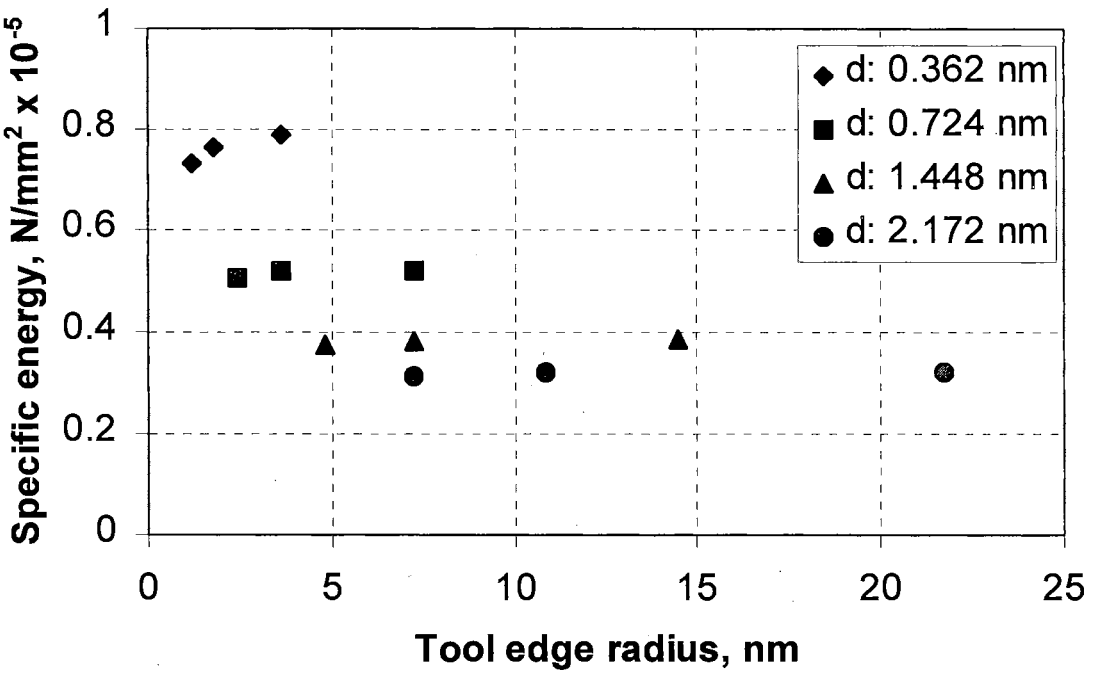

Figure 5.18. Variation of specific energy with radius in MD simulation of cutting

5.3.3.2.2. Effect of depth of cut

Figures 5.19 (a) - (c) show the variation of the cutting and the thrust forces, and the ratio of the thrust force to the cutting force with depth of cut for various d/r ratios, respectively. It can be seen that the cutting force increases linearly with increase in the depth of cut. Also, the values for different d/r ratios more or less coincide indicating that they are independent of the d/r ratio. This is important to recognize for if d/r ratio is not maintained constant, then one would not get such a result because in that case both depths of cut and the edge radius varies. On the other hand, when the d/r ratio is maintained constant, by varying the depth of cut, one can study the effect of depth of cut exclusively. Figure 5.19 (b) shows the variation of thrust force with depth of cut showing a much wider variation in the values for different d/r ratios. Also, the variation in the thrust force with d/r seems to saturate at higher depths of cut. The ratio of thrust force to cutting force

with depth of cut [Figure 5.19 (c)] shows a slight decrease in the ratio indicating more cutting and less subsurface plastic deformation with increase in depths of cut.

Figure 5.20 shows the variation of specific energy with depth of cut, indicating a rapid increase in specific energy with decrease in depth of cut when the depth of cut reaches more or less atomic dimensions. In other words, the so-called 'size effect' one normally refers to in conventional machining and grinding does not seem to occur until one approaches close to the atomic dimensions. Therefore, an increase in specific energy with decreasing depth of cut (in the micrometer range) reported in conventional machining and grinding may be attributed to change in the rake angle and/or tool wear and not necessarily due to 'size effect'. Also, one can see very little scatter in the results for different d/r ratios (except at the lowest depth of cut of 0.362 nm) indicating that in cases where there is a definite edge radius, one has to maintain the ratio of d/r constant if one were to investigate the effect of depth of exclusively.

5.3.3.2.3. Effect of Ratio of Depth of Cut to Edge Radius (d/r)

Figures 5.21 (a) - (c) show the variation of the cutting and the thrust force, and the ratio of the thrust force to the cutting force with the ratios of depth of cut/edge radius (d/r), for different depths of cut, respectively. It can be seen that the cutting force is more or less independent of the d/r ratio [Figure 5.21 (a)] with the level of the force increasing with increasing depth of cut. The thrust force on the other hand shows a decreasing trend with increasing d/r ratio [Figure 5.21 (b)] with the level of the force increasing with increasing depth of cut. Also, the difference in the level of the force decreases with

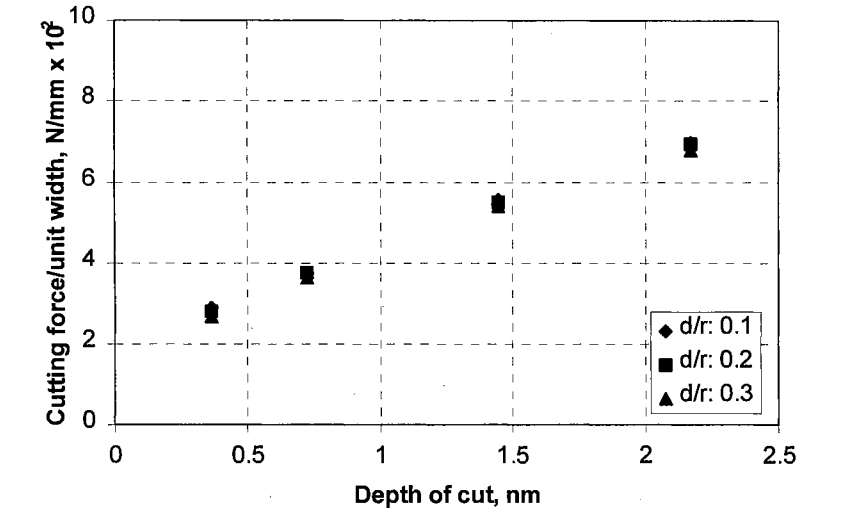

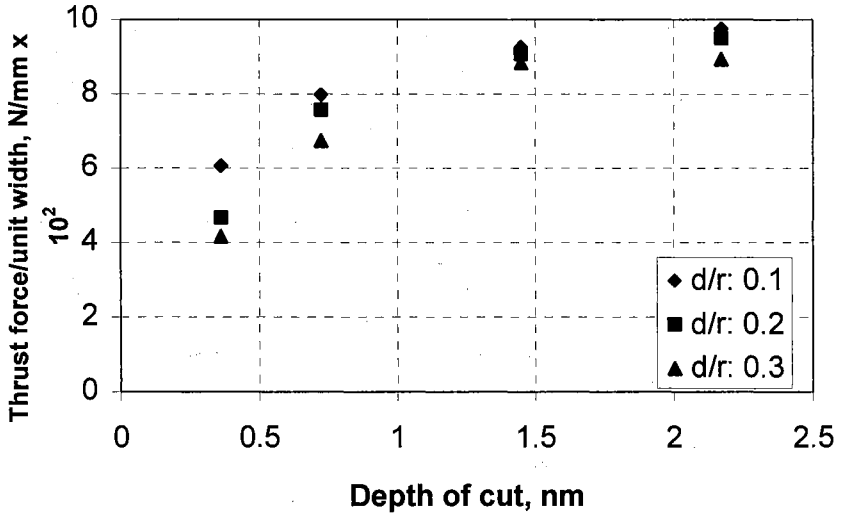

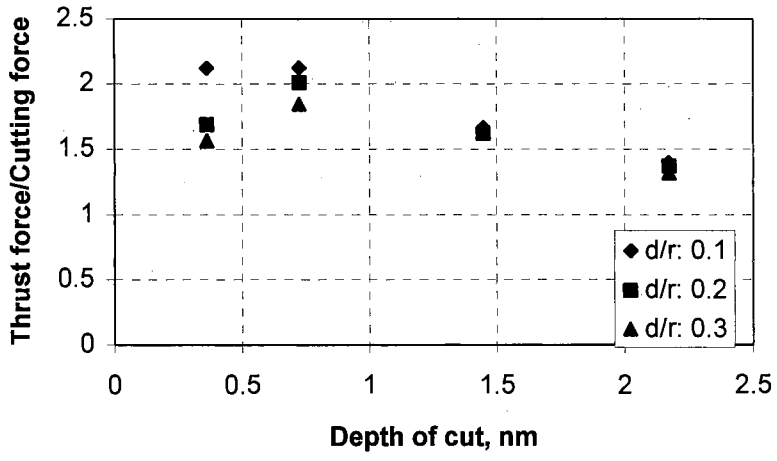

Figures 5.19 (a) - (c) Variation of the cutting and the thrust force, and the force ratio with depth of cut, for different d/r ratios, respectively

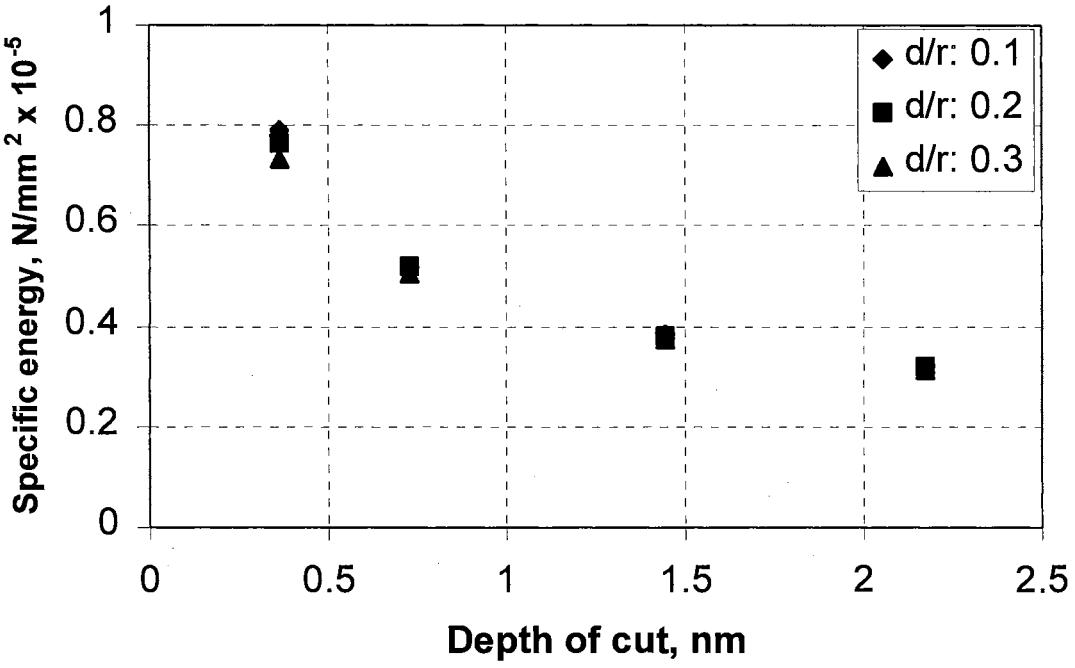

Figure 5.20. Variation of specific energy with depth of cut in nanometric cutting

increase in the depth of cut. The force ratio shows a slight decrease with increase in the d/r ratio. This value is also found to be less at higher depths of cut than for lower depths of cut. Figure 5.22 shows the variation of the specific energy with the d/r ratio. The specific energy shoes a slight decrease with increase in the d/r ratio with higher specific energy corresponding to lower depths of cut.

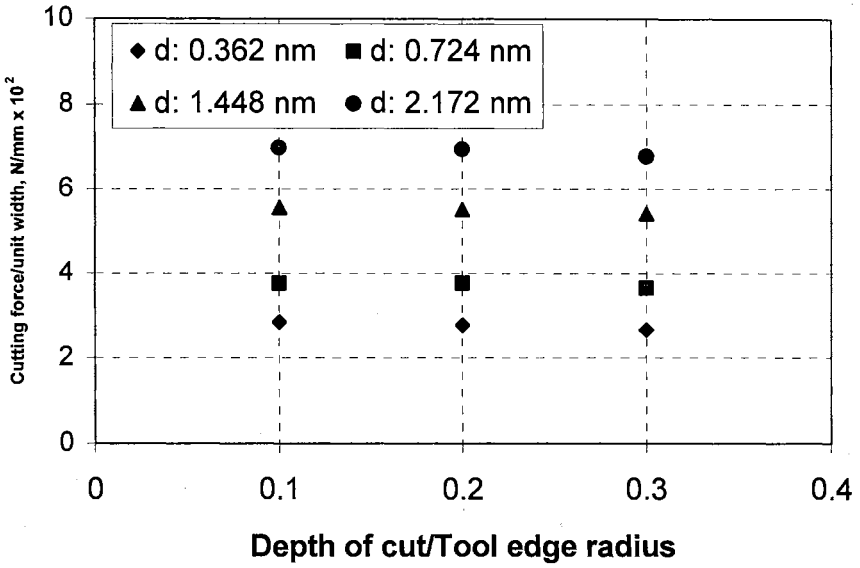

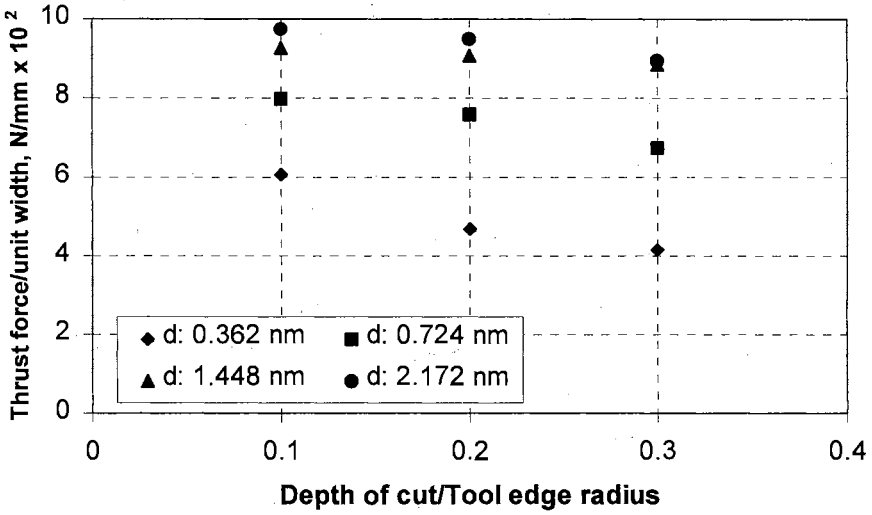

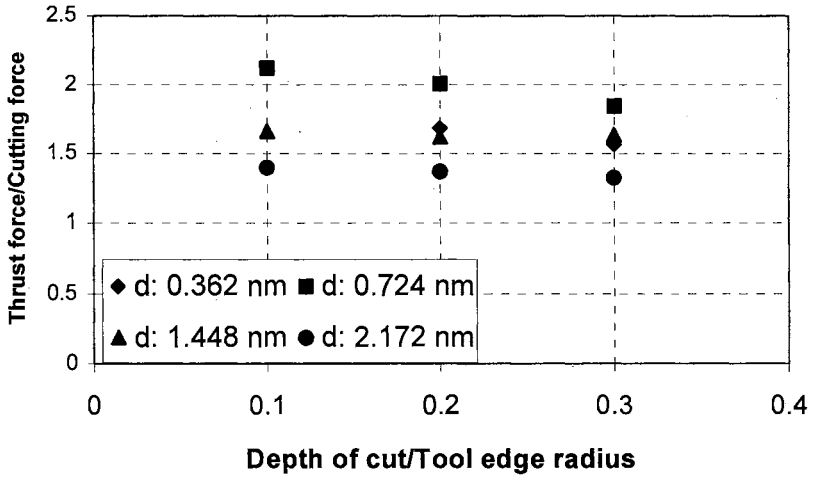

Figures 5.21 (a) - (c) Variation of forces and force ratio with d/r ratio for various depths

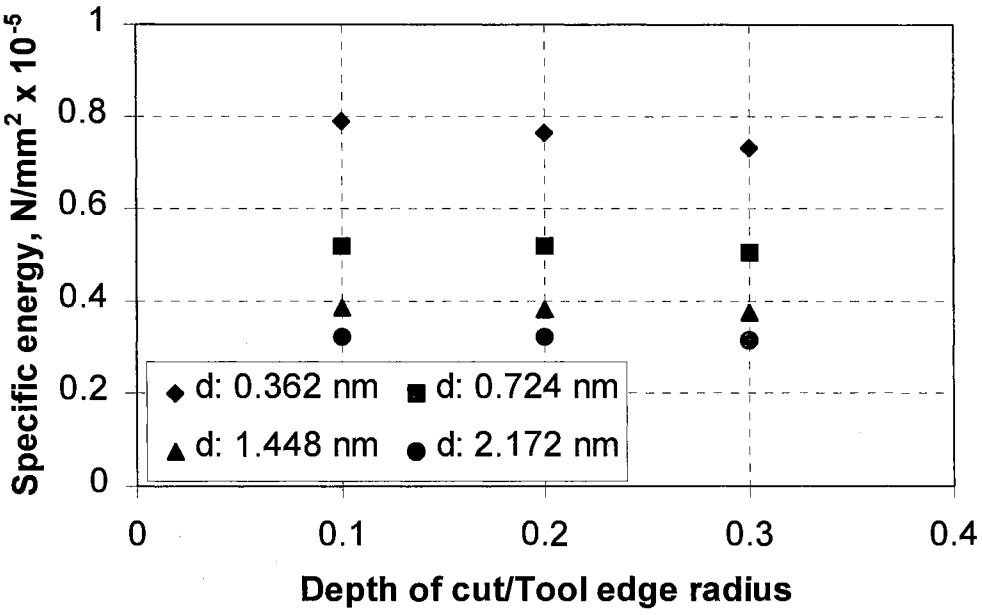

Figure 5.22 Variation of specific energy with the d/r ratio for various cut depths

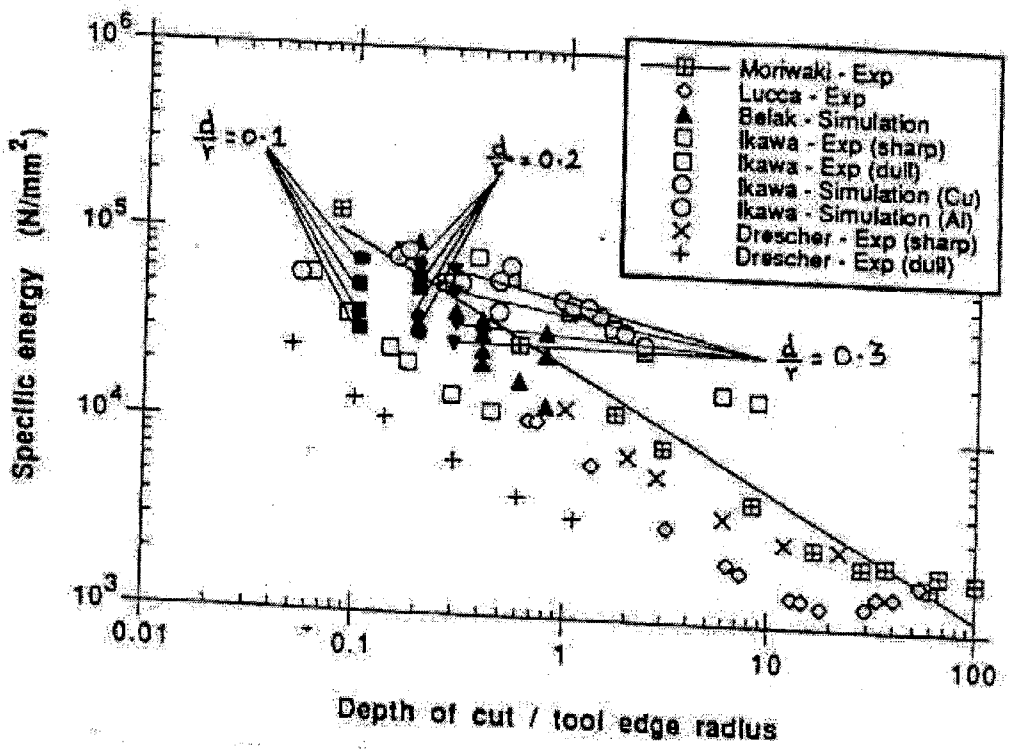

Figure 5.23. Variation of specific energy with d/r ratio from experimental and simulation results

Figure 5.23 shows the compilation of data of the variation of specific energy with the ratio of the depth of cut to the tool edge radius, from the UPM experimental and MD simulation results reported in the literature (Belak et al., 1991). Also shown is MD simulation data obtained in the present investigation. It can be seen from the figure that the MD simulation results are in reasonable agreement with the results reported in the literature (both experimental and MD simulation). The specific energy for a given tool edge radius is higher at lower depths of cut as can be seen from Figure 5.22. This suggests an increased subsurface deformation, which is the characteristic of machining with high negative-rake-angle tools and/or at low depths of cut.

5.3.4. Conclusions

MD simulation studies were conducted with various tool edge radii (1.81-21.72 nm) and depths of cut (0.362-2.172 nm) at constant ratios of depth of cut to tool edge radius (d/r of 0.1, 0.2, and 0.3), to investigate the effect of tool geometry in nanometric cutting. It was observed that to study the effect of depth of cut when machining with an edge radius tool, it is necessary to maintain the ratio of d/r constant. By doing so, the depth effect can be separated from the edge radius effect. Even though, in the literature, experimental and MD simulation data was plotted showing a decrease in specific energy with increase in the ratio of depth of cut to tool edge radius, in the narrow range of d/r ratios investigated (0.1 to 0.3), this was not found to be the case.

5.4. Material Removal Mechanisms From Conventional Machining to Indentation-Sliding

In ultraprecision machining or grinding at fine depths of cut, most tools used have large edge radii (relative to the depth of cut) and large negative rake angles. For example, in single point machining of silicon wafers, negative rake angles as high as -30° or higher are typically used in industrial practice. It is the severe negative rake angle that provides the necessary hydrostatic pressures to enable plastic deformation of the workmaterial beneath the indenter. One should not liken this type of plastic deformation with the concentrated plastic deformation, which occurs ahead of the tool in the case of conventional machining of metals with positive rake tools. In fact, plastic deformation in the case of brittle materials with large negative rake angle tools is energy intensive and inefficient compared to machining metals with positive rake angle tools. Based on the MD simulations of nanometric cutting with tools of various rake angles and edge radius relative to depth of cut a material removal mechanism from conventional machining to indentation-sliding is proposed.

For the case of conventional machining, the tool geometry is such that the rake angle is close to zero or slightly negative (-5°). With a positive rake tool, the cutting force is generally about twice the thrust force. The deformation ahead of the tool is either in a concentrated shear plane or in a narrow shear zone [Figure 5.24 (a)]. In grinding, although one cannot identify a definite rake angle as it is unknown and varies continuously during the process due to wear and self-sharpening of the abrasive, it is

generally accepted that the tool presents a large negative rake angle of -60 °. Also, the cutting force is about half of the thrust force [Figure 5.24 (b)]. In ultraprecision machining (e.g., single point diamond turning) at depths of cut smaller than the tool edge radius, the tool presents a large negative rake angle and the radius of the tool edge acts as an indenter [Figure 5.24 (c)]. The final progression in this series, which represents a rotation of the resultant force vector downward towards the workmaterial (or counterclockwise), is indentation-sliding of a blunt indenter across the work surface. This situation could represent the case when the tool is rigidly supported and cuts the workpiece under a stress state that no median vents are generated but material underneath the tool is plastically deformed due to large hydrostatic pressure [Figure 5.24 (d)].

It is apparent when one considers the force system which results over a range of tool-workmaterial interactions, there is an obvious progression from conventional machining with positive rake angles, to grinding, to ultraprecision machining, and finally to indentation-sliding. It appears that an indentation-sliding model would be more appropriate when considering machining brittle materials with tools of large edge radius relative to the depth of cut or large negative rake angle tools. Similarly, in grinding of ductile materials [Figure 5.24 (b)] the appropriate model would involve either using tools of large edge radius relative to depth of cut or large negative rake angle tools.

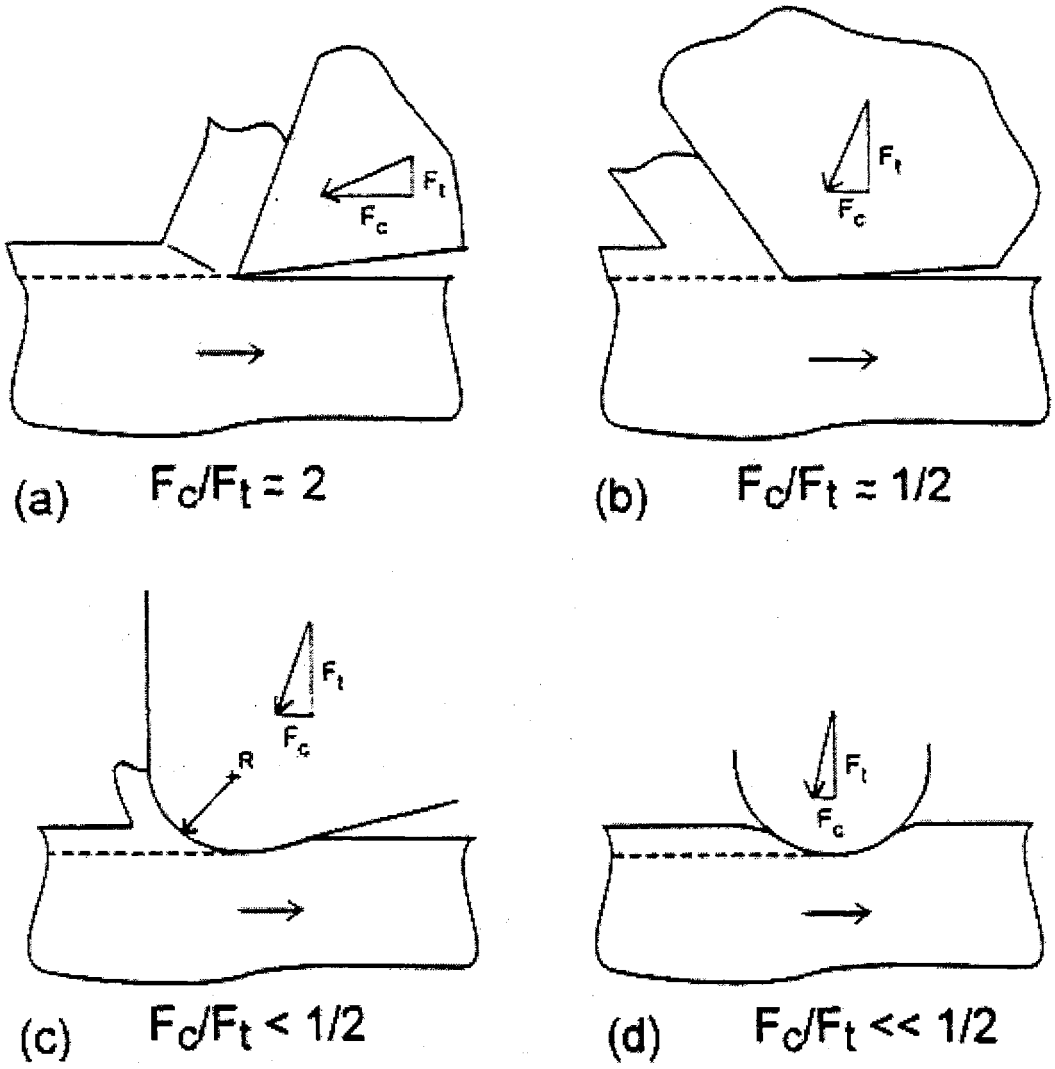

Figure 5.24. The progression of tool/work interactions which result in the rotation of the resultant force anticlockwise downward towards the workpiece surface (a) conventional cutting, (b) grinding, (c) ultra-precision machining, and (d) indentation-sliding

CHAPTER 6

EFFECT OF CRYSTAL ORIENTATION AND DIRECTION OF CUTTING OF SINGLE CRYSTAL ALUMINUM [a, b]

6.1. INTRODUCTION

Studies on the machining of metals and their alloys are generally conducted on polycrystalline materials, as most engineering materials are polycrystalline in nature. However, in the case of nanometric cutting and ultraprecision grinding, the depth of cut is far less than the average grain size of a conventional polycrystalline material. Consequently, UPM/UPG basically involves cutting within a single grain with periodic interruptions at the grain boundaries. Since grain orientation changes from one crystal to another in a polycrystalline aggregate, the cutting tool in nanometric cutting experiences workmaterial with different crystallographic orientations and directions of cutting.

---

a - R. Komanduri, N. Chandrasekaran, L. M. Raff, 1999, "Orientation Effects in Nanometric Cutting of Single Crystal Materials: An MD Simulation Approach," Annals of CIRP, 48/1, 67-72

b - R. Komanduri, N. Chandrasekaran, L. M. Raff, 2000, "M.D. simulation of nanometric cutting of single crystal aluminum-effect of crystal orientation and direction of cutting," Wear, 242, 60-88

However, there is hardly any information on the effect of orientation and direction of cutting aluminum workmaterial. In addition, there are many precision engineering applications where single crystal materials like silicon, germanium are finished by nanometric cutting. Since, some of the single crystal materials are anisotropic in their physical and mechanical properties, it is necessary to investigate their behavior, namely, the variation of the cutting forces, mechanics of chip formation, specific energy, etc. in different orientations and cutting directions. This is the objective of the present investigation.

Material removal at small depths of cut involves plastic deformation ahead of the tool and elastic recovery of the finished surface (machined surface underneath the clearance face of the tool). The elastic recovery of the machined surface results in small upward projection of material at the machined surface near the tool tip and consequent rubbing of it with the clearance face of the tool. In conventional cutting where the depth of cut is significant, the elastic effects are rather small compared to the plastic deformation effects and hence may be neglected. This is not the case in nanometric cutting due to extremely small depths of cut, on the order of a few nanometers or less. Thus, the variation in the elastic modulus with crystallographic orientation can significantly affect the finish, accuracy, and surface integrity of the machined components. Consequently, the accuracy of the machining process and the quality of the finished surface (surface integrity) depend upon both the plastic and elastic behavior of the material being machined.

Since the binding forces are strongly affected by the distance between the atoms in a crystal, the elastic constants of a single crystal will vary with the direction. For example, the modulus of elasticity in any direction of a cubic crystal is given by (Dieter, 1986),

$$\frac{1}{E} = S_{11} - 2[(S_{11}-S_{12}) - \frac{1}{2}S_{44}](l^2m^2+m^2n^2+l^2n^2)$$

where S_{ij} are the elastic constants in different orientations and l, m, and n are the direction cosines.

Table 6.1. Summary of Properties of Single and Polycrystalline Aluminum

Elastic modulus (GPa), Polycrystalline	70.30
Shear Modulus (GPa), Polycrystalline	26.1
Poisson's ratio, Polycrystalline	0.345
Burger's Vector	2.86
Relative degree of anisotropy *	1.219
E_{111} (GPa)	76.1
E_{100} (GPa)	63.7
E_{110} (GPa)	72.59
$\frac{E_{111}}{E_{100}}$	1.19
C_{11} (10^{10}Pa)	10.82
C_{12} (10^{10}Pa)	6.13
C_{44} (10^{10}Pa)	2.85
S_{11} (10^{-11}Pa^{-1})	1.57
S_{12}(10^{-11}Pa^{-1})	-0.57
S_{44} (10^{-11}Pa^{-1})	3.51

Aluminum is used extensively in the disc drives, which are finished to very high accuracy, finish, and flatness before they are coated with nickel. It is also used extensively for mirrors in lasers, rotating mirrors in copying machines, to name a few. Consequently, the study of the nanometric cutting of aluminum can be very useful to the computer, optical, laser, and printing industries in addition to its scientific relevance.

Table 6.1 gives a summary of the elastic properties of polycrystalline and single crystal aluminum in different directions (stiffness, compliance constants, and elastic

anisotropy). It may be noted that aluminum has a degree of anisotropy of 1.219 in the elastic region. In comparison, copper has been reported to have much higher degree of anisotropy of 3.203 (Hertzberg, 1996). A somewhat similar anisotropy in the plastic range can also be anticipated of these materials. For example, it is well known that for the FCC metals, slip is predominant on the {111} planes and [110] directions. In nanometric cutting one would, therefore, expect these planes and directions to result in easy slip and perhaps lower cutting forces. It would be interesting to investigate the degree of anisotropy of aluminum in nanometric cutting and compare it with its value in the elastic region, which is 1.219. Variations in the plastic behavior of the material in cutting with different crystallographic orientations can thus be determined.

In this section, the results of the Molecular Dynamics (MD) simulation of nanometric cutting of single crystal aluminum of different orientations and in specific cutting directions with tools of different rake angles are reported to investigate the anisotropic behavior of this material.

6.2. LITERATURE REVIEW

6.2.1 Machining of Single Crystal Materials

One of the pioneering studies on the micromachining of single crystal copper and aluminum was made by von Turkovich and Black (1970) who used ultramicrotome to study the chip formation process at a cutting speed of 1 mm/s using a glass knife edge of 75° included angle, a rake angle of 13-14°, and a clearance angle of 2-3°. The cutting directions investigated in Cu and Al single crystals were: <100> parallel to the (100) plane, and <110> parallel to the (112) plane. They reported for the first time that shear ahead of the tool occurs in a shear front whose thickness is of the order of a few tens or

hundreds of atomic spacing implying strain rates much larger than 10^4 sec^{-1} even at very low speed of cutting (~ 1 mm/s) [Figure 6.1]. This was followed by the work of Black (1971) who observed the discontinuous nature of the machining process on a microscale leading to the systematic formation of shear lamella separated by shear fronts. He observed large variations in the chip thickness ratio (ratio of chip thickness to the uncut chip thickness) with variation in the crystal orientation.

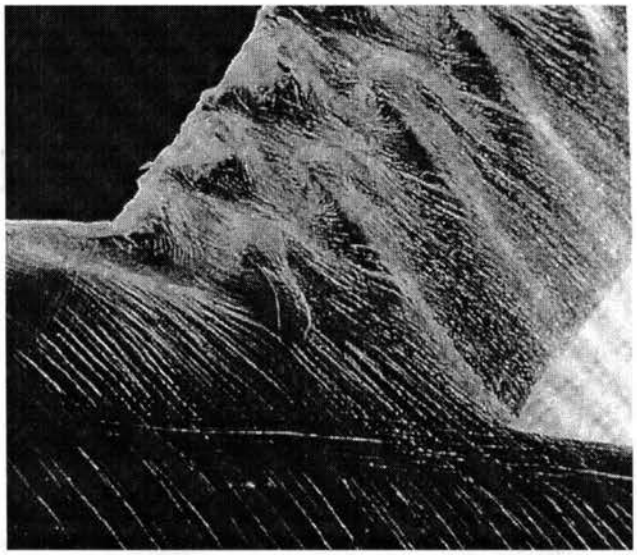

Figure 6.1. SEM micrograph of a chip root showing plastic deformation occurring in a shear zone (after von Turkovich and Black, 1970)

Ramalingam and Hazra (1973) conducted cutting experiments on single crystal aluminum of known crystal orientations. They found the dynamic shear stress (DSS) to remain constant for all orientations and consequently concluded the DSS to be a material property. They also reported a wide variation in the shear angle with orientation. Several other research workers have suggested the constancy of DSS and attributed DSS as a true material property (Chao et al., 1952, 1959; Kobayashi and Thompson, 1959).

Williams and Gane (1977) conducted orthogonal cutting experiments on single crystal copper in two orientations - one with the (111) plane parallel to the slip plane and the other parallel to the cutting direction. In contrast to the results reported by Ramalingam and Hazra (1973), they observed the shear angle to be relatively unchanged and the resolved shear stress (RSS) dependent on the orientation. They also observed the shear stress to be ~40% lower when the (111) plane was parallel to the shear plane as this orientation favored easy chip formation. In a subsequent work, Williams (1993) observed copper to display a dependence of RSS with orientation while aluminum did not, thus validating the results of both Ramalingam and Hazra (1973) and Williams and Gane (1977). He attributed this difference to the variation in the nature of dislocation motion in aluminum as compared to copper due to differences in the stacking fault energy and equilibrium spacing of the atoms in the crystal.

Ueda *et al.* (1980) investigated the mechanism of chip formation, variation of cutting forces, and shear angle with the crystallographic orientation during diamond cutting of β-brass. They observed typical lamellar slip structure and reported the formation of discontinuous chip in a particular range of crystal orientations. They observed the shear angle to vary from ~15^{o} - 60^{o} with changes in crystallographic orientations. These measured values were found to be in reasonable agreement with the estimated values based on Schmid factor. The cutting forces and surface roughness values were also observed to depend on the material anisotropy. However, no explanation was offered for these unusually high shear angles.

In most theoretical analysis of the cutting process, the workmaterial is assumed to be isotropic and homogeneous for convenience. Lee (1990) proposed a physical model to predict the variation of cutting forces due to different crystallographic orientations based on the changes in the shear angle of the crystal being machined. In a subsequent study,

Lee *et al.* (1993) proposed a microplasticity model to analyze the effect of crystallographic orientation on the shear zone formation in micromachining. They proposed that the most likely shear angle is the one that has the most negative texture softening factor among the ones with the same minimum shear strength. Based on this, they concluded that the variation in microcutting force could be predicted if the change in crystallographic orientation of the substrate material with respect to the cutting direction is known.

Konig and Spenrath (1991) conducted cutting experiments on monocrystalline copper (OFHC) substrate with {100}, {110}, and {111} oriented crystals along different cutting directions. They observed a significant dynamic component of the cutting force along the <100> cutting direction, which they attributed to the resulting poor surface quality of the machined surface. However, when the substrate was machined along the <110> direction, the dynamic component of the cutting force was low and consequently, a high surface quality was obtained. They also predicted the plastic material properties to be the cause for the surface slip encountered at the grain boundaries.

Moriwaki *et al.* (1991) conducted *in situ* machining experiments inside the SEM on a single crystal copper in the (110) and (111) planes and in various cutting directions at a depth of cut ranging from 0.1 to 5 μm and a cutting speed of 120 μm/min. They found the crystallographic orientation affects the chip formation process in terms of magnitude of the shear angle and the cutting force. While in some orientations, the shear angles were reported to be $<45^{o}$ [Figure 6.2 (a)], in other orientations they were as high as 60^{o}. However, no explanation was offered for the unusually high values. Moriwaki *et al.* (1991) observed that the mechanics of chip formation was not much influenced as the depth of cut was reduced from conventional to micrometer (or even submicrometer) depths of cut. Moriwaki *et al.* (1993) in a subsequent study, based on ultraprecision

orthogonal microdiamond cutting of single crystal copper, concluded that the cutting forces, shear angle, and surface roughness are not much influenced by the crystal orientation when the depth of cut is decreased to submicrometer level (< 1 μm).

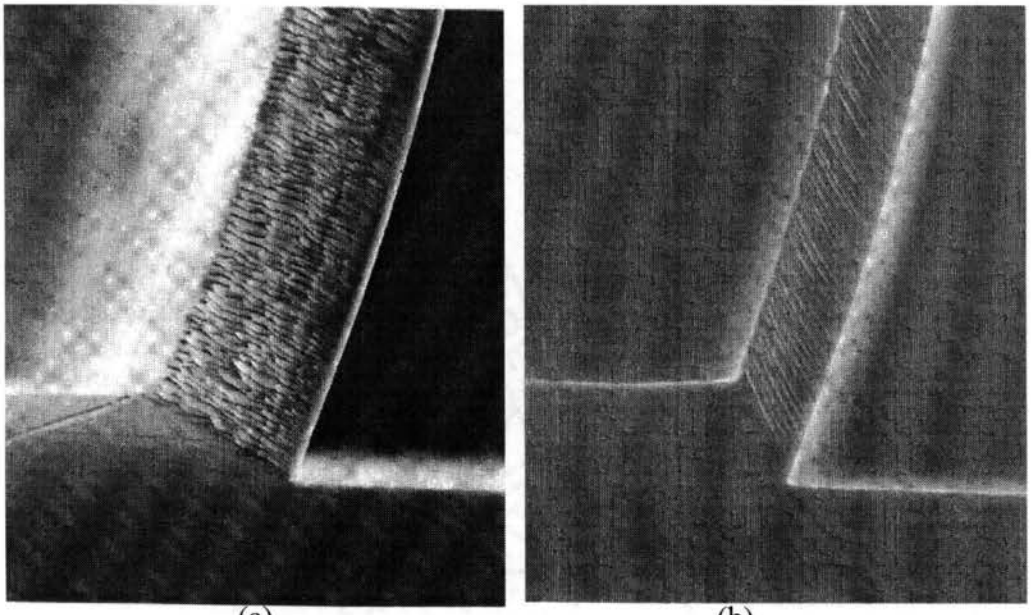

(a) (b)

Figure 6.2. SEM Micrographs of Chiproot of a Single Crystal Copper Showing (a) Shear Angle < 45 deg. (Orientation Angle = 55deg.) and (b) Shear Angle > 45 deg. (Orientation Angle = 90 deg.) [after Moriwaki et al., 1991]

Sato *et al.* (1991) conducted microcutting experiments on aluminum single crystals oriented along different crystallographic planes. They reported a better surface finish when cutting along [0-11] direction as compared to [1-21] direction. To *et al.* (1997) conducted diamond turning of aluminum single crystal rods with crystallographic axes normal to <100>, <110>, and <111> using a cutting tool of 0.635 mm edge radius, 0^{o} rake angle and 5^{o} clearance angle and depths of cut in the range of 1-10 μm. Continuous chip formation was observed under all cutting conditions. They reported highest cutting force for the {110} oriented crystals and lowest for the {111} oriented crystals. They

also observed the (001) oriented crystals to exhibit a relatively low magnitude of the dynamic component of the force compared to the (110) or (111) oriented crystals. To *et al.* (1997) suggest a high surface finish with (001) plane but a poor surface finish when turning was carried out on the (110) plane. According to the authors, the depth of cut had negligible effect on the surface roughness over the range of depth of cut (1-10 μm) studied in their experiments.

Only limited results in the ultraprecision machining of single crystal aluminum in different orientations have been reported in the literature. A reason for the limited effort in the study of single crystal materials is their high cost and difficulties involved in setting up a proper orientation and direction of cutting of the crystal. Another limitation of the above studies is that they are either postmortem in nature or done at not high enough resolution for investigation of the dislocation motion during machining. MD simulation is an alternative approach.

6.3. METHODOLOGY FOR MD SIMULATION OF NANOMETRIC CUTTING

6.3.1. Cutting Model and Simulation Conditions

MD simulations of nanometric cutting were conducted on single crystals of aluminum using a Digital α- workstation (Model 500) with a clock speed of 433 MHz to study the effect of crystallographic factors, namely, crystal orientation and direction of cutting. The schematic of the MD simulation model used in this study is shown in Figure 6.3. Machining studies were conducted along specific combinations of the orientation of the work material {(111), (110), and (001)} and cutting direction <[$\bar{1}$10], [$\bar{2}$11], [100]> at a cutting speed of 500 m/sec and different depths of cut (0.81-1.62 nm). The specific combinations for the (111) orientation are the cutting directions [$\bar{1}$10] and [$\bar{2}$11], for the

(110) orientation are the cutting directions [$\bar{1}10$] and [001], and for the (001) orientation are the cutting directions [$\bar{1}10$] and [100], respectively. In addition, tools with different positive rake angles (0^o, 10^o, and 40^o) were used to investigate their effect on the mechanics of nanometric cutting. For convenience, an infinitely hard (tungsten) tool was used in these simulations, as tool wear is hardly a problem when machining pure aluminum.

Table 6.2 gives the computational parameters, details of the workmaterial and tool dimensions, width of cut, depth of cut, length of cut, and tool geometry used in the simulations. Figure 6.4 shows the various crystal orientations and the corresponding cutting directions for cubic crystals (Sato et al., 1991) that are used in this investigation. Figure 6.5 shows schematically the orientation of the workmaterial with respect to the direction of cutting (Shirakashi et al., 1991). It should be noted that while the simulation size of the workmaterial is maintained constant for all the crystal orientations and cutting directions (Table 6.2), the number of planes and consequently, the total number of atoms considered in the simulation size depend on the crystal orientation. The number of atoms in the workmaterial varies from 4852 to 3960 depending on the crystal set-up. Table 6.2 also tabulates the total number of atoms in the workmaterial for various combinations of crystal orientation and cutting direction. Consequently, the number of atoms to be cut for a particular depth and width of cut will change with orientation and cutting direction. While, the workmaterial orientation is varied the tool orientation is maintained constant in all the simulations (Table 6.2). The tool has 506 total number of atoms. The potential used in the simulations is a pairwise sum of Morse potential.

Table 6.2. Computation parameters used in the MD simulation of nanometric cutting

Configuration	3-D cutting
Potential used (potential parameters for the workmaterial)	Morse potential (D_L=0.2703 eV, α_L=1.1646 / A, r_{eL}=3.253 A and r_c=5.624 A)
Workmaterial dimension	4ax30ax25a, a-lattice constant
Number of atoms in the workmaterial based on crystal set-up	Crystal set-up -> No. of atoms (111)[$\bar{1}$10] -> 4852 (111)[$\bar{2}$11] -> 4687 (110)[$\bar{1}$10] -> 4046 (110)[001] -> 4658 (001)[$\bar{1}$10] -> 4728 (001)[100] -> 3960
Tool dimension	4ax12ax20a, a-lattice constant 506 total tool atoms
Tool material	Infinitely hard
Tool edge radius	Sharp edge
Tool rake angle	0°, 10°, and 40°
Tool Clearance angle	5°
Depth of cut	0.81 - 1.62 nm
Width of cut	1.62 nm
Cutting speed	500 m/sec
Bulk temperature	293 K

Table 6.3 gives the atomic density and the distance between the planes with respect to the orientation of an aluminum crystal (Dieter, 1986). The atomic density for aluminum, an FCC material, is maximum for the octahedral (111) plane and minimum for the dodecahedral (110) plane. Note that the planes of greatest atomic density (atoms per unit area) also are the most widely spaced planes. Both the atomic density and the distance between the atoms in a given direction of cutting are important considerations, for slip will occur on the densest planes and the shortest directions. Thus, a combination of both these factors affect the nature of plastic deformation of this material in nanometric cutting.

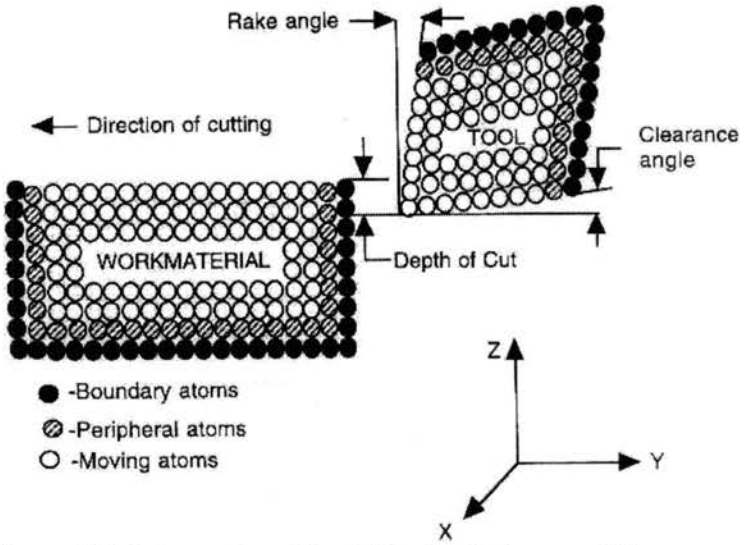

Figure 6.3. Schematic of the MD simulation model

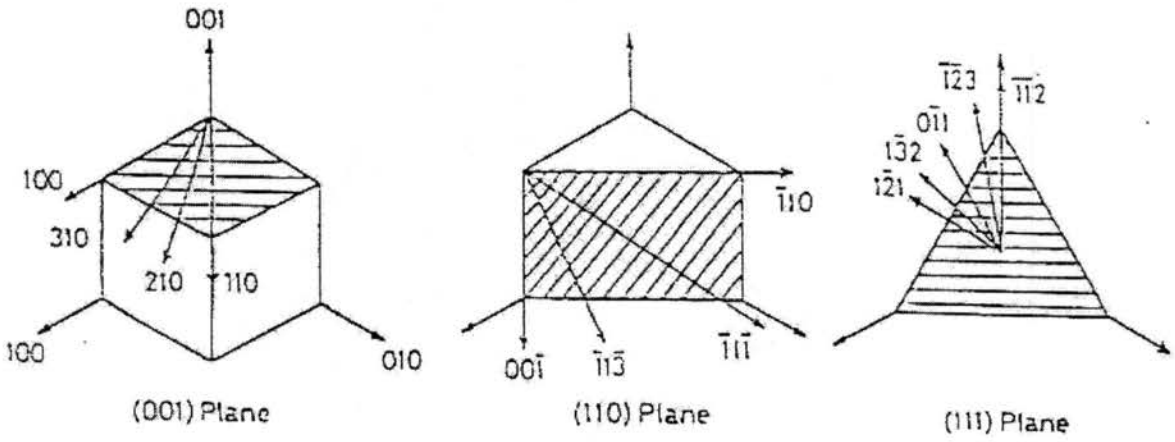

Figure 6.4. Various crystal orientations and cutting directions for cubic material

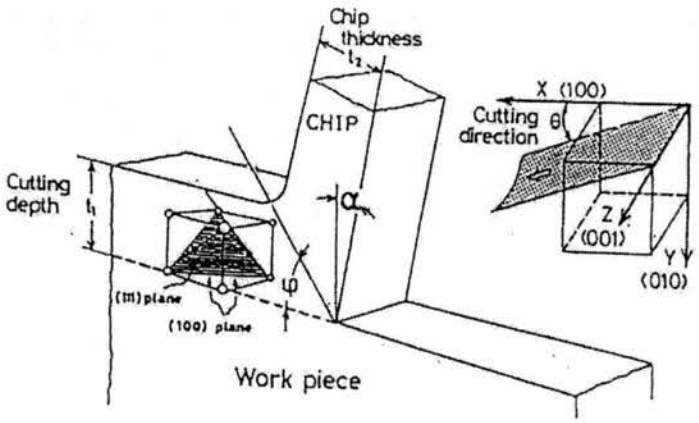

Figure 6.5. Schematic showing the orientation of the workmaterial with respect to the cutting direction

Table 6.3. Atomic density and distance between planes for Al crystal (Dieter, 1986)

Orientation	Atomic density per unit area, /Å	Distance between planes, Å
Octahedral {111}	$4/\sqrt{3}a^2$ (0.141)	$a/\sqrt{3}$ (2.338)
Cube {100}	$2/a^2$ (0.122)	a/2 (2.025)
Dodecahedral {110}	$2/\sqrt{2}a^2$ (0.086)	$a/2\sqrt{2}$ (1.432)

6.4. RESULTS AND DISCUSSION

6.4.1. Effect of Crystal Orientation and Direction of Cutting on Nanometric Cutting of Single Crystal Aluminum

6.4.1.1 On the nature of deformation in cutting

Figures 6.6 (a) - (d) to 6.11 (a) - (d) are MD simulation plots of nanometric cutting showing various stages for specific combinations of workpiece orientations, namely, (111), (110), and (001), and cutting directions, namely, [$\bar{1}$10], [$\bar{2}$11], and [100] with a 10^{o} rake tool. For example, for the (111) orientation, the cutting directions used are [$\bar{1}$10] and [$\bar{2}$11]; for the (110) orientation they are [$\bar{1}$10] and [001]; and for the (001) orientation they are [$\bar{1}$10] and [100]. It may be noted that the discussion of results presented in the following is based not only on the MD simulation plots of the various stages of cutting [Figures 6.6 (a) - (d) to 6.11 (a) - (d)] but also on the detailed study of the animation of the nanometric cutting process under various conditions. The animations were accomplished using a special program developed at OSU. It will be shown that the nature of deformation ahead of the tool, the generation and propagation of the dislocations, and the subsurface deformation of the workmaterial all depend very much on the orientation and the direction of cutting. Even the mechanism of chip

formation will be shown to vary significantly depending on the crystal orientation and direction of cutting. It will also be shown that while the chip formation mechanism is similar to the conventional shear ahead of the tool in the case of a polycrystalline material for the workmaterial-cutting direction combination of (001) [100], they are distinctly different in other combinations. It will also be shown that the elastic recovery along the machined surface of the workmaterial is different for different combinations of crystallographic orientations and cutting directions, thereby affecting the surface finish and integrity of the finished surface. Some of the elastic recovery relaxes the atoms in the crystal near the machined surface to their nearly original state, thereby reducing the subsurface deformation.

Figures 6.6 (a) - (d) show various stages of MD simulation of nanometric cutting of a single crystal aluminum along $[\bar{1}10]$ direction and (111) crystal orientation. Initially, the material is deformed ahead of the tool with minimal deformation in the vicinity of the cutting tool [Figure 6.6 (a)] as in conventional cutting at large depths of cut. Apart from this the uncut material in the workpiece seems to be little affected by the motion of the tool. The chip formation appears to be predominantly due to compression ahead of the tool combined with shear along the cutting direction [Figures 6.6 (b) & (c)]. As cutting progresses, the deformation ahead of the tool in the depth of cut region as well as below this in the workpiece leading to subsurface deformation in the machined surface (under the clearance surface of the tool) [Figure 6.6 (b)] can be seen. It may be noted that the $(111)[\bar{1}10]$ combination involves the densest plane with the cutting performed along the close packed direction (see Table 6.3). As a result, the material ahead of the tool is compressed significantly with cutting. As cutting progresses, not only the material ahead of the tool is deformed but also several layers below the uncut material ahead of the tool tip is affected [Figures 6.6 (b) & (c)]. As the tool passes this region partial elastic recovery of the deformed subsurface region takes place. From Figure 6.6 (d), which is the

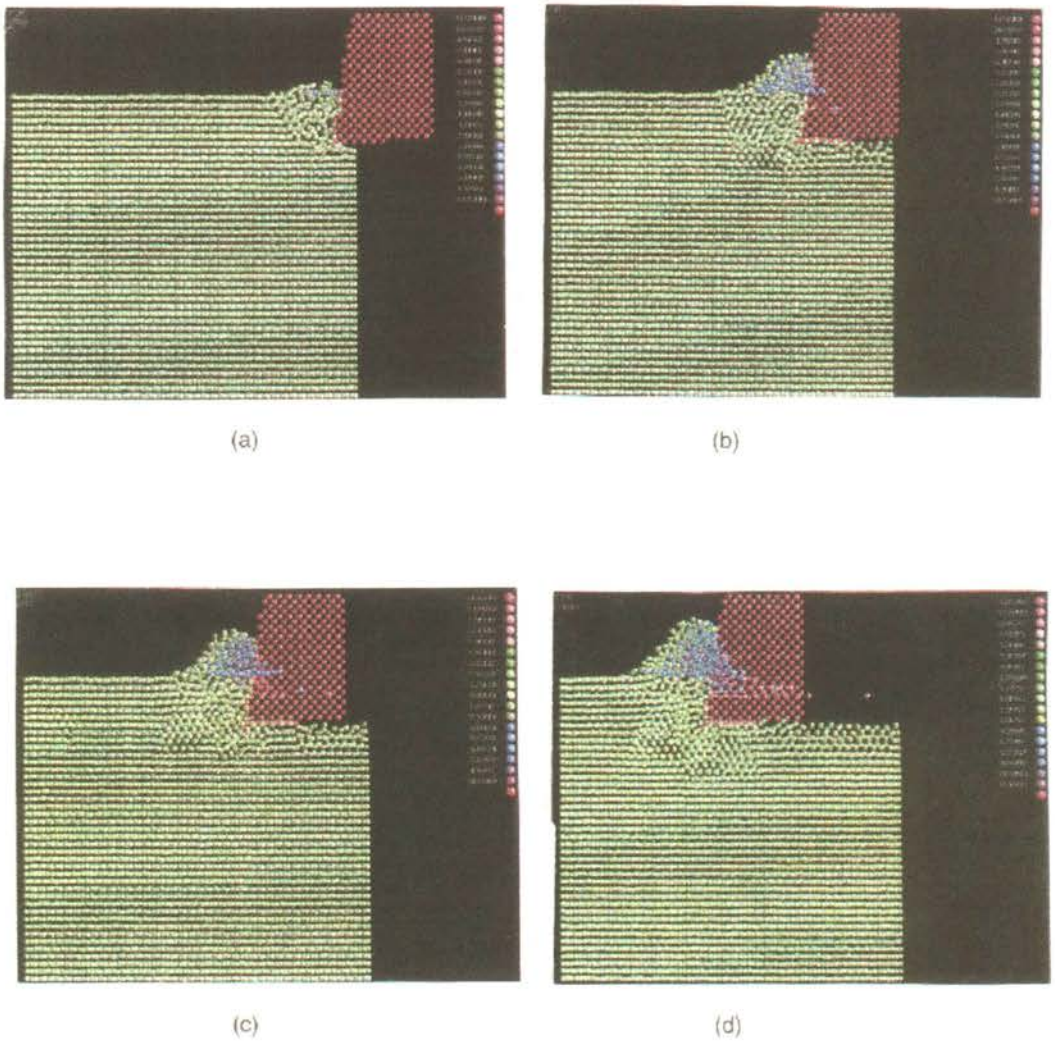

Figures 6.6 (a) - (d) MD simulation plots showing various stages of nanometric cutting of Al single crystal. Cutting along [-110] direction and (111) crystal orientation. Rake angle 10^{o}

final stage of the cutting process, the amount of subsurface deformation appears to be nearly equal to the depth of cut. However, as the tool progresses further, some of the subsurface deformation underneath and ahead of the tool tip is released, resulting in the subsurface deformation of only about half the depth of cut [as in Figure 6.6 (c)]. Also, much of the remaining workmaterial is undisturbed, as no disorder in the crystal can be seen. The chip appears to be thick and shorter due to predominant compression ahead of the tool together with shear along the cutting direction.

Figures 6.7 (a) - (d) show various stages of MD simulation of nanometric cutting when cutting along the $[\bar{2}11]$ direction and (111) crystal orientation. Figure 6.7 (a) shows the generation and propagation of dislocations into the workmaterial at an angle of $\sim 60^{o}$ to the cutting direction (anticlockwise). It may be noted that the direction of dislocation motion in this case is different to the dislocation motion observed in Figures 6.6 (a) - (d). Though the crystal orientation is the same in both cases, the cutting directions are different. Incidentally for a cube system, the angle between the slip plane (111) and the slip direction [-211] is 61^{o} 52' (Wood, 1963). The material in the shear zone also seems to be deforming at an angle of $\sim 60^{o}$, as though a mirror image of the dislocations propagating into the workmaterial [Figures 6.7 (b) & (c)]. As cutting progresses, multiple dislocations are observed to travel through the entire depth of the workmaterial [Figure 6.7 (b)]. Figure 6.7 (d) shows the final stage of the cutting process with minimal subsurface deformation except for the dislocations. However, the elastic recovery enables the movement of many of the dislocations to the free surface (machined surface) resulting in minimal subsurface deformation. The chip appears to be thinner than that observed with the (111) $[\bar{1}10]$ combination [Figure 6.6 (d)]. The machined surface indicates better finish and integrity than that observed with the (111) $[\bar{1}10]$ combination [Figure 6.6 (d)].

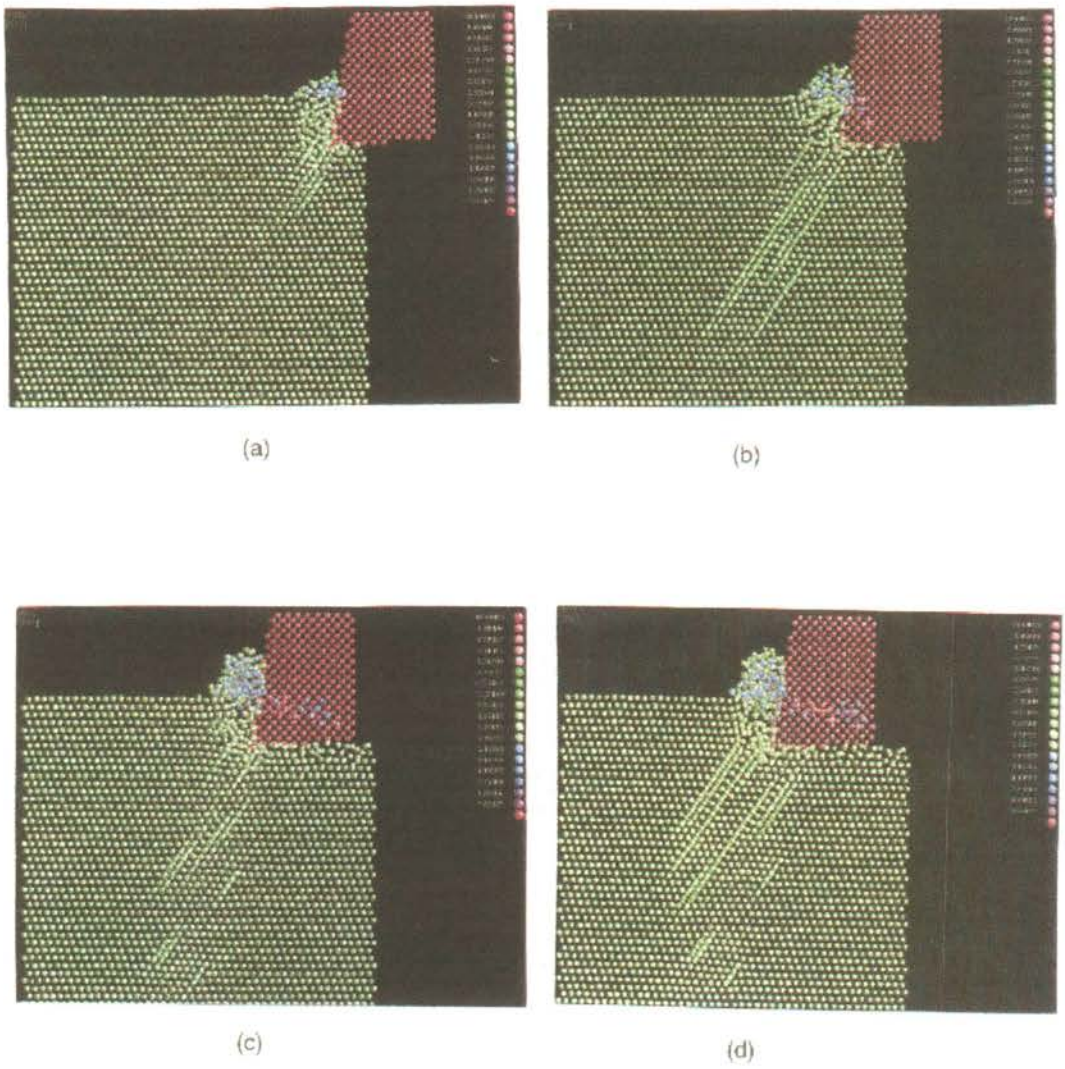

Figures 6.7 (a) - (d) MD simulation plots showing various stages of nanometric cutting of Al single crystal. Cutting along [-211] direction and (111) crystal orientation. Rake angle 10°

Also, Figure 6.7 (d) shows lesser amount of plastic deformation ahead of the tool in comparison to Figure 6.6 (d). This is due to the differences in the dislocation motion as it leads to variations in the nature of plastic deformation. This, consequently, leads to the variation in forces, force ratio, specific energy, and subsurface deformation, as will be discussed shortly.

Figures 6.8 (a) - (d) show the MD simulation of nanometric cutting at various stages when cutting along the $[\bar{1}10]$ direction with a (110) crystal orientation. It can be seen from Figures 6.8 (a) and (c) that dislocations are generated parallel to the cutting direction in the region of depth of cut of the workmaterial as well as perpendicular to the cutting direction into the workmaterial underneath the tool. Also seen in Figures 6.8 (a), as well as from the animation studies, are the planes within the depth of cut which glide past one another along the cutting direction like a deck of cards sliding over one other. Consequently, there is very little subsurface deformation underneath the tool initially. It may be noted that slip of the layers within the uncut depth along the cutting direction ($[\bar{1}10]$) [as in Figure 6.8 (a)] was not observed with the (111) orientation [Figure 6.6 (a)], even though the cutting direction was the same. In Figure 6.6 (b), subsurface deformation below the depth of cut in the workmaterial was observed in the initial stages itself. In contrast, Figure 6.8 (b) shows no such deformed layer below the depth of cut though the cutting direction is the same in both cases. Figure 6.8 (c) shows the generation and propagation of additional dislocations perpendicular (into the workmaterial) to the cutting direction as a result of dislocations generated along the cutting direction. It is also possible that these dislocations may have been generated due to the boundary atoms located farther from the tool in the cutting direction, which can obstruct the dislocations propagating parallel to the cutting direction. However, it will be shown [Figures. 6.10 (a) - (d)] that in the case of $(001)[\bar{1}10]$ combination where the

dislocations propagate parallel to the cutting direction [similar to Figures 6.8 (a)-(d)] no such dislocations propagating perpendicular to the cutting direction was observed. It, therefore, appears probable that the dislocations propagating perpendicular to the cutting direction in this case may have been generated due to the orientation effect. Figure 6.8 (d) shows the final stage of the cutting process where the perpendicular dislocations into the workmaterial observed in Figure 6.8 (c) under the tool tip are no longer present in the workmaterial although new dislocations are generated instead. It was found from the animation of the MD simulation process that many of the dislocations generated perpendicular to the cutting direction terminated through the free surface due to elastic recovery of the workmaterial after cutting. The initiation of the perpendicular dislocations resulted in minor disorder of the atoms near the surface towards the end of the cutting process. However, some of these dislocations were observed to travel through the entire depth of the workmaterial. Those that could not escape completely through the machined surface due to elastic recovery were found to introduce minor lattice disorders in the machined surface. The chip length is observed to be shorter than the earlier combinations as can be seen by comparing Figures 6.6 (d), 6.7 (d), and 6.8 (d).

Figures 6.9 (a) - (d) show the MD simulation of nanometric cutting at various stages when cutting along the [001] direction with a (110) crystal orientation. In contrast to the other orientations and cutting directions presented earlier, the dislocations are seen generated perpendicular to the cutting direction ahead of the tool and propagated both below and above the workmaterial [Figure 6.9 (b)]. This mode of deformation is somewhat peculiar to single crystal material as no such effect was observed in conventional machining with polycrystalline materials. Hence, the plastic deformation around the tool is constrained to this region only. As the dislocations are generated perpendicular to the cutting direction, the deformation ahead of the tool tip is accompanied by shear in this direction resulting in very high values of the shear angle.

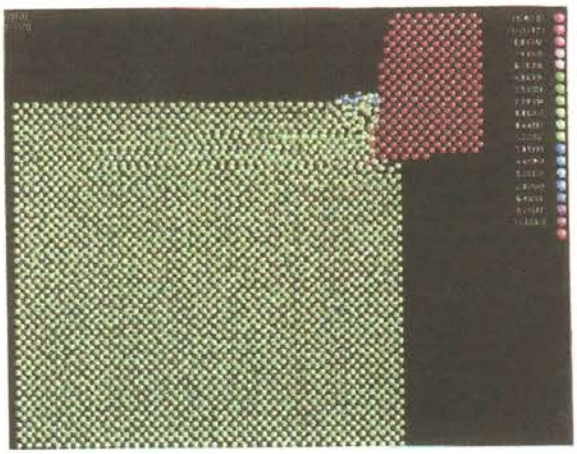

(a)

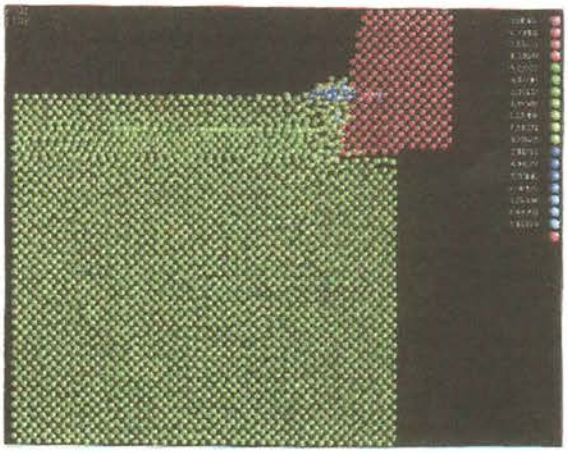

(b)

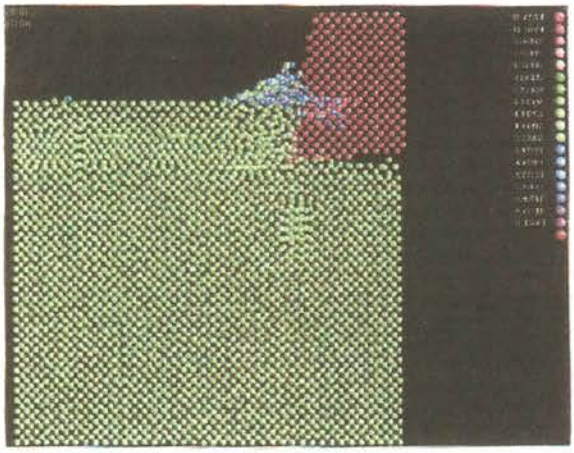

(c)

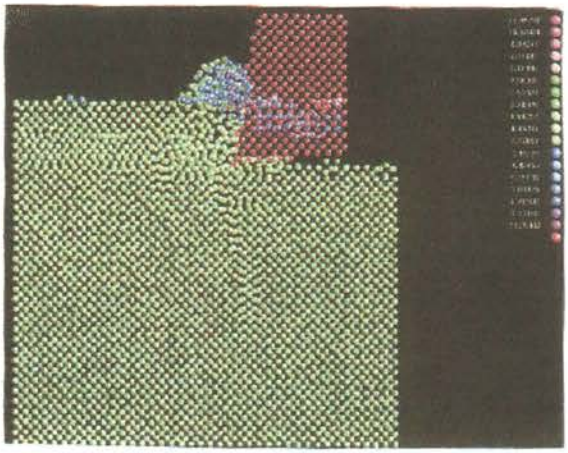

(d)

Figures 6.8 (a) - (d) MD simulation plots showing various stages of nanometric cutting of Al single crystal. Cutting along [-110] direction and (110) crystal orientation. Rake angle 10°

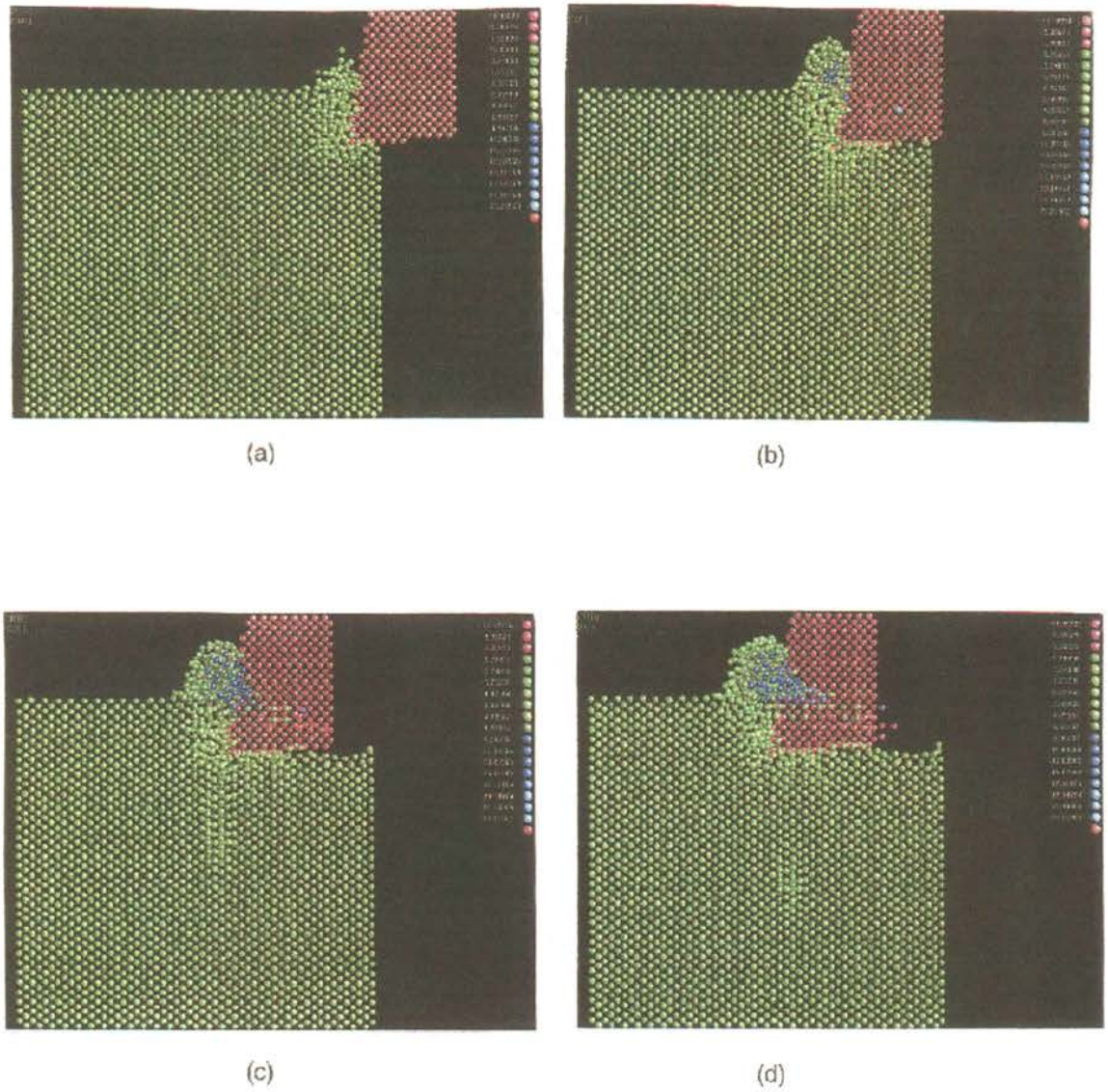

Figures 6.9 (a) - (d) MD simulation plots showing various stages of nanometric cutting of Al single crystal. Cutting along [001] direction and (110) crystal orientation. Rake angle 10°

This, however, was not the case with the other combinations of crystal orientations and cutting directions discussed earlier. Though there was a difference in the amount of plastic deformation ahead of the tool [Figures 6.6, 6.7, and 6.8 (a) - (d)], the deformation was more of shear than compression. As cutting proceeds [Figures 6.9 (b) - (d)] the subsurface deformation is observed to be rather low. The dislocations (or the subsurface deformation) observed in Figures 6.9 (b) or 6.9 (c) are no longer seen in Figures 6.9 (c) or 6.9 (d). From a study of the animation of the MD simulation process, it was observed that the elastic recovery was rather rapid for this combination. Though, a large number of dislocations were observed to propagate into the workmaterial, many of them escaped through the machined surface. The rest of the dislocations deep in the workmaterial rearranged themselves by the end of the process leaving behind practically no disorder in the workmaterial. Figure 6.9 (d) shows the chip to be thin and longer with minimal subsurface deformation except for the atoms at or near the surface. The chip thickness was observed to be minimum for this particular combination in comparison to the combinations discussed earlier.

Figures 6.10 (a) - (d) show MD simulation plots of the various stages of the nanometric cutting process along the $[\bar{1}10]$ direction with a (001) crystal orientation. Similar to the observations made earlier with the (110) $[\bar{1}10]$ [Figures 6.8 (a) - (d)] combination, dislocations propagating along the cutting direction are seen from Figure 6.10 (a). Figure 6.10 (b) shows the stage after the tool has moved a few nanometers into the workmaterial showing extensive slip along the cutting direction. Also, dislocations moving along the cutting direction in the workmaterial under the depth of cut region can be seen. However, this was not the case with the other two orientations [(111) and (110)] machined along the $[\bar{1}10]$ cutting direction. In the case of (111) orientation [Figure 6.6 (b)], subsurface deformation was observed in the form of lattice disorder. In the case of

(110) orientation [Figure 6.8 (b)] dislocations propagating into the workmaterial perpendicular to the cutting direction were observed. However, with the (001) orientation, dislocations move along the cutting direction in the workmaterial as well as in the depth of cut region. The amount of subsurface deformation increases as the cutting proceeds along the $[\bar{1}10]$ direction. However, the dislocations in the subsurface continue to move along the cutting direction [Figures 6.10 (c) and (d)]. The rest of the workmaterial seems to be undisturbed by the cutting process as can be observed from the final stage of cutting [Figure 6.10 (d)]. The subsurface disorder seen in Figures 6.10 (b) and (c) can still be seen in Figure 6.10 (d) but to a lesser extent. From this, the amount of elastic recovery seems to be very low in the case of (001) orientation. The amount of minor disorder in the atoms at and near the subsurface is estimated to be about the depth of cut.

Figures 6.11 (a) - (d) show MD simulation plots of the various stages of the nanometric cutting process along the [100] direction with a (001) crystal orientation. Figure 6.11 (a) shows plastic deformation ahead of the tool and dislocations propagating into the workmaterial at an angle of $\sim 45^{o}$ to the cutting direction. Figure 6.11 (b) shows multiple dislocations generated from the tool tip and propagating into the workmaterial. It may be noted that in the case of (111) [-211] combination, the dislocations are observed to propagate at an angle of $\sim 60^{o}$ with respect to the cutting direction [Figure 6.7 (b)]. Figure 6.11 (c) shows an intermediate stage where the dislocations have propagated deep into the workmaterial. Also, seen from the figure is the elastic recovery of the surface atoms as the tool moves forward. Figure 6.11 (d) shows the final stage of the cutting process where the dislocations propagate into the entire depth of the workmaterial. Disorder in the lattice arrangement of the crystal (or subsurface deformation) immediately beneath the machined surface was observed to be limited to a fraction of the depth of cut.

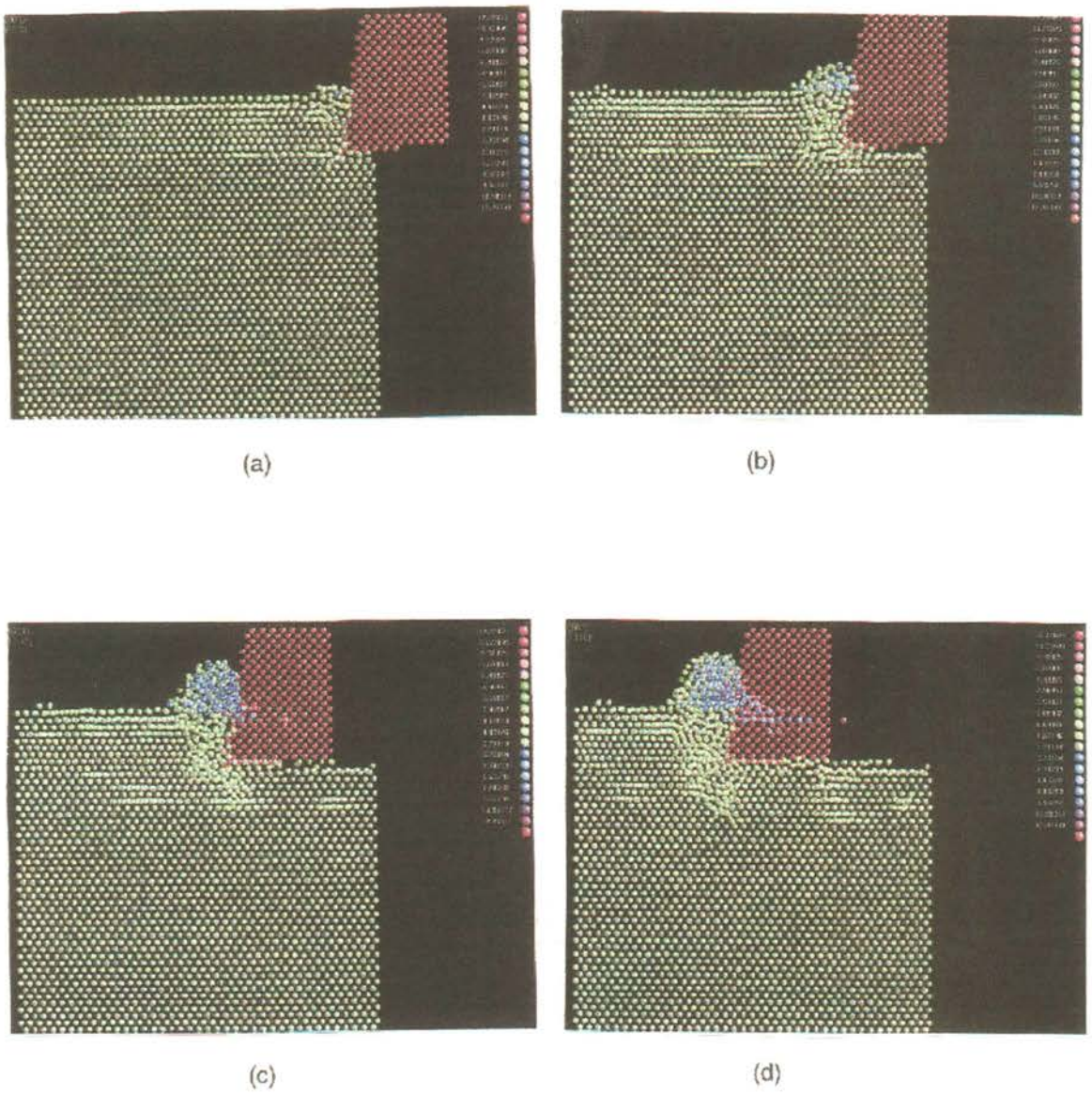

Figures 6.10 (a) - (d) MD simulation plots showing various stages of nanometric cutting of Al single crystal. Cutting along [-110] direction and (001) crystal orientation. Rake angle 10^{o}

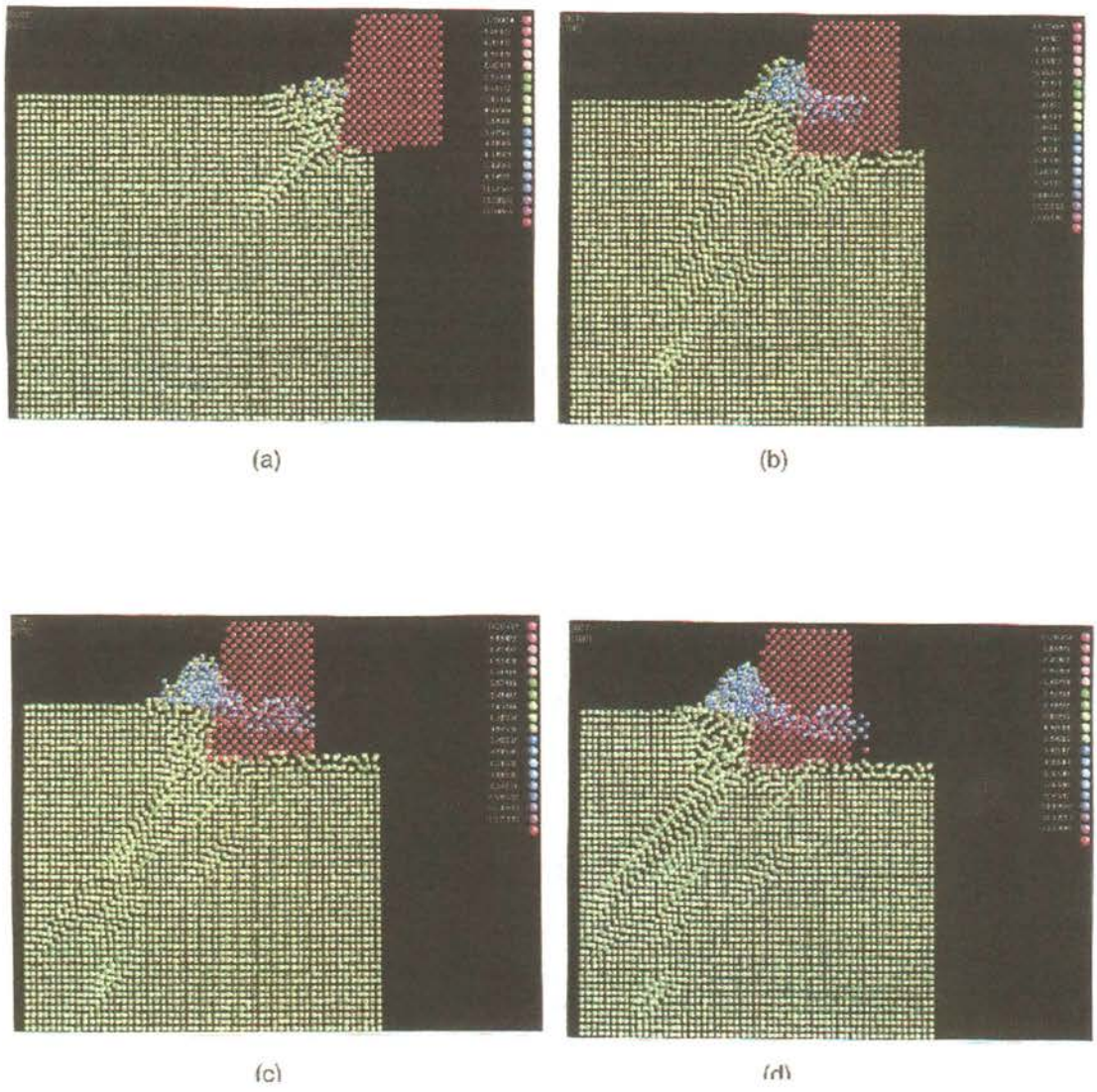

Figures 6.11 (a) - (d) MD simulation plots showing various stages of nanometric cutting of Al single crystal. Cutting along [100] direction and (001) crystal orientation. Rake angle 10^{o}

Closer examination of Figures 6.6 (a) - (d) to 6.11 (a) - (d) as well as the animations of the MD simulation of nanometric cutting of aluminum crystals of different crystal orientations and directions of cutting indicates a significant difference in the mechanism of shear as well as the shear angle for different orientations. For example, Figure 6.11 (d) shows that the shear plane orientation is much closer to conventional ($<45^{o}$). However, in the case of (001) $[\bar{1}10]$ combination, dislocations propagating parallel to the cutting direction both in the depth of cut region as well as beneath the depth of cut region in the workmaterial were observed. In the case of (111) orientation and in the $[\bar{2}11]$ direction, the dislocations are generated at $\sim 60^{o}$ to the cutting direction. The material in the shear zone also seems to be deforming at an angle of $\sim 60^{o}$, as a mirror image of the dislocations propagating into the workmaterial. The shear angle for (111) [-110] is far below the shear angle as observed with (111) $[\bar{2}11]$. In the case of (110) crystal orientation and $[\bar{1}10]$ cutting direction, the dislocations are generated along the cutting direction. Consequently, there is very little subsurface deformation. However, the secondary dislocations created perpendicular into the workmaterial do result in some degree of subsurface deformation. In contrast in the (110) crystal orientation but in the [001] cutting direction, the dislocations are generated perpendicular to the cutting direction. Consequently, the deformation ahead of the tool is accompanied by shear perpendicular to the cutting direction. Also, with the (110) [001] combination, a large amount of elastic recovery was observed. Consequently, minimum subsurface deformation was observed towards the end of the process suggesting this combination as a possibility for obtaining better finish in the finished component.

Table 6.4 summarizes the mode of dislocation generation and propagation for various crystallographic orientations and cutting directions. This variation in the dislocation generation and propagation can also be explained in terms of the angle between the

cutting direction and the family of slip direction <110> of a FCC crystal. For example, the angle between [100] cutting direction and the slip direction corresponds to either 45^{o} or 90^{o} (Wood, 1963). From the simulations, the dislocations in the case of (001)[100] combination seem to propagate at ~45^{o} to the cutting direction [Figures 6.11 (a)-(d)]. In the case of (110)[001] combination the dislocations seem to propagate perpendicular (90^{o}) to the cutting direction [Figures 6.9 (a)-(d)]. In both these combinations the cutting direction corresponds to the <100> family. In the case of cutting along $[\bar{1}10]$ direction the angle between the cutting direction and the slip direction can be either 0^{o}, 60^{o}, or 90^{o} (Wood, 1963). Consequently, cutting along this particular direction produced dislocations either parallel to [Figures 6.10 (a)-(d)] or both parallel and perpendicular to [Figures 6.8 (a)-(d)] the cutting direction. Finally the angle between $[\bar{2}11]$ cutting direction and the slip direction can be 30^{o}, 54^{o}, 73^{o}, or 90^{o} (Wood, 1963). In the current study the dislocations in the case of (111)$[\bar{2}11]$ combination was observed to propagate at an angle of 60^{o} to the cutting direction. Based on the current study it seems possible to predict the direction of primary dislocation propagation based on the angle between the cutting direction and the slip direction of the crystal.

The thickness of the chip was observed to be minimum with (110) [001] combination and maximum in the case of (111) $[\bar{1}10]$ combination. The variation in the chip thickness and the shear angle are due to the shear plane aligning itself for different orientations to enable easy glide or easy material removal and consequent lower forces (minimum energy). The differences in the dislocation motion lead to variations in the nature of plastic deformation and consequently the cyclic variation of forces, specific energy, force ratio, and subsurface deformation.

Table 6.4. Mode of dislocation generation and propagation as well as standard deviation of force variation for various crystal orientations and cutting directions

No.	Cutting Plane	Cutting Direction	Dislocation Generation and Propagation	Standard Deviation of Force Variation, N/mm x 10^2
1	(111)	$[\bar{1}10]$	Compression and shear	1.040
2		$[\bar{2}11]$	~60°	1.093
3	(110)	$[\bar{1}10]$	Parallel and perpendicular to the cutting direction	1.248
4		[001]	Perpendicular to the cutting direction	2.043
5	(001)	$[\bar{1}10]$	Parallel to the cutting direction	1.233
6		[100]	~45°	0.996

6.4.1.2. On the nature of variation of the forces and energy

Table 6.5 summarizes the results (the magnitudes of the cutting and thrust forces, the force ratio, the resultant force, and the specific energy) of the MD simulation of nanometric cutting on single crystal aluminum for different orientations, cutting directions, and depths of cut (0.81 nm - 1.62 nm). An infinitely hard tool with a 10^{o} rake angle and a 5^{o} clearance angle cutting was used at a velocity of 500 m/sec.

Table 6.5: Results of MD simulation study conducted on aluminum single crystals for different orientations and different directions of cutting for various depths of cut with a 10^{o} rake tool

Crystal orientation	Cutting direction	Cut depth, nm	Cutting force/unit width, N/mm x 10^2	Thrust force/unit width, N/mm x 10^2	Thrust force/Cutting force	Resultant force/unit width, N/mm x 10^2	Specific energy, N/mm^2 x 10^{-5}
111	-110	0.810	1.723	1.563	0.907	2.326	0.213
		1.215	2.186	1.511	0.691	2.657	0.180
		1.620	3.306	1.732	0.524	3.732	0.204
	-211	0.810	2.395	1.728	0.722	2.953	0.296
		1.215	3.174	1.664	0.524	3.584	0.261
		1.620	4.010	1.289	0.321	4.212	0.248
110	-110	0.810	1.648	1.209	0.734	2.044	0.203
		1.215	2.725	1.468	0.539	3.095	0.224
		1.620	3.529	2.304	0.653	4.215	0.218
	001	0.810	2.143	1.091	0.510	2.405	0.265
		1.215	3.661	2.520	0.688	4.444	0.301
		1.620	4.454	1.005	0.226	4.566	0.275
001	-110	0.810	2.145	2.080	0.970	2.988	0.265
		1.215	3.116	2.617	0.840	4.069	0.256
		1.620	4.228	3.110	0.736	5.249	0.261
	100	0.810	1.857	1.471	0.792	2.369	0.229
		1.215	2.494	1.798	0.721	3.075	0.205
		1.620	3.437	1.708	0.497	3.838	0.2122

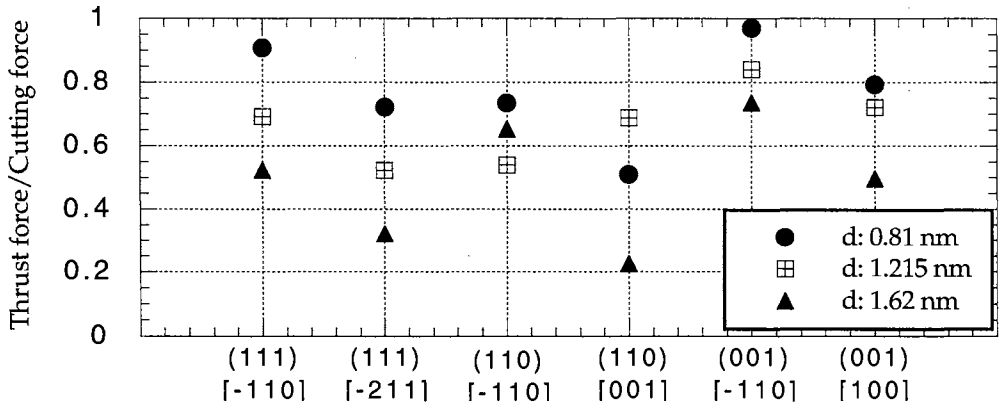
Thrust force/Cutting force
1
0.8
0.6
0.4
0.2
0
d: 0.81 nm
d: 1.215 nm
d: 1.62 nm
(111) [-110]
(111) [-211]
(110) [-110]
(110) [001]
(001) [-110]
(001) [100]

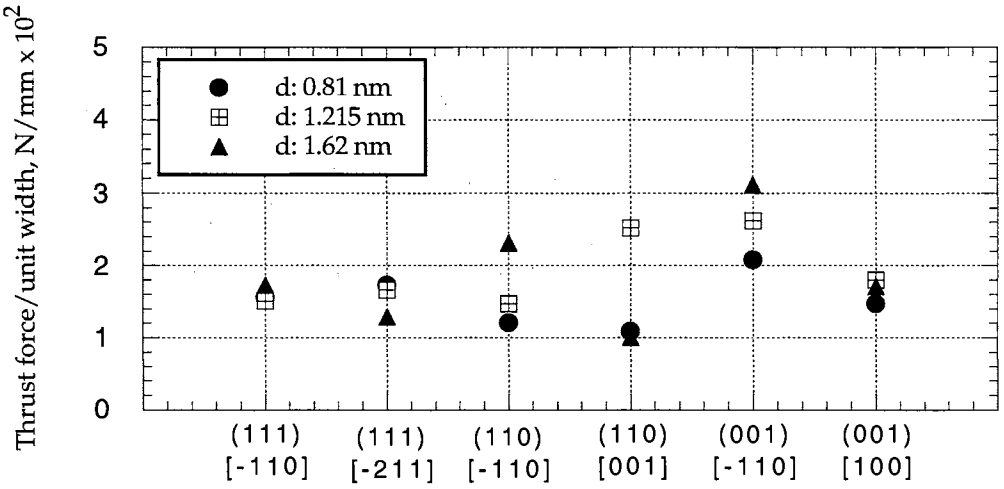
Thrust force/unit width, N/mm x 10^2
5
4
3
2
1
0
d: 0.81 nm
d: 1.215 nm
d: 1.62 nm
(111) [-110]
(111) [-211]
(110) [-110]
(110) [001]
(001) [-110]
(001) [100]

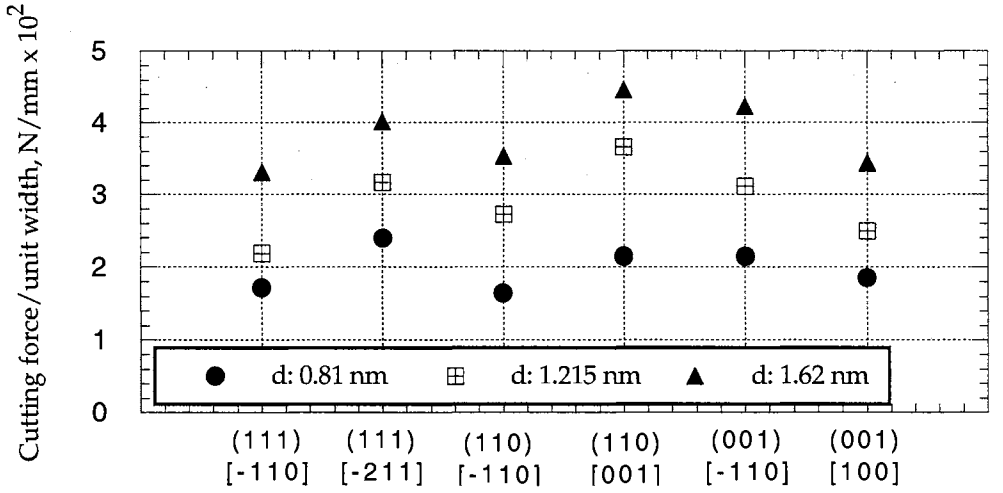
Cutting force/unit width, N/mm x 10^2
5
4
3
2
1
0
d: 0.81 nm
d: 1.215 nm
d: 1.62 nm
(111) [-110]
(111) [-211]
(110) [-110]
(110) [001]
(001) [-110]
(001) [100]

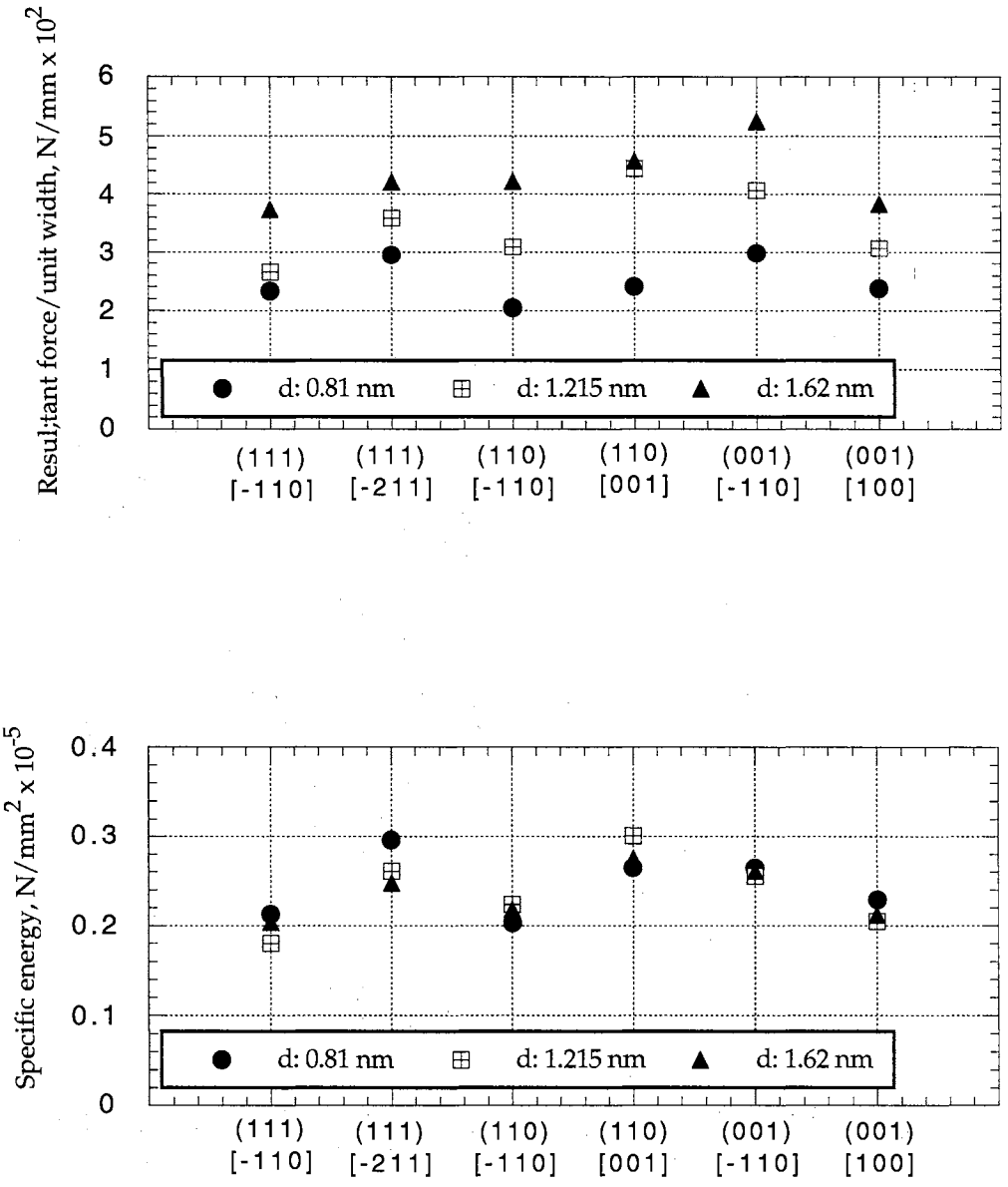

Figures 6.12 (a)- (e) Variation of the cutting and thrust forces, the ratio of thrust force to cutting force, the resultant force, and the specific energy, respectively, for different depths of cut (0.81 nm - 1.62 nm), different crystal orientations, and different cutting directions. Rake angle 10^{o}

Figures 6.12 (a) - (e) show the variation of the cutting and thrust forces, the ratio of the thrust force to the cutting force, the resultant force, and the specific energy, respectively, for different depths of cut (0.81 nm - 1.62 nm), different crystal orientations, and different cutting directions. Among all planes and directions investigated, the cutting force was minimum in nanometric cutting on the (111) plane along the $[\bar{1}10]$ cutting direction. This can be attributed to the fact that the (111) plane is the close packed plane and the $[\bar{1}10]$ is the close packed direction. Consequently, they constitute the easy slip system for a FCC crystal and hence result in the lowest values of the forces. It may be noted that along a particular cutting direction ($[\bar{1}10]$), the cutting force is minimum on the (111) plane and maximum on the (001) plane. However, according to theory the (110) plane offers the maximum resistance to slip as the distance between two (110) planes is minimum and (110) is also the less densely packed plane (Table 6.3). Consequently, referring to Table 6.3 one would expect the forces to be maximum on the (110) plane, which is not in agreement with the MD simulation results. However, it may be observed from Fig. 6.12 (a) that the results are consistent for different depths of cut. It can also be inferred from Figure 6.12 (a) that for a particular orientation, the cutting force is least along the $[\bar{1}10]$ direction with the (001) plane being an exception. On the (001) plane, minimum force is experienced along the [100] direction. The thrust force [Figure 6.12 (b)] does not seem to follow any particular trend as the cutting force. This is expected as the energy required for plastic deformation is determined by the cutting force. However, the minimum and the maximum thrust forces occur for the same orientations as the cutting force.

From Figure 6.12 (d) it can be seen that the resultant force follows the same trend as the cutting force. This suggests that the cutting force is the major variable affected by the orientation when machining is carried out with positive rake tools. The thrust force

seems to play a negligible effect on the resultant force experienced by the tool. From Figure 6.12 (e), it can be seen that the specific energy tends to increase with decreasing depth of cut, indicating a possible size effect reported by many previous researchers. It can be seen that the specific energy is significantly influenced by both the orientation of the workmaterial and the cutting direction.

Figures 6.13 (a) - (c) show the variation of the cutting force with cutting distance for three different combinations of workpiece orientations and cutting directions, namely, (111) [$\bar{1}$10], (110) [$\bar{1}$10], and (001) [100], respectively. Table 6.4 tabulates the standard deviation of the force values from the mean for different combinations. The standard deviation was used to define the dynamic force variation for various combinations. Even though, the other combinations studied in this investigation, namely, {(111) [$\bar{2}$11], (110) [001], and (001) [$\bar{1}$10]}, are not shown here, they exhibited higher dynamic force variation in comparison to the combinations presented here (Table 6.4). Each plot of force variation for a particular orientation and cutting direction was so chosen as to yield the minimum force for that particular orientation. For example, in the case of (110) orientation, [$\bar{1}$10] cutting direction, the force exhibits a standard deviation value of 0.0125 N/mm in comparison to 0.0204 N/mm with [001] cutting direction. Consequently, [$\bar{1}$10] cutting direction was selected as it yields the minimum dynamic force variation for (110) orientation. The biased method (n-method) was used for evaluating the standard deviation of the force curves, which defines how widely the force values are dispersed from the average value. The formula used to determine the standard deviation of the force values is given in the following:

$$\sqrt{\frac{n\Sigma x^2 - (\Sigma x^2)}{n^2}}$$

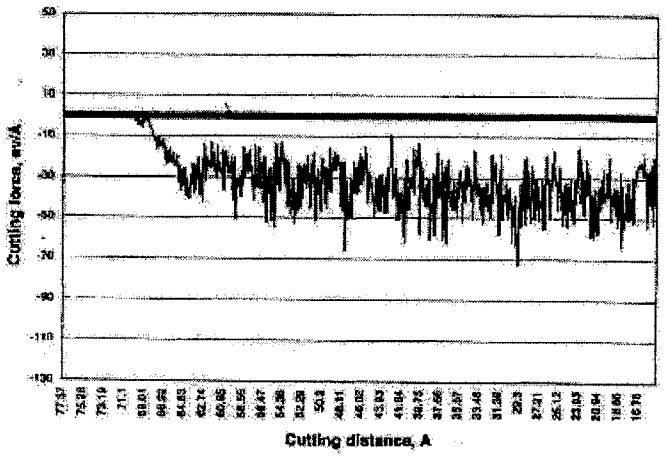

(a)

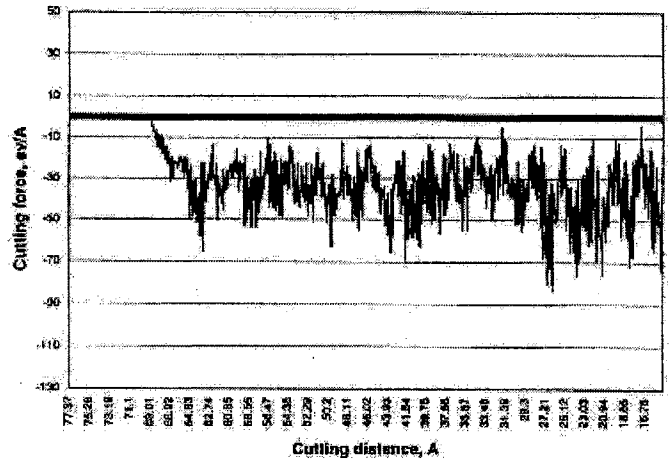

(b)

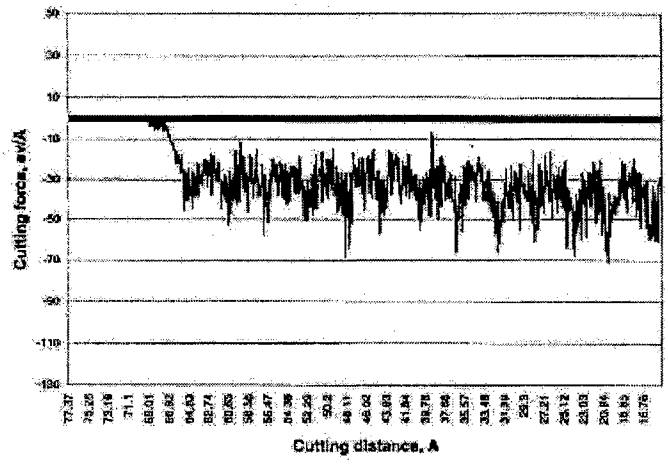

(c)

Figures 6.13. (a) - (c) Variation of the cutting force with cutting distance for three different combinations of crystal orientation and cutting directions, namely, (a) (111)[-110], (b) (110)[-110], and (c) (001)[100], respectively

where, x is the value of the cutting force and n is the total number of values for which all the points in the curve [Figs. 6.13 (a) - (c)] are considered. The standard deviations of the force curves were observed to be 0.0104 N/mm for the (111) [$\bar{1}$10] combination, 0.0125 N/mm for the (110) [$\bar{1}$10] combination, and 0.00996 N/mm for the (001)[100] combination. It can be seen that (110) [$\bar{1}$10] combination presents the highest force variation [Figure 6.13 (b)]. Also, the dynamic components of the force for the (111) [$\bar{1}$10] and the (001) [100] combinations [Figures 6.13 (a) & (c)] were found to be similar although the amplitude of force variation was lower for the (001) [100] combination than (111) [$\bar{1}$10] combination. This result is in agreement with the results reported by To *et al.* (1998).

6.4.2. Effect of Rake Angle on Nanometric Cutting of Single Crystal Aluminum

6.4.2.1 On the nature of deformation in cutting

In this series of tests, MD simulations of nanometric cutting were conducted on single crystal aluminum for different orientations, namely, {(111), (110), and (001)} and cutting directions, namely, <[$\bar{1}$10], [$\bar{2}$11], [100]> by varying the tool rake angle (i.e., 0^o, 10^o, and 40^o). The depth of cut was maintained constant at 1.62 nm. Figures 6.14 (a) - (d) to 6.19 (a) - (d) are the MD simulation plots of nanometric cutting with a 40^o rake tool for various orientations and cutting directions, respectively. The MD simulation plots for the 0^o rake tool are not given here as the differences in the nature of deformation between 0^o and 10^o rake tools are not significant.

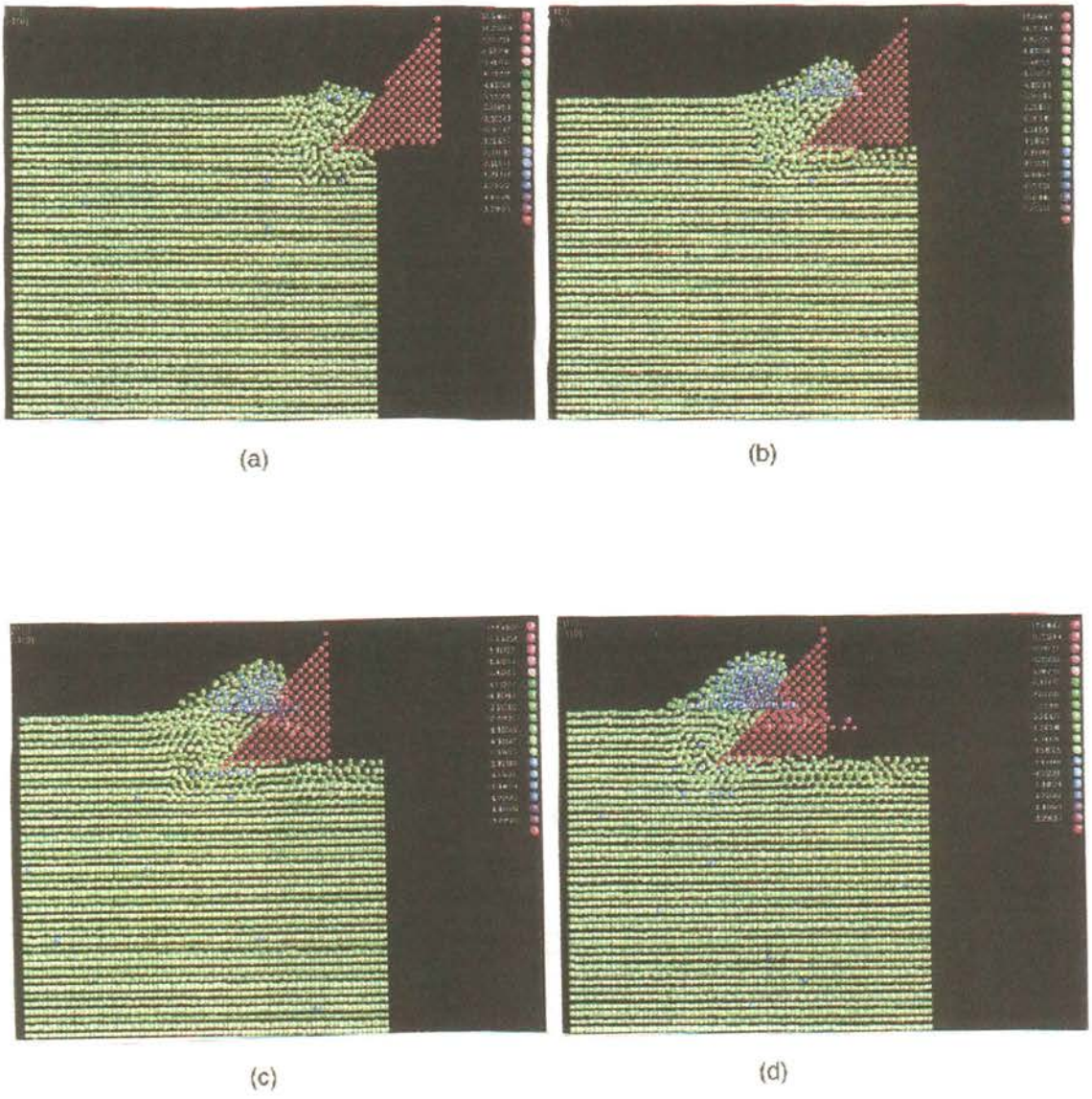

Figures 6.14 (a) - (d) MD simulation plots showing various stages of nanometric cutting of Al single crystal. Cutting along [-110] direction and (111) crystal orientation. Rake angle 40°

Figures 6.14 (a) - (d) show MD simulation plots of the various stages of the nanometric cutting process along the $[\bar{1}10]$ direction with a (111) crystal orientation. A comparison of the same combination of crystal orientation and cutting direction but with different rake angles [Figures 6.14 (a) - (d) for 40^{o} rake with Figures 6.6 (a) - (d) for 10^{o} rake] indicate some similarities but other differences. For example, a comparison of the initial stages of deformation [Figures 6.14 (a) and 6.6 (a)] shows that the deformation is found to be predominantly in front of the tool with a 10^{o} rake while with a 40^{o} tool it is ahead of the tool as well as below the uncut material. The smaller included angle thus provides more uniform distribution of stresses in the workmaterial at the tool tip resulting in deformation both in the shear zone in the depth of cut region and below the uncut material of the workpiece. With the progress of cut, the subsurface deformation is found to be somewhat similar to a 10^{o} rake tool although more with the latter. Comparison of Figures 6.14 (b) - (c) with Figures 6.6 (b) - (c) suggests lower amount of plastic deformation ahead of the tool with a 40^{o} rake tool than with a 10^{o} rake tool. Further, as can be expected, the shear angle with a 40^{o} rake tool is much higher (and the chip longer) [Figure 6.14 (d)] than that with a 10^{o} rake tool [Figure 6.6 (d)]. Figure 6.14 (d) shows the final stage of the cutting process where the amount of subsurface deformation seems to be somewhat lesser than that observed with a 10^{o} rake tool [Figure 6.6 (d)].

Figures 6.15 (a) - (d) show MD simulation plots of the various stages of the nanometric cutting process along the $[\bar{2}11]$ direction with a (111) crystal orientation. From Figures 6.15 (a) and (b) it can be noted that the dislocations propagate at about the same angle (i.e., $\sim 60^{o}$, measured anticlockwise with respect to the cutting direction), as observed earlier [Figures 6.7 (a) and (b)] with a 10^{o} rake tool. The material ahead of the tool in the shear zone was deforming at an angle of $\sim 60^{o}$, as though a mirror image of the

dislocations propagating into the workmaterial. However, the number of dislocations observed in Figure 6.15 (b) is far less than that observed in Figure 6.7 (b) though the combination studied is the same except for the tool rake angle. Also, the subsurface dislocations observed in Figs. 6.15 (a) and (b) are no longer observed in Figure 6.15 (c). This indicates that elastic recovery has taken place, thus relieving these dislocations. However, no significant elastic recovery was observed in Figures 6.7 (a) - (d). With a 10^{o} rake tool, the dislocations generated traveled through the depth of the workmaterial and could not reach the surface by elastic recovery. But, in the case of a 40^{o} rake tool, the dislocations have propagated no more than a few layers beneath the tool tip. Consequently, the dislocations escape through the machined surface as the tool advances. Figure 6.15 (d) shows the final stage of the cutting process. In comparison to Figure 6.7 (d), Figure 6.15 (d) shows minimal subsurface deformation with very few dislocations. This shows that the tool geometry plays an important role in addition to the orientation and cutting direction effects. Hence, the results observed for the same orientation and cutting direction can vary significantly, if not in the nature, in the magnitude. The subsurface deformation appears to be minimal with this tool geometry.

Figures 6.16 (a) - (d) show MD simulation plots of the various stages of the nanometric cutting process along the $[\bar{1}10]$ direction with a (110) crystal orientation. Figure 6.16 (a) shows the dislocations moving parallel along the cutting direction similar to the one observed with a 10^{o} rake tool [Fig. 6.8 (a)]. However, as cutting progresses, an increasing number of dislocations perpendicular to the cutting direction are generated [Figures 6.16 (b), (c) & (d)]. This is due to the differences in the chip formation process for different rake tools, as explained earlier [also can be seen by comparing Figures 6.16 (b) - (c) and 6.8 (b) - (c)]. With a 10^{o} rake tool, all the atom layers in the depth of cut were observed to glide along the cutting direction [Figure 6.8 (a)].

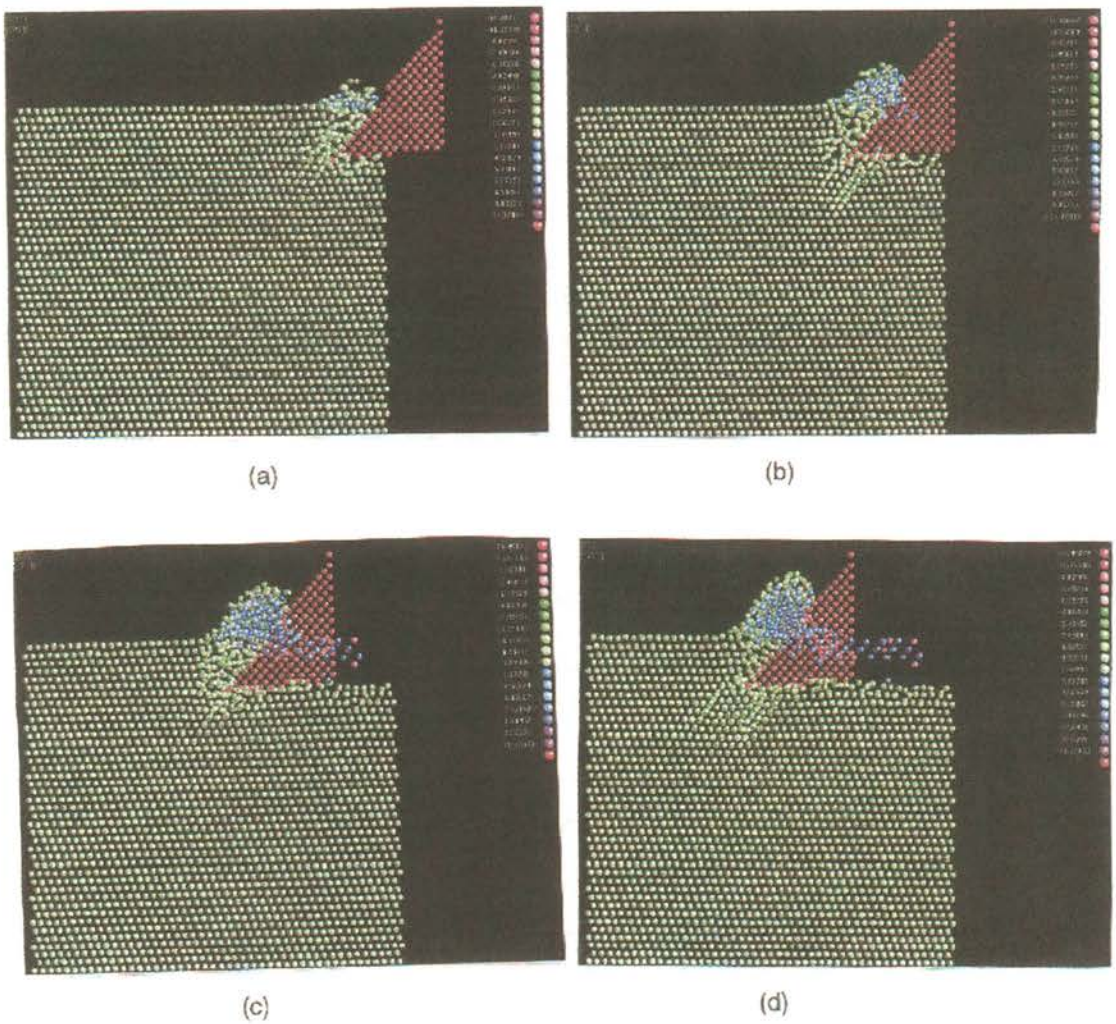

Figures 6.15 (a) - (d) MD simulation plots showing various stages of nanometric cutting of Al single crystal. Cutting along [-211] direction and (111) crystal orientation. Rake angle 40°

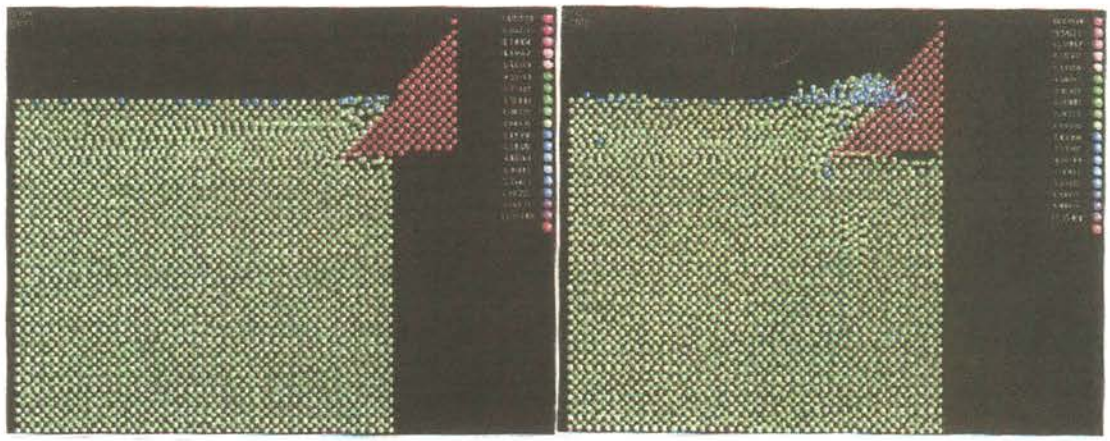

(a) (b)

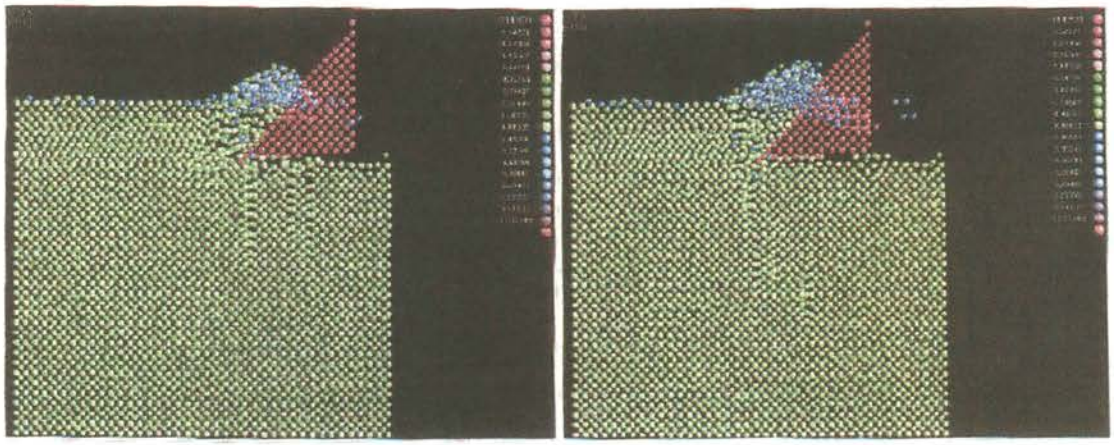

(c) (d)

Figures 6.16 (a) - (d) MD simulation plots showing various stages of nanometric cutting of Al single crystal. Cutting along [-110] direction and (110) crystal orientation. Rake angle 40°

In the case of a 40^{o} rake tool, the planes at the lower end of the depth of cut glide along the cutting direction initially, followed by the planes at the upper end. Consequently, this leads to an increased amount of cross slip and hence, more dislocations were observed to propagate into the workmaterial perpendicular to the cut depth [Figure 6.16 (d)]. The chip length does show an increase, in comparison with a 10^{o} rake tool, for a similar combination but is lower than the other combinations studied thus far. The subsurface deformation is also seen to be minimal as most of the dislocations generated perpendicular to the cutting direction are relieved due to elastic recovery.

Figures 6.17 (a) - (d) show MD simulation plots of the various stages of the nanometric cutting process along the [001] direction with a (110) crystal orientation. Figures 6.17 (a) - (d), similar to Figures 6.9 (a) - (d), show dislocations generated in front of the tool. However, with a 40^{o} rake tool [Figures 6.17 (a) - (d)] the chip formation process is in such a way that the dislocations generated ahead of the tool moved towards the free surface rather than into the workmaterial. The animations of the MD simulation process showed some of the dislocations escaping into the free surface of the unmachined part of the workmaterial with the rest being carried away by the chip. Also, no dislocations propagating into the workmaterial perpendicular to the cutting direction are seen [Figures 6.17 (a) - (d)] in contrast to dislocations moving into the workmaterial perpendicular to the cutting direction with a 10^{o} rake tool [Figures 6.9 (a) - (d)]. As already mentioned, this mode of deformation is rather unusual in machining and is peculiar to single crystal material. Figure 6.17 (d) shows very low subsurface deformation, in comparison to Figure 6.9 (d), due to the absence of perpendicular dislocations propagating into the workmaterial. Most of the deformation process and the dislocations are generated within the depth of cut and are carried away by the chip leaving a better finish and the workmaterial with practically very few residual defects.

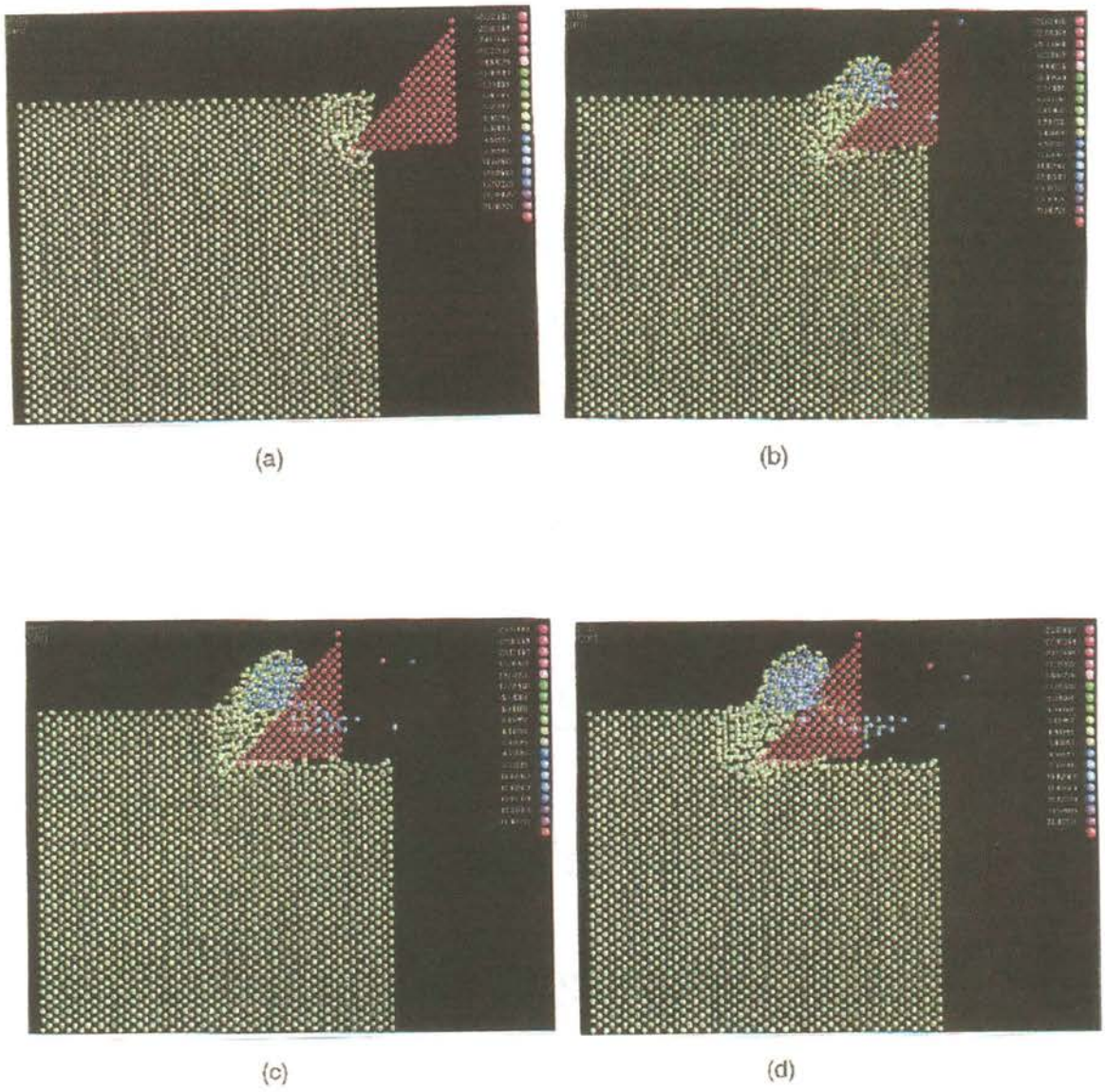

Figures 6.17 (a) - (d) MD simulation plots showing various stages of nanometric cutting of Al single crystal. Cutting along [001] direction and (110) crystal orientation. Rake angle 40^{o}

Figures 6.18 (a) - (d) show MD simulation plots of the various stages of the nanometric cutting process along the $[\bar{1}10]$ direction with a (001) crystal orientation. The dislocations move parallel to the cutting direction and the planes within the depth of cut glide over each other [Fig. 6.18 (a)]. As the cutting progresses, more dislocations are generated in the workmaterial and all the dislocations propagate along the cutting direction [Figures 6.18 (b) and (c)]. The amount of subsurface deformation seems to be much less [Figure 6.18 (d)] than that produced by a 10^{o} rake tool [Figure 6.10 (d)]. The rest of the workmaterial remains completely unaffected.

Figures 6.19 (a) - (d) show MD simulation plots of the various stages of the nanometric cutting process along the [100] direction with a (001) crystal orientation. Figure 6.19 (a) shows plastic deformation ahead of the tool and dislocations propagating into the workmaterial. The dislocations propagate at an angle of $\sim 45^{o}$ with respect to the cutting direction. Figure 6.19 (b) shows multiple dislocations generated from the tool tip and propagating into the workmaterial. It may be noted that in the case of (111) [-211] combination the dislocations are observed to propagate at an angle of $\sim 60^{o}$ with respect to the cutting direction [Figure 6.15 (b)]. However, the extent of dislocation generation and the depth to which they propagate into the workmaterial are significantly lower for a 40^{o} rake tool [Figures 6.19 (c) and (d)] than for a 10^{o} rake tool [Figure 6.11 (d)]. Figure 6.19 (c) shows another case of generation of cross slip where dislocations are generated at right-angle to the first set of dislocations in the workmaterial. However, this was not observed for the same orientation and cutting direction for a 10^{o} rake tool [Figures 6.11 (a) - (d)]. As can be seen from Figure 6.19 (c), dislocations generating at $\sim 45^{o}$ (with respect to the cutting direction) align and propagate parallel to the shear plane as in conventional machining with a polycrystalline workmaterial at normal depths of cut.

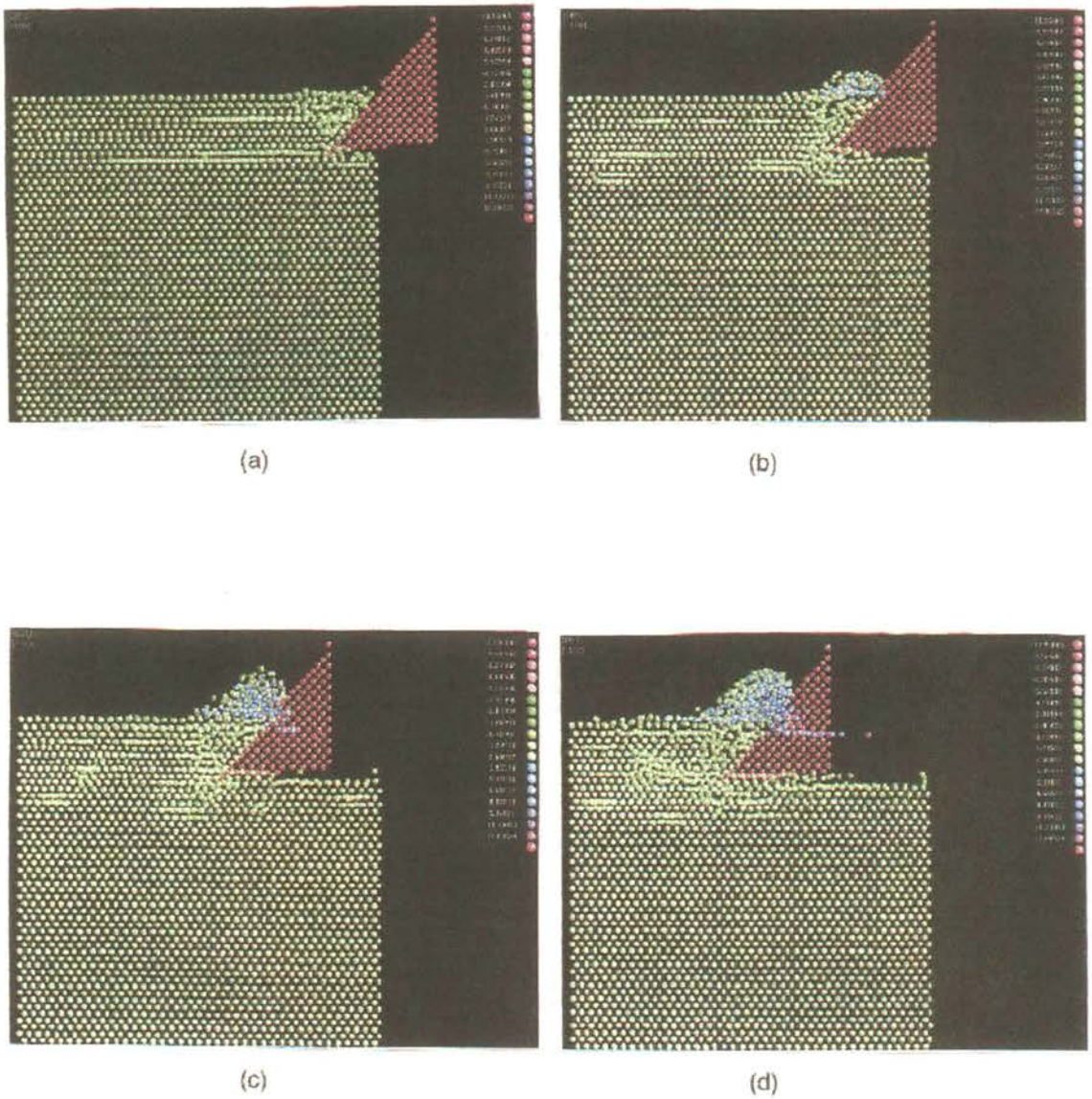

Figures 6.18 (a) - (d) MD simulation plots showing various stages of nanometric cutting of Al single crystal. Cutting along [-110] direction and (001) crystal orientation. Rake angle 40°

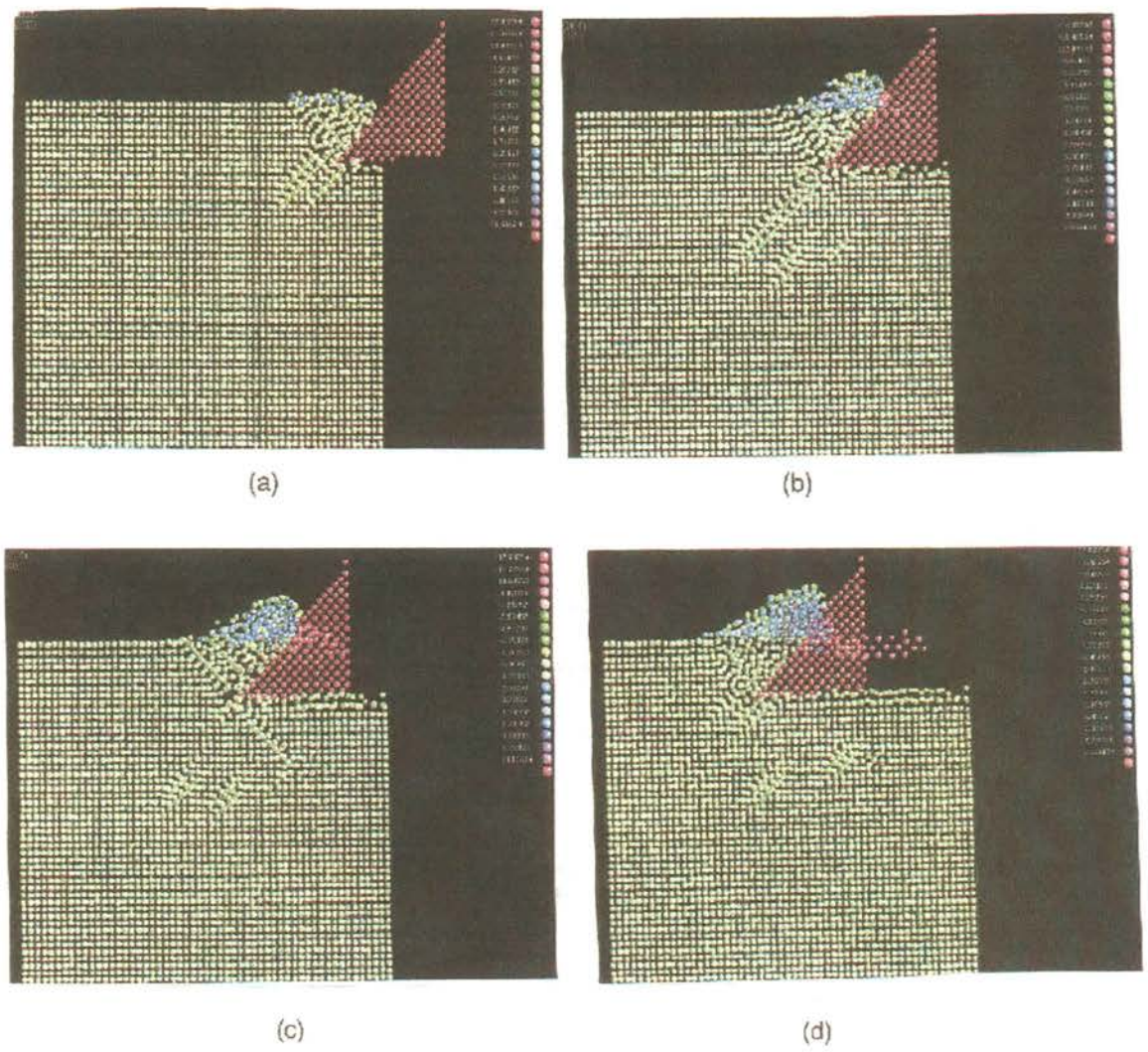

Figures 6.19 (a) - (d) MD simulation plots showing various stages of nanometric cutting of Al single crystal. Cutting along [001] direction and (100) crystal orientation. Rake angle 40°

However, in the case of 10^{o} rake tool, the dislocations were observed to travel into the workmaterial and ahead of the tool tip at ~90^{o} to the shear plane (i.e., shear plane at ~45^{o} relative to the cutting direction and dislocations at 45^{o} below cutting direction).

In summary, the chip length was observed to increase and the subsurface deformation to decrease for the same orientations as the rake angle is increased. Also, the number of dislocations and the distance traveled into the workmaterial were observed to decrease with increasing tool rake angle. In the case of (110) [001] combination, the dislocations were observed to generate within the cut depth and escape through the unmachined free surface of the workmaterial and the rest being carried away by the chip. No dislocations were observed to propagate into the workmaterial and the subsurface damage was observed to be minimal with practically no visible disorder in the workmaterial near the finished surface. Generation of cross slip was observed in the case of (001) [100] combination, which was not observed for the similar combination with a 10^{o} rake tool.

6.4.2.2. Nature of variation of the forces and energy

Table 6.6 summarizes the results (magnitudes of the cutting and thrust forces, the resultant force, the force ratio, and the specific energy) of the MD simulation of nanmometric cutting on aluminum single crystals for different orientations and cutting directions at different tool rake angles (0^{o}, 10^{o}, and 40^{o}). The depth of cut was maintained constant at 1.62 nm. The cutting speed used was 500 m/sec. Figures 6.20 (a) - (e) show the variation of the cutting and the thrust forces, force ratio, the resultant force, and the specific energy for different rake angles, respectively.

Table 6.6: Results of MD simulation study conducted on aluminum single crystals for different crystal orientations, different cutting directions, and different rake angles at a depth of cut of 1.62 nm

Tool rake angle, degrees	Crystal orientation	Cutting direction	Cutting force/unit width, N/mm x 10^2	Thrust force/unit width, N/mm x 10^2	Thrust force/ Cutting force	Resultant force/unit width, N/mm x 10^2	Specific energy, $N/mm^2 \times 10^{-5}$
0°	111	-110	3.324	2.840	0.854	4.372	0.205
		-211	4.110	2.490	0.606	4.805	0.254
	110	-110	3.643	2.762	0.758	4.487	0.225
		001	4.341	2.275	0.524	4.900	0.268
	001	-110	4.237	3.863	0.912	5.734	0.262
		100	3.440	2.175	0.632	4.070	0.212
10°	111	-110	3.306	1.732	0.524	3.732	0.204
		-211	4.010	1.289	0.321	4.212	0.248
	110	-110	3.529	2.304	0.653	4.215	0.218
		001	4.454	1.005	0.226	4.566	0.275
	001	-110	4.228	3.110	0.736	5.249	0.261
		100	3.437	1.708	0.497	3.838	0.2122
40°	111	-110	2.548	1.197	0.470	2.815	0.157
		-211	3.204	1.136	0.355	3.399	0.198
	110	-110	2.879	1.207	0.419	3.122	0.178
		001	3.106	1.083	0.349	3.289	0.192
	001	-110	3.78	1.557	0.412	4.088	0.233
		100	2.867	1.575	0.549	3.271	0.177

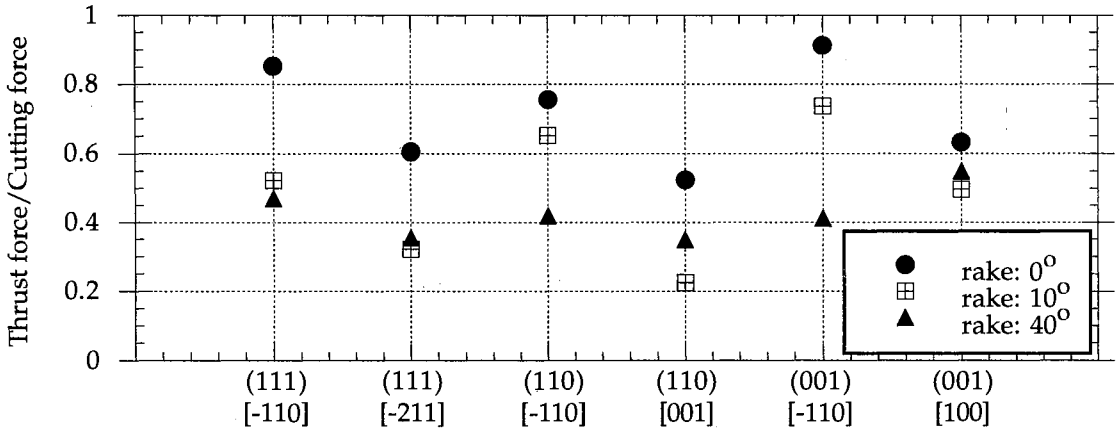
Thrust force/Cutting force
1
0.8
0.6
0.4
0.2
0
rake: 0°
rake: 10°
rake: 40°
(111) [-110]
(111) [-211]
(110) [-110]
(110) [001]
(001) [-110]
(001) [100]

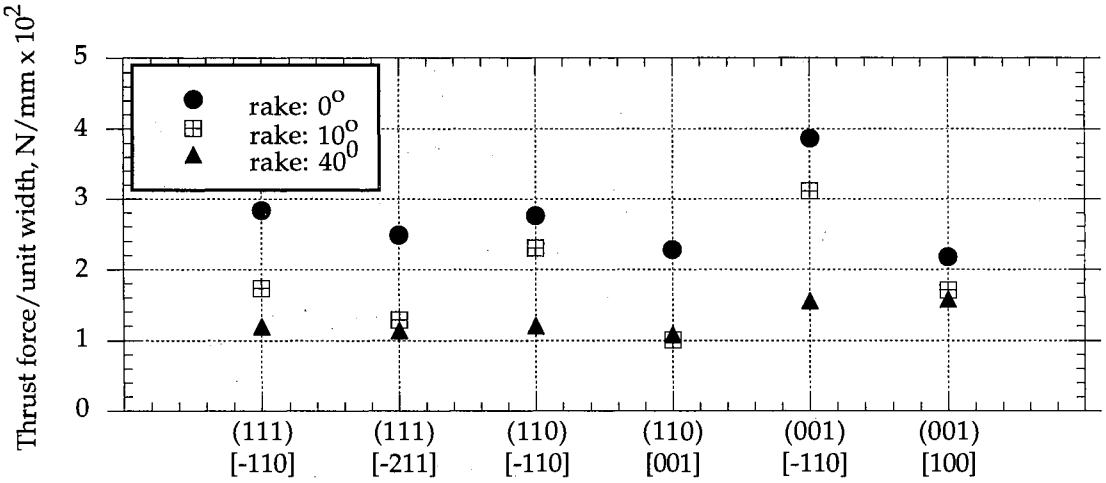
Thrust force/unit width, N/mm x 10^2
5
4
3
2
1
0
rake: 0°
rake: 10°
rake: 40°
(111) [-110]
(111) [-211]
(110) [-110]
(110) [001]
(001) [-110]
(001) [100]

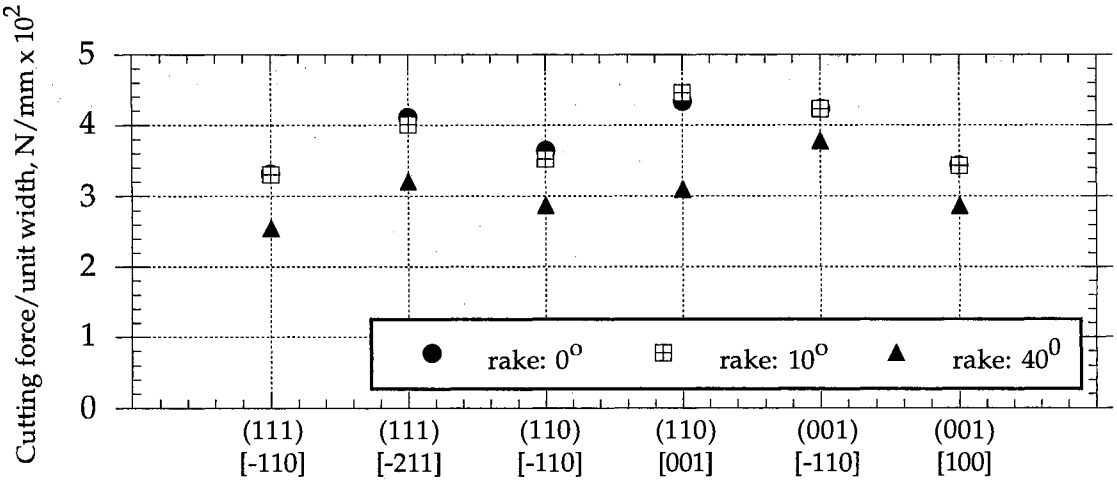
Cutting force/unit width, N/mm x 10^2
5
4
3
2
1
0
rake: 0°
rake: 10°
rake: 40°
(111) [-110]
(111) [-211]
(110) [-110]
(110) [001]
(001) [-110]
(001) [100]

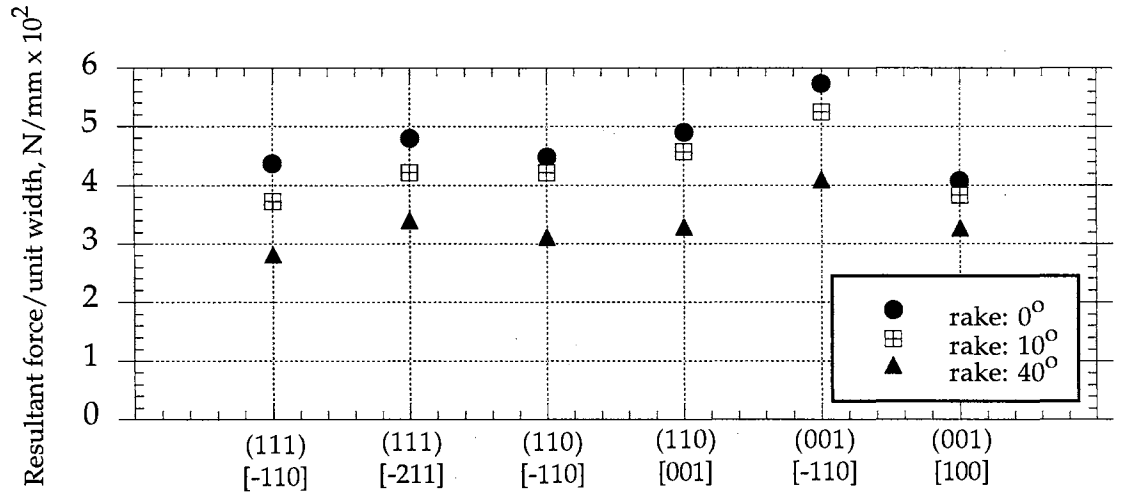

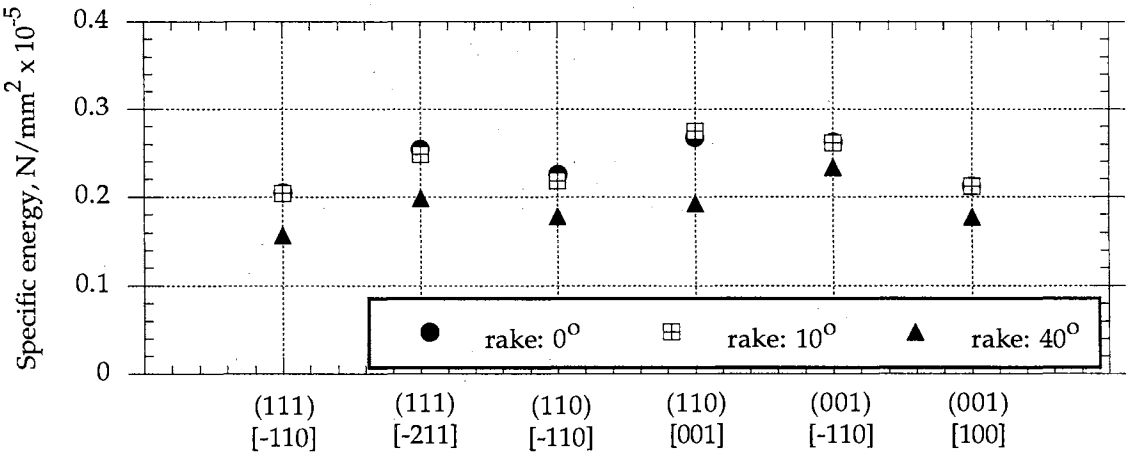

Figures 6.20 (a) - (e) Variation of the cutting and thrust forces, the ratio of thrust force to cutting force, the resultant force, and the specific energy, respectively, for different crystal orientations, different cutting directions, and different rake angles at a depth of cut of 1.62 nm

It can be seen from Figures 6.20 (a) - (c) that the forces and the force ratio tend to show very little variation with orientation and cutting direction when the rake angle is high (~40^{o}). This is partly due to overall lower forces with a 40^{o} rake compared to a 10^{o} rake. However, as the rake angle decreases, the anisotropy of forces and the force ratio become significant. For example, Figure 6.20 (a) shows the variation in the cutting force with orientation indicating higher values with a 0^{o} and 10^{o} rake tool compared to a 40^{o} rake tool. This result is more significant with the thrust force and the force ratio [Figures 6.20 (b) and (c)] as rake angle more or less controls the magnitude of the thrust force increasing more rapidly with decreasing rake angle. The resultant force shows much larger variation with orientation for lower rake tools than for a 40^{o} rake tool [Figure 6.20 (d)]. The specific energy follows the same trend as the cutting force with least variation with orientation for the 40^{o} rake tool [Figure 6.20 (e)]. This may be one of the reasons why some researchers could not find much variation in the forces, shear angle, and DSS with variation in crystal orientation and cutting direction at they used higher rake angles.

6.4.3. Effect of Width of the Workmaterial

In order to investigate the effect of the width of the workmaterial, simulations were conducted with an increased width of the workmaterial from 1.62 nm to 3.24 nm. Based on these simulations, it was observed that the shear angle as well as the deformation ahead of the tool remained essentially unchanged with the increase in the width of the workmaterial. It was also observed that the orientation of the dislocations with the cutting direction did not change. A decrease in the extent of dislocations and subsurface damage was observed. This in part is due to stacking up of more number of layers, which made it difficult to observe the dislocation propagation. Also, an increase in the number of atoms in the width direction increases the force required for the

dislocations to propagate into the workmaterial. Consequently, it can be said that while some differences were observed by increasing the width of the workmaterial, the basic process phenomenon, such as the shear angle and the dislocation generation and propagation, remain unchanged.

Table 6.7. Estimation of the Statistical Error % With Change in the Work Width

Variables	Crystal Set-Up	Width of Cut 1.62 nm (3.24 nm)	Statistical Error %
Cutting Force, N/mm X 10^2	(111)[$\bar{1}$10]	1.723 (1.854)	7.6
	(111)[$\bar{2}$11]	2.395 (2.539)	6.01
	(001)[100]	1.857 (2.019)	8.72
Specific Energy, $N/mm^2 \times 10^{-5}$	(111)[$\bar{1}$10]	0.213 (0.229)	7.51
	(111)[$\bar{2}$11]	0.296 (0.313)	5.74
	(001)[100]	0.229 (0.249)	8.73

Table 6.7 summarizes the results of the MD simulations, namely the cutting force, specific energy, and the statistical error % for the two different widths of cut simulations (1.62 and 3.24 nm), for three different crystal set-up, namely (111)[$\bar{1}$10], (111)[$\bar{2}$11], and (001)[100]. It can be noted that the variation in the forces and the specific energy is <10% as the width is increased by twice. It can also be noted that amongst the three crystal set-ups, the cutting force is minimum with (111)[$\bar{1}$10] combination, followed by (001)[100] and (111)[$\bar{2}$11] combinations, respectively. This trend is in agreement with the results observed when the width of the workmaterial was 1.62 nm. Consequently, based on the

animations and the forces, it appears that while the width of the workmaterial may have some effect on the magnitude of the observed phenomenon and collected data, it does not seem to affect the basic mechanics of the process significantly.

6.4.4. Modes of deformation in machining single crystals of different orientations and cutting directions

Based on the detailed examination of the chip formation process in MD simulation of nanometric cutting of single crystal aluminum, the nature of deformation is found to vary significantly with the crystal orientation and cutting direction. This is because, in the case of single crystal materials, slip occurs on a specified plane for a given orientation and direction of cutting.

Figure 6.21 (a) - (c) show schematically three modes of plastic deformation in the shear zone in nanometric cutting, based on the current investigation. Figure 6.21 (a) shows the case of chip formation process and the shear plane orientation, similar to the one commonly experienced in conventional machining of polycrystalline materials at conventional depths of cut. In this investigation, the chip formation process and the shear angle orientation in the case of (001) orientation and [100] direction of cutting were found to be very similar to the conventional shear ahead of the tool material as shown in Figure 6.21 (a). Thus, it is recommended that this combination be used for simulating machining if only one orientation has to be used. However, in certain other combinations of crystal orientation and cutting direction, the shear angles were found to be much higher than 45^{o}. For example, in the case of (110) orientation and [001] direction, the dislocations are generated at right angle to the direction of cutting. Consequently, the shear angle is much higher than 60^{o}.

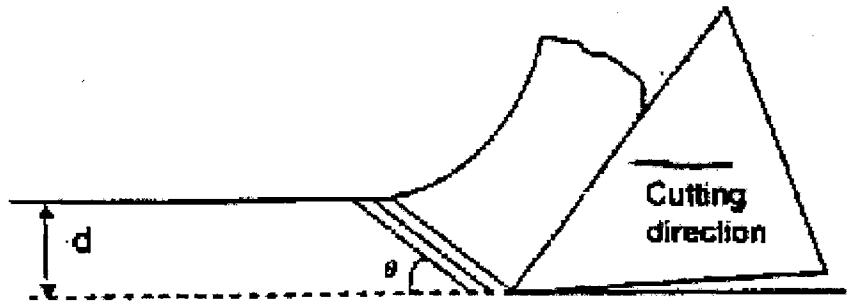

(a)

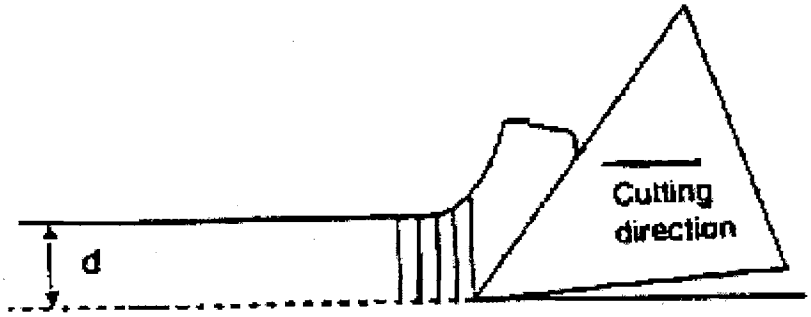

(b)

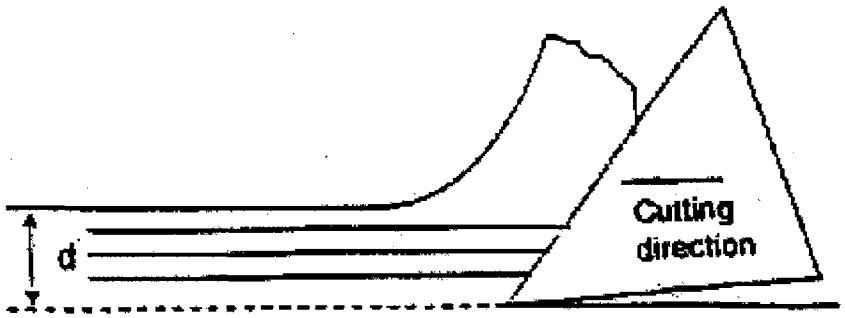

(c)

Figures 6.21 (a) - (c) Schematic Showing Three Modes of Plastic Deformation in the Shear Zone in Nanometric Cutting of Single Crystals in Different Crystal Orientations and Cutting Directions

This mode of dislocation generation and plastic deformation in the shear zone, which is rather unique and not known in the conventional machining with polycrystalline work materials, is shown schematically in Figure 6.21 (b). In contrast, when machining in the (001) orientation and $[\bar{1}10]$ direction, the dislocations are generated parallel to the cutting direction. Consequently, the material is deformed parallel to the cutting direction and the shear angle is much lower than 45^{o}. This mode of dislocation generation and plastic deformation in the shear zone is shown schematically in Figure 6.21 (c).

Such variations in the mode of deformation were not reported earlier as most of the machining tests were conducted on polycrystalline aluminum. Even though some researchers (Ueda et al., 1980; Moriwaki et al., 1991) reported shear angle $>45^{o}$ and as high as 60^{o}, no explanation was offered for this unusual behavior of single crystal materials. This is because it is not easy to observe the cutting process continuously by other experimental techniques, while animation of the MD simulation of nanometric cutting permits such unusual observations.

6.5. CONCLUSIONS

Molecular Dynamics (MD) simulation of nanometric cutting on single crystal aluminum in different orientations, namely, {(111), (110), and (001)}, and cutting directions, namely, <$[\bar{1}10]$, $[\bar{2}11]$, and [100]> were conducted in specific combinations, with cutting tools of different positive rake angles (0^{o}, 10^{o}, and 40^{o}) and different depths of cut (0.81-1.62 nm) and at a cutting speed of 500 m/sec to investigate the degree of anisotropy of this material. Specific combination of orientation and cutting direction used are for the (111) orientation, the cutting directions are $[\bar{1}10]$ and $[\bar{2}11]$; for the (110)

orientation, the cutting directions are [$\bar{1}10$] and [001]; and for the (001) orientation, the cutting directions are [$\bar{1}10$] and [100]. Specific conclusions that may be arrived based on this study are given in the following:

1. When the aluminum crystal was oriented in the (111) plane and cut in the [$\bar{1}10$] direction, the plastic deformation ahead of the tool was found to be predominantly compression along with shear in the cutting direction. As cutting progresses, not only the material ahead of the tool in the depth of cut region is deformed but also several layers below the depth of cut region ahead of the tool tip. As the tool progresses, some of the dislocations causing subsurface deformation underneath and ahead of the tool tip are released, resulting in the subsurface deformation of only about half the depth of cut.

2. When the workmaterial was oriented in the (001) plane and cut in the [$\bar{1}10$] direction, the dislocations were found to generate parallel to the cutting direction. In contrast, when the crystal was oriented in the (110) plane but cut in the [001] direction, the dislocations were generated normal to the cutting direction. When the crystal is oriented in the (110) plane and cut in the [$\bar{1}10$] direction, dislocations were found to generate both along and normal to the cutting direction. Although movement of dislocations to the machined surface takes place due to elastic recovery, latter orientation, namely, the (110) plane cut in the [$\bar{1}10$] direction seems to provide minimal subsurface deformation.

3. In the case of (001) orientation and [100] cutting direction, extensive dislocation motion at $\sim 45^{o}$ to the cutting direction was observed while in the case of (111) orientation and [$\bar{2}11$] cutting direction, the dislocation motion at $\sim 60^{o}$ to the cutting direction was observed.

4. The cutting forces were found to vary cyclically with the orientation of the crystal and the direction of cutting. Minimum cutting forces were generated when machining in the $[\bar{1}10]$ directions on the (111) or (110) orientations. This is followed by cutting in the (001) direction on the [100] orientation. The cutting force was maximum when machining in the [001] direction on the (110) orientation.

5. A systematic variation of the cutting forces and specific energy with crystal orientation and direction of cutting was observed. Variation in the magnitude of the cutting force for a given depth of cut with different orientations and directions of cutting was in the range of 25% which is close to the anisotropy of this material in the elastic range (21.9%). Variation of specific energy was found to range from 25.8 to 40 % which is higher than the anisotropy in the elastic range. The lower degree of anisotropy in the case of aluminum, an FCC material, may be attributed to the high stacking fault energy ($\sim 200 \times 10^{-3}$ J m^{-2}) and low equilibrium spacing (2 atomic layers) enabling cross slip more easily.

6. Subsurface deformation was observed to vary with different orientations of the crystal and direction of cutting. Subsurface deformation was seen to be minimum when the dislocation motion was parallel to or perpendicular to the cutting direction. In the former case, no dislocations were generated in the subsurface while in the latter case the dislocations generated into the workmaterial are seen to move towards the machined surface due to elastic recovery.

7. A decrease in the cutting force with increase in the rake angle was observed. The forces, force ratio, and the specific energy showed least variation with orientation for

higher rake tools (40^{o}). However, as the rake angle was decreased (i.e., 10^{o} and 0^{o}) high anisotropy in the magnitude of the forces, force ratio, and the specific energy with orientation was observed.

8. When the dislocations were moving at an angle to the workmaterial, as in the case of (001) orientation and [100] cutting direction or in the case of (111) orientation and $[\bar{2}11]$ cutting direction, they were found to propagate into the workmaterial at depths several times the depth of cut. However, with a rake tool of 40^{o}, the dislocation motion was limited to only a few layers beneath the tool tip. This suggests that tool geometry also plays an important role in addition to the orientation and cutting direction effects. Hence, the results observed for the same orientation and cutting direction can vary significantly, if not in the nature, in the magnitude.

9. Shear angles much higher than 45^{o} were observed when machining in specific planes and cutting directions, in the machining of single crystal aluminum. For example, in the (110) orientation and <001> direction, the dislocations are at right angle to the direction of cutting. Material is deformed perpendicular to the cutting direction. The shear angle is $> 60^{o}$. Similarly, when machining in the (001) orientation and $[\bar{1}10]$ direction, the dislocations are generated parallel to the cutting direction. This is because, in the case of single crystal materials, slip occurs on a specified plane for a preferred orientation and direction of cutting. Such variations in the mode of deformation were not reported earlier as most of the machining tests were conducted on polycrystalline aluminum. Even though some researchers reported shear angle $> 45^{o}$, no explanation was offered for this unusual behavior of single crystal materials. This is because it is not possible to observe continuously by other experimental techniques, while animation of the MD simulation of nanometric cutting permits observation of such unusual phenomena.

10. Based on the MD simulation of nanometric cutting in different crystallographic planes and cutting directions, three modes of deformation were observed in the shear zone. In the first case, namely, [(001) orientation and [100] direction], the chip formation process and the shear plane orientation were similar to the one commonly experienced in conventional machining of polycrystalline materials at conventional depths of cut. In the second case, namely, [(110) orientation and [001] direction], the dislocations are generated at right angles to the direction of cutting, i.e., material is deformed perpendicular to the cutting direction. Consequently, the shear angle is extremely high ($< 60^{o}$). In the third case, namely, [(001) orientation and $[\bar{1}10]$ direction], the dislocations are generated parallel to the cutting direction. Consequently, the material is deformed parallel to the cutting direction and the shear angle is $> 45^{o}$.

CHAPTER 7

EXIT FAILURE IN NANOMETRIC CUTTING [a]

7.1. INTRODUCTION

In most machining operations, be it turning, milling, or grinding, undesirable burrs are invariably formed in the workmaterial at the exit end of the cut. Burr formation modifies the nature of the chip formation and the associated forces, stresses, and strains both in the workmaterial as well as in the tool towards the exit. This can have a detrimental effect on the chipping and fracture of brittle cutting tools, such as ceramics, cemented carbides etc., in interrupted cutting of high-strength materials at high speeds and/or feeds (Shaw, 1979). While there are numerous studies on the entry and exit effects on the tool fracture (Loladze, 1975; Uehara, 1977; Shaw, 1979; Takagi and Shaw, 1983; Lee et al., 1984; Sampath et al., 1984; Ramaraj et al., 1988), relatively few studies were focused on the burr formation in the workmaterial at exit (Pekelharing, 1978; Lucca, 1982). This investigation is a contribution in that direction.

---

a - R. Komanduri, N. Chandrasekaran, L. M. Raff, "MD simulation of exit failure in nanometric cutting," accepted for publication in Mat. Sci. Engg., 2001

Pioneering work on the exit failure in the workmaterial as well as in the tool in interrupted cutting was conducted by Pekelharing (1978). Figure 7.1 is an optical micrograph of a polished and etched workmaterial showing the exit failure and the foot formation, after Pekelharing (1978). It shows a drastic change in the mechanism of chip formation (termed as "negative shear') near the end of the cut. The separation is always noticeably curved indicating that the foot rotates during the negative shear period and leaves with the chip. The separation of the chip during the last part of the cut (the "foot" on the chip) is not of a brittle nature, but begins as a negative shearing process until separation takes place. Shaw (1979) also pointed out that in addition to the "foot" formation, a reversal of the normally compressive stress at the tool tip might occur on unloading at the exit to cause failure of the tool tip.

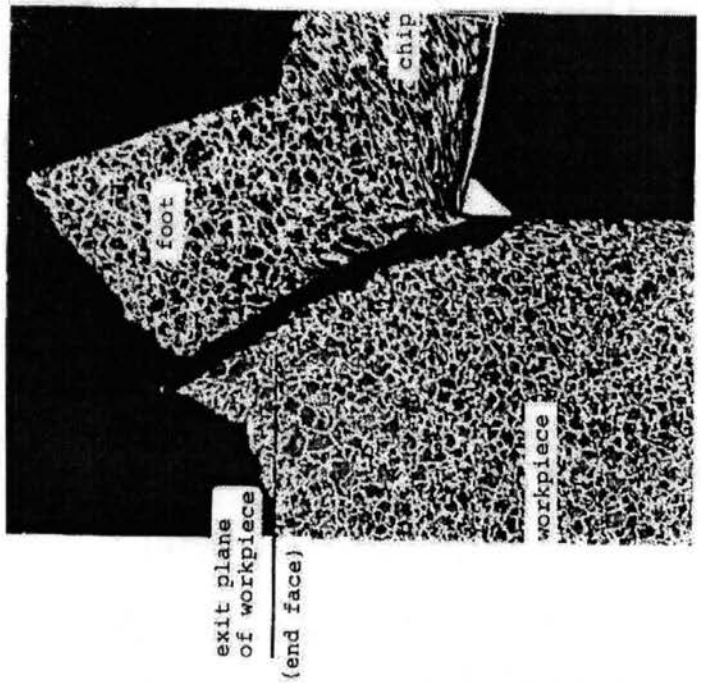

Figure 7.1. Micrograph of the Chip Root Showing the Exit Failure, Negative Shear, and Foot Formation (after Pekelharing, 1978)

Ramaraj et al (1988) investigated the "foot" formation in connection with the tool fracture at exit. They pointed out that it would be more accurate to describe the change in

the shear plane direction from positive to negative as a "sudden jump" rather than "rotation," since rotation infers a gradual change. They considered this as a sudden change from shear in the shear plane to fracture along the negative shear plane in the workmaterial forming a "foot." Takagi and Shaw (1983), with reference to cutting tools, pointed out that crack initiation may be more important in the case of brittle materials and crack propagation in the case of ductile materials. A similar situation may exist in the case of exit failure of ductile versus brittle workmaterials.

Lucca (1982) conducted a systematic experimental study of the exit failure in different materials (AISI 1020 steel, 6061-T6 Al, and commercially pure A-55 titanium) under different machining conditions (15^{o}-135^{o} entry and exit angles and 0.008", 0.009", 0.01" depth of cut), using high speed photography. It was observed in that study that the exit chip separation process is a ductile shear type failure of workmaterial due to inadequate elastic constraint at the exit. Foot formation at the exit is reported to occur on all test materials with 90^{o} exit angle on odd numbered cuts as reported earlier by Pekelharing (1978). The depth of the exit separation chamfer is reported to equal the depth of cut. The exit chip separation angle is reported to be constant for each workmaterial and between 20-25^{o}. The behavior of foot formation process is reported to be different for various materials. Consequently, the sudden shock on the tool due to release of cutting energy will be more severe when machining brittle or limited ductility materials (e.g. titanium) compared to much ductile materials (e.g. aluminum).

Nakayama and Arai (1987) classified the machining burrs formed in various cutting operations by a combination of two systems: (1) by cutting edge directly concerned and (2) by the mode and direction of burr formation. They observed that the size of the sideward burr is minimized by decreasing the undeformed chip thickness, decreasing the

shear strain of the chip, increasing the strength of the workpiece edge by increasing the including angle and, turning the direction of cutting force towards the workpiece. A decrease in the chip shear strain can be achieved by using high rake angle tools, high cutting speed, lubricant, and cold working of the workpiece. Forward burrs are reported at exit in the cutting of ductile materials while fracture at exit is reported as the brittleness of the workmaterial increases. The size of forward burr at the exit of cutting is often minimized by the fracture at the chip root.

Hashimura et al. (1995) conducted *in situ* oblique cutting experiments on aluminum workmaterial (Al 2024-O) in a scanning electron microscope with a micromachining device to investigate 3-D burr formation and the effect of tool inclination angle. Two types of burrs are reported, namely, exit burr on the exit edge of the workpiece and side burr on the side of the workpiece. The exit burr thickness decreases and the side burr size increases with increase in the inclination angle. They observed the exit burr to be smaller and the side burr larger in oblique cutting than in orthogonal cutting. For a feed of 50 μm, edge break out is reported for inclination angles from 0^{o} to 45^{o}. For a feed of 20 μm, break out did not occur for inclination angles > 30^{o}. Breakout is considered to be caused by the smaller strain experienced in oblique cutting compared to orthogonal cutting.

In a recent study, Hashimura et al. (1999) conducted *in situ* machining experiments inside scanning electron microscope and FEM studies of the exit failure in orthogonal cutting. Two workmaterials of different ductilities, namely, copper to represent a more ductile material and aluminum (Al 2024-O) to represent a less ductile or more brittle material (according to the authors), were used in this study. Machining experiments were performed with a HSS tool (rake angle 15^{o}), two tool edge radii (10 and 150 mm)], a cutting speed of 0.025 mm/s, and feed rates in the range of 20-200 mm. They found that

ductile materials (copper) behaved differently from brittle materials (Al-2024-O) in burr formation, in particular in the crack propagation.

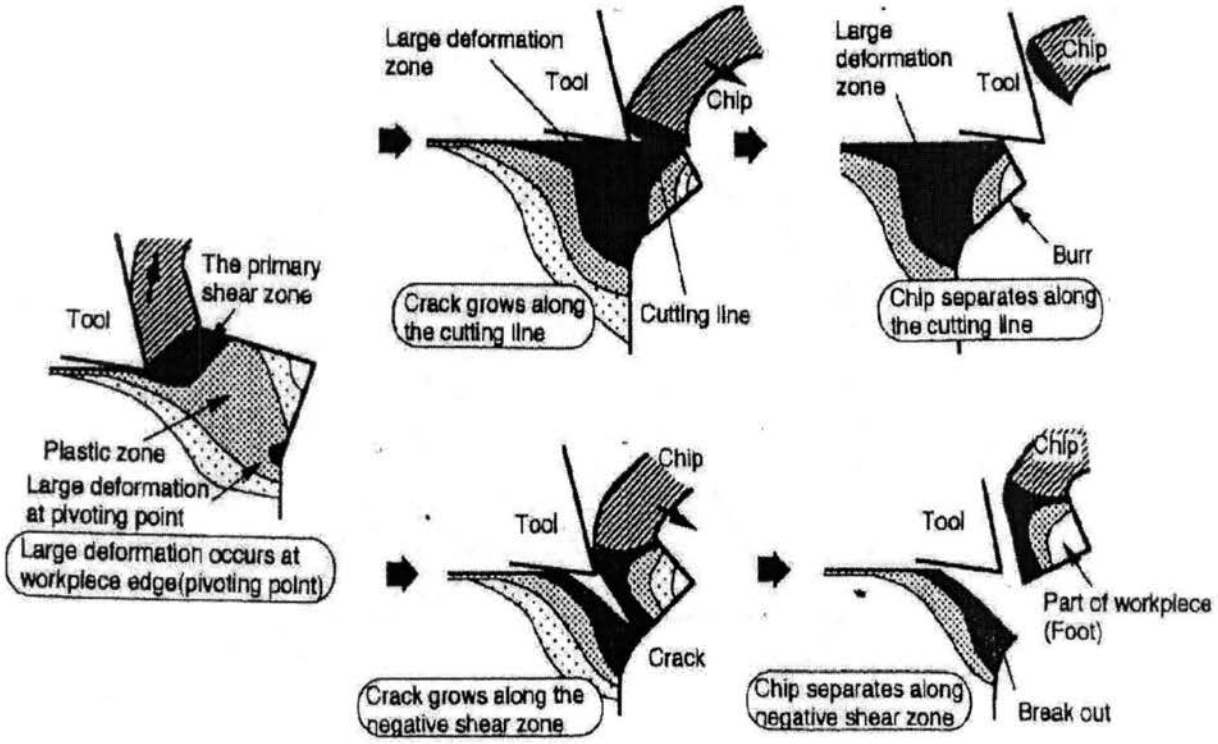

Figures 7.2. Schematic of the exit Failures with (a) Cu and (b) Al-2024-O (after Hashimura et al., 1999)

Figures 7.2 (a) and (b) are schematics of the exit failures in a 'ductile' (Cu) and a 'brittle' (Al-2024-O) workmaterial, respectively, after Hashimura et al (1999). According to them, for both type of workmaterials, as the cut approaches the exit end, large deformation occurs at the workpiece edge causing negative shear. However, for ductile materials, a crack initiates at the tool tip in the primary shear zone and moves in the direction of the depth-of-cut line. This causes separation of the chip along the depth-of-

cut line and formation of a positive burr on the workpiece. For brittle (or not-so-ductile) materials a crack initiates at the tool tip in the negative shear zone and propagates in the direction of the pivoting point. The tool induces crack growth and the crack mode changes from a shearing type to a crack opening mode. The crack separates the chip along with a part of the workpiece ("foot") above the negative shear line. Consequently, the fractured surface as well as a small deformed material remains on the workpiece edge, similar to the "foot" formation showed by Pekelharing (1978). In this case, the burr is of a break out type, also termed negative burr. As the undeformed chip thickness was increased, they found an increase in the resulting burr thickness as well as an increase in both the distance and depth of the initial pivoting point of the burr from the tool edge.

While significant amount of work has been done and still in progress to reduce tool chipping, very limited work has been reported from the standpoint of damage to the workmaterial. A reduction in the foot formation at the workmaterial exit might reduce tool chipping. Also, precision finishing of expensive semiconducting and brittle materials, such as silicon, germanium, and glasses, for various technological applications demand minimum deviation from the required form and finish accuracy. The tool chipping can result in poor surface finish while the exit failure of the workmaterial can cause significant wastage of material. In addition, fracture of single crystal diamond tools, usually used to finish such materials, alleviates the cost of the process. Experimental studies on the burr formation can be rather expensive and time consuming in view of the vast number of process parameters involved. Hence, simulation of the process, such as the MD simulation, can be an attractive alternative. In this investigation, molecular dynamics (MD) simulations of nanometric cutting were conducted at various cutting conditions to investigate the exit failure and burr formation in the machining of metals. The effect of relative ductility of the workmaterial (e.g. soft versus hard), tool rake angle (-30^{o} to 60^{o}), depth of cut (1.45 to 3.62 nm), and the effect of elastic

constraint at the end of cut on the exit failure were investigated and the simulation results were compared with some of the experimental results reported in the literature.

7.2. MD SIMULATION OF EXIT FAILURE IN NANOMETRIC CUTTING

Figures 7.3 (a) and (b) show the schematic of the models used for the MD simulation of nanometric cutting of exit failure. The boundary atoms on the exit side were removed to create conditions similar to "no elastic constraint" at the exit side of the workmaterial as shown schematically in Figure 7.3 (a). This model was used in the studies relating to the effect of workmaterial ductility, tool rake angle, and depth of cut. In the study on the effect of external constraint at exit, boundary atoms were placed till the depth of cut line to simulate the external constraint at the exit side of the workmaterial as shown in Figure 7.3 (b). For convenience, an infinitely hard tool was used in these simulations as the emphasis is on the workmaterial failure at exit.

The potential used in the simulations is a pairwise sum of Morse potentials between the lattice atoms of the workmaterial plus a second summation of pairwise Morse potentials between the atoms of the tool and those in the workmaterial. Two model FCC materials (one to represent a ductile material [D] and the other to represent a brittle material [B]) were chosen by varying the appropriate Morse potential parameters [D, α, r_{eq}]. Table 7.1 gives the computational parameters, details of the workmaterial and tool dimensions, workmaterial Morse parameters (for ductile [D] and brittle [B] workmaterials), depth of cut, cutting speed, and tool geometry used in the simulations. Figure 7.4 shows the variation of the potential curve with interatomic distance for the ductile and the brittle materials used in the current study. The potential was calculated using the Morse potential parameters given in Table 7.1.

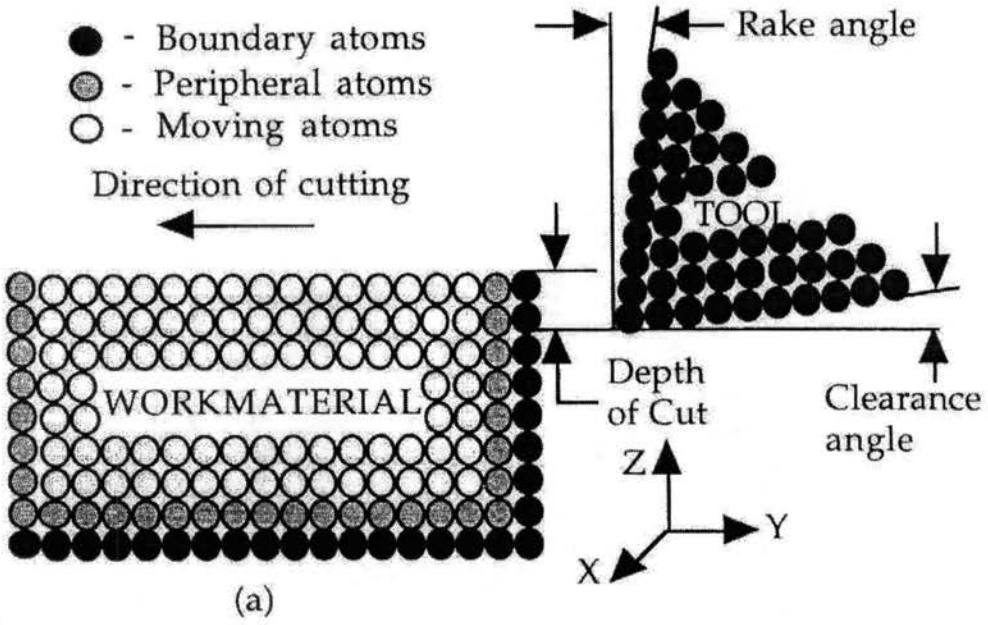

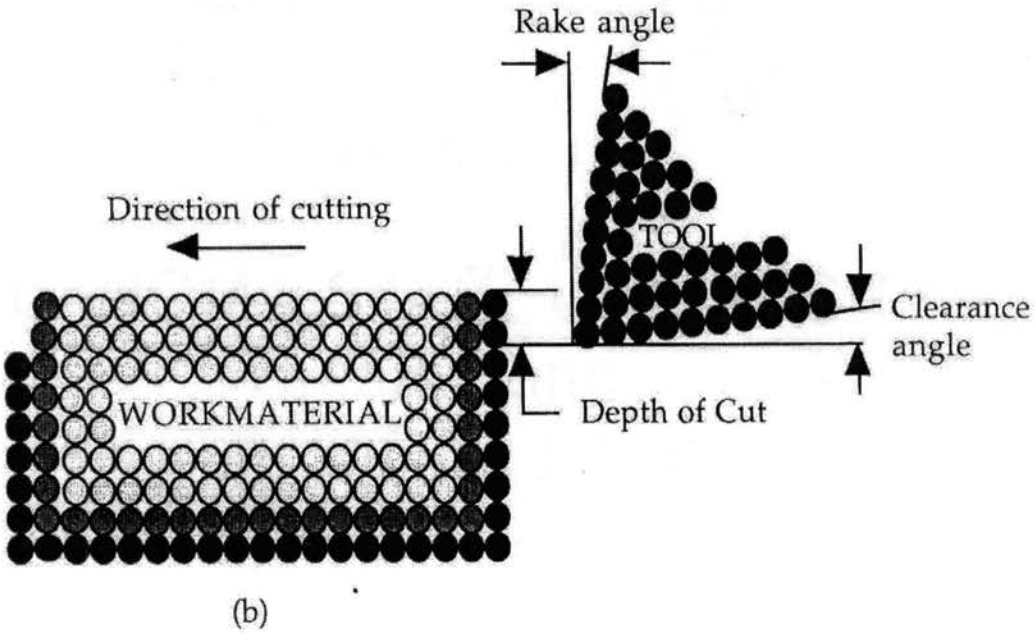

Figures 7.3 (a) and (b) show the schematic of the models used for the MD simulation of nanometric cutting of exit failure

Table 7.1. Computational parameters in MD simulation of nanometric cutting

Configuration	2-D
Workmaterial	Ductile (D) and Brittle (B)
Crystal structure	FCC
Lattice constant (a)	3.62 A (D) and 3.17 (B)
Potential used	Morse potential
Morse potential parameters	for ductile (D) material : D: 0.343 eV, α: 1.359 A^{-1}, r_{eq}: 2.87 A
	for brittle (B) material : D: 0.54 eV, α: 2.47 A^{-1}, r_{eq}: 2.6 A
Workmaterial dimensions	1ax70ax50a a - lattice constant
Tool dimensions	2ax20ax50a
Tool material	Infinitely hard
Tool edge radius	Sharp edge
Tool rake angle	-30^o, -15^o, 0^o, 15^o, 30^o, 45^o, and 60^o
Depth of cut (nm)	1.45, 2.17, and 3.62
Workmaterial geometry at exit	90^o
Cutting speed (m/sec)	500
Bulk temperature (K)	293

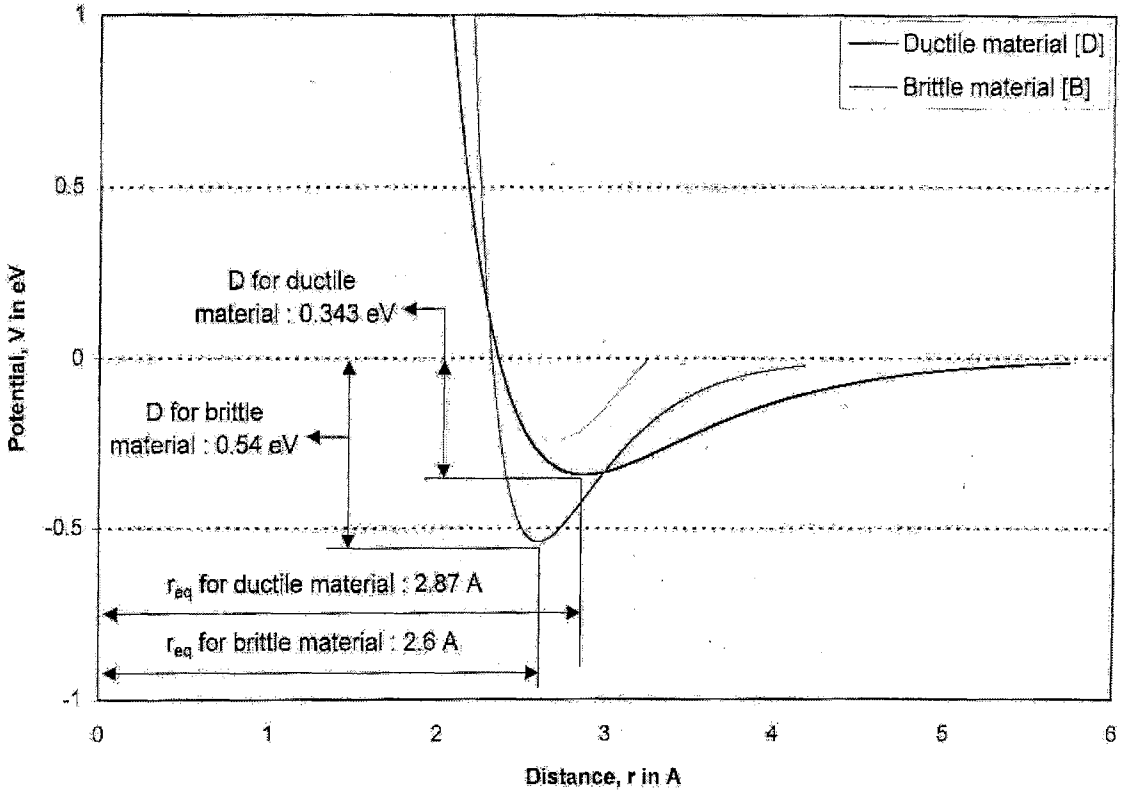

Figure 7.4. Variation of the potential curve with interatomic distance for the ductile and the brittle materials

7.3. RESULTS AND DISCUSSION

7.3.1. Effect of Workmaterial Type

In order to investigate the effect of workmaterial's ductility, two model FCC materials (one to represent a ductile material [D] and the other to represent a brittle material [B]) were chosen by altering the appropriate Morse potential parameters (Table

7.1 and Figure 7.4). A tool rake angle of -30^{o} and a depth of cut of 6 lattice spacing were used in the simulations. The boundary condition used is as shown in Figure 7.3 (a). Figures 7.5 (a) and (b) and Figures 7.6 (a) and (b) show a comparison of typical exit failures of a brittle [B] and a ductile [D] workmaterial, respectively. For a brittle workmaterial [B], as the cutting tool approaches the exit, a crack initiates at the tool tip [Figure 7.5 (a)] and propagates into the workmaterial [Figure 7.5 (b)]. This negative shear and failure is close to the mirror image of the primary shear above the depth of cut line. Thus, the chip along with the "foot" is removed by the tool. This results in a negative burr formation, similar to that shown by Hashimura et al. (1999) [Figure 7.2]. In the case of cutting a ductile material [D], as the cutting tool approaches the exit, initiation of negative shear from the tool tip into the workmaterial can be seen [Figure 7.6 (a)] similar to that reported by Pekelharing (1978) and Hashimura et al. (1999). This negative shear is again close to the mirror image of the primary shear above the depth of cut line. However, no sudden crack is seen to develop along the negative shear zone [Figure 7.6 (b)] unlike that in the case of brittle material [B]. The chip is subsequently removed along the depth of cut line by a shearing process and not by brittle fracture [Figure 7.6 (b)]. From the animations of the nanometric cutting process, the pivot point was observed to change due to rotation of the foot during cutting. This results in a constant reduction in the depth of cut as cutting progresses. Consequently, for a ductile material the formation of a positive burr with a curved surface is seen at exit. These results on the effect of workmaterial ductility on the exit failure are in agreement with the experimental observations of Pekelharing (1978), Nakayama and Arai (1987), and Hashimura et al. (1999) [compare Figures 7.5 and 7.6 with Figure 7.2]. Based on this, it can be inferred that the type of failure at exit (either negative or positive burr formation) for a given cutting condition depends on the extent of ductility of the workmaterial. Hashimura et al. (1999) attributed this variation to the difference in the critical fracture strain of ductile versus brittle materials.

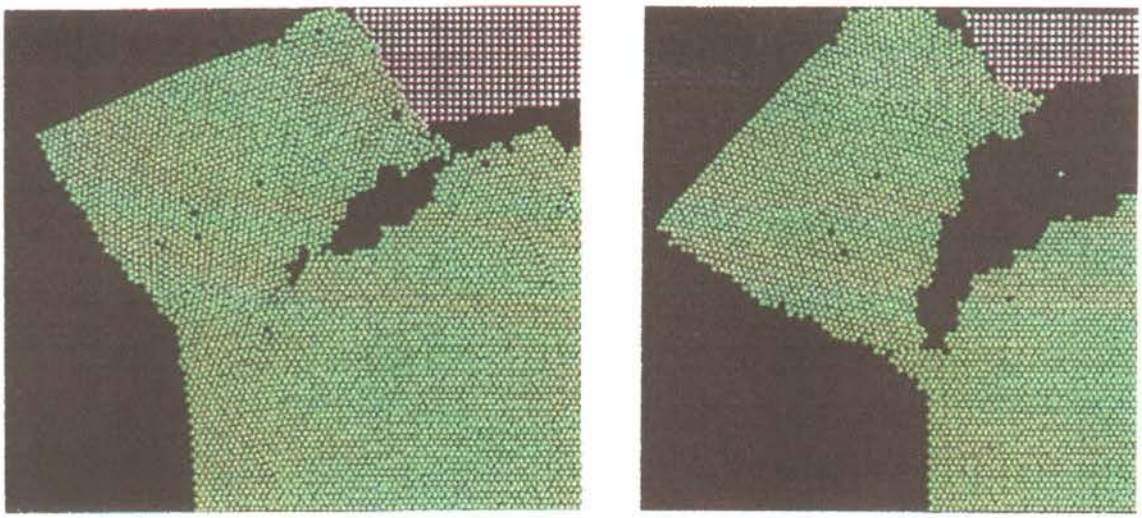

(a) (b)

Figures 7.5 (a) and (b) Two stages of the exit failure in nanometric cutting of a brittle workmaterial with no elastic constraint

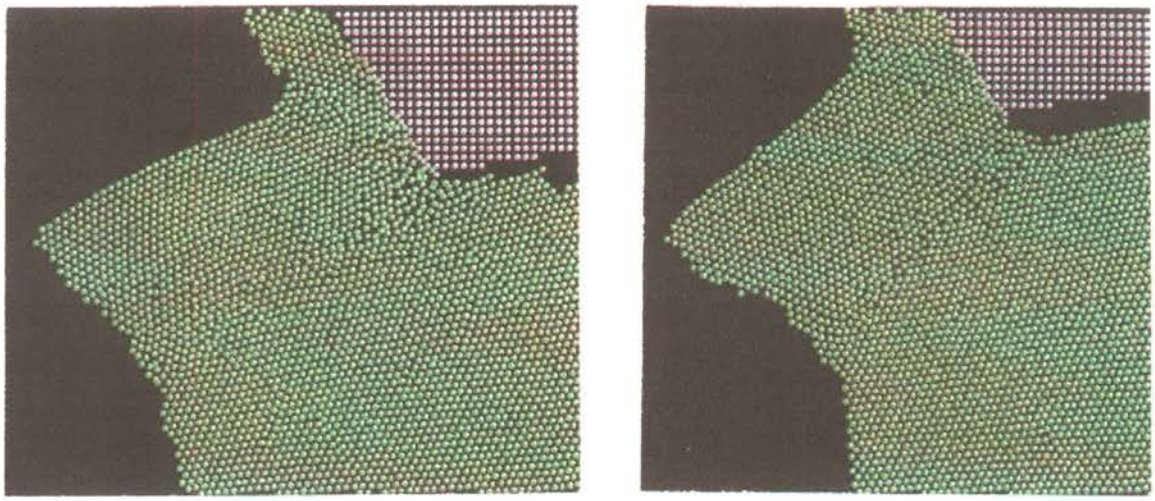

(a) (b)

Figures 7.6 (a) and (b) Two stages of the exit failure in nanometric cutting of a ductile workmaterial with no elastic constraint

7.3.2. Effect of Tool Rake Angle

Figures 7.7 (a) - (f) and Figures 7.8 (a) - (f) show the exit stage of nanometric cutting of a ductile workmaterial [D] and a brittle workmaterial [B], respectively with various rake tools, namely, -15^{o}, 0^{o}, 15^{o}, 30^{o}, 45^{o}, and 60^{o}. The depth of cut was maintained constant at 6 lattice spacings. Figures 7.5 (b) and 7.6 (b) show the exit stage of a brittle and a ductile workmaterial under similar cutting conditions for a tool rake angle of -30^{o}. In the following discussion, the point at the exit edge about which the workmaterial fails is referred to as the 'pivoting point' and the distance from the workmaterial starting edge at which failure began is referred to as 'failure starting point (FSP)'. It should be noted that the workmaterial-tool plots as shown in Figures 7.5 to 7.8 are magnified and only the exit region where failure occurs is focussed. The workmaterial size is maintained significantly large (Table 7.1) to avoid boundary effects in all the simulations conducted.

In the case of ductile material, formation of negative shear zone into the workmaterial can be observed with all the rake angles. However, the width of the shear zone is high with a high negative rake tool (-30^{o}) [Figure 7.6 (b)] and decreases as the negative rake angle decreases [compare Figure 7.6 (b) with Figures 7.7 (a) - (f)]. Positive burr formation can be observed with all rake angle tools though to a varying degree. From the animations of the nanometric cutting process, it was observed that the FSP at which exit failure began decreases with increasing negative rake tool. In addition, Figures 7.7 (a) - (f) indicate an increase in the depth of the pivot point (d) from the depth of cut line and the length (l) from the tool tip at which pivoting occurs with increasing negative rake tool. The dimensions d and l were measured when prominent pivoting was observed at the exit edge of the workmaterial. An increase in the thickness of the burr (t)

and the height of the burr (h) (measured after cutting) with increasing negative rake tool was also observed. From the animations of the nanometric cutting process and the measured burr dimensions (as will be shown below), it was observed that the pivot point for a ductile material constantly changes as the cutting progresses and the initial pivot dimensions (d and l) are not the same as the final burr dimensions (t and h).

In the case of a brittle material, the increase in the positive rake angle of the tool results in a decrease in the fracture dimensions (thickness [t] and height [h] of burr) [compare Figures 7.8 (a) - (f)]. With a 60^{o} rake tool, practically no burr formation is observed and the chip seems to be separated from the workmaterial along the depth of cut line [Figure 7.8 (f)]. However, as the negative rake angle increases, formation of 'foot' and subsequent separation of the chip along with a part of the workmaterial can be observed [Compare Figures 7.8 (a) - (e)]. In the case of a brittle workmaterial, the FSP and the dimensions d and l could not be measured as the time between fracture initiation and propagation and subsequent exit failure was significantly low. Consequently, only the thickness (t) and height (h) of the fractured workmaterial after cutting were measured.

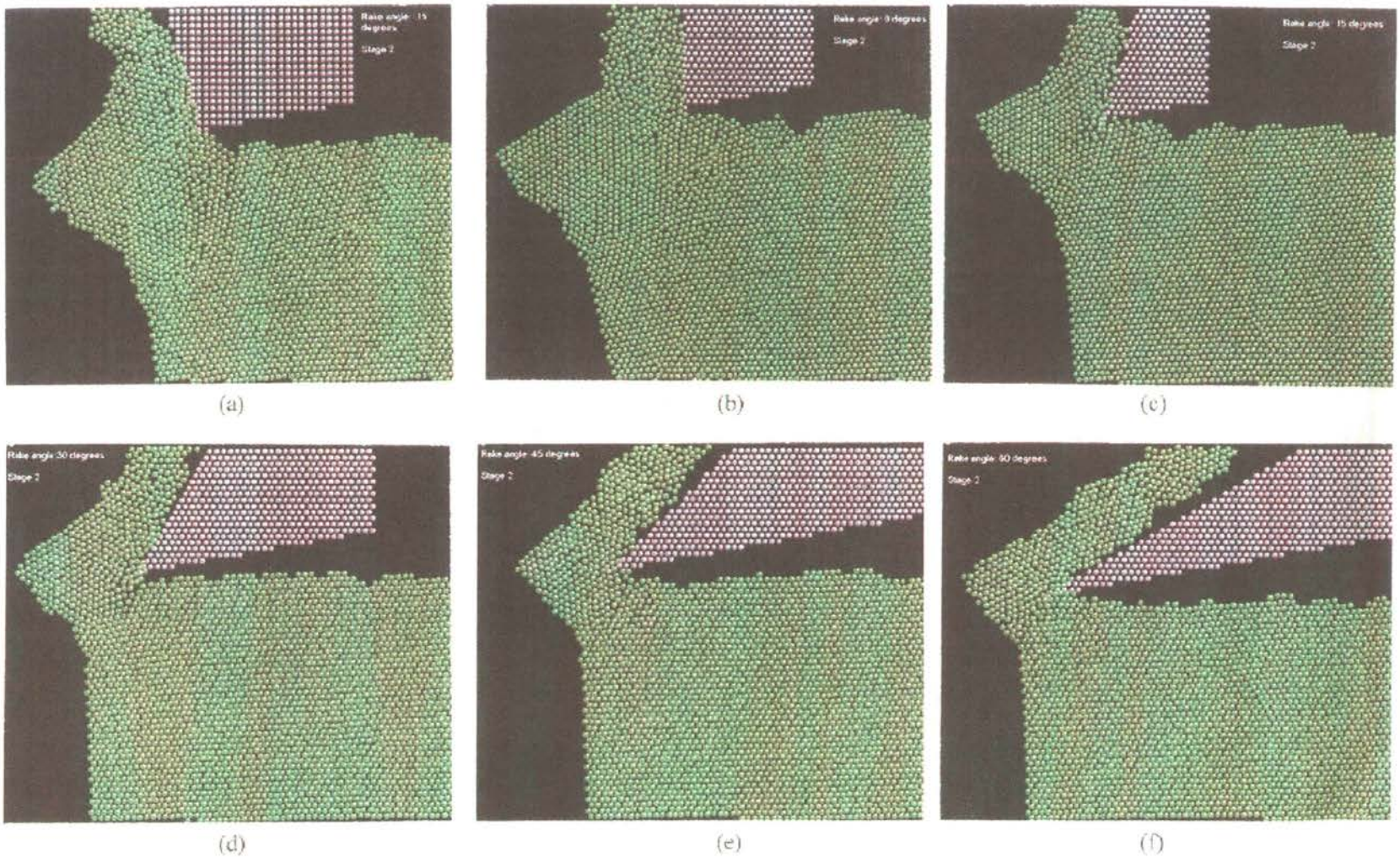

Figures 7.7 (a) - (f) MD simulation plots of the nanometric cutting process performed on a ductile workmaterial with no elastic constraint at the exit for various tool rake angles (a) -15° (b) 0° (c) 15° (d) 30° (e) 45° and (f) 60°

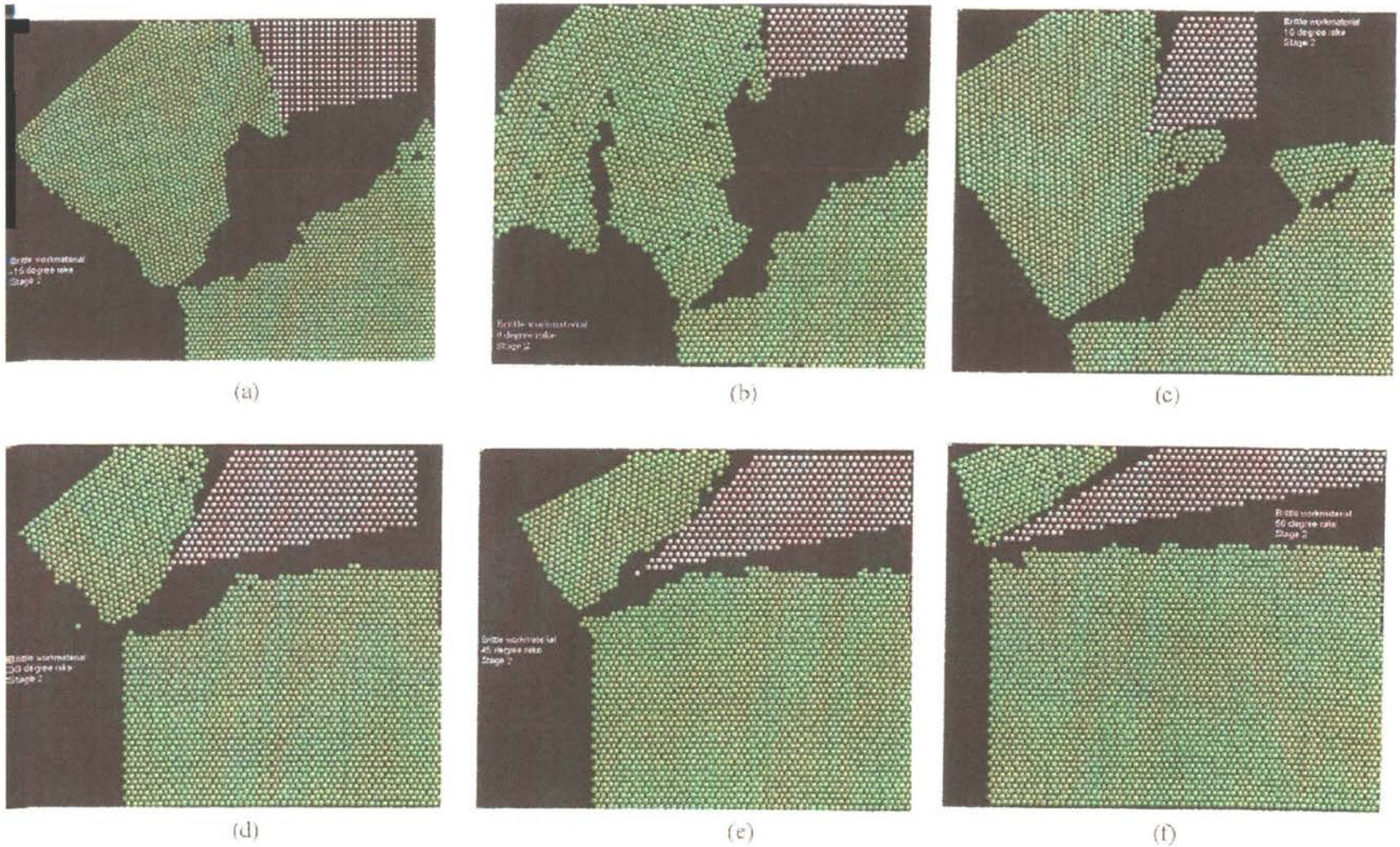

Figures 7.8 (a) - (f) MD simulation plots of the nanometric cutting process performed on a brittle workmaterial with no elastic constraint at the exit for various tool rake angles (a) -15° (b) 0° (c) 15° (d) 30° (e) 45° and (f) 60°

7.3.3. On the Burr Dimensions Measured After Exit Failure

Tables 7.2 (a) - (c) give dimensions of the exit failure measured on the workmaterials (D and B) machined with different rake tools at the point of pivot initiation and after completion of the cut (see Figure 7.9 for details).

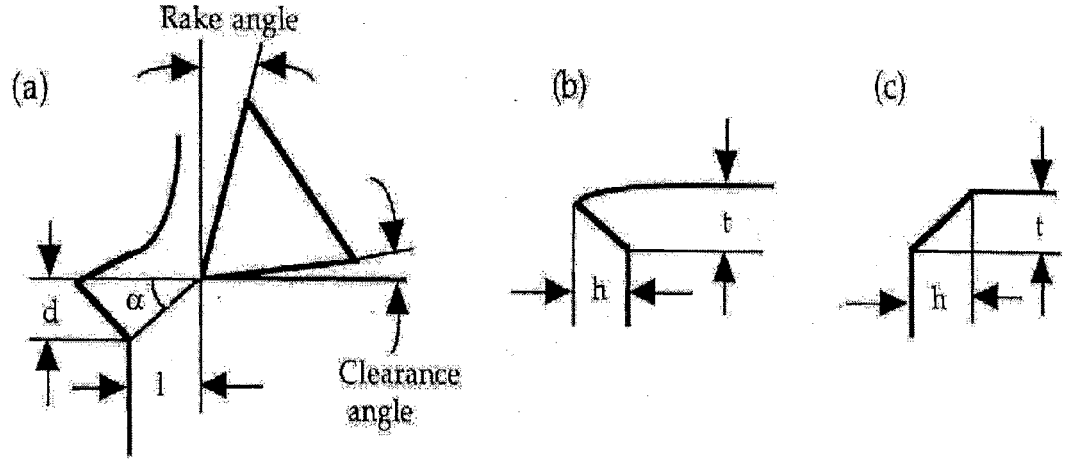

Figure 7.9. Schematic of the various dimensions measured at the exit failure

From Table 7.2 (a), it can be seen that for a ductile workmaterial, the FSP (measured from the entry side) decreases with increasing negative rake tool, as is also observed from the animations of the nanometric cutting process. Based on Figure 7.10 (a) [as well as Table 7.2 (a)], it can be seen that both d and l for a ductile material [D] increases with increasing negative rake tool. Also, the increase in d is at a higher rate in comparison to increase in l. In the case of a positive rake tool, the plastic deformation zone is mainly concentrated around the tool tip and the primary shear zone. As the positive rake angle decreases, the plastic deformation extends deep into the workmaterial. In addition, with high negative rake tools, the radius of the plastic deformation zone is higher compared to those with positive rake tools. Consequently, the plastic/elastic zone approaches the exit edge earlier and deeper with a negative rake tool. Hence, both d and l increase as the tool negative rake angle increases.

Table 7.2 (a): Dimensions of pivoting for ductile workmaterial [Figure 7.10 (a)]

Rake Angle (degrees)	Failure Starting Point (FSP), nm	Depth of Pivot (D), nm	Distance of Pivot from Exit (L), nm
-30	7.54	11.21	5.52
-15	8.75	9.91	5.0
0	10.56	7.76	4.31
15	11.46	5.34	3.28
30	12.67	4.22	2.76
45	15.38	3.45	2.41
60	19.60	2.76	2.07

Table 7.2 (b): Dimensions of burr after failure [Figure 7.10 (b)]

Rake angle (degrees)	Pivot after depth failure (t), nm		Pivot height after failure (h), nm	
	Ductile [D]	Brittle [B]	Ductile [D]	Brittle [B}
-30	10.34	22.90	8.28	20.82
-15	8.79	19.78	7.41	18.74
0	7.07	17.20	6.90	17.59
15	4.83	13.04	5.52	14.96
30	3.28	4.16	4.31	8.33
45	2.41	3.05	3.79	6.68
60	2.07	1.08	3.62	2.40

Table 7.2 (c): Ratio of dimensions for Cu and W, resultant force and negative shear angles with respect to cutting direction and force ratio

Rake Angle (degrees)	D/L for ductile material [D]	t/h for ductile material [D]	t/h for brittle material [B]	Force Ratio $(F_t/F_c)^*$	Negative Shear Angle (ϕ), degrees	Orientation of Resultant Force $(\theta)^*$, degrees
-30	2.03	1.25	1.1	1.4	40	54.46
-15	1.98	1.19	1.06	1.09	30.96	47.33
0	1.80	1.02	0.98	0.86	30.11	40.63
15	1.63	0.88	0.87	0.60	28.81	30.75
30	1.53	0.76	0.50	0.57	24.23	29.68
45	1.43	0.64	0.46	0.50	26.57	26.38
60	1.33	0.57	0.45	-	24.00	-

Figure 7.10 (b) shows the variation of t and h with tool rake angle for a ductile [D] and a brittle [B] workmaterial. Both, t and h increase with increasing negative rake tool [also Table 7.2 (b)]. Nakayama and Arai (1987) showed that the side burr dimensions decrease with increasing positive tool rake angle. Figure 7.10 (b) also shows that the burr thickness (t) increases at a higher rate in comparison to burr height (h) with increasing negative tool rake angle. The magnitude of t and h are higher with a brittle workmaterial in comparison to a ductile workmaterial [Figure 7.10 (b) and Table 7.2 (b)]. As the positive tool rake angle increases, the dimensions seem to converge and for a 60^{o} rake tool the dimensions overlap to a near constant value irrespective of the workmaterial type. This was also seen from Figures 7.7 (f) and 7.8 (f) where minimal or practically insignificant burr formation resulted with a 60^{o} rake tool. Also, the curves for t and h crossover at 0^{o} rake for both ductile and brittle workmaterials. This trend is very much similar to the thrust (F_t) and cutting force (F_c) trends observed in cutting (both simulation and experimental) for various rake tools.

Figure 7.10 (c) shows the variation of the burr dimension ratios, namely, d/l for material D and t/h for materials D and B, respectively. It also shows the ratio of the thrust force to the cutting force (F_t/F_c) in nanometric cutting. The corresponding forces and the force ratio values in nanometric cutting for various rake tools were collected from the earlier investigation on the effect of tool rake angle in nanometric cutting (Chapter 5). In that investigation, 3-D MD simulation of nanometric cutting was performed on a copper workmaterial with the tool rake angle varying from -75^{o} to $+45^{o}$. The numerical values of the ratios used to plot Figure 7.10 (c) are given in Table 7.2 (c). The ratio of burr dimensions shows a decrease with increasing positive tool rake angle.

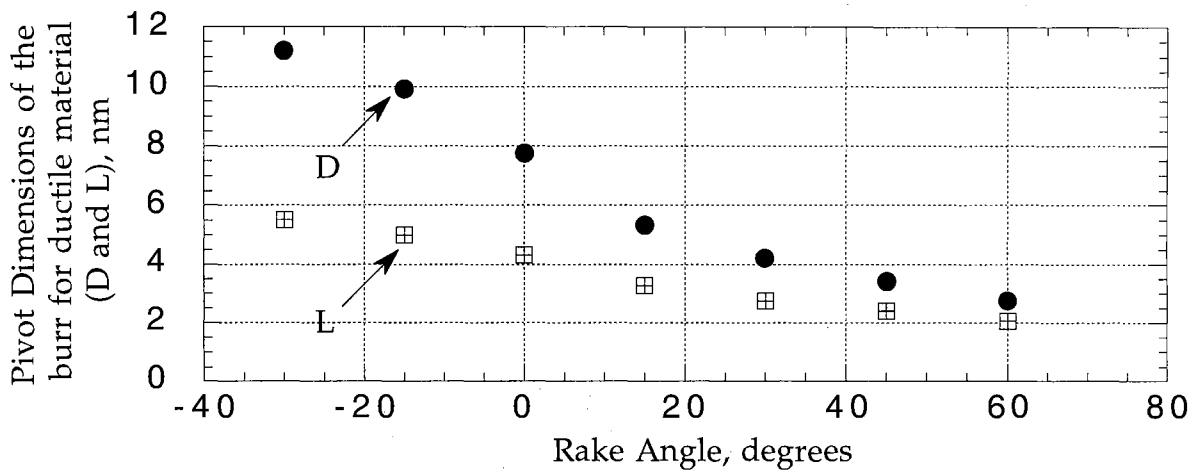

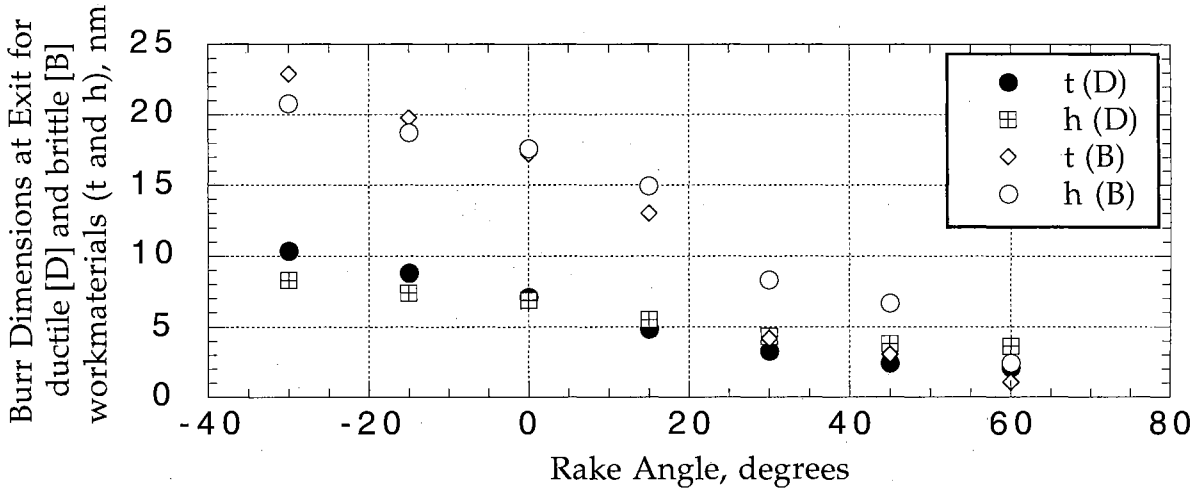

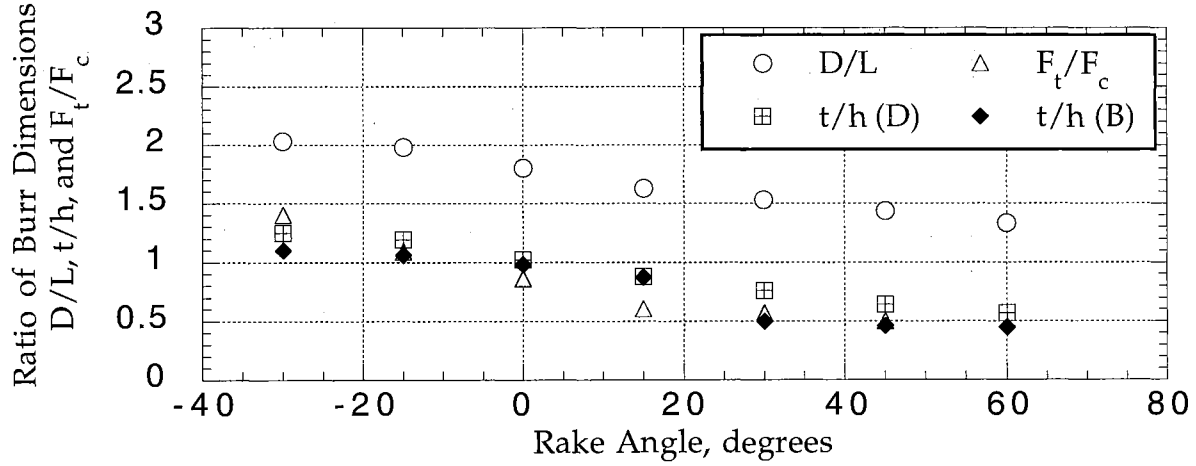

Figures 7.10 (a) - (c) Variation of the burr dimensions with the rake angle in the of (a) the pivot during cutting (D and L), (b) burr at exit after cutting (t and h) and (c) ratio of dimensions

One can observe that the t/h curves for the ductile and brittle materials match closely with the F_t/F_c curve. This can also be observed from Table 7.2 (c). Consequently, it appears that a relationship exists between the force ratio (F_t/F_c) and the burr dimensions (t and h) for various rake tools. Sampath et al. (1984) suggested that the magnitude and location of the maximum probability of tool fracture depend not only on the magnitude of the cutting forces but upon their relative values. Since, tool fracture is also related to the exit failure of the workmaterial it is reasonable that the force ratio affects the burr dimensions at exit.

The close agreement observed between the force ratio (F_t/F_c) and the burr dimension ratio (t/h) can also be explained in terms of the resultant force and its angular orientation from the cutting direction. Table 7.2 (c) gives the orientation of the resultant force vector with respect to the cutting direction for various rake tools (Chapter 5). The table also gives the magnitude of the measured negative shear angle for various rake tools for both the ductile and brittle workmaterials. Figure 7.11 plots the variation of the resultant force vector orientation and the negative shear angle (both ductile and brittle) variation with tool rake angle. It can be seen that as the positive rake angle of the tool increases the angle between the resultant force vector and the cutting direction decreases. The negative shear angle also follows a similar trend. A good agreement between the negative shear angle and the resultant force vector is observed with high positive rake tools ($+15^o$ to $+45^o$). As the rake angle becomes more negative, the negative shear angle values are found to be lower than the angle between the resultant force vector and the cutting direction. However, the trend still shows an increase with decreasing tool rake angle. Figure 7.11 and Table 7.2 (c) indicate that the resultant force vector rotates pointing deep into the workmaterial as the tool rake angle decreases. The negative shear zone tends to follow the line of the resultant force into the workmaterial. The insert in

Figure 7.11 represents this schematically. The angle (θ) of the resultant force (R) from the depth of cut line depends on the magnitude of the cutting (F_c) and thrust force (F_t) which in turn depends on the tool rake angle. Consequently, with increasing positive rake tool, the resultant force rotates towards the depth of cut line (decreasing force ratio) and as a result, the angle (θ) decreases. This rotation of the resultant force results in a rotation of the negative shear zone towards the depth of cut line with increasing positive rake angle. Consequently, the burr dimensions decrease as the tool rake angle increases which explains the close agreement observed between the ratio of burr dimensions and the force ratio. Based on Figures 7.7 and 7.8 it can be seen that the negative shear inside the workmaterial appears as a mirror image of the positive shear zone above the depth of cut line. The positive shear angle depends on the magnitude and orientation of the resultant force vector. It was observed from Figure 7.11 that the negative shear angle is also affected by the resultant force vector. This relation possibly contributes towards creating a negative shear zone from the tool tip into the workmaterial that tends to be a mirror image of the positive shear zone above the depth of cut line.

Based on Figures 7.10 (a) and (b) as well as Table 7.2 it can be seen that the values of d and t are different although they are the same dimensions measured during and after cutting [Figure 7.9]. It can also be seen that the magnitude of d is higher compared to the magnitude of t. Figure 7.10 (c) indicates that the ratio d/l is much higher than the ratio t/h for a particular rake tool. This implies that the dimensions of the pivot change constantly from the time of pivot initiation to the end of cut. This, in part, can be attributed to the rotation of the resultant force vector even for a particular rake tool as cutting progresses. Once the exit failure has began (pivot initiation), the depth of cut reduces constantly which can be clearly observed from the animations. This results in

force variations and subsequent rotation of the resultant force vector causing changes in the burr dimensions as cutting progresses.

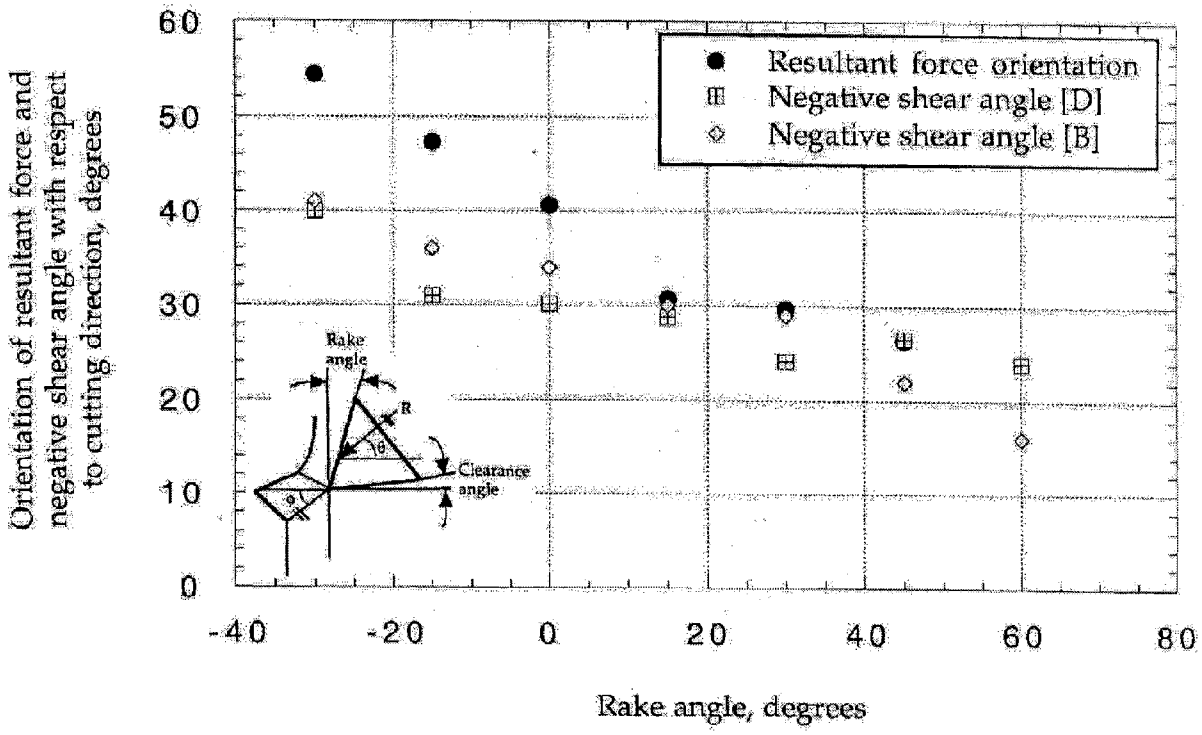

Figure 7.11 Variation of the shear angle of the resultant force vector and the negative shear angle with tool rake angle

7.3.4. Effect of Depth of Cut

Figures 7.12 (a) - (c) show the exit stages of nanometric cutting of the ductile material [D] for various depth of cuts, namely, 1.45 nm, 2.9 nm, and 3.62 nm. Figure 7.7 (b) is a similar stage for a depth of cut of 2.17 nm. The tool rake angle (0^O) was maintained constant in all these simulations. The exit burr formed seems to be similar although the scale of the burr increases with increasing depths of cut. As the undeformed

chip thickness increases, the resulting burr thickness as well as the distance and depth of the initial pivoting point of the burr from the tool edge increases. For example, the depth (d), length (l), height (h), and thickness (t) increase as the depth of cut increases from 1.45 nm to 3.62 nm [Figures 7.12 (a) - (c)]. Similar results have also been suggested by Nakayama and Arai (1987), Hashimura et al. (1999), and Hofman and Kvasnicka (1999). It can also be noted that in the case of depths of cut of 1.45 nm [Figure 7.12 (a)], 2.17 nm [Figure 7.7 (b)], and 2.9 nm [Figure 7.12 (b)] no crack propagation was observed into the workmaterial. In other words, positive burr formation was observed as the depth of cut was varied from 1.45 nm to 2.9 nm. However, in the case of 3.62 nm depth of cut [Fig. 7.12 (c)], crack initiation from the tool tip into the workmaterial was observed [Figure 7.12 (c)]. This resulted in negative burr formation. Hence, it is possible that depending on the scale of the cutting process there can be a transition from positive burr formation to negative burr formation even with ductile materials. This is not altogether surprising as increase in the undeformed chip thickness of a nominally ductile material can alter the nature of the chip from a continuous to a brittle discontinuous chip. Thus, for a particular material, tool fracture probability might increase with increasing depth of cut due to increasing stresses around the tool tip. Nakayama and Arai (1987) also suggested an increase in the side burr dimensions with increasing undeformed chip thickness.

7.3.5. Effect of External Constraint

The effect of external constraint was investigated by setting boundary atoms along the exit edge till the depth of cut as shown schematically in Figure 7.3 (b). Figure 7.13 shows a snapshot of the simulation process, which shows absence of exit failure as suggested originally by Pekelharing (1978) and Lucca (1982).

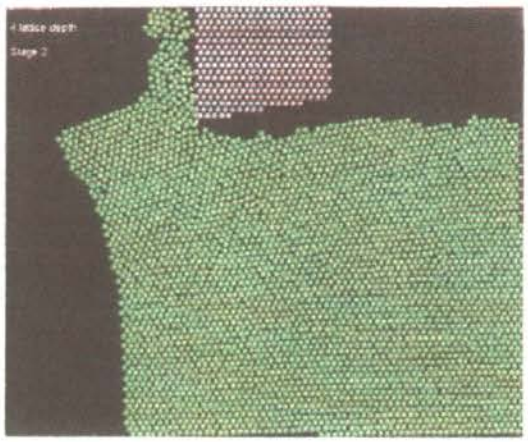

(a)

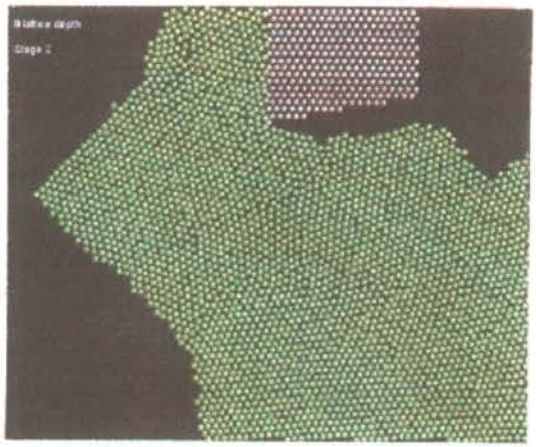

(b)

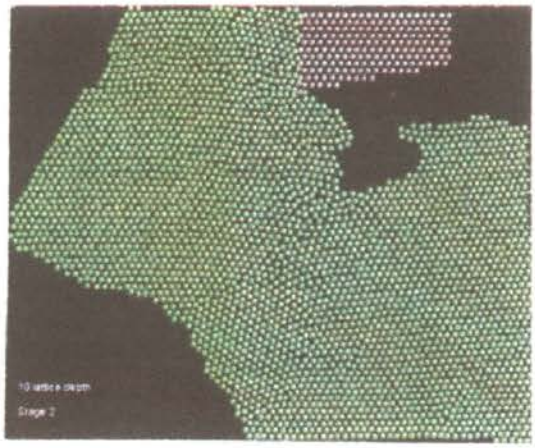

(c)

Figure 7.12 (a) - (c) Effect of depth of cut on the exit failure in nanometric cutting of a ductile workmaterial (a) 4 lattice spacings (b) 8 lattice spacings and (c) 10 lattice spacings

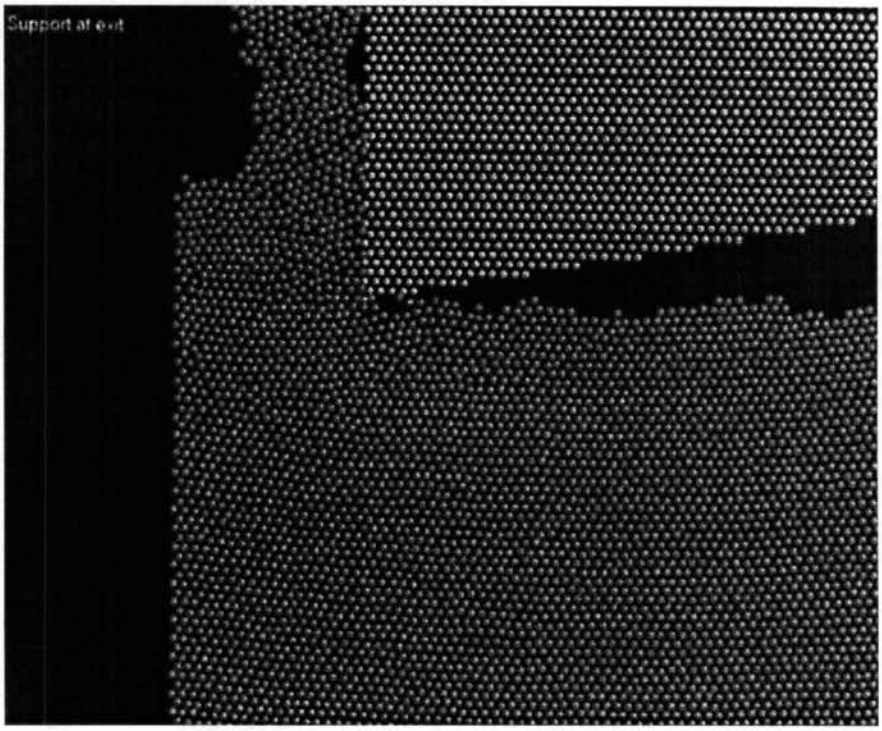

Figure 7.13 Snapshot of the simulation process with external constraint

7.4. CONCLUSIONS

MD simulations of nanometric cutting were conducted under different cutting conditions to study exit failure in metals. The following are some specific conclusions based on this study.

1. The mode of failure resulting in either positive or negative burr formation depends on the workmaterial type (ductile/brittle). Although negative shear occurs in both cases, positive burr formation with no crack propagation into the workmaterial was observed with the more ductile metal. In contrast, negative burr formation with crack propagation into the workmaterial was observed with the not-so-ductile or brittle material.

Consequently, tool fracture probability at exit might be higher when machining not-so-ductile materials compared to ductile materials under similar cutting conditions.

2. From the pivoting point (initiation of burr) to the final burr formation at the exit (as tool leaves the workmaterial), a constant reduction in the depth of cut was observed. This can effect the forces and the orientation of the resultant force vector. Consequently, the pivot point rotates during the cutting process. The dimensions of the initial pivot were observed to be much higher than the final burr at exit.

3. The dimensions of the burr [depth (t) and height (h)] after cutting were observed to decrease with decreasing negative rake tools (more positive rake). Similar trends in the cutting force and the thrust force were observed in nanometric cutting with various rake tools.

4. The ratio of t/h was observed to agree closely with the force ratio (F_t/F_c) for various rake tools in nanometric cutting. This agreement can be attributed to the dependence of the negative shear zone on the resultant force vector orientation with change in the tool rake angle.

5. The depth of cut was observed to influence the mode of failure at exit. As the undeformed chip thickness was increased, the resulting burr dimensions as well as the distance and depth of the initial pivoting point of the burr from the tool edge was observed to increase. Crack initiation with a nominally ductile material was observed as the depth of cut was increased from 1.45 nm to 3.62 nm. Consequently, it is possible that the scale of the cutting process can effect the mode of failure at the exit.

6. It is shown in this investigation that the presence of external elastic constraint at exit prevents the foot formation of the workmaterial at exit.

7. It is shown that the foot formation observed using MD simulation is similar to that reported in the literature at macro and micro level based on extensive experimentation. For example, comparison of MD simulation results with the foot formation reported by Pekelharing (1978), the effect of workmaterial properties reported by Lucca (1982), Nakayama and Arai (1987), and Hashimura et al. (1999), and the effect of depth of cut reported by Nakayama and Arai (1987), Hashimura et al. (1999), and Hofman and Kvasnicka (1999) show good agreement. Consequently, MD simulation can be used as an inexpensive tool to study the process parameters before conducting extensive and expensive experimentation.

CHAPTER 8

NANOMETRIC CUTTING OF SILICON [a]

8.1. INTRODUCTION

It is well known that ductility of a material depends, in general, on its ability to withstand a general homogeneous strain involving an arbitrary shape change of the crystal (Hertzberg, 1996). For metals, slip occurs predominantly on the crystallographic planes of maximum atomic density and in the close-packed directions. The more firmly the valence electrons are bound, the more brittle the material is likely to be. In the case of covalently bonded materials, such as silicon, additional restrictions apply, namely, strong directional bonding and sharing of the valence electrons. Under these conditions, atomic movements are energetically unfavorable. Therefore, the number of potential slip systems in these materials is restricted and as is their overall ductility. As a result, silicon is essentially a brittle material under normal conditions of temperature and pressure.

---

a - R. Komanduri, N. Chandrasekaran, L. M. Raff, "MD simulation of nanometric cutting of silicon," accepted for publication in Phil. Mag. B, 2001

Ductility can be imparted to silicon at higher temperatures by providing more electrons in the conduction band and thus rendering the material more metallic in character (in terms of conductivity and limited ductility). When subjected to hydrostatic pressure (ca 11 GPa), the covalent diamond structure of silicon can be transformed into a metallic, body-centered tetragonal structure (β-tin structure) (Donohue, 1974). Such a structural change is typical of silicon undergoing pressure-induced phase transformation (Gerk and Tabor, 1978; Pharr et al., 1991; Cahn, 1992).

Silicon is a covalently bonded material with a diamond cubic structure comprising of two FCC lattices displaced from each other by ¼ of the body diagonal. The atoms of silicon touch each other along the four <111> directions and the nearest neighbor distance is $\sqrt{3}a/4$. Covalent bonded materials, in general, are characterized by a strong directional bonding, low Poisson's ratio, strong temperature sensitive yield strength, and narrow dislocations with large Peierls-Nabarro forces. In addition, dislocations with some edge component will have unsatisfied bonds (dangling bonds). The slip system is <110> {111}. Slip does not occur by pure edge dislocations; instead it occurs by pure screw dislocations with a Burger's vector at 60^{o} to the dislocation line.

Table 8.1 lists various properties of single crystal silicon (Donohue, 1974; Runyan, 1999). At atmospheric pressure, β-silicon has a lattice constant of 5.43 A, a bond distance of 2.352 A, and an atomic volume of 18.38 A^3. The high-pressure β-silicon phase has a body-centered tetragonal structure (β-tin structure) with the following lattice constants a = 4.686 A, c = 2.585 A, and c/a = 0.5516. In this structure, each silicon atom has four

nearest neighbors at 2.43 A and the two next neighbors are at a distance of 2.585 A. The atomic volume is 14.19 A^3. The α to β transformation, therefore, results in a significant reduction in the atomic volume from 18.38 A^3 to 14.19 A^3 per atom or a densification reduction of ~22.8% (Donohue, 1974). Although, the Tersoff potential used in the present study does not include the long-range forces required to properly simulate sharp phase transitions, it should be possible to observe some of these features in the MD simulation of nanometric cutting of silicon, at least qualitatively.

Table 8.1 Properties of single crystal α-Silicon (Donohue, 1974; Runyan, 1999)

Bond type	Covalent
Lattice structure	Diamond cubic
Lattice constant, A	5.43
Density, g/cm^3	2.328
Melting point, ^oC	1414
Debye temperature, K	654
Young's Modulus, GPa	130
Elastic constants, GPa	C_{11} : 165.7 C_{12} : 63.9 C_{44} : 79.57
Poisson's ratio, v	0.28
Bulk modulus, GPa	100
Fracture stress, GPa	6.47
Fracture toughness, Mpa. $mm^{1/2}$	15
Hardness, Hv, kg/mm^2	950-1150
Resistivity at 300 K,	2.3×10^5

8.2. BRIEF REVIEW OF LITERATURE

The technical feasibility of single-point diamond turning of silicon when the size of cut is below a critical value, usually in the sub-micrometer range, has been demonstrated (Komanduri et al., 1997). This has been termed 'ductile-regime' machining by some researchers indicating plastic deformation and chip formation ahead of the tool, as in the machining of ductile materials. Nakasuji *et al.* (1990) reported that negative rake angle tools permit higher cut depths prior to the occurrence of brittle fracture. Interestingly, in most literature, on the machining of silicon in particular, and other nominally brittle materials in general, cutting tools with a high negative rake angle (-25^{o} to -45^{o}) or with a high tool edge radius relative to depth of cut ($d/r<<1$) have been used. Komanduri *et al.* (1997) attributed this to the generation of high hydrostatic pressure underneath the tool in nanometric cutting resulting in microcrack-free machining. This was demonstrated to be the case in the indentation of silicon by FEM numerical analysis (Yoshino et al., 2001) as well as by experimental work involving the use of a special apparatus that produces high external hydrostatic pressures (up to 400 MPa) during the machining process (Yoshino et al., 2001; Chandrasekaran et al., 2000).

Yan *et al.* (2001) reported the critical depth of cut to increase with increase in the negative rake angle up to about -40^{o} and then to decrease thereafter. The observed decrease is attributed to increased side flow and plowing of the material ahead of the tool with increasing tool negative rake angle (Komanduri, 1971). Komanduri (1971) also showed that side flow is not only dependent on the tool geometry but also on the ratio of

width of cut (w) to the cut depth (d), or w/d, especially when high negative rake tools are used. Consequently, the effect of tool geometry (rake angle) and machining parameters, such as cut depth and width of cut, on the material removal mechanisms in the finishing of silicon are of significant interest.

Puttick *et al.* (1994) investigated the near surface damage caused in nanomachining of single crystal silicon using transmission electron microscopy (TEM). They reported the mean depth of permanent damage consisting of a dense array of dislocations to lie in the range of 100-400 nm. They also observed the occurrence of cracks, several hundred nanometers deep, beneath many of the deeper grooves. They further reported intermittent regions showing the formation of amorphous silicon. They proposed a mechanism of material removal in silicon based on extrusion of plastically deformed material ahead of the tool, similar to the model originally proposed by Shaw (1984) for grinding of ductile materials. The MD simulations of silicon reported in this section supports this mechanism.

Shibata *et al.* (1994) also investigated the damage generated in diamond-turned single crystal silicon surfaces using TEM. They used a - 40^{o} rake tool and reported conversion of several layers of the machined surface into amorphous layers (~150 nm deep) and the formation of continuous ribbon-like chips.

Thus, even though good finish and accuracy can be generated by ultraprecision machining/grinding of silicon, subsurface damage, especially at the atomic level, may

still be an inherent limitation of these processes. To produce defect-free surface at an atomic level, this damaged layer (or permanently deformed layer on the machined surface) has to be removed by subsequent finishing operation, such as chemo-mechanical polishing. For example, Kunz *et al.* (1996) investigated damage induced by lapping and single-point diamond turning (using -25° rake tool) of silicon (100). They reported that complete damage-free material removal is possible only when a chemical component to polishing is present.

In the field of MD simulation of silicon, a significant amount of work has been reported on indentation (Kallman et al., 1993; Rentsch and Inasaki, 1995; Brenner et al., 1996; Zhang and Tanaka, 1999; Cheong and Zhang, 2000), grinding (Tanaka et al., 1999), and nanometric cutting (Belak et al., 1993; Shimada et al., 1995; Nozaki et al., 1998; Inamura et al., 1997, 1999). In the following, only literature pertaining to the nanometric cutting of silicon will be briefly reviewed to focus on the main topic of this investigation.

Belak *et al.* (1993) conducted pioneering work on the MD simulation of nanometric machining of silicon with a diamond tool using a Tersoff potential (1988, 1989) at a cutting speed of 540 ms^{-1}. The silicon chips and the first few layers of the newly cut surface were reported to be heavily deformed resembling an amorphous structure or even possibly molten silicon. This transformation was attributed on the basis that the energy requirements for the transformation of the crystal into an amorphous solid are less than that required for shear within the crystal.

Inamura *et al.* (1997, 1999) conducted theoretical studies of nanometric cutting of silicon using Renormalized Group Molecular Dynamics (RGMD) employing a Tersoff potential. They were mainly concerned with the transition from brittle to ductile behavior of silicon and the associated critical depth of cut. They postulated that silicon could be machined in the 'ductile' mode at any depth of cut in vacuum. However, neither the actual values were specified nor the justification for this postulate was given. They pointed out that under normal atmospheric conditions, the material exhibits brittle-ductile transition depending on the scale of machining. Initiation of microcrack-like defects are reported when the machining depth is ~1 μm. The defect generation was attributed to the interaction between a local static stress distribution and a global dynamic stress associated with acoustic waves.

Shimada *et al.* (1995) conducted MD simulations of nanoindentation/scratch experiments with a 90^{o} included angle tool on silicon using a Tersoff potential. They observed movement of many cavities-like vacancies (or voids) at regular intervals. Based on this observation they suggested the presence of elastic/thermal shock wave generation and propagation repeatedly from the tool-work interface. If, however, when the depth of cut is in the nanometer range, they found that the stored potential energy is too small for the shock wave to supply the necessary energy to initiate a crack or propagate a pre-existing crack.

Nozaki *et al.* (1998) reported MD simulations of (111) silicon with an atomically sharp edge, 0^{o} rake tool and depth of cut varying from 2 to 6 atom layers. A Stillinger-Weber potential (1985) was used to model the silicon lattice. The plastic deformation in silicon is reported to be highly limited compared to metals. They reported the chips, the cut surface, and the area around the tool to exhibit a crystalline to amorphous transformation. They also reported absence of dislocations, which they attribute to the cutting speeds (10-50 ms-1), used. The surface generated was reported to be smoother when the cut depth was higher.

Tanaka *et al.* (1999) used a Tersoff potential to simulate nanometric cutting of silicon. A cutting tool with a 2.1 nm edge radius, a 0^{o} rake, and a 10^{o} clearance angle was used to machine silicon at cut depths of 1.9 nm and 3.19 nm. They reported the absence of dislocations in their simulations. Based on this observation, they suggested that an inelastic deformation via amorphous phase transformation and viscous flow deformation within the amorphous layer is an energetically more dominant mechanism than the plastic deformation involving the generation and propagation of dislocations at nanometric scale.

Zhang and Tanaka (1999) and Cheong and Zhang (2000) have conducted MD simulation of nanoindentation of silicon single crystals. Their results show that elastic deformation occurs only in an extremely narrow regime with no indication of dislocation generation. Densification beneath the indenter was found to involve a phase transition from α to β-silicon induced by the large pressures present in the simulation. The authors reach this conclusion by monitoring the positions of the atoms within the model crystal

and noting that the distributions of Si-Si bond lengths and the number of nearest neighbors changes from those characteristics of α-silicon to a broader distribution that can be viewed as consisting of components of both α and β forms. Consequently, the computations are suggestive of the presence of such transitions even though no sharp phase transition is observed due to the lack of long-range forces in the Tersoff potential function.

It can be seen, from the above brief review of literature, that while there were significant contributions towards our understanding of the mechanics of material removal in nanometric cutting of silicon, there are yet several unanswered questions or questions needing further clarification. The objective of this investigation is to address these critical issues that are not only fundamental in nature but are also of technological significance. For example, can one generate defect-free surfaces in silicon, at an atomic level, under any conditions of machining? If so, what are those cutting conditions? Or, if not, what are the underlying reasons for this limitation? Is there a lower limit on the extent of subsurface damage independent of the process used in ultraprecison machining/grinding? Similarly, what is the nature of chip formation in nanometric cutting of silicon? It may be noted that when we conduct nanometric cutting experiments and examine the chips and the machined surface, the analysis is *post mortem* in nature and we have to link them to analyze the process. With the MD simulation of nanometric cutting, it is possible to freeze the cutting process at different stages of cutting and analyze the process as it occurs. Here, the workpiece and the chip are intact and hence analysis of the chip formation process in the primary deformation zone is possible.

8.3. MD SIMULATION CONDITIONS

In this investigation, 3D-MD simulations of nanometric cutting of silicon were conducted with cutting tools of different geometry (rake angles from $+60^{o}$ to -60^{o}, and clearance angles from 10^{o} to 30^{o}) and cutting conditions (widths of cut from 1.1 nm to 4.34 nm and depths of cut from 0.01 nm to 2.72 nm) to investigate the effect of these parameters on the nature of deformation and material removal. In order to isolate the effect of rake angle from the effect of tool edge radius, the cutting tool in this study is considered to be infinitely sharp. It may also be pointed out that it is very simple and straightforward to incorporate edge radius, if that is of interest, as shown earlier. Similarly, to separate the chip formation effects from the chip-tool interaction effects, an infinitely hard tool was used in the simulations. Some 6300 initial workpiece atoms and 500 tool atoms were considered in the simulation. The number of tool atoms considered does not actually make any difference in the simulation as an infinitely hard tool is assumed in this investigation. A Digital α-workstation (with a clock speed of 600 MHz) was used for the simulations.

In order to reduce the computational time and memory requirements without limiting the length of the workpiece (or the length of cut), the Length Restricted MD (LRMD) simulation introduced originally by Belak *et al.* (1993) and subsequently implemented by Chandrasekaran *et al.* (1998) was incorporated in this investigation. The length of cut, crystal orientation (001), cutting direction [100], and cutting speed (500 ms^{-1}) were maintained constant for any given simulation. Table 8.2 gives details of various

computational parameters used in the MD simulations. It may be noted that the analysis of chip formation, as well as discussion of the results presented here, are based not only on the MD simulation plots of various stages of cutting but also on the detailed study of the animation of the nanometric cutting process under various conditions. Tersoff-type 3-body potential (1989) was considered for the interaction between Si-Si atoms.

Table 8.2: Computational parameters used in the MD simulation of nanometric cutting of silicon

Potential used	Tersoff potential
Initial Workmaterial dimension	6a X 12a X 10a, where a is 0.543 nm
Crystal Orientation	(001)
Cutting Direction	[100]
Tool dimension	12a x 12a x 20a
Tool material	Infinitely hard
Tool geometry	Edge radius: Sharp Rake angle: -60° to + 60° Clearance angle: 5°, 10°, and 30°
Depth of cut (nm)	0.25, 0.5, 0.75, and 1.1
Width of cut (nm)	1.1,1.63, 2.172, 3.26, 3.8, and 4.34
Cutting speed (m/s)	500
Bulk temperature (K)	293

8.4. MD SIMULATION OF NANOMETRIC CUTTING OF SILICON

8.4.1. On the Nature of Chip Formation

Figures 8.1 (a) and (b) are MD simulations of the nanometric cutting of aluminum and silicon, respectively (tool rake angle: 0^o, depth of cut: 0.81 for Al and 1.1 nm for Si, and width of cut: 3.26 nm) showing for comparison significant differences in the nature of deformation in these two materials owing to the differences in their ductilities. Figure 8.1 (a) shows plastic deformation in the primary shear zone due to the generation and propagation of dislocations ahead of the tool (as well as into the workmaterial) at ~45^o to the cutting direction in the case of aluminum. In contrast, Figure 8.1 (b) shows an extrusion-like chip formation process in the case of silicon. For the case of aluminum, the dislocations generated at ~45^o to the cutting direction were observed to penetrate deep into the workmaterial requiring the size of the workpiece to be increased considerably to avoid boundary effects. This was not found to be the case with silicon.

Based on the animations of the cutting process, the dislocations generated in aluminum are found to be highly elastic in nature resulting in their rearrangement into the original crystal structure behind the tool due to elastic recovery but this was not so for silicon, where permanent deformation with no elastic recovery is observed. This can be seen in Figure 8.1 (a) where the dislocations ahead of the tool recover elastically once underneath or behind the tool in the case of aluminum but not for silicon [Figure 8.1 (b)] where significant permanent deformation and subsurface damage is observed. The highly

compressed region in the machined surface is attributed here to the pressure-induced phase transformation of silicon under high hydrostatic pressure present under the tool during nanometric cutting.

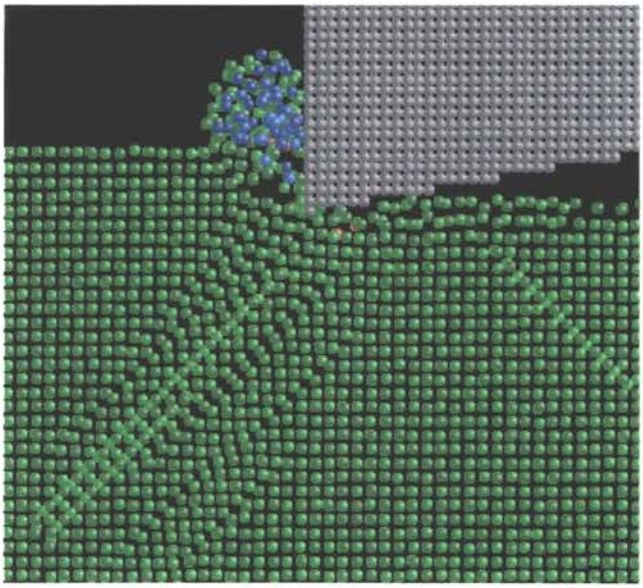

Figure 8.1 (a) MD simulation of nanometric cutting of Al

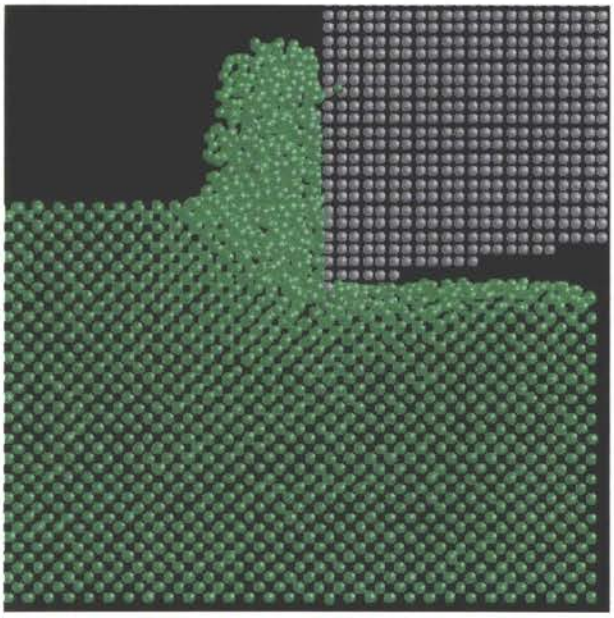

Figure 8.1 (b) MD simulation of nanometric cutting of Si

Yoshino *et al.* (2001) showed numerically, using FEM, that high hydrostatic pressure underneath the indenter could be generated in the indentation of silicon. Such hydrostatic pressures can trigger phase transformation of silicon. Figure 8.1 (b) suggests that the effects of phase transition can be seen in MD simulations even though the potential lacks the long-range forces required to accurately model the transition.

Figures 8.2 (a) to (d) show MD simulations of nanometric cutting of silicon at various stages of chip formation with a -30° rake angle. The example of -30° rake tool is taken here to illustrate typical industrial practice of machining silicon. Based on Figures 8.2 (a) to (d) and animations of the MD simulations of nanometric cutting of silicon, it can be seen that the material removal occurs in four ways, namely, compression of the workmaterial ahead of the tool in the primary deformation region, formation of the chip by a mechanism akin to an extrusion-like process, subsurface deformation of the material underneath the tool in the machined surface, and side flow. It may be noted that the relative contribution of these four removal mechanisms depends on the cutting conditions and the tool geometry used (as will be shown later). The chip formation process in nanometric cutting of silicon closely resembles an extrusion-like process similar to the one proposed by Puttick *et al.* (1994) for silicon and originally introduced by Shaw (1984) for the grinding of ductile materials.

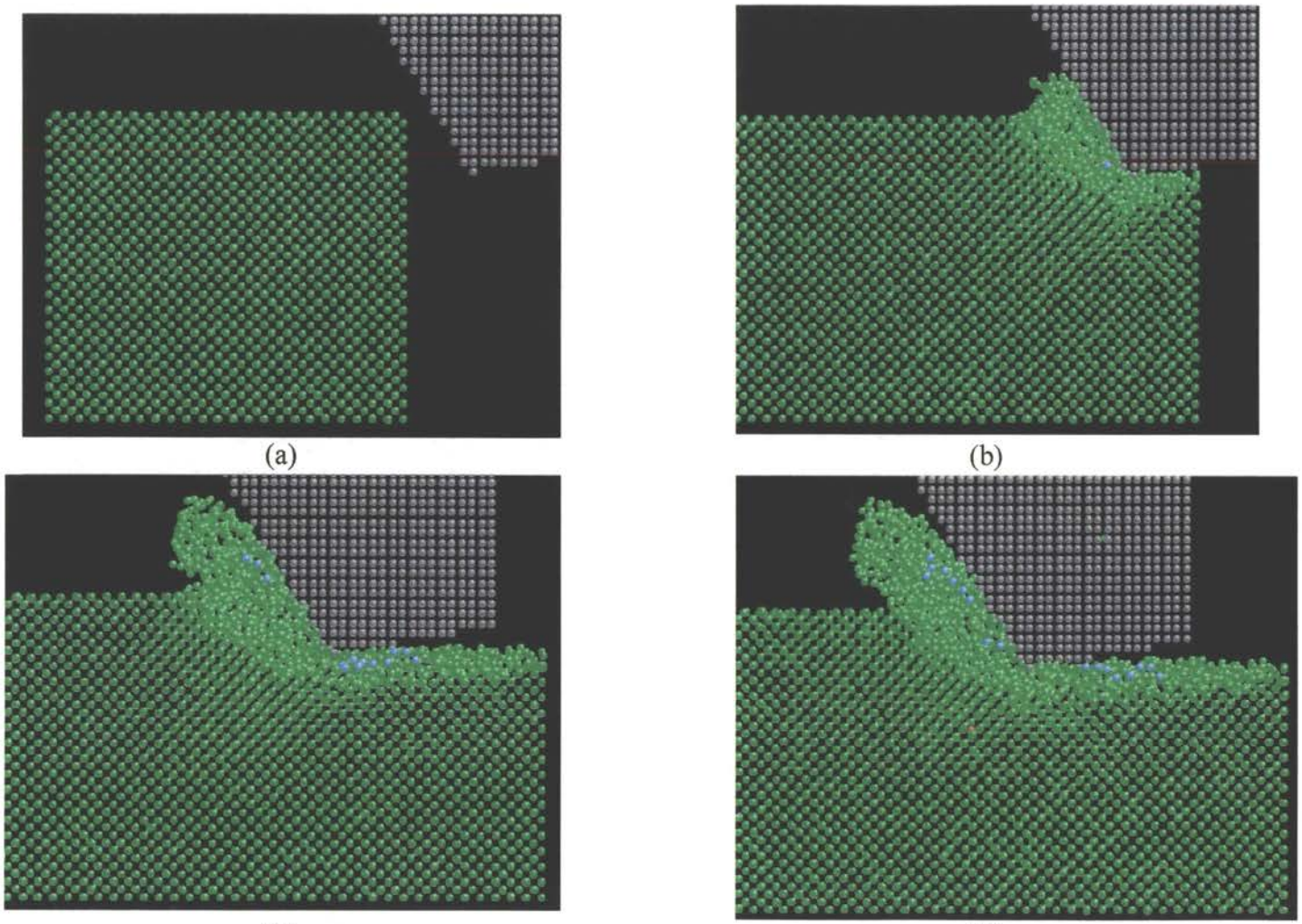

Figures 8.2 (a) to (d) MD simulation of nanometric cutting of silicon (-30 deg. Rake; 1.1 nm depth; 3.26 nm width)

It can also be seen that the material ahead of the tool in the primary zone, the chip, and the subsurface deformation in the machined surface underneath the tool are subjected to considerable compaction or densification suggestive of structural transformation from diamond cubic (α-silicon) to body-centered tetragonal (β-tin structure). This is one of the reasons why the amount of chip material in Figures 8.2 (a) to (d) is not the same as the amount of workmaterial removed (compare the chip volume with the volume of the workmaterial removed from the beginning of the cut to the position of the tool at any given time). The other reason being the extent of side flow that takes place, especially with high negative rake angle tools, as will be shown subsequently (Section 8.4.4). Since the change in volume is significant in the transformation of α to β silicon, it would be valuable to compare this aspect in the original workmaterial and the chips generated in experimental nanometric cutting of silicon.

The presence of α to β-silicon phase transition induced by high hydrostatic pressure leads to a 22.8% densification of the material during cutting and indentation. The effect, which is generally absent for most ductile materials such as aluminum or copper, appears to be the main reason for the subsurface deformation of the machined silicon surface that is observed irrespective of the rake angle or depth of cut (as will be shown later). This possibility, apparently, has not been considered earlier, as significant volume changes due to phase changes in nanometric cutting are rare and in the majority of cases for most ductile metals, no volume changes are involved in plastic deformation. If silicon responds, for example, only in a brittle manner (with no phase transformation), i.e., as α-silicon, then the nature of chip formation should be in conformity with the response of a

typical brittle material under the action of cutting, namely, separation of material by the formation of microcracks and their coalescence into large cracks. Also, any disturbances caused on the machined surface should be elastic in nature and should be fully recovered after cutting. This is generally the case as shown by indentation/ scratching experiments, which are conducted at very low speeds. But in nanometric cutting of silicon, we observe permanent deformation and a highly compressed material ahead of the tool, in the chip, and in the machined surface. This can only be possible if the nanometric cutting process induces a phase transformation from a diamond cubic covalent bonding (α-silicon) to a body-centered tetragonal bonding (β-silicon) with an accompanying increase in the ductility. This will be examined more in detail, in the next section.

8.4.2. On the Pressure Induced Phase Transformation

The damaged layer on the surface of silicon has been attributed to the pressure induced phase transformation (from α to β-silicon) and/or an amorphous structure in various investigations on indentation (Cheong and Zhang, 2000) and nanometric cutting (Belak et al., 1993). Cheong and Zhang (2000) showed that the phase transformation from α to β-silicon is accompanied by a change in the interatomic distance from 0.235 nm to 0.243 nm for 4 bonds and 0.258 nm for the remaining 2 bonds (β-silicon) resulting in a change in the coordination number between silicon atoms from 4 to 6.

In this investigation, based on Cheong and Zhang's work (2000), the distribution of atoms in three dimensions at various interatomic distances and coordination were

determined from the MD simulation data before and after nanometric cutting in various regions of interest, namely, the subsurface deformation region in the machined surface, in the compression zone ahead of the tool in the primary deformation zone, and in the chip. Figures 8.3 (a) and (b) are plots of the distribution of atoms at various interatomic distances and the coordination structure for silicon before and after nanometric cutting in the subsurface deformed zone underneath the cutting tool. Figure 8.3 (a) shows that before cutting, all the atoms are positioned at an equilibrium distance of 0.235 nm corresponding to α-silicon. After machining [Figure 8.3 (b)], a significant decrease in the number of bonds at 0.235 nm and a corresponding increase in the number of bonds at 0.243 nm and 0.258 nm interatomic distances can be noted. Figure 8.3 (b) also shows a high peak at 4 and a smaller peak at 2 coordination before nanometric cutting. The peak at 4 for silicon is indicative of a covalently bonded system with a diamond cubic structure. The peak at 2 is indicative of the termination of bonds (dangling bonds) on the surface and sides of the workmaterial. After machining, the number of atoms with 4 coordination was found to decrease with a corresponding increase in the number of atoms of 5 and 6 coordination. A relatively small increase in the 7 and 8 coordination was also observed. A similar structure was observed between the atoms in the chip and in the compression zone ahead of the tool.

Raghavachari and Logovinsky (1985) have shown by *ab initio* molecular orbital calculations that numerous other coordination, n (n up to 30) of silicon (such as 5 in this case) are possible under different conditions leading to the formation of various types of

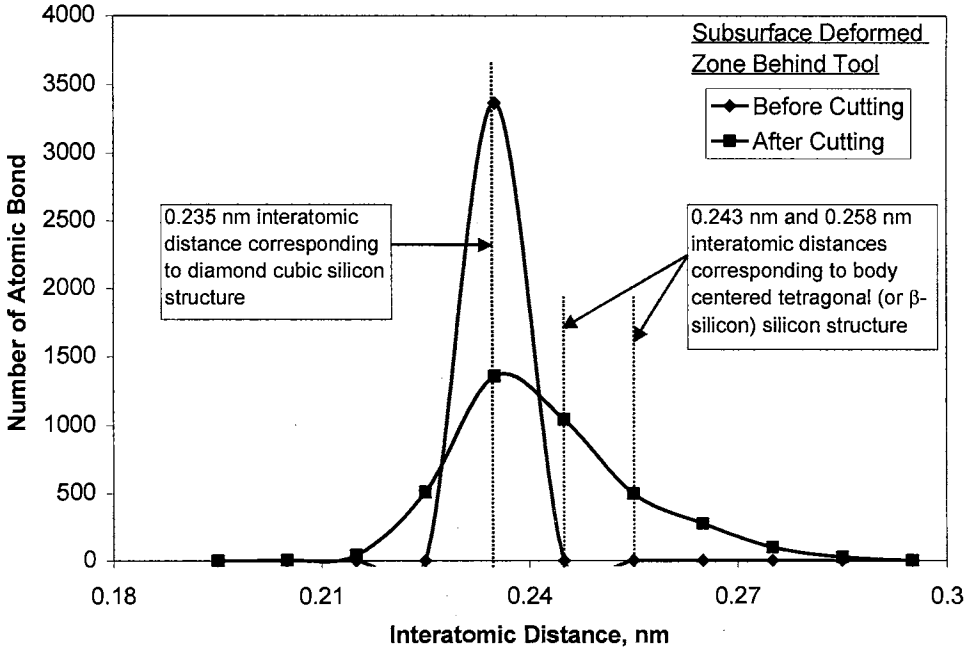

(a)

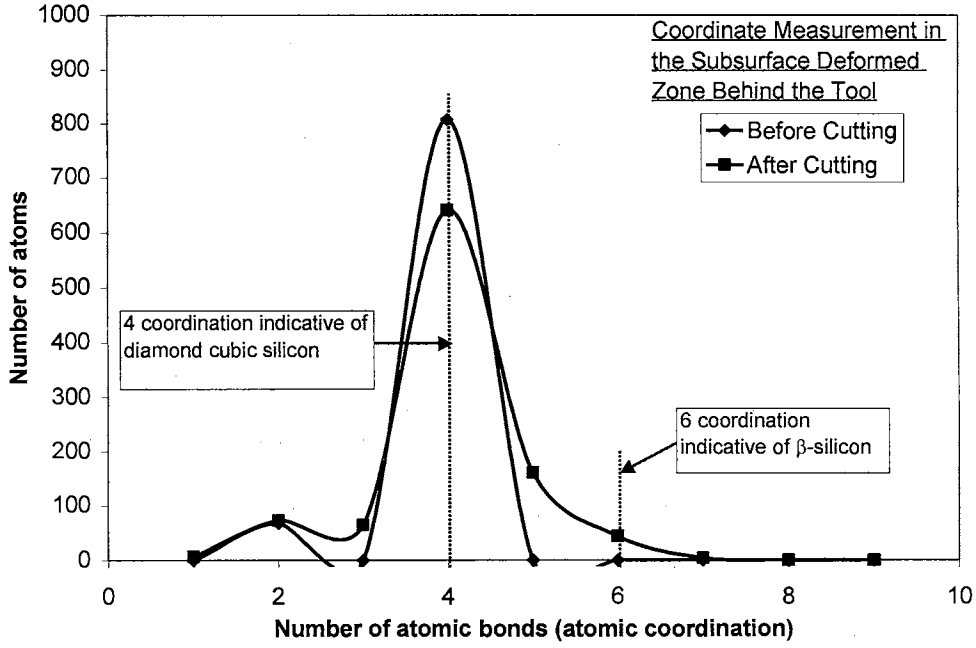

(b)

Figures 8.3 (a) and (b) Plots of the distribution of atoms at various interatomic distances and coordination structure for silicon before and after nanometric cutting in the subsurface deformed zone underneath the cutting tool (tool rake angle: -30°; depth of cut: 1.1 nm; and width of cut: 3.26 nm)

clusters, crystals, and surfaces of silicon. It may be noted that although silicon and diamond are both covalent, this is where their similarity ends. For example, carbon can assume only two crystalline structures, namely, hexagonal graphite and covalent diamond cubic, while silicon can assume many more forms. Also, within the diamond structure no other transformations are known, whereas the Si (111) surfaces are known to undergo reconstruction into a 7x7 symmetric configuration (1994).

The results presented here [Figures 8.3 (a) and (b)] indicate the possibility that the material of the chip, the material ahead of the tool in the primary zone, and the subsurface deformation (or the damaged layer) underneath the tool in the case of silicon can undergo a structural transformation (from α to β-silicon) and a significant densification as a consequence during nanometric cutting. Without the presence of long-range forces in the Tersoff potential, a sharp, unequivocal phase transition may not be observable in the MD simulations. The existence of such a phase change can only be inferred by the broadened distributions seen in Figures 8.3 (a) and (b) and by the lack of elastic response of the lattice upon indentation and machining. Similar conclusions have previously been drawn by Zhang and Tanaka (1999) and Cheong and Zhang (2000).

This highly densified and not so well ordered structure underneath the tool in the machined surface is also referred to as an amorphous structure by some researchers. Whether or not this material is body centered tetragonal or amorphous structure is an important side issue, as evidence was presented for the existence of both these forms using TEM (Pharr et al., 1991; Puttick et al., 1994; Shibata et al., 1994; Kunz et al.,

1996). However, based on the distribution of atoms in three dimensions at various interatomic distances and the coordination numbers, it appears that the highly densified material in the chip, ahead of and underneath the tool appears to be the phase transformed body centered tetragonal structure. This does not mean that there is no formation of amorphous structure in nanometric cutting of silicon but merely states that at this time no means is available, to the knowledge of the authors, for evaluating this aspect using the MD simulation results.

8.4.3. Effect of Width of Cut (w)

Figures 8.4 (a) - (d) are MD simulations of nanometric cutting of silicon for different widths of cut, namely, 1.1 nm, 1.63 nm, 2.2 nm, and 3.26 nm, respectively. The depth of cut and the tool rake angle are 1.1 nm and -30^{o}, respectively. It can be seen that relative to the amount of material removed, the chip volume is less in Figure 8.4 (a) than in Figure 8.4 (d). The difference stems from higher side flow in Figure 8.4 (a). However, the subsurface deformation in the machined surface underneath the tool is relatively large when the w/d is large. To minimize subsurface deformation, it may be preferable to use narrower width and let the material be removed by side flow. In fact, in the grinding of silicon with fine abrasives, this may be the main mode of material removal as the width of cut due to the cutting action by any individual grain is rather small. What is really required in silicon machining/grinding is removal of material without much subsurface deformation or without the formation of microcracks rather than machining at the so-called 'ductile regime' grinding conditions. This may be accomplished by narrow size

cuts relative to the depth. Figures 8.5 (a) and (b) show the plan view of the distributions of the atoms in the X-Y plane for two widths of cut, namely, 1.1 nm and 3.26 nm [corresponding to Figures 8.4 (a) and 8.4 (d)], respectively, in the uncut material, in the chip and shear zone ahead of the tool (mid zone), and in the machined surface after the cut. The densification of the material after the cut can be clearly seen by comparing the packing of the atoms before and after cutting. Also, the densification in the machined surface after the cut for two different w/d ratios can also be seen by the relative packing of the atoms in that region in Figures 8.5 (a) and (b). It can be seen that the atoms are more closely packed in Figures 8.5 (b) (i.e., higher w) than in Figure 8.5 (a) (i.e., lower w). Also, the side flow is much higher with a lower w [Figure 8.5 (a)] (due to more plane stress conditions) than a higher w (less plane stress or more plane strain conditions).

In the following, the number of workpiece atoms in the compressed zone ahead of the tool, in the chip, in the subsurface deformation underneath the tool in the machined surface, and by side flow are normalized with respect to the number of atoms removed from the workpiece in the depth of cut region. This enables a comparison of the aforementioned four quantities independent of the width of workmaterial.

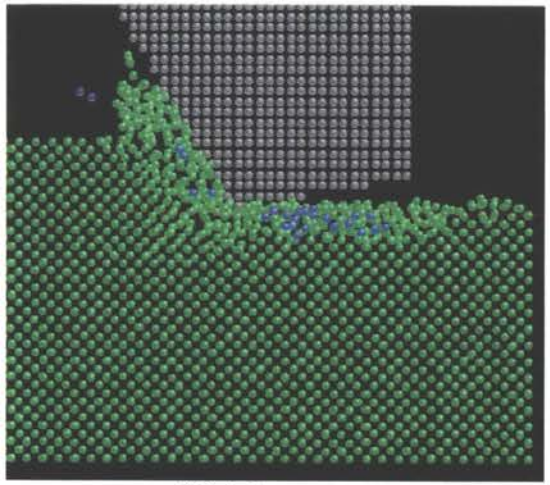

(a) 1.1 nm

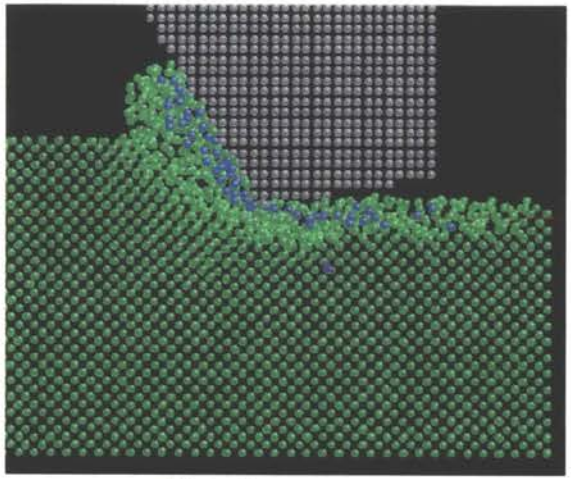

(b) 1.63 nm

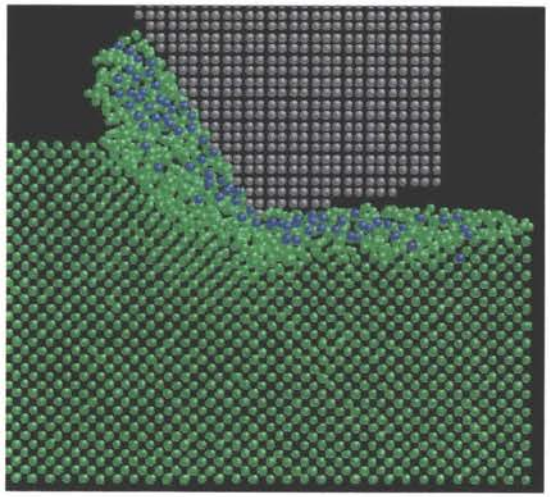

(c) 2.2 nm

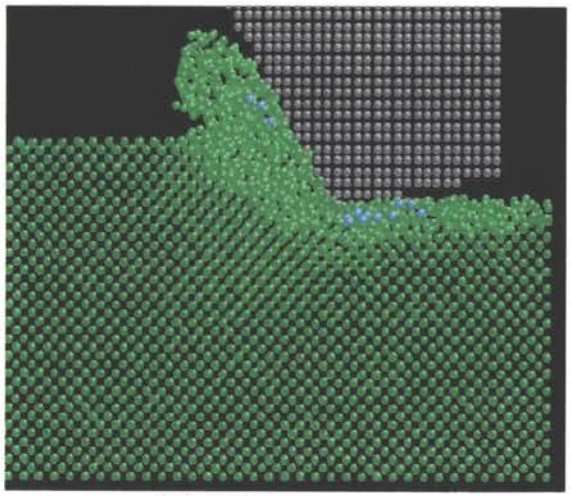

(d) 3.26 nm

Figures 8.4 (a) - (d) MD simulations of nanometric cutting of silicon for different widths of cut (-30 deg. Rake; 10 deg clearance; 1.1 nm depth; 1.1 nm width)

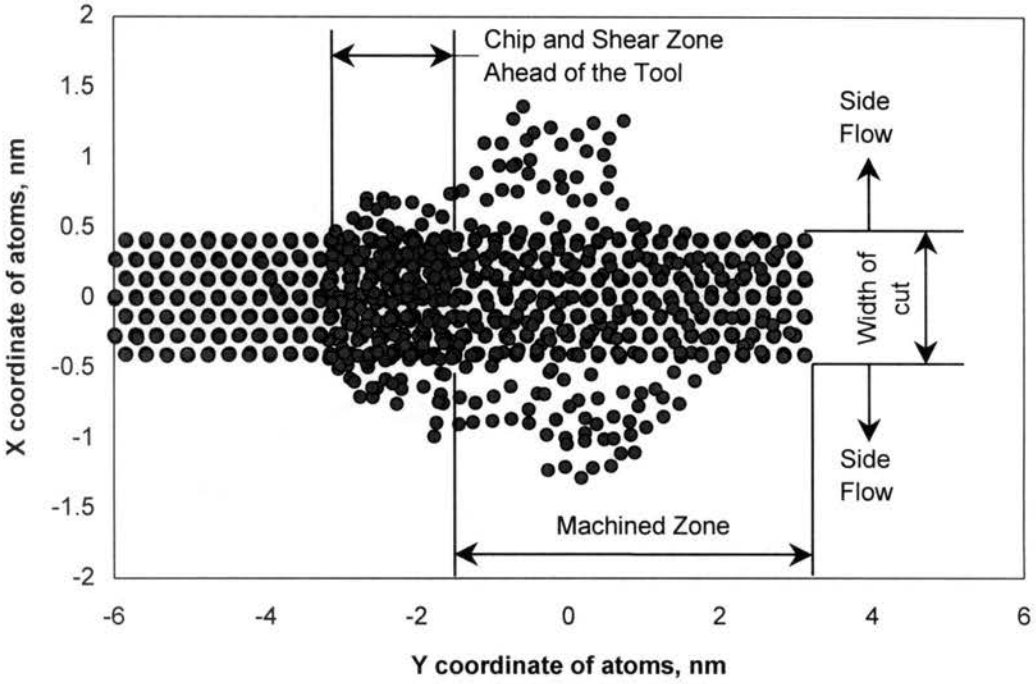

(a)

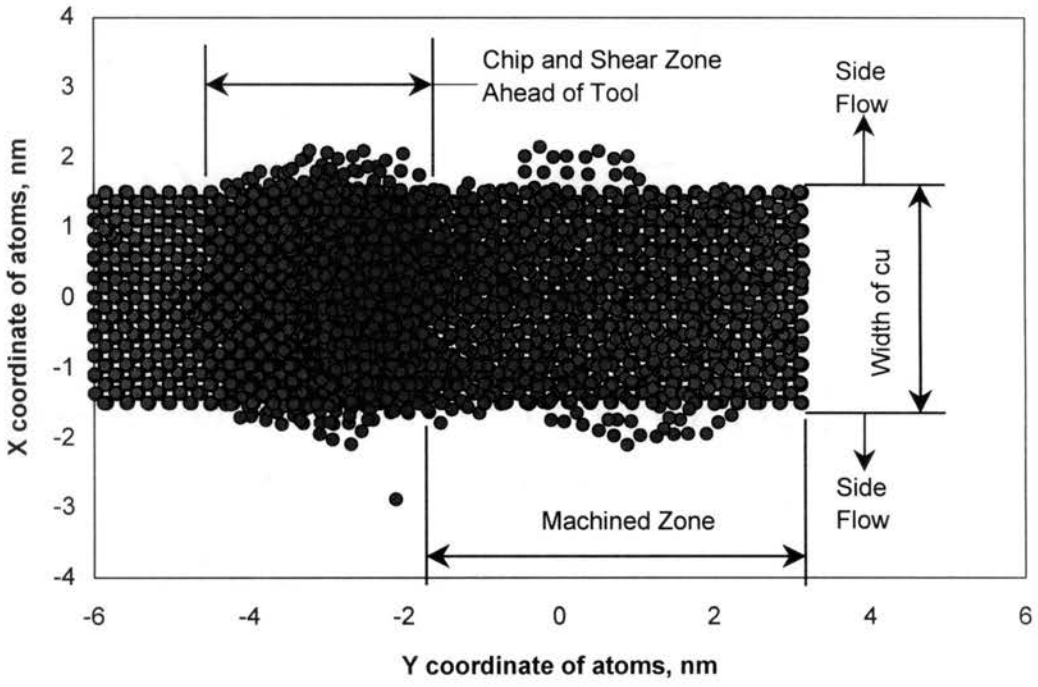

(b)

Figures 8.5 Plots showing the plan view of the distributions of the atoms in the X- Y plane for two widths of cut, namely, (a) 1.1 nm and (b) 3.26 nm, respectively (tool rake angle: -30° and depth of cut: 1.1 nm)

Figure 8.6 shows the variation of the normalized values of side flow (SF), chip count (CC), subsurface compression (SC), and shear zone compression (SZC) with the width of cut (w). It can be seen that the sum of four normalized quantities, namely, [SF + CC + SC + SZC] is equals to unity, indicating that one or the other of the four mechanisms, accounts for all material removal. As the width of cut (w) increases, a rapid increase in the normalized chip count and a similar decrease in the side flow, followed by a slight increase in the subsurface deformation and the shear zone compression can be seen. For example, as the width of cut (w) increases from 1.1 nm to 3.26 nm, the chip count increases from ~20% to ~60%, while the side flow decreases from ~60% to 10%. At a width of cut of 3.26 nm, the chip count accounts for ~65% of material removal, while the other three quantities are in the range of 10-15% each.

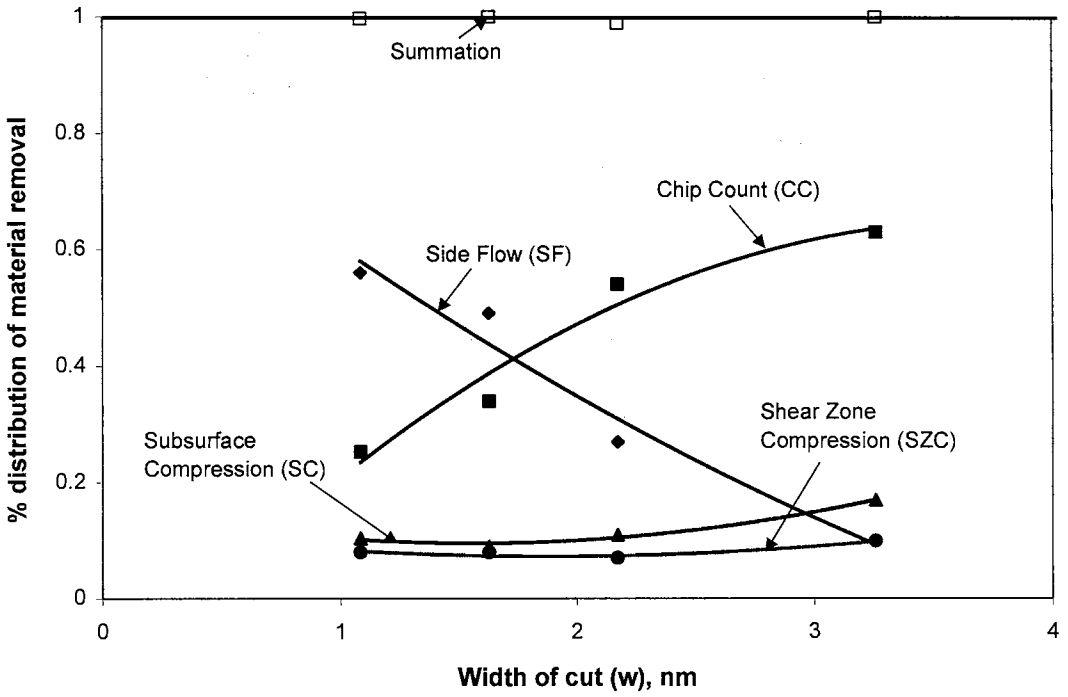

Figure 8.6 Variation of the normalized values of side flow (SF), chip count (CC), subsurface deformation (SC), and shear zone compression (SZC) with the width of cut (w) (tool rake angle: -30° and depth of cut: 1.1 nm)

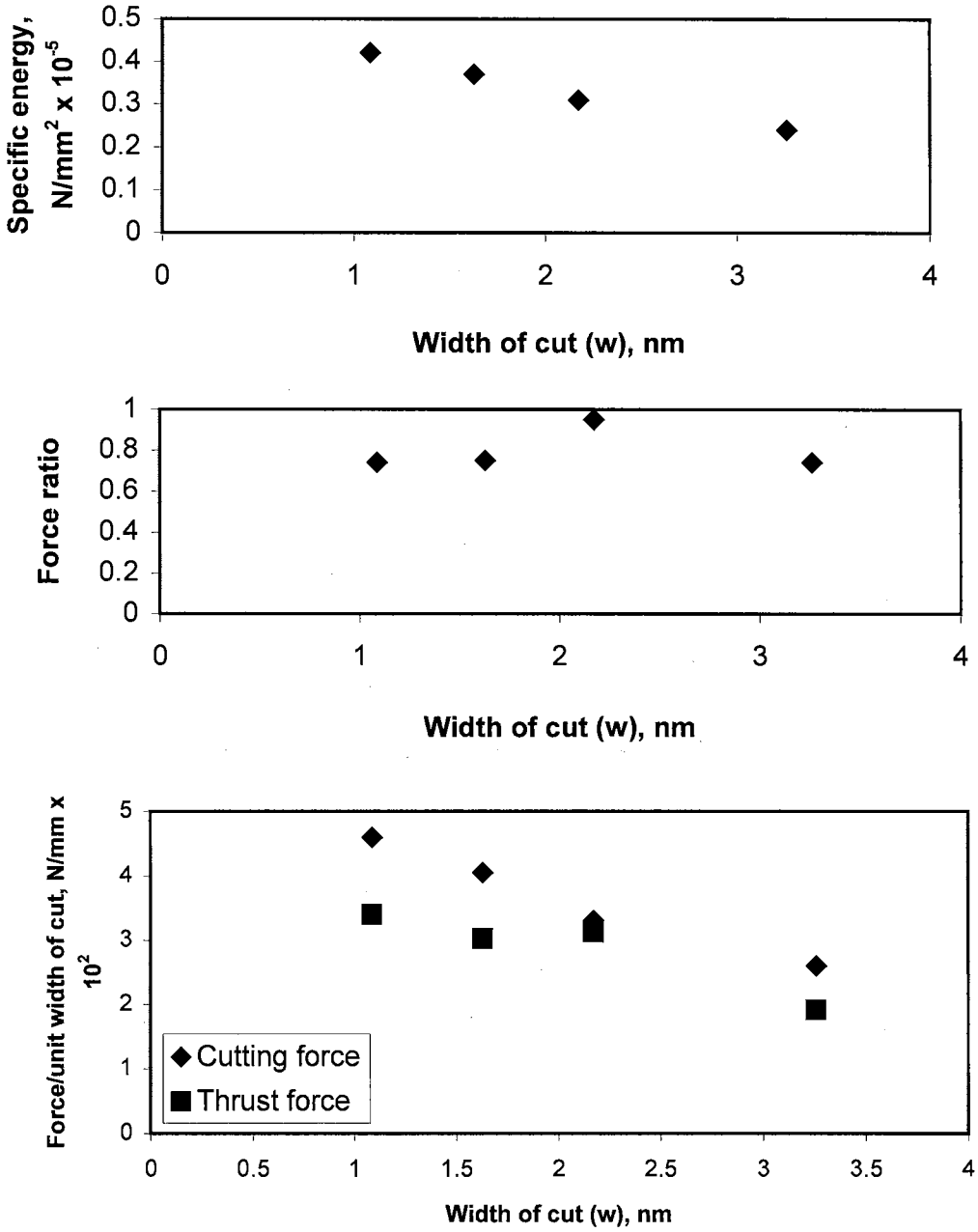

Figures 8.7 (a) - (c) Variation of the cutting force (F_c) and the thrust force (F_t) per unit width of cut, the force ratio (F_t/F_c), and specific energy with the width of cut (w)

Figures 8.7 (a) - (c) show the variation of the cutting force (F_c) and the thrust force (F_t) per unit width of cut, the force ratio (F_t/F_c), and specific energy with the width of cut (w). Even though the forces are normalized with respect to the width of cut, an increase in both the cutting and the thrust forces can be observed with decreasing width of cut [Figure 8.7 (a)]. Consequently, the specific energy, namely, the energy required for removing unit volume of the workmaterial, also increases with decreasing width of cut [Figure 8.7 (c)]. This increase can be attributed to the boundary effects when the width of cut is smaller relative to the depth of cut. The force ratio, in contrast, remains constant or independent of the width of cut [Figure 8.7 (b)], which is what is anticipated.

8.4.4. Effect of Rake Angle

Figures 8.8 (a) - (i) are MD simulations of nanometric cutting of silicon over a wide range of rake angles from $+60^{\circ}$ and -60° at a width of 3.26 nm and a depth of cut of 1.1 nm. Considerable subsurface deformation in the machined surface can be seen in all cases. It can be seen that the extent of deformation ahead of the tool and particularly under the tool increases with increase in negative rake. The extent of deformation under the tool seems to be minimum up to about 0° rake and increases significantly with increase in the negative rake angle from $\sim -15^{\circ}$. As previously noted, chip formation is very similar to an extrusion-like process, as *Puttick et al.* (1994) proposed. This becomes even clearer at higher negative rake angles. Incidentally, as the negative rake is increased there is less space to accommodate the chip between the work and the tool resulting in a significant increase in side flow, which would be the path of least resistance.

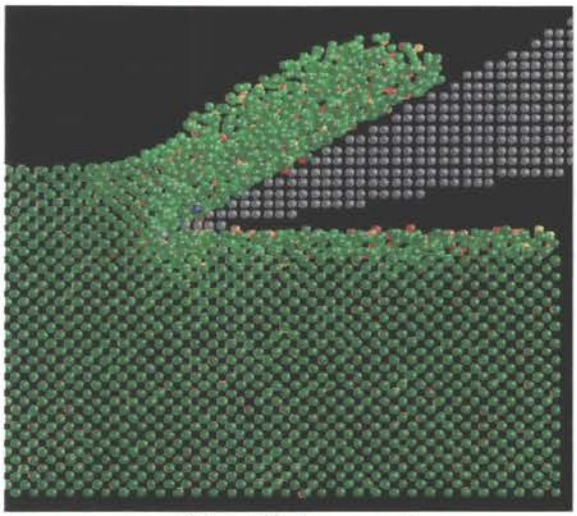

(a) + 60 degree rake

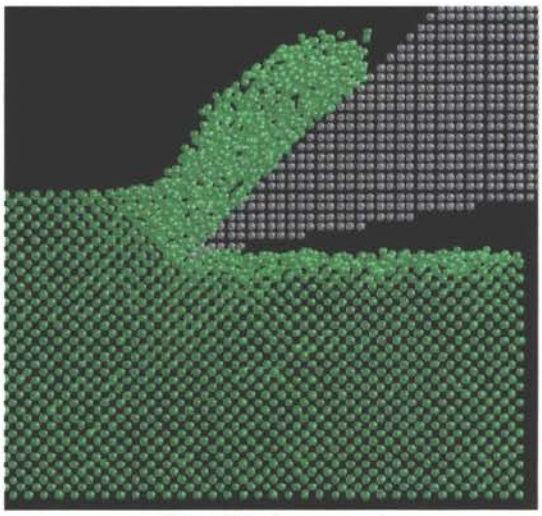

(b) +45 degree rake

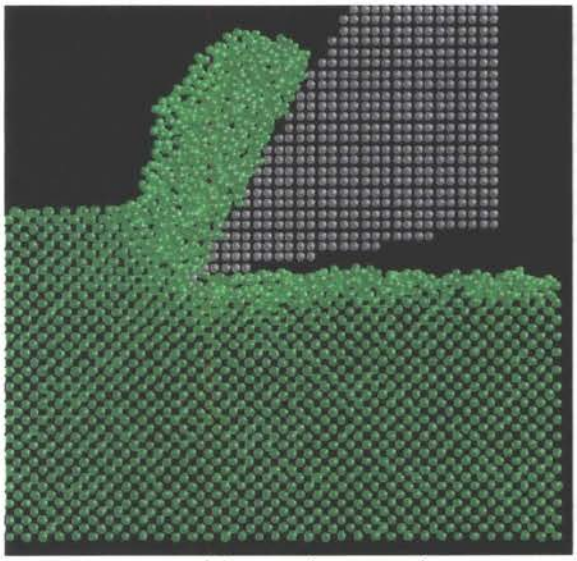

(c) +30 degree rake

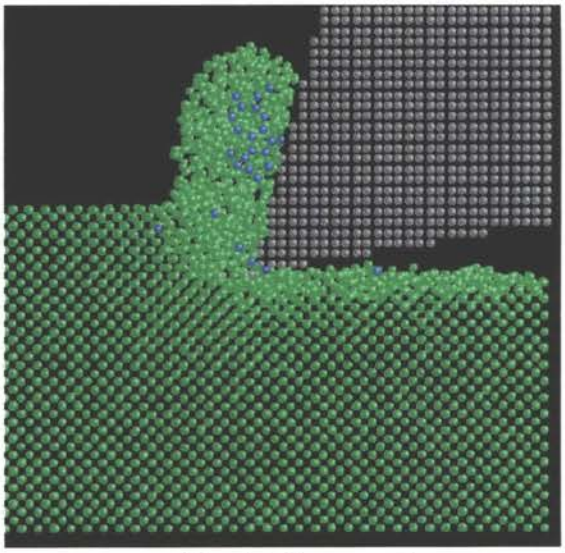

(d) +15 degree rake

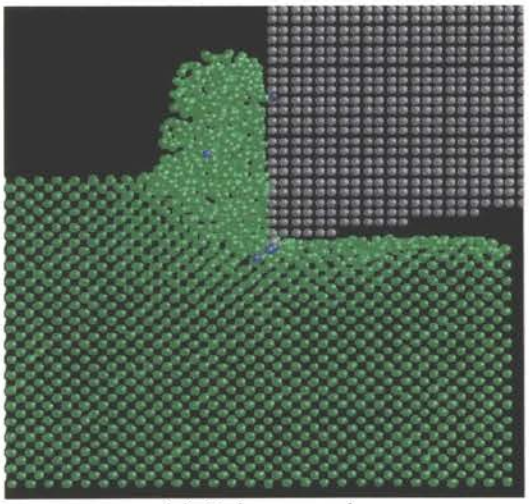

(e) 0 degree rake

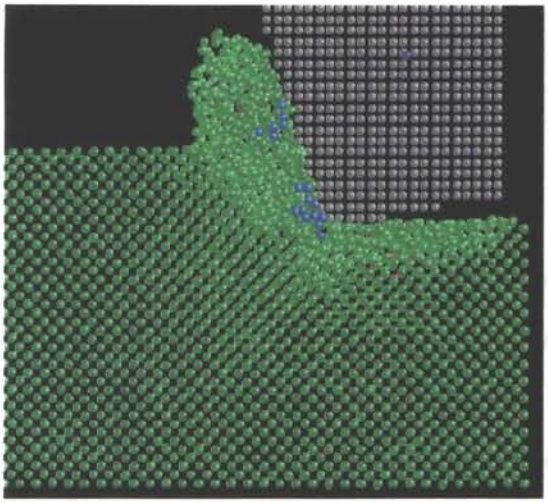

(f) -15 degree rake

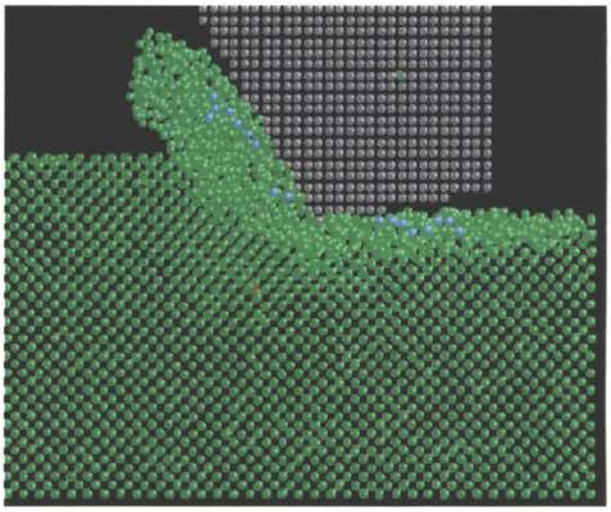

(g) -30 degree rake

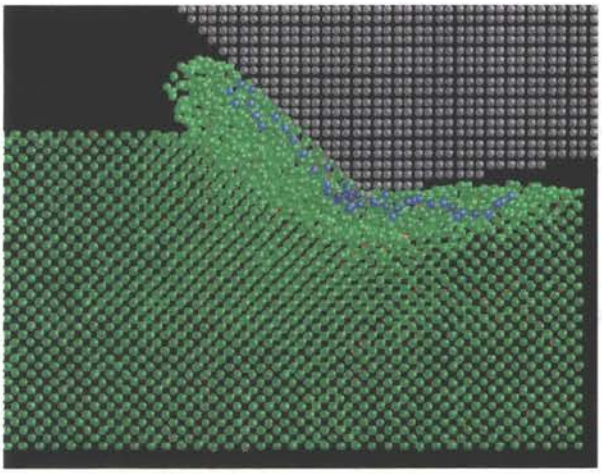

(h) -45 degree rake

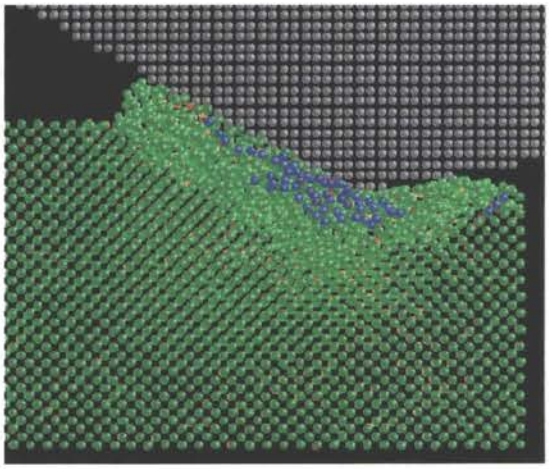

(i) -60 degree rake

Figures 8.8 (a) - (i) MD simulations of nanometric cutting of silicon over a wide range of rake angles from +60° and -60° (width: 3.26 nm and depth of cut: 1.1 nm)

The decrease in the chip volume with increasing negative rake is associated with an increase in the side flow and ploughing of the tool into the workmaterial. Also, subsurface deformation can be seen over a wide range of rake angles from - 60° to + 60° with the main difference being the degree of compaction of the atoms at or near the machined surface, as the rake angle is varied, namely, less compaction with high positive rake tools.

Figure 8.9 shows the variation of normalized values of side flow (SF), chip count (CC), subsurface compression (SC), and shear zone compression (SZC) with the tool rake angle. It can be seen that with increase in rake angle, there is a rapid increase in the chip count, a decrease in the side flow, subsurface deformation, and shear zone compression. For example, as the rake angle is increased from - 60° to +15°, the chip count (CC) increase from ~20% to ~80%, while the subsurface compression (SC) decreases from ~20% to ~10%. Similarly, the side flow (SF) decreases from ~25% to ~1%. This decrease is much more rapid for rake angles from –60° to -30°. The shearzone compression (SZC) similarly decreases from ~30% to ~5%. All four measured quantities seem to stabilize at rake angles above 0° with the chip count accounting for ~80% while each of the other three quantities are in the ~ 5-10% range.

Figure 8.10 shows the variation of the cutting force (F_c), thrust force (F_t), the force ratio (F_t/F_c), and the specific energy with rake angle. It can be seen that these values increase with increase in the negative rake angle, as expected. Also, the values of specific are not particularly high (~50% more than aluminum) (Chapter 6). Consequently, any

difficulty associated with the machining of silicon is not due to particularly high forces or energy requirements but due to other factors, such as the tool wear when machining with single crystal diamond tools or subsurface deformation in the machined surface underneath the tool.

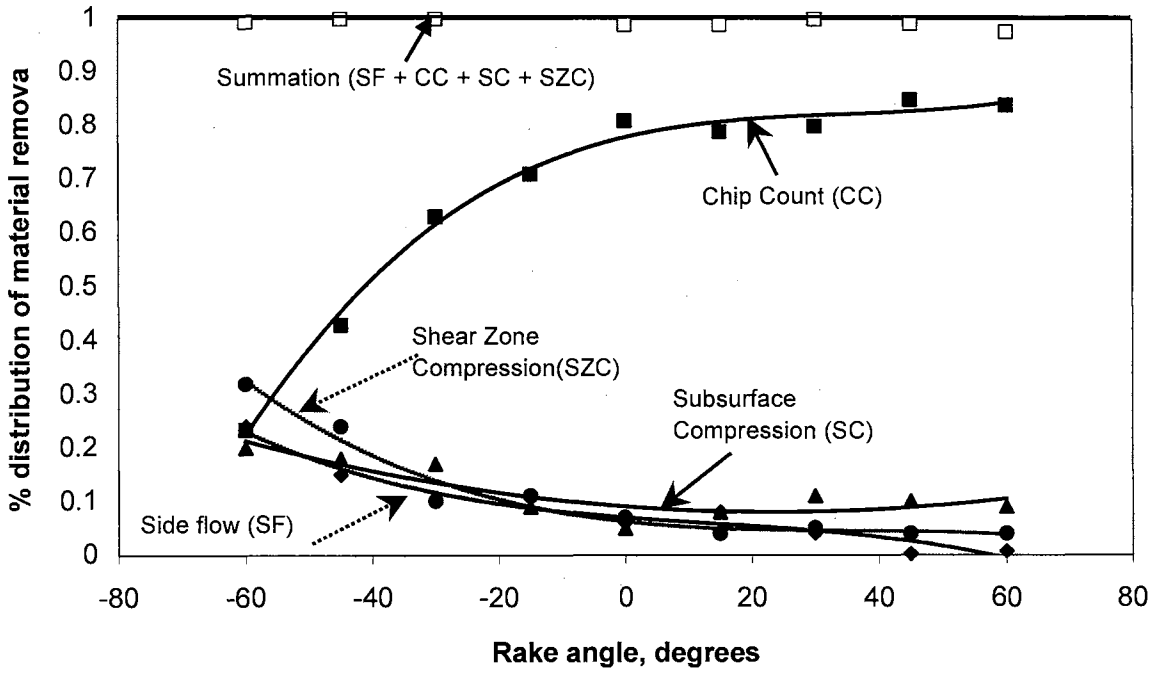

Figure 8.9 Variation of normalized values of side flow (SF), chip count (CC), subsurface deformation (SD), and shear zone compression (SZC) with the tool rake angle (width of cut: 3.26 nm and depth of cut: 1.1 nm)

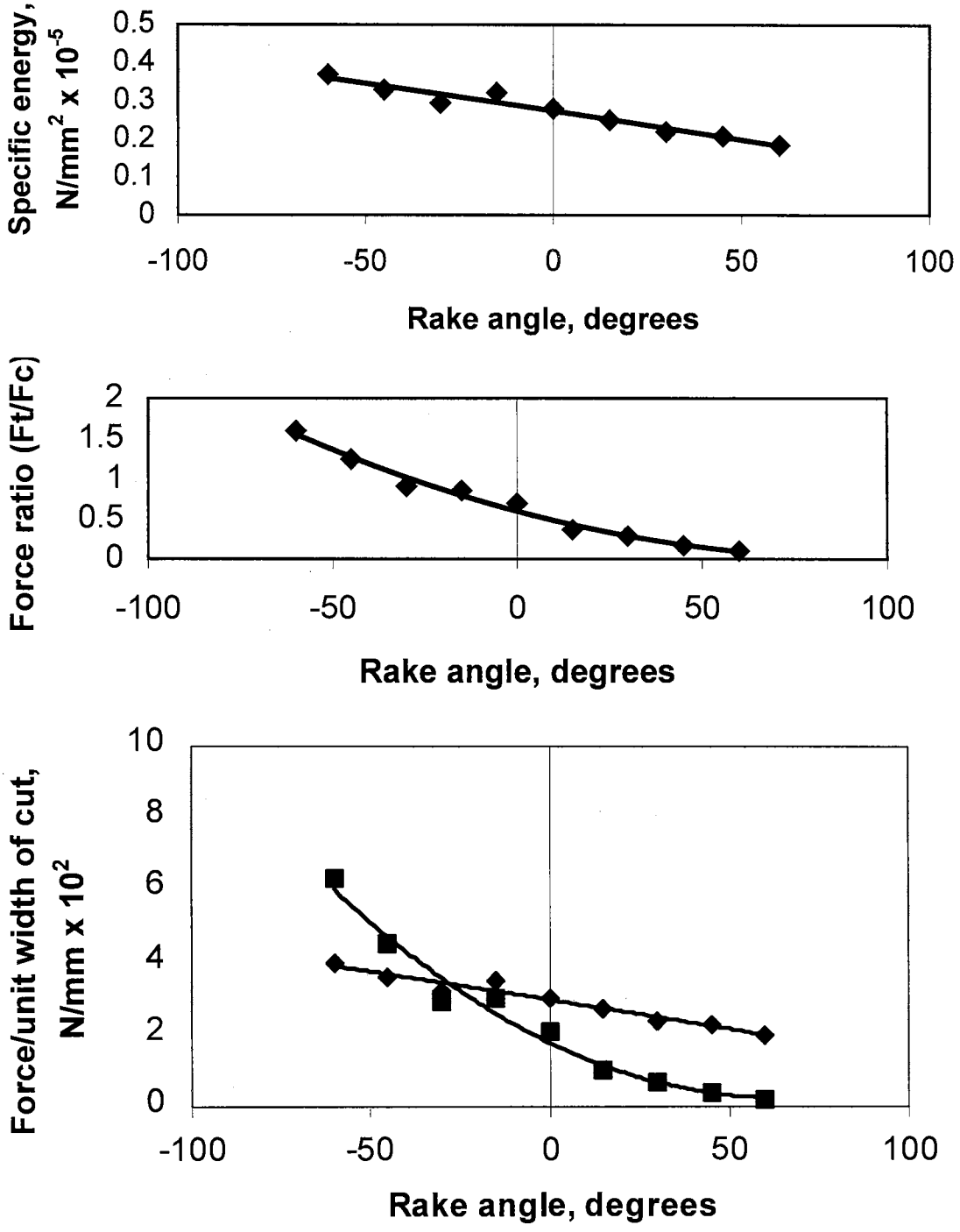

Figure 8.10 Variation of the cutting force (F_c), thrust force (F_t), the force ratio (F_t/F_c), and the specific energy with rake angle

8.4.5. Effect of Depth of Cut

Since it is logical to consider that the extent of subsurface deformation could decrease with lighter cuts, i.e. lower depths of cut or lower forces, MD simulations were conducted at various depths of cut from ~ 0.01 nm to 2.72 nm [Figures 8.11 (a) to (f)]. It can be seen that even at the lowest depth of cut used [Figure 8.11 (a)], where the tool is merely sliding on the workmaterial surface, there is considerable structural change in the material of the surface underneath the tool. As the depth of cut is increased, the subsurface deformation also increases. However, the subsurface deformation as a fraction of the depth of cut increases as the depth of cut is decreased. It is, therefore clear that subsurface deformation cannot be eliminated altogether by reducing the depth of cut.

Figure 8.12 shows the variation of the normalized values of side flow (SF), chip count (CC), subsurface compression (SC), and shear zone compression (SZC) with the depth of cut (d). As the depth of cut (d) increases, a rapid increase in the normalized side flow and a decrease in the chip count as well as the subsurface compression are observed. Both, the subsurface and the shear zone compression are significantly low at high cut depths due to an increased percentage of the removed material being accommodated by side flow.

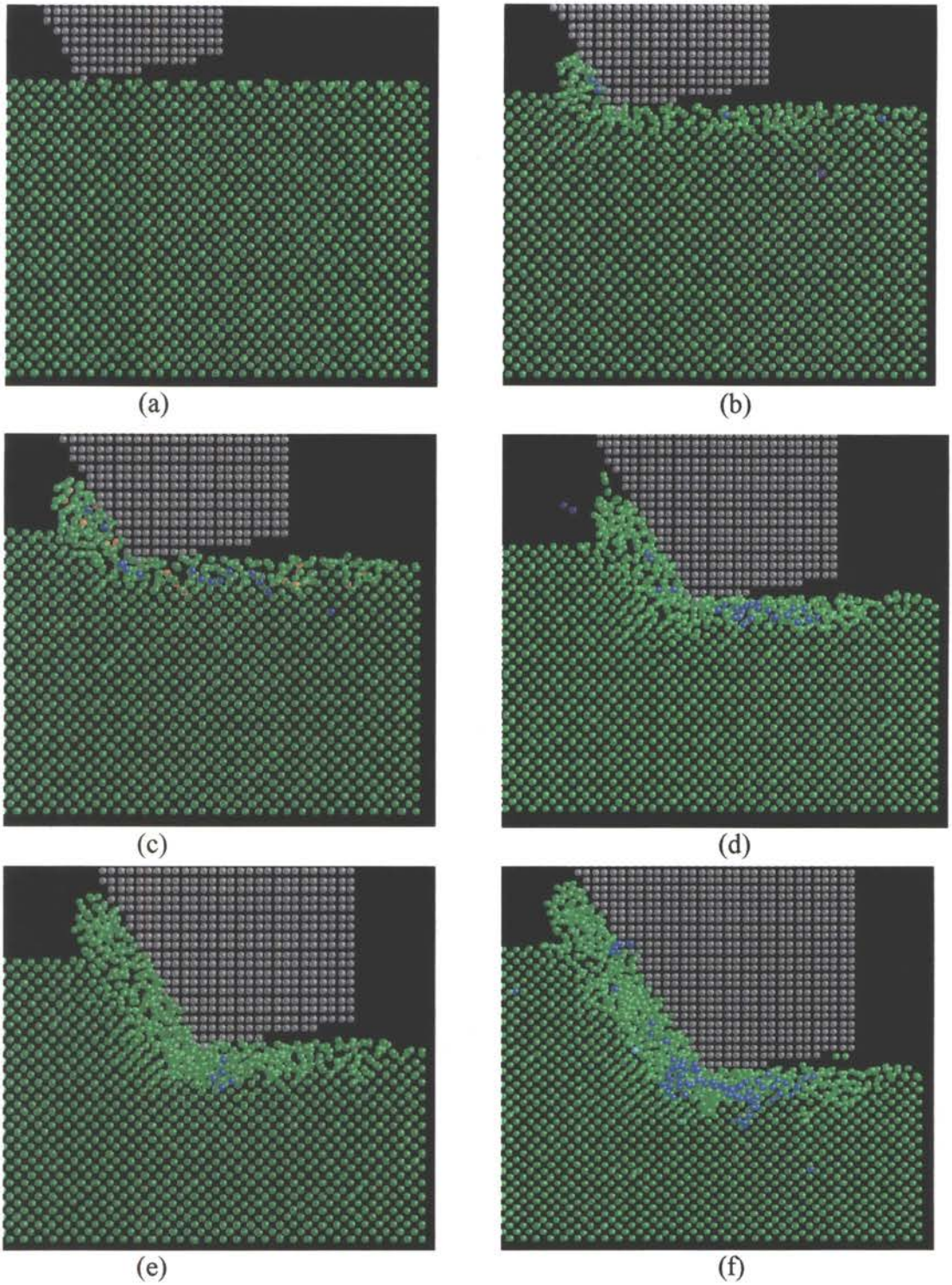

Figures 8.11 (a) - (f) MD Simulations of Nanometric Cutting of Silicon at Various Depths of Cut (a) ~0.01 nm (b) 0.272 nm (c) 0.543 nm (d) 1.1 nm (e) 1.63 nm and (f) 2.72 nm (-30 deg. rake; 1.1 nm width)

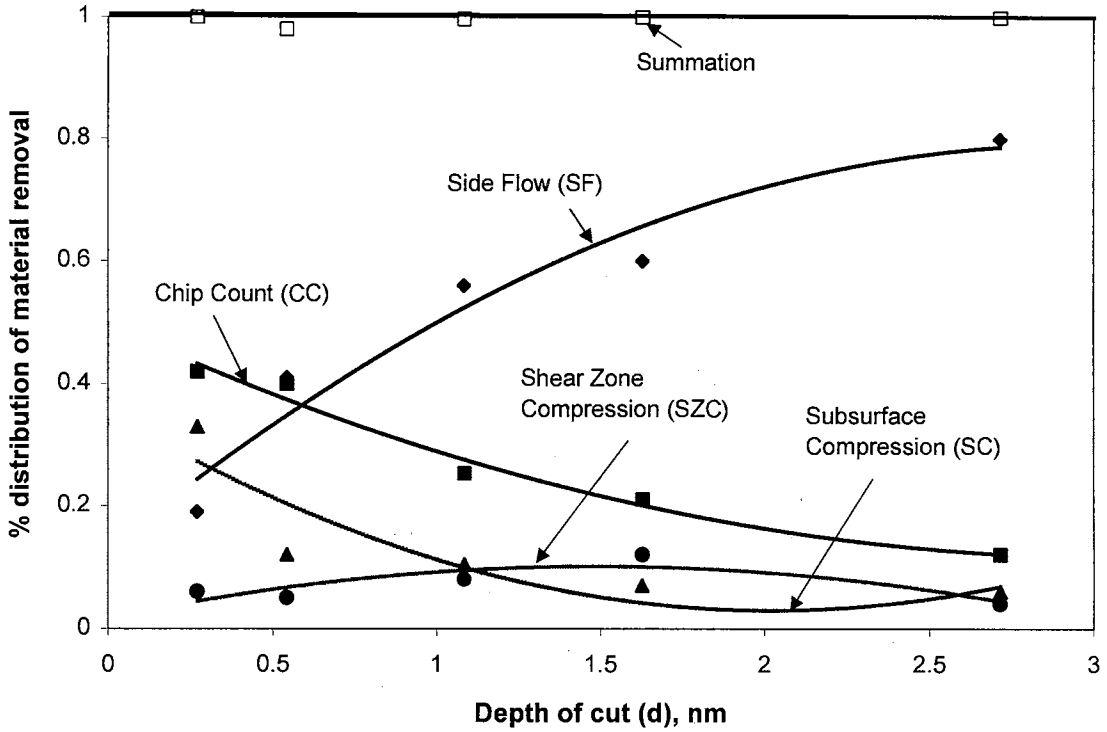

Figure 8.12 Variation of normalized values of side flow (SF), chip count (CC), subsurface deformation (SD), and shear zone compression (SZC) with the depth of cut (tool rake angle: -30° and width of cut: 1.1 nm)

Figures 8.13 (a) - (c) show the variation of the cutting force (F_c) and the thrust force (F_t) per unit width of cut, the force ratio (F_t/F_c), and specific energy with the depth of cut (d). Both, the cutting and the thrust forces, increase with increasing depth of cut [Figure 8.13 (a)], as can be expected. However, the specific energy increases with decreasing depth of cut [Figure 8.13 (c)] which can be attributed to the so called *size effect* similar to that reported by many other researchers based on experimental and simulation results (Nakayama and Tamura, 1968, for example). The force ratio remains nearly constant (~0.8) and independent of the depth of cut [Figure 8.13 (b)] as expected.

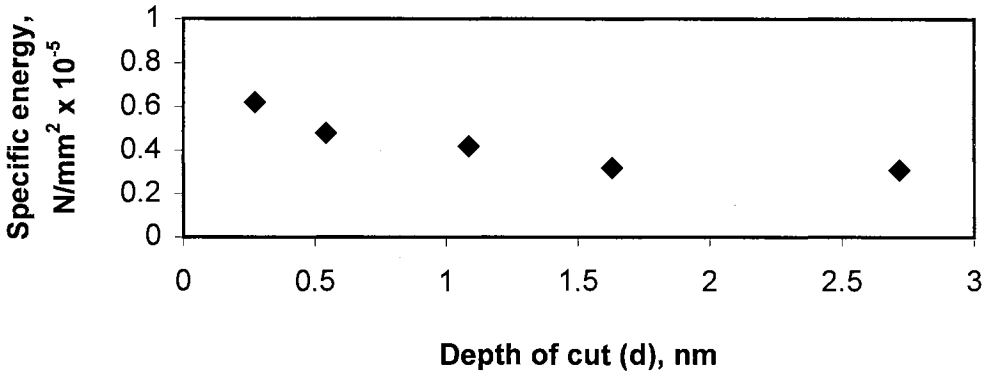

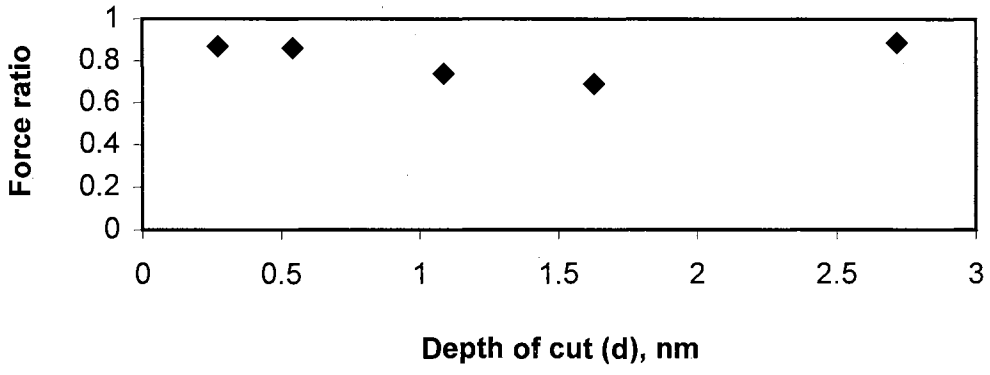

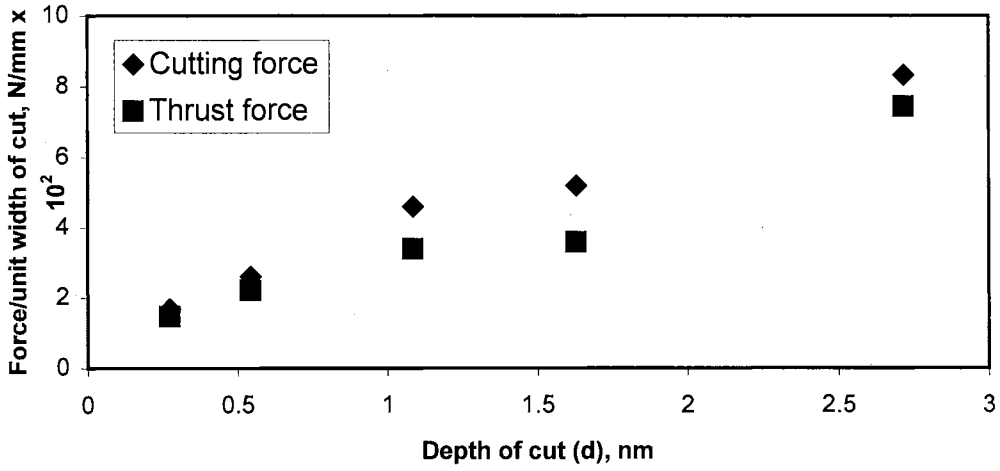

Figures 8.13 (a) - (c) Variation of the cutting force (F_c) and the thrust force (F_t) per unit width of cut, the force ratio (F_t/F_c), and specific energy with the depth of cut (d)

8.4.6. Effect of Ratio of Width of Cut to Depth of Cut (w/d)

The normalized chip count (CC) and side flow (SF) exhibited opposite trends as the width of cut (w) [Figure 8.6] and depth of cut (d) [Figure 8.12] were varied. In order to evaluate the distribution of the four material removal quantities irrespective of the width (w) and depth of cut (d), the measured quantities were plotted against the ratio of the width of cut and the depth of cut (w/d). Figure 8.14 shows the variation of the normalized values of side flow (SF), chip count (CC), subsurface compression (SC), and shear zone compression (SZC) with the ratio w/d. As the ratio of w/d increases, a rapid increase in the normalized chip count and an even more rapid decrease in the side flow can be observed. For example, as w/d increases from 0.5 to 6, the chip count increases from ~10% to ~65%, while the side flow decreases from ~80% to 5%. Thus, while the chip count depends both on the width of the workmaterial as well as the rake angle of the tool, the side flow is dependent mainly on w/d. All the four quantities tend to stabilize as w/d approaches 3 with the chip count accounting for ~65% while each of the other three quantities are in the range of ~ 5-15% each. In fact, for obtaining conditions close to the plane strain conditions (i.e., no side flow), the w/d ratio may have to be as high as 30 depending on the magnitude of the negative rake angle used (Komanduri, 1971); the higher the negative rake angle, the higher the w/d ratio must be to attain plane strain conditions. Figures 8.15 (a) - (c) show the variation of the cutting force (F_c) and the thrust force (F_t) per unit width of cut, the force ratio (F_t/F_c), and specific energy with the ratio w/d. It can be seen that these quantities asymptotically approach their limiting values as w/d approaches 6.

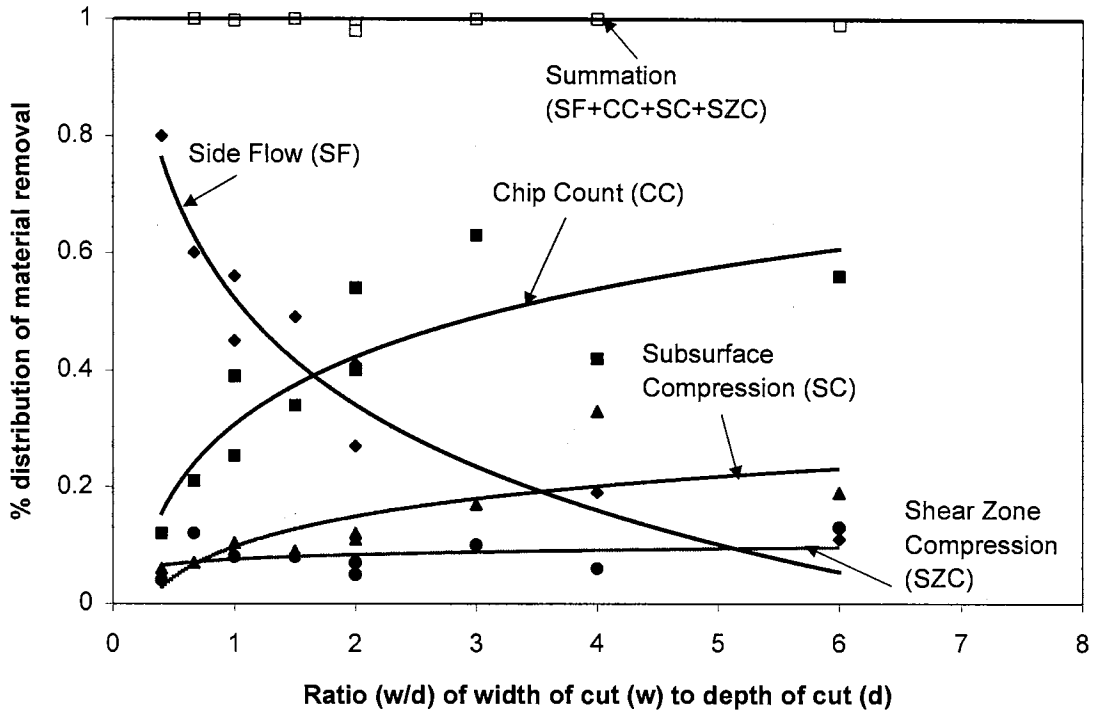

Figure 8.14 Variation of normalized values of side flow (SF), chip count (CC), subsurface deformation (SD), and shear zone compression (SZC) with the ratio of the width of cut (w) to the depth of cut (d), i.e., (w/d)

Figures 8.16 (a) and (b) show the variation of the difference in the number of atomic bonds before and after cutting measured in the subsurface deformed zone with interatomic distance and number of atomic bonds/atom (or coordination number), respectively, for different values of w/d. It can be seen from Figure 8.16 (a) that, as w/d increases, the difference decreases for the atomic distance of 0.235 nm and increases for the atomic distances of 0.243 nm and 0.258 nm. Similarly, Figure 8.16 (b) shows a decreasing 4-coordination number with a corresponding increase in the 6-coordination number as w/d increases. Again, the figures suggest that a phase transformation is taking place during nanometric cutting of silicon. Thus, to reduce subsurface damage, it may be preferable to use lower values of w/d.

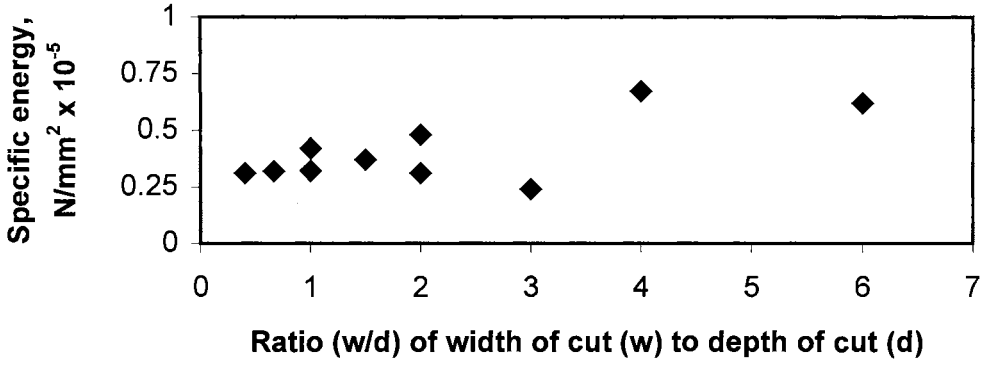

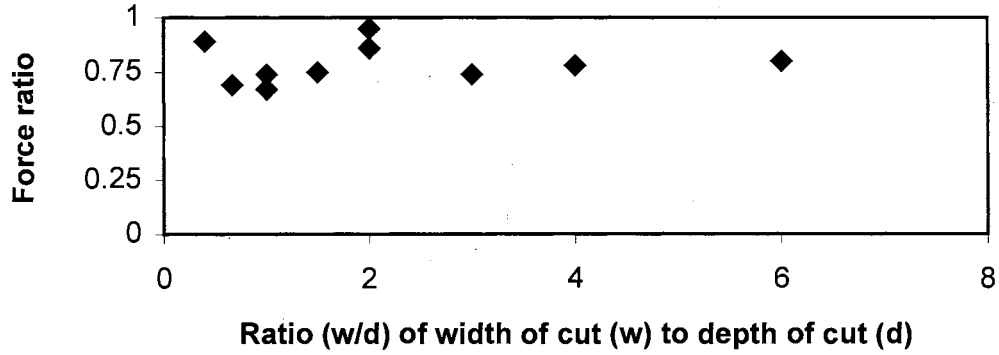

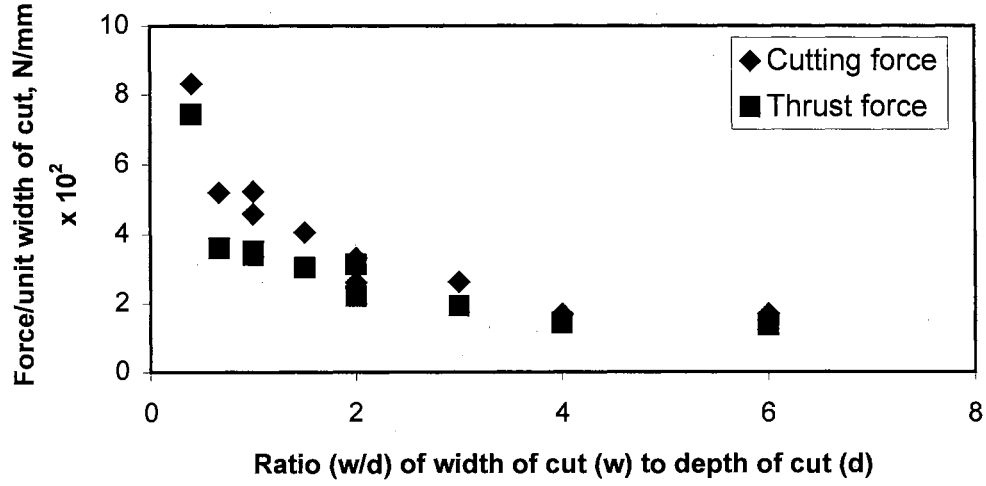

Figures 8.15 (a) - (c) Variation of the cutting force (F_c) and the thrust force (F_t) per unit width of cut, the force ratio (F_t/F_c), and specific energy with the ratio w/d

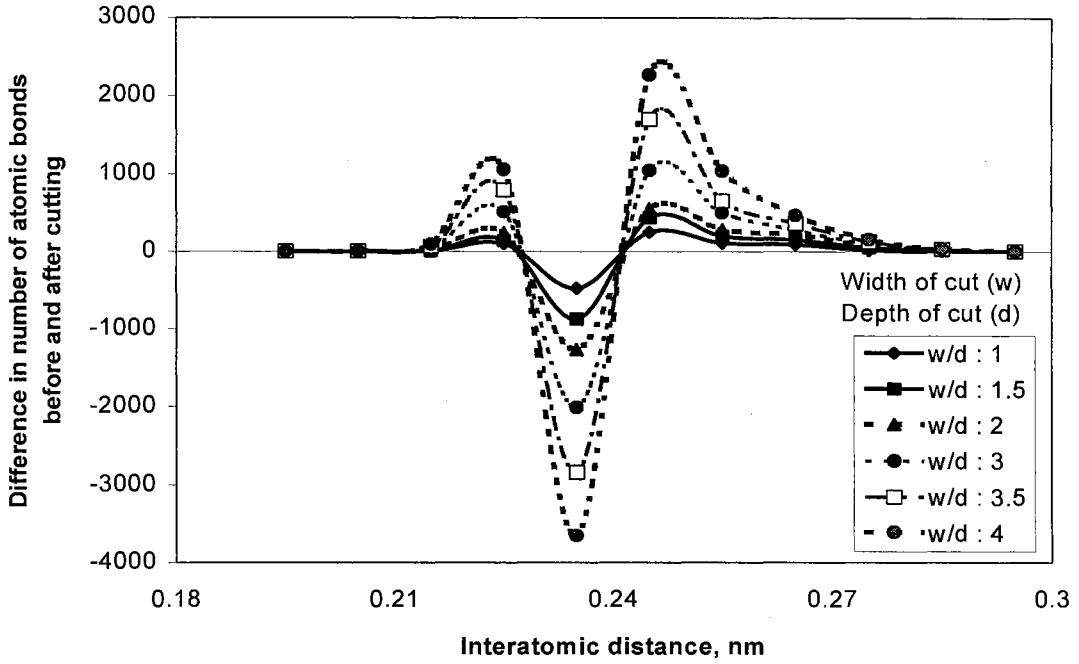

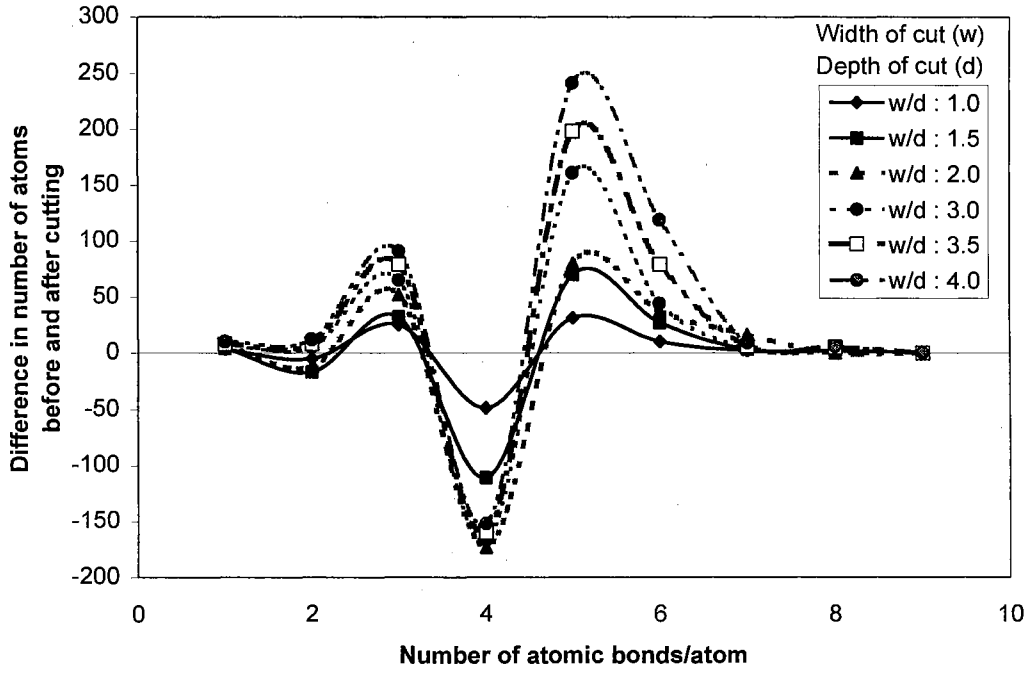

Figures 8.16 Variation of the difference in the number of atomic bonds before and (a) and (b) after cutting measured in the subsurface deformed zone with interatomic distance and number of atomic bonds/atom (coordination number), respectively, for different values of w/d (tool rake angle: -30°)

8.4.7. Effect of Clearance Angle

As shown earlier, subsurface deformation in the machined surface underneath the tool is observed for all rake angles and depths of cut. To investigate if clearance angle plays a role in influencing the extent of subsurface deformation, MD simulations were conducted with tools having clearance angles of 10^{o} and 30^{o} and rake angles of -30^{o} and $+30^{o}$, respectively, in specific combinations. The results are shown in Figures 8.17 (a) - (c). It can be seen that even with a clearance angle of $+30^{o}$, there is still considerable subsurface deformation in the machined surface underneath the tool, similar to the one with a 10^{o} clearance angle tool. The main difference is in the degree of compaction of the machined surface underneath the tool. It is, therefore, clear that this subsurface deformation is not due to rubbing of the clearance face on the machined surface but rather due to compression of the material beneath the tool.

8.4.8. Effect of Cutting Conditions and Tool Rake Angle On the Subsurface Damage in Nanometric Cutting of Silicon

Figures 8.18 (a) - (d) show the variation of the ratio of subsurface damage to the depth cut with cutting conditions (depth of cut [Figure 8.18 (a)], width of cut [Figure 8.18 (b)], and the ratio w/d [Figure 8.18 (c)]) and tool rake angle [Figure 8.18 (d)]. It can be seen from Figure 8.18 (a) that the subsurface damage as a fraction of the depth of cut increases with decreasing depth of cut. This increase is significant at lower depths of cut suggesting the possibility of a near constant subsurface damage inherent to silicon

machining, even as the depth of cut is reduced to atomic dimensions. Figure 8.18 (b) shows a small increase in the subsurface damage to depth ratio as the width of cut is increased. It was shown earlier that with increasing width of cut, the degree of compaction in the subsurface region increases. However, based on Figure 8.18 (b) it seems that the effect of width of cut on the depth of subsurface damage is minimal. Figure 8.18 (c) shows a constant increase in the subsurface damage with increasing w/d ratio. Figure 8.18 (d) shows an increase in the subsurface damage with increasing tool negative rake angle. This can be attributed to the resultant force vector direction (into the workmaterial) and the less space available for the chip to flow, resulting in increased side flow as the tool negative rake angle is increased. This increase in the subsurface damage with increasing tool negative rake angle can lead to the formation of microcracks, as was also observed by Yan et al. (2000). Based on Figures 8.18 (a) - (d) it is possible to suggest that the depth of cut and the tool rake angle are the two major factors affecting the depth of subsurface deformation in machining of silicon.

8.5. CONCLUSIONS

MD simulations of nanometric cutting of silicon were performed using cutting tools of various rake angles (from - 60^{o} to + 60^{o}), clearance angles (from 10^{o} to 30^{o}), depths of cut (0.01 nm to 2.72 nm), and widths of cut (1.1 nm to 4.34 nm) to investigate the nature of the chip formation process. The following conclusions may be drawn based on these studies:

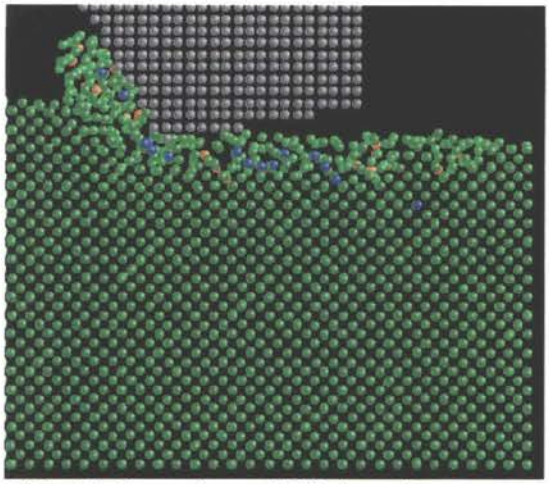

(a) -30 deg. rake and 10 deg. clearance

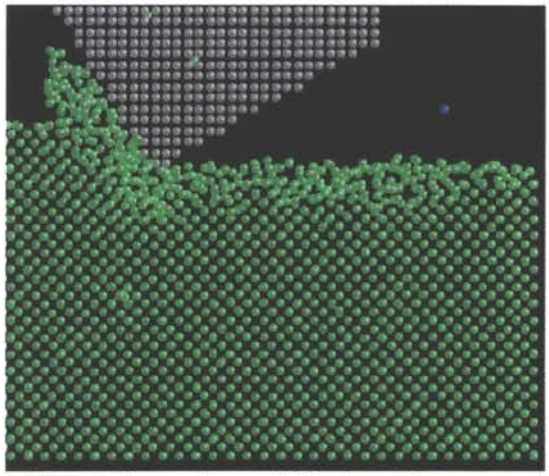

(b) -30 deg. rake and 30 deg. clearance

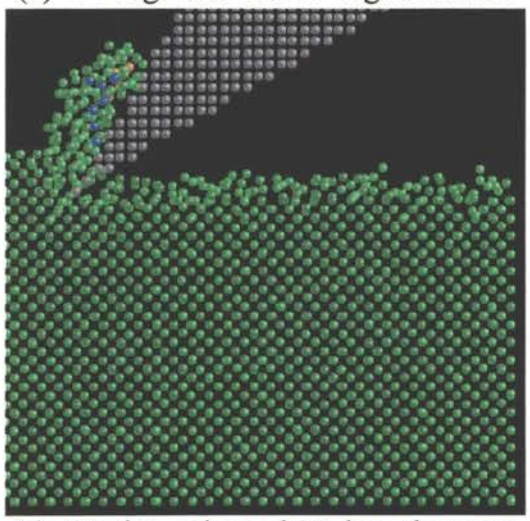

(c) +30 deg. rake and 30 deg. clearance

Figures 8.17 (a) - (c) Effect of Clearance Angle in Nanometric Cutting of Silicon (1.1 nm; width; 0.543 nm depth)

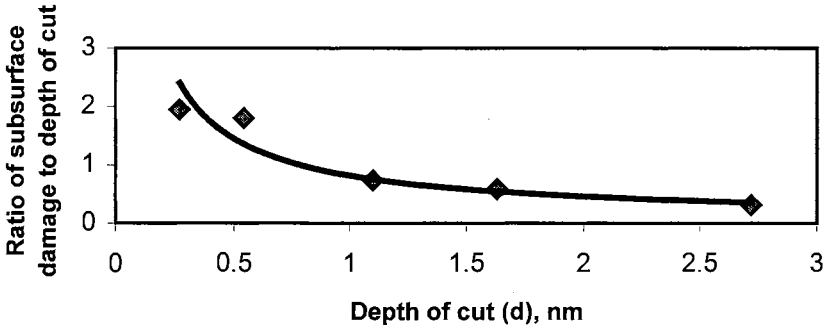

(a)

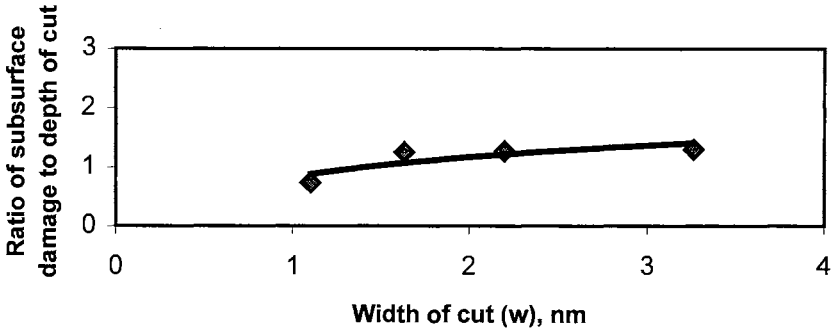

(b)

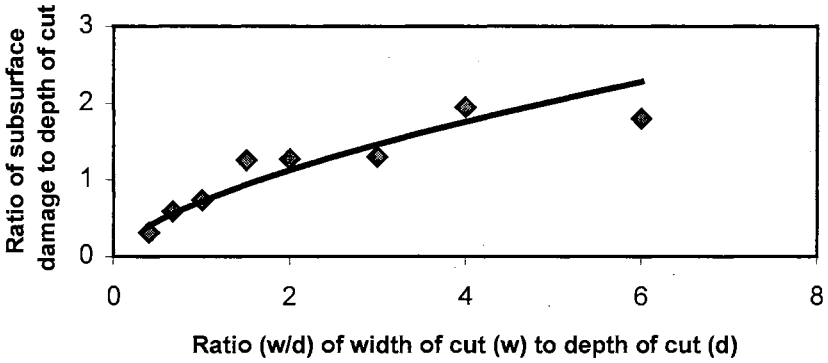

(c)

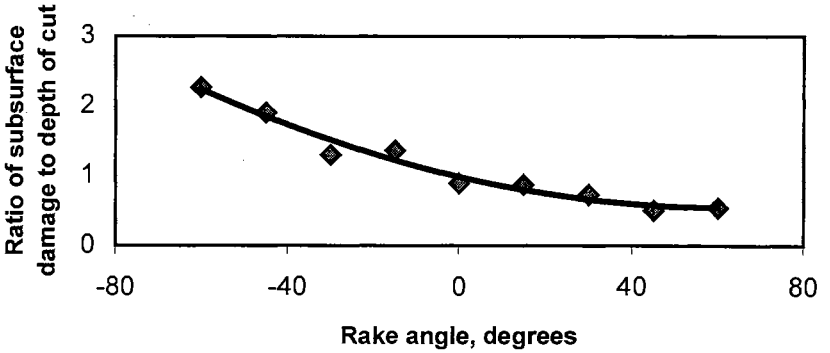

(d)

Figures 8.18 (a) - (d) Effect of (a) depth of cut [d] (b) width of cut [w] (c) ratio of width of cut to depth of cut [w/d] and (d) tool rake angle on the ratio of subsurface damage to depth of cut in nanometric cutting of silicon

1. A comparison of the MD simulation of nanometric cutting of aluminum and silicon shows significant differences due to differences in ductility. This includes the nature of deformation ahead of the tool in the primary zone and the extent of deformation in the bulk workmaterial.

2. While the chip formation process in the machining of ductile materials, such as aluminum is one of plastic deformation on preferred crystallographic planes and directions ahead of the tool in the primary shear zone, the chip formation process with silicon seems to be similar to an extrusion-like process without a specific crystallographic preference (Puttick et al., 1994). This appears to be due to phase transformation from α to β-silicon under hydrostatic pressure and consequent densification of the material.

3. Based on the determination of the distribution of interatomic distances and coordination numbers before and after cutting, a possible phase transformation from α to β-silicon in nanometric cutting is inferred. Such a phase transition produces densification of the material ahead of the tool, in the chip, and in the machined surface beneath the tool. Since, most ductile materials do not exhibit phase transitions and a concomitant densification upon machining or indentation, permanent subsurface deformation is generally not observed. Instead, strain lines and dislocations appear, many of which disappear by elastic recovery once the tool is removed.

4. Subsurface deformation was observed over a wide range of rake angles (from -60° to +60°) and at all cut depths down to 0.01 nm. From this, it appears that some subsurface damage in the machined surface of silicon is inherent with nanometric cutting. As Kunz *et al.* (1996) suggested, complete damage-free material removal may be possible only when a chemical component to polishing is involved.

5. The fact that subsurface deformation was observed under all conditions of cutting, indicates that in all likelihood a pressure induced phase transformation has taken place. In the absence of such a phase transformation, silicon would be brittle and subsurface deformation would recover elastically, which is not the case.

6. Material removal in nanometric cutting of silicon occurs by four mechanisms, namely, compression of the workmaterial ahead of the tool, formation of a chip akin to an extrusion-like process, by side flow, and by subsurface deformation in the machined surface beneath the tool.

7. Based on the analysis of various components of the material removal process in nanometric cutting of silicon, it can be seen that side flow decreases rapidly with increase in width of cut (Figure 8.6) and increases with increase in depth of cut (Figure 8.12). Their combined effect can be considered using the ratio of w/d. As the ratio of w/d increases, the side flow decreases rapidly (Figure 8.14). The chip count on the other hand increases with increase in rake angle as well as increase in the ratio of w/d. Both these conditions decrease the degree of side flow. The subsurface

compaction decreases with increase in rake angle (Figure 8.9) but increases with increase in the ratio of w/d.

8. When the ratio of width to depth of cut (w/d) is low, the material removal is dominated by side flow with very little chip formation ahead of the tool (Figure 8.14). When the ratio of w/d is large, the chip count increases with a corresponding decrease in the side flow. However, the subsurface compression increases with increase in the ratio of w/d. To minimize subsurface deformation, it may be preferable to use narrower widths and obtain material removal by side flow. In fact, in grinding of silicon with fine abrasives, this may be the main mode of material removal.

CHAPTER 9

TRIBOLOGY AT THE ATOMIC SCALE [a, b]

9.1. INTRODUCTION

Magnetic hard disks (usually made of aluminum) are used extensively in information storage systems. They are generally finished very rapidly and very efficiently by ultraprecision machining using single point diamond tools on an expensive, highly rigid, high precision machine tool. The stored information is protected from the read/write head (slider) by means of a thin coating (tungsten, nickel etc.) in addition to a lubricant layer between the protective layer and the head. The coatings applied on the surface should have sufficient strength and wear resistance to withstand the force applied by the slider. When the thickness is on the order of a few nanometers or less, even the slightest load can cause atomic rearrangement, which can result in the alteration of the mechanical and electrical properties. Hence, it is of paramount importance that the process should be investigated at the atomic level while performing low load, indentation and scratch experiments.

---

a - R. Komanduri, N. Chandrasekaran, L. M. Raff, 2000, "MD Simulation of Indentation and Scratching of Single Crystal Aluminum," Wear, 240, 113-143

b - R. Komanduri, N. Chandrasekaran, L. M. Raff, 2000, "Molecular Dynamics Simulation of Atomic-Scale Friction," Phys. Rev. B, 61/20, 14007-14019

As the demand for higher storage space increases, the distance between the magnetic disk and the slider is being reduced significantly to nanometric dimensions (1-10 nm). Wear of the disk will further reduce this distance. As a result, the possibility of contact between the head and the disk resulting in adhesion, asperity contact, friction, and wear is increased significantly (Forehand and Bhushan, 1997). This will especially be the case if the lubricant fails. Also, sliders having extremely small mass (<10 mg) and light contact loads (< 1 μN) are being considered for ultrahigh-density recording devices using the point-recording technique (Kaneko, 1993). A similar situation applies for micro electro mechanical systems (MEMS) and ultrahigh density recordings. Friction and wear under these conditions are believed to be due to surface interaction forces at the atomic level rather than the load (Kaneko et al., 1996) because of light loads and the extremely light weights of the sliders. It appears that the traditional macroscopic theories of friction cannot be extended under these conditions.

The ultimate goal of nanotribology is to design practically zero wear devices with very small mass and extremely light loads. Fundamental atomic scale friction studies are anticipated to throw light on the nature of the friction process, the magnitudes of the friction force as well as the friction coefficient, and ultimately the relation between friction and wear, if any. Is the friction coefficient, low or high, under nanotribological conditions? What is its magnitude? What is its significance? Is it dependent on the normal load? Answers to these and other questions are important in pursuance of our knowledge in nanotribology. Understanding the science of nanotribology, therefore, is not only an intellectual curiosity but also a definite technological need. The fact that a lubricating layer is provided between the disc and the read/write head (slider) to reduce friction and wear is an indication that without that, the friction coefficient is anticipated to be high. However, some experimental studies using atomic force microscope and other devices report rather low friction values (Mate et al., 1987; Erlandsson et al., 1998). Of

course, these studies may involve the introduction of a low friction coefficient lubricant either intentionally or formed *in situ* with the environment.

Nanotribology involves dynamic atomic interactions at the interface of two materials in relative contact. This includes adhesion, contact formation, nano-indentation, scratching, nanocutting, friction, wear, and lubrication [Bhushan, 1999]. Considerable research has been focused on the macroscopic, microscopic, and atomistic behavior of friction. Oftentimes, the microscopic and atomic behaviors are combined into nanometric behavior. A number of theories such as the surface roughness theory (Coulomb, 1785), the adhesion theory (Bowden and Tabor, 1954), the delamination theory (Suh, 1973), and friction due to molecular interactions (Tomlinson, 1929; Mori et al., 1980; McClelland, 1989) have been put forward to explain the origin of friction. However, surface roughness theories fail to explain energy dissipation and adhesion theories assume friction *a priori*. Other mechanisms such as phonon interactions (Cieplak et al., 1994) and electron excitation (Persson, 1994) have also been suggested. A new regime of friction, termed *superlubricity*, where friction between two contacting bodies in relative motion under extremely light loads completely vanishes has been postulated (Hirano and Shinjo, 1990; 1993). This is based on the situation where (sliders with extremely small mass and very light contact loads), the friction is independent of the normal force and is mainly due to atomic scale surface interactions. The phenomenon appears when the sum of the forces on each moving atom against the entire system vanishes. Theories explaining the dependence of the friction coefficient on such extrinsic factors as surface roughness (Lim et al., 1989; Rabinowicz, 1992; Garzino and Lama, 1996; You and Yu, 1997), load (Casey and Wilks, 1973; Tsukizoe and Sakamoto, 1975; Enomoto and Tabor, 191; Rabinowicz, 1992), sliding speed (Tsukizoe and Sakamoto, 1975; Lim et al., 1989; Rabinowicz, 1992; Krim, 1996), and hardness (Mokhtar, 1982) have also been proposed. However, significant discrepancies exist on the nature and magnitude of friction coefficient and its dependence on the extrinsic factors.

Indentation and scratch tests have long been used to determine the hardness, the friction and wear characteristics, and the elastic properties of materials (Vlassak and Nix, 1994; Doerner and Nix, 1997). Hardness and friction coefficient are important properties when a slider moves on a substrate as in the case of disk drives and other nanotribological applications. The hardness test provides a means to measure the resistance to permanent or plastic deformation and the scratch test provides information regarding abrasion, friction coefficient, wear resistance, etc. In the field of tribology, hardness and coefficient of friction are considered as two important characteristics that can provide significant insight into the frictional and wear behavior of two contacting surfaces.

When the depth of indentation-scratching is in the range of nanometers (as in nanoindentation), indentation or scratching is performed within a single grain of a polycrystalline workmaterial as the average grain size is significantly larger (generally, several micrometers). Consequently, nanoindentation or scratching of a polycrystalline material basically involves machining a single grain with periodic interruptions at the grain boundaries. It is also known that the grain orientation changes from one crystal to another in a polycrystalline aggregate. Hence, the indenter experiences workmaterial with different crystallographic orientations and scratch directions. In addition, there are many precision engineering applications where single crystal materials, such as silicon and germanium, are finished by nanometric cutting. The properties of these single crystal materials are determined by means of nanoindentation and sliding experiments.

It was shown earlier [Chapter 6] that the crystallographic factors affect the forces and force ratio in nanometric cutting. Similarly, the crystal orientation and the indentation/scratch directions affect the measured hardness and friction coefficient. The frictional anisotropy is of significant importance in nanotribology to achieve zero wear state. Also, the variation of friction coefficient with load suggests the dependence of the mechanism of friction on the scale of interaction (Kim and Suh, 1994). Hence, it is

necessary to understand the mechanism of friction and the dependence of friction coefficient on extrinsic and intrinsic factors at the atomic level. Consequently, in this study the nature of atomic scale friction and the effect of various factors on the friction coefficient and hardness are investigated in detail.

9.2. LITERATURE REVIEW

9.2.1. Experimental Study of Indentation and Sliding Process

While numerous studies has been reported on indentation, sliding, and the anisotropy in hardness and friction on a range of workmaterials, only a limited number of them were directed to aluminum and specifically on single crystal aluminum. In this investigation, since the focus of our study is on the latter, only the literature relevant to indentation and sliding of single crystal aluminum in different crystallographic orientations and direction of sliding are covered. The important conclusions of the studies on other materials are briefly summarized for completeness.

Petty (1962) experimentally investigated the anisotropy in hardness of single crystal aluminum and its relation to the preferred orientation and earing using the Vicker's, Brinell, and Knoop indenters. As the anisotropy in hardness by a Vicker's pyramid or a Brinell ball could not be determined, a less symmetrical Knoop indenter was chosen. The {100}, {110}, and {111} planes of aluminum were indented along different directions. The minimum and maximum hardness on the cube face were found to be along the <110> and <100> directions, respectively. The Knoop hardness on the {110} face of high-purity aluminum was reported to increase as the indenter direction moved from <110> to <100>. The hardness level on the {110} plane was found to be slightly higher than that of {100} plane. This was attributed to the increased resistance to compression offered by the {110} plane. However, it was also stated that this could be due to the differences in the purity of the samples. The {111} plane was reported to

exhibit a lower degree of hardness variation with a minimum in the <110> direction. Petty concluded that the form of variation of hardness with direction depended on the orientation of the surface, which can be related to the patterns in which the available slip systems intersected the surface and also to the interactions between the available slip systems.

Garfinckle and Garlick (1968) conducted Knoop hardness tests on single crystal aluminum of different orientations {(100), (110), and (210)} and indentation directions (<100>, <110>, <210>, <211>, <221>, <421>). They concluded that the hardness anisotropy was essentially dependent on the direction of the long axis of the indenter and not on the plane of indentation. The hardness values were found to be nearly the same for a given direction of indentation regardless of the plane of indentation. For example, on the {100}, {110}, and {210} planes along the <100> direction, they observed the hardness values to be 23.1, 22.6, and 22.1, respectively. Similar results were reported for other combinations of crystallographic orientation and direction of indentation. The maximum and the minimum hardness were reported to be in the <100> and the <111> directions, respectively. With the hardness reported as a function of the indentation direction alone, they suggested the possibility of predicting the hardness anisotropy of a crystal on a standard stereographic triangle.

Based on a number of studies on the anisotropy in hardness and friction of a range of workmaterials by various researchers, the following conclusions may be drawn.

* The anisotropy in hardness is an intrinsic property of all crystalline solids (Bowden and Brookes, 1966).

* The extent of anisotropy in hardness is determined essentially by the crystal structure and the primary slip systems which accommodate dislocation motion during indentation.

* The varying extent of work hardening associated with indentations does not appear to influence the anisotropy (Brookes et al., 1971).

* An increase in strength with a decrease in the deformed area is generally observed. If the stressed volume is small enough that it lies between dislocations, a much higher strength might result.

* Dislocations can propagate in the indented area and hence, can account for the plastic deformation in the region of indentation (Gane and Bowden, 1968).

* An increase in the hardness value with decreasing indentation depth (Chen and Hendrickson, 1971)) is observed.

* The dislocation density in the regions surrounding the indenter has an effect on the hardness (Pharr and Oliver, 1989). An increase in the hardness occurs due to difficulty with which the dislocations are nucleated in the near surface region.

* Frictional anisotropy is reported to disappear below a critical load (~0.1 N), which is proportional to the square of the radius of curvature of the stylus, implying a critical contact pressure for Hertzian deformation (Enomoto and Tabor, 1981).

* The plastic strain field after indentation is complicated and multiple slip systems have to be activated at the same time (Vlassak and Nix, 1994).

9.2.2. Experimental Study of Atomic Scale Friction

Atomic Force Microscopy (AFM) and Scanning Tunneling Microscopy (STM), introduced a decade or so ago, following the pioneering work of Binnig and Rohrer in 1982, are used extensively to investigate tribological interactions, such as adhesion, contact formation, friction, wear, microindentation etc.

Mate et al. (1987) conducted pioneering atomic scale friction studies of a tungsten tip on graphite in the load range of 1 μN using an AFM in ambient air. They discovered that as the tip slides over the graphite surface, which has a hexagonal periodic arrangement of surface atoms, the tip experienced a periodic friction force with the same periodicity as the graphite structure, thus relating for the first time the friction force variations with the atomic structure of one of the sliding elements. They reported the friction coefficient to be extremely low and in the range of 0.005-0.015, depending on the tip geometry. Erlandsson et al. (1988) extended the friction studies of a tungsten tip on a muscovite mica and found similar results. Analogous to the graphite-tungsten combination, they found the friction force to vary with the same periodicity as the hexagonal layers of SiO_4 units that form the cleavage planes of mica. They estimated the average friction coefficient to be ~0.09.

Skinner et al. (1971) also reported extremely low friction coefficients (0.005-0.02) for a tungsten tip sliding on graphite surface in vacuum for loads in the range of 10- 400 μN. They considered at length the origin of the frictional force in the case of a tungsten stylus sliding on the basal plane of graphite with little or no deformation. Flaking of graphite was discounted as a possible mechanism for friction at low loads as flaking is produced by a cleavage mechanism and not friction. They also pointed out that plastic deformation or shear is not observed in their experiments. Based on these observations, they proposed that the chief component of friction arise from an adhesion-type mechanism at the stylus/graphite interface. This is very similar to Kaneko's suggestion that friction and wear at extremely light loads are due to surface interaction forces at the atomic level rather than the load (Kaneko et al., 1996).

Rabinowicz (1992) observed high friction coefficients at low loads of 0.001 g, which he attributed to the surface energy of adhesion. These high values are in contrast to the results obtained using AFM's where the friction coefficients has been reported to be

very low (10^{-2} - 10^{-3} range) when the loads applied are in the nanogram range. Significantly higher values for friction force (10^{-6} N) are observed as the load tends to zero, which corresponds to a friction coefficient of infinity (Kaneko et al., 1988).

9.2.3. MD Simulation of Indentation - Sliding and Atomic Scale Friction Process

Pioneering research in the field of MD simulation of indentation was conducted by Landman and his colleagues (1989-1992, 1996) at Georgia Institute of Technology. While some MD simulations of indentation (Hoover et al., 1990; Belak et al., 1993; Landmann et al., 1989-1992, 1996) and sliding (Harrison et al., 1992; Kim and Suh, 1990; Hirano and Shinjo, 1990; Buldum and Ciraci, 1998) studies have been reported in the literature, there are practically no investigations on the indentation and scratching of single crystal aluminum and in specific, the effect of crystallographic orientation. The principal materials for which indentation and sliding that have been studied include Cu (Belak et al., 1993; Yan and Komvopoulos, 1998; Buldum and Ciraci, 1998), Au (Landmann and Luedtke, 1991; 1996), and Ag (Belak et al., 1993). Also, the wide variation in the friction coefficient observed by experimental and simulation techniques is not addressed in detail. The literature pertaining to MD simulation of nanoindentation was covered in detail in Chapter 4. Therefore, in this section, we shall provide only a very brief review of a few examples of MD simulations of the atomic scale friction. In the present investigation, the emphasis of the indentation/sliding studies is not on the details of the indentation process *per se* but to determine the anisotropy in hardness and friction coefficient with crystal orientation.

Landman et. al. (1989) conducted MD simulation of two contacting solids to evaluate the critical shear stress. The failure was reported to take place along the weakest plane of the softer material. In contrast to the low friction coefficients (0.005-0.015) reported using AFM, Landman et al. report friction coefficient values in the range of

0.77. Buldum et al. (1998) conducted MD simulation of nanoindentation and sliding of a Ni tip on a Cu substrate, with a sharp Ni (111) tool on Cu (110) surface and a blunt Ni (001) tip on Cu (001) surface. An embedded atom potential was used to simulate the metallic bonds of Ni and Cu. A quasiperiodic variation in the force was reported during sliding of the sharp Ni tip on the Cu substrate. This was attributed to the stick-slip process involving phase transitions. Accordingly, one layer of the asperity deforms and matches the substrate during the first slip followed by two asperity layers merging into one through structural transition during the second slip. The ratio of the static to kinetic friction force was reported to be ~2.

Kim and Suh (1994) conducted MD simulations of friction for a single atom sliding non-destructively over a triangular surface with a 2D Lennard-Jones potential and a specified normal force. The normal force was kept very low to avoid mechanical interactions such as plowing, asperity deformation, etc. The interfacial interaction was kept strictly repulsive based on the justification that the repulsive forces are short range forces and primarily responsible for supporting loads at the point of contact between two solids under applied force. In the case of static simulations, a periodic oscillation of the tangential force and the normal force as the atom scans the lattice was reported. The friction coefficient was observed to oscillate between -0.8 and 0.8 for a case when the scan height was 1.1 a, where 'a' is the lattice parameter of the surface. In the case of constant force simulations at similar scan height, the friction coefficient was reported to vary between -1.0 and 1.0. Average friction coefficients of ~ 0.05 was reported for elastic interaction between the atom sliding over the work surface. Of course, this value would be much higher had they considered plastic interactions as is the case of atomic scale friction involving material removal.

Shimizu et al. (1998) conducted MD simulation of friction of a rigid diamond-like tool on a single crystal copper in the (111) plane at 1 m/s to investigate stick-slip

phenomena such as those observed using an AFM. A Morse potential was used for the copper atoms and an interaction potential proposed by Inamura and Takezawa (1992) was used between copper and diamond atoms. It may be noted that no diamond potential is actually used in this case. Instead, an infinitely hard indenter was considered. They confirmed the atomic scale stick-slip phenomenon in friction. They, also, reported the average friction coeffients to vary from ~0.5 to 5 while the maximum friction coefficient from ~4-19, depending on the spring constant (5-100 N/m) and spring force (0.1-0.6) of the system used.

Even though, significant research has been reported in the literature on the mechanics of indentation-sliding process at nanometric level, a number of problems still remain. In many of the indentation studies, it is implicitly assumed that there is chemical interaction between the indenter and the workmaterial, while most practical indentation tests are conducted with a tool that is chemically incompatible with the workmaterial. It, thus, appears that in the modeling of the indentation, the tool should be considered as infinitely rigid with no interaction between the indenter and the workmaterial. This can simulate many of the hardness tests with cemented tungsten carbide and diamond indenters when indenting a range of workmaterials. It is, also, not clear whether hardness anisotropy depends on the plane of indentation, or direction of indentation, or a combination.

A wide range of friction coefficient values varying from extremely low (0.005) (Mate et al., 1987), to intermediate values of ~0.13 (Kim and Suh, 1991), to high values of 1.2 (Garzino and Lama, 1995) and 5 (Shimizu et al., 1998) has been reported in the literature. Consequently, there is a genuine concern whether atomic scale friction differs significantly from the macroscopic or even microscopic friction. In nanoscratching, what may be relevant is the value of the friction force at light loads rather than the friction coefficient, as the latter is merely the ratio of the two forces, namely, the scratch force to

the normal force. The numerical value of the ratio can be high even though the values of the individual forces can be extremely low. It may be noted that the use of the scanning probe microscopes, such as AFM and STM involves significant cost, time, and technological constraints. Also, the results can be influenced by such extrinsic factors as surface contaminants, surface state, geometry of the slider, depth of sliding etc. resulting in friction coefficient values much higher or lower than reality.

It should, also, be noted that the experiments reported in the literature relating to the effect of anisotropy are performed at the micrometer level. It would be of great interest to extend this problem to the nanometric-atomic level for many nanotribological applications. The effect of anisotropy on hardness and friction coefficient has not yet been attempted at the atomic level, as previous MD studies of indentation-sliding did not specifically address this problem. The effect of crystallographic orientation and direction of scratching on the friction coefficient are also not well understood. In this investigation, the variation of the indentation and scratching process mechanics with crystallographic factors and the nature of atomic scale friction are discussed in some detail. The effect of crystallographic factors is also discussed in terms of anisotropy in hardness, friction coefficient, forces, force ratio, and specific energy.

9.3. METHODOLOGY OF MD SIMULATION OF INDENTATION/SLIDING

9.3.1. MD Simulation Model and Conditions

Figure 9.1 is a schematic of the model used in the MD simulation studies on atomic scale friction and the effect of crystallographic factors in indentation and scratch tests of single crystal aluminum. Table 9.1 gives the computational parameters, details of the workmaterial and tool dimensions, the indentation/scratch depth, and the length of slide used in the simulations. The simulations were conducted using a Digital a-workstation with a clock speed of 433 MHz. For convenience, an infinitely hard tool was

used in the simulations, as wear of the indenter is not considered. The empirical potential used was a pairwise sum of Morse potentials.

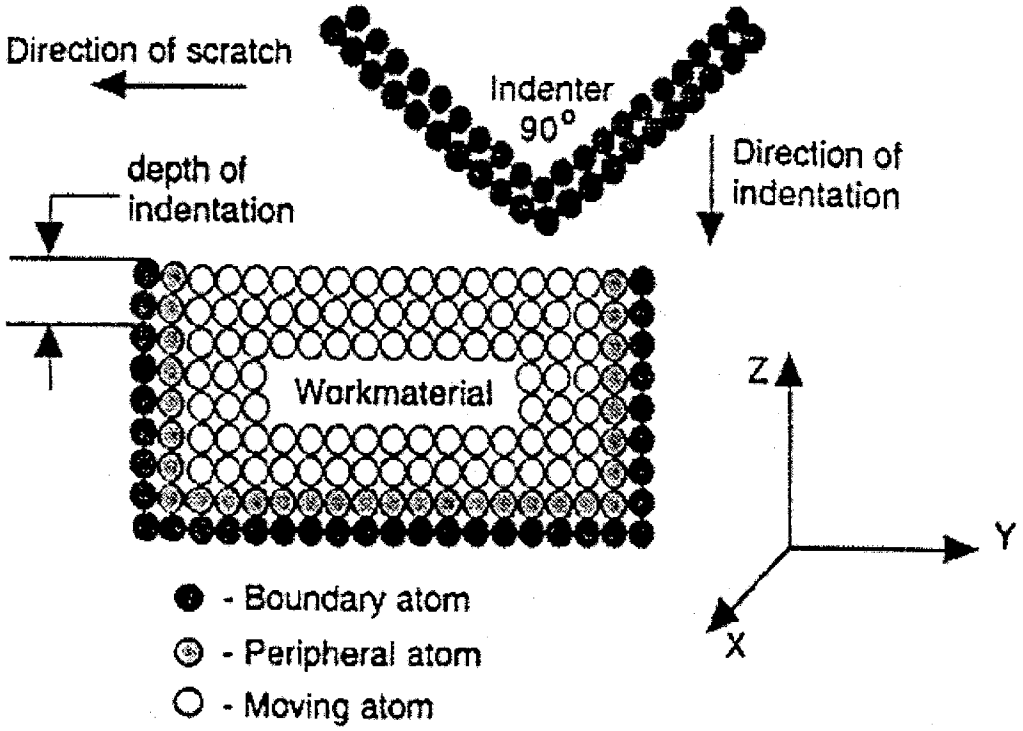

Figure 9.1. Schematic of the indentation-scratch model used in the MD simulation

MD simulations of indentation and scratching were conducted on single crystals of aluminum to study the effect of crystallographic factors, namely, crystal orientation, and indentation and scratch directions. Indentation and scratching were conducted along specific combinations of the orientation of the work material {(111), (110), (001), and $(\bar{1}20)$} and scratch direction <$[\bar{1}10]$, $[\bar{2}11]$, [100], [210], and [221]> at a speed of 500 m s^{-1}. The indentation/scratch depth was maintained constant at 0.81 nm in all simulations. The specific combinations for the (111) z-axis are the 'y' directions $[\bar{1}10]$ and $[\bar{2}11]$, for the (110) z-axis are the 'y' directions $[\bar{1}10]$ and [001], for the (001) z-axis are the 'y' directions $[\bar{1}10]$ and [100], and for the $(\bar{1}20)$ z-axis the 'y' direction is [210] and for the

$(01\bar{2})$ z-axis the y-direction being [221] respectively. In the following discussion, the crystal set-up is referred to as (z)<y>. For example, (001)<100> represents the crystal being set-up with (001) as the z-axis and <100> as the y-axis. The planes perpendicular to the 'z' and the 'y' axis have the same Miller indices. For example, the plane perpendicular to <100> direction will be (100). The indentation is performed along the z-axis and the scratch is performed along the y-axis.

Figure 9.2 shows the various crystal orientations and the corresponding directions for cubic materials. It should be noted that while the simulation size of the workmaterial is maintained constant (Table 9.1) the number of planes and consequently, the total number of atoms considered in the simulation size depend on the crystal orientation. Consequently, the indentation/scratch width will change with orientation and scratch direction. While, the workmaterial orientation is varied, the tool orientation is maintained constant in all the simulations (Table 9.1).

To simulate sliding at extremely small depths (in the order of nm), MD simulations of nanoindentation followed by nano-scratching were conducted on a single crystal aluminum (with (001)[100] combination of crystal orientation and [100] direction of scratching) at extremely fine scratch depths (0.8 nm to almost zero). Values of the forces, the specific energy, the friction coefficient, the indentation hardness, and the scratch hardness for various scratch depths and crystallographic orientations were determined. The emphasis of the current investigation is not on the details of the indentation/scratching process but to study the nature of atomic scale friction and frictional anisotropy.

Table 9.1. Computation parameters used in the MD simulation of Al

Configuration	3-D indentation-scratch
Potential used (potential parameters for the workmaterial)	Morse potential (D_L=0.2703 eV, α_L=1.1646 / A, r_{eL}=3.253 A and r_c=5.624 A)
Workmaterial dimension	6ax25ax15a, a-lattice constant
Number of atoms in the workmaterial based on crystal set-up	Crystal set-up No. of atoms (111) [$\bar{1}$10] -> 5131 (111) [$\bar{2}$11] -> 5092 (110) [$\bar{1}$10] -> 4550 (110) [001] -> 4382 (001) [$\bar{1}$10] -> 4998 (001) [100] -> 4410 (01$\bar{2}$) [221] -> 4802 ($\bar{1}$20) [210] -> 4940
Indenter dimension	6ax15ax15a, a-lattice constant 2551 total tool atoms
Indenter material	Infinitely hard
Indenter edge radius	Sharp edge
Indenter rake angle	-45°
Indenter included angle	90°
Indentation/ scratch depth	0.81 nm
Width of scratch	2.12 nm
Indentation/ scratch speed	500 m/sec
Bulk temperature	293 K

It may be noted that width of the indenter was kept the same as the width of the workmaterial and the tool center coincided with the workmaterial origin during indentation-sliding. Even though, in practice, the indenter's width is smaller than the workmaterial width, this approach is adapted here for a better visualization of the deformation process during MD simulation, which will not be the case when the width of the indenter is smaller than the workmaterial. In that respect, the indenter has a 2-D geometry. The semi-included angle of the indenter was 45°. This corresponds to a -45° negative rake angle of the indenter during the scratch process.

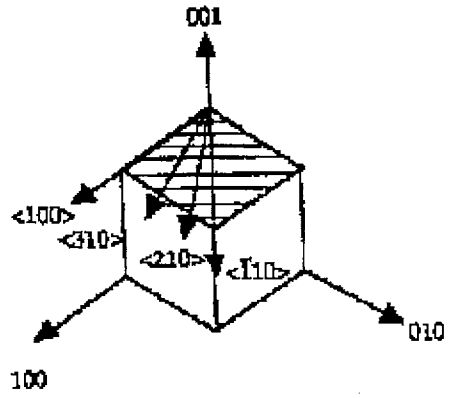

(001) Plane

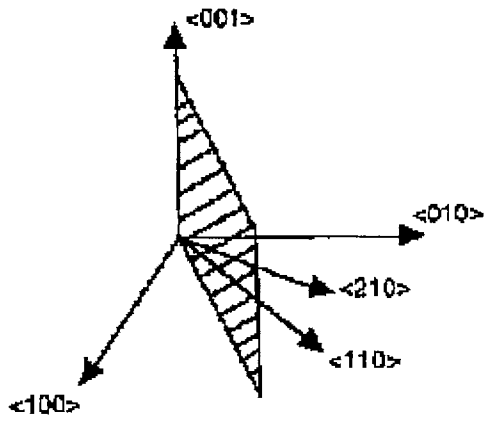

(-120) plane

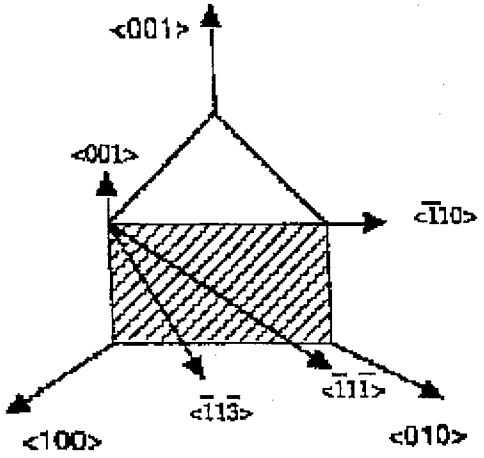

(110) Plane

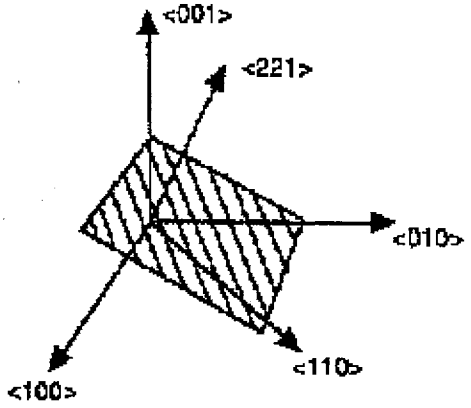

(01-2) plane

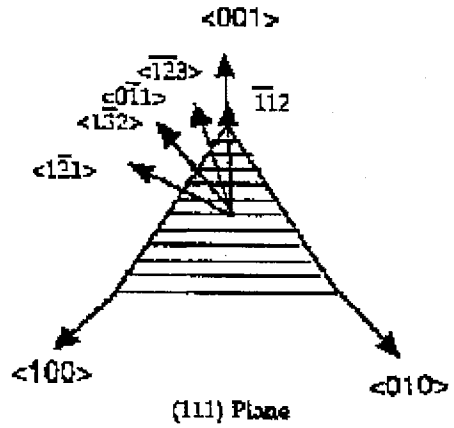

(111) Plane

No.	Indentation/ Scratch Plane	Scratch Direction
1	(111)	[1̄10]
2		[2̄11]
3	(110)	[110]
4		[001]
5	(001)	[110]
6		[100]
7	(1̄20)	[210]
8	(012̄)	[221]

Figures 9.2. Schematic showing various crystal orientations and the corresponding directions for cubic materials

9.4. RESULTS AND DISCUSSION

9.4.1. Effect of Crystal Orientation and Indentation/Scratch Direction

9.4.1.1. M.D. Simulation Results

In the following, results of MD simulation of the indentation-scratch process on single crystal aluminum in different orientations and scratch directions are presented to investigate the process dependence on crystallographic factors. It may be noted that the description of the process is based not only on the simulation plots but also on the detailed studies conducted of the animations of the MD simulation process. Since, scratching of a single crystal aluminum in various orientations and scratching directions with the indenter, in the present investigation, is somewhat similar to the nanometric cutting of a single crystal aluminum in various orientations and cutting directions with a 10^{o} rake tool reported earlier (Chapter 6), they will be compared where appropriate. It should, however, be noted that the scratching tests were conducted with the indenter presenting a high negative rake angle (-45^{o}) while the nanometric cutting was performed with a positive rake tool (10^{o}).

Figures 9.3 (a) - (e) show various stages of the MD simulation of the indentation-scratching test with the workmaterial set-up in the $(111)[\bar{1}10]$ orientation. Figure 9.3 (a) shows a zone of disturbed material (~8 layers) from the surface (covering the entire length) extending into the workmaterial in the form of an inverted trapezium prior to contact by the indenter. Prior to this the atoms were found to be in the relaxed condition. The trapezium is symmetrically located with respect to the workmaterial even though the indenter is approaching at one end. It is also not clear what role the boundary atoms play in truncating the sides of the trapezium. In addition, some voids or missing atoms can also be seen. These are attributed to the initial attractive forces followed by repulsive

forces experienced by the workmaterial atoms as the indenter approaches. As will be shown shortly, the zone of disturbed (shape and size) material prior to contact by the indenter on the workmaterial was found to vary with the orientation. The maximum was observed along the $(111)[\bar{1}10]$ orientation. It should be pointed out that the initial disturbance in the workmaterial was not observed in the case of nanometric cutting [Figure 6.6 (a)]. This might be due to the presence of the boundary atoms between the workmaterial and the tool as the tool approaches the workmaterial. Animation of the indenter approaching the workmaterial in the present investigation showed compression of the top layers of the workmaterial as a result of an increase in the forces as the work-indenter separation distance was decreased.

Figure 9.3 (b) shows indentation into the workmaterial and the displacement of some atoms from the workmaterial towards the surface. The pile up is higher on the right of the indenter, due to placement of the boundary atoms closer to the indentation site on that side. The wide zone of disturbed material, which was present prior to indentation into the workmaterial, was no longer present during the indentation process under the indenter. The length of the trapezium on the surface is reduced and is determined by the contact point of the indenter at the surface. Figure 9.3 (c) shows the indenter at the maximum indentation depth and just prior to the initiation of the scratch process, showing a small region of plastically deformed material directly underneath the indenter. In addition, slip along the sides of the indenter can also be seen.

Figure 9.3 (d) is an intermediate stage of the scratch process showing displacement or pile-up of material ahead of the indenter in the form of a chip similar to machining with a high negative rake angle (here, it is -45^{o}) or plowing. It may be noted that in nanometric cutting of single crystal aluminum [Chapter 6] with a 10^{o} positive rake tool, for a similar orientation and cutting direction, i. e. $(111)[\bar{1}10]$, dislocations moving

parallel to the cutting direction were clearly observed [Figures 6.6 (a) - (d)]. Also, the animation studies showed the zone of disturbed material under the tool to disappear due to elastic recovery once the tool had passed the machined zone. In the current study, due to the formation of a band of disturbed material in the workmaterial underneath and ahead of the indenter, it was difficult to observe clearly the movement of dislocations parallel to the direction of scratching during the indentation process (extensive compression) [Figure 9.3 (d)]. Also, the atoms in the disturbed region have to be rearranged during the indentation process. Animation of the scratching process showed slip to take place on layers of material parallel to the cutting direction ahead of the indenter (within the scratch depth). In nanometric cutting, the deformation ahead of the tool was in the form of compression combined with shear along the cutting direction with the $(111)[\bar{1}10]$ orientation. In this study, compression ahead of the indenter to a greater extent can be observed from Figure 9.3 (e). It may be noted that the $(111)[\bar{1}10]$ combination involves the densest plane with scratching performed along the close packed direction. Figure 9.3 (e), the final stage of the scratch process, shows considerable amount of subsurface deformation, estimated to be equal to the indentation-scratch depth. In nanometric cutting [Chapter 6], for a 10^{o} rake tool the subsurface deformation for similar conditions was observed to be much lower [Figure 6.6 (d)]. This suggests that with increase in the negative rake, the extent of subsurface deformation increases. Some elastic recovery of the workmaterial following the indentation-scratch process can also be observed from Figure 9.3 (e) and animation of the process. The material removal process during scratching is predominantly plowing due to high negative rake angle of the indenter.

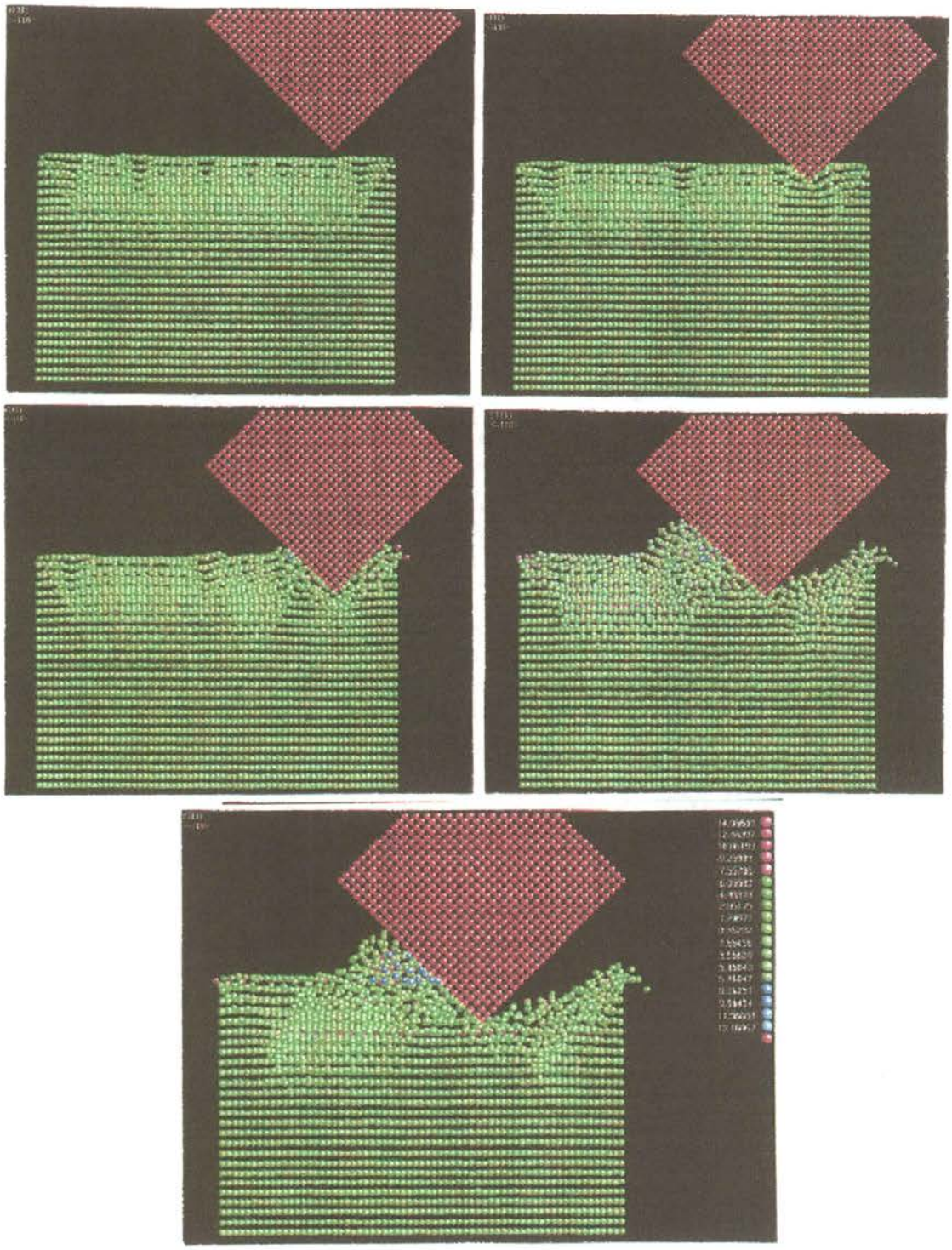

Figures 9.3 (a) – (e) Stages of MD simulation of indentation – scratching of Al workmaterial with (111)[-110] orientation

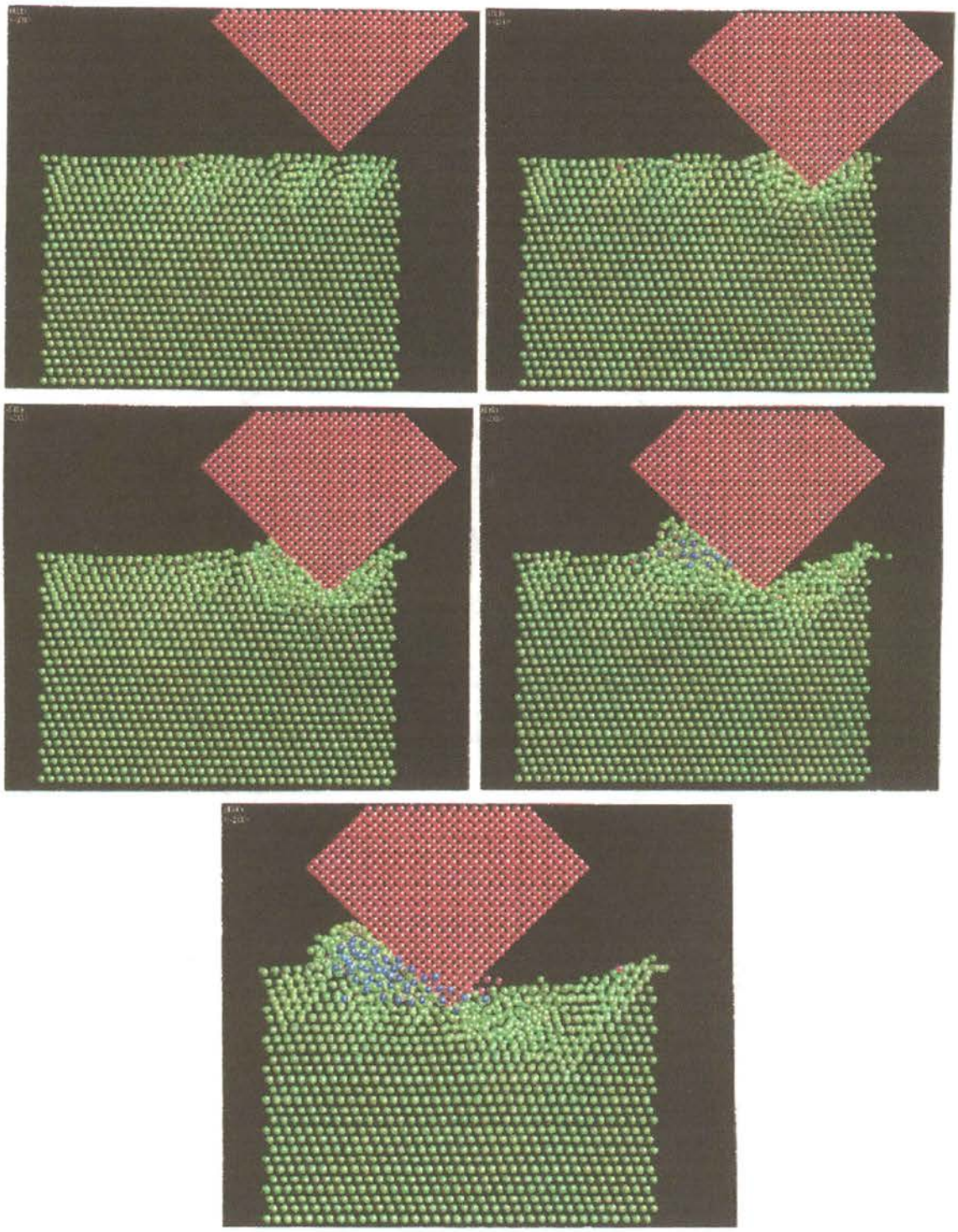

Figures 9.4(a) – (e) Stages of MD simulation of indentation – scratching of Al workmaterial with (111)[-211] orientation

Figures 9.4 (a) - (e) show the stages of the MD simulation of the indentation-scratching process with the workmaterial set-up in the (111)[$\bar{2}$11] orientation. Figure 9.4 (a) shows the initial disturbance in the form of trigons (in the shape of inverted triangles with each triangle slightly separated from each other) near the surface of the workmaterial prior to contact with the indenter. However, the extent of this disturbance is less in comparison to the (111)[$\bar{1}$10] orientation [Figure 9.3 (a)] indicating differences in the forces experienced by the workmaterial prior to contact by the indenter. Figure 9.4 (b) shows the plastic deformation to be concentrated around as well as the sides of the indenter. Figure 9.4 (c) shows the indenter at the maximum indentation depth (0.81 nm) and just prior to the initiation of the scratch process. The deformation around the indenter as well as the region of deformation appears to be quite extensive [compare Figures 9.4 (c) and 9.3 (c)]. Also, the trigon under the indenter is no longer prominent due to extensive plastic deformation [Figure 9.4 (c)]. The amount of pile-up of the workmaterial seems to be higher in this case compared to the earlier orientation [compare Figures 9.4 (c) and 9.3 (c)].

Figure 9.4 (d) is an intermediate stage of the scratch process showing displacement or pile-up of material ahead of the indenter in the form of a chip similar to machining with a high negative rake angle (-45^{o}). The deformation in the chip in the form of slip appears to be taking place predominantly parallel to the tool face [Figure 9.4 (e)]. In the case of nanometric cutting [Chapter 6] for a similar crystal orientation with a 10^{o} rake tool, dislocations were found to be generated $\sim 60^{o}$ to the cutting direction in the workmaterial [Figures 6.7 (a) - (d)]. In the present investigation, due to large negative rake angle of the indenter, the direction of slip seems to be controlled by the tool rake face. However, their presence can be seen in Figure 9.4 (e) in the machined surface after

the indenter had advanced during scratching. Incidentally, the two sides of the inverted trigons observed prior to indentation were also formed at 60^{o} to the scratch direction. Comparison of Figures 9.3 (e) and 9.4 (e) indicates higher elastic recovery with the (111)[$\bar{2}$11] orientation than (111)[$\bar{1}$10]. The subsurface deformation and the chip volume appear to be lower with the (111)[$\bar{2}$11] orientation compared to (111)[$\bar{1}$10] [Figure 9.3 (e)].

Figures 9.5 (a) - (e) show stages of the MD simulation of the indentation-scratching process with the workmaterial setup in the (110)[001] orientation. Figure 9.5 (a) shows practically negligible initial disturbance on the top layers of the workmaterial. Animation studies of the indentation process indicated that what little disturbance that was present was distributed uniformly. Figure 9.5 (b) and (c) are stages of indentation. They, along with the animation studies, show dislocations generating underneath the tip of the indenter in the direction of indentation and moving towards the free surface of the workmaterial. A similar observation was made in nanometric cutting with a 10^{o} rake tool with the dislocations generating both below and above the workmaterial in the shear zone [Figures 6.9 (a) - (d)]. Significant differences in the shape of the deformation region in the work material due to indentation can be observed depending on the crystal orientation [compare Figures 9.3 (c), 9.4 (c), and 9.5 (c)]. It was, also, reported that this mode of deformation was unique as no such mode was observed in conventional machining. In the scratch process, because of the large negative rake of the indenter, the deformation of the material was found to occur nearly parallel to the indenter face [Figures 9.5 (d) and (e)]. This suggests that the geometry of the tool can strongly affect the mode of dislocation generation and propagation even though the crystal orientation and other factors remain the same. Figure 9.5 (e) also indicates that the chip volume and subsurface deformation to be slightly lower than the other two cases discussed so far [Figures 9.3 (e) and 9.4 (e)].

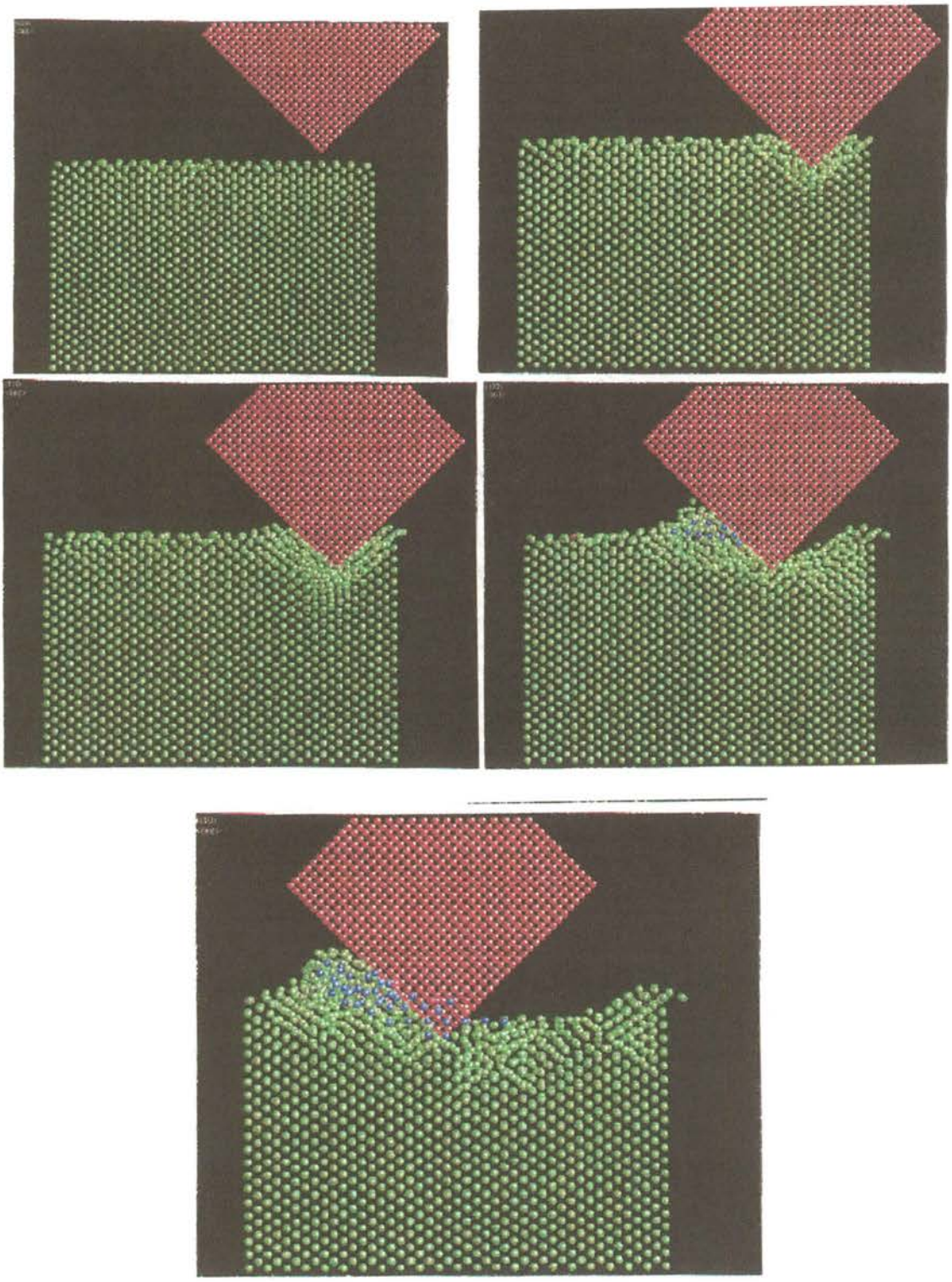

Figures 9.5 (a) – (e) Stages of MD simulation of indentation – scratching of Al workmaterial with (110)[001] orientation

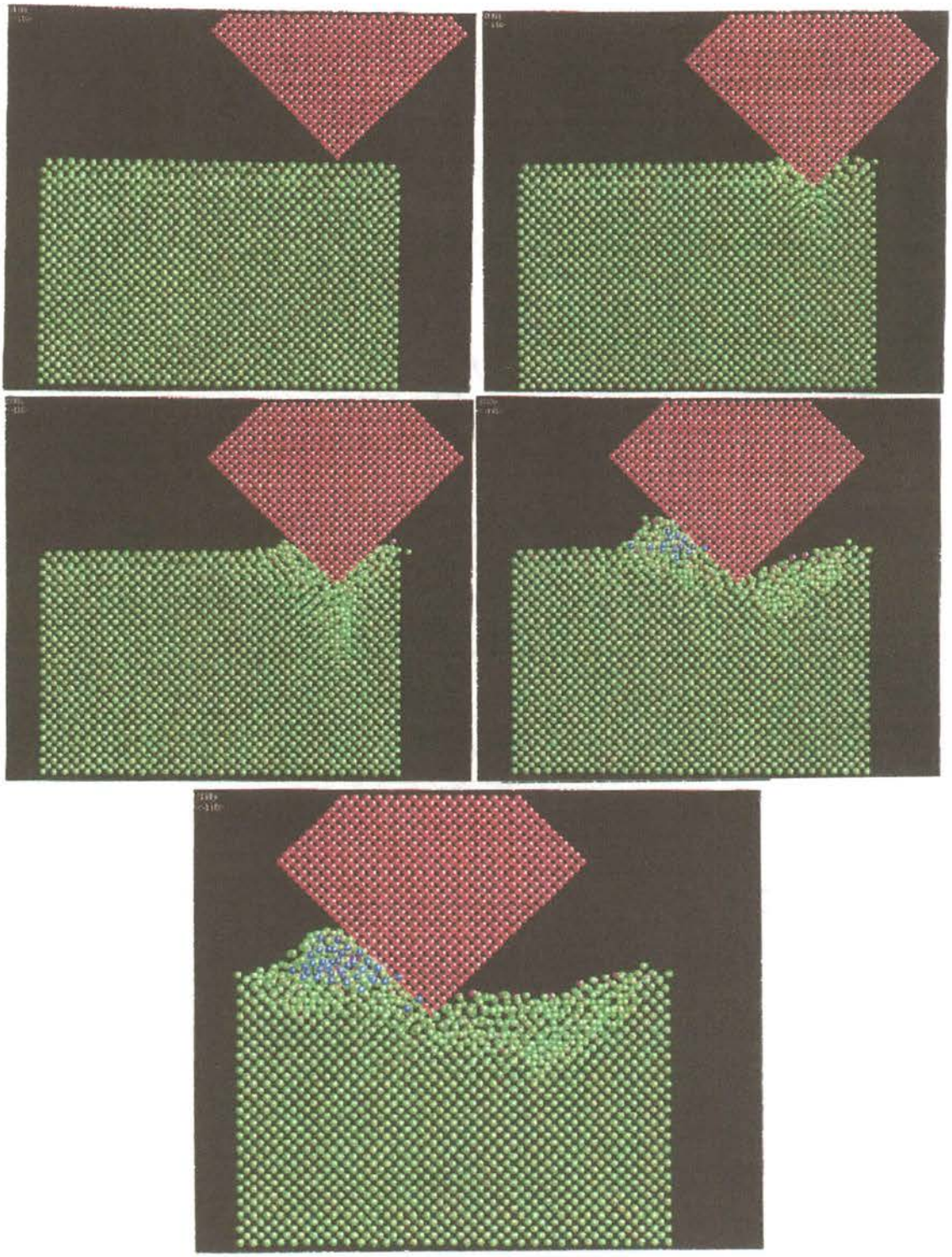

Figures 9.6 (a) – (e) Stages of MD simulation of indentation – scratching of Al workmaterial with (110)[-110] orientation

Figures 9.6 (a) - (e) show various stages of the MD simulation of the indentation - scratching process performed with the (110)[$\bar{1}$10] orientation. Figure 9.6 (a) shows practically negligible disturbance in the workmaterial prior to the contact of the indenter. Figure 9.6 (b) shows the amount of initial deformation to be minimal and around the indenter. Indentation along [$\bar{1}$10] direction on the crystal with (110)[$\bar{1}$10] orientation generated dislocations both parallel and perpendicular to the indentation direction although the former were more obvious [Figure 9.6 (c)]. A similar observation was made in the MD simulation of nanometric cutting for a similar orientation [Figures 6.8 (a) - (d)]. This is attributed to the fact that [110] is the easy slip direction and when either indented or machined along that direction will generate dislocations along <110> direction. Cross slip from the indenter's tip towards the free surface and into the workmaterial can be observed from Figure 9.6 (c). As the indenter moved along the [$\bar{1}$10] direction the dislocations generated underneath the tool disappear due to elastic recovery [Figure 9.6 (d)].

Comparison of Figures 9.5 (d) and 9.6 (d) suggests a higher degree of plastic deformation ahead of the tool with the (110)[001] orientation. However, in the previous study [Chapter 6], (110)[$\bar{1}$10] crystal set-up was observed to show higher degree of plastic deformation ahead of the tool in contrast to the current observation. The degree of elastic recovery seems to be higher with the current crystal set-up. Figure 9.6 (e) shows the final stage of the indentation-scratch process. The elastic recovery can be observed to be higher than that experienced with (111) combinations [Figures 9.3 (e) and 9.4 (e)]. However, the chip volume is lower than (111)[$\bar{1}$10] [Figure 9.3 (e)] and (111)[$\bar{2}$11] [Figure 9.4 (e)] and seems to be nearly equal to that of (110)[001] orientation [Figure 9.5 (e)]. The subsurface deformation can be estimated to be nearly equal to the scratch depth [Figure 9.6 (e)] and is higher in comparison to (110)[001] orientation [Figure 9.5 (e)].

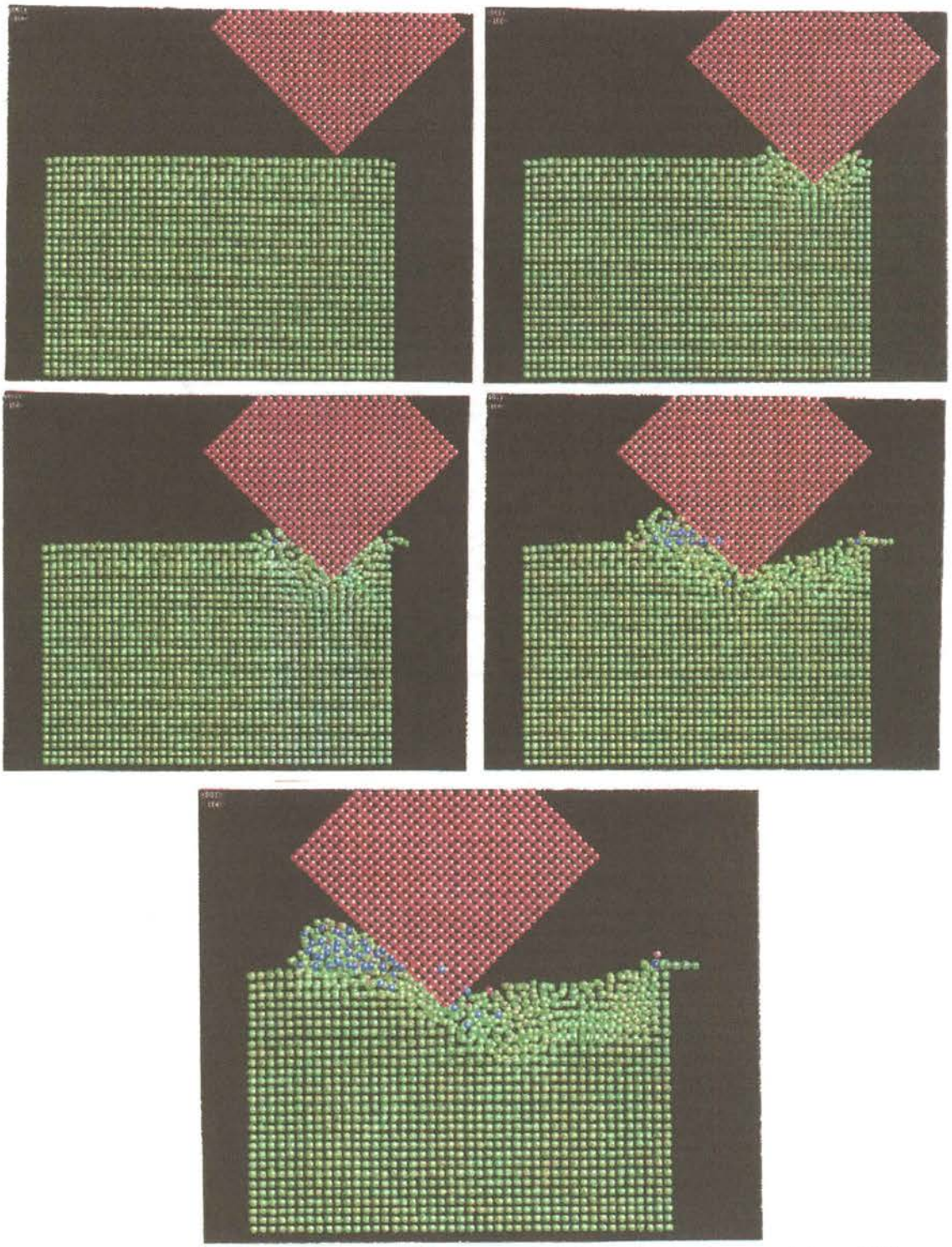

Figures 9.7 (a) – (e) Stages of MD simulation of indentation – scratching of Al workmaterial with (001)[001] orientation

Figures 9.7 (a) - (e) show various stages of the MD simulation of the indentation - scratching process performed with the (001)[100] orientation. Negligible disturbance in the work material prior to the contact of the indenter was observed [Figure 9.7 (a)]. No visible dislocation pattern was observed during the initial stages of the indentation process. Initiation of dislocations at ~45^{o} into the workmaterial was observed during the animation (at maximum depth) but were observed to be highly elastic in nature. Consequently, as soon as the scratch process commences, the dislocations were observed to rearrange or escape towards the free surface. Figure 9.7 (c) shows the final stage of the indentation process wherein the workmaterial is largely undisturbed except for the region around the indenter. Displacement of atoms towards the free surface of the workmaterial by the indenter can be observed from Figure 9.7 (c). Figure 9.7 (d) is an intermediate stage of the scratch process along [100] direction showing the material removal taking place as in conventional machining with the generation of a chip via the shear zone. However, the dislocations propagating at ~45^{o} into the workmaterial and ~45^{o} in the shear zone which was clearly observed in nanometric cutting [Figures 6.11 (a) - (d)] was not observed during the scratch process. Figure 9.7 (e), the final stage of the scratch process, shows that the deformation ahead of the indenter in the scratch process is rather limited. The elastic recovery is significantly higher and is comparable with (111)[$\bar{2}$11] orientation [Figure 9.4 (e)]. The subsurface deformation is comparable with the (110)[$\bar{1}$10] crystal set-up [Figure 9.6 (e)].

Figures 9.8 (a) - (e) show various stages of the MD simulation of the indentation - scratching process performed with the (001)[$\bar{1}$10] orientation. Figure 9.8 (a) shows that only the top layer is disturbed prior to the indenter's contact with the workmaterial. Figure 9.8 (b) shows the progress of indentation. It is interesting to note dislocations propagating along the [$\bar{1}$10] direction which is perpendicular to the direction of

indentation, even before the commencement of the scratch process. This is found to be unique to this particular combination of crystal set-up. Dislocations propagating parallel to the cutting direction ([$\bar{1}$10]) were also observed in nanometric cutting for similar crystal combination ((001)[$\bar{1}$10]) in nanometric cutting [Figures 6.10 (a) - (d)]. As scratching progresses [Figures 9.8 (d) and (e)], the number of dislocations propagating along the scratch direction was observed to increase. This is because [$\bar{1}$10] is the close packed direction for the FCC crystal set-up and consequently, slip is predominant when scratching along [$\bar{1}$10] direction. In the earlier study [Chapter 6] additional dislocations moving parallel to the cutting direction even below the depth of cut was observed [Figures 6.10 (a) - (d)]. However, no such additional dislocations are seen propagating in the current study.

Figures 9.9 (a) - (e) show various stages of the MD simulation of the indentation - scratching process performed with the ($\bar{1}$20)[210] orientation. Figure 9.9 (a) shows minimal disturbance of the top layer of the workmaterial prior to the indenter's contact with the workmaterial. Figures 9.9 (b) and (c) show the deformation limited to the region around the indenter. Figures 9.9 (d) and (e) show two stages during the scratch process. Slip seems to take place along the [210] direction although modified by the large negative rake angle presented by the indenter as the indenter moves during the scratch process. Plastic deformation is limited to a small region ahead of the tool with the subsurface deformation extending to ~3-4 layers beneath the scratch depth.

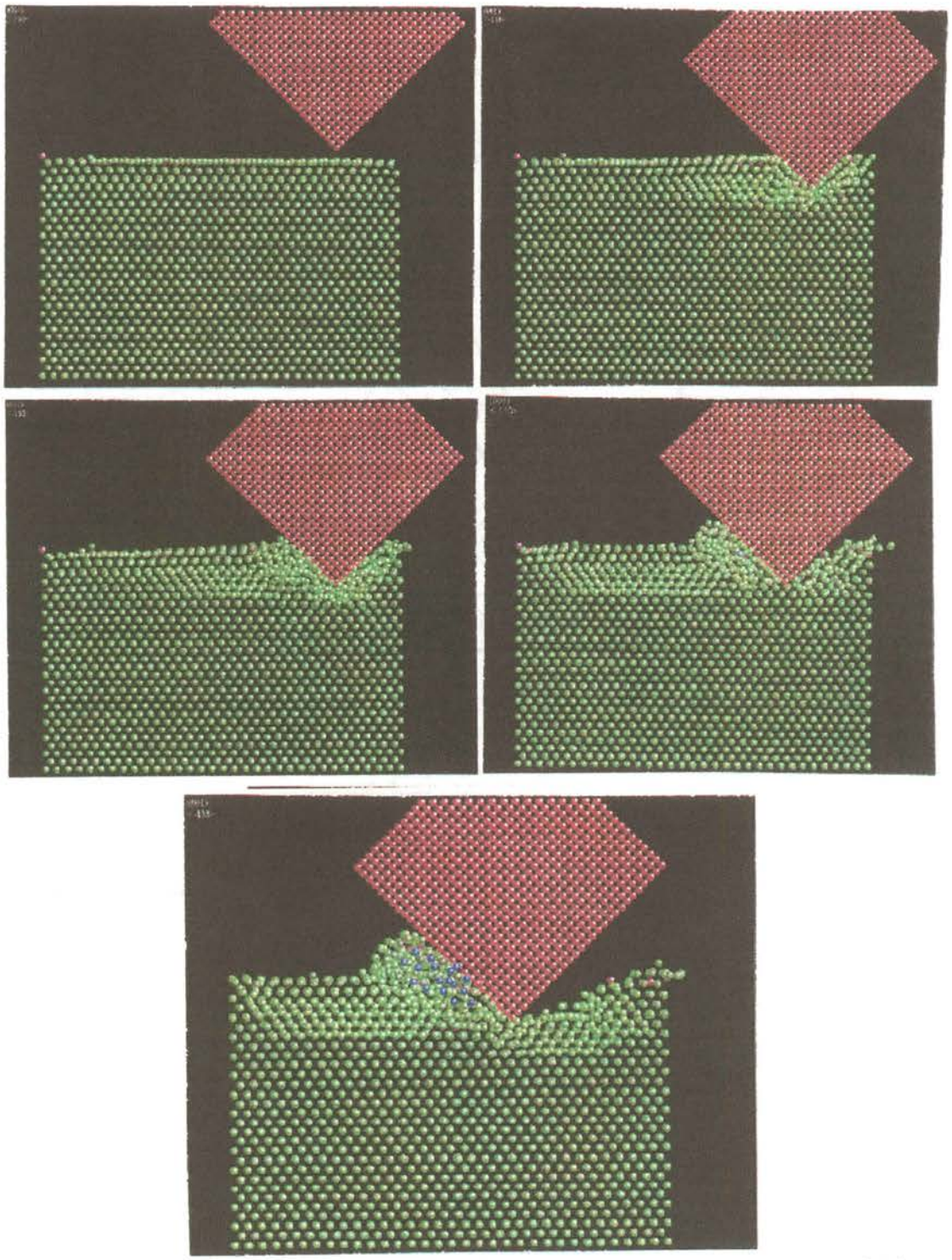

Figures 9.8 (a) – (e) Stages of MD simulation of indentation – scratching of Al workmaterial with (001)[-110] orientation

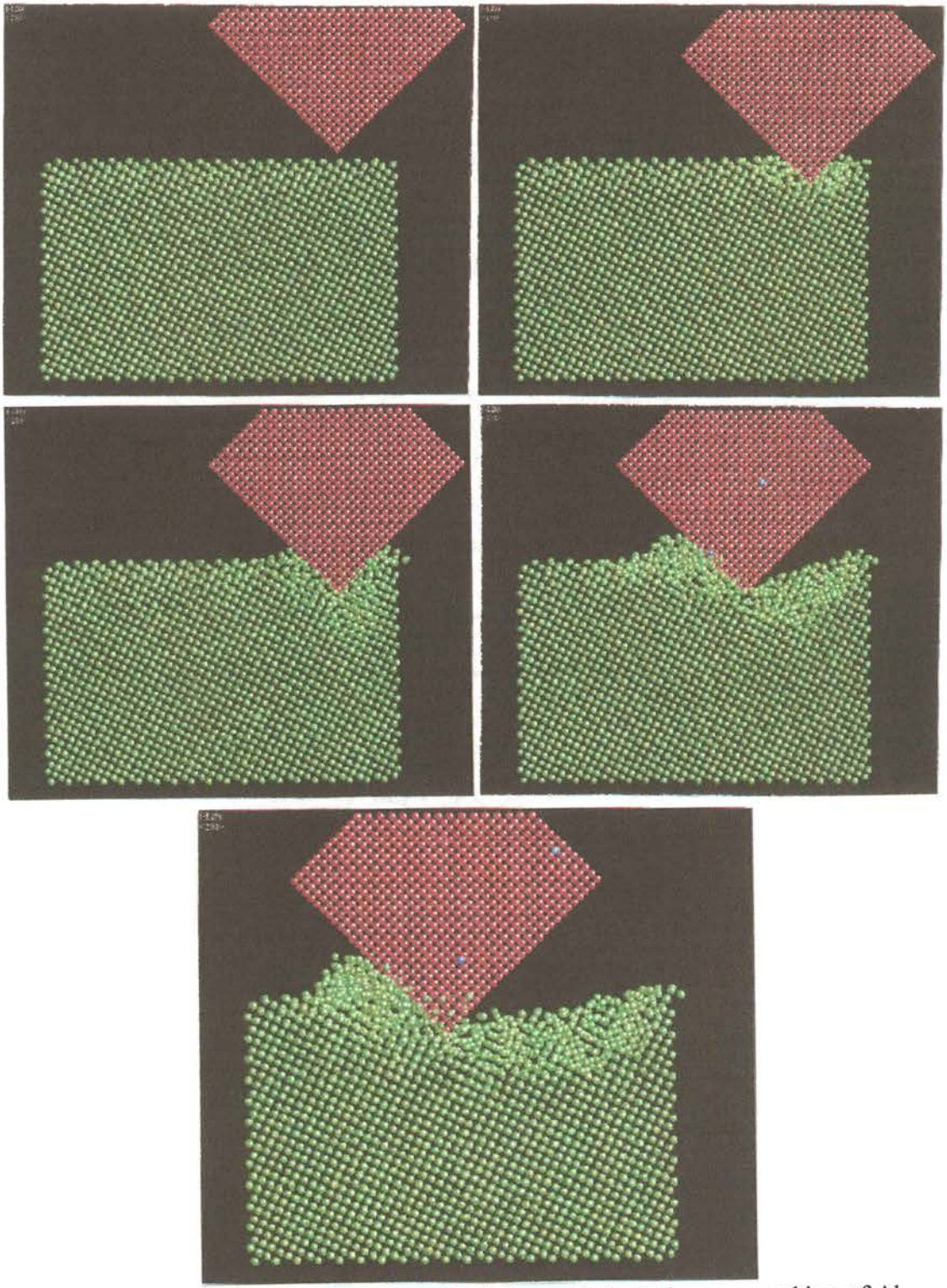

Figures 9.9 (a) – (e) Stages of MD simulation of indentation – scratching of Al workmaterial with (-120)[210] orientation

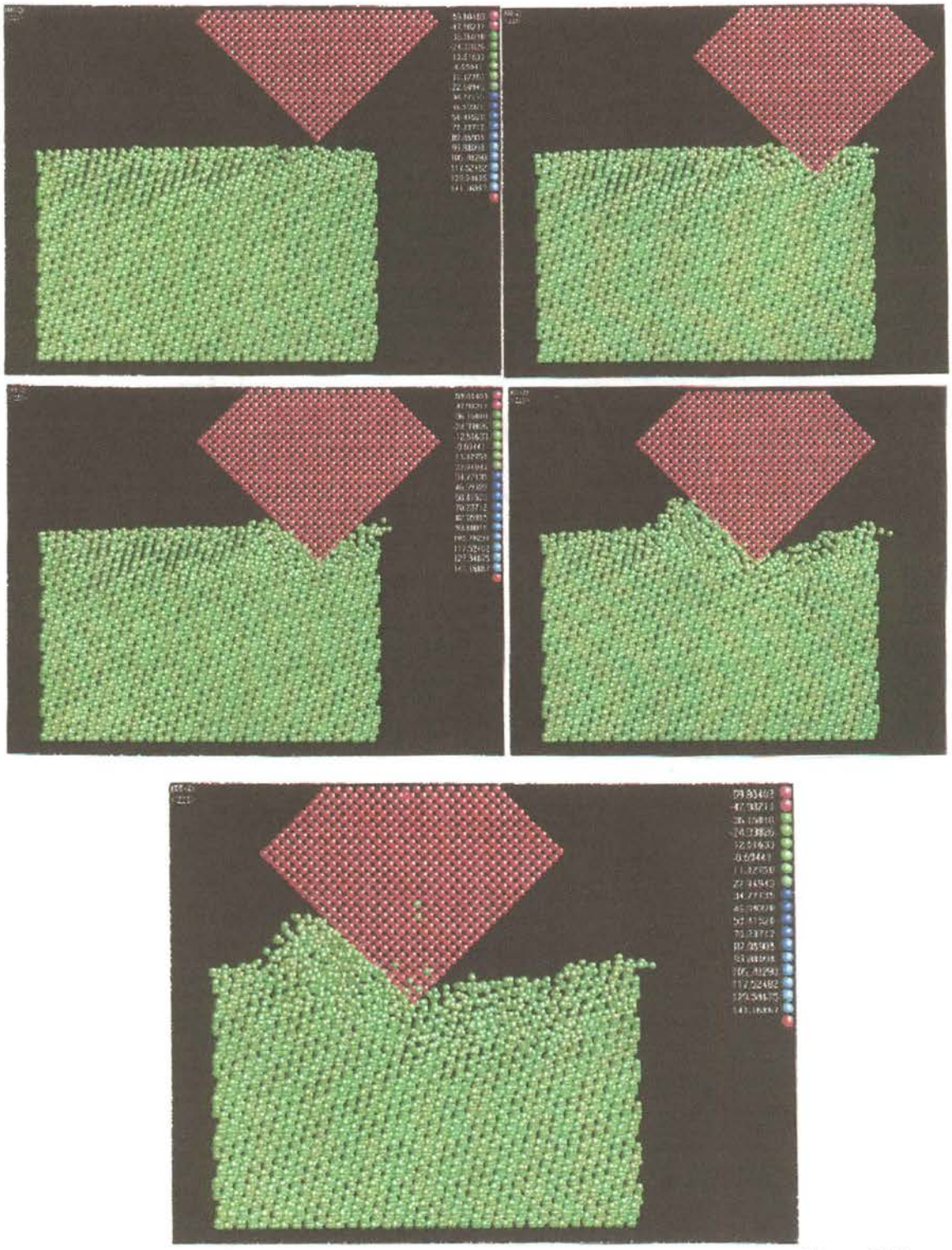

Figures 9.10 (a) – (e) Stages of MD simulation of indentation – scratching of Al workmaterial with (01-2)[221] orientation

Figures 9.10 (a) - (e) show various stages of the MD simulation of the indentation - scratching process performed with the $(01\bar{2})[221]$ orientation. Some initial disturbance of the top layers of the workmaterial prior to the indenter's contact with the workmaterial was observed [Figure 9.10 (a)]. Deformation is concentrated near the indenter during indentation [Figures 9.10 (a) and (b)] and takes place parallel to the indenter face during scratching [Figures 9.10 (d) and (e)]. It may be noted that this orientation resulted in minimum forces.

In Figures 9.3 to 9.10 (a) - (e), the generation and propagation of dislocations can be seen contrary to some of the experimental work where no dislocations were reported for indentation depths of less than 50 nm (Pharr and Oliver, 1989). During indentation, dislocations were observed to propagate both parallel and perpendicular to the indentation direction in the case of $(110)[\bar{1}10]$ combination. Dislocations propagating parallel to the indentation direction are observed in the case of $(001)[\bar{1}10]$ combination. Some of these dislocations have been found to escape towards the free surface or rearrange themselves to proper crystal symmetry, due to elastic recovery as the indenter was removed from the workmaterial or moved away from the indent during scratching. The amount of plastic deformation during indentation was observed to be maximum on the (111) plane with different directions of indentation investigated. The pile up of the workmaterial around the tool was observed to be maximum in the case of $(111)[\bar{2}11]$ combination. During sliding, the elastic recovery was observed to be minimum for the case of $(001)[\bar{1}10]$ combination and maximum for the $(111)[\bar{2}11]$ combination. The elastic recovery in the case of (001)[100] combination is found to be comparable to that of $(111)[\bar{2}11]$ combination. The subsurface deformation towards the end of the sliding process was observed to be maximum for the case of (111) and the directions of sliding considered with subsurface deformation along $[\bar{1}10]$ scratch direction slightly higher than that of

[$\bar{2}$11]. The minimum subsurface deformation was observed in the case of (001)[$\bar{1}$10] orientation. The chip volume at the end of the scratch process was observed to be maximum for the case of (111)[$\bar{1}$10] combination and minimum in the case of ($\bar{1}$20)[210] combination. The dislocations do facilitate the initiation of the plastic deformation as seen above, in addition to the vacancies as mentioned by Belak *et al.* (1993) [observed during the animation process]. The presence of vacancies supplement the hypothesis proposed by Belak *et al.* (1993) that plasticity in the case of small scale indentation is likely due to creation and movement of point defects.

9.4.1.2. On the nature of variation of the forces prior to indentation

A comparison of Figures 9.3 (a) - 9.10 (a) shows that the disturbance of the workmaterial prior to indenter's nominal contact to be maximum in the case of (111)[$\bar{1}$10] and (111)[$\bar{2}$11] combinations, and then by (110)[001] and (001)[$\bar{1}$10] combinations. Insignificant or practically no disturbance was observed for the other combinations, namely, ((110)[$\bar{1}$10], (001)[100], (01$\bar{2}$)[221], and ($\bar{1}$20)[210]) studied. Since the response of the workmaterial atoms prior to indenter's contact is different for different crystal set-ups, the corresponding forces prior to indenter's contact should also exhibit similar differences. In order to study this phenomenon, force data were collected during the initial stages of indentation prior to indenter's contact with the workmaterial.

Figures 9.11 (a) to (h) show the variation of the normal (indentation direction) and tangential forces (scratch direction) with distance along the direction of indention prior to the contact of the indenter with workmaterial for various crystal set-ups. It can be seen that as the indenter approaches the work, the force interactions commence at ~0.2 nm. Coincidentally, this is about half the jump-to-contact (JTC) reported by Landman and

Luedtke (1992, 1996) and Buldum and Ciraci (1998). However, in their cases, both the workmaterial and the indenter are free to interact whereas, in the present investigation, only the workmaterial is free and the indenter is infinitely rigid. Thus, the disturbance of the workpiece atoms when the indenter approaches nearly 0.2 nm appears reasonable. The workmaterial in the present investigation is aluminum, whereas Landman and Luedtke were using gold and Buldum and Ciraci were using nickel as the work material, respectively. Consequently, the material differences can also account partially for the differences in the magnitude of the initial forces prior to the contact of the indenter. Also, the surfaces of the workmaterial in different orientations are not atomically smooth but are affected by the size of the atoms, the lattice spacing, the crystallographic orientation, and direction of sliding. Thus, the roughness of the surface on an atomic level will vary depending on the workmaterial as well as its crystallographic orientation and this can affect the initial forces as the indentation process commences.

The frequency of oscillation as well as the magnitudes of the forces tends to vary with the crystallographic orientations. It can be seen that maximum force variations occur in the case of (111)[$\bar{1}$10] and (111)[$\bar{2}$11] crystal set-ups. This is reflected by significant disturbance of the workmaterial in both the cases [Figures 9.3 (a) and 9.4 (a)]. It is, however, not clear why the magnitude of force is not significantly higher in the former case, as significant disturbance in the form of an inverted trapezium is observed in the first case and less disturbed, only trigons in the second case. In the case of (001)[$\bar{1}$10], (110)[001], and (001)[100] combinations, there is some disturbance of the workmaterial atoms near the surface and this is reflected by a smaller magnitude of forces. In contrast, very little disturbance of the workmaterial atoms was observed in the cases of ($\bar{1}$20)[210]) and (110)[$\bar{1}$10], and this is reflected in very small variation of the forces not until the indenter is close to 0.05 nm from the workmaterial surface.

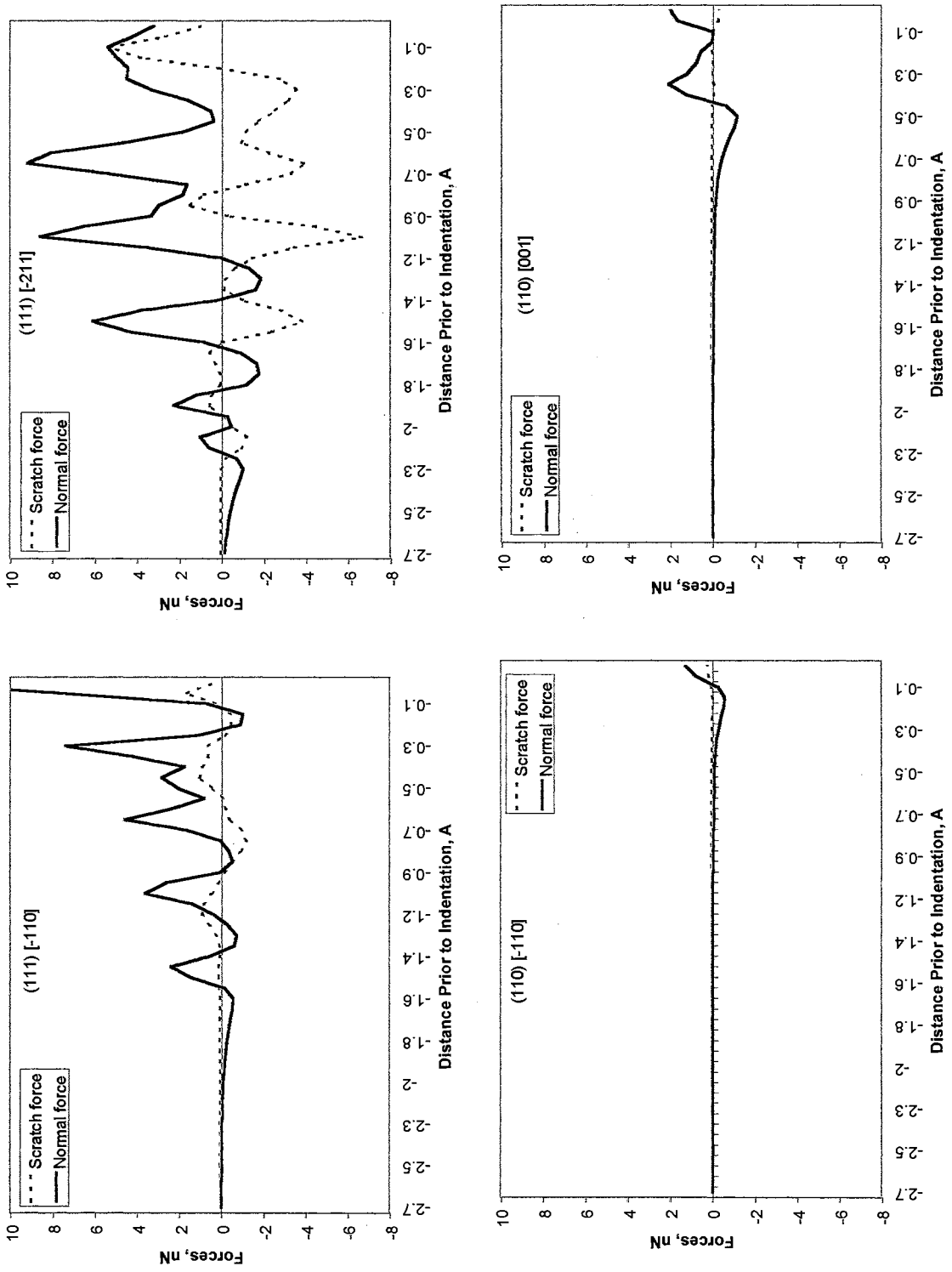
(111) [-211]
(111) [-110]
(110) [001]
(110) [-110]
Scratch force
Normal force
Forces, nN
Distance Prior to Indentation, A

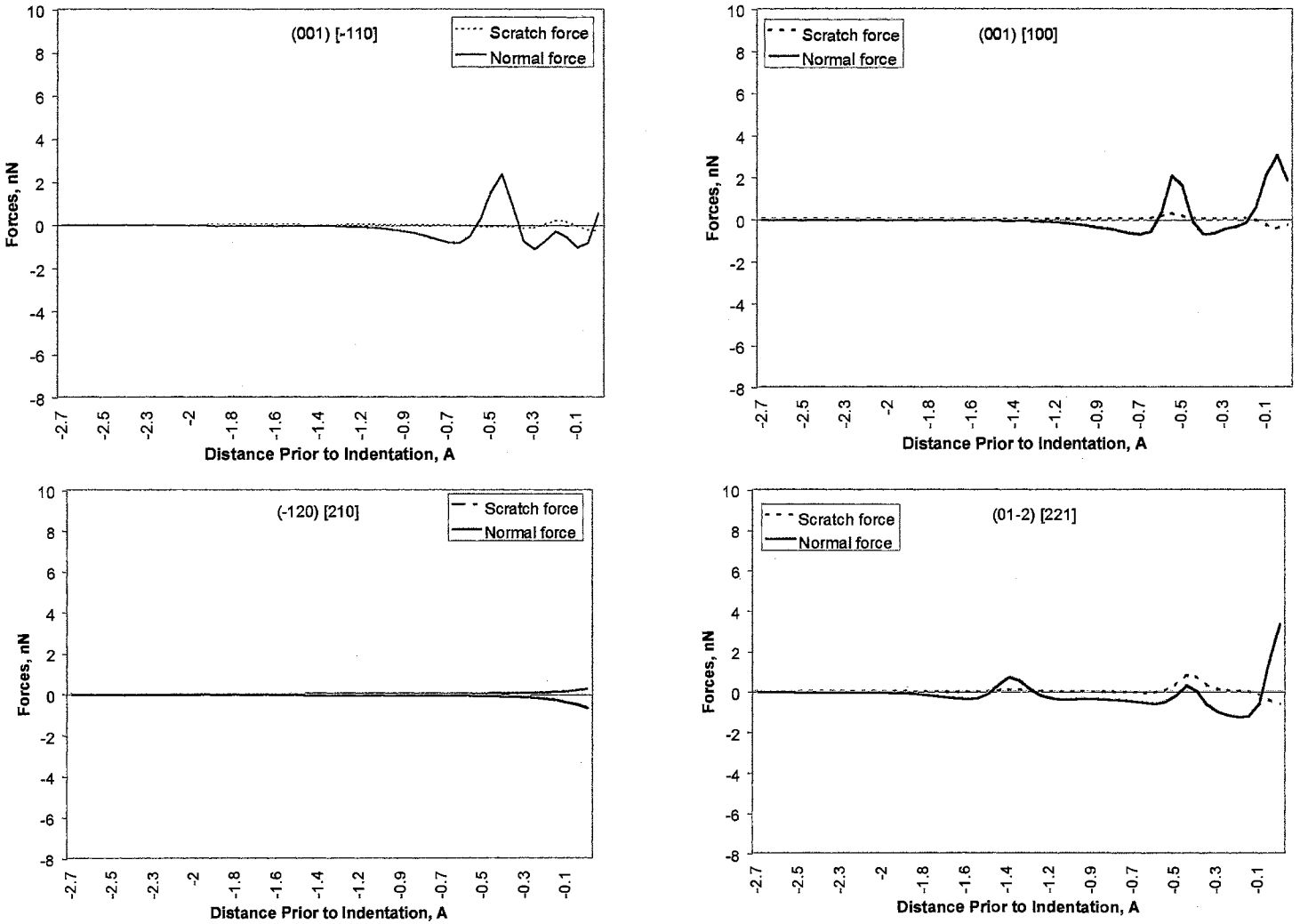

Figures 9.11 (a) - (h) Variation of the normal (indentation direction) and tangential forces (scratch direction) with distance along the direction of indention prior to the contact of the indenter with workmaterial for various crystal set-ups

9.4.1.3. Some quantitative analysis of the lattice disturbances, subsurface deformation, and chip Volume

In order to quantitatively estimate the lattice disturbance prior to indentation, subsurface deformation at maximum indentation depth and after scratching, elastic recovery, and number of atoms in the chip after scratching for various crystal orientations and scratch directions, the workmaterial was divided into various zones as shown schematically in Figure 9.12.

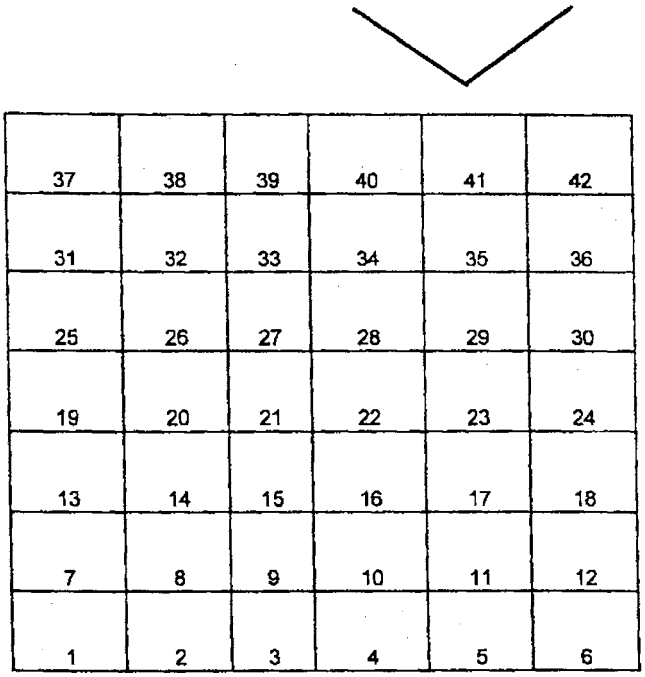

Figure 9.12. Schematic of the work showing division of the workmaterial into zones

In order to evaluate the above quantities a new variable termed, "the atom count ratio" is defined as follows:

$$\text{Atom count ratio (R)} = \frac{N_t}{N_{eq}}$$

where, N_t and N_{eq} are the number of atoms in a particular zone at time t and at equilibrium, respectively. This ratio was evaluated at three time instants, namely, prior to indentation, at maximum indentation depth, and after retraction, and plotted against the corresponding zone number.

Standard deviation of the atom count ratio from the mean was also evaluated for different combinations of crystal orientation. The biased method (n-method) was used for evaluating the standard deviation of the atom count ratio curves which defines how widely the ratio is dispersed from the average value of 1. The formula used to determine the standard deviation of the atom count ratio is given in the following:

$$\sqrt{\frac{n\Sigma x^2 - (\Sigma x^2)}{n^2}}$$

where, x is the value of the atom count ratio and n is the total number of values, which will be 42 in the current study (42 zones in the workmaterial).

Figures 9.13 (a) - (h) show the variation of the atom count ratio (ACR) in various zones for different combinations of crystal orientation and scratch direction, respectively. In the graphs, one can observe that zones 1 through 24 are nearly unaffected by the indentation/scratching process (for example, consider the (111)[$\bar{1}$10] [Figure 9.13 (a)] and (110)[$\bar{1}$10] [Figure 9.13 (c)] combinations). This suggests that, in the current study, the height of the crystal is sufficient to avoid boundary effects along the height of the crystal. With some combinations, for example (111)[$\bar{2}$11] [Figure 9.13 (b)], we observe minor fluctuations of the atom count ratio in zones 1 through 24. This is attributed to the movement of a few atoms across the zone boundaries, which are strictly defined. When the coordinates of these atoms were monitored, it was observed that the change was in the farther decimal digits (4th or 5th decimal digit). This small change in the ACR can be due

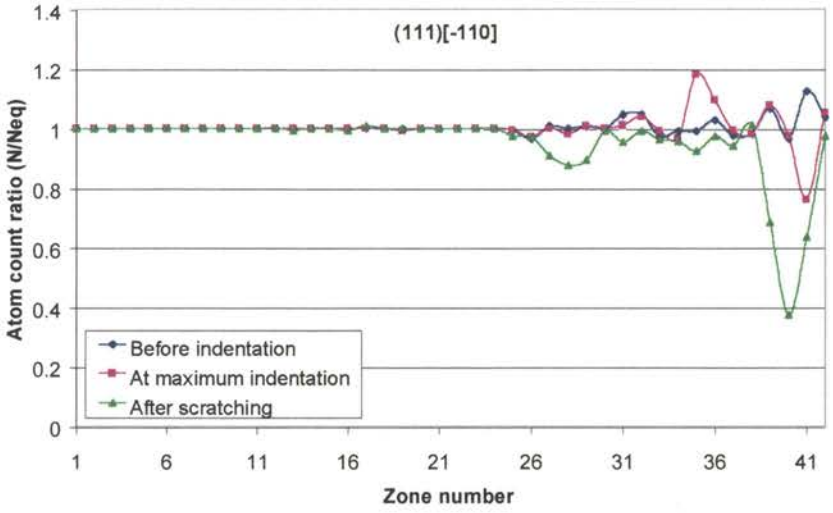
(111)[-110]
Atom count ratio (N/Neq)
Zone number
Before indentation
At maximum indentation
After scratching

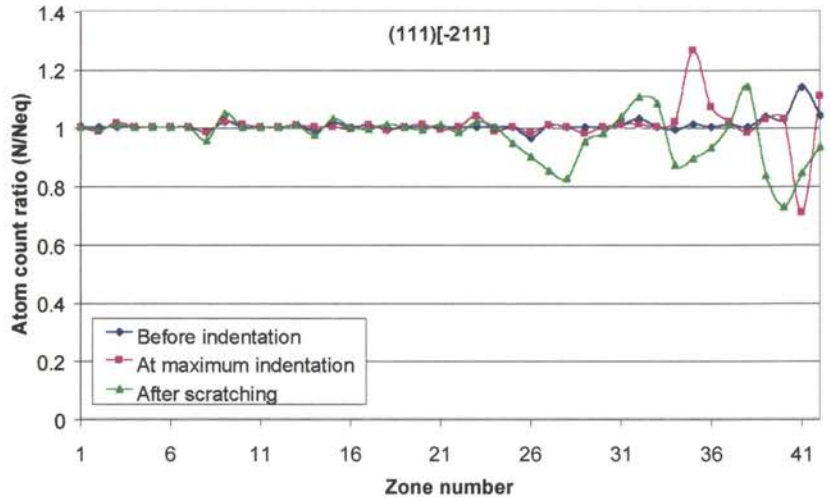
(111)[-211]
Atom count ratio (N/Neq)
Zone number
Before indentation
At maximum indentation
After scratching

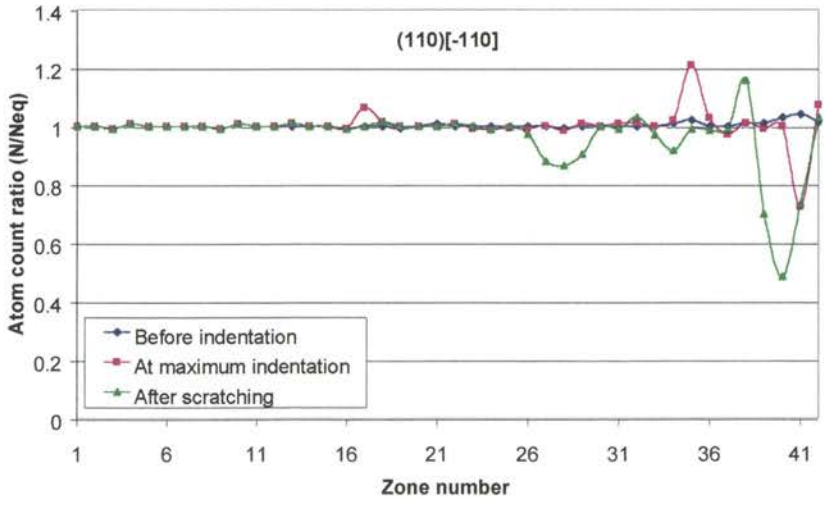
(110)[-110]
Atom count ratio (N/Neq)
Zone number
Before indentation
At maximum indentation
After scratching

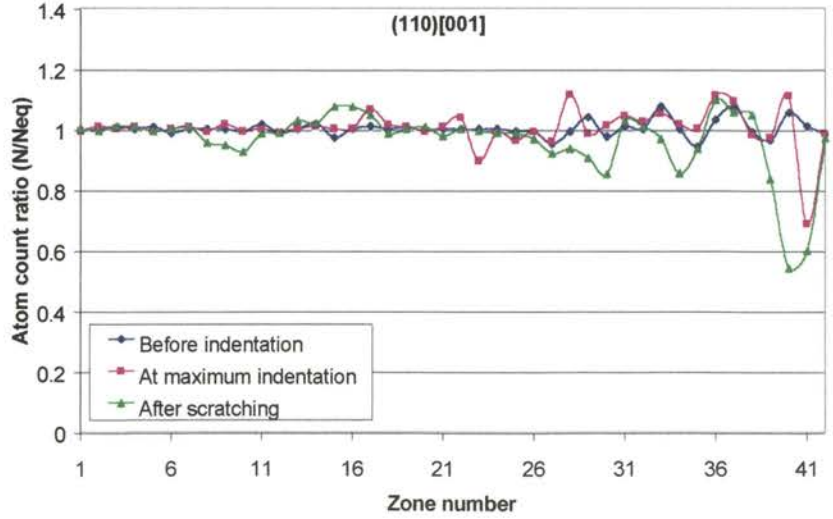
(110)[001]
Atom count ratio (N/Neq)
Zone number
Before indentation
At maximum indentation
After scratching

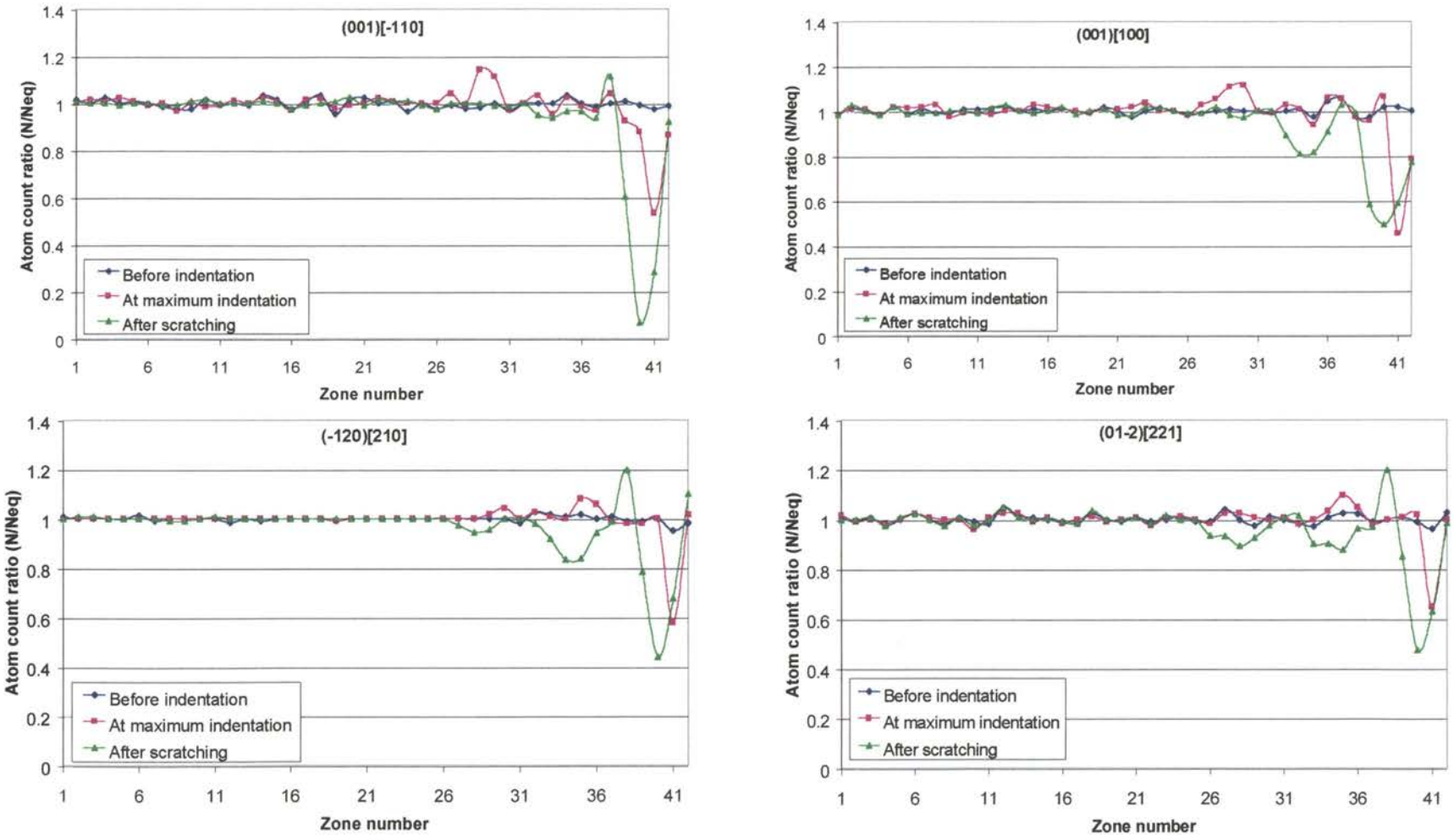

Figures 9.13 (a) - (h) Variation of the atom count ratio (ACR) in various zones for different combinations of crystal orientation and scratch direction, respectively

to the atomic vibrations or shock waves propagated through the crystal during scratching. This results in a change in the atom count ratio. Consequently, these small variations are not considered as lattice disturbances but rather as the dynamic fluctuation of the atom count ratio. It is interesting to note that the dynamic fluctuation of the atom count ratio is different for different crystallographic orientations. If one would consider these fluctuations to be due to atomic vibrations or shock waves then it is appropriate to consider that these properties also vary with crystal orientation and scratch direction.

In the following discussion atom count ratio curves for two combinations, namely, (111)[$\bar{1}$10] [Figure 9.13 (a) and (110)[$\bar{1}$10] [Figure 9.13 (c)], will be discussed in detail. Comparison of the atom count ratio curves prior to indentation in Figures 9.13 (a) and (c) suggest higher lattice disturbances in the case of (111)[$\bar{1}$10] combination in comparison to (110)[$\bar{1}$10] combination. This was, also, observed earlier from Figures 9.3 (a) and 9.6 (a). At maximum indentation depth, the atom count ratio in zone 41 is significantly low for both combinations. This is because this zone is the indented zone and the atoms in this zone are being pushed to the side and lower zones. Consequently, both graphs show an increase in the atom count ratio in zones 42, 40, 39, 36, 35, and 34 which are the zones immediately surrounding the indent. The increase in the atom count ratio for zone 35 is slightly higher in the case of (110) [$\bar{1}$10] combination [Figure 9.13 (c)] in comparison to (111)[$\bar{1}$10] combination [Figure 9.13 (a)]. This can be attributed to the dislocations propagating parallel to the indentation direction with (110)[$\bar{1}$10] combination [Figure 9.13 (c)] which were not observed with the (111)[$\bar{1}$10] combination [Figure 9.3 (c)]. In the case of (110)[$\bar{1}$10] [Figure 9.13 (c)] the atom count ratio remains around 1 from zone 26 to zone 18. However, zone 17 shows an increase in the atom count ratio. Once again, this might be due to the dislocations propagating parallel to the indentation direction with

this particular combination. With (110)[$\bar{1}$10] we observed the indentation damage to penetrate deep into the workmaterial [Figure 9.13 (c)] but the radius of the damaged zone [Figure 9.6 (c)] was not large in comparison to (111)[$\bar{1}$10] combination [Figure 9.3 (c)]. Similar analysis was also applied to the atom count ratio after scratching and repeated for the other orientations as well.

Figures 9.14 (a) - (d) show the variation of standard deviation of atom count ratio, number of chip atoms, elastic recovery, and subsurface deformation for various orientations. Table 9.2 tabulates the corresponding numerical values. Also, in Table 9.2 each combination of crystal orientation is given an orientation number which is used in Figures 9.14 (a) - (d). The elastic recovery was estimated as the ratio of the number of total atoms in zones 33, 34, 35, 39, 40, and 41 after scratching to that at equilibrium. The higher this ratio, the higher is the elastic recovery of the orientation. Subsurface deformation is estimated from the atom count ratio curves. Based on the deviation of the atom count ratio from its mean value, the zone up to which damage extends is evaluated. From this, the subsurface deformation is defined in terms of number of atomic layers. It should be noted that while the subsurface deformation for two orientations might be same in terms of number of atomic layers along the depth direction, it might vary significantly in its radius. Hence, caution should be exercised when interpreting these quantitative results.

Figure 9.14 (a) shows a high standard deviation of atom count ratio prior to indentation for (111)[$\bar{1}$10] and (111)[$\bar{2}$11] combinations. The lowest is observed with the (110)[$\bar{1}$10] combination. Similar results were, also, observed from the MD simulation plots [Figures 9.3 (a), 9.4 (a), and 9.6 (a)]. At maximum indentation depth, the standard deviation is maximum with (001)[100] crystal set-up and minimum with

(111)[$\bar{1}$10] crystal set-up. After scratching, the standard deviation is maximum with (001)[$\bar{1}$10] orientation and minimum with (111)[$\bar{2}$11] orientation. Figure 9.14 (b) plots the variation of the number of chip atoms showing maximum with (111)[$\bar{1}$10] combination and minimum with ($\bar{1}$20)[210] combination. Figure 9.14 (c) plots the variation of elastic recovery with orientation where maximum and minimum elastic recovery are observed with (111)[$\bar{2}$11] and (001)[$\bar{1}$10] combinations, respectively. This is in agreement with the MD simulation plots [Figures 9.4 (e) and 9.8 (e)]. Figure 9.14 (d) shows the variation of the subsurface deformation for various orientations prior to, at maximum depth, and after scratching. Prior to indentation we observe maximum and minimum subsurface deformation with (111)[$\bar{1}$10] and (110)[$\bar{1}$10] combinations which is in agreement with the simulation plots [Figures 9.3 (a) and 9.6 (a)]. This was also stated earlier based on the forces prior to indentation [Figures 9.11 (a) - (h)]. Reasonable agreement was also obtained for the subsurface deformation at maximum indentation depth and after scratching.

9.4.1.4. On the Nature of Variation of Forces and Energy

In general, indentation tests are conducted at constant load. However, in this investigation, a constant velocity condition is used instead for convenience. Consequently, the indentation force is taken as the average of the forces during the entire indentation process. The hardness of the workmaterial is evaluated as the average force over the contact area of the indenter with the workmaterial. The specific energy is defined, as the energy required for removing unit volume of the workmaterial. The friction coefficient is evaluated as the ratio of the scratch force over the normal force, where the forces are the average values over the scratch length. The scratch hardness was calculated as the average normal force during scratching over the deformation supporting area of the indenter.

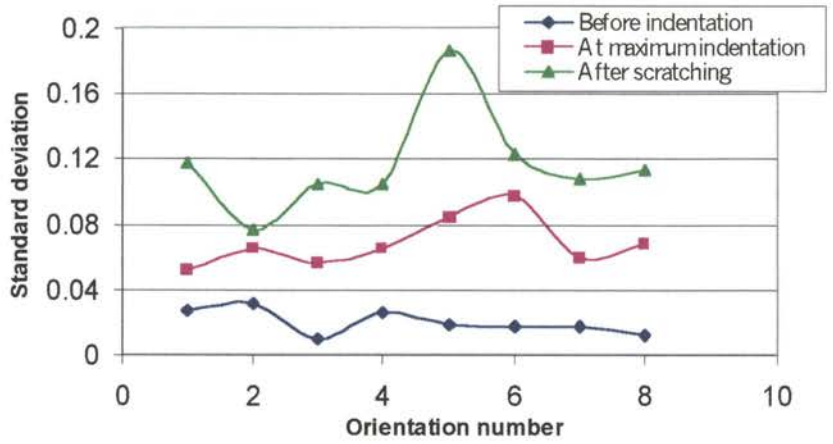

(a)

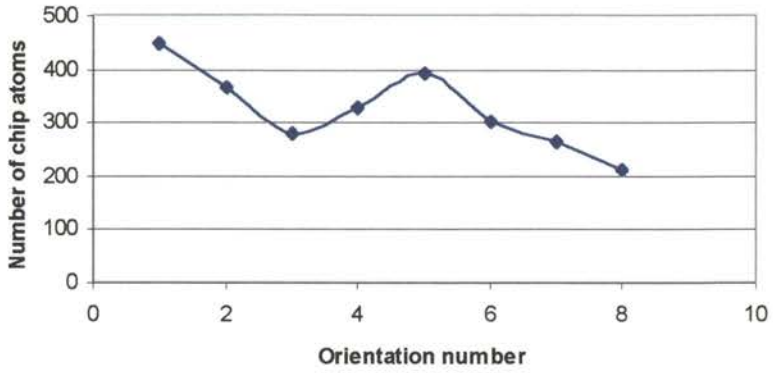

(b)

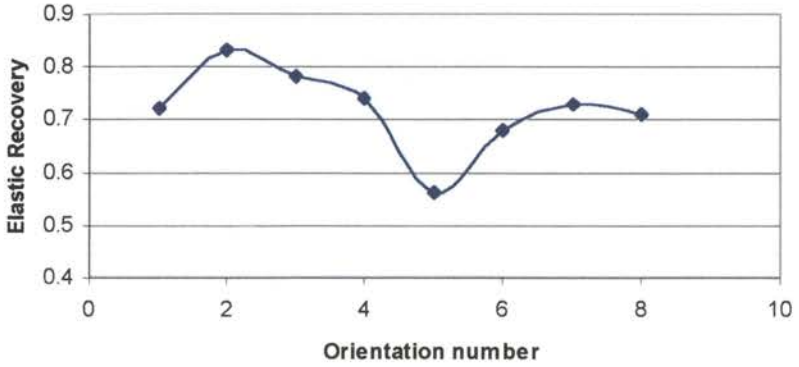

(b)

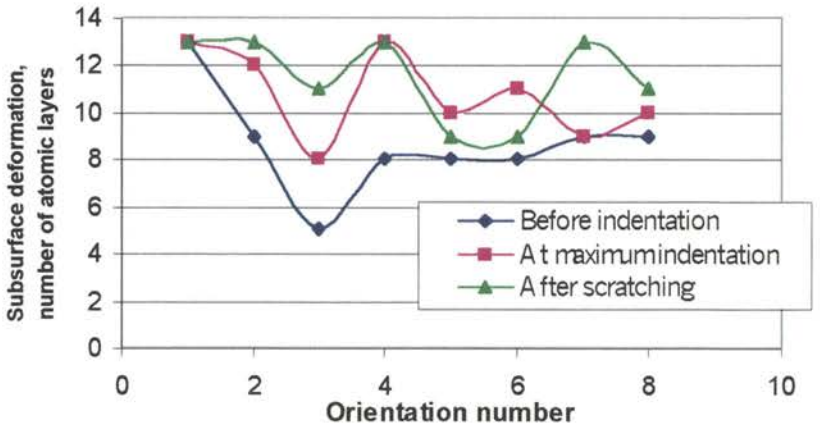

(d)

Figures 9.14 (a) - (d) Variation of standard deviation of atom count ratio, number of chip atoms, elastic recovery, and subsurface deformation for various orientations

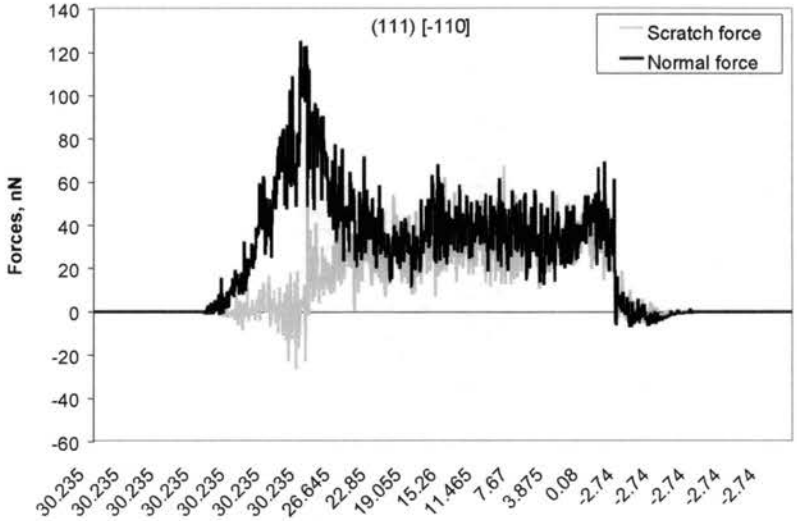
(111) [-110]
Scratch force
Normal force
Forces, nN
140
120
100
80
60
40
20
0
-20
-40
-60
30.235
30.235
30.235
30.235
30.235
30.235
30.235
26.645
22.85
19.055
15.26
11.465
7.67
3.875
0.08
-2.74
-2.74
-2.74
-2.74
-2.74

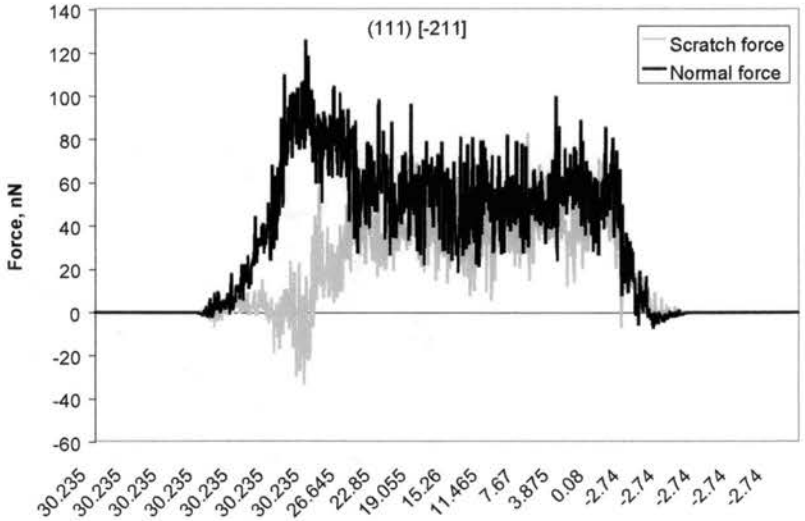
(111) [-211]
Scratch force
Normal force
Force, nN
140
120
100
80
60
40
20
0
-20
-40
-60
30.235
30.235
30.235
30.235
30.235
30.235
30.235
26.645
22.85
19.055
15.26
11.465
7.67
3.875
0.08
-2.74
-2.74
-2.74
-2.74
-2.74

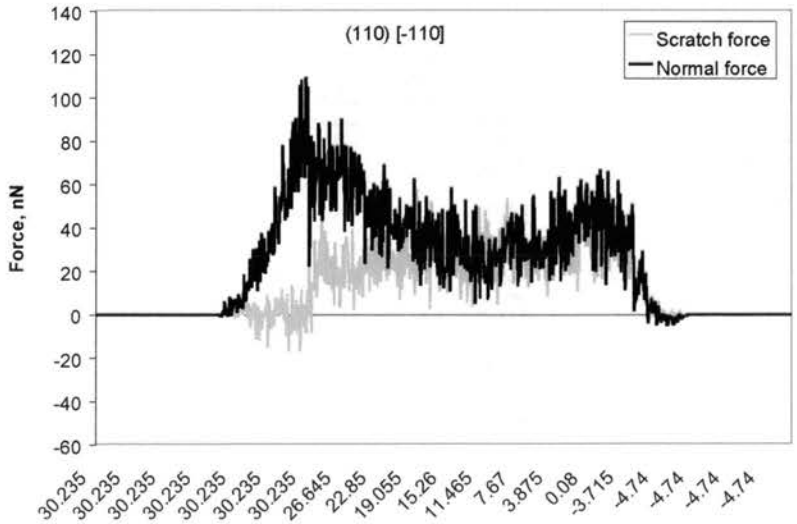
(110) [-110]
Scratch force
Normal force
Force, nN
140
120
100
80
60
40
20
0
-20
-40
-60
30.235
30.235
30.235
30.235
30.235
30.235
30.235
26.645
22.85
19.055
15.26
11.465
7.67
3.875
0.08
-3.715
-4.74
-4.74
-4.74
-4.74

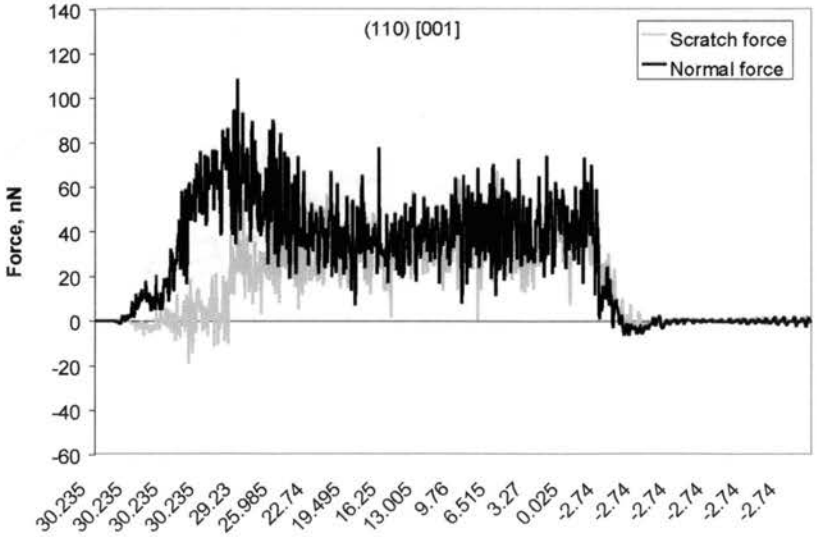
(110) [001]
Scratch force
Normal force
Force, nN
140
120
100
80
60
40
20
0
-20
-40
-60
30.235
30.235
30.235
30.235
29.23
25.985
22.74
19.495
16.25
13.005
9.76
6.515
3.27
0.025
-2.74
-2.74
-2.74
-2.74
-2.74
-2.74

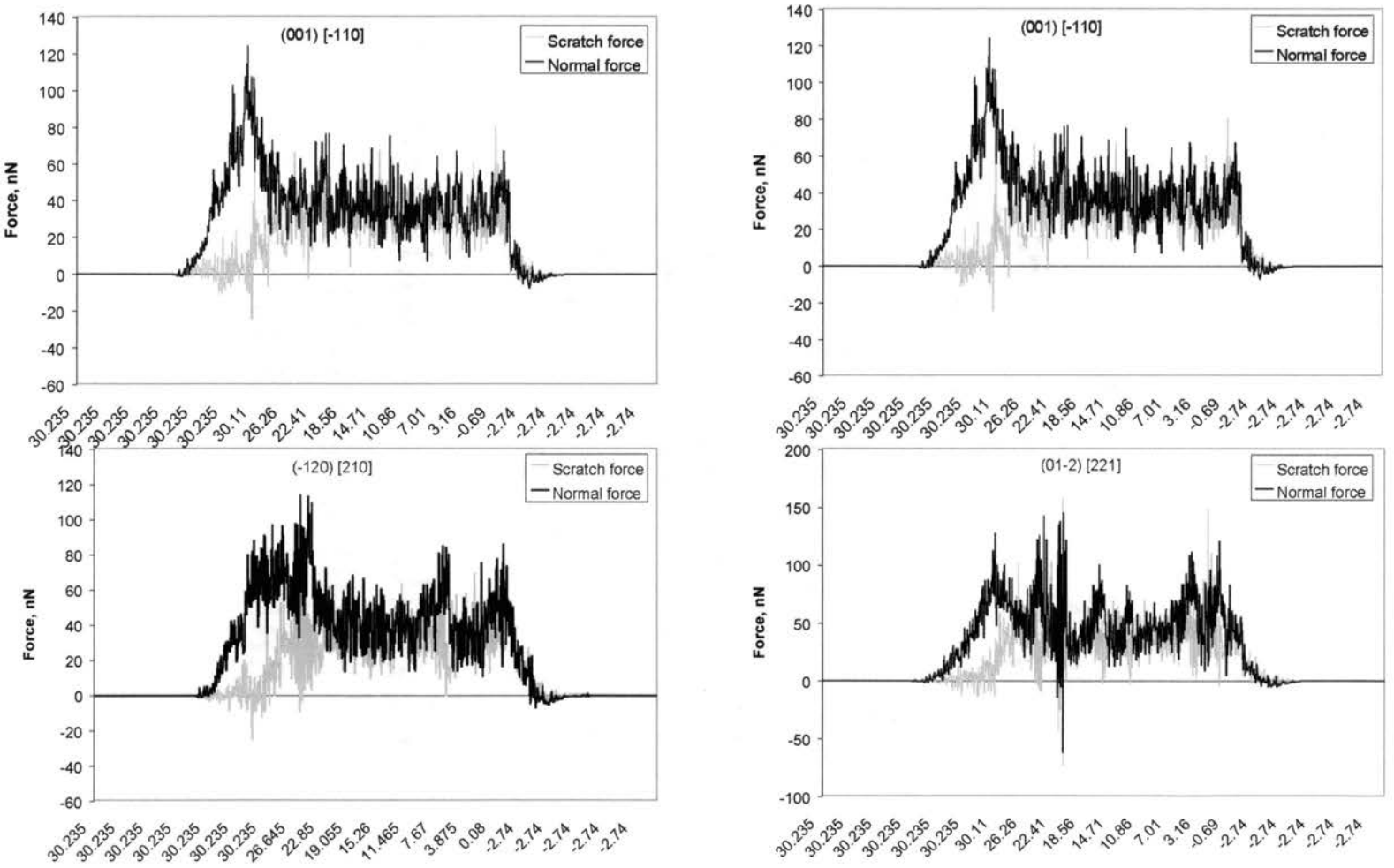

Figures 9.15 Variation of the normal (indentation direction) and tangential forces (scratch direction) with distance along the (a) - (h) direction of indention and scratch for various crystal set-ups

Table 9.2 : Quantitative Estimates of Standard Deviation of Atom Count Ratio, Chip Atom Count, Elastic Recovery, and Subsurface Deformation for Various Combinations of Crystal Orientation and Scratch Direction

No.	Crystal Orientation	Standard Deviation of Atom Count Ratio			Chip Atom Count	Elastic Recovery	Subsurface Deformation, number of atomic layers		
		Before Indentation	At Max. Ind. Depth	After Scratching			Before Indentation	At Max. Ind. Depth	After Scratching
1	(111) [-110]	0.0268	0.0519	0.1176	447	0.72	13	13	13
2	(111) [-211]	0.031	0.0649	0.0767	364	0.83	9	11	13
3	(110) [-110]	0.0094	0.0561	0.1044	278	0.78	5	8	11
4	(110) [001]	0.0253	0.064	0.1044	327	0.74	8	19	13
5	(001) [-110]	0.0185	0.0844	0.186	391	0.56	8	10	9
6	(001) [100]	0.0169	0.097	0.123	300	0.68	8	11	9
7	(01-2) [221]	0.0177	0.0587	0.108	264	0.74	9	9	13
8	(-120) [210]	0.0114	0.0673	0.113	212	0.71	9	10	11

Table 9.3: Results of MD simulation of nanoindentation - scratch

No	Crystal Orientation	F_c, N/mm x 10^2	F_t, N/mm x 10^2	F_c/F_t	F_R, N/mm x 10^2	Specific energy, $N/mm^2 \times 10^{-5}$	Indentation hardness, GPa	Scratch hardness, GPa
1	(111)[$\bar{1}$10]	1.193	1.556	0.767	1.960	0.147	4.797	15.624
2	(111)[$\bar{2}$11]	1.590	2.278	0.698	2.778	0.196	4.933	22.879
3	(110)[$\bar{1}$10]	1.076	1.666	0.646	1.983	0.133	4.251	16.733
4	(110)[001]	1.319	1.709	0.772	2.159	0.163	3.982	17.165
5	(001)[$\bar{1}$10]	1.297	1.567	0.828	2.034	0.160	5.063	15.738
6	(001)[100]	1.485	2.127	0.698	2.594	0.183	5.068	21.360
7	($\bar{1}$20)[210]	1.299	1.894	0.686	2.297	0.1604	3.891	19.023
8	(01$\bar{2}$)[221]	1.551	2.108	0.736	2.617	0.191	3.599	21.172

Figures 9.15 (a) to (h) are the force-displacement curves obtained in MD simulation of indentation and scratching for different orientations and scratch directions. They provide the raw data for further analysis. Table 9.3 summarizes the results of the MD simulation studies of indentation-scratching conducted on a single crystal aluminum for different orientations and directions of scratching. It shows the magnitude of the scratching force, the normal force, the resultant force, the specific energy, the friction coefficient, indentation hardness, and scratch hardness for various orientations and scratch directions.

In the following, the nature of the force - displacement curves will be discussed for a specific combination, {(001)<100>} as an example. The repulsive force is considered positive. During indentation, the normal force increases rapidly and the tangential force remains almost zero. The increase in the forces is essentially uniform exhibiting minor fluctuations. After the indentation process, when the indenter was slid along the scratch direction, the normal force drops significantly. Further, during the scratch process, the primary force is along the scratch direction and, hence, the normal force drops significantly. However, it can be noted from the figure that the scratching force increases with a drop in the normal force. It can also be noted from the figure that the scratching force is lower than the normal force (also taken as the average values in Table 9.3) during sliding, as the indenter presents a high negative rake angle (-45^{o}) during the sliding process. Once the indenter has moved through the specified scratch distance, it was retracted from the workmaterial. The force corresponding to this segment of the simulation drops to zero as the tool-work separation increases. Hysterisis in the indentation-retraction curve can also be seen.

Figure 9.16 shows the variation of hardness for different combinations of crystal setups. They were represented with increasing angle between the (111) and other planes

considered here. It can be seen that the calculated hardness values are an order of magnitude higher than the engineering values. This can be attributed to the fact that the depth of indentation is significantly smaller and at such small scales of indentation, it is possible that plastic deformation is governed by the theoretical yield strength. This increase is attributed to the well known Size effect. Belak et al. (1993) reported in the MD simulation of indentation of silver substrate, hardness of 5.4 GPa, which is close to the theoretical hardness value of 4.5 GPa. They also proposed a similar rationale for the high values. It can also be noted from Figure 9.16 that the hardness value is not only a function of the indentation direction or plane of indentation alone but also depends on the crystal orientation.

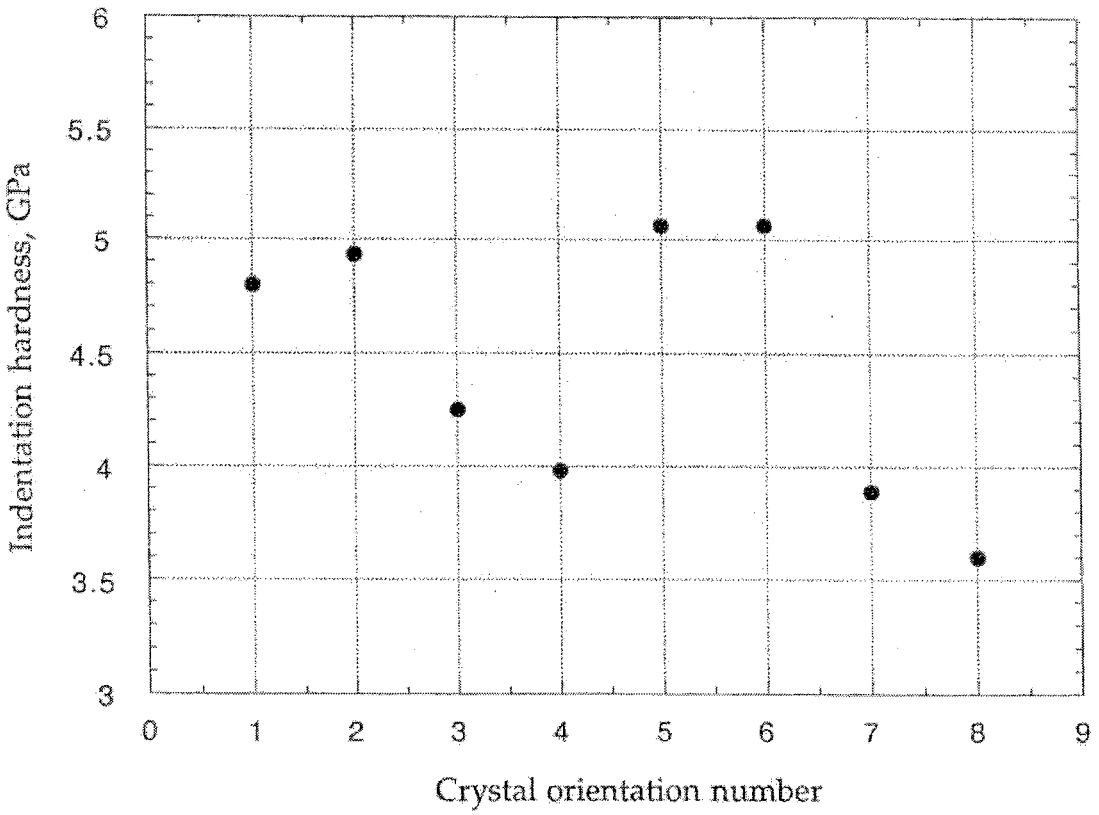

Figure 9.16. Variation of hardness for different combinations of orientations and scratch directions

In Table 9.3, 'z' represents the plane of indentation as well as the direction of indentation since indentation was performed perpendicular to the 'z' plane. It can be noted that the calculated hardness value shows variation even when the plane of indentation and the indentation direction are maintained constant. Among the orientations studied, the maximum hardness value is found with the (100)[001] combination and the minimum with the $(01\bar{2})[221]$ combination. The maximum hardness direction [100] is in fact the same as the indentation direction of maximum hardness, proposed by Garfinkle and Garlick (1968). For the combinations studied, Figure 9.16 also shows the anisotropy to be the least for the (001) orientation with indentation performed along [001] direction. The hardness variation is found to be maximum for the (110) orientation with the indentation performed along the [110] direction (Figure 9.16). From Table 9.3, the hardness anisotropy of aluminum with different crystal set-up is calculated to be ~29 %, which is close to the anisotropy of this material in the elastic, range (21.9 %). A similar anisotropy is anticipated in the plastic range.

Figures 9.17 (a) - (c) show the variation of the scratching force, the normal force, the resultant force, the friction coefficient, and the specific energy during the scratch process for various combinations of crystal set-ups. Figure 9.17 (a) is the variation of the scratching force, the normal force, and the resultant force with crystal orientation. Minimum in the scratching force was obtained along the $(110)[\bar{1}10]$ orientation and maximum along the $(111)[\bar{2}11]$ orientation. This is not in total agreement with the argument that the minimum scratching force for an FCC material should be along the most favorable slip system, i. e. in the $(111)[\bar{1}10]$ combination. However, the indenter used here had a high negative rake of -45^{o} and, consequently, the normal force during scratching would be the dominant force. It, therefore, appears that the theoretical predictions regarding the magnitude of forces with orientation should perhaps be

considered for the normal force and not for the scratching force. It can be seen from Figure 9.17 (a) that the normal force is minimum along the (111)[$\bar{1}$10] orientation, which is the most favored slip system for a FCC material. This reasoning is substantiated by similar trends in the resultant force and the thrust force [Figure 9.17 (a)] which show minimum and maximum values along (111)[$\bar{1}$10] and (111)[$\bar{2}$11], respectively. In an earlier MD simulation study on the effect of crystal orientation and cutting direction of aluminum single crystals [Chapter 6] with a positive rake tools, the minimum and the maximum forces were experienced with the (111)[$\bar{1}$10] combination and the (110)[001] combination, respectively. The differences in the results once again highlight the influence of the tool geometry on the resultant force system.

Figure 9.17 (b) shows the variation of friction coefficient with crystal orientation. The highest friction coefficient is found to be along the (001)[$\bar{1}$10] orientation and the lowest along the (110)[$\bar{1}$10] orientation. The friction coefficients obtained in this investigation are high and in the range of 0.6 - 0.9. Even though the loads are significantly low, the friction coefficients are higher. The high friction coefficients observed in this study are attributed to the material removal in scratching with a high negative rake tool (-45^{o}). In general, the friction coefficient in grinding where the abrasives present a high negative rake angle ($\sim -60^{o}$) is estimated to be ~0.5 (Komanduri, 1971). In the present investigation, the indenter presents a high negative rake angle of -45^{o} during the scratch process. The large negative rake angles, in general, are typical for most indenter geometries. Consequently, even though the normal force (load) is significantly low (nN range) the tool nomenclature results in an approximately equivalent decrease in the scratch force. This can result in high friction coefficient even with loads in the nN range. It is also possible that the contact pressure exerted by the tool can be significantly higher resulting in increased friction coefficient values.

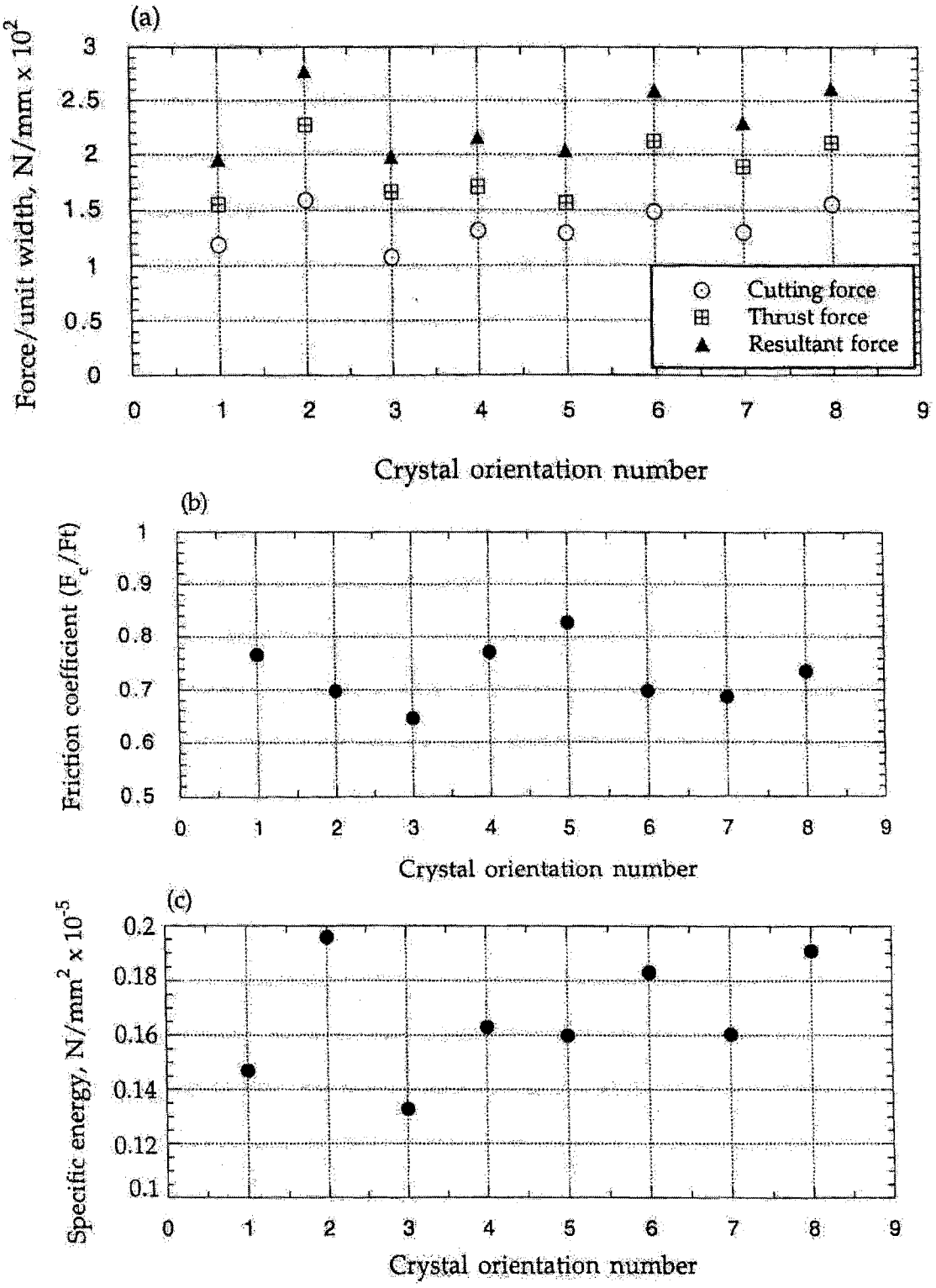

Figures 9.17 (a) - (c) Variation of (a) the cutting force, the thrust force, and the resultant force, (b) the friction coefficient, and (c) the specific energy during the scratch process for various crystal orientations and scratch directions

The friction coefficient shows maximum variation with scratch direction when sliding along the (110) plane (16.32%). This is followed by (001) (15.7%) and the minimum (9%) with (111) plane. This is attributed to the fact that the (110) is the least packed plane and (111) is the most packed plane with (001) in between. Figure 9.17 (c) shows the variation of specific energy with crystal orientation. It follows a similar trend as the cutting force [Figure 9.17 (a)]. Figure 9.18 shows the variation of the scratch hardness with crystal orientation. It was found to be minimum along the $(111)[\bar{1}10]$ orientation and maximum along the $(111)[\bar{2}11]$ orientation [Figure 9.18 and Table 9.3]. The anisotropy of scratch hardness of single crystal aluminum was found to be in the range of 30%.

In order to estimate the statistical error of the numerical quantities evaluated, for example, indentation hardness, three indentation simulations were performed (for a particular crystal orientation, namely, $(110)[\bar{1}10]$) with the indentation process starting at various time instants. This was achieved by altering the initial position of the tool relative to the surface of the workmaterial. This process will have some effect on the atom positions, as the equations of motion are being evaluated for various time intervals before indentation begins. Figure 9.19 plots the indentation curves for the three simulations mentioned above. It can be observed from this figure that, apart from small variations in the dynamic fluctuations, the variations in the force curves are insignificant. Table 9.4 tabulates the indentation hardness for simulations starting at various time instants. It can be observed that the difference between the indentation hardness values is less than 2%.

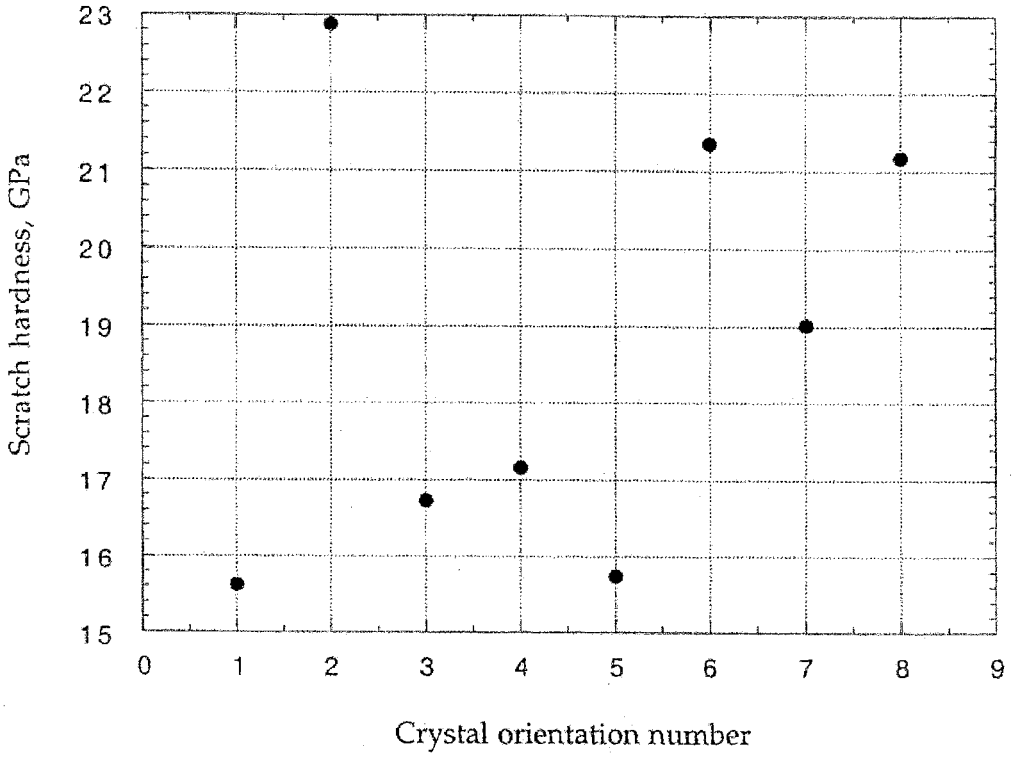

Figure 9.18 Variation of Scratch Hardness With Crystal Orientation and Indentation Direction Combination

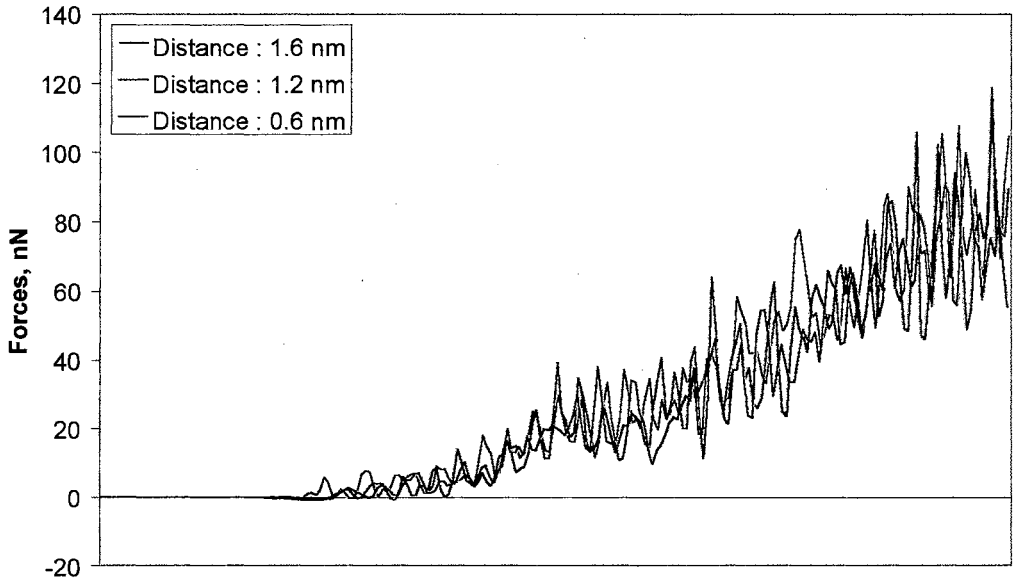

Figure 9.19 Indentation Curves for Simulations on (110)[-110] Combination Started at Various Time Instants in Order to Estimate the Statistical Error of Indentation

Table 9.4 Statistical error estimate of indentation hardness for (110)[$\bar{1}$10] orientation

No	Distance of Indenter from Work Surface, nm	Time Before Indentation Begins, s x 10^{-14}	Indentation Hardness, GPa	Error %
1	1.6	320	4.25	0
2	1.2	240	4.20	1.2
3	0.6	120	4.18	1.7

9.4.1.5. CONCLUSIONS

Molecular Dynamics (MD) simulation of indentation-scratching was conducted on single crystal aluminum in different orientations and scratch directions, namely, {(111)[$\bar{1}$10], (111)[$\bar{2}$11], (110)[$\bar{1}$10], (110)[001], (001)[$\bar{1}$10], (001)[100], ($\bar{1}$20)[210], (01$\bar{2}$)[221]}, to investigate the extent of anisotropy in hardness and friction coefficient of this material. Specific conclusions that may be drawn from this study are given in the following. In some cases, only experimental observations are summarized, as specific reasons for their behavior are not known at this stage.

1. The calculated hardness values were found to be an order of magnitude higher than the engineering hardness values. The magnitude of hardness was found to increase significantly as the indentation depths were reduced to atomic level.

2. At very low indentation depths, i. e. nanoindentation, plastic deformation appears to be governed by the theoretical yield strength of the workmaterial.

3. The hardness anisotropy of aluminum with different crystal set-ups was observed to be in the range of 29%. This may be compared to the anisotropy of this material in the elastic range (21.9%). It would be more useful to compare the anisotropy of this material in the plastic range, if available.

4. Maximum hardness value was experienced with the (001)[100] and the minimum with the $(01\bar{2})[221]$. Anisotropy of hardness was observed to depend on the crystal orientation in addition to the indentation direction and the plane of indentation.

5. During indentation, dislocations were observed to propagate both parallel and perpendicular to the indentation direction in the case of $(110)[\bar{1}10]$ orientation. In contrast, the dislocations were observed to propagate only parallel to the indentation direction in the case of $(001)[\bar{1}10]$ orientation. At other orientations, they were generally oriented at an angle to the direction of scratching which depends on the crystal orientation and the direction of scratching.

6. Initial disturbance of the atoms near the surface of the workmaterial prior to indentation (i. e. as the indenter was brought close to the workmaterial), was observed to vary with crystallographic factors. This was observed to be maximum in the case of $(111)[\bar{1}10]$ followed by $(111)[\bar{2}11]$ orientation. Minimum disturbance of the top layers of the workmaterial was found to be in the case of (110)[001] and $(001)[\bar{1}10]$ orientations. Insignificant, or practically zero, disturbance was observed for the remaining combinations investigated, namely, $(110)[\bar{1}10]$, (001)[100], $(\bar{1}20)[210]$, and $(01\bar{2})[221]$. Instantaneous forces as the indenter approached the workmaterial in different crystallographic directions were found to correlate reasonably well with the degree of

disturbance of the workmaterial. Why this disturbance and why it varied with the crystal orientation is not clear at this stage.

7. The friction coefficient, defined as the ratio of the scratching force to the normal force, during scratching was observed to be high, i. e. in the range of 0.6 - 0.9. Even though both the forces are very low, the friction coefficients are found to be rather high. This is attributed to the high negative rake angle (-45^{o}) presented by the indenter and the resulting high contact pressure exerted by the indenter. During scratching, bonds between the atoms have to be broken and reformed at an atomic level and it may not be possible to have low friction coefficients unless the contact between them involves a physisorbed layer, as in van der Waals bonding.

8. The resultant force during the scratch process was found to be minimum along the $(111)[\bar{1}10]$ orientation and maximum along the $(111)[\bar{2}11]$ orientation. The highest friction coefficient was observed to be along $(001)[\bar{1}10]$ and the lowest along $(110)[\bar{1}10]$ orientation. The reasons for this are not clear at this stage.

9. The scratch hardness was observed to be minimum along the $(111)[\bar{1}10]$ orientation and maximum along the $(111)[\bar{2}11]$ orientation. The reasons for this, again, are not clear at this stage. The anisotropy of scratch hardness of aluminum was also found to be in the range of 30%.

10. The extent of elastic recovery, subsurface deformation, and chip volume were found to vary with the crystallographic orientation.

9.4.2. Nature of Atomic Scale Friction

9.4.2.1. MD Simulation Results

In the following, MD simulation results of the indentation/sliding on a single crystal aluminum at extremely fine depths (0-0.8 nm) are presented. The crystal was set-up with (001) orientation and scratching was performed in the [100] direction. MD simulation plots at different stages of the process are given for a better appreciation of the process. It may be noted that the width of the tool in this investigation was taken as being equal to the width of the workmaterial (perpendicular to the paper). The tool center coincides with the workmaterial origin during the indentation-sliding process. Even though in practical cases the tool width is less than the workmaterial width, this approach is used to facilitate observation of the deformation process more clearly than by having the tool width less than that of the workmaterial. The discussion of the indentation/sliding process is based not only on the MD simulation plots but also on the detailed observation of the animations of the process.

In the MD simulations, the indentation/scratch depth was reduced from 0.8 nm to practically zero (tool sliding on the surface) in steps. Even at nominally zero scratch depth, some contact between the tool and the workmaterial and subsequent material removal was observed (as will be shown) due to relaxation of the atoms in the structure. This condition is termed here as sliding slightly below the surface. In order to simulate a zero scratch depth condition, the tool was initially set slightly above the workmaterial so that after relaxation, the surface of the workmaterial was just beneath the tool tip, i.e., touching but no removal. This situation is termed as sliding on the surface. For this reason, indentations were performed only in the depth range of 0.8 - 0.1 nm and not in the two special cases discussed above.

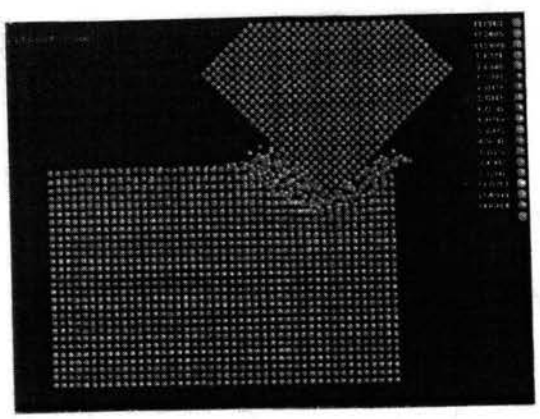

(a)

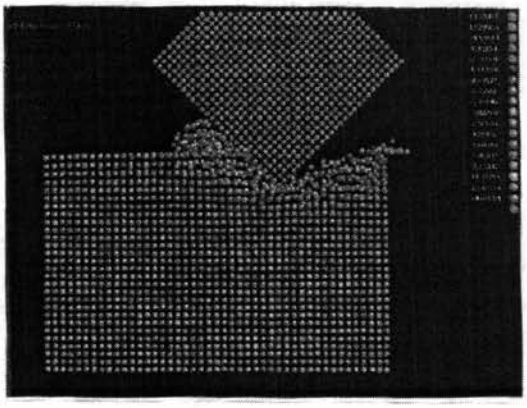

(b)

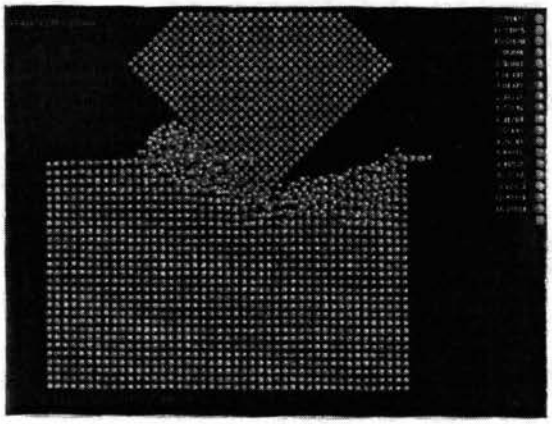

(c)

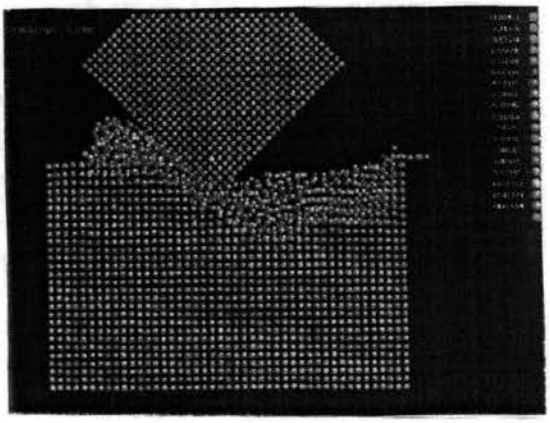

(d)

Figures 9.20 (a) - (d) MD simulation plots showing various stages of the scratch process at a scratch depth of 0.8 nm

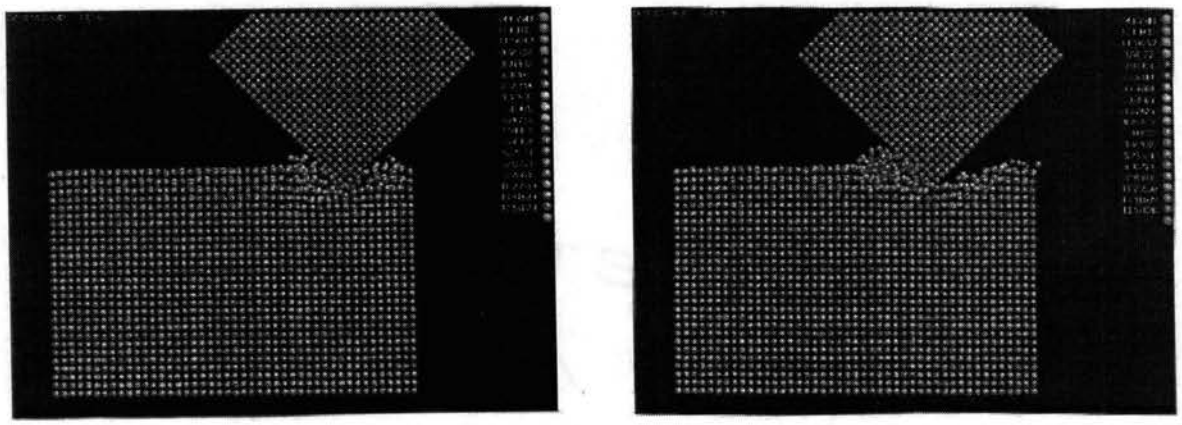

(a) (b)

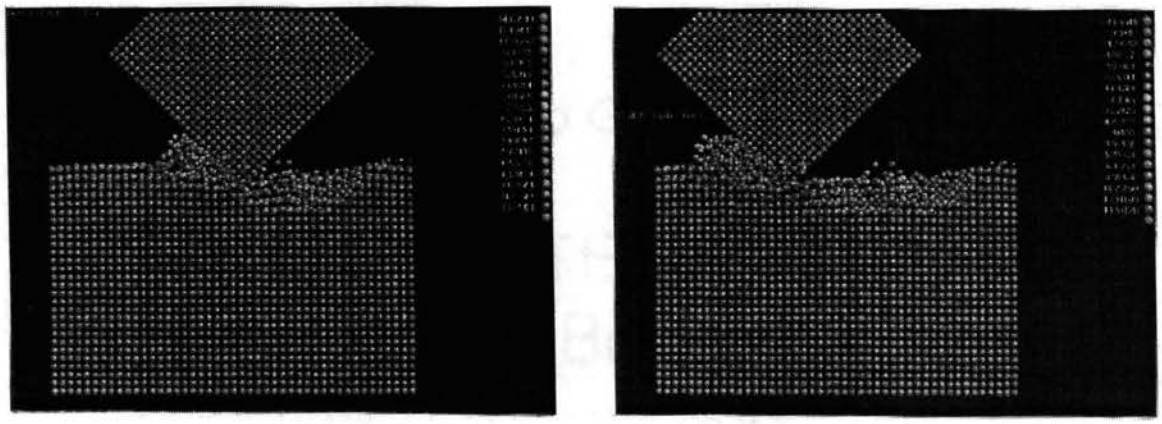

(c) (d)

Figures 9.21 (a) - (d) MD simulation plots showing various stages of the scratch process at a scratch depth of 0.4 nm

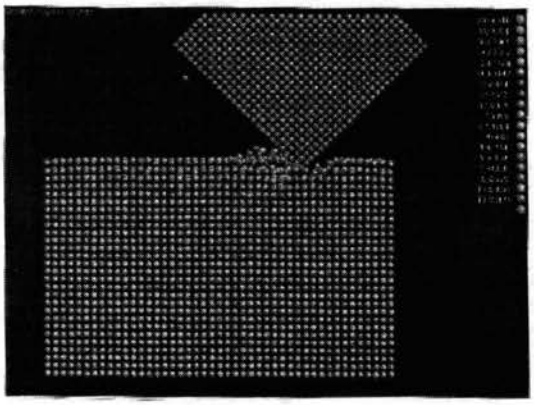

(a)

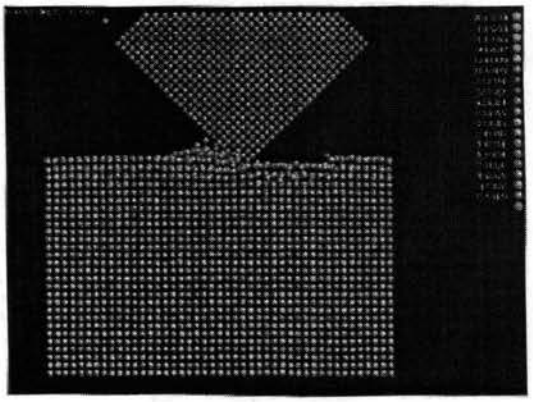

(b)

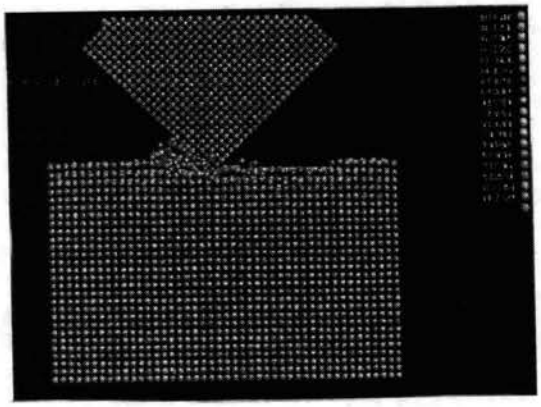

(c)

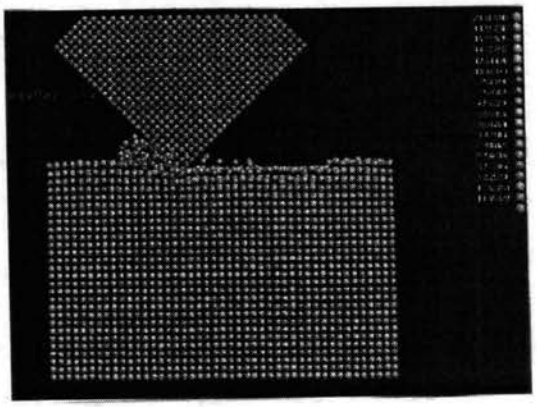

(d)

Figures 9.22 (a) - (d) MD simulation plots showing various stages of the scratch process at a scratch depth of 0.2 nm

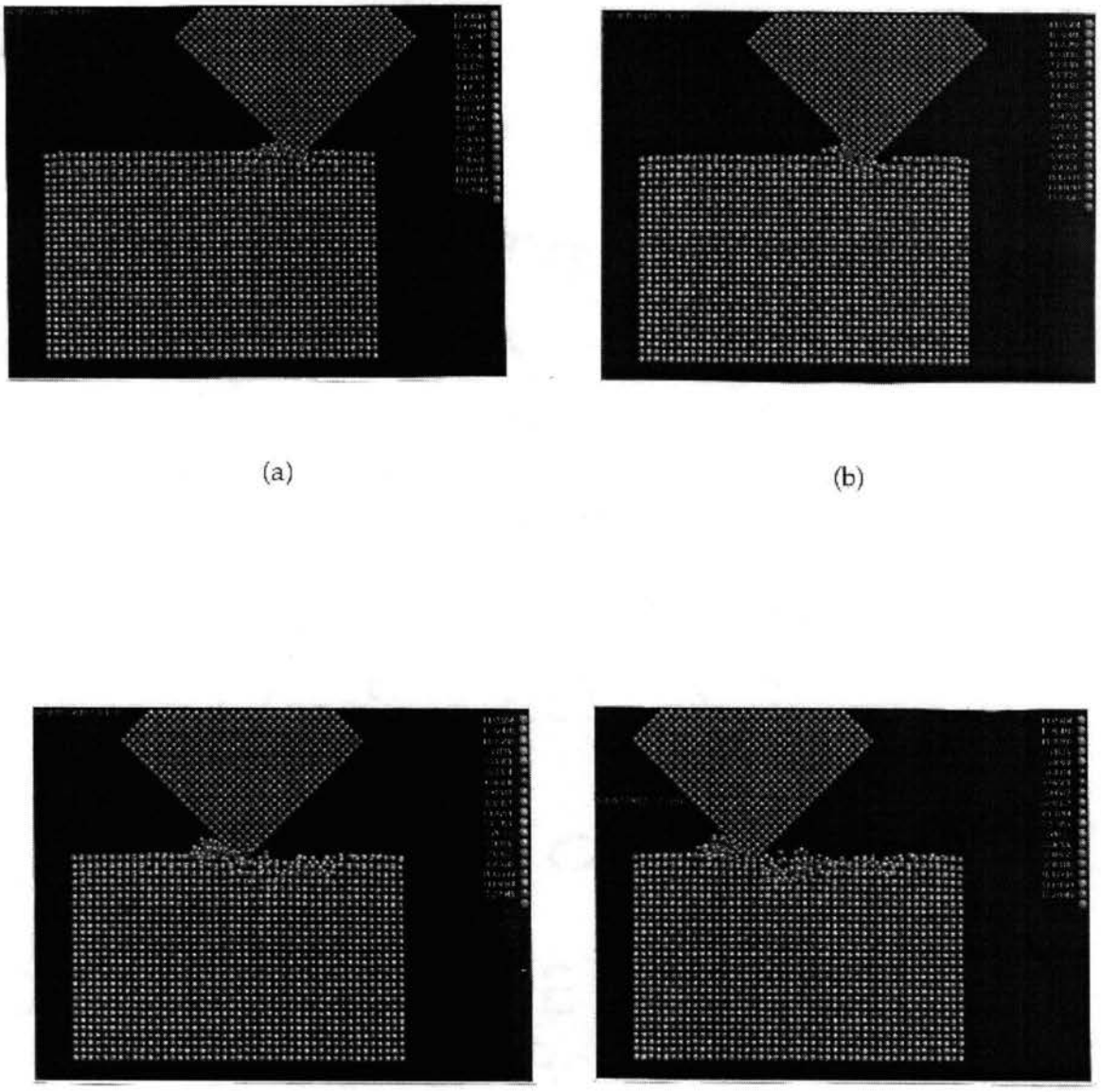

Figures 9.23 (a) - (d) MD simulation plots showing various stages of the scratch process at a scratch depth of 0.1 nm

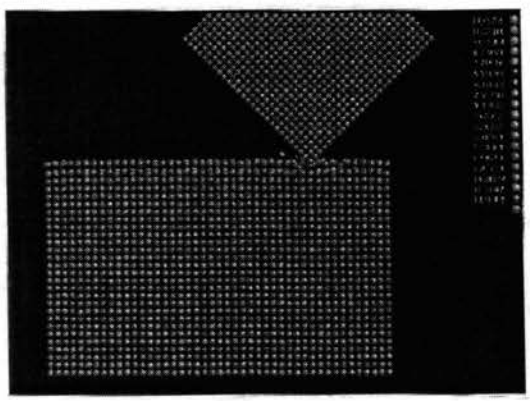

(a)

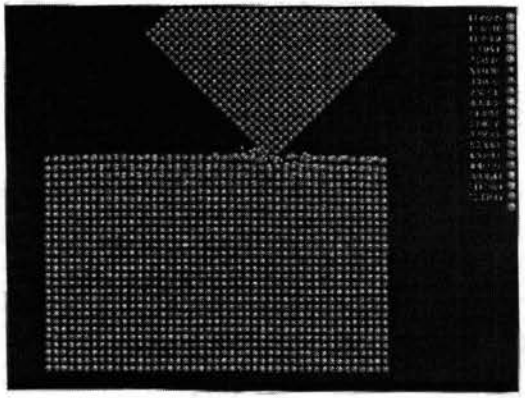

(b)

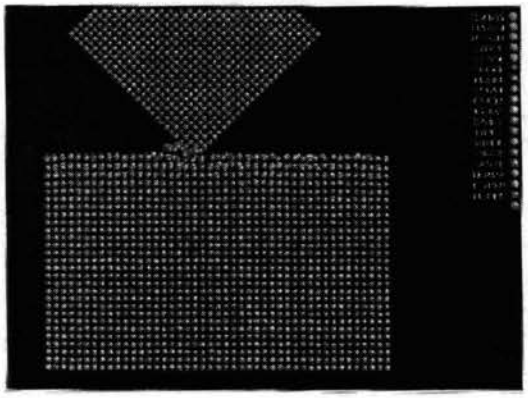

(c)

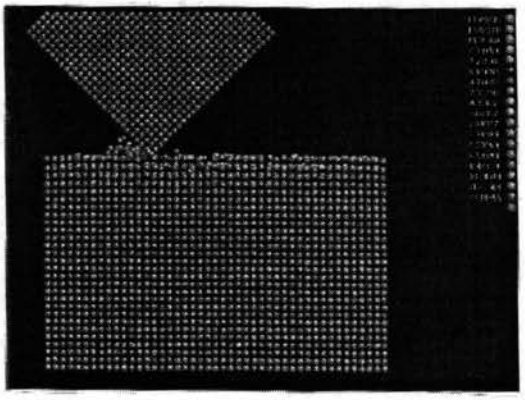

(d)

Figures 9.24 (a) - (d) MD simulation plots showing various stages of the scratch process with the indenter sliding slightly below the surface

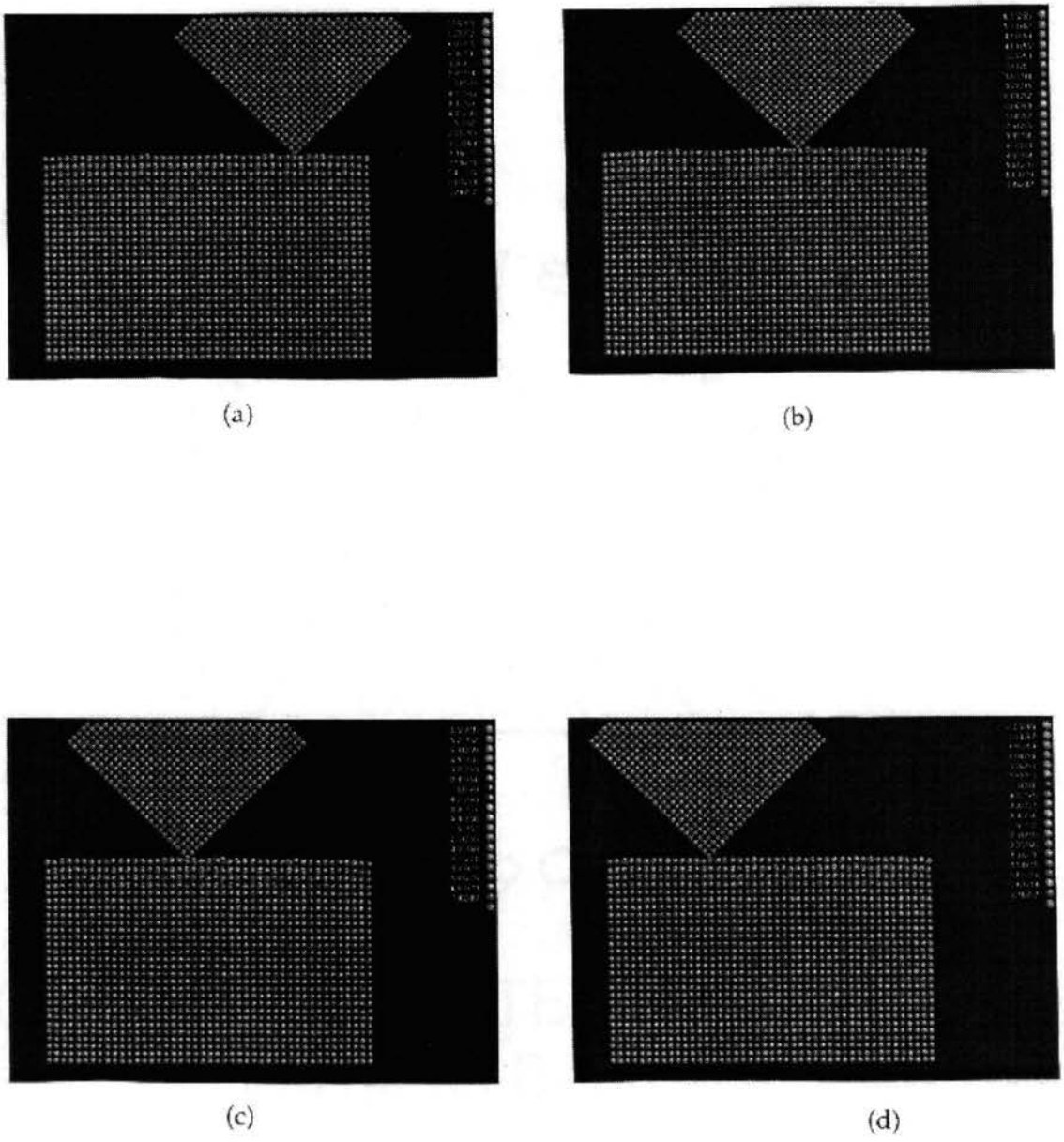

Figures 9.25 (a) - (d) MD simulation plots showing various stages of the scratch process with the indenter sliding slightly above the surface

Figures 9.20 (a) - (d) to 9.25 (a) - (d) are MD simulation plots showing the initial and the final stages of the scratch process at various scratch depths (0.8 - 0.1 nm, sliding slightly below surface, and sliding on the surface) showing the nature of deformation ahead of the indenter and material removal in the form of chips. Figures 9.20 (a) - 9.25 (a) are initial stages of the scratch process (after indentation) performed at 0.8, 0.4, 0.2, and 0.1 nm scratch depth, respectively. Figures 9.20 (b) to (d) to Figures 9.25 (b) to (d) show subsequent stages of scratching. They show the material removal taking place via the generation of chips as in conventional machining. However, due to the use of a high negative rake angle (-45^{o}) for the indenter, it can be likened more to plowing than cutting. Some subsurface deformation, estimated to be approximately equal to the indentation-scratch depth, especially at larger scratch depths can also be seen. In the case of the tool sliding slightly below the surface, chip formation is not very prominent although a few atoms being removed from the top surface of the workmaterial can be seen [Figures 9.24 (a) - (d)]. Absence of material removal can be seen when the tool was slid on the surface of the workmaterial without scratching [Figures 9.25 (a) and (d)].

9.4.2.2. On the Nature of Variation of the Forces and Energy

Figures 9.26 (a) to (f) are the force - displacement plots obtained in MD simulation of indentation/scratching at various depths [0.8 nm to almost zero]. They are the raw data that are used in the analysis. Table 9.5 summarizes the results of the MD simulation giving the values of the scratch force, normal force, resultant force, specific energy, friction coefficient, indentation hardness, and scratch hardness for various scratch depths.

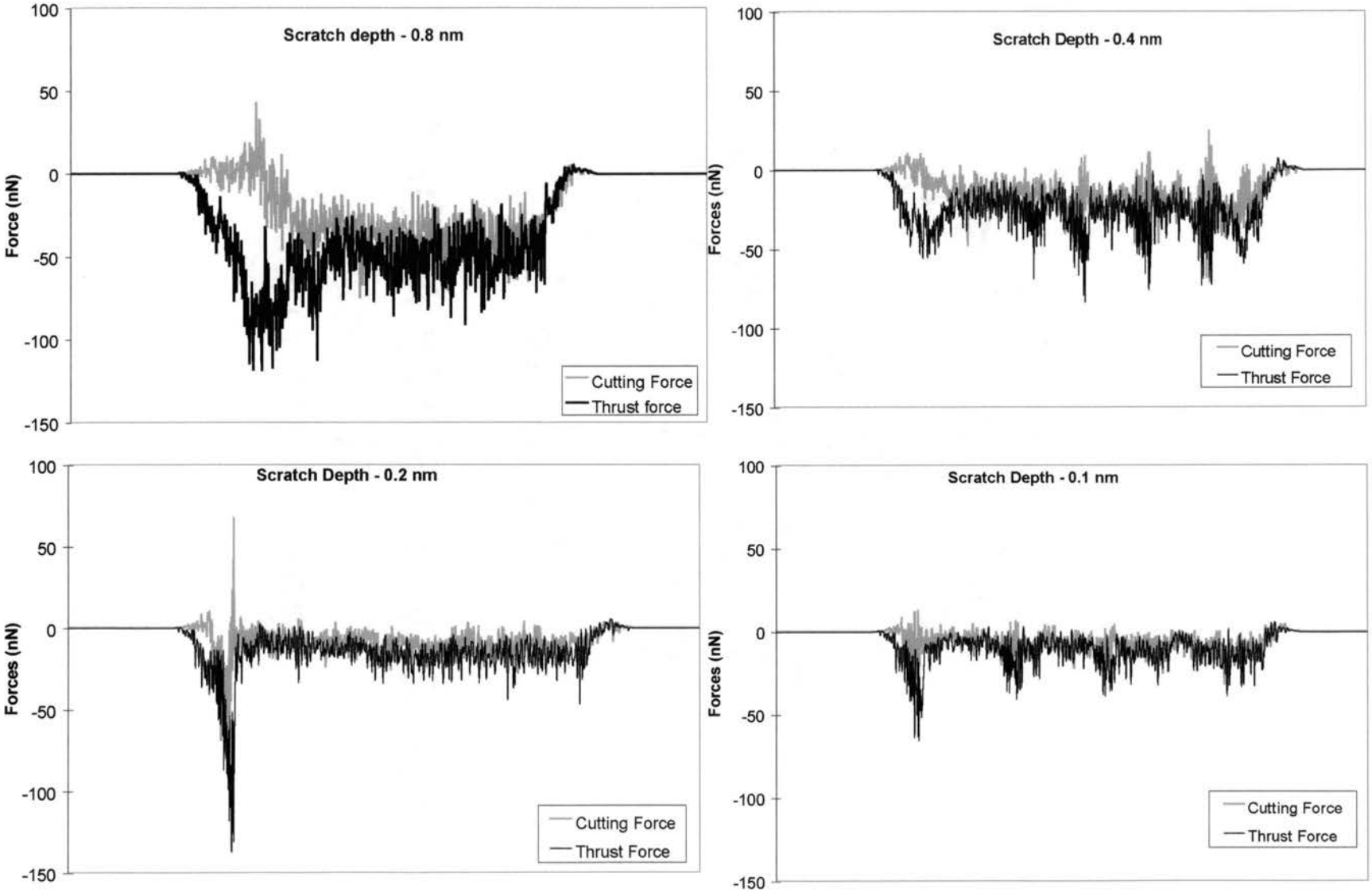
Scratch depth - 0.8 nm
Force (nN)
100
50
0
-50
-100
-150
Cutting Force
Thrust force
Scratch Depth - 0.4 nm
Forces (nN)
Cutting Force
Thrust Force
Scratch Depth - 0.2 nm
Forces (nN)
Cutting Force
Thrust Force
Scratch Depth - 0.1 nm
Forces (nN)
Cutting Force
Thrust Force

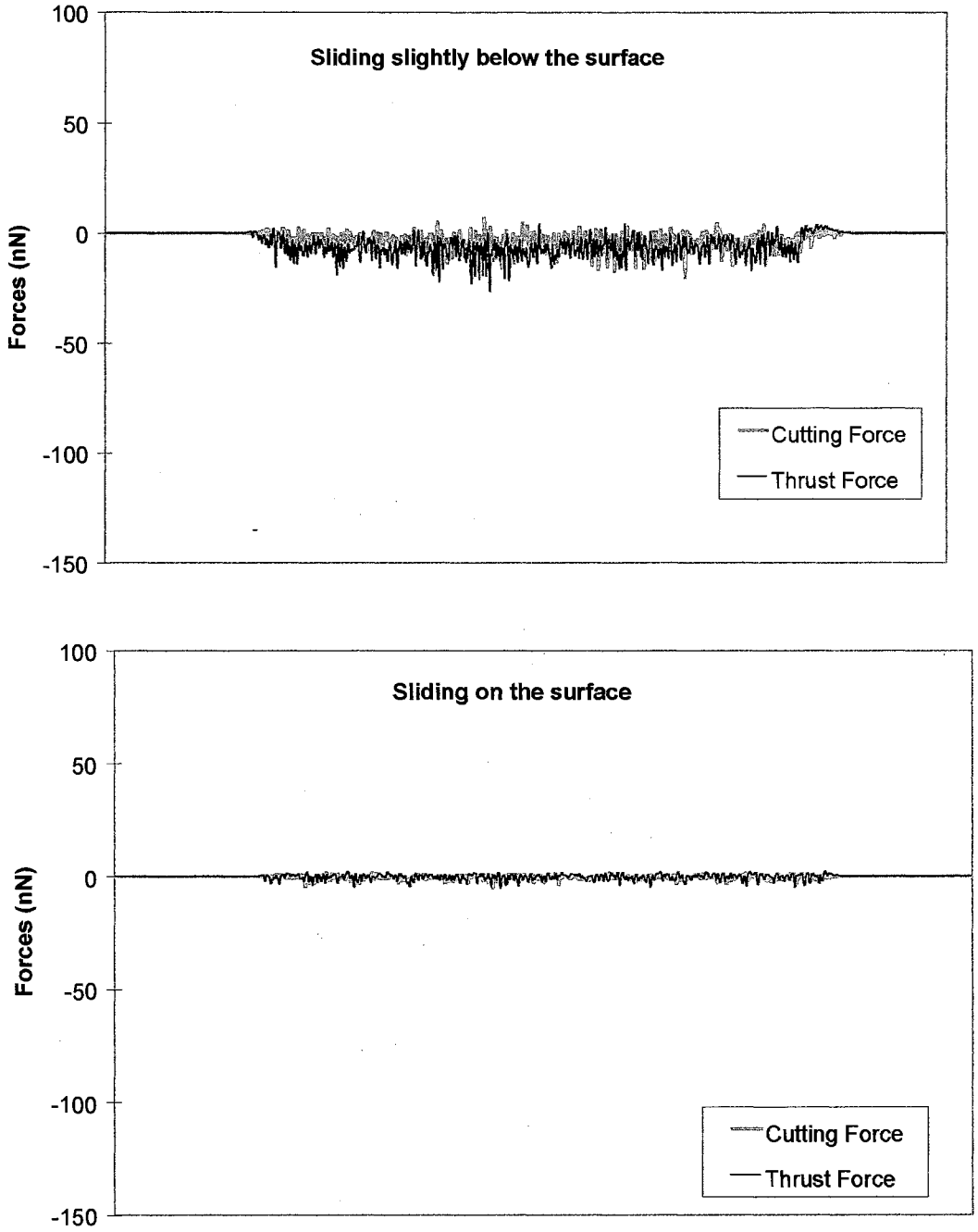

Figures 9.26 (a) - (f) Force-displacement curves from MD simulations of indentation/scratching at various depths (a) 0.8 nm (b) 0.4 nm (c) 0.2 nm (d) 0.1 nm (e) sliding slightly below the surface and (f) sliding on the surface

Table 9.5: Results of MD simulation study of nanoindentation - sliding conducted on aluminum single crystals with (001)[100] orientation for different depths

Depth of indentation-scratch, nm	Scratch force/ unit width (F_s), N/mm x 10^2	Normal force/ unit width (F_n), N/mm x 10^2	Friction coefficient (F_s/F_n)	Resultant force /unit width (F_R), N/mm x 10^2	Specific energy, GPa	Indentation hardness, GPa	Scratch hardness, GPa
0.8	1.485	2.127	0.698	2.594	18.3	5.068	21.360
0.4	0.741	1.148	0.645	1.366	18.3	5.460	23.074
0.2	0.443	0.724	0.612	0.848	21.9	5.930	30.486
0.1	0.337	0.510	0.661	0.611	33.3	5.871	40.974
Slightly below the surface	0.167	0.296	0.565	0.334	-	-	-
Sliding on the Surface	0.019	0.009	2.111	0.021	-	-	-

In the following, the nature of the force - displacement curves [Figures 9.26 (a) - (f)] is presented. The attractive force is considered negative. During indentation, the normal force increases rapidly and the scratch force (tangential force) remains nearly zero. The increase in the attractive force, though exhibiting minor fluctuations, is essentially uniform. After the indentation process, when the indenter was slid along the scratch direction, the normal force drops significantly. Further, during the scratch process, the primary force is along the scratch direction and hence the normal force drops significantly. As scratching proceeds, the scratching force increases while the normal force decreases [Figures 9.26 (a) - (f)]. It can also be noted that the scratching force is lower than the normal force (also taken as the average values in Table 9.5) as the indenter presents a high negative rake angle (-45^{o}) during the sliding process. Once the indenter has moved through a specified scratch distance, it was retracted from the workmaterial. The force corresponding to this segment of the simulation drops to zero as the tool-work separation increases. Hysterisis in the indentation-retraction curve can also be seen. In the cases of sliding slightly below the surface and on the surface, indentation were not performed. Consequently, Figures 9.26 (e) and (f) do not have indentation force trends. Even as the sliding depth is reduced from 0.8 nm to 0.1 nm, the position of the thrust force curve with respect to the cutting force curve seems to be constant. In other words, comparison of Figures 9.26 (a) to (e) suggests that the ratio of the cutting force to the thrust force is nearly constant as will be shown in the subsequent discussion. In the case of sliding on the surface both the forces seem to be close to zero [Figure 9.26 (f)].

Figures 9.27 (a) - (c) show the variation of the scratching force, the normal force, the resultant force, the friction coefficient, and the specific energy during the scratch process for various scratch depth. Figure 9.27 (a) is the variation of the scratching force, the normal force, and the resultant force with scratch depth. A depth of ~0.05 nm is assumed in the case of the indenter sliding slightly below the surface. The force values in

the case of the indenter sliding on the surface is plotted before the force values in the case of the indenter sliding slightly below the surface (0.05 nm). The forces can be observed to reduce with decreasing scratch depth. Both, the scratch and the normal forces seem to follow a straight line relationship with scratch depth. Also, the normal force is higher than the scratch force in all the cases (except for sliding on the surface) suggesting that scratching is performed with a high negative rake tool. Figure 9.27 (b) shows the variation of friction coefficient with scratch depth. Since the forces in the case of sliding on the surface were observed to be very close to zero (Table 9.5), the friction coefficient value is not plotted for this case. It can be seen that the friction coefficient is nearly constant for various depths of scratching. Figure 9.27 (c) shows the variation of specific energy with scratch depth which shows an increasing trend with decreasing scratch depth. This can be attributed to the size effect similar to the ones reported by other researchers (Furukawa and Morunuki, 1988; Nakayama and Tamura, 1968; Lucca et al., 1991)

Figure 9.28 shows the variation of the scratch hardness with scratch depth. The scratch hardness can be seen to increase with decreasing scratch depth. This increase is small as the depth is reduced from 0.8 nm to 0.4 nm. However, further reduction in the scratch depth results in a significant increase in the scratch hardness as shown in Fig. 9.28. Figure 9.29 shows the variation of indentation hardness with depth of indentation. At the extremely small indentation depths used in this study, an increase in indentation hardness with decreasing depth of indentation can be seen, again indicating a size effect.

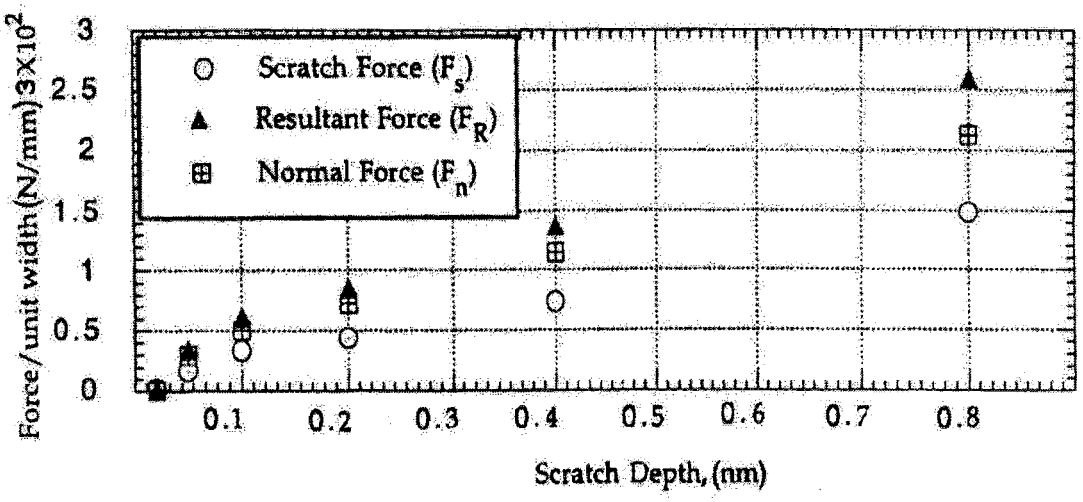

(a)

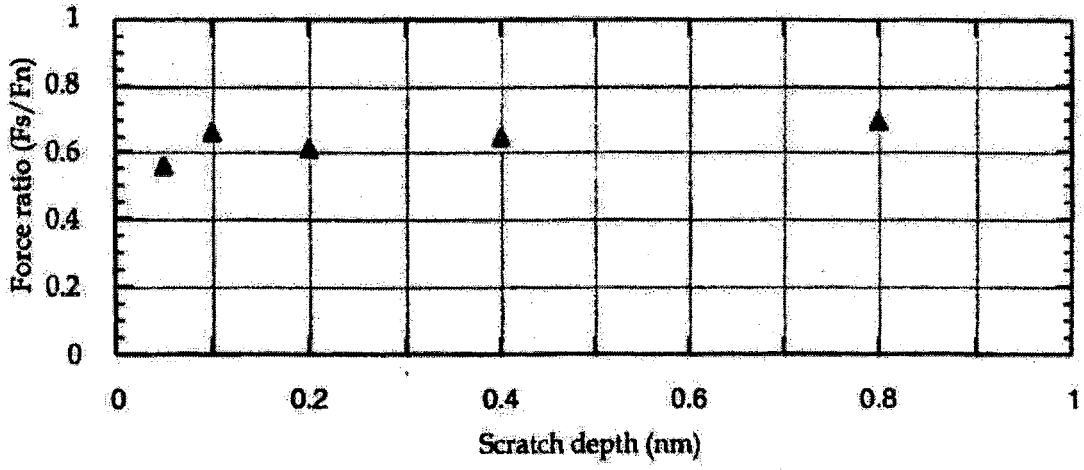

(b)

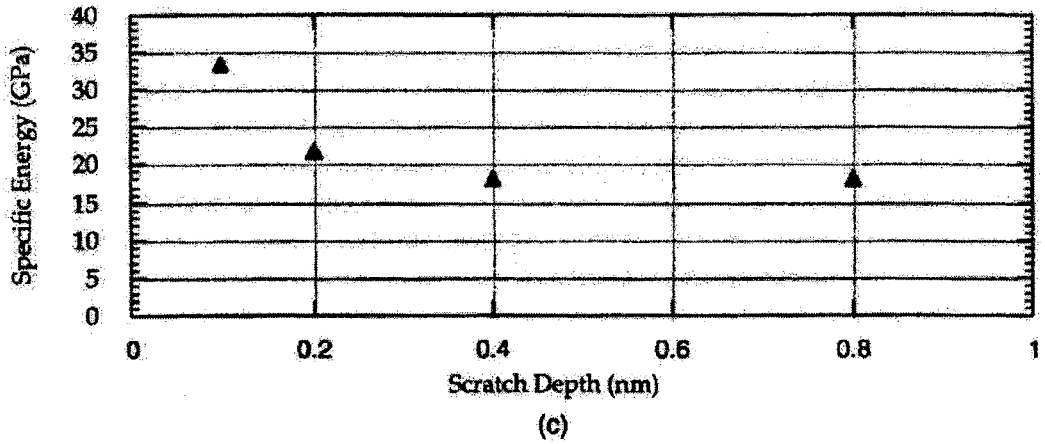

(c)

Figures 9.27 (a) - (c) Variation of (a) scratching force, the normal force, the resultant force, (b) the friction coefficient, and (c) the specific energy during the scratch process for various scratch depths

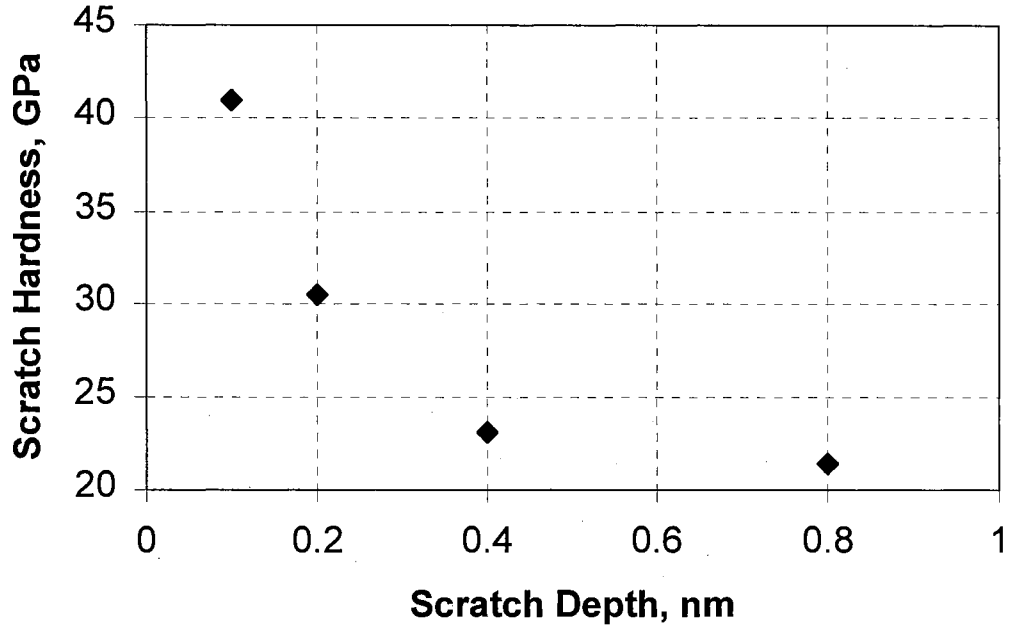

Figure 9.28. Variation of scratch hardness with scratch depth

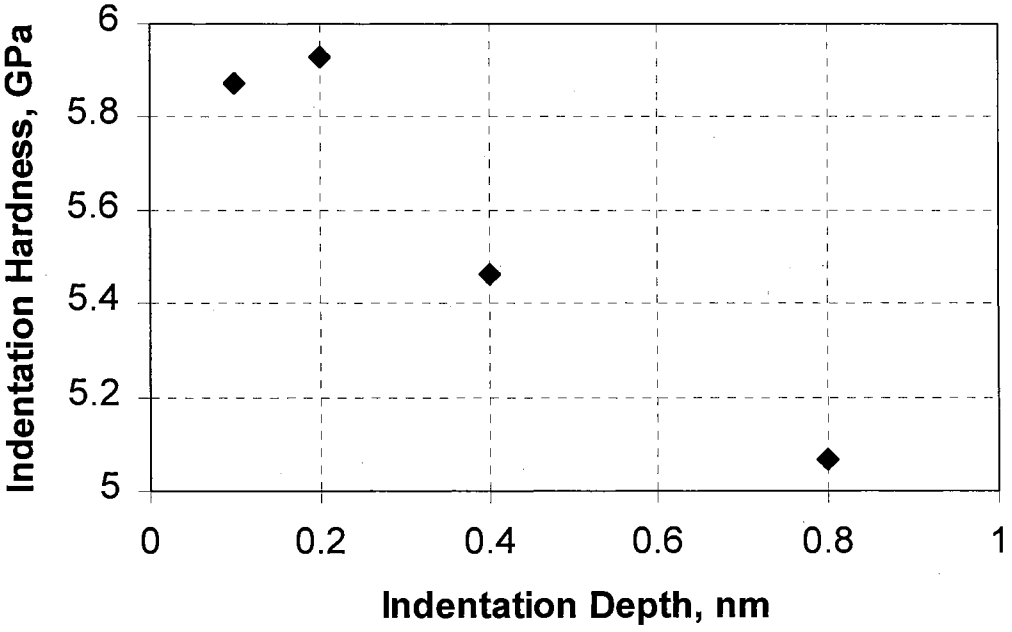

Figure 9.29. Variation of indentation hardness with indentation depth

9.4.2.3. Sensitivity of Results Due to Variation in the D Parameter of the Morse Potential

It is always a question as to how well the Morse potential parameters represent the system potential. For that, one can conduct sensitivity studies by varying the Morse parameters, slightly, say +/- 5%. However, one needs to be careful not to vary to such an extent that the potential approaches that for another metal. A case in point is aluminum and lead. If the D parameter of aluminum is reduced by 10%, the potential would represent lead more than aluminum as the other two Morse parameters (α and r_o) are very close. In this investigation, a sensitivity analysis is conducted for one scratch depth (0.1 nm) by varying the most important of the Morse parameters, namely, the D parameter by +/- 5%.

Table 9.6 summarizes the results of the sensitivity analysis. It can be seen that the scratch force, the normal force, and the resultant force decrease with decreasing D parameter. However, the variation is within experimental error limits. As the D parameter is reduced, with the other Morse parameters remaining constant, the well depth of the Morse potential curve decreases. This results in a reduction in the force required to deform the atomic bonds. Consequently, both the scratch and the normal forces decrease with decreasing D parameter. The reverse holds true when the D parameter is increased resulting in an increase in the forces. However, the data in Table 9.6 show that when the D parameter is varied by +/- 5%, the corresponding friction coefficient values vary by <1%.

Table 9.6. Results of sensitivity analysis

Variation of D parameter	Scratch force/unit width, N/mm x 10^2	Normal force/unit width, N/mm x 10^2	Resultant force/unit width, N/mm x 10^2	Friction coefficient
0.2703	0.337	0.510	0.611	0.661
0.2568 (-5%)	0.310	0.465	0.559	0.667
0.2838 (+5%)	0.348	0.525	0.630	0.663

9.4.2.4. DISCUSSION

It can be seen from Figure 9.27 (b) that the friction coefficient is independent of the depth of sliding and the values of friction coefficient are significantly high (~0.6). This is attributed to the tool (slider) presenting a high negative rake angle of -45^o during sliding. It may be noted that the 90^o indenter used in the present investigation is considered as a sharp indenter in the indentation field which in fact is a blunt tool with a -45^o rake. Other pyramidal or conical indenters with higher included angles as well as spherical indenters present even higher negative rake angles. Marshall and Shaw (1952) reported the mean grinding coefficient, which is the ratio of the cutting force to thrust force for grinding to be 0.47 for silicon carbide wheel. In an earlier MD simulation study, on the effect of tool rake angle, the ratio of cutting to thrust force for a -45^o rake tool was observed to be 0.58. In a subsequent study on the effect of tool geometry in nanometric cutting, carried out by varying the tool edge radius and depths of cut, the ratio of cutting to thrust force was observed to be in the range of 0.5-0.8 due to the high effective negative rake presented by the tool edge radius relative to the depth of cut. Based on the results of the simulations presented here, it can be seen that the friction coefficient values are in close agreement with those reported in the literature. Since the rake angle remains constant, even with

decreasing depths during the scratch process, the resulting ratio of the scratch force to normal force (friction coefficient) should be nearly constant as found in this investigation.

It can be noted from the review of literature that a wide range of friction coefficient value were reported from an extremely low (0.005-0.015) (Skinner et al., 1971; Mate et al., 1987; Erlandsson et al., 1988) to extremely high (1.2) (Garzino et al., 1995) and (~19) (Shimizu et al., 1998). In one of the simulations conducted in the present investigation with the indenter just sliding on the surface (without material removal) of the workmaterial, the friction coefficient was found to be somewhat high (2.1) (see Table 9.5). However, based on the force values reported in Table 9.5 as well as the raw force data [Figure 9.26 (f)], it can be seen that the magnitude of the forces are extremely low and close to zero. Hence, it is possible that in sliding friction processes where the slider moves on the surface without material removal, the forces can be extremely low and very close to zero. However, when the slider is moving on the surface at a finite depth, in addition to the molecular interactions, mechanical contact and subsequent damage of the substrate are possible (Kim and Suh, 1991). Under such conditions, it is not appropriate to assume that sliding experiments are nondestructive. A similar situation exits when measuring the surface finish with a stylus type of instrument, especially on soft materials (e.g. aluminum and copper used in optical mirrors). One can clearly observe the scratches made by the stylus with a sensitive instrument. Use of a noncontact surface finish measuring instrument, such as an optical interference contrast microscope is the only alternate to measure surface roughness. Indeed, the nature of scratching by a stylus type instrument has to be reevaluated in terms of elastic and plastic deformation of a blunt indenter at extremely light loads.

When the sliding process is destructive resulting in permanent deformation of the substrate, it very much resembles the atomic scale scratching process. In such a case, the

forces are defined by the tool nomenclature in addition to various other factors (depth of sliding, workmaterial properties etc.). Even when sliding is performed at a few atomic layers depth, the tip of an AFM or STM presents a high effective negative rake angle similar to a spherical indenter. Consequently, based on this study, it is proposed that as long as the rake angle of the tool plays a significant role in the scratch process, the friction coefficient will be a measure of the force ratio. However, when the slider slides on the surface without any material removal and the rake angle effect is insignificant, the friction coefficient depends on a number of other factors including the accuracy of the instrumentation used to measure forces and the surface state. Unless the surface is covered by a lubricant, it is unlikely that the friction coefficient would be low, as some researchers reported earlier. For example, Mate et al. (1987) and Erlandsson et al. (1988) reported friction coefficient values in the range of 0.005-0.015. However, their experiments were conducted in ambient air. It is possible that the surfaces may have been covered with a monolayer of a weak film which may act as a lubricant. In such cases, sliding involves breaking of weak van der Waal bonds as opposed to the much stronger metallic bonds we are representing with Morse potentials which can result in very low friction coefficient values. In the case of MD simulations, the surfaces are atomically smooth and totally free from any contaminant.

9.4.2.5. CONCLUSIONS

MD simulations of indentation/scratching were performed on single crystal aluminum at extremely low depths (0-0.8 nm) to investigate atomic scale friction, such as the variation of friction coefficient and hardness with scratch/indentation depth. The following are some of the specific conclusions that may be drawn based on this investigation.

1. The ratio of scratch force to the normal force (friction coefficient) was observed to be significantly high (~0.6) and independent of the normal force on the indenter in the nano-Newton range. One reason for the higher friction coefficient values is that in MD simulations, the surfaces are totally free from any contaminant.

2. The friction coefficient was found to be constant and independent of scratch depth except when the indenter was slid on the surface of the crystal without any material removal (zero scratch depth). This indicates that when material removal is involved in atomic scale friction, the friction coefficient is dependent on the rake angle presented by the indenter and does not depend either on the scratch depth or the normal force.

3. That the friction coefficient is independent of the normal force in atomic scale friction involving material removal can be explained on the basis of large negative rake angle presented by the indenter during sliding. As the scratch depth increases, the normal force also increases, but the friction coefficient remains nearly constant due to constant rake angle.

4. Both the indentation and scratch hardness values are found to increase with decreasing depth strongly suggesting a size effect.

5. Based on the MD simulation results, it appears that the low values of friction coefficient reported in the literature are possible only when the surfaces are covered with a lubricant. In such cases, sliding involves breaking of weak van der Waal bonds, which can result in very low friction coefficient values. Extrinsic factors such as surface contaminants, load, environment etc. may affect the friction coefficient values in addition to molecular interactions between the contacting surfaces.

CHAPTER 10

CONCLUSIONS AND FUTURE WORK

Molecular Dynamics (MD) computer simulations are constantly making important contributions to our fundamental understanding of the material behavior at the atomic level under a variety of processing conditions. It has been shown in this investigation that MD simulation technique is an extremely powerful and valuable tool in addressing a range of machining, materials testing, and tribological problems revealing several hidden mechanisms and correlations which underlie the macroscopic behavior. It is rather amazing that starting with a simple atomic model of a crystal, one can directly compute numerically the behavior of the model to elucidate as complex a physical phenomenon as machining. In the following, some of the specific conclusions of this investigation are briefly summarized.

10.1. MATERIALS TESTING

Measurement of mechanical properties of nano structures (with no or very few defects and strength close to their theoretical values) is an important problem in the field

of micro-electro-mechanical-systems (MEMS). In this investigation, MD simulations of nano-uniaxial tension and nanoindentation were performed on various materials (both, metals and semiconductors).

- The measured hardness, ultimate tensile strength, and elastic modulus were found to be in reasonable agreement with the experimental and the simulation results reported in the literature.
- The calculated hardness values were found to be an order of magnitude higher than the engineering hardness values. In nanoindentation, plastic deformation appears to be governed by the theoretical yield strength of the workmaterial.
- In order to reduce the computational time, MD simulations are normally conducted at very high speeds (100-500 m/s). The fracture strains were observed to be significantly higher at such high strain rates. However, the effect of simulation rate on the nature of deformation and the measured mechanical properties (elastic modulus, ultimate tensile strength, and hardness) was observed to be minimal.
- From the simulations of nano-uniaxial tension, it appears that the Morse potential used to model metals in this investigation, may not represent the deformation behavior of BCC metals as accurately as the FCC metals and an alternate potential may need to be considered.
- The deformation behavior of metals was observed to be associated with the generation and propagation of dislocations. In contrast, no dislocations were observed with silicon and germanium.

- The nanoindentation simulations on silicon indicate the possibility that the material around and underneath the indenter can undergo a structural transformation (from α- to β-silicon) and a significant densification as a consequence of nanoindentation.

10.2. MACHINING

MD simulations of nanometric cutting were conducted to study various problems, including, effect of workmaterial properties (ductile vs brittle), effect of tool geometry, effect of depth of cut and width of cut, effect of crystal orientation and cutting direction, and exit failure, at the atomic scale.

- The chip formation process in the machining of ductile materials, such as aluminum is one of plastic deformation on preferred crystallographic planes and directions ahead of the tool. In contrast, the chip formation with relatively brittle materials, such as silicon, seems to be an extrusion-like process without a specific crystallographic preference. This appears to be due to phase transformation from α- to β- silicon under hydrostatic pressure and consequent densification of the material.
- A material removal model explaining the modes of material removal in nanometric cutting of silicon is proposed.
- The degree of side flow was observed to depend not only on the tool geometry but also on the ratio of width of cut to depth of cut.
- It was observed that to study the effect of depth of cut (d) when machining with an edge radius (r) tool, it is necessary to maintain the ratio of d/r constant. By doing so, the depth effect can be separated from the edge radius effect.

- A material removal mechanism was proposed that would cover the range from conventional machining to grinding, to ultraprecision machining, and finally to the indentation-sliding as a cognate transition for material removal operation.
- The simulations on the effect of crystal orientation and cutting direction provided plausible explanations for the high and low shear angles reported by researchers in microcutting of single crystal materials. Dislocations were observed to propagate parallel, perpendicular, parallel and perpendicular, and at an angle to the cutting direction depending on the crystal orientation and the cutting direction. In addition, the shear angle was also observed to vary depending on the crystal orientation and cutting direction resembling a mirror image of the dislocations in the workmaterial.
- It was shown that it is possible to predict the nature of dislocation motion depending on the knowledge of the crystal orientation, cutting direction, and the slip system of the workmaterial. Three modes of material removal mechanisms in machining of single crystal materials are proposed.
- Exit failure in nanometric cutting was observed to be similar to that at micro- and macro-scale cutting, reported based on experimental evidence. The mode of failure resulting in either positive or negative burr formation was observed to depend on the workmaterial type (ductile/brittle). The ratio of burr dimensions was observed to agree closely with the force ratio for various rake tools in nanometric cutting. A model is proposed to explain the dependence of burr dimensions on tool geometry.
- The force and the specific energy trends observed during nanometric cutting in this investigation are in line with the results reported based on microcutting experiments.

The force ratio magnitude agrees reasonably well with the experimental results reported in the literature.

10.3. TRIBOLOGY AT THE ATOMIC SCALE

Nanoscale indentation and scratch experiments were conducted on aluminum single crystals under various indentation/scratch conditions (depth of indentation, crystal orientation and direction, scratch depth, etc.) to understand the nature of friction at the atomic scale.

- The indentation and scratch hardness anisotropy of aluminum with different crystal set-ups was observed to be in the range of 30%. This may be compared to the anisotropy of this material in the elastic range (21.9%). Anisotropy of hardness was observed to depend on the crystal orientation in addition to the indentation direction and the plane of orientation.
- Initial disturbance of the atoms near the surface of the workmaterial prior to indentation was observed. The degree of the initial surface disturbance was observed to depend on the crystal set-up.
- The study on the nature of atomic scale friction showed that whenever material removal is involved even at extremely fine scratch depths, the magnitude of friction coefficients can be high, dependent on the rake angle presented by the tool, and independent of the normal force.

These results suggest that MD simulation is a versatile and inexpensive tool that can be used with reasonable success to simulate a variety of problems at the atomic scale not possible (or extremely expensive and difficult) to conduct experimentally.

10.4.FUTURE WORK

Central to the success of MD simulation is the incorporation of an interatomic potential energy function, which accurately represents the material behavior. Interatomic forces are not simple because the atom itself is not an elementary particle but a composite body consisting of nucleus and orbital electrons which must be treated quantum mechanically. Consequently, any model of the interatomic forces or potential must deal with the complicated problem of many-body interactions. At the same time, limitations on the computational speed is in favor of using simple pairwise potentials which reasonably represent simple metals. However, the constant development of more and more realistic potentials for a range of materials starting from simple cubic metals to hexagonal metals, to covalent materials such as diamond and silicon, to some ionic/covalent materials such as silicon nitride, silicon carbide, to amorphous materials such as glass are enabling extension of the approach to a range of materials.

Since real materials involve imperfections (point, line, area, and volume), it is necessary to introduce them in the modeling process. While some success has been reported in some aspects, more work is needed to mimic real materials. Also, the computational speed is limiting the number of atoms to be considered as well as the speed of cutting. For a realistic simulation, it is necessary to consider more number of atoms (millions to a billion) and cutting speeds close to 1-2 m/s instead of 100-500 m/s currently used. Advances in hardware in computers in terms of processing speed, memory content, and parallel processing will advance this goal. Similar advances are

needed in the software as well. The following are some of the future works suggested based on the current investigation.

- Study the effect of imperfections in the workmaterial, such as voids, defects, grain boundaries, and dislocations, to name a few.
- Effect of various potential energy functions in modeling a given material. For example, the applicability of Morse potential to simulate metals has been subjected to significant criticisms. It was shown in this investigation that Morse potential couldn't simulate BCC materials as accurately as FCC metals. It will be interesting to study similar problems with the modified embedded atom potential and compare the results with those obtained using the Morse potential.
- Simulate nanometric cutting of more complex materials, such as ceramics and glasses using complex potential energy functions. For example, the shell potential model can be used to simulate nanometric cutting of ceramics.
- The problems associated with simulation size and speed can be overcome by investigating new simulation methodologies. For example, the constraint on the simulation size can be overcome to some extent by combining MD simulation technique with the continuum mechanics approach (Molecular Dynamics - Finite Element Modeling). The speed limitations can be overcome by conducting combined Molecular Dynamics - Monte Carlo simulations (hybrid MD/MC).
- Parallel processing can be an effective technique in reducing the computational time. A project is underway at OSU to introduce a 128-node cluster to enable MD

simulations of machining and materials testing with an increased simulation size and at reasonable simulation speeds.

- The high strain rates and cutting speeds used in the MD simulations can affect the temperature distribution in the workmaterial, which in turn can affect the mode of material behavior. Consequently, a detailed study on the temperature distribution in the workmaterial and its dependence on speed need to be performed. Also, such data (temperature distribution vs speed) is necessary to perform hybrid MD/MC simulations, as there is no direct speed variable in the MC simulation technique.
- The degree of phase transformation of silicon was observed to increase with increasing tool rake angle and indenter included angle. This was attributed to the increasing hydrostatic pressure underneath the tool/indenter with increasing negative rake angle. An investigation on the stress distribution in the workmaterial in nanoindentation and nanometric cutting simulations can shed more light on this issue.

REFERENCES

Abraham, F. F., Brodbeck, D., Rafey, R. A., and Rudge, W. E., 1994, "Instability Dynamics of Fracture: A Computer Simulation Investigation," Phys. Rev. Lett., 73/2, p. 272

Agrawal, P. M., Raff, L. M., and Thompson, D. L., 1988, Surface Sciences, 188, 402-

Alder, B., and Wainwright, T., 1959, "Studies in Molecular Dynamics. I. General Method," J of Chemical Physics, 31, No. 2, p. 459

Alder, B., and Wainwright, T., 1960, "Studies in Molecular Dynamics. II. Behavior of a Small Number of Elastic Spheres," J of Chemical Physics, 33, No. 5, p. 1439

Backer, W. R., Marshall, E. R., and M. C. Shaw, 1952, "The Size Effect in Metal Cutting," Trans ASME. 74, p. 61

Baskes, M. I., 1992, "Modified Embedded Atom Potentials for Cubic Materials and Impurities," Phys. Rev. B, 46, p. 2727

Belak, J. and I. F. Stowers, 1990, " A Molecular Dynamics Model of the Orthogonal Cutting Process," Proc. ASPE Annual Conf., Rochester, NY, p. 76

Belak, J., Lucca, D. A., Komanduri, R., Rhorer, R. L., Moriwaki, T.,Okuda, K., Ikawa, Shimada, S., Tanaka, H., Dow., T. A., Drescher, J. D., and I. F. Stowers, 1991, "Molecular Dynamics Simulation of the Chip Forming Process in Single Crystal Copper and Comparison with Experimental Data," Proc. of the ASPE Annual Conference, p. 100

Belak, J., Boercker, D. B., and Stowers, I. F., 1993, Simulation of Nanometer Scale Deformation of Metallic and Ceramic Surfaces, MRS Bulletin, 18, p. 55

Belak, J., 1994, "Nanotribology: Modelling Atoms When Surfaces Collide," Energy & Technology Review, Lawrence Livermore Laboratory, p. 13

Benton, T., and Kramer, B. M., 1988, "A Finite Element Analysis of Metal Cutting Using a Strain Rate and Temperature Dependent Constitutive Model," Trans. ASME, J. Eng. Mat. Tech.

Bhattacharya, A. K., and Nix, W. D., 1988, "Finite Element Simulation of Indentation Experiments," Materials research, 1, p. 601

Bhushan, B., Israelachvill, J. N., and Landman, U., 1975, "Nanotribology: Friction, Wear, and Lubrication at the Atomic Scale," Nature, 374 (4), p. 607

Bhushan, B., "Handbook of Micro/Nano Tribology," 1995, CRC Press, NY

Binnig, G., Rohrer, H., Gerber, Ch., and Weibel, E., 1982, "Surface Studies by Scanning Tunneling Microscopy," Phys. Rev. Lett., 49, p. 57

Biswas, R., and Hamann, D. R., 1985, "Interatomic Potentials for Silicon Structural Energies," Phys. Rev. Lett., 55/19, p. 2001

Black, J. T., 1971, "On the Fundamental Mechanism of Large Strain Plastic Deformation," Trans. ASME, J. of Eng. for Industry, 93, p. 507

Blake, P. N., and Scattergood, R. O., 1990, "Ductile-Regime Machining of Germanium and Silicon," J. Am. Cer. Soc., 73/4, p. 949

Bolding, B. C., and Andersen, H. C., 1990, "Interatomic Potential for Silicon Clusters, Crystals, and Surfaces," Phys. Rev. B, 41, p. 10568

Born, M., and Meyer, M. G., 1933, Handbuch der Physik (Berlin)

Bowden, F. P., and Tabor, D., "The Friction and Lubrication of Solids (Part I)," Clarendon Press, Oxford, 1954.

Bowden, F. P., and Brookes, C. A., 1966, "Frictional Anisotropy in Non-Metallic Crystals," Proc. R. Soc. Lond. A, 295, p. 244.

Brantley, W., 1973, "Calculated Elastic Constants for Stress problems Associated With Semiconductor Devices," J. Appl. Phys., 44/1, p. 534

Brenner, D. W., and Garrison, B. J., 1986, "Dissociative Valence Force Field Potential for Silicon," Phys. Rev. B, 34/2, p. 1304

Brenner, D. W., 1990, "Empirical Potential for Hydrocarbons for Use in Simulating the Chemical Vapor Deposition of Diamond Films," Phys. Rev. B, 42/15, p. 9458

Brenner, D. W., Sinnott, S. B., Harrison, J. A., and Shenderova, O. A., 1996, "Simulated Engineering of Nanostructures, Nanotechnology," 7, p. 161.

Bridgman, P. W., 1947, "The Effect of Hydrostatic Pressure On the Fracture of Brittle Substances," J. Appl. Phys., 18, 246-259

Brookes, C. A., O'Neill, J. B., and Redfern, B. A. W., 1971, "Anisotropy in the Hardness of Single Crystals," Proc. Roy. Soc. Lond. A, 322, p. 73.

Bryan, J. B., 1979, Precision Engineering, 1, p. 13

Buldum, A., and Ciraci, S., 1998, "Contact, Nanoindentation, and Sliding Friction," Physical Review B, Vol. 57, No. 4, p. 2468

Burnham, N. A., Colton, R. J., and Pollock, H. M., 1991, "Interpretation Issues in Force Microscopy," J. Vac. Sci. Technol. A, 9, p. 2548.

Cahn, R. W., 1992, "Metallic Solid Silicon," Nature, 357, p. 645

Casey, M., and Wilks, J., 1973, "The Friction of Diamond Sliding on Polished Cube Faces of Diamond," J. Phys. D Appl. Phys., 6, p. 1772.

Chandrasekaran, N., 1997, "Length Restricted Molecular Dynamics (MD) Simulation of Nanometric Cutting," M.S. Thesis, Oklahoma State University, Stillwater, OK, USA

Chandrasekaran, N., Noori-Khajavi, A., Raff, L. M., and Komanduri, R., 1998, "A New Method for Molecular Dynamics Simulation of Nanometric Cutting," Philosophical Magazine B, 77(1), p. 7

Chandrasekaran, N., Yoshino, M., Aoki, T., and Komanduri, R., 2000, "Micro Crack-Free Scratching of Silicon Under External Hydrostatic Pressure," Proc. of ASPE, 15th Annual Meeting, Scottsdale, p. 78

Chandrasekaran, N., Yoshino, M., Aoki, T., and Komanduri, R., 2001, "Defect-Free Finishing of Glass Under External Hydrostatic Pressure," submitted for publication

Chang, X, Perry, M., Peploski, J., Thompson, D, and Raff, L., 1993, "Theoretical Studies of Hydrogen-Abstraction Reactions from Diamond and Diamond-like Surfaces,"J. Chem. Phys. , 99, p. 4748

Chang, X., Thompson, D., and Raff, L., 1993, "Minimum-Energy Reaction Paths for Elementary Reactions in Low Pressure Diamond-Film Formation," J. Chem. Phys., 97, p. 10112.

Chang, X., Thompson, D., and Raff, L., 1994, "Hydrogen-Atom Migration on a Diamond (111) Surface," J. Chem. Phys., 100, p. 1765

Chao, B. T., Trigger, K. J., and Zylstra, L. B., 1952, "Thermophysical Aspects of Metal Cutting," Trans. ASME, 74, p. 1039

Chao, B. T., and Trigger, K. J., 1959, "Controlled Contact Cutting Tools," Trans ASME, J Eng. Industry, 81, p. 139

Chen, C. C., and Hendrickson, A. A., "Dislocation Etch Pits in Silver," J. Appl. Phys., 1971, 42, p. 2208

Cheong, W. C. D., and Zhang, L. C., 2000, "Molecular Dynamics Simulation of Phase Transformations in Silicon Monocrystals due to Nano-Indentation," Nanotechnology, 11, p. 173

Cieplak, M., Elizabeth, E. D., and Robbins, M. O., 1994, "Molecular Origins of Friction: The Force on Adsorbed Layers," Science, 265, p. 1209.

Cohen, S. R., Neubauer, G., and McClelland, G. M., 1990, "Nanomechanics of Au-Ir Contact Using a Bidirectional Atomic Force Microscope," J. Vac. Sci. Technol. A, 8, p. 3449.

Conte, S. D., and de Boor, C., 1972, "Elementary Numerical Analysis: An Algorithm Approach," McGraw-Hill, NY, Chapter 6

Coulomb, C. A., *Memoires de Mathematique et de Physics de l'Academie Royale,* 1785, 161.

Crawford, J. H., and Merchant, M. E., 1953, Trans. ASME, 75, p. 561

Crossland, B., and Dearden, W. H., 1958, "The Plastic Flow and Fracture of a Brittle Material (Gray Cast Iron) With Particular reference to the Effect of Fluid Pressure," Proc. Inst. Mech. Eng. (Lon.), 172, p. 805

Daniels, F. W., Dunn, C. G., 1949, "The Effect of Orientation On Knoop Hardness of Single Crystals of Zinc and Silicon Ferrite," Trans. Am. Soc. Metals, 41, p. 419.

Daw, M. S., and Baskes, M. I., 1984, "Embedded Atom Method : Derivation and Application to Impurities, Surfaces, and Other Defects in Metals," Phys. Rev. B, 29, p. 6443

Dieter, G. E. 1986, "Mechanical Metallurgy," 3rd Edition, McGraw-Hill Inc, New York, NY

Dodson, B. W., 1990, "Molecular Dynamics Modeling of Vapor-Phase and Very-Low-Energy Ion-Beam Crystal Growth Processes," Solid State and Materials Sciences, 16, No. 2, p. 115

Doerner, M. F., and Nix, W. D., 1986, "A Method for Interpreting the Data from Depth Sensing Indentation Instruments," Material Research, 1, p. 601

Donohue, J., 1974, "The Structures of Elements," John Wiley & Sons, Inc., NY

Doyama, M., 1995, Nucl. Instrum. Methods Phys. Res. B, 102, p. 107

Elizabeth A. Wood, 1963, "Crystal Orientation Manual," Columbia University Press, Newyork and London

Enomoto, Y., and Tabor, D., 1981, "The Frictional Anisotropy of Diamond," Proc. R. Soc. Lond. A, 373, p. 405

Erlandsson, R., Hadziioannou, G., Mate, C. M., McClelland, G. M., and Chiang, S., 1988, "Atomic Scale Friction Between the Muscovite Mica Clevage Plane and a Tungsten Tip," J. Chem. Phys., 89/8, p. 5190

Fatikow, S., and Rembold, U., "Microsystem Technology and Microrobotics," 1997, Springer-Verlag, Berlin, Germany

Forehand, S. M., and Bhushan, B., 1997, *"In Situ* Studies of Wear Mechanisms in Magnetic Thin Film Disks," Tribology Transactions, 40 (4), p. 549

Furukawa, Y., and Moronuki, N., 1988, "Effect of Material Properties on Ultra Precise Cutting Processes," Annals of CIRP, 37/1, p. 113

Gane, N., and Bowden, F. P.,1968, "Microdeformation of Solids," J of Appl. Phy., 39, p. 1432

Garifalco, L. A., and Weizer, V. G., 1959, "Application of the Morse Potential Function to Cubic Metals," Phys. Rev., 114/3, p. 687

Garfinkle, M., and Garlick, R. G., 1968, "A Stereographic Representation of Knoop Hardness Anisotropy," Trans. of the Metallurgical Society of AIME, 242, p. 809

Garzino-Demo, G. A., and Lama, F. L., 1995, "Friction and Wear of Metallic and Non-metallic Surfaces," Surface and Coatings Technology, 76-77, p. 487.

Garzino, G. A., Lama, F. L., 1996, "Effect of Surface Finish and of Materials Matching On Friction and Wear of Uncoated and Unlubricated Sliding Bodies," Surface and Coatings Technology, V 86-87, n 1-3, pt. 2, p. 603.

Gerk, A. P. and Tabor, D., 1978, "Indentation Hardness and Semiconductor-Metal Transition of Germanium and Silicon, Nature, 271, p. 732

Germann, G. J., Cohen, S. R., Neubauer, G., McClelland, G. M., and Seki, H., 1993, "Atomic Scale Friction of a Diamond Tip on Diamond (100) and (111) Surfaces," J. Appl. Phys., 73/1, p. 163

Goldstein, H., 1965, "Classical Mechanics," Addison-Wesley, Reading, MA.

Hahn, R. S., 1956, "The Relation Between Grinding Conditions and Thermal Damage in the Workpiece," Trans. ASME, 78, p. 807

Haile, J. M., 1992, "Molecular Dynamics Simulation - Elementary Methods," John Wiley & Sons, NY

Hamada, E., and Kaneko, R., as referred in Kaneko, 1991 reference

Handin, J., Heard, H. C., and Magouirk, J. N., 1967, "Effects of the Intermediate Principal Stress On the Failure of Limestone, Dolomite, and Glass at Different Temperatures and Strain Rates," J. Geo. Res., 72/2, p. 611

Harrison, J. A., Brenner, D. W., White, C. T., and Colton, R. J., 1991, "Atomistic Mechanisms of Adhesion and Compression of Diamond Surfaces," Thin Solid Films, 206, p. 213

Harrison, J. A., White, C. T., Colton, R. J., and Brenner, D. W., 1992, "Molecular Dynamics Simulations of Atomic Scale Friction of Diamond Surfaces," Phys. Rev. B, 46/15, p. 9700

Hashimura, M., Ueda, K., Dornfeld, D., and Manabe, K., 1995, "Analysis of three - dimensional burr formation on oblique cutting," Annals of CIRP, 44/1, p. 27.

Hashimura, M., Chang, Y. P., and Dornfeld, D., 1999, "Analysis of Burr Formation Mechanism in Orthogonal Cutting," J. Manufacturing Science and Engineering, 121, p. 1

Heino, P., Hakkinen, H., and Kaski, K., 1998a, "Molecular-Dynamics Study of Mechanical Properties of Copper," Europhys. Lett., 41/3, p. 273

Heino, P., Hakkinen, H., and Kaski, K., 1998b, "Molecular-Dynamics Study of Copper With Defects Under Strain," Phys. Rev. B, 58/2, p. 641

Heinzelmann, H., Meyer, E., Rudin, H., and Guntherodt, H. J., 1990, "Force Microscopy, Scanning Tunneling Microscopy and Related Methods," p. 443.

Hertzberg,R. W., 1996, "Deformation and Fracture Mechanics of Engineering Materials," Fourth Edition, John Wiley & Sons, Inc.

Hill, R., 1954, "The Mechanics of Machining: A New Approach," J. Mech. Phys. Solids, 3, p. 57

Hillebrecht, F. U., M. Sc thesis, Oxford University, 1981.

Hirano, M., and Shinjo, K., 1990, "Atomistic Locking and Friction," Phys. Rev. B, 41/17, p. 11837

Hirano, M., and Shinjo, K., 1993, "Superlubricity and Frictional Anisotropy," Wear, 168, p. 121

Hofman, P., and Kvasnicka, I., 1999, "A study of grinding burrs formation," Abrasives Magazine, /10, p. 29

Hoover, W. G., 1986,"Molecular Dynamics," Lecture Notes in Physics, 258 Springer-Verlag, Berlin, p. 13

Hoover, W. G., Hoover, C. G., and I. F. Stowers, 1989, "Interface Tribology by Nonequilibrium Molecular Dynamics," Fabrication Technology, Mat. Res. Symposium, 140, p. 119

Hoover, W. G., De Groot, A. J., Hoover, C. G., Stowers, I. F., Kawai, T., Holian, B. L., Boku, T., Ihara, S., and Belak, J., 1990, "Large Scale Elastic-Plastic Indentation Simulations via Non-equilibrium Molecular Dynamics," Physical Review A, 42/10, p. 5844

Ikawa, N., Shimada, S., Tanaka, H., and Ohmori, G., 1991, "An Atomistic Analysis of Nanometric Chip Removal as Affected by Tool-Work Interaction in Diamond Turning," Annals of the CIRP, 40/1, p. 551

Inamura, T., Suzuki, H., and Takezawa, N., 1991, "Cutting Experiments in a Computer Using Atomic Models of Copper Crystal and a Diamond Tool," Int. J. Japan Soc. Prec. Eng., 25/4, p. 259

Inamura, T., Takezawa, N., and Taniguchi, N., 1992, "Atomic-Scale Cutting in a Computer Using Crystal Models of Copper and Diamond," Annals of the CIRP, 41/1, p. 121

Inamura, T., Takezawa, N., and Kumaki, Y., 1993, "Mechanics and Energy Dissipation in Nanoscale Cutting," Annals of the CIRP, 42/1, p. 79

Inamura, T., Takezawa, N., Kumaki, Y., and Sata, T., 1994, "On a Possible Mechanism of Shear Deformation in Nanoscale Cutting," Annals of the CIRP, 43/1, p. 47

Inamura, T., Shimada, S., Takezawa, N., and Nakahara, N., 1997, "Brittle/Ductile Transition Phenomena Observed in Computer Simulations of Machining Defect-Free Monocrystalline Silicon," Annals of CIRP, 46/1, p. 31

Inamura, T., Shimada, S., Takezawa, N., and Ikawa, N., 1999, "Crack Initiation in Machining Monocrystalline Silicon," Annals of CIRP, 48/1, p. 81

Iwata, K., Osakada, K., Terasaka, Y., 1984, "Process Modeling of Orthogonal Cutting by the Rigid-Plastic Finite Element Method," Trans. ASME, J. Eng. Mat. Techn., 106, p. 132

Kallman, J. S., Hoover, W. G., Hoover, C. G., De Groot, A. J., Lee, S. M., and Wooten, F., 1993, "Molecular Dynamics of Silicon Indentation," Physical Review B, 47/13, p. 7705

Kaneko, R., Nonaka, K., and Yasuda, K., 1988, "Summary Abstract: Scanning Tunneling Microscopy and Atomic Force Microscopy for Microtribology," J. Vac. Sci. Technol. A, 6, p. 291

Kaneko, R., 1991, "Microtribology Related to MEMS - Concept, Measurements, Applications," IEEE Proceedings On MEMS, p. 108

Kaneko, R., 1993, "Microtribology Today and Tomorrow," Wear, 168, p. 1.

Kaneko, R., Umemura, S., Hirano, M., Andoh, Y., Miyamoto, T., and Fukui, S., 1996, "Recent Progress in Microtribology," Wear, 200, p. 296.

Kim, D. E., and Suh, N. P., 1991, "On Microscopic Mechanisms of Friction and Wear," Wear, 149, p. 199

Kim, D. E., and Suh, N. P., 1994, "Molecular Dynamics Investigation of Two Dimensional Atomic Scale Friction," Trans. ASME, J of Tribology, 116, p. 225

Kita, Y., and Ido, M., 1982, ASME Winter Annual Meeting, Washington D. C. 82-Prod 16

Kitamura, T., Yashiro, K., and Ohtani, R., 1997, "Atomic Simulation On Deformation and Fracture of Nano-Single Crystal of Nickel in Tension," JSME Int. Journal Series A, 40/4, p. 430

Kobayashi, S., and Thomson, E. G., 1959, "Some Observations of the Shearing Process in Metal Cutting," Trans. ASME, 81, p. 251

Kohno, A., and Hyodo, S., 1974, "The Effect of Surface Energy on the Microadhesion between Hard Solids," J. Phys. D: Appl. Phys., 7, p. 1243

Komanduri, R., 1971, "Some Aspects of Machining with Negative Rake Tools Simulating Grinding," Int. J. Mach. Tool Des., 11, p. 223

Komanduri, R., 1993, "Machining and Grinding: A Historical Review of the Classical Papers," ASME Applied Mechanics Review, 46/3, p. 80

Komanduri, R., 1996, "On Material Removal Mechanisms in Finishing of Advanced Ceramics and Glasses," Annals of CIRP, 45/1, p. 509

Komanduri, R., Lucca, D. A., and Tani, Y., 1997, Technological Advances in Fine Abrasive Processes, Annals of CIRP, 46/2, p. 545

Komanduri, R., and Raff, L. M., 1999, "Molecular Dynamics Simulation of Machining," in New Developments in the Finishing of Advanced Materials, p. 153, Proceedings of the US-Japan Symposium, 1999, Oklahoma State University

Konig, W. B., and Spenrath, N., 1991, "The Influence of the Crystallographic Structure of the Substrate Material on Surface Quality and Cutting Forces in Micromachining," Progression Precision Engineering, Springer-Verlag, Braunschweig, Germany, 141

Krim, J., 1996, "Friction at the Atomic Scale," Scientific American, Oct., p. 74.

Kunz, R. R., Clark. H. R., Nitishin, P. M., and Rothschild, 1996, "High Resolution studies of Crystalline Damage Induced by Lapping and Single-point Diamond Machining of Si(100)," J Mater. Res. 11, p. 1228

Landman, U., Luedtke, W. D., and Ribarsky, M. W., 1989, "Micromechanics and Microdynamics via Atomistic Simulations," Mat. Res. Soc. Symp. Proc., 140, p. 101.

Landman, U., Luedtke, W., Burnham, N., and Colton, R., 1990, "Atomistic Mechanisms and Dynamics of Adhesion, Nano-indentation, and Fracture," Science, 248/17, p. 454

Landman, U., and Luedtke, W. D., 1991, "Nanomechanics and Dynamics of Tip-Substrate Interactions," J. Vac. Sci. Technol, 9, p. 414.

Landman, U., Luedtke, W. D., and Ringer, E. M., 1992, "Atomistic Mechanisms of Adhesive Contact Formation and Interfacial Processes," Wear, 153, p. 3.

Landman, U., and Luedtke, W. D., 1996, "Atomistic Dynamics of Interfacial Processes: Films, Junctions, and Nanostructures," Applied Surface Science, 92, p. 237

Lee, E. H., and Shaffer, B. W., 1951, "Theory of Plasticity Applied to the Problem of Machining," Trans. ASME, J. Appl. Mech., 18, p. 405

Lee, Y. M., Sampath, W. S., and Shaw, M. C., 1984, "Tool fracture probability of cutting tools under different exiting conditions," Trans ASME, J. Eng. Ind., 106, p. 168.

Lee, W. B., 1990, "Prediction of Micromachining Force Variation in Ultraprecision Machining," Precision Eng., 12(1), p. 25

Lee, W. B., and Zhou, M., 1993, "A Theoretical Analysis of the Effect of Crystallographic Orientation on Chip Formation in Micromachining," Int. J. of Mach. Tool and Manuf., 33, p. 439

Lennard-Jones, J. E., 1926, "Forces Between Atoms and Ions," Proc. of the Roy. Soc. (Lon) A, 110, 230-234 and Proc. Roy. Soc. A (Lon), 109, 1925, p. 584

Li, X., Kopalinsky, E. M., and Oxley, P. L. B., 1995, "A Numerical Method for Determining Temperature Distributions in Machining With Coolant Part 1. Modeling the Process and Part 2. Calculation Method and Results," Proc. Of the I. Mech. E. (Lon), J. Engg. Manuf., 209/1, 33-43 and 45-52

Lifshits, V. G., Saranin, A. A., and A. V. Zotov, "Surface Phases of Silicon," John Wiley & Sons, New York, NY (1994)

Lim, S. C., Ashby, M. F., and Brunton, J. H., 1989, "The Effect of Sliding Conditions On the Dry Friction of Metals," Acta Metall., 37 (3), p. 767.

Loladze, T. N., 1975, "Nature of brittle failure of cutting tools," Annals of CIRP, 24/1, p. 13

Lucca, F. L., An Investigation On the Transient Effects in Interrupted Cutting by Simulated Orthogonal Machining, RPI, NY, 1982

Lucca, D. A., Rhorer, R. L., and Komanduri, R., 1991, "Energy Dissipation in Ultraprecision Machining of Copper," Annals of CIRP, 40/1, p. 83

Lynden-Bell, R. M., 1992, "The Fracture of Perfect Crystals Under Uniaxial Tension At High Temperatures," J Phys. Condens. Matter, 4, p. 2172

Lynden-Bell, R. M., 1994, "Computer Simulations of Fracture at the Atomic Level," Science, 263, p. 1704

Lynden-Bell, R. M., 1995, "A Simulation Study of Induced Disorder, Failure and Fracture of Perfect Metal Crystals Under Uniaxial Tension," J. Phys. Condens. Matter, 7, p. 4603

Macmillan, N. H., and Kelly, A., 1972, "The Mechanical Properties of Perfect Crystals," Proc. R. Soc. Lond. A, 330, p. 291

Maekawa, K., and Itoh, A., 1995, "Friction and Tool Wear in Nanoscale Machining - Molecular Dynamics Approach," Wear, 188, p. 115

Marshall, E. R., and Shaw, M. C., 1952, "Forces in Dry Surface Grinding," Trans. ASME, 74, p. 51

Mate, C. M., McClelland, G. M., Erlandsson, R., and Chiang, S., 1987, "Atomic Scale Friction of a Tungsten Tip on a Graphite Surface," Phys. Rev. Lett., 59, p. 1942.

McClelland, G. M., in "Adhesion and Friction," (M. Grunge and H. J. Kreuger Eds.), Springer Series in Surface 17, Springer Verlag, 1989, Berlin, p. 1.

McKeown, P. A., 1987, "The Role of Precision Engineering in Manufacturing of the Future," Annals of CIRP, 36, p. 495

Merchant, M. E., 1944, "Basic Mechanisms of the Metal Cutting Process," Trans. ASME, 66, p. A65

Miyamoto, T., Kaneko, R., and Ando, Y., 1990, "Interaction Force Between Thin Film Disk Media and Elastic Solids Investigated by Atomic Force Microscope," Trans. ASME: J. Tribology, 112, p. 567

Mokhtar, M. O. A., 1982, "The Effect of Hardness on the Frictional Behavior of Metals," Wear, p. 297

Mori, Y., Endo, K., Yamamoto, K., Wang, H., and Ide, T., J. Jpn. Soc. Precision Eng., 1990, 56, p. 679 (in Japanese)

Moriwaki, T., and Okuda, K., 1989, "Machinability of Copper in Ultraprecision Microdiamond Cutting," Annals of CIRP, Vol. 38/1, p. 115

Moriwaki, T., Sugimura, N., Manabe, K., and Iwata, K., 1991, "A Study on Orthogonal Micromachining of Single Crystal Copper," Transactions of NAMRI/SME, p. 177

Moriwaki, T., Okuda, K., and Jian Guo Shen, 1993, "Study of Ultraprecision Orthogonal Microdiamond Cutting of Single Crystal Copper," JSME Int. J. Series C, 36(3), p. 400

Morse, P. M., 1929, "Diatomic Molecules According to the Wave Mechanics II Vibrational Levels," Phys. Rev., 34, p. 57

Nakasuji, T., Kodera, S., Hara, S., Matsunaga, H., Ikawa, N., and Shimada, S., 1990, "Diamond Turning of Brittle Materials for Optical Components," Annals of CIRP, 39/1, p. 89

Nakayama, K., and Tamura, K., 1968, "Size Effect in Metal-Cutting Force," Trans. ASME, J. of Eng. for Ind., 80, p. 119

Nakayama, K., and Arai, M., 1987, "Burr formation in metal cutting," Annals of CIRP, 36/1, p. 33

Nozaki, T., Doyama, M., Kogure, Y., and Yokotsuka, T., 1998, "Micromachining of Pure Silicon by Molecular Dynamics," Thin Solid Films, 334, p. 221

Oxley, P. L. B., 1989, "Mechanics of Machining: An Analytical Approach to Assessing Machinability," John Wiley & Sons, NY

Parrinello, M., and Rahman, A., 1981, "Polymorphic Transitions in Single Crystals: A New Molecular Dynamics Method," J. Appl. Phys., 52/12, p. 7182

Pekelharing, A. J., 1978, "The Exit Failure in Interrupted Cutting," Annals of CIRP, 27/1, p. 5

Peploski, J., Thompson, D. and Raff, L., 1992,"Molecular Dynamics Studies of Elementary Surface Reactions of C_2H_2 and C_2H in Low-Pressure Diamond Film Formation," J. Chem. Phys., 96, p. 8538

Perry, M., and Raff, L., 1994, "Theoretical Studies of Elementary Chemisorption Reactions on an Activated Diamond Ledge Surface," J. Phys. Chem., 98, p. 4375

Perry, M., and Raff, L., 1994, "Theoretical Studies of Elementary Chemisorption Reactions on an Activated Diamond(111) Terrace,"J. Phys. Chem., 98, p. 8128

Persson, B. N. J., 1994, "Theory of Friction: The role of Plasticity in Boundary Lubrication," Phys. Rev. B, 50, p. 4771

Pethica, J. B., Hutchings, R., and Oliver, W. C., 1983, "Hardness Measurements At Penetration Depths As Small As 20 nm," Philosophical Magazine A, 48/4, p. 593

Petty, E. R., 1962, "The Hardness Anisotropy of Aluminum Single Crystals," J. of the Institute of Metals, 91, p. 54

Pharr, G. M., and Oliver, W. C., 1989, "Nanoindentation of Silver-Relations Between Hardness and Dislocation Structure," J. Mater. Res., 4, p. 94

Pharr, G. M., Oliver, W. C., and Harding, D. S., 1991, "New Evidence for a Pressure Induced Phase Transformation During the Indentation of Silicon," J. Mater. Res., 6/6, p. 1129

Puttick, K. E., Rudman, M. R., Smith, K. J., Franks, A., and Lindsey, K., 1989, "Single Point Diamond Machining of Glasses," Proc. R. Soc. Lond. A, 426, p. 19

Puttick, K. E., Whitmore, L. C., Chao, C. L., and Gee, A. E., 1994, "Transmission Electron Microscopy of Nanomachined Silicon Crystals," Phil. Mag. A, 69, p. 91

Rabinowicz, E. , 1992, "Friction Coefficients of Noble Metals Over a Range of Loads," Wear, 159, p. 89

Raff, L. M., and Thompson, D. L., 1985, "The Classical Trajectory Approach to Reactive Scattering," in Theory of Chemical Reaction Dynamics, CRC press, Vol. III, Chapter

Raff, L. M., 1998, "Theoretical Investigations of Chemical and Physical Processes Under Matrix Isolation Conditions," in Modern Methods for Multidimensional Dynamics Computations in Chemistry, Editor: D. L. Thompson, World Scientific Publishing Co., NJ, pp. 266-354

Raff, L. M., 1992, "Effects of Lattice Morphology Upon Reaction Dynamics in Matrix-Isolated Systems," J. Chem. Phys. 97, p. 7459

Raghavachari, K., and Logovinsky, V., 1985, "Structure and Bonding in Small Silicon Clusters," Phys. Rev. Lett., 55, p. 2853

Ralston, A., 1962, "Runge-Kutta Methods With Minimum Error Bounds," Math. Comput., 16, p. 431

Ramalingam, S., and Hazra, J., 1973, "Dynamic Shear Stress-Analysis of Single Crystal Machining Studies," Trans. ASME, J. of Eng. for Industry, 95B, p. 939

Ramaraj, T. C., Santhanam, S., and Shaw, M. C., 1988, "Tool fracture at the end of a cut - Part I: Foot formation," Trans ASME, J. Eng. Ind., 110, p. 333

Rentsch, R., and Inasaki, I., 1994, "Molecular Dynamics Simulation for Abrasive Processes," Annals of CIRP, 43/1, p. 327

Rentsch, R., and Inasaki, I., 1995, "Indentation Simulation on Brittle Materials by Molecular Dynamics," SPIE, 2596, p. 214

Riley, M. E., Coltrin, M. E., and Diestler, D. J., 1988, "A Velocity Reset Method of Simulating Thermal Motion and Damping in Gas-Solid Collisions,"J. of Chemical Physics, 88, p. 5943

Rubenstein, C., Groszmann, F. K., and Koenigsberger, 1966, Proc. Int. Industrial Diamond Conf., Oxford, Vol. 1, 161, Industrial Diamond Information Bureau, London

Runyan, W. R., 1999, "Silicon and Silicon Alloys," Concise Encyclopedia of Chemical Technology, 4th Edition, John Wiley & Sons, Inc., New York, NY, p. 1809

Salmeron, M., Folch, A., Neubauer, G., Tomitori, M., Ogletree, D. F., and Kolbe, W., 1992, "Nanometer Scale Mechanical Properties of Au(111) Thin Films," Langmuir, 8, p. 2832

Sampath, W. S., Lee, Y. M., and Shaw, M. C., 1984, "Tool fracture probability under steady state cutting conditions," Trans ASME, J. Eng. Ind., 106, p. 161

Sato, M., Yamazaki, T., Shimizu, Y., Nakagawa, T., and Takabayashi, T., 1991, "A Study on the Microcutting of Aluminum Single Crystal," JSME, 34 III, p. 531

Sato, K., Shikida, M., Yoshioka, T., Ando, T., and Kawabata, T., 1997, "Micro Tensile-Test of Silicon Film Having Different Crystallographic Orientations," Proc. Int. Conf. Solid-State Sensors and Actuators, Chicago, IL, USA, p. 595

Selinger, R. L. B., Wang, Z. G., and Gelbart, W. M., 1991, "Statistical Thermodynamic Approach to Fracture," Phys. Rev. A, 43/8, p. 4396

Selinger, R. L. B., Lynden-Bell, R. M., and Gelbart, W. M., 1993, "Stress-Induced Failure and Melting of Ideal Solids," J. Chem. Phys., 98/12, p. 9808

Shaw, M. C., 1950, "A Quantized Effect of Strain Hardening as Applied to Cutting of Metals," J. Appl. Phys., 21, p. 599

Shaw, M. C., 1972, A New Theory of Grinding, Mech. Chem. Trans. Inst. Eng. Aust., Vol. MC*, No. 1, p. 73

Shaw, M. C., 1979, "Fracture of metal cutting tools," Annals of CIRP, 28/1, p. 19.

Shaw, M. C., 1984, "Metal Cutting Principles," Oxford University Press, Oxford,U.K.

Shaw, M. C., 1996, "Principles of Abrasive Processes," Clarendon Press, Oxford

Shibata, T., Ono, A., Kurihra, K., Makino, E., and M. Ikeda, 1994, "Cross Sectional Transmission Electron Microscope Observations of Diamond-Turned Single –Crystal Si Surfaces," Appl.Phys. Lett. 65, p. 2553

Shimada, S., Ikawa, N., Ohmori, G., and Tanaka, H., 1992, "Molecular Dynamics Analysis as Compared with Experimental Results of Micromachining," Annals of the CIRP, 41/1, p. 117

Shimada, S., Ikawa, N., Tanaka, H., Ohmori, G., Uchikoshi, J., and Yoshinaga, H., 1993, "Feasibility Study on Ultimate Accuracy in Microcutting Using Molecular Dynamics Simulation," Annals of the CIRP, 42/1, p. 91

Shimada, S., Ikawa, N., Tanaka, H., and Uchikoshi, J., 1994, "Structure of Micromachined Surface Simulated by Molecular Dynamics Analysis," Annals of the CIRP, 43/1, p. 51

Shimada, S., 1995, "Molecular Dynamics Analysis of Nanometric Cutting Process," Int. J of Japan Soc. Prec. Eng., 29, No.4, p. 283

Shimizu, J., Eda, H., Yoritsune, M., and Ohmura, E., 1998, "Molecular Dynamics Simulation of Friction on the Atomic Scale," Nanotechnology, 9, p. 118

Shirakashi, T., Yoshino, M., and Kurashima, H., 1991, "Study on Cutting Mechanism of Single Crystal Based on Simple Shear Plane Model," Int. J. Japan Soc. Prec. Eng., 25/2, p. 96

Sieradzki, K., Dienes, G. J., Paskin, A., and Massoumzadeh, B., 1988, "Atomistics of Crack Propagation," Acta Metall., 36/3, p. 651

Skinner, J., Gane, N., and Tabor, D., 1971, "Micro-friction of Graphite," Nature, Phys. Sci., 232, p. 195

Stillinger, F. H., and Weber, T. A., 1985, "Computer Simulation of Local Order in Condensed Phases of Silicon," Phys. Rev. B, 31, p. 5262

Strenkowski, J. S., and Carroll, J. T., 1985, "A Finite Element Model of Orthogonal Metal Cutting," Trans. ASME, J. Eng. Ind., 107, p. 349

Suh, N. P., 1973, "Delamination Theory of Wear," Wear, 25, p. 111

Suh, N. P., and Saka, N., 1987, "Surface Engineering," Annals of CIRP, 36, p. 403

Takagi, J., and Shaw, M. C., 1983, "Brittle fracture initiation under complex stress state," Trans ASME, J. Eng. Ind., 105, p. 143

Tanaka, H., Zhang, L. C., and Shimada, S., 1999, "Molecular Dynamics Analysis On Microstructure of Silicon Surfaces Finished by Mechanical Processes," Precision Sci. and Tech. for Perfect Surfaces, Ed. By Furukawa, Y., Mori, Y., and Kataoka, T., JSPE Publication Series No. 3, Osaka, Japan, p. 1019

Taniguchi, N., 1983, "Current Status in, and Future Trends of, Ultraprecision Machining and Ultrafine Materials Processing," Annals of CIRP, 32/2, p. 573

Tay, A. O., Stevenson, M. G., and G. de Vahl Davis, 1974, "Using the Finite Element Method to Determine Temperature Distributions in Orthogonal Machining," Proc. I. Mech. E. (Lon), 188, p. 627

Tersoff, J., 1988, "New Empirical Approach for the Structure and Energy of Covalent Systems," Physical Review B, 37/12, p. 6991

Tersoff, J., 1989, "Modeling Solid State Chemistry: Interatomic Potential for Multicomponent Systems," Physical Review B, 39, p. 5566

To, S., Lee, W. B., and Chan, C. Y., 1997, "Ultraprecision Diamond Turning of Aluminum Single Crystals," J. of Mat. Proc. Tech., 63, p. 157

Tomagnini, O., Ercolessi, F., and Tosatti, E., 1993, "Microscopic Interaction Between a Gold Tip and Lead Surface," Surface Science, 287/288, p. 1041

Tomlinson, G. A., 1929, "Molecular Theory of Friction," Philos. Mag., 7, p. 905

Torrens, I. M., 1972, "Interatomic Potentials," Academic Press, NY

Tsukizoe, T., and Sakamoto, T., 1975, "Friction in Scratching Without Metal Transfer," Bulletin of the JSME, 18 (115), p. 65

Ueda, K., and Iwata, K., 1980, "Chip Formation Mechanism in Single Crystal Cutting of Beta-Brass," Annals of CIRP, 41(1), p. 65

Uehara, K., 1977, "On the chipping phenomena of carbide cutting tools," Annals of CIRP, 25/1, p. 11

Usui, E., and Shirakashi, T., 1982, "Mechanics of Machining-From Descriptive to Predictive Theory," On the Art of Cutting Metals-75 Years Later, ASME Publication PED-Vol. 7, p. 13

Vitek, V., 1996, "Pair Potentials in Atomistic Computer Simulations," MRS Bulletin, p. 20

Vlassak, J. J., and Nix, W. D., 1994, "Measuring the Elastic Properties of Anisotropic Materials By Means of Indentation Experiments," J. Mech. Phys. Solids, 42, No. 8, p. 1223

von Turkovich, B. F., and Trigger, K. J., 1963, "Theoretical Aspects of High-Speed Shear in Face Centered Cubic Metals," Trans. ASME, J. Eng. Ind., 85, p. 357

von Turkovich, B. F., 1967, "Dislocation Theory of Shear Stress and Strain Rate in Metal Cutting," Proc. Of the 8th Int. MTDR Conf., Eds. S. A. Tobias and F. Koenigsberger, p. 531

von Turkovich, B. F., and Black, J. T., 1970, "Micromachining of Copper and Aluminum Crystals," Trans. ASME, J. Engg. Ind., 2, p. 130

Voter, A. F., 1996, "Interatomic Potentials for Atomic Simulations," MRS Bulletin, p. 17

Williams, J. A., and Gane, N., 1977, "Some Observations On the Flow Stress of Metals During Metal Cutting," Wear, 42, p. 341

Williams, J. A., 1993, "Small Scale Effects in Metal Cutting," Thin Films in Tribology, p. 289

Wilson, C. J., and Beck, P. A., 1996, "Fracture Testing of Bulk Silicon Microcantilever Beam Subjected to a Side Load," J. Microelectromech. Syst., 5(3), p. 142

Yan, W., and Komvopoulos, K., 1998, "Three Dimensional Molecular Dynamics Analysis of Atomic Scale Indentation," Journal of Tribology, 120, p. 385

Yan, Y., Yoshino, M., Kuriagawa, T., Shirakashi, T., Syoji, K., and Komanduri, R, 2001, "On the Ductile Machining of Silicon for Micro Electro-Mechanical (MEMS), Opto-Electronic, and Optical Applications," Mater. Sci. and Engg. A, 297, p. 230

Yoshino, M., Aoki, T., N., Shirakashi, T., and Komanduri, R., 2001a, "Some Experiments on the Scratching of Silicon : *In situ* scratching inside an SEM and scratching under high external hydrostatic pressure," Int. J of Mech. Sci. 43, p. 335

Yoshino, M., Aoki, T., Chandrasekaran, N., Shirakashi, T., and Komanduri, R., 2001b, "finite Element Simulation of Plane Strain Plastic-Elastic Indentation on Single Crystal Silicon," Int. J of Mech. Sci. 43, p. 313

You, H. I., and Yu, C. S., 1997, "Effect of Surface Roughness On Low Sliding Friction for Lubricated and Dry Surfaces With Elastic Contact," J. of the Chinese Society of Mechanical Engineers, 18 (4), p. 371

Young, H. T., and Chou, T. L., 1994, "Modeling of Tool-Chip Interface Temperature Distribution in Metal Cutting," Int. J. Mech. Sci., 36/10, p. 931

Zhang, L. C., and Tanaka, H., 1999, "On the Mechanics and Physics in the Nano-Indentation of Silicon Monocrystals," JSME Int. J. A, 42/4, p. 546

Zhong, Z., and Venkatesh, V. C., 1994, "Generation of Parabolic and Toroidal Surfaces on Silicon and Silicon Based Compunds Using Diamond Cup Grinding Wheels," Annals of CIRP, 43/1, p. 323

Zhou, S. J., Beazley, D. M., Lomdahl, P. S., and Holian, B. L., 1997, "Large Scale Molecular Dynamics Simulations of Three-Dimensional Ductile Failure," Phys. Rev. Lett., 78/3, p. 479

APPENDIX I

LIST OF PUBLICATIONS

[1] Chandrasekaran, N., Noori-Khajavi, A., Raff, L. M., and Komanduri, R., 1998, "A New Method for Molecular Dynamics Simulation of Nanometric Cutting," Philosophical Magazine B, 77(1), 7-26

[2] Komanduri, R., Chandrasekaran, N., and Raff, L. M., 1998, "Effect of Tool Geometry in Nanometric Cutting: A Molecular Dynamics Simulation Approach," Wear, 219, 84-97

[3] Komanduri, R., Chandrasekaran, N., and Raff, L. M., 1999, "Some Aspects of Machining with Negative Rake Tools Simulating Grinding," Phil. Mag. B, 79/7, 955-968

[4] Komanduri, R., Chandrasekaran, N., and Raff, L. M., 1999, "Orientation Effects in Nanometric Cutting of Single Crystal Materials: An MD Simulation Approach," Annals of CIRP, 48/1, 67-72

[5] Komanduri, R., Chandrasekaran, N., and Raff, L. M., 2000, "MD Simulation of Nanometric Cutting of Single Crystal Aluminum-Effect of Crystal Orientation and Direction of Cutting," Wear 242, 60-88

[6] Komanduri, R., Chandrasekaran, N., and Raff, L. M., 2000, "MD Simulation of Indentation and Scratching of Single Crystal Aluminum," Wear, 240, 113-143

[7] Komanduri, R., Chandrasekaran, N., and Raff, L. M., 2000, "Molecular Dynamics Simulation of Atomic Scale Friction," Phys. Rev. B, 61/20, 14007-14019

[8] Komanduri, R., Chandrasekaran, N., and Raff, L. M., "MD Simulation of Exit Failure in Nanometric Cutting," accepted for publication in Mat. Sci. Engg., 2001

[9] Komanduri, R., Chandrasekaran, N., and Raff, L. M., "MD Simulations of Uniaxial Tension," accepted for publication in J. Mat. Sci., 2001

[10] Komanduri, R., Chandrasekaran, N., and Raff, L. M., "MD Simulation of Nanometric Cutting of Silicon," accepted for publication in Phil. Mag. B, 2001

[11] Komanduri, R., Chandrasekaran, N., and Raff, L. M., "Nano- Tensile Testing of Semiconducting Materials for MEMS Applications," submitted for publication, 2001

[12] Komanduri, R., Chandrasekaran, N., and L. M. Raff, "MD Simulation of Nanoindentation of Silicon," to be submitted for publication, 2001

APPENDIX II - MD SIMULATION PLOTS

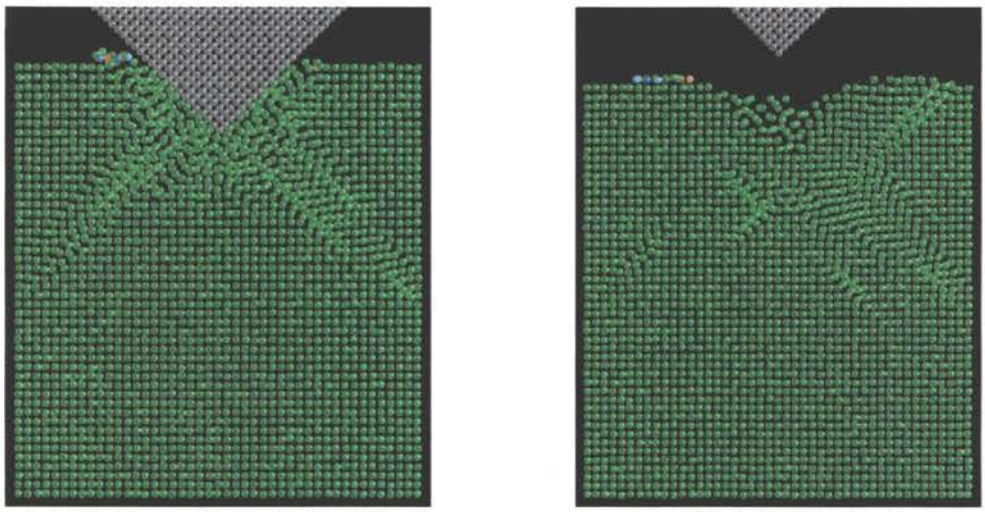

(a) Maximum Indentation Depth (b) After Retraction

Figures AII.1 (a) - (b) MD Simulation Plots of Nanoindentation of Copper

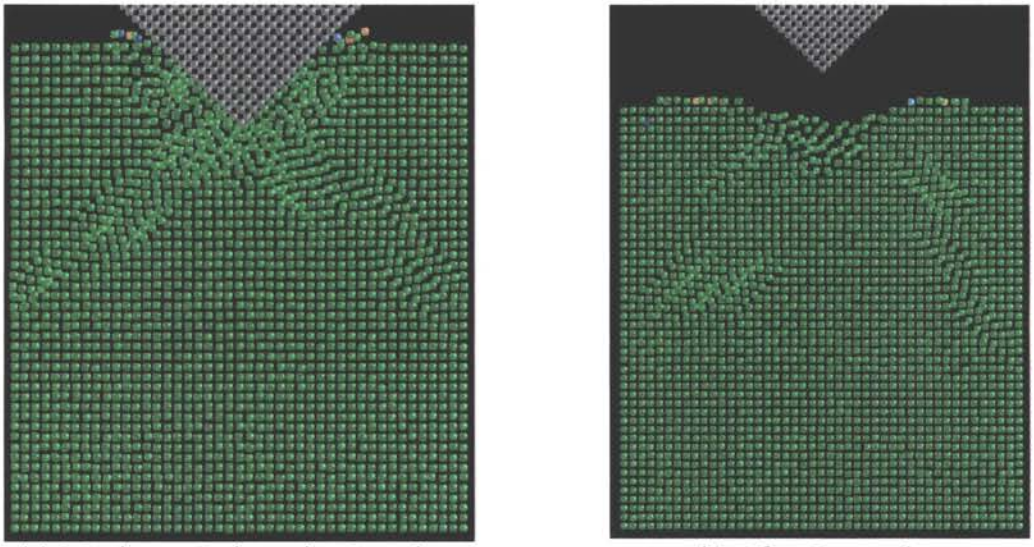

(a) Maximum Indentation Depth (b) After Retraction

Figure AII.2 (a) - (b) MD Simulation Plots of Nanoindentation of Nickel

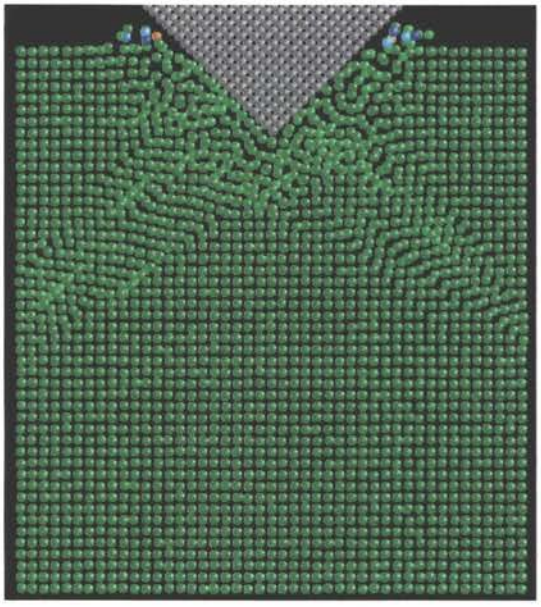

(a) Maximum Indentation Depth

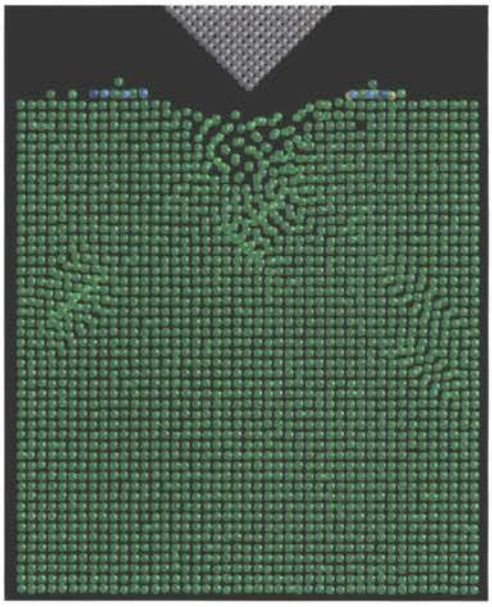

(b) After Retraction

Figures AII.3 (a) - (b) MD Simulation Plots of Nanoindentation of Silver

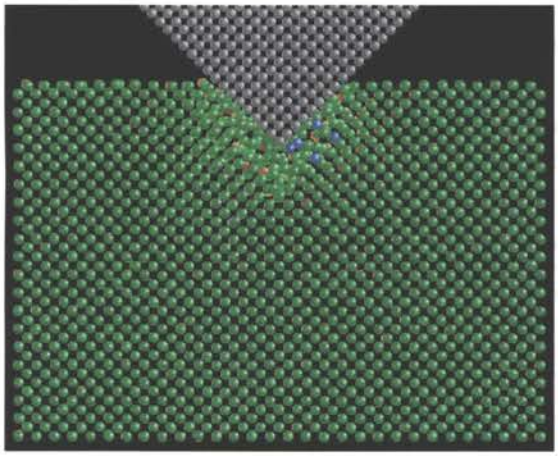

(a) Maximum Indentation Depth

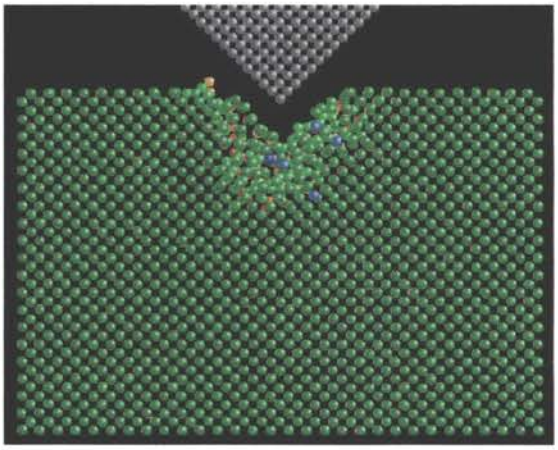

(b) After Retraction

Figures AII.4 (a) - (b) MD Simulation Plots of Nanoindentation of Germanium

VITA

Nagasubramaniyan Chandrasekaran

Candidate for the Degree of

Doctor of Philosophy

Thesis: MOLECULAR DYNAMICS SIMULATIONS OF MACHINING, MATERIALS TESTING, AND TRIBOLOGY AT THE ATOMIC SCALE

Major Field: Mechanical Engineering

Biographical:

Personal Data: Born in Madras, Tamilnadu, India, on February 15, 1974, the son of V. Chandrasekaran and T. V. Vijayalakshmi

Education: Received Bachelor of Engineering degree in Mechanical Engineering from the University of Madras, Tamilnadu, India, in May 1995. Received Master of Science in Mechanical Engineering from the Oklahoma State University, Stillwater, Oklahoma, in May 1997. Completed requirements for the Doctor of Philosophy degree with a Major in Mechanical Engineering at Oklahoma State University, Stillwater, Oklahoma, in May, 2001

Professional Experience: Research Assistant, Department of Mechanical Engineering, Oklahoma State University, Stillwater, Oklahoma, January 1996 - May 2001.
Teaching Assistant, Department of Mechanical Engineering, Oklahoma State University, Stillwater, Oklahoma, January 1996 - December 2000.

Professional Memberships: Member of American Society of Mechanical Engineers (ASME), American Society for Precision Engineering (ASPE)